Search for heavy neutral Higgs bosons decaying into the fully hadronic di-tau final state with ATLAS

Dissertation

zur Erlangung des akademischen Grades

Doctor rerum naturalium
(Dr. rer. nat.)

vorgelegt von

Max Märker
geboren am 22.04.1992 in Dresden

TECHNISCHE UNIVERSITÄT DRESDEN
INSTITUT FÜR KERN- UND TEILCHENPHYSIK
FAKULTÄT PHYSIK
BEREICH MATHEMATIK UND NATURWISSENSCHAFTEN

24. Januar 2022

Abstract

Although the Standard Model of particle physics is one of the most successful and well-tested theories in physics, many extensions to the Standard Model were proposed that aim to resolve its shortcomings. Many of these models extend the Standard Model by adding additional symmetries such as Supersymmetry with one of the simplest being the Minimal Supersymmetric Standard Model (MSSM). Supersymmetric models also require the presence of a second Higgs-doublet field which predicts the existence of additional Higgs bosons. Hence, the search for these additional Higgs bosons provides an important window into investigating physics beyond the Standard Model.

In this thesis, the search for additional heavy neutral Higgs bosons A and H decaying into a fully hadronic tau lepton pair is presented based on $139\,\text{fb}^{-1}$ of data taken by the ATLAS detector during the full LHC Run-2 data taking period from 2015 to 2018. Since no significant excess of data with respect to the background estimation was found, the results are presented in terms of $95\,\%$ CL upper exclusion limits on the cross-section times branching ratio for Higgs bosons produced via gluon-gluon fusion and b-associated production. Different Higgs boson mass hypotheses are taken into account ranging from $200\,\text{GeV}$ to $2500\,\text{GeV}$. A combination with the semi-leptonic search channel is performed whose exclusion limits are transformed into the m_A-$\tan\beta$ parameter space of the hMSSM and various m_h^{125} benchmark model scenarios. The combined exclusion limit set in the hMSSM model is compared to the previous publications by the ATLAS and CMS collaboration based on early Run-2 data of $36.1\,\text{fb}^{-1}$ and $35.9\,\text{fb}^{-1}$ respectively. Compared to previous exclusion limits set by ATLAS (CMS) for the hMSSM scenario, significant improvements are observed ranging between $11\,\%$ ($10\,\%$) at $m_A = 500\,\text{GeV}$ up to $63\,\%$ ($67\,\%$) at $m_A = 1200\,\text{GeV}$.

In addition to the Higgs boson search, a novel algorithm is presented to identify and select charged particle tracks reconstructed in the ATLAS inner detector originating from hadronic tau lepton decays. The identification of these tracks is an important part of the tau lepton reconstruction and identification at ATLAS and provides information about the decay multiplicity and charge of the tau lepton. By deploying state-of-the-art recurrent neural networks the reconstruction efficiency for tau leptons with a true decay multiplicity of 1 and 3 charged hadrons improves by about $10\,\%$ and $20\,\%$ respectively. With this improvement, the neural networks achieve a reconstruction efficiency close to the maximum efficiency possible. By exploiting the flexibility of the neural networks, they can be optimized for both offline data analysis and fast software trigger applications.

Kurzfassung

Obwohl das Standardmodell der Teilchenphysik eines der erfolgreichsten physikalischen Theorien der modernen Geschichte ist, wurden schon früh viele theoretische Erweiterung entwickelt, welche versuchen, die offenen Fragen des Standardmodells zu lösen. So bietet das Standardmodell keine Erklärung für die Existenz der dunklen Materie oder eine vereinheitlichte Theorie der fundamentalen Wechselwirkungen an. Viele der Modelle erweitern das Standardmodell mit zusätzlichen Symmetrien wie zum Beispiel der Supersymmetrie. Die einfachste supersymmetrische Erweiterung des Standardmodells ist das Minimal Supersymmetrische Standardmodell (MSSM). Diese Modelle sagen die Existenz eines zweiten Higgs-Dublette Feldes voraus, welches die Präsenz zusätzliche Higgs-Bosonen zur Folge hätte. Daher ist die Suche nach zusätzlichen Higgs-Bosonen ein wichtiges Fenster zur Suche nach Physik jenseits des Standardmodells.

In dieser Arbeit wird die Suche nach zusätzlichen, schweren und neutralen A und H Higgs-Bosonen im voll-hadronischen di-Tau Zerfallskanal präsentiert. Die Suche basiert auf dem vollständigen LHC Run-2 Datensatz, aufgezeichnet vom ATLAS Detektor in der Zeit von 2015 bis 2018. Die aufgezeichneten Daten entsprechen einer intrigierten Luminosität von $139\,\mathrm{fb}^{-1}$. Da kein signifikanter Überschuss an Daten im Verhältnis zur Untergrundabschätzung beobachtet wurde, werden die Resultate der Suche in Form von Ausschlussgrenzen auf den Wirkungsquerschnitt mal dem Verzweigungsverhältnis für Higgs-Bosonen mit Massen zwischen $200\,\mathrm{GeV}$ und $2500\,\mathrm{GeV}$, welche via Gluon-Gluon-Fusion oder b-assoziierter Produktion generiert wurden, angegeben. Die Ausschlussgrenzen werden berechnet mit einem Vertrauensniveau von $95\,\%$. Die Resultate des voll-hadronischen Zerfallskanals werden kombiniert mit denen des semi-leptonischen Zerfallskanals und anschließend in den m_A-$\tan\beta$ Parameterraum des hMSSM Modells als auch weiterer m_h^{125} Modellvarianten transformiert. Die kombinierten Ausschlussgrenzen im Parameterraum des hMSSM Modells werden mit jener vorherigen Analysen publiziert durch die ATLAS und CMS Kollaboration verglichen, welche auf einem vorläufigen Run-2 Datensatz basieren. Im Verhältnis zu den vorherigen Resultaten von ATLAS (CMS) wurde eine signifikante Verbesserung von $10\,\%$ ($11\,\%$) für $m_A = 500\,\mathrm{GeV}$ bis hin zu $63\,\%$ ($67\,\%$) für $m_A = 1200\,\mathrm{GeV}$ beobachtet.

Des Weiteren wird in dieser Arbeit ein neuartiger Algorithmus, basierend auf moderner rekurrenten neuronalen Netzen vorgestellt, welcher Spuren im inneren Detektor des ATLAS Experiments hadronisch zerfallenden Tauonen zuordnen kann. Die Zuordnung der Spuren zu Tauonenzerfällen ist ein integraler Bestandteil der Rekonstruktion hadronisch zerfallender Tau-Leptonen bei ATLAS und liefert wichtige Informationen über dessen Ladung und Zerfallsmultiplizität. Durch Verwendung neuronaler Netze kann ein erheblicher Zuwachs in der Rekonstruktionseffizienz von $10\,\%$ und $20\,\%$ für hadronische Tauonzerfälle mit einer Zerfallsmultiplizität von 1 und 3 erreicht werden. Aufgrund dieser Verbesserungen erreicht der neue Algorithmus eine Rekonstruktionseffizienz nahe der maximal möglichen Effizienz. Zusätzlich ist es möglich, durch Ausnutzen der inhärenten Flexibilität neuronaler Netze das Training so zu verändern, dass die Netze unterschiedliches verhalten auf QCD Untergrund aufweisen. Es werden zwei Trainingskonfigurationen beschrieben, welche für die offline Datenanalyse oder die Anwendung in Trigger-Entscheidungen optimiert wurden.

Contents

1. Introduction

Fundamental particle physics is a relatively new field of physics established during the 20th century which aims to describe the motion and interactions of the the smallest particles that make up the universe. Its birth is marked by the discovery of the electron as the first elementary particle by J. J. Thompson in 1892 [1]. Later, in the first half of the 20th century experiments with nuclear radiation revealed that the nucleus of the atom itself is made up out of protons and neutrons. This sparked an enduring search for further particles like mesons and baryons which are later found to consist of quarks themselves.

However, the emergence of quantum mechanics and special relativity posed a problem to the theoretical description of the observed particle zoo. Finally, in the 1940s Tomonaga [2], Schwinger [3], Feynman [4, 5], and Dyson [6, 7] successfully formulated a relativistic quantum field theory of the electromagnetic interaction, called Quantum Electro Dynamics (QED), where the interaction is described as a gauge symmetry group acting on particle fields [8]. This concept was later adopted by Fritzsch, Gell-Mann, and Leutwyler [9] in the development of the theory of Quantum Chromo Dynamics (QCD) which describes the strong interaction. At the same time Glashow [10], Salam [11], and Weinberg [12] proposed a model which unifies the flavor changing weak interaction with electromagnetic interaction to form the theory of the electro-weak force. However, all theories can not comprehensively explain the generation of particle masses without breaking the gauge symmetry. Hence, a mechanism was invented in 1964 by three independent groups: Peter Higgs [13], François Englert and Robert Brout [14] as well as C. R. Hagen, Gerald Guralnik, and Tom Kibble [15]. The Higgs mechanism proposes the existence of a weak iso-doublet scalar field that interacts with fermions and gauge bosons to give rise to their masses. Combined with the Higgs mechanism, the QCD and electro-weak theory form the Standard Model of particle physics (SM). As of now, all elementary particles predicted by the Standard Model were discovered with the last being the Higgs boson in 2012 by the ATLAS and CMS experiments.

Although the Standard Model is one of the most precisely tested theories in history, there are still problems and observations that can not be resolved satisfactorily within the Standard Model. One example is the hierarchy problem which asks why the electro-weak energy scale and the Planck scale at which gravitational physics is expected to become important are many orders of magnitude apart. Furthermore, the SM completely lacks a theoretical description of gravity as the fourth fundamental force next to the strong, weak and electromagnetic interaction. These inherent shortcomings suggest that there should be physics beyond the Standard Model.

A more direct indication of the existence of physics beyond the Standard Model is provided by experiments such as the observation of the impact of dark matter on the movements of galaxies [16] and the development of the Universe [17]. As of now, the Standard Model does not provide an explanation of what dark matter might consist of. One of the strongest indications of new physics, however, comes from the measurement of the anomalous magnetic moment of the muon $(g-2)$. New results from the Muon $(g-2)$ experiment of the Fermilab National Accelerator Laboratory in combination with previous findings of the E821 experiment located at the Brookhaven National Laboratories found a $4.2\,\sigma$ discrepancy between the measured value of the anomalous moment and Standard Model prediction [18, 19].

Many theory models which try to explain these phenomena extend the Standard Model with additional symmetries and fields. A commonly used extension is Supersymmetry (SUSY) which predicts the existence of supersymmetric partner particles for each of the known elementary particle degree of freedom of the Standard Model [20]. The simplest supersymmetric extension is the Minimal Supersymmetric Standard Model (MSSM). In addition to the supersymmetric partners, SUSY models predict the existence of an additional Higgs iso-doublet field, the presence of which would lead to two additional neutral and two charged Higgs bosons [21].

With the commissioning of increasingly powerful particle accelerators like the Large Electron-Positron Collider at CERN [22] or Tevatron at Fermilab [23], it was possible to perform searches for additional particles predicted by the many extensions of the Standard Model through the study of particle collisions at the 100 GeV to 1 TeV energy scale. In 2008 the Large Hadron Collider (LHC), hosted in the tunnel of the predecessor LEP, was commissioned, marking the beginning of the search for new physics beyond the TeV scale. During Run-1 the LHC operated with a center of mass energy of 7 TeV which was significantly increased to 13 TeV at the beginning of the Run-2 operation, lasting from 2015 to 2018. Thanks to the enormous increases in the collision energy, experiments located at the LHC, such as ATLAS and CMS, were able to search for additional heavy particles. Although no new non-SM particle was observed yet, the results of the LHC experiments excluded many of the potential beyond Standard Model theory candidates and significantly improved our understanding of the physics at the TeV scale.

A particularly promising way of probing potential SUSY theory candidates is the search for additional Higgs bosons. Since many models predict the presence of additional Higgs doublets, the results can be easily interpreted into various potential model hypotheses. At hadron colliders like the LHC, one of the most sensitive search channels is the decay of the Higgs bosons into a pair of tau leptons. These tau leptons themselves quickly decay before they can be detected by the Detectors, with about $\sim 65\,\%$ of them decaying into hadrons like pions and a tau neutrino.

In this thesis, the search for additional neutral heavy Higgs bosons decaying into the fully hadronic di-tau final state at the ATLAS detector using the full Run-2 dataset is presented. The analysis results contributed to the paper published in the *Physical Review Letters* in 2020 (see Reference [24]) together with the search in the semi-leptonic di-tau decay channel of the Higgs boson. In addition to the search results, improvements to the background estimation and validation are developed which leads to better agreement between the expected background and data. The results of the analysis are presented in terms of 95 % CL upper exclusion limits on the cross-section times branching ratio of the Higgs boson production as well as the parameter space of commonly used MSSM benchmark models.

Since the reconstruction and identification of hadronically decaying tau leptons at the ATLAS detector is crucial for many searches and measurements of processes with tau leptons in their final state, such as the search presented here, a new algorithm is presented which selects and identifies inner detector tracks that belong to hadronic tau decays. The new algorithm deploys state-of-the-art recurrent neural networks in order to achieve optimal reconstruction performance.

In the first two chapters a theoretical and experimental overview is given. After a detailed description of the particle signature reconstruction at ATLAS and a brief introduction to recurrent neural networks, the results of the neural network based track identification algorithm are presented. The last part of this thesis is concerned with the search for additional heavy neutral Higgs bosons decaying in the di-tau final state in the fully hadronic search channel and its combination with the semi-leptonic channel.

2. Theoretical Framework

2.1. The Standard Model of Particle Physics and Electro-Weak Symmetry Breaking

The Standard Model of particle physics (SM) is the theoretical foundation with which elementary particles and their interactions are described. It explains three of the four known fundamental forces of nature: the strong force, the weak- and electromagnetic force. The latter two can be combined as a single unified Electro-Weak (EW) interaction by the Weinberg–Salam theory [10–12]. Although the SM describes processes of particles under these interactions with remarkable precision, it does not provide a description of gravity and general relativity.

Within the SM all matter consists of fermions with spin $\frac{1}{2}$ which are separated in leptons and quarks [8]. A total of 6 different leptons are predicted by the SM consisting of electrons, muons, and tau leptons which have the same electric charge of $Q_l = -1\,$e but differ in their mass, as well as their corresponding uncharged neutrinos. The quark sector also contains 6 quarks: up, down, charm, strange, top, and bottom which carry electric charges of $Q_q = +\frac{2}{3}$ for up, charm and top or $Q_q = -\frac{1}{3}$ for down, strange and bottom. Similar to the charged leptons, the quarks differ strongly in their respective mass, ranging from $m_{\mathrm{up}} = 2.16\,$MeV to $m_{\mathrm{top}} = 172.76\,$GeV [25]. For each of the matter fermions, the SM also predicts the existence of a corresponding anti-matter particle with an opposite charge.

The theoretical description of the SM is based on a relativistic Lagrangian field formalism where particles correspond to discrete excitations of quantum fields [26]. The strong and EW interactions are described by a gauge theory that introduces symmetry transformations under which the Lagrangian density function is locally invariant [8]. In this framework the strong interaction corresponds to a $SU(3)_{\mathrm{C}}$ gauge symmetry group acting on quarks that carry the associated color charge, forming a charge triplet. Hence, the theory of the strong interaction is also called the Quantum Chromo Dynamic (QCD) theory. The EW interaction on the other hand is described by a $SU(2)_{\mathrm{L}} \times U(1)_{\mathrm{Y}}$ symmetry group which introduces a hypercharge Y_f as well as an isospin $\boldsymbol{I}$ quantum number which is quantized along its third component denoted by I_f^3. These relate to the electric charge Q via $Y_f = 2Q_f - 2I_f^3$ for any given fermion f. The $SU(2)_{\mathrm{L}}$ only acts on left-handed fermions or right-handed anti-fermions, which form iso-doublets with $I_{f\,\mathrm{L}}^3 = \pm\frac{1}{2}$ while right-handed fermions and left-handed anti-fermions are iso-singlets with $I_{f\,\mathrm{R}}^3 = 0$.

The leptons and quarks are grouped in 3 generations with increasing particle mass, each described by left-handed doublets and right-handed singlets according to [27]:

$$
L_{1\,\mathrm{L}} = \begin{pmatrix} \nu_e \\ e^- \end{pmatrix}_{\mathrm{L}}, \quad l_{1\,\mathrm{R}} = e_{\mathrm{R}}^-, \quad Q_{1\,\mathrm{L}} = \begin{pmatrix} u \\ d \end{pmatrix}_{\mathrm{L}}, \quad u_{1\,\mathrm{R}} = u_{\mathrm{R}}, \quad d_{1\,\mathrm{R}} = d_{\mathrm{R}},
$$

$$
L_{2\,\mathrm{L}} = \begin{pmatrix} \nu_\mu \\ \mu^- \end{pmatrix}_{\mathrm{L}}, \quad l_{2\,\mathrm{R}} = \mu_{\mathrm{R}}^-, \quad Q_{2\,\mathrm{L}} = \begin{pmatrix} c \\ s \end{pmatrix}_{\mathrm{L}}, \quad u_{2\,\mathrm{R}} = c_{\mathrm{R}}, \quad d_{2\,\mathrm{R}} = s_{\mathrm{R}}, \tag{2.1}
$$

$$
L_{3\,\mathrm{L}} = \begin{pmatrix} \nu_\tau \\ \tau^- \end{pmatrix}_{\mathrm{L}}, \quad l_{3\,\mathrm{R}} = \tau_{\mathrm{R}}^-, \quad Q_{3\,\mathrm{L}} = \begin{pmatrix} t \\ b \end{pmatrix}_{\mathrm{L}}, \quad u_{3\,\mathrm{R}} = t_{\mathrm{R}}, \quad d_{3\,\mathrm{R}} = b_{\mathrm{R}},
$$

with $L_{i\,\mathrm{L}}$ and $Q_{i\,\mathrm{L}}$ being the left-handed doublets and $l_{i\,\mathrm{R}}$, $u_{i\,\mathrm{R}}$, and $d_{i\,\mathrm{R}}$ the weak isospin

singlets for leptons, up-, and down-type quarks. It is assumed that the neutrinos are massless, thus no right-handed neutrino fields are considered. This is a sufficient approximation for the phenomenology discussed in this thesis. However, the observation of neutrino oscillation indicates that neutrinos have a non-zero but small mass [28, 29] which is currently constrained to $m_\nu < 1.1\,\text{eV}$ [25]. The full Lagrangian density function of the SM is then given by:

$$\mathcal{L}_{\text{SM}} = \sum_{\psi_{\text{L}} \in \{L_{i\,\text{L}}, Q_{i\,\text{L}}\}} \bar{\psi}_{\text{L}} i D_\mu \gamma^\mu \psi_{\text{L}} + \sum_{\psi_{\text{R}} \in \{l_{i\,\text{R}}, u_{i\,\text{R}}, d_{i\,\text{R}}\}} \bar{\psi}_{\text{R}} i D_\mu \gamma^\mu \psi_{\text{R}}$$
$$- \frac{1}{4} G^a_{\mu\nu} G^{\mu\nu}_a - \frac{1}{4} W^a_{\mu\nu} W^{\mu\nu}_a - \frac{1}{4} B_{\mu\nu} B^{\mu\nu}, \tag{2.2}$$

where the covariant derivative is defined by[1][2]:

$$D_\mu \psi = \left(\partial_\mu - i g_s \tilde{T}_a G^a_\mu - i g_2 T_a W^a_\mu - i g_1 \frac{Y_f}{2} B_\mu \right) \psi. \tag{2.3}$$

The first two terms of Equation (2.2) contain the equations of motion for the left- and right-handed fermion fields of the form $\bar{\psi} i D_\mu \gamma^\mu \psi$. Enforcing local gauge symmetry of the Lagrangian density requires additional terms in the covariant derivative, introducing the fields $G^{1,\dots,8}_\mu$, $W^{1,2,3}_\mu$ and B_μ. These correspond to the respective $SU(3)_\text{C}$ gauge group with the 8 Gell-Mann matrices $\tilde{T}^{1,\dots,8} = 1/2 \cdot \lambda_{1,\dots,8}$ as generators, $SU(2)_\text{L}$ with generators $T^{1,2,3} = 1/2 \cdot \tau_{1,2,3}$ derived from the three Pauli matrices and $U(1)_\text{Y}$ which generator is a scalar. In the SM the fields G^a_μ are identified as gluons, the massless carrier bosons of the strong interactions. The fields W^a_μ and B_μ are the four massless Goldstone bosons which are the mediators of the EW force. Hence, Equation (2.3) also includes fermion-boson interactions. The last three terms in Equation (2.2) describe the equations of motion of the gauge fields with the general structure of:

$$V^a_{\mu\nu} = \partial_\mu V^a_\nu - \partial_\nu V^a_\mu + g_x x^{abc} V^b_\mu V^c_\nu, \qquad V^a_\mu \in \{G^a_\mu, W^a_\mu, B_\mu\}, \tag{2.4}$$

with g_x the coupling constants of the $SU(3)_\text{C}$ (g_s), $SU(2)_\text{L}$ (g_2) and $U(1)_\text{Y}$ (g_1). Since $SU(3)$ and $SU(2)$ are non-Abelian groups, the last term contains the structure constants $x^{abc} = f^{abc}$ and ϵ^{abc} of the respective commutation relations of the group generators. Because $U(1)$ is an Abelian group, the last term in Equation (2.4) is zero for the B_μ field.

The Lagrangian density in Equation (2.2) does not contain mass generating terms for the EW bosons or any of the fermions as they would break the local gauge invariance of the $SU(2)_\text{L} \times U(1)_\text{Y}$ group. However, all charged fermions and at least 3 of the EW gauge bosons do have non-zero masses [25]. As a solution, the Higgs mechanism was proposed as a way to introduce mass terms for these particles without breaking local gauge invariance [13–15].

The Higgs mechanism introduces a complex $SU(2)$ iso-doublet of scalar fields:

$$\Phi = \begin{pmatrix} \phi^+ \\ \phi^0 \end{pmatrix}, \tag{2.5}$$

with hypercharge $Y_\phi = +1$ and $I^3_{\phi^{+/0}} = \pm\frac{1}{2}$. Thus, the upper component has a positive electric charge while the lower one is neutral. The Lagrangian density function of the new

---

[1]Using Einstein notation: $X_\alpha Y^\alpha = \sum_{\alpha=1}^{n} X_\alpha Y^\alpha$

[2]This is the covariant derivative for a quark. For leptons, the second term corresponding to the $SU(3)_\text{C}$ group would vanish as they do not a carry color charge.

field with its potential $V(\Phi)$ is of the form:

$$\mathcal{L}_{\text{Higgs}} = \frac{1}{2} \left(D^\mu \Phi\right)^\dagger \left(D_\mu \Phi\right) - V(\Phi),$$

$$V(\Phi) = \mu^2 \Phi^\dagger \Phi + \lambda \left(\Phi^\dagger \Phi\right)^2. \tag{2.6}$$

The shape of the Higgs potential depends on the mass term μ^2 and Higgs field self-coupling λ. If μ^2 and λ are positive the potential has its minimum, and therefore Vacuum Expectation Value (VEV) at $\langle\Phi\rangle_0 = \langle 0|\Phi|0\rangle = 0$. For the case of $\mu^2 < 0$, the minimum of the potential is at non-zero values of the Higgs field. Since the vacuum state is expected to be electrically neutral in order to preserve $U(1)_{\text{QED}}$, the charged component ϕ^+ is set to zero. This makes the minimum of the potential only dependent on the imaginary and real part of ϕ^0. Figure 2.1.1 illustrates the shape of the potential for this case.
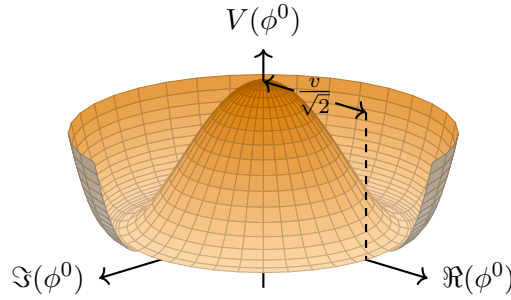
Figure 2.1.1.: Sketch of the SM Higgs potential for $\mu^2 < 0$ and $\lambda > 0$ parameterized in the real and imaginary part of the neutral component of the Higgs field ϕ^0. The minima form a ring with radius $|\phi^0| = \frac{v}{\sqrt{2}}$ with rotational symmetry in the complex plane.

Given these preconditions, the VEV of the Higgs field can then be found at:

$$\langle\Phi\rangle_0 = \begin{pmatrix} 0 \\ \frac{v}{\sqrt{2}} \end{pmatrix}, \qquad \text{with } v = \sqrt{-\frac{\mu^2}{\lambda}}. \tag{2.7}$$

Expanding the neutral component of the doublet field with a term $H(x)$ around the VEV and expressing the field in terms of the components $\theta_{1,2,3}(x)$, followed by a gauge transformation of the field gives [27]:

$$\Phi = \begin{pmatrix} \theta_1(x) + i\theta_2(x) \\ \frac{1}{\sqrt{2}}(v + H(x)) - i\theta_3(x) \end{pmatrix} \rightarrow e^{-i\sqrt{2}\theta_a(x)\tau^a/v} \Phi = \begin{pmatrix} 0 \\ \frac{1}{\sqrt{2}}(v + H(x)) \end{pmatrix}. \tag{2.8}$$

By plugging in Equation (2.8) and the covariant derivative (2.3) into the Higgs Lagrange density (2.6), the kinetic term decomposes into:

$$\left(D^\mu \Phi\right)^\dagger \left(D_\mu \Phi\right) = \frac{1}{2}(\partial_\mu H)^2 + g_2^2 \frac{1}{4} W_\mu^+ W^{-\mu}(v+H)^2 + \frac{g_1^2 + g_2^2}{8} Z_\mu Z^\mu (v+H)^2, \tag{2.9}$$

with four new vector boson fields $W_\mu^\pm$, Z_μ, and A_μ created by mixing the Goldstone boson fields:

$$W_\mu^\pm = \frac{1}{\sqrt{2}}\left(W_\mu^1 \mp iW_\mu^2\right), \quad Z_\mu = \frac{g_2 W_\mu^3 - g_1 B_\mu}{\sqrt{g_1^2 + g_2^2}}, \quad A_\mu = \frac{g_2 W_\mu^3 + g_1 B_\mu}{\sqrt{g_1^2 + g_2^2}}. \tag{2.10}$$

Equation (2.9) does not only contain VVH and $VVHH$ couplings but also mass terms for the $W_\mu^\pm$ and Z_μ fields of the form:

$$m_W^2 W_\mu^+ W^{-\mu} + \frac{1}{2} m_Z^2 Z_\mu Z^\mu \qquad \text{with } m_W = \frac{1}{2} v g_2, \; m_Z = \frac{v\sqrt{g_1^2 + g_2^2}}{2}. \qquad (2.11)$$

The massive boson fields are associated with the Z and $W^\pm$ vector bosons observed with a rest mass of $\sim 91\,\text{GeV}$ and $80\,\text{GeV}$ respectively while the massless A_μ field corresponds to the photon. When the Higgs field assumes its VEV at $\mu < 0$ the $SU(2)_\text{L} \times U(1)_\text{Y}$ symmetry spontaneously breaks leaving behind a $U(1)_\text{QED}$ symmetry with the associated electric charge Q.

Inserting Equation (2.8) into the Higgs potential reviles the mass terms of the H field:

$$V(\Phi) = \lambda v^2 H^2 + \lambda v H^3 + \frac{\lambda}{4} H^4, \qquad (2.12)$$

with a mass of $m_H^2 = 2\lambda v^2 = -2\mu^2$. This scalar H field is associated with the Higgs boson which was found by the ATLAS and CMS experiments with a mass of $m_H \approx 125\,\text{GeV}$ [30–33]. The vacuum expectation value as a parameter of the Higgs-sector can be derived from measurements of weak processes like the muon decay as it is connected with the Fermi constant via: [34]

$$v = \frac{1}{\left(\sqrt{2} G_\text{F}\right)^{\frac{1}{2}}} = 246\,\text{GeV}, \qquad (2.13)$$

which sets the typical energy scale for EW processes.

Masses for fermions are produced by introducing Yukawa terms in the Lagrangian for each of the fermion fields of Equation (2.1) which are invariant under $SU(2)_\text{L} \times U(1)_\text{Y}$ transformation:

$$\begin{aligned} \mathcal{L}_\text{Yukawa} &= -\lambda_{l_i} \bar{L}_{i\,\text{L}} \Phi l_{i\,\text{R}} - \lambda_{u_i} \bar{Q}_{i\,\text{L}} i\tau_2 \Phi^* u_{i\,\text{R}} - \lambda_{d_i} \bar{Q}_{i\,\text{L}} \Phi d_{i\,\text{R}} + h.c. \\ &= - \sum_{\psi \in \{e,\mu,\tau,u,d,...\}} \frac{\lambda_\psi}{\sqrt{2}} (v + H) \bar{\psi}_\text{L} \psi_\text{R} + h.c.. \end{aligned} \qquad (2.14)$$

The Yukawa Lagrangian contains terms of the form $-\frac{\lambda_f}{\sqrt{2}} v \bar{\psi}_\text{L} \psi_\text{R} + h.c.$ which are associated with fermion masses of $m_f = \frac{\lambda_f v}{\sqrt{2}}$ while keeping the neutrinos massless. The Yukawa couplings λ_f are parameters in the SM which are determined by the measurements of the fermion mass. Additionally, the Yukawa Lagrangian also contains fermion-Higgs boson interaction terms with a coupling constant of:

$$g_{Hff} = \frac{m_f}{v}, \qquad \text{for } f \in \{e,\,\mu,\,\tau,\,u,\,d,\,c,\,s,\,t,\,b\}. \qquad (2.15)$$

Thus, Higgs bosons couple stronger to fermions with high invariant mass such as tau leptons or top and bottom quarks.

In summary, after the Higgs field assumes its VEV for $\mu^2 < 0$ the $SU(2)_\text{L} \times U(1)_\text{Y}$ gauge symmetry spontaneously breaks, creating massive gauge vector bosons and fermions, as well as a massive spin 0 Higgs boson. Three degrees of freedom of the broken symmetry are absorbed in the massive Z and $W^\pm$ bosons while the remaining one forms the photon which is associated with the $U(1)_\text{QED}$ gauge group of the Quantum Electro Dynamic (QED) theory. The phenomenology of the Higgs mechanism and the spontaneously EW symmetry coincides with the particle content and interactions observed in the universe and therefore is an integral part of the SM.

2.2. Minimal Supersymmetric Extension of the Standard Model

The general goal of particle physics is to provide a complete theory of the known fundamental forces, particles, and their interactions. The theory of the electro-weak and strong force of the SM is already capable of describing the data measured at experiments like ATLAS or CMS [35, 36] with incredible precision. Therefore, the SM is regarded as one of the most successful theories in the field of physics. However, it is not able to fully explain observation from cosmic measurements and also comes with theoretical deficiencies [21]. Firstly, the SM completely lacks a description of gravity. Additionally, the SM introduces the strong and EW interaction as separate gauge groups with separate charges. In general, one would like the $SU(3)_\mathrm{C} \times SU(2)_\mathrm{L} \times U(1)_\mathrm{Y}$ symmetry group of the SM to emerge from a single larger, spontaneously broken symmetry group with one charge [37]. Such a Grand Unified Theory (GUT) would require the strong and EW couplings to converge to a common value at a GUT scale of $\Lambda_\mathrm{GUT} \sim 10^{16}\,\mathrm{GeV}$.

Also, when calculating radiative corrections to the bare Higgs mass, correction terms with quadratic divergence in the cut-off scale Λ_Cut appear. If this scale is chosen to be of the order of the GUT scale or Planck scale $\Lambda_\mathrm{Cut} \sim 10^{18}\,\mathrm{GeV}$ at which new physics is thought to emerge, the corrections to the Higgs mass would need to be unnaturally fine-tuned at the order $\sim \mathcal{O}(10^{-30})$ if the Higgs mass is set to a value around the EW scale. This problem is called the fine-tuning or naturalness problem. Although, it is not a strict phenomenological problem that falsifies the theory it is usually considered unnatural that parameters need to be adjusted with such high precision. The fine-tuning problem is also related to the hierarchy problem which poses the question of why the electro-weak scale is so much smaller than the Planck scale.

Furthermore, the existence of dark matter, first indirectly observed in the movements of galaxy clusters [16], poses an unsolvable problem to the SM as it does not predict particles candidates that could explain the observed dark matter content of the universe. These discrepancies lead to the notion that the SM is incomplete. One possibility of resolving these shortcomings is to extend the SM by introducing new symmetries and fields.

A popular extension is called Supersymmetry (SUSY). The SUSY theory proposes the existence of a new symmetry where a generator $\mathcal{Q}$ transforms bosons with integer spin into half-spin fermion and vice versa [37]:

$$\mathcal{Q}\left|\mathrm{Fermion}\right\rangle = \left|\mathrm{Boson}\right\rangle, \qquad\qquad \mathcal{Q}\left|\mathrm{Boson}\right\rangle = \left|\mathrm{Fermion}\right\rangle. \qquad (2.16)$$

The generator has to fulfill the commutation and anti-commutation relations:

$$\{\mathcal{Q},\, \mathcal{Q}^\dagger\} = P^\mu, \qquad \{\mathcal{Q},\, \mathcal{Q}\} = \{\mathcal{Q}^\dagger,\, \mathcal{Q}^\dagger\} = 0, \qquad [P^\mu,\, \mathcal{Q}] = [P^\mu,\, \mathcal{Q}^\dagger] = 0. \qquad (2.17)$$

This additional symmetry predicts the existence of fermionic and bosonic superpartners for each of the particles in the SM which differ in the spin but otherwise hold the same charges. The smallest possible supersymmetric extension to the SM with the smallest set of newly predicted particles is the Minimal Supersymmetric Standard Model (MSSM). Within this extended model, many of the aforementioned problems of the SM can be solved. For example, in the MSSM the couplings strengths of the QCD and EW interaction converge at the GUT scale as shown in Figure 2.2.1 depending on the choice of SUSY parameters [20]. The charged and neutral superpartners of the EW gauge and Higgs bosons mix, forming the 4 fermionic neutralino and chargino mass eigenstates. The mass eigenstates of the fermion superpartners are mixtures of their left- and right-handed mass states. The splitting of these mass eigenstates is proportional to the mass of their fermionic partners and thus can be particularly large for third-generation sfermions. Depending on the choice of SUSY parameters, the mass splitting of the sfermions can be significant. Hence, the eigenstates
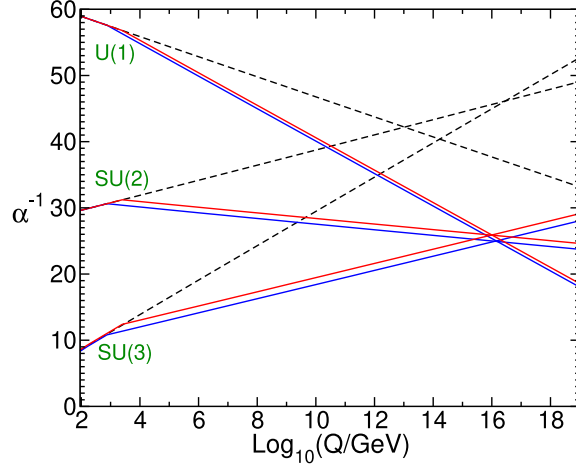
Figure 2.2.1.: Evolution of the inverse coupling $\alpha^{-1}(Q)$ predicted by the SM (dashed lines) and the MSSM (solid lines) over the renormalization group scale Q [20]. The lines of the MSSM model are derived by varying the supersymmetric particle masses between the commonly used range of $750\,\text{GeV}$ to $2.5\,\text{TeV}$ and α_S from 0.117 to 0.12.

for third-generation sfermions are usually distinguished by subscripts, e.g. $\tilde{t}_{1,2}$, $\tilde{b}_{1,2}$, and $\tilde{\tau}_{1,2}$.

By introducing R-parity in order to preserve lepton and baryon number conservation in the MSSM, the lightest supersymmetric particle becomes stable. If this particle is a weakly interacting heavy neutralino, it can serve as a candidate for dark matter. Finally, a supersymmetric model would prevent the appearance of quadratic terms in the radiation corrections to the Higgs mass, subsequently solving the fine-tuning problem.

More importantly for the scope of this thesis, the MSSM requires the existence of two Higgs doublets with 8 degrees of freedom, which, after Electro Weak Symmetry Breaking (EWSB), produces the three vector gauge bosons $W^\pm$, Z, and A as well as 5 scalar Higgs bosons, two massive charged bosons $H^\pm$ and three neutral bosons of which two are CP-even h and H, while the third one is the CP-odd A boson. Within the framework of SUSY, their presence also comes with an equal amount of charged and neutral gauginos and higgsino superpartners. A depiction of the full particle content of the MSSM is given in Figure 2.2.2.

2.2.1. Higgs Sector of the MSSM

Since the superpartners of the SM-like particles were not yet observed at experiments like ATLAS and CMS [38, 39], it has to be assumed that SUSY is broken, creating large differences between the mass of ordinary particles and their superpartners of the order of $> 1\,\text{TeV}$. To achieve supersymmetry breaking, the Lagrangian of the SUSY potential contains a soft SUSY breaking term which explicitly breaks the symmetry while preventing the appearance of quadratic cut-off scale dependencies in the perturbative mass corrections of the scalar fields [21].

In the MSSM two Higgs doublets are necessary in order to generate the masses for up- and down-type fermions:

$$\Phi_1 = \begin{pmatrix} \phi_1^0 \\ \phi_1^- \end{pmatrix}, \text{with } Y_{\Phi_1} = -1, \qquad \Phi_2 = \begin{pmatrix} \phi_2^+ \\ \phi_2^0 \end{pmatrix}, \text{with } Y_{\Phi_2} = +1. \tag{2.18}$$

SM-like particles

Generation

I   II   III

Quarks

| 2.16 MeV $\frac{2}{3}$ $\frac{1}{2}$ / u / Up | 1.27 GeV $\frac{2}{3}$ $\frac{1}{2}$ / c / Charm | 172.76 GeV $\frac{2}{3}$ $\frac{1}{2}$ / t / Top | 0 eV 0 0 / g / Gluon | 125.1 GeV 0 0 / h / SM-Higgs | 0 0 / H / H-Higgs |

Up: 2.16 MeV, $\frac{2}{3}$, $\frac{1}{2}$, $\frac{1}{2}$, 1 — u
Charm: 1.27 GeV, $\frac{2}{3}$, $\frac{1}{2}$, $\frac{1}{2}$, 1 — c
Top: 172.76 GeV, $\frac{2}{3}$, $\frac{1}{2}$, $\frac{1}{2}$, 1 — t
Gluon: 0 eV, 0, 0, 1, 1 — g
SM-Higgs: 125.1 GeV, 0, 0, 0, 1 — h
H-Higgs: 0, 0, 0, 1 — H

Down: 4.67 MeV, $-\frac{1}{3}$, $-\frac{1}{2}$, $\frac{1}{2}$, 1 — d
Strange: 93 MeV, $-\frac{1}{3}$, $-\frac{1}{2}$, $\frac{1}{2}$, 1 — s
Bottom: 4.81 GeV, $-\frac{1}{3}$, $-\frac{1}{2}$, $\frac{1}{2}$, 1 — b
Photon: 0 eV, 0, 0, 1, 1 — γ
A-Higgs: 0, 0, 0, 1 — A
$H^{\pm}$-Higgs: 0, ±1, 0, 1 — $H^{\pm}$

Higgs Sector

Leptons

e-Neutrino: <1.1 eV, 0, $\frac{1}{2}$, $\frac{1}{2}$, 1 — ν_e
μ-Neutrino: <0.19 MeV, 0, $\frac{1}{2}$, $\frac{1}{2}$, 1 — ν_μ
τ-Neutrino: <18.2 MeV, 0, $\frac{1}{2}$, $\frac{1}{2}$, 1 — ν_τ
W-Boson: 80.38 GeV, ±1, ±1, 1, 1 — $W^{\pm}$

Electron: 0.51 MeV, -1, $-\frac{1}{2}$, $\frac{1}{2}$, 1 — e
Muon: 105.7 GeV, -1, $-\frac{1}{2}$, $\frac{1}{2}$, 1 — μ
Tau: 1.78 GeV, -1, $-\frac{1}{2}$, $\frac{1}{2}$, 1 — τ
Z-Boson: 91.19 GeV, 0, 0, 1, 1 — Z

Gauge Bosons

Legend

m_X — q — l^3 — s — X — P_R — Name

Superpartners

Squarks

Sup: $\frac{2}{3}$, $\frac{1}{2}$, 0, -1 — $\tilde{u}$
Scharm: $\frac{2}{3}$, $\frac{1}{2}$, 0, -1 — $\tilde{c}$
Stop: $\frac{2}{3}$, $\frac{1}{2}$, 0, -1 — $\tilde{t}_{1,2}$
Gluino: 0, 0, $\frac{1}{2}$, -1 — $\tilde{g}$
$\tilde{\chi}^0_1$: 0, 0, $\frac{1}{2}$, -1
$\tilde{\chi}^{\pm}_1$: -1, ±1, $\frac{1}{2}$, -1

Sdown: $-\frac{1}{3}$, $-\frac{1}{2}$, 0, -1 — $\tilde{d}$
Sstrange: $-\frac{1}{3}$, $-\frac{1}{2}$, 0, -1 — $\tilde{s}$
Sbottom: $-\frac{1}{3}$, $-\frac{1}{2}$, 0, -1 — $\tilde{b}_{1,2}$
$\tilde{\chi}^0_2$: 0, 0, $\frac{1}{2}$, -1
$\tilde{\chi}^{\pm}_2$: -1, ±1, $\frac{1}{2}$, -1

Charginos

Sleptons

e-Sneutrino: 0, $\frac{1}{2}$, 0, -1 — $\tilde{\nu}_e$
μ-Sneutrino: 0, $\frac{1}{2}$, 0, -1 — $\tilde{\nu}_\mu$
τ-Sneutrino: 0, $\frac{1}{2}$, 0, -1 — $\tilde{\nu}_\tau$
$\tilde{\chi}^0_3$: 0, 0, $\frac{1}{2}$, -1

Selectron: -1, $-\frac{1}{2}$, 0, -1 — $\tilde{e}$
Smuon: -1, $-\frac{1}{2}$, 0, -1 — $\tilde{\mu}$
Stau: -1, $-\frac{1}{2}$, 0, -1 — $\tilde{\tau}_{1,2}$
$\tilde{\chi}^0_4$: 0, 0, $\frac{1}{2}$, -1
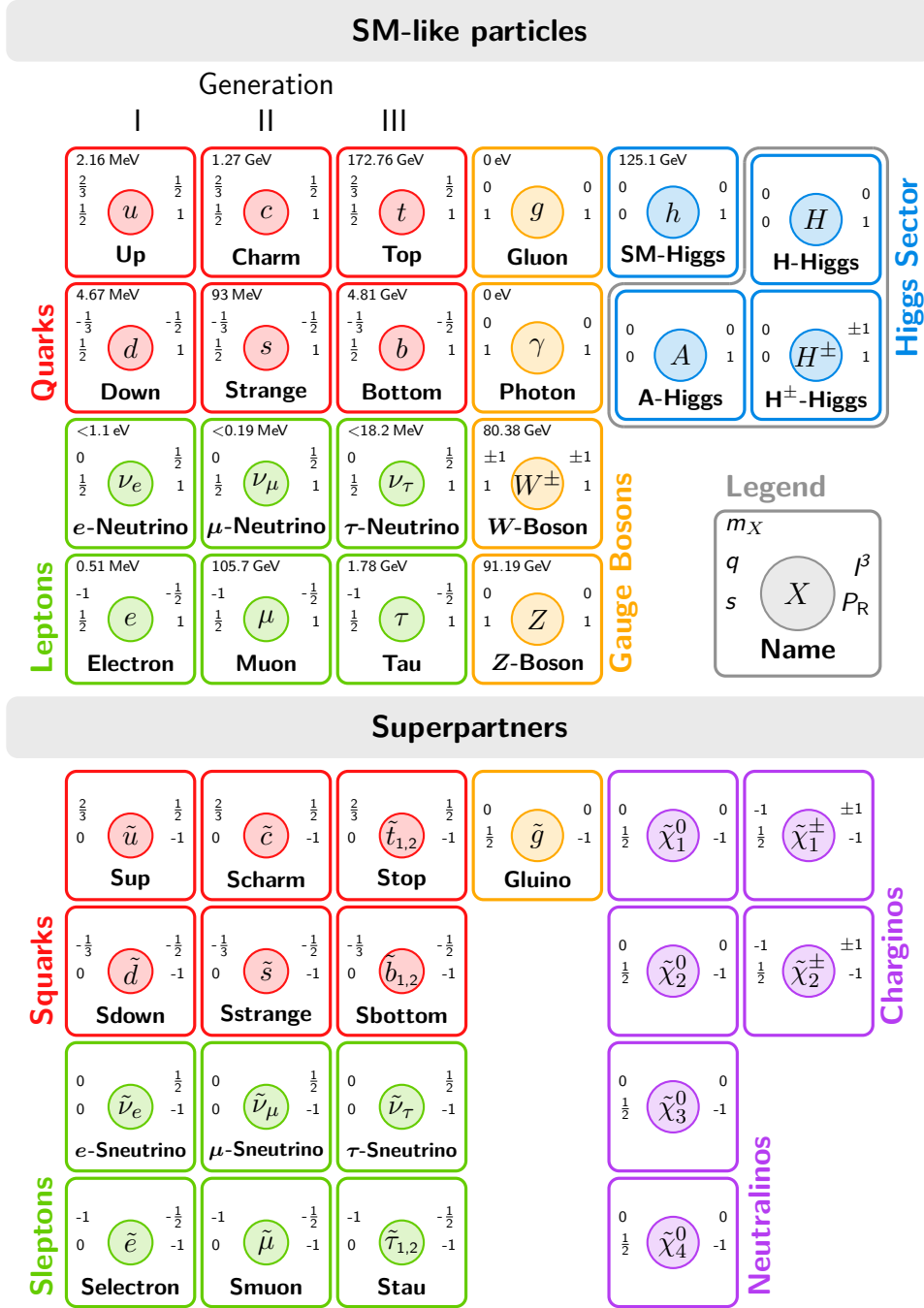
Neutralinos

Figure 2.2.2.: Particle content of the MSSM in their mass eigenstates. The weak isospin of fermions refers to their left-handed component [21]. Masses of SM particles are taken from Reference [25]. The MSSM predicts the existence of an extended Higgs-sector with additional neutral and charged Higgs bosons.

The corresponding full Higgs potential in the MSSM is defined by:

$$V_{\text{Higgs, MSSM}} = \left(|\mu|^2 + m_{\Phi_1}\right)|\Phi_1|^2 + \left(|\mu|^2 + m_{\Phi_2}\right)|\Phi_2|^2 - \mu B \epsilon_{ij}\left(\Phi_1^i \Phi_2^j + h.c.\right)$$
$$+ \frac{g_1^2 + g_2^2}{8}\left(|\Phi_1|^2 - |\Phi_2|^2\right)^2 + \frac{1}{2}g_2^2|\Phi_1^\dagger \Phi_2|^2, \tag{2.19}$$

where the first two terms contain mass terms of the Φ_1 and Φ_2 fields which explicitly break SUSY[3], while the third term contains bilinear combinations of the Higgs fields with the coupling parameter B.

Similar to the Standard Model case, the EW symmetry breaks if $\mu^2 < 0$. Then, the neutral components of both Higgs fields assume the VEV of:

$$\Phi_1 = \begin{pmatrix} \frac{v_1}{\sqrt{2}} \\ 0 \end{pmatrix}, \qquad\qquad \Phi_2 = \begin{pmatrix} 0 \\ \frac{v_2}{\sqrt{2}} \end{pmatrix}, \tag{2.20}$$

with the ratio of the two VEV defined by:

$$\tan\beta = \frac{v_2}{v_1} = \frac{v\sin\beta}{v\cos\beta}, \tag{2.21}$$

corresponding to a rotation around the angle β of the VEV $v^2 = v_1^2 + v_2^2$ as defined in Equation (2.13). With Equations (2.11) and (2.21) the minimum of the potential is reached if:

$$\mu^2 = \frac{m_{\Phi_2}^2 \sin^2\beta - m_{\Phi_1}^2 \cos^2\beta}{\cos(2\beta)} - \frac{m_Z^2}{2},$$
$$B\mu = \frac{1}{2}\left[\left(m_{\Phi_1}^2 - m_{\Phi_2}^2\right)\tan(2\beta) + m_Z^2 \sin(2\beta)\right]. \tag{2.22}$$

Similar to the SM case, the Higgs fields are expanded around the VEV:

$$\Phi_1 = \frac{1}{\sqrt{2}}\begin{pmatrix} (v_1 + H_1^0) + iP_1^0 \\ H_1^- \end{pmatrix}, \qquad \Phi_2 = \frac{1}{\sqrt{2}}\begin{pmatrix} H_2^+ \\ (v_2 + H_2^0) + iP_2^0 \end{pmatrix}, \tag{2.23}$$

where the imaginary part of the neutral components mix to create a neutral CP-odd pseudoscalar A and a massless G^0 Goldstone boson, while the real part gives rise to the CP-even h and H bosons. The mass eigenstates that diagonalize the imaginary part of the mass matrix are mixed by a rotation of the imaginary Higgs field parts with angle β from Equation (2.21):

$$\begin{pmatrix} G^0 \\ A \end{pmatrix} = \begin{pmatrix} \cos\beta & \sin\beta \\ -\sin\beta & \cos\beta \end{pmatrix}\begin{pmatrix} P_1^0 \\ P_2^0 \end{pmatrix}, \tag{2.24}$$

with the tree-level A boson mass of:

$$m_A^2 = -\frac{2B^2\mu^2}{\sin(2\beta)}. \tag{2.25}$$

Similarly, the charged Higgs boson mass eigenstates are mixed from the charged Higgs field components:

$$\begin{pmatrix} G^\pm \\ H^\pm \end{pmatrix} = \begin{pmatrix} \cos\beta & \sin\beta \\ -\sin\beta & \cos\beta \end{pmatrix}\begin{pmatrix} H_1^\pm \\ H_2^\pm \end{pmatrix}, \tag{2.26}$$

generating massless charged Goldstone and massive $H^\pm$ bosons with mass:

$$m_{H^\pm}^2 = m_A^2 + m_W^2. \tag{2.27}$$

---

[3]This is only one part of the SUSY breaking potential. In the MSSM, further SUSY breaking terms for sfermions and gauginos are present in the SUSY potential.

The CP-even neutral mass eigenstates are generated by rotating the real parts of the neutral Higgs field components with a mixing angle α:

$$\begin{pmatrix} H \\ h \end{pmatrix} = \begin{pmatrix} \cos\alpha & \sin\alpha \\ -\sin\alpha & \cos\alpha \end{pmatrix} \begin{pmatrix} H_1^0 \\ H_2^0 \end{pmatrix}, \tag{2.28}$$

where the rotation angle α relates to β by:

$$\alpha = \frac{1}{2}\arctan\left(\tan(2\beta)\frac{m_A^2 + m_Z^2}{m_A^2 - m_Z^2}\right). \tag{2.29}$$

The resulting masses of the CP-even eigenstates are then given at tree-level by:

$$m_{h,H}^2 = \frac{1}{2}\left[m_A^2 + m_Z^2 \mp \sqrt{(m_A^2 + m_Z^2)^2 - 4m_A^2 m_Z^2 \cos^2(2\beta)}\right]. \tag{2.30}$$

As a convention, the h boson is defined to be the lighter of the two CP-even Higgs bosons. Thus, the entire Higgs-sector of the MSSM can be described at tree level by two parameters m_A and $\tan\beta$. With Equation (2.30) the lightest Higgs boson is constrained from above at tree level:

$$m_h \leq \min(m_A, m_Z) \cdot |\cos(2\beta)| \leq m_Z. \tag{2.31}$$

In the MSSM models considered in this thesis, the h boson is usually associated with the SM-like Higgs boson with a mass of $\sim 125\,\text{GeV}$ which is already substantially larger than the Z boson mass. However, higher-order corrections to the Higgs boson masses can raise the mass of h by several GeV bringing it close to the SM value. The other Higgs bosons are thought to be heavier with masses ranging from a couple of hundred GeV up to many TeV.

Similarly to the SM case, masses of gauge bosons are generated by evaluating the kinematic terms of the Higgs field Lagrangian:

$$\mathcal{L}_{\text{Higgs, kin.}} = (D^\mu \Phi_1)^\dagger (D_\mu \Phi_1) + (D^\mu \Phi_2)^\dagger (D_\mu \Phi_2), \tag{2.32}$$

while fermion masses are generated by adding Yukawa terms. In the case of the MSSM, the Higgs field Φ_1 only couples to up-type and Φ_2 to down-type fermions to prevent flavor-changing neutral currents. The resulting Yukawa terms are then defined by:

$$\mathcal{L}_{\text{Yukawa}} = -\lambda_{l_i}\bar{L}_{i\,\text{L}}\Phi_2 l_{i\,\text{R}} - \lambda_{u_i}\bar{Q}_{i\,\text{L}}\Phi_2 u_{i\,\text{R}} - \lambda_{d_i}\bar{Q}_{i\,\text{L}}\Phi_1 d_{i\,\text{R}} + h.c.. \tag{2.33}$$
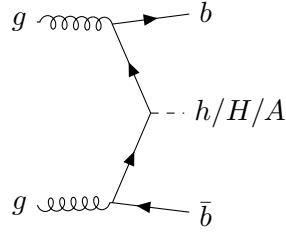
Evaluating the Yukawa terms at the VEV with Equation (2.21) gives rise to the fermion masses:

$$m_{u_i} = \frac{\lambda_{u_i} v_2}{\sqrt{2}} = \frac{\lambda_{u_i}\sin\beta}{\sqrt{2}}, \qquad m_{d_i,l_i} = \frac{\lambda_{d_i,l_i} v_1}{\sqrt{2}} = \frac{\lambda_{d_i,l_i}\cos\beta}{\sqrt{2}}, \tag{2.34}$$
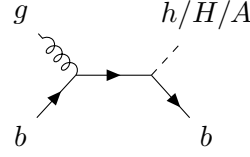
and neutral Higgs boson couplings to up- and down-type fermions:

$$\begin{aligned}
g_{huu} &= i\frac{m_u}{v}\left[\sin(\beta-\alpha) + \cot\beta\cos(\beta-\alpha)\right], \\
g_{hdd} &= -i\frac{m_d}{v}\left[\sin(\beta-\alpha) - \tan\beta\cos(\beta-\alpha)\right], \\
g_{Huu} &= i\frac{m_u}{v}\left[\cos(\beta-\alpha) - \cot\beta\sin(\beta-\alpha)\right], \\
g_{Hdd} &= i\frac{m_d}{v}\left[\cos(\beta-\alpha) + \tan\beta\sin(\beta-\alpha)\right], \\
g_{Auu} &= \frac{m_u}{v}\gamma_5\cot\beta, \\
g_{Add} &= \frac{m_d}{v}\gamma_5\tan\beta.
\end{aligned} \tag{2.35}$$

b-associated production in 4 FS

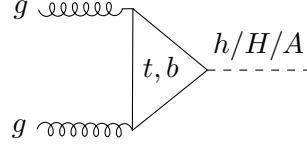*b*-associated production in 5 FS

gluon-gluon fusion

Figure 2.2.3.: Main neutral Higgs production channels at proton-proton colliders.

Hence for large $\tan\beta$ the coupling to down-type fermions with large mass, like b quarks or τ leptons, is enhanced while couplings to up-type quarks is suppressed.

The prediction of additional massive Higgs bosons after EWSB can be exploited to probe the MSSM by searching for these new heavy resonances and excluding regions of the m_A-$\tan\beta$ parameter space. The search presented in this thesis aims to search for new heavy neutral Higgs bosons H and A produced at the LHC particle accelerator that decay into pairs of taus. Despite the coupling to bottom quarks being larger than that to tau leptons, the latter provides a cleaner signature which is easier to separate from the abundant QCD-process background present in proton-proton accelerators. Thus, the search for the additional Higgs bosons decaying into di-tau final states is particularly sensitive to a potential signal in the high $\tan\beta$ regime.

At proton-proton colliders like the LHC, the most dominant production channels for heavy neutral Higgs bosons are gluon-gluon fusion and b-associated production. The former process is mediated via a top or bottom loop. The b-associated production is dominated by two processes where either a bottom quark is present in the initial state (5 flavor scheme) or not (4 flavor scheme). However, in both b-associated production processes, additional b-hadrons are present in the final state. Figure 2.2.3 shows the Feynman diagrams for the leading Higgs production processes considered in this thesis. Further production channels like vector-boson fusion or Higgs radiation are neglected as their contribution is strongly suppressed by the signal region selection described in Chapter 7.

2.2.2. Benchmark Models

Although the Higgs-sector in the MSSM is described at tree level by m_A and $\tan\beta$, the phenomenology of the MSSM model is also strongly dependent on other model parameters when including higher-order corrections. Input parameters from the SM sector that have a large impact on the phenomenology of the Higgs-sector are the bottom-quark mass and top-quark pole-masses (m_b and $m_{\text{top}}^{\text{pole}}$) as well as the gauge boson masses (m_Z and m_W), the strong coupling parameter $\alpha_S(m_Z)$ evaluated at the Z mass energy scale and the Fermi constant G_{F}.

From the ~ 100 parameters in the soft SUSY breaking Lagrangian only a small subset of parameters that strongly influence the Higgs-sector phenomenology are frequently used

to adjust the model configurations. These are the third generation squark masses m_{Q_3}, m_{u_3}, and m_{d_3}[4], the third generation slepton masses m_{L_3} and m_{l_3}, as well as their trilinear Higgs to sfermions coupling parameters A_t, A_b, and A_τ. Sometimes A_t is not directly fixed but rather determined by the stop-mixing parameter:

$$X_t = A_t - \mu \cot\beta, \qquad (2.36)$$

which also appears in the off-diagonal elements of stop mass matrix and thus determines the mixing of the left- and right-handed stop fields $\tilde{t}_L$ and $\tilde{t}_R$ giving rise to their mass eigenstates $\tilde{t}_1$ and $\tilde{t}_2$. Other frequently adjusted SUSY parameters are the masses of the gauginos m_1, m_2, and m_3 for binos, winos and gluinos respectively.

Depending on the configuration of these parameters, different benchmark models are defined. In the following section, an overview of the configuration of the hMSSM model and three variants of the m_h^{125} benchmark models are presented.

The hMSSM Model

After the discovery of an SM-like Higgs boson, the hMSSM model was proposed in References [40–43] as an alternative SM extension. In this model, the lightest Higgs boson h is associated with the SM-like Higgs boson with a mass of $m_h \approx 125\,\text{GeV}$ based on the Run-1 data measurements from CMS and ATLAS [30,31]. To account for the fact that no supersymmetric particle has been observed yet, the SUSY mass scale $M_S = \sqrt{m_{\tilde{t}_1} \cdot m_{\tilde{t}_2}}$ is assumed to be much larger than $1\,\text{TeV}$ thus evading the sensitivity of the ATLAS and CMS experiments. Since the dominant contributions to the radiative Higgs mass corrections originate from the top-stop sector, the mass of the SM-like h boson can be fixed to $m_h = 125\,\text{GeV}$ within a theoretical uncertainty of $\pm 3\,\text{GeV}$ by adjusting parameters like X_t over a large range of m_A-$\tan\beta$ [44,45]. Since there are no strong constraints applied on the SUSY sector, the hMSSM model is well suited as a benchmark to compare and combine results from multiple searches for additional heavy Higgs bosons.

A description of the cross-section and branching ratio calculations is given in Reference [46]. Gluon-gluon fusion production cross-sections for neutral Higgs bosons are calculated with SuSHi 1.5.0 [47,48] with full Next-to Leading Order (NLO) QCD corrections [49] and Next-to-Next-to Leading Order (NNLO) corrections to top contributions [50–52], as well as NNLO EW contributions of lighter quarks [53,54]. Cross-sections for the b-associated production channel are provided for the 4 and 5 flavor scheme production processes at NLO and NNLO precision respectively [55–57], which are combined using the Santander matching scheme [58–62]. All cross-section calculations are conducted using the MSTW2008 Parton Density Function (PDF) set [63].

To account for theoretical uncertainties, the factorization and renormalizations scale μ_F and μ_R are varied by a factor of two where the scale uncertainty is then determined by the envelope of the independent variations. Uncertainties on the PDF are derived from variations on the strong coupling parameter α_S of the chosen PDF set.

Masses of the Higgs bosons are calculated by FEYNHIGGS 2.10.4 [44,64–70] while branching ratios are computed using HDECAY 6.42 [71,72]. The resulting branching ratios are calculated at Leading Order (LO) for decays into leptons and bosons, and Next-to-Next-to NNLO (N^{4}LO) in QCD for quark pair decays.

The phase space investigated in the search for additional Higgs bosons covers a region of $0.8 \leq \tan\beta \leq 60$ and $130\,\text{GeV} \leq m_A \leq 2000\,\text{GeV}$ with branching ratios and cross-sections provided by the LHC Higgs Cross Section Working Group [73].

---

[4]Masses with capital letter subscripts refer to left-handed iso-doublet sfermion masses while the ones with lowercase letters are the masses for right-handed iso-singlets

An example of the leading branching ratios for the decays of *A* and *H* bosons is showcased in Figure 2.2.4. As expected, the decay into top pairs is the dominant contribution at
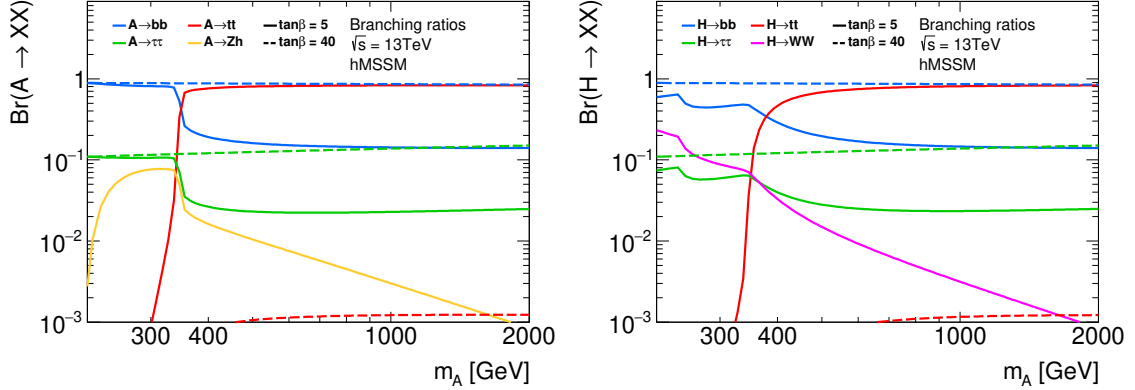

Figure 2.2.4.: Leading branching ratios of *A* (left) and *H* (right) bosons decays in the hMSSM for $\tan\beta = 5$ (solid lines) and $\tan\beta = 40$ (dotted lines). Branching ratios were computed with HDECAY [71, 72] and are provided by the LHC Higgs Cross Section Working Group [73].

low values of $\tan\beta$. However, if the Higgs masses do not pass the threshold of top pair production $m_{H/A} < 2 \times m_{\text{top}} \approx 346\,\text{GeV}$ then top decays are suppressed and the Higgs bosons decay mainly into taus or bottom quarks. In the high $\tan\beta$ regime, couplings to down-type fermions are enhanced, and thus the Higgs bosons decay preferably into pairs of bottom quarks or tau leptons, making them the most sensitive search channels.

The m_{h}^{125} Models

Although the hMSSM provides a flexible benchmark scenario, some problems arise due to the choice of approximations applied. Namely, neglecting radiative corrections of the CP-even mass matrix not related to the top-stop sector might be not well justified for small values of m_A and large values of $\tan\beta$. Also, enforcing the SM-like Higgs mass throughout the entire parameter space forces the stop mass to be of the order of the GUT scale for small values of m_A-$\tan\beta$, raising the SUSY scale to large energies [46, 74].

In the light of new constraints on the MSSM parameters, 4 new benchmark scenarios are proposed in Reference [74]: the m_{h}^{125} scenario with heavy super particles, the $m_{\text{h}}^{125}(\tilde{\tau})$ scenario predicting the existence of a light stau particle, the $m_{\text{h}}^{125}(\tilde{\chi})$ containing light gauginos as well as the m_{h}^{125} (alignment) scenario which predict that one of the CP-even Higgs bosons has SM-like couplings.

In all scenarios, the neutral Higgs boson masses are calculated using FEYNHIGGS 2.14.3 at full LO precision with partial NLO corrections. FEYNHIGGS is also used to produce the branching ratios with up to NLO precision for decays into fermions, photons, and gluons. Branching ratios for decays into vector bosons are calculated by reweighting the NLO branching ratios predicted for an SM-like Higgs boson using PROPHECY4F [75, 76].

Cross-sections are computed with SUSHI 1.7.0 in combination with SUSHIMI at full NLO precision with NNLO contributions from the top sector. Cross-sections for *b*-associated production are provided at fixed order plus next-to-leading log precision with the 4 and 5 flavor scheme contributions combined by applying a Santander matching. Depending on the order of the radiative contributions the PDF4LHC_NLO_MC and PDF4LHC_NNLO_MC PDF sets are used [77]. The cross-section uncertainties are derived by varying the renormaliza-

tion scale μ_R as well as by replacing the nominal PDF set with the systematic variations, including variations in α_S. Uncertainties originating from μ_F variations are known to be small in the m_h^{125} scenarios and are neglected. The total theory uncertainty is defined as the square sum of the three uncertainty sources.

All cross-sections and branching ratios are provided by the LHC Higgs Cross Section Working Group spanning over the parameter phase space of $0.5 \leq \tan\beta \leq 60$ and $70\,\text{GeV} \leq m_A \leq 2600\,\text{GeV}$ for the m_h^{125} model and all its variations except for the m_h^{125} (alignment) model.

In the following, the different m_h^{125} models and their configurations are explained.

The m_h^{125} scenario: The first model assumes that sfermion masses are large enough to only cause a small effect on Higgs production and decay. Additionally, this causes heavy Higgs bosons to only decay in SM particles up to masses of $m_{A,H} = 2\,\text{TeV}$. A list of relevant parameters is given by [74]:

$$
\begin{aligned}
m_{Q_3} = m_{u_3} = m_{d_3} &= 1.5\,\text{TeV}, \\
m_{L_3} = m_{l_3} &= 2\,\text{TeV}, \\
m_1 = m_2 = 1\,\text{TeV}, \quad m_3 &= 2.5\,\text{TeV}, \\
\mu = 1\,\text{TeV}, \quad X_t &= 2.8\,\text{TeV}, \\
A_b = A_\tau &= A_t.
\end{aligned}
\tag{2.37}
$$

Here the trilinear coupling parameters are not directly fixed but indirectly constrained by the stop mixing parameter X_t. The choice of parameters allows the light Higgs mass to stay around $m_h = 125 \pm 3\,\text{GeV}$ over a large range in the m_A-$\tan\beta$ space.

The $m_h^{125}(\tilde{\tau})$ scenario: A possible alteration of the above model predicts light staus and EW gauginos with masses of the order of a few hundred GeV as there are no strong constraints on uncolored super particles in this region. The presence of these light super particles can explain some of the differences observed in the measurement of the anomalous magnetic moment of the muon [18, 19, 78, 79]. If not stated otherwise the parameter configuration is the same as in Equations (2.37) except for:

$$
\begin{aligned}
m_{L_3} = m_{l_3} &= 350\,\text{GeV}, \\
m_1 = 180\,\text{GeV}, \quad m_2 &= 300\,\text{GeV}, \\
A_b = A_t, \quad A_\tau &= 800\,\text{GeV},
\end{aligned}
\tag{2.38}
$$

with a significantly lower stau, bino, and wino mass as well as fixed trilinear Higgs-to-stau couplings.

The $m_h^{125}(\tilde{\chi})$ scenario: This scenario is a variation of the m_h^{125} model with an uncolored super particles spectrum containing light EW gauginos and higgsinos. The model configuration is given by:

$$
\begin{aligned}
m_1 = 160\,\text{GeV}, \quad m_2 &= 180\,\text{GeV}, \\
\mu = 180\,\text{GeV}, \quad X_t &= 2.5\,\text{TeV},
\end{aligned}
\tag{2.39}
$$

with all other parameters set to the same values as stated in Equations (2.37). Reducing the EW gaugino mass and Higgs potential to values of $\sim 100\text{-}200\,\text{GeV}$ results in a strong mixing of gauginos and Higgsinos into chargino and neutralino mass eigenstates with a highly compressed mass spectrum. Due to the lightest neutralino mass $m_{\tilde{\chi}_1^0}$ ranging between 105

to 118 GeV the branching ratio of A and H bosons to neutralinos is significantly enhanced over a large area of the m_A-$\tan\beta$ parameter space, reaching 80 % for $m_A > 500$ GeV and $\tan\beta < 10$. This might explain why the additional Higgs bosons were not yet observed in their SM decay channels.

The m_h^{125} (alignment) scenario: The m_h^{125} (alignment) model aims at studying the scenario of alignment without decoupling where one of the CP-even Higgs fields is aligned with the SM Higgs VEV, thus assuming the same couplings to fermions and gauge bosons as predicted for the SM Higgs. This alignment occurs naturally at the decoupling limit where $m_A \gg m_Z$. Here, however, the parameters are chosen such that the light Higgs h is aligned to the SM coupling values in a band around $\tan\beta \approx 7$ with CP-odd A Higgs boson masses as low as $m_A > 170$ GeV. Simultaneously, the trilinear stop sector couplings are set to a value that maximizes the light h mass to match the SM-like Higgs boson mass at a value of $\tan\beta \approx 6$. The parameter setup of this model is given by:

$$\begin{aligned}
m_{Q_3} = m_{u_3} = m_{d_3} &= 2.5\,\text{TeV}, \\
m_{L_3} = m_{l_3} &= 2\,\text{TeV}, \\
m_1 = 500\,\text{GeV} \quad m_2 &= 1\,\text{TeV}, \quad m_3 = 2.5\,\text{TeV}, \\
\mu = 7.5\,\text{TeV}, \quad A_b &= A_\tau = A_t = 6.25\,\text{TeV}.
\end{aligned}$$
(2.40)

Note, in this configuration X_t is not set to a constant value but rather defined by the fixed A_t according to Equation (2.36). Due to the strong constraints placed on the model parameters from measurements of the SM-like Higgs properties, the phase space investigated covers the region of $1 \leq \tan\beta \leq 20$ and $120\,\text{GeV} \leq m_A \leq 1000\,\text{GeV}$.

An overview of the phase space excluded by a mismatch of the SM-like Higgs bosons properties for each of the discussed m_h^{125} scenarios is given in Section 2.2.3.

2.2.3. Current State of Searches for Additional Higgs Bosons

Many analyses at the ATLAS and CMS experiments are searching for new Higgs bosons predicted by beyond SM theories. Since the Higgs bosons are considered to be very heavy, they decay quickly at the point of interaction before they can reach the detector. Thus only their decay products are detected from which conclusions about the mass, cross-section, and branching ratios of the potential Higgs bosons can be drawn. However, so far no decay of a heavy neutral resonance has been observed. Thus, the results of the searches are interpreted in terms of exclusion limits on the parameter space of different benchmark models. Figure 2.2.5 shows a summary of the most recent results from analyses at ATLAS searching for additional Higgs bosons, interpreted in the hMSSM model. Constraints on low values of m_A-$\tan\beta$ come from searches looking for heavy neutral Higgs bosons decaying to vector bosons or from Higgs pair production, most notably $H \to hh \to bb\,bb/\gamma\gamma/\tau\tau$ [81] and $H \to ZZ \to 4l/ll\nu\nu$ [82]. Additional phase space is excluded by measurements of Higgs couplings, excluding the region of $m_A \lesssim 500$ GeV where the h couplings predicted by the hMSSM do not match the measured values.

As already discussed, the analysis searching for Higgs decays in a di-tau final state is especially sensitive at high values of $\tan\beta$ and provides the strongest constraints on the upper values of the m_A-$\tan\beta$ plane. The analysis described in this thesis in Chapter 7 is part of the results from Reference [24] shown in Figure 2.2.5 based on the full Run-2 dataset of ATLAS data-taking.

The analysis presented in this thesis will be also compared to previous results from ATLAS [83] and CMS [84] searching for neutral heavy Higgs boson decays in the di-tau
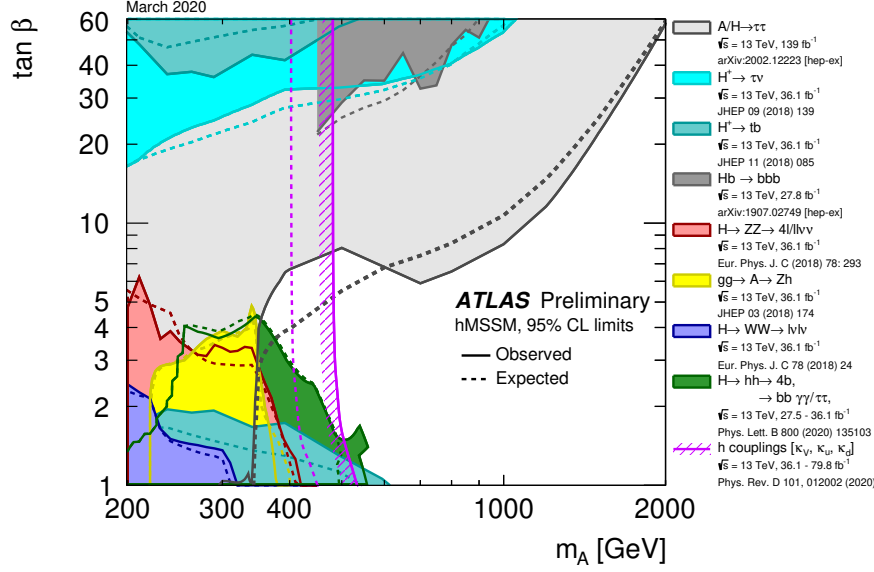
Figure 2.2.5.: Summary of ATLAS searches setting limits in the hMSSM parameter space presented in Reference [80]. The exclusion regions are derived from direct and indirect searches for heavy Higgs bosons as well as from measurements of Higgs couplings. Overall, the search for Higgs decaying into pairs of tau leptons sets the strongest upper exclusion contours in the m_A-$\tan\beta$ space.

final state. These previous results were based on $36.1\,\mathrm{fb}^{-1}$ and $35.9\,\mathrm{fb}^{-1}$ from LHC 2015-2016 data-taking periods for ATLAS and CMS respectively. Exclusion limits of these searches are presented in Figure 2.2.6.

Finally, exclusion limits on the different m_h^{125} scenarios are provided in Reference [74] and shown in Figure 2.2.7. Here, three sources of constraints on the parameter phase space are considered: the predicted mass of the light h bosons which has to be within a $\pm 3\,\mathrm{GeV}$ uncertainty range around the measured SM-like Higgs mass, measurements of SM Higgs boson production and decay rates, as well as constraints derived from direct searches for heavy Higgs boson decays. Constrains on the light Higgs properties are derived using the HiggsSignals package version 2.2.0beta [85] which contains numerous results from CMS and ATLAS based on full Run-1 and $36\,\mathrm{fb}^{-1}$ of Run-2 data-taking. Exclusion limits on the other hand were calculated using the HiggsBounds framework version 5.2.0beta [86–89] which calculates limits based on previous $36\,\mathrm{fb}^{-1}$ $H/A \to \tau\tau$ search results of ATLAS [83] and CMS [84].
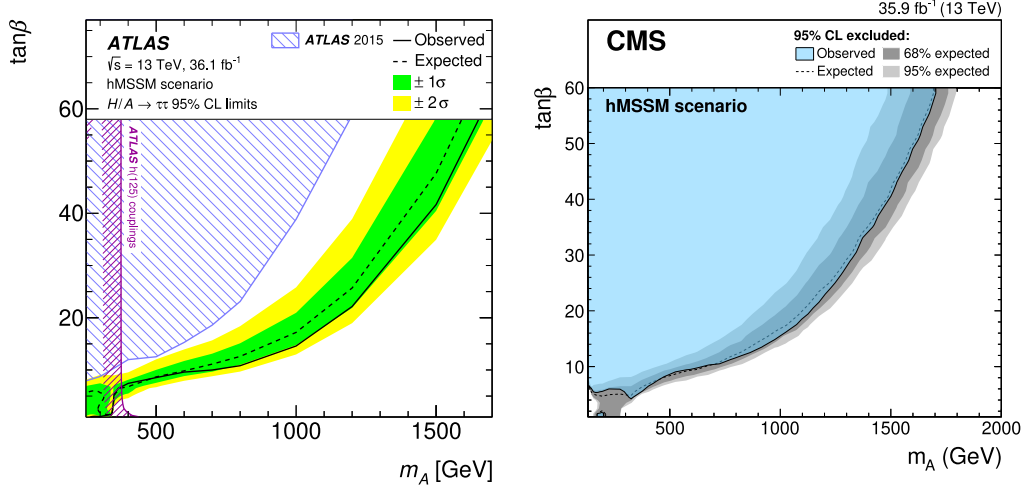
Figure 2.2.6.: Exclusion limit results from previous early Run-2 papers of the ATLAS (left) [83] and CMS (right) [84] experiments based on $36.1\,\mathrm{fb}^{-1}$ and $35.9\,\mathrm{fb}^{-1}$ of data respectively.
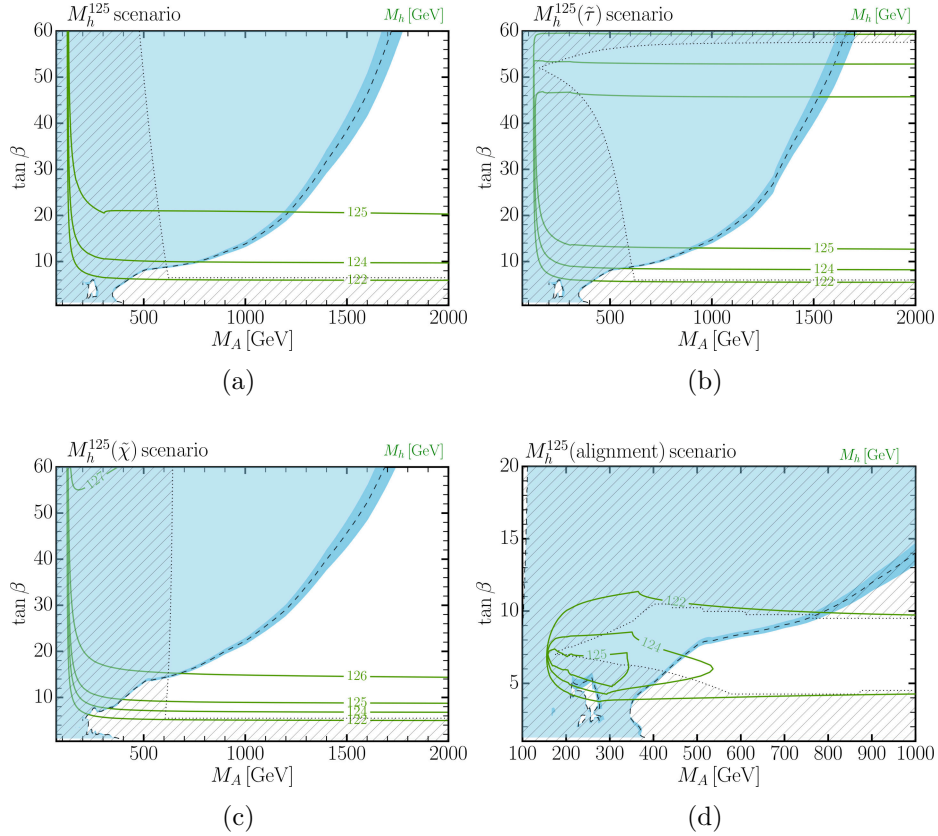
Figure 2.2.7.: Exclusion limits on the m_A-$\tan\beta$ plane for (a) the nominal m_h^{125}, (b) the $m_h^{125}(\tilde{\tau})$, (c) $m_h^{125}(\tilde{\chi})$ and (d) m_h^{125} (alignment) benchmark scenarios, taken from Reference [74]. The exclusion regions are derived from the predicted light Higgs mass contours (solid green line), Higgs coupling measurements (shaded green) and direct search for $H/A \rightarrow \tau\tau$ from CMS and ATLAS.

2.3. Physics of Tau Leptons

Similar to the heavy Higgs bosons which can decay into pairs of tau leptons, tau leptons themselves are unstable and mostly decay before reaching the inner parts of the ATLAS detector. Instead, the kinetic properties of tau leptons are reconstructed from their decay products. With an invariant mass of $m_\tau = 1776.86 \pm 0.12$ MeV and a mean lifetime of $\tau = 290.3 \times 10^{-15}$ s [25], the tau lepton is the heaviest of the leptons. Due to its large mass tau decays have a richer particle spectrum with more kinematically allowed final states compared to the lighter muons [90]. Tau leptons decay via emission of a virtual W boson into tau neutrinos, where the vector boson further decays into lighter charged leptons and lepton neutrinos but also pairs of light quarks. The Feynman diagram of this process is given in Figure 2.3.1.
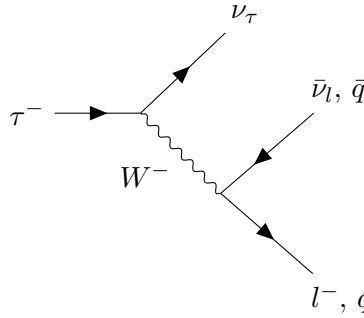

Figure 2.3.1.: Feynman diagram of the tau decay at tree level. The emitted W further decays into light leptons or quark pairs.

The light leptons from the fully leptonic tau decay are considered to be stable particles. Quarks from the W decay on the other hand undergo hadronization and form a multitude of colorless hadrons, predominantly pions and kaons. Due to the presence of the tau neutrino, this final state is called semi-leptonic tau decay. However, neutrinos are not detected in detectors like ATLAS or CMS. Hence, tau lepton decays with hadrons in the final state are referred to as hadronic tau decays.

Hadronically decaying tau leptons always decay into an odd number of charged hadrons like $\pi^\pm$ because of the conservation of charge but can be accompanied by multiple neutral mesons. However, the number of hadrons created in the tau decay is kinematically limited by the invariant mass of the tau lepton. Thus, for on-shell processes, only decay modes where the sum of the invariant mass of the decay products is equal or smaller than that of the tau lepton mass are observed. Decays with higher multiplicity are kinematically suppressed. Table 2.3.1 lists the dominant and most important decay modes of the tau lepton. With a branching ratio of 64.79 %, taus decay almost twice as frequently into hadrons than into lighter leptons. In ~ 50 % of the cases, the tau lepton decay contains one charged hadron, of which the majority are charged pions accompanied by up to 3 neutral pions, while decays in 3 charged hadrons occur with ~ 15 %. Decays with higher charged hadron multiplicity are much rarer and are usually neglected due to their small branching ratio compared to the background produced at hadron colliders. Thus, when searching for Higgs bosons decaying into tau leptons, final states where one or both tau leptons decay hadronically provide the largest branching ratio. The search presented in this thesis focuses on the fully hadronic final state which contributes to the results in Reference [24] in conjunction with the semi-leptonic final state search channel.

Decay mode	Fraction Γ_i/Γ [%]	Decay mode	Fraction Γ_i/Γ [%]
Fully leptonic decays		Hadronic decays	
$\tau^- \to e^- \bar{\nu}_e \nu_\tau$	17.82	Charge multiplicity of 3	
$\tau^- \to \mu^- \bar{\nu}_\mu \nu_\tau$	17.39	$\tau^- \to 2\pi^- \pi^+ \nu_\tau$	9.31
Hadronic decays		$\tau^- \to 2\pi^- \pi^+ \pi^0 \nu_\tau$	4.62
Charge multiplicity of 1		Charge multiplicity of 5	0.099
$\tau^- \to \pi^- \pi^0 \nu_\tau$	25.49		
$\tau^- \to \pi^- \nu_\tau$	10.82	Total leptonic	35.21
$\tau^- \to \pi^- 2\pi^0 \nu_\tau$	9.26	Total hadronic	64.79
$\tau^- \to K^*(892)^- \nu_\tau$	1.20		
$\tau^- \to \pi^- 3\pi^0 \nu_\tau$	1.04		

Table 2.3.1.: List of the most important decay modes of the tau lepton decay [25]. Note that the branching ratios do not add up to 100 % since minor decay modes are not listed.

3. The ATLAS Experiment at the LHC

3.1. The Large Hadron Colider

The Large Hadron Collider (LHC) is a two-ring particle accelerator located at the French-Swiss border near Geneva [91] and was built by the European Organization for Nuclear Research, CERN. It is designed as a synchrotron that is capable of accelerating and colliding two beams of protons or lead ions in opposite directions to energies at the TeV scale. The accelerator ring itself is installed in a circular tunnel with a circumference of 27 km and lays between 45 to 170 m beneath the surface. The tunnel was previously built for the Large Electron-Positron Collider (LEP) and consists of 8 straight sections connected by 8 arcs. Four intersection points are located along these straight segments at which the two opposing particle beams cross each other.

The two counter-rotating beams are guided in two separate beam pipes that are enclosed in one support structure. To accelerate the particles in the beam pipes, superconducting radio frequency cavities are used. Guiding the trajectory of the particle beams around a circular path of the LHC is achieved by 1232 superconducting dipole magnets, while further 392 quadrupole magnets focus the beams when entering and leaving the arc sections. Particularly strong quadrupole magnets are placed close to the intersection points to focus the beam and increase the probability of particle collisions. All magnets are made from a niobium-titanium alloy which is cooled to temperatures below 2 K using superfluid Helium. In the superconducting phase, the magnets can produce a magnetic flux density of more than 8 T.

The LHC was designed to collide beams at a Center of Mass Energy (CME) of 14 TeV when running in the proton-proton mode, which corresponds to beam energies of 7 TeV. However, the design beam energy was not directly reached after commissioning in the first run of data-taking [92]. Instead, the beam energy was increased gradually starting at 7 TeV CME at the beginning of Run-1 (2010-2011) which was raised to 8 TeV CME during the last third of Run-1 data-taking (2012). After the following long shutdown from 2013 to 2014, the proton beam energy was raised to 6.5 TeV, which increases the CME for proton-proton collisions to 13 TeV, almost matching the design collision energy. This beam energy was kept during the entire Run-2 of collision data-taking from 2015 to 2018.

Although the LHC synchrotron ring accelerates particles to their final collision energy, the collider itself is fed by a chain of pre-accelerators that raise the beam energy high enough to meet the minimum energy requirement of the LHC ring [91]. Proton beams are created at the LINAC 2 linear accelerator where they are stripped from their electrons and accelerated to an energy of 50 MeV. The beams then enter the Proton Synchrotron Booster (PSB) where their energy is increased to 1.4 GeV. In the next stage, the Proton Synchrotron (PS) accelerates the protons to 25 GeV before they enter the final injection stage and are fed in the Super Proton Synchrotron (SPS). In the SPS the beam energy is again raised to 450 GeV and the protons are injected into the LHC accelerator ring.

The proton beams in the LHC are packed in bunches containing $\sim 1.1 \times 10^{11}$ protons, with up to 2544 bunches per beam circulating the accelerator [93]. These bunches are organized in trains with a bunch spacing of 25 ns. In this configuration, the LHC was able to reach a peak instantaneous luminosity of $\mathcal{L}_{\text{inst, peak}} = 19 \times 10^{33} \, \text{cm}^{-2}\text{s}^{-1}$ which is almost twice the design luminosity.

At each of the intersection points, detectors are located that measure, record, and analyze the particle collisions. Two large general purpose-detectors, the ATLAS [94] and CMS (Compact Muon Solenoid) [95] detectors, are placed at opposite sides of the LHC accelerator ring. At the remaining intersections points the ALICE (A Large Ion Collider Experiment) [96] and LHCb (LHC-beauty) [97] detectors are located. The former detector is specialized in recording proton-lead and lead-lead collisions in order to explore the creation and behavior of quark-gluon plasma, while the latter focuses primarily on studying *b*-hadron physics. Furthermore, three smaller experiments are located within or near the cavities of the 4 larger experiments which are LHCf (LHC forward) [98], TOTEM (Total Elastic and Diffractive Cross Section Measurement) [99], and MoEDAL (Monopole and Exotics Detector at the LHC) [100]. The LHCf is located in the forward direction of each side of the ATLAS detector and aims to measure high-energy QCD processes in order to improve the Monte Carlo simulation used in modeling cosmic ray showers. The TOTEM experiment is installed in both directions of the CMS cavity, studying the proton structure by measuring the elastic and diffractive scattering cross-section of protons collisions at the interaction point at small forward angles. Located in the chamber of the LHCb is the MoEDAL experiment. Designed as a long-term experiment the detector searches for the existence of magnetic monopoles and stable massive ionizing particles by recording their trajectories in polymeric track etch detectors. A schematic overview of the LHC accelerator complex is given in Figure 3.1.1.
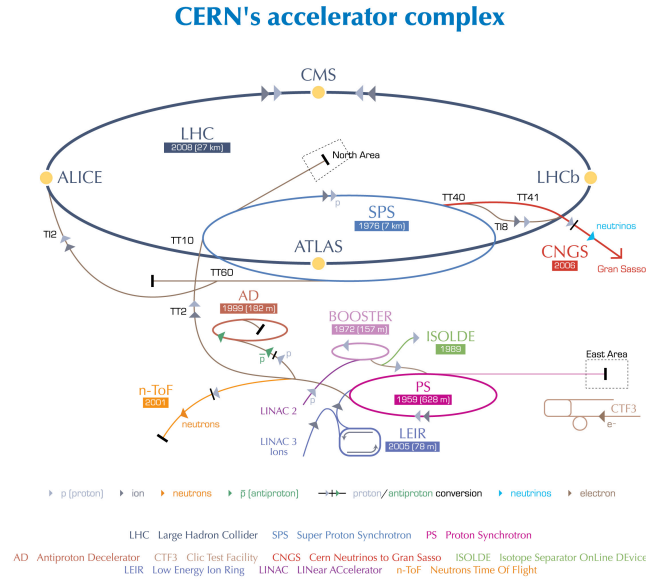
Figure 3.1.1.: Schematic overview of the accelerator complex of the LHC at CERN [101].

3.2. The ATLAS Experiment

The A Toroidal LHC ApparatuS (ATLAS) detector is a multipurpose detector located beneath the main CERN site in Meyrin [94]. Its main objective is to precisely measure physics processes created by the high energy collisions at the beam intersection point and search for new physics beyond the SM. ATLAS itself consists of multiple sub-detectors, arranged in concentric layers around the beam pipe, which are specialized in different aspects of measuring and reconstructing particles coming from proton beam collisions.

Starting with the Inner Detector (ID) system, the ID measures the trajectory of traversing charged particles. It is directly built around the beam pipe and surrounded by a solenoid magnet. Enclosing the solenoid are the electromagnetic and hadronic calorimeters. The outer layer hosts the toroidal magnet system and the muon spectrometer. The entire detector system is of cylindrical shape with a length of 44 m and a diameter of 25 m. A sketch of the ATLAS detector and its sub-systems are shown in Figure 3.2.1.
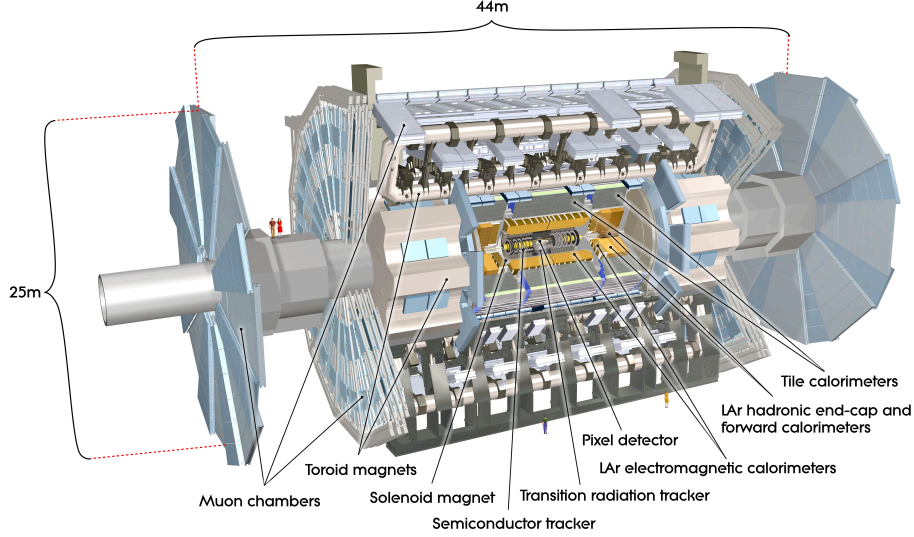

Figure 3.2.1.: Schematic cross-section of the ATLAS detector and its sub-components [94].

To determine locations within the ATLAS detector a variety of coordinate systems are commonly used. In the Cartesian coordinate system, the z-axis points in the direction of the particle beam while the x-y coordinates span the detector plane orthogonal to the z-axis, with the y-axis pointing upwards and the x-axis pointing towards the center of the LHC. The x and y coordinates are frequently replaced by polar coordinates (r, ϕ) to describe the transverse plane with the polar angle $\phi = 0$ pointing in the direction of the x-axis. Together with the z coordinate, (r, ϕ, z) form the cylindrical coordinate system. By introducing a longitudinal angle θ, positions can also be expressed in terms of spherical coordinates (R, ϕ, θ) where $\theta = 0$ aligns with the z-axis.

However, in most cases, θ is replaced by the pseudo-rapidity η defined by:

$$\eta = \frac{1}{2} \ln \left(\frac{|\boldsymbol{p}| + p_z}{|\boldsymbol{p}| - p_z} \right) = -\ln \left[\tan \left(\frac{\theta}{2} \right) \right], \tag{3.1}$$

with the absolute value of the four-momentum $|\boldsymbol{p}|$. For massless particles or particles with negligible invariant mass, the momentum can be approximated by $|\boldsymbol{p}| \approx E$. This means, that for highly relativistic particles, the rapidity $y = \frac{1}{2} \ln \left(\frac{E + p_z}{E - p_z} \right)$ approaches the pseudo-rapidity. Choosing η over θ yields two major advantages: the particle production at hadron colliders is roughly constant as a function of η, while differences in η of two particles $\Delta \eta = \eta_1 - \eta_2$ are invariant under Lorentz transformation in the z-axis direction. Therefore, measures in $\Delta \eta$ are then invariant under the different energy sharing between the colliding partons in the hard proton-proton scattering. A sketch of the coordinate systems at ATLAS is shown in Figure 3.2.2. Radial difference between two locations in the ATLAS detector can be expressed in terms of ϕ and η by the radial distance parameter:

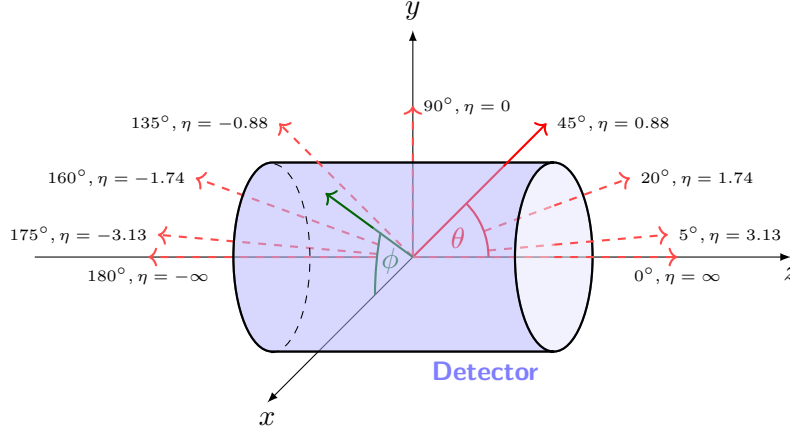$$\Delta R = \sqrt{(\phi_1 - \phi_2)^2 + (\eta_1 - \eta_2)^2}, \tag{3.2}$$

Figure 3.2.2.: Sketch of the ATLAS coordinate systems [94].

which is also invariant under Lorentz transformation along the z-axis.

In the following section, an overview of the individual detector components is given.

3.2.1. The Inner Detector

The Inner Detector (ID) is the detector system closest to the beam pipe and aims to measure the trajectory of charged particles emerging from the proton-proton collisions [102]. The ID itself consists of three different types of sub-detectors, each measuring traversing charged particles with different granularity. All ID components are contained within a solenoid magnet which produces a magnetic field of 2 T along the z-axis, bending the flight path of charged particles. Based on the Larmor radius of the particle trajectory the sign of the charge and the particle momentum can be calculated. An overview of all different ID component parts is given in Figure 3.2.3.
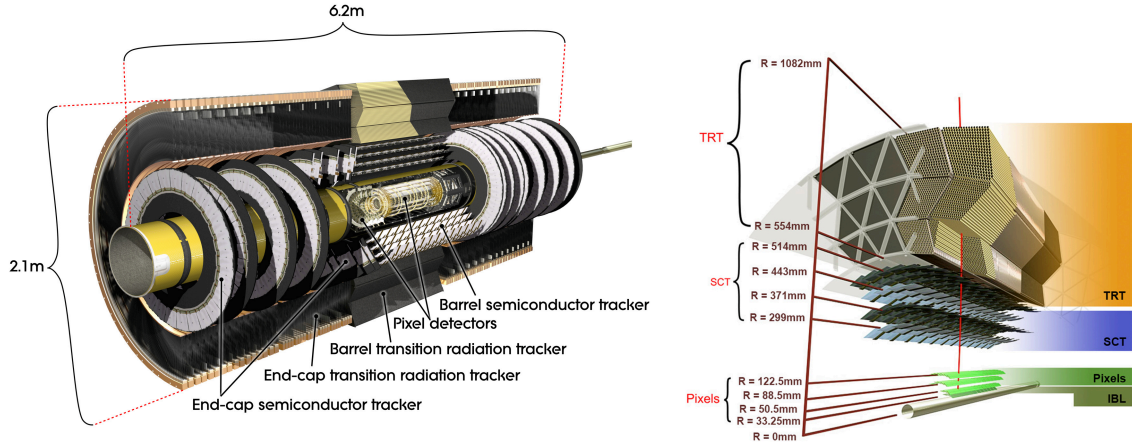
Figure 3.2.3.: Cross-sectional view of the ATLAS Inner Detector showing the overall dimension and sub-detector placement (left) as well as the cross-sectional view of the transverse plane in the barrel region (right) [102, 103].

The pixel detector: The innermost part of the ID is the pixel detector [104, 105] which is separated into a barrel and end-cap region, together covering a range of $|\eta| < 2.5$. In the barrel region, the detector is made up of 3 concentric layers of overlapping pixel modules

while the two end-caps on each side consist of three disks holding pixel modules. Each module hosts silicon-based sensor arrays as well as the read-out and front-end electronics and is attached to a support structure. The sensors are designed as an array of bipolar diodes of n-type bulk material with a p^+ region on the front side and an n^+ region on the readout side, measuring 256 µm in thickness. The diodes are operated in reverse bias mode creating a depletion region between the doped sides, with an operating bias voltage of up to $V_{\text{bias}} \approx -600$ V depending on the amount of radiation the module was exposed to. Charged particles passing through the sensors induce charges in the depletion area which are drained by the electrodes and create a measurable current. In total there are approximately 80 million pixels and read-out channels contained within the Pixel Detector, designed to deliver an intrinsic spatial resolution of ~ 10 µm in r-ϕ and 115 µm in z [103].

During the long shut-down between the LHC runs 1 and 2 the Innermost B-Layer (IBL) was introduced as the fourth pixel layer alongside the new and thinner beam pipe [106,107]. The IBL deploys two different sensor designs: planar sensors, similar to the sensors of the adjacent Pixel Detector layers, are used in the central region, while at the edges sensors with the new 3D design are mounted. In sensors using the 3D design, the electrodes run in columns through the substrate instead of being positioned at the surface. This allows for improved radiation hardness and reduces the impact of the Lorentz angle on the cluster size. The IBL contributes about 12 million channels, covering a range of up to $|\eta| < 3$. Adding a new layer close to the particle beam improves the track reconstruction efficiency which results in significantly improved b-tagging and vertex reconstruction performance.

The semiconductor tracker: The Pixel Detector is followed by the Semiconductor Tracker (SCT) [108, 109]. Similar to the Pixel Detector the SCT consists of 4088 modules arranged in four concentric layers in the barrel region and 9 disks in the two end-caps, covering a region up to $|\eta| < 2.5$. Each module hosts four sensor chips with strips made of p-type doped silicon on n-type bulk material with an average pitch of 80 µm. For most modules, the strips of two sensor chips are daisy-chained together forming strips with a length of about 12 cm. Two sensors are glued together back-to-back at a stereo angle of 40 mrad which measurements are combined to determine the space-point of a particle hit. In the barrel region, the sensors are of rectangular shape with the strips aligned to the direction of the magnetic field created by the solenoid, while the sensors in the disks are of trapezoidal shape with the strips pointing in the radial direction. The sensors are operated in reversed bias mode with a nominal operating voltage of $V_{\text{bias}} = -150$ V which is increased depending on the module irradiation. In total, the SCT provides an intrinsic resolution of 17 µm in r-ϕ and 580 µm in z (r) in the barrel (end-cap) region [94]

The transition radiation tracker: The Transition Radiation Tracker (TRT) makes up the outermost part of the ID and is designed to provide track information in the r-ϕ plane [110,111]. The TRT consists of 298304 drift tubes with a diameter of 4 mm containing a 31 µm thick, gold-plated tungsten wire. In the barrel region of $|\eta| < 1$ the straws are oriented in the beam direction and tightly packed around the TRT, forming a layer with a thickness of about 520 mm [112]. Each side of the barrel is followed by end-caps which cover the region of $1 < |\eta| < 2$ and where the straws are aligned perpendicular to the beam, mounted on 20 wheels containing 8 straw layers each [113].

Between the inner wire and the straw walls, an electric potential of around -1.5 kV is applied. Most straws are filled with a xenon-based gas mixture (70 % Xe, 27 % CO_2 and 3 % O_2). However, due to leaks observed in some detector parts after the end of Run-1, the xenon-based filling gas in areas experiencing high gas leakage was replaced with an argon-based gas mixture (70 % Ar, 27 % CO_2 and 3 % O_2) [114]. Particles crossing the

straws cause the gas to ionize along the particle trajectory. The gas ions are collected by the anode wire, creating a drift current which is measurable as a pulse. Two thresholds, high and low, are defined depending on the height of the pulse over which the Time-Over-Threshold (TOT) is measured. The low threshold TOT measurements are used for track reconstruction where the track coordinate is obtained by exploiting the correlation of the drift time and the drift radius relative to the anode wire. Thus, the TRT achieves a position accuracy of 130 μm for charged particles with $p_T > 0.5$ GeV [111].

The TRT also provides excellent particle identification capabilities. The spaces between the straws are filled with polymer fiber sheets (barrel) and foils (end-cap). Charged particles passing through the interface of the polymer media emit Transition Radiation (TR) in form of soft X-rays which get absorbed by the filling gas causing an increase of high threshold TRT hits. Since the intensity is dependent on the γ-factor of the particle, the measurement of TR allows the differentiation of high γ-factor electrons from pions which generate significantly less TR. Thus, an electron identification probability can be calculated based on the high threshold TRT hits.

3.2.2. The Calorimeter System

The ATLAS calorimeter system surrounds the inner solenoid magnet [94]. Its main purpose is to absorb showers caused by electromagnetically and hadronically interacting particles and measure their energy. Additionally, it also the reduces punch-through of particles other than muons to the outer muon spectrometer. The calorimeters also provide the granularity to measure the shape of these particle showers which are reconstructed as jets. The calorimeter system is separated into the inner EM Calorimeter (ECAL) and outer Hadronic Calorimeter (HCAL) subsystems which are optimized to absorb electromagnetically or hadronically interacting particles. An additional Forward Calorimeter (FCal) is placed on each side of the detector around the beam pipe to enable jet energy measurements in the forward regions with $|\eta|$ up to 4.9. Figure 3.2.4 provides an overview of the different calorimeter systems in the ATLAS detector. In the following, a description of the calorimeter systems is given.

Figure 3.2.4.: Cross-sectional view of the ATLAS calorimeter systems [94].
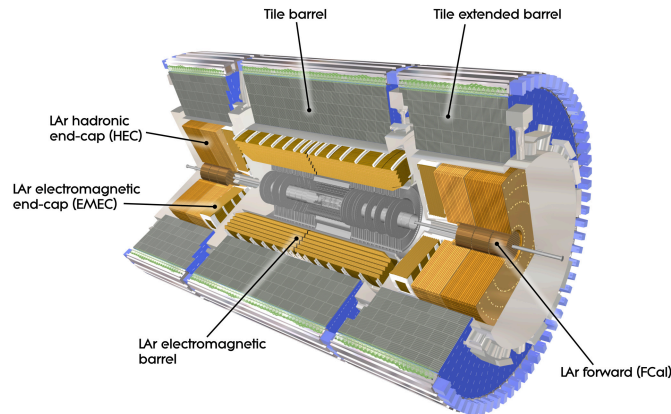
LAr EM calorimeters: The Liquid Argon (LAr) EM calorimeter is a sampling calorimeter that is divided into a barrel region, covering $|\eta| < 1.475$ and two end-cap regions extending the coverage to $|\eta| < 3.2$ [94, 115]. While the barrel calorimeter is hosted in its own cryostat, the end-caps share the same cryostat as the hadronic end-cap and forward

calorimeter. In the calorimeter, lead plates enclosed by stainless-steel sheets are used as an absorber material where the gaps between the absorber plates are filled with liquid argon as an active detector medium. Three-layered copper read-out electrodes are placed between two absorber plates and held in place by spacers, thus dividing the LAr gap into two chambers. The outer copper plates are connected to the high voltage supply and provide a potential difference of $-2\,\mathrm{kV}$ while the inner electrode is capacitively coupled and serves as a read-out channel. High energy electromagnetically interacting particles crossing the EM calorimeter interact with the absorber material and produce a shower of secondary particles along its trajectory until it is fully absorbed. These lower energy secondary particles create ions in the LAr active medium which drift to the high-voltage electrodes and are then detected as pulses on the readout electrode. If the particle gets fully absorbed its energy can be reconstructed from the signal measured by the active medium. In order to achieve a homogeneous energy reconstruction efficiency over a wide spatial range, the plates and electrodes are folded and stacked with an accordion-like geometry.

The barrel region consists of 3 layers with axial folds parallel to the z-axis. The first layer is designed for high granularity in η of $0.025/8 \times 0.1$ in $\Delta\eta \times \Delta\phi$ for $|\eta| < 1.4$. In the region of $1.4 < |\eta| < 1.475$, plates with a granularity of 0.025×0.025 are used. The second layer is thicker than the first layer, thus absorbing the largest energy fraction of an electromagnetic shower. It achieves a granularity of 0.025×0.025 for $|\eta| < 1.4$ and 0.075×0.025 in the barrel-end-cap transition section of $1.4 < |\eta| < 1.475$. The third layer absorbs the upper part of the EM shower but at a coarser granularity of 0.05×0.025 in $\Delta\eta \times \Delta\phi$.

The two end-caps consist of two co-wheels separated at $\eta = 2.5$ with the outer wheel covering $1.475 < \eta < 2.5$ and the inner wheel $2.5 < \eta < 3.2$. Within the precision region of $1.5 < \eta < 2.5$, the outer wheel has three longitudinal layers with the middle layer matching the granularity of the barrel.

A presampler layer stretches over the entire range of the LAr calorimeter forming the innermost part of the ECAL. It consists of one active LAr layer with a thickness of $1.1\,\mathrm{cm}$ in the barrel region and $0.5\,\mathrm{cm}$ in the end-cap region. It is used to correct the energy of electrons and photons and provides a granularity of 0.025×0.1 in $\Delta\eta \times \Delta\phi$. In total the LAr ECAL has a thickness measured in radiation length of at least $22\,X_0$ reaching up to $38\,X_0$ at $\eta = 2.5$.

Tile calorimeter: The tile calorimeter is part of the hadronic calorimeter system [94, 116]. Similar to the LAr ECAL it is designed as a sampling calorimeter with steel as the absorber and plastic scintillator as the active medium. The barrel region covers a range of $|\eta| < 1$ which is followed by two extended barrels on each side with a range of $0.8 < |\eta| < 1.7$. Scintillating tiles are sandwiched between steel plates. The steel-tile assemblies are organized in cells forming 3 layers with the tiles aligned in the radial direction. Typically the tiles of each cell are grouped by fiber optic cables and read out by one photomultiplier for each edge [117]. Between the gaps of the barrel and the barrel extension are smaller steel-tile or tile-only cells placed to recover some acceptance in the crack region.

With an inner radius of $2.28\,\mathrm{m}$ and an outer radius of $4.25\,\mathrm{m}$, translating to a thickness of 9.7 hadronic interaction lengths at $\eta = 0$, the tile calorimeter has good absorption capabilities while also providing a reasonable granularity in $\Delta\eta \times \Delta\phi$ of 0.1×0.1 in the first two layers and 0.2×0.1 in the last layer. Thus, it plays a crucial role in reconstructing the shape and energy of hadronic showers.

LAr hadronic end-cap: The LAr hadronic end-caps are detector wheels placed on each side of the LAr ECAL end-caps, covering a range of $1.5 < |\eta| < 3.2$ [94, 115, 118]. Each wheel is divided into two sub-wheels in the longitudinal direction. It is designed as a sampling calorimeter with flat copper sheets as absorber material and LAr as an active detector medium. Within the active medium, three electrodes divide the LAr-filled gaps into 4 drift zones. Each electrode is individually supplied with a typical operating voltage of $-1.8\,\text{kV}$ and is connected forming an electrostatic transformer. The middle electrode hosts readout pads of the size 0.1×0.1 for $|\eta| < 2.5$ and 0.2×0.2 in $\Delta\eta \times \Delta\phi$ for higher pseudo-rapidity regions which also determines the granularity of the hadronic end-cap detector.

LAr forward calorimeter: Contained within the same cryostat as the LAr ECAL and HCAL end-caps are the LAr forward calorimeter system [94, 115]. One FCal is placed on each side of the detector and consists of three $45\,\text{cm}$ long submodules stacked in a longitudinal direction followed by a copper-alloy shielding to minimize punch-through into the muon spectrometer. The first module, FCal1, uses a copper matrix as the absorber and is optimized to absorb electromagnetic showers. The other two modules, FCal2 and FCal3, are hadronic calorimeters optimized for large absorption lengths, which is achieved by mainly using tungsten as absorber material.

The FCal1 is made out of copper plates stacked longitudinally with holes running parallel to the beam pipe. Electrodes are inserted in the holes which consist of an outer copper pipe and an inner copper rod with a LAr-filled gap.

The hadronic FCal2 and FCal3 modules are made from two copper end-plates which are connected by the copper electrode pipes. To increase the tungsten content, the space between the electrodes is filled with tungsten slugs while the copper of the inner electrode rods is replaced with tungsten. In total, the three modules together have a thickness of approximately 10 hadronic interaction lengths.

Multiple electrode rods within a module (9, 6, or 4) are combined to one readout channel, resulting in a total of 1762 channels per side. Due to the nature of its design, the FCal provides varying granularity over η with the lowest granularity of $\Delta x \times \Delta y = 5.4\,\text{cm} \times 4.7\,\text{cm}$ reached at $3.32 < |\eta| < 4.6$.

3.2.3. The Muon Spectrometer

The ATLAS Muon Spectrometer (MS) is the outermost part enclosing the calorimeter system [94, 119]. It aims to precisely measure and identify muons which mostly pass the subjacent detector layers without being absorbed. Four different detector designs are deployed throughout the MS system: Monitored Drift Tubes (MDT) and Cathode Strip Chambers (CSC) for precision tracking, as well as Resistive Plate Chambers (RPC) and Thin Gap Chambers (TGC) for fast muon event trigger capabilities. These modules are placed around and within the toroidal magnet system. The toroid magnet itself consists of a large superconducting barrel magnet and two end-cap toroids producing a magnetic field of approximately 1.5 - $5.5\,\text{Tm}$ in the barrel and 1 - $7.5\,\text{Tm}$ in the end-caps which bends the trajectory of traversing muons in the η plane. An overview of the MS system is given in Figure 3.2.5.

The MS is separated into a barrel region ($|\eta| < 1$) and end-cap regions ($1 < |\eta| < 2.7$). In both regions, MDT modules are primarily used for precision tracking. A MDT module consists of 3-4 layers of tubes mounted on each side of a support frame which also acts as a spacer. The tubes are approximately $30\,\text{mm}$ in diameter, filled with an Ar-CO_2 gas mixture (93/7), with a $50\,\mu\text{m}$ wide gold plated coaxial tungsten-ruthenium wire running over the length of the tube. The tubes are designed to be operated at a potential difference of $3080\,\text{V}$
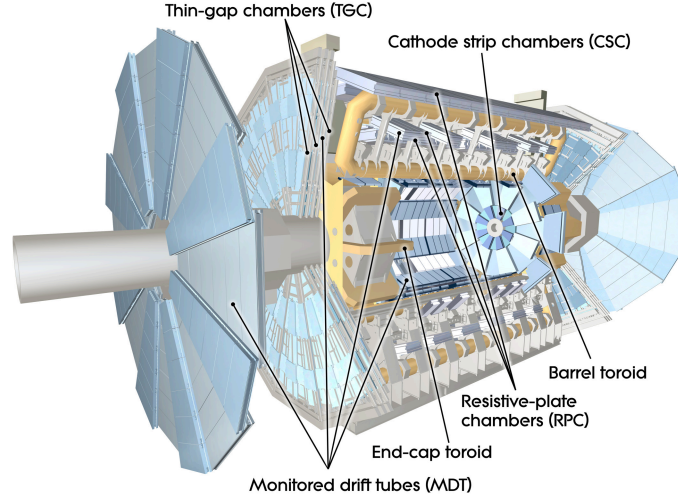
Figure 3.2.5.: Cross-sectional view of the ATLAS muon spectrometer [94].

between the wire and the tube. Muons traversing the tubes ionize argon atoms which drift to the wire where they are picked up as an electric pulse. Depending on the pulse shape and duration the drift radius can be measured with a design precision of $\sim 80\,\mu$m. In the barrel region, three layers of rectangular MDT modules are placed before, within, and outside the toroid magnet with the tubes oriented in the ϕ-direction. The end-cap region consists of 3 wheels with trapezoidal MDT modules with the inner wheel placed on the inside of the end-cap toroid magnet and the other two on a large support structure on the outside of the magnet system An additional smaller wheel is placed between the first and second wheel to improve the coverage in the barrel-end-cap region.

The ring closest to the beam pipe of the inner wheel is equipped with CSC modules instead of MDT modules due to their higher count rate and better radiation tolerance. The CSCs are multi-wire proportional chambers consisting of an Ar-CO$_2$-filled chamber with cathode strips and radially running anode wires. Each module is made out of four layers of CSC chambers. In the second CSC layer, the anode wires run parallel to the strips which allow for measuring the ϕ component. When applying the operating voltage of $1.9\,$kV between wire and strips, muons passing through the gas cause charge avalanches to form between the cathode and anode. The resulting signal is read out at the cathode strips. CSC modules are designed to achieve a resolution of $\sim 40\,\mu$m in the bending plane.

To trigger events with high energy muons, fast operating trigger chambers are deployed throughout the MS which provide coarser location and momentum measurements. In the barrel region the, middle and outer layers of MDT modules are equipped with RPC modules. A RPC consists of two resistive plastic layers with a $2\,$mm wide gap filled with a gas mixture of tetrafluoroethane, isobutane and sulfur hexafluoride. The resistive plates are coated with graphene electrodes which apply an electric field of $4.9\,$kV/mm. Similar to the CSC, traversing muons cause charge avalanches in the gas. Readout strips mounted on each side of the restive plat, which are capacitively coupled to the RPC chamber, collect the signals induced by the avalanches from which the space point coordinates of the muons are derived. Each RPC module consists of two radially stacked RPCs which translates into 6 measurements along each muon trajectory.

The MDT chambers of the end-cap wheels are accompanied by TGC modules to trigger events containing muons, but also to provide complementary measurements of the pseudo-rapidity angle. Similar to CSC the TGCs are multi-wire proportional chambers filled with a highly quenching gas mixture of CO$_2$ and n-pentane. On one side of the chamber are

readout strips running orthogonal to the wires. A TGC module consists of multiple layers of chambers. Tree layers of TGC modules are placed around the second MDT wheel, with one placed in front and two behind the main wheel, while an additional inner layer of TGC modules is placed in front of the innermost MDT wheel. In total the TGC system is designed to provide an azimuthal resolution of 2-3 mrad. The combined RPC and TGC trigger chamber system covers a total pseudo-rapidity region of $|\eta| < 2.4$.

3.2.4. ATLAS Forward Detectors

In addition to the main detector structure, four forward detectors are placed in both directions of the beam pipe: LUCID-2 (LUminosity Cherenkov Integrating Detector) [120], the ZDC (Zero Degree Calorimeters) [121], the ALFA (Absolute LuminosityFor ATLAS) detector [122], and the AFP (Atlas Forward Proton) detector [123]. An overview of the location of the forward detectors with respect to the intersection point is given in Figure 3.2.6.
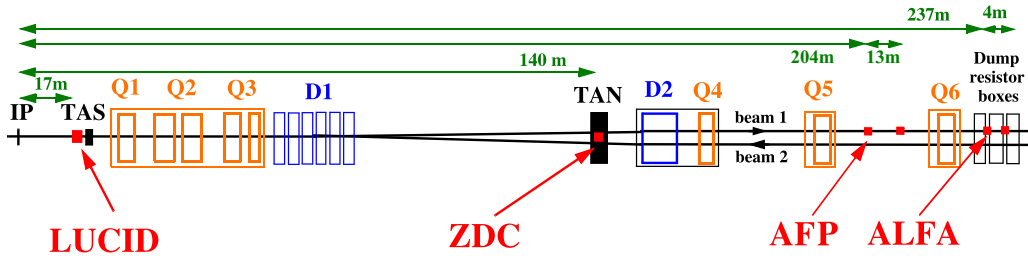

Figure 3.2.6.: Overview of the ATLAS forward detectors showing their locations along one side of the beamline. The figure is taken from Reference [94] and is modified to include the AFP detectors [123].

The LUCID-2 detector is the forward detector closest to the collision point and located within the ATLAS detector between the middle and outer MS wheel, inside the shielding. It consists of 16 photomultiplier tubes per side placed around the beam pipe. The main purpose of the detector is to provide a fast and precise measurement of the luminosity delivered to the ATLAS detector [93]. This is done by measuring the Cherenkov radiation produced by inelastically scattering protons when passing through the quartz windows of the photomultipliers. The luminosity can then be calculated from the inelastic cross-section measurements via the optical theorem.

Located within the TAN (Target Absorber Neutral) absorber on both sides of the beam pipe is the ZDC detector. Its main purpose is to measure very forward neutrons during heavy-ion runs in order to determine the centrality of the ion collisions and provide minimum-bias trigger capabilities. During runs in proton-proton mode, the detector can be used for initial beam tuning and as a way to locate collisions along the z-axis without evaluating the data of the tracking detectors.

The AFP and ALFA detectors are furthest away from the intersection point located at one branch of the beam pathway with the AFP detectors placed between the quadrupole magnets Q5 and Q6 and ALFA placed behind Q6. Both detectors follow a Roman pot design and aim to measure elastic and diffractive proton scattering in the forward direction, which allows measuring the elastic and diffractive cross-section. Additionally, by measuring diffractive proton scattering interesting physics can be investigated like the search for pomeron particles.

3.3. Trigger System of the ATLAS Detector

During the Run-2 operation of the LHC proton bunches within a bunch-train were collided approximately every 25 ns, resulting in a collision rate of 40 MHz [124, 125]. However, the rate at which the detector components can be read out is limited by the physical properties of the detector and read-out electronics as well as by the available computational power and bandwidth needed to store the collected data. Thus a preselection needs to be applied to only select events containing interesting physics processes. To reduce the read-out rate to a maintainable level a two-staged trigger system is deployed which schedules the full detector read-out based on predefined online trigger decisions. An overview of the ATLAS trigger system is given in Figure 3.3.1.
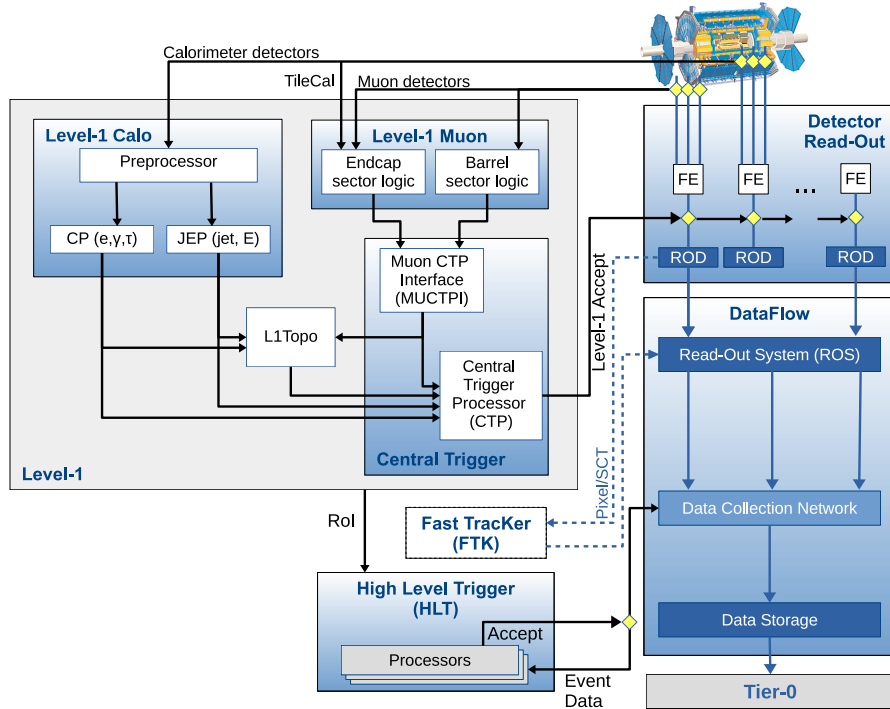

Figure 3.3.1.: Overview of the ATLAS trigger system [125]. It is designed as a two-stage trigger system. The FTK (Fast TracKer) [126] was commissioned during Run-2 but not yet used in HLT trigger decisions.

The first stage is formed by the hardware-based Level-1 (L1) trigger which is divided into a calorimeter (L1Calo) and muon (L1Muon) trigger sub-systems. Decisions in the L1Muon trigger are derived from measurements of the TGC and RPC modules of the MS. Coincidence measurements between the inner and outer MS trigger module layers as well as the tile calorimeter allow for good separation of muon signals from the background. The L1Calo decisions are based on the reduced-granularity calorimeter input which is processed in parallel in the Cluster Processor (CP) and Jet/Energy-sum Processor (JEP). The former provides initial identification capabilities to separate clusters from taus, electrons, or photons while the latter identifies jets and calculates the missing transverse energy of the event. While L1Muon and L1Calo trigger on physical properties like p_T, the L1Topo triggers events based on the topological structure of the trigger objects reconstructed at the previous L1 trigger stages. If interesting events are found that pass the L1 trigger decision the Central Trigger Processor (CTP) accepts the event causing the entire detector

to be read out. In this case, the front-end electronics send the data to Read-Out Drivers (ROD) for initial formatting before detector data is temporally stored in Read-Out System (ROS). Additionally, the L1 trigger forms Regions of Interests (ROI) parameterized in ϕ and η to aid the decision-making in later trigger stages. In total, the L1 trigger decision reduces the rate at which the detector is read out to about 100 kHz.

After the events are preselected by the L1 trigger, a software-based High-Level Trigger (HLT) is deployed using the higher granularity information stored in the ROS as well as the RoI. From the input data, the HLT reconstructs physics objects such as muons or electrons on which various kinetic cuts and identification algorithms are applied. Multiple HLT decisions are deployed consecutively forming a trigger chain that aims to select certain physics objects passing specific kinetic and topological cuts. Since the algorithms of the HLT are computationally more expensive than the one of the L1 trigger, they are computed in parallel on a batch farm. If an event is accepted by one of the HLT trigger chains it is written out to the permanent storage, reducing the read-out rate to 1.2 kHz.

Since only limited bandwidth is available to write out data to the permanent storage, some triggers can be prescaled to reduce their acceptance rate. A prescale-factor thus determines the probability that an accepted event gets written out. Most high-level trigger selecting for specific physics objects come with increasing kinetic threshold cuts, for example HLT tau triggers that apply cuts on the reconstructed transverse momentum of the tau candidate of 80, 125, or 160 GeV. The lowest unprescaled trigger then references the lowest threshold HLT witch has a prescale-factor of one.

Usually, multiple collisions are captured during one read-out cycle of the detector alongside the hard scatter event that triggered the read-out. These overlapping collision events are called pile-up events which can be classified into two categories. Firstly, pile-up which is caused by multiple scatter events within the same bunch crossing as the hard scatter event is called *in-time* pile-up. Contrary, pile-up events recorded from bunch collisions before or after the hard scatter event are called *out-of-time* pile-up. In an analysis, both sources are considered simultaneously as pile-up events and are usually parameterized by the mean number of interactions per bunch crossing $\langle \mu \rangle$.

3.4. Data Taking at ATLAS

During Run-2 the ATLAS detector collected an integrated luminosity of 147 fb^{-1} of the 156 fb^{-1} total luminosity delivered by the LHC [93]. After the application of data quality selections (see Section 7.2.1) a total of 139 fb^{-1} of data is available for physics analyses with an associated uncertainty of 1.7 %. The data has been taken over the course of four years from 2015 to 2018 with varying run conditions such as the peak instantaneous luminosity and pile-up. The total integrated luminosity is primarily determined by the LUCID-2 detector measurements and is aggregated with measurements of the ATLAS calorimeter system. On average the mean number of interactions per bunch crossing over all data-taking periods is $\langle \mu \rangle = 33.7$. Figure 3.4.1 shows the accumulated integrated luminosity and pile-up distribution over the data-taking periods.

At the ATLAS detector, the smallest continuous block of data considered is called a luminosity block. One luminosity block corresponds to a fixed time interval of approximately one minute of data-taking and also resembles the smallest unit of data for which luminosity measurements are available. Multiple luminosity blocks form a run which is identified by a unique 6 digit run number. These runs cover a time period starting before the proton beam injection and ending with dumping the beam [128]. A list of all data runs on which the search for heavy neutral Higgs bosons is based can be found in Appendix B.2.

During the data-taking, the status of the detector, proton beam, and LHC magnet
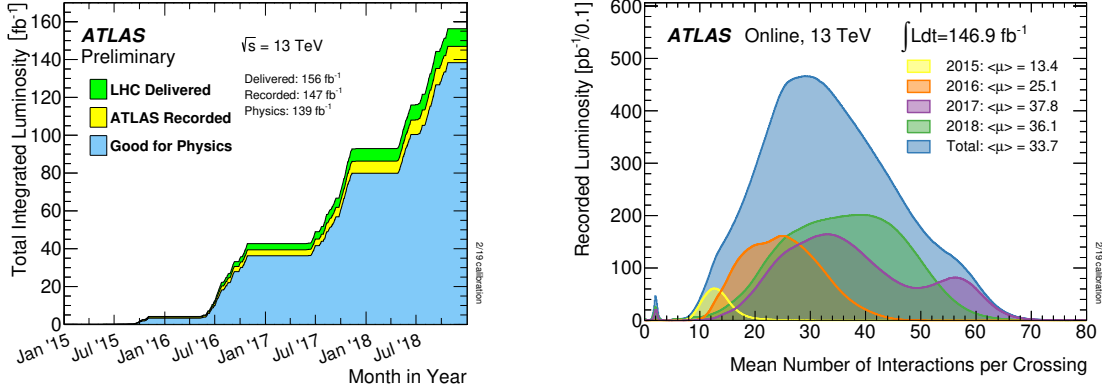
Figure 3.4.1.: Cumulative integrated luminosity (left) and pile-up (right) measured during the Run-2 data-taking from 2015 to 2018 [127].

system is constantly monitored. Based on the operation status a data quality assessment is conducted. The main goal is to provide a list of luminosity blocks in which the detector was fully operational [128, 129]. This list is given in XML format and is called Good Run List (GRL) containing all luminosity blocks approved to be used for physics analyses.

3.5. Monte Carlo Simulation

Estimating contributions of background and signal processes requires simulating the proton-proton collisions at the LHC using Monte Carlo generators [130]. In fact, in many cases simulating specific processes like top-quark production is the only way of reliably estimating background contributions while almost all searches for new physics rely on Monte Carlo simulated signal events. Hence, the generation and simulation of events play a crucial part in searches conducted at ATLAS.

The simulation of events is a multi-staged process that is managed by the ATHENA software framework [131–133]. In a first step events of a specific hard scatter collision process are generated by using Monte Carlo generators which produce possible initial and final state particles based on the matrix element calculations. Generators responsible for the initial part of the event generation are also called Matrix Element (ME) Monte Carlo generators. The hard partons originating from the hard scatter event are usually unstable and undergo hadronization and radiative corrections which produce particle showers, consisting of hadrons, called jets. The hadronization and showering of the partons are simulated by Parton Shower (PS) Monte Carlo generators. Some Monte Carlo generators such as PYTHIA 8 [134] or SHERPA [135] are designed as multi-purpose generators which cover both ME and PS calculations. However, many generators like MADGRAPH5_AMC@NLO [136] are only used to calculate the matrix element of the hard scattering process. Events generated by these programs have to be interfaced with another generator in order to apply the parton showering. Most ME and PS generators simulate collision events at a fixed order in the underlying perturbative theory and use externally provided PDF sets to model the parton content of the hadrons. These PDFs are derived from multiple measurements as the parton density functions can not be derived easily by the first principles of the underlying QCD theory.

Besides the hard scatter process, softer interaction processes are also taken into account to model the complete collision event. These soft interactions include contributions from Initial State Radiation (ISR), Final State Radiation (FSR), and Multi Parton Interaction (MPI), which describe additional lower energy radiation and hard scatter events within the

same proton-proton collision as the main scatter event. These processes are collectively referred to as the underlying event. The underlying event is also generated by the Monte Carlo generators used during the event generation and is usually applied in the PS stage. Since the underlying QCD processes are difficult to model by perturbative calculations, the generator relies on an effective description of low-energy parton shower and underlying event. This effective model can be tuned by varying free parameters such as factorization and renormalization scale or the momentum cut-of up to which the partons decay is propagated. The parameters are chosen based on comparisons with data. One example is the A14 tune which is frequently used to configure the PYTHIA 8 shower generator [137]. A visual representation of a hard scatter event including the underlying event as well as radiative corrections and parton showering is given in Figure 3.5.1.
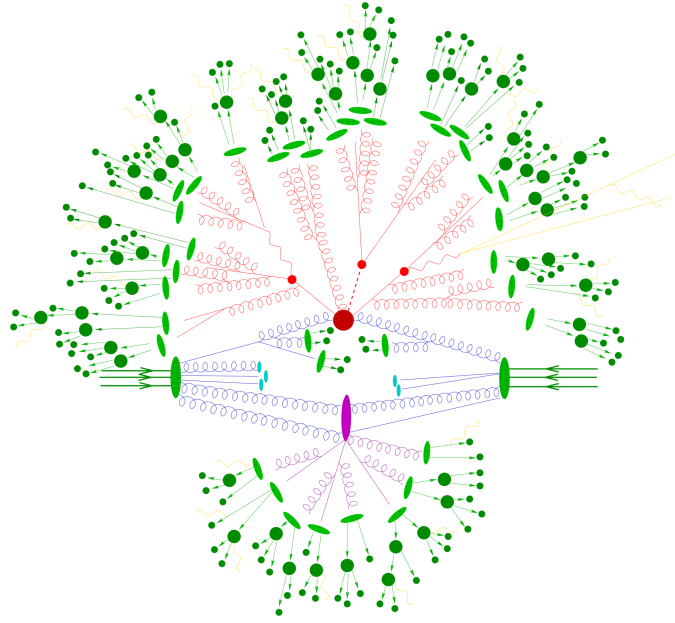

Figure 3.5.1.: Schematic depiction of a simulated $t\bar{t}h$ event at the proton-proton collider [138] with proton beams coming in from left and right (green arrows). The partons of the proton interact in the hard scatter event (large red circle) from which the final state products arise (small red circles). Partons created by the interaction emit additional QCD radiation before undergoing parton showering (light green ellipses). The resulting hadrons can further decay in more stable particles (dark green circles). In addition to the hard scatter event, the residual parton of the protons can initiate secondary interactions which are part of the underlying event (purple).

After the hard scatter and underlying events are generated, the detector response is simulated. This process requires a high-detail model of the entire ATLAS detector, consisting of the active and passive detector material, support structure, and magnetic fields. The detector geometry is implemented using the GEOMODEL software package [139, 140] and is interfaced to the GEANT4 framework which simulates the detector response [141–143].

To achieve high accuracy, the evolution of particle decays and the detector response is fully simulated within the GEANT4 framework. However, the full simulation of the detector response is very computationally expensive and is a major time-consuming step during the event generation. Unfortunately, some studies and physics analyses require a large number of simulated events to be generated in order to achieve reasonable statistical coverage. The precision of these studies would be limited by the amount of time it takes to simulate the

full detector response. To speed up this process the ATLFAST-II simulation model can be used [133]. In this case, the simulation of the calorimeter system is conducted by the ATLAS Fast Calorimeter Simulation (FastCaloSim) package [144] while the simulation of the inner detector and muon spectrometer is still done with GEANT4. The parametric approach of FastCaloSim provides a significant increase of the event simulation speed by reducing the time needed for the detector simulation by approximately an order of magnitude while achieving good agreement with the full GEANT4 simulation.

Based on the simulated detector response, the events undergo the same reconstruction procedure as data recorded by the detector described in Chapter 4. In addition to the reconstructed event record, Monte Carlo simulations also store the truth record of particles.

To emulate the in-time and out-of-time pile-up present in data, the hard scatter event is overlayed with multiple minimum-bias events which are produced by Monte Carlo generators or directly taken from zero-bias data measurements [145]. While the latter approach is predominantly used in simulations of heavy ion collisions, samples simulating proton-proton collisions use Monte Carlo pile-up event samples which are generated by PYTHIA 8.186 [146] configured with the NNPDF2.3LO [147] parton distribution function set and using the A3 [148] generator tune.

The pile-up overlay is sampled according to the ATLAS detector run condition and the pile-up distributions measured or expected in data. To improve the granularity and statistical coverage with which the different detector run conditions are represented in the Monte Carlo simulations, the generated event samples are split into three campaigns, each sampled to match the run condition of specific data-taking periods [149]. The campaigns are denoted by MC16a, MC16d, and MC16e. Samples produced with the MC16a campaign setup match the run conditions encountered during the 2015 to 2016 data-taking periods and are generated with a pile-up profile measured during the same period. Similarly, samples of the MC16d campaign match the pile-up profile and run condition of the 2017 data-taking period. However, since the event generation and detector simulation was mostly finalized before the end of Run-2, the MC16e campaign matches the expected conditions of the 2018 data-taking period based on the extrapolation of previous periods. To further reduce a potential mismatch in the generated and measured pile-up distribution between Monte Carlo simulations and data, a pile-up reweighting procedure is deployed that corrects the simulated events with a scale-factor [150].

Similar to the data sample run numbers, Monte Carlo simulated event samples are enumerated by six-digit Dataset Identifier (DSID) numbers. Each physics process sample is assigned a unique DSID. Hence, samples that are generated with a different generation or reconstruction setup, such as different Monte Carlo campaigns, but simulate the same physics processes are also assigned the same DSID.

4. Physics Object Reconstruction

The inelastic scattering of protons accelerated by the LHC gives rise to many particles such as leptons, quarks, and bosons. A majority of these particles however are unstable and quickly decay into more stable ones, or undergo hadronization and create large showers of particles. The resulting stable particles finally reach the detector with which they interact and get absorbed in. A multitude of highly specialized algorithms is deployed to recreate the trajectories and energy of the decay particles based on the signatures left behind in the various detector parts. In searches for new physics, the reconstruction and identification of these particles play a crucial role as many hypothetic signals are not observed directly but through their decay products. Thus the performance of the algorithms used directly impacts the sensitivity of the measurements.

This chapter lays out how physics objects are reconstructed and identified at the ATLAS experiment starting from simple structures like clusters and tracks which are combined to form higher-level objects like electrons, muons, or jets.

4.1. Low-Level Physics Objects

The raw data recorded by the detector provides highly granular information about the locality of particle hits in the ID and MS as well as the energy deposited in the various calorimeter systems. From this information, the first set of low-level quantities are calculated and reconstructed. These low-level objects build the foundation from which higher-level objects like electron or muon candidates are derived. The most basic low-level objects considered and explained in this section are tracks, vertices, and calorimeter clusters.

4.1.1. Track Reconstruction

Tracks are reconstructed from hits in the inner detector [151]. The reconstruction starts by clustering hits in each layer of the pixel and SCT detector using a connected component analysis [152]. Three of these clusters are then used to form a track seed. To suppress purely combinatorial track seeds and to increase the purity of tracks created by charged particles, cuts on the impact parameter and momentum of the fitted seed are applied. A Kalman filter [153] is used on the seed tracks in conjunction with the remaining silicon hits to extrapolate the trajectory of the seed track to the TRT. The track candidates then enter an ambiguity-solving phase. In this phase, a score is assigned to the tracks to determine the goodness of the track candidate based on the trajectory fit quality and possible missing but expected clusters along the track trajectory. This score is then used to resolve cases where tracks share common clusters, preferring higher score tracks. Additionally, a neural network is deployed to identify cases where clusters are shared due to merging track trajectories. This step increases the reconstruction efficiency of tracks in high-track density environments. Tracks with too many shared clusters or failing the quality requirements of the ambiguity solver are rejected. After the ambiguity resolving phase, tracks are fitted with the high-resolution ATLAS global track fitter [154] assuming a pion hypothesis. Tracks that pass this step are added to the final track collection. Physical quantities like charge and momenta

are calculated based on the curvature of the fitted trajectory in the magnetic field of the inner detector.

4.1.2. Primary Vertex Reconstruction

The reconstruction of interaction vertices is crucial to distinguish objects originating from different interaction points. Primary vertices are defined as space points where inelastic proton-proton collisions occurred. In ATLAS the vertex reconstruction is performed in a two-stage process using reconstructed tracks passing the selection criteria described in Reference [155]. In the vertex finding stage, a vertex seed is constructed as a space point with the transverse coordinate set to the center of the beam collision point. The z-coordinate of the seed is then derived from the distribution of the closest points of approach of the tracks to the beam axis. In the second stage, an iterative fitting algorithm is applied to determine the exact position of the vertex. In each iteration tracks less compatible with vertex are weighted down, reducing the impact on the fit. If a track is incompatible with the presumed position of the fitted vertex, it is removed from the fit and used to reconstruct other vertices while the iterations continue with the reduced set of tracks until the vertex position converges. The tracks associated with the fitted vertex are then removed and the procedure is repeated starting with a new vertex seed based on the remaining tracks until no track is left or no further vertex is found. In the analysis, only the primary vertex with the highest sum of squared transverse momenta of the associated tracks, $\sum p_{\mathrm{T}}^2$, is considered as the hard scatter vertex.

4.1.3. Calorimeter Clusters

After passing the inner detector, particles will eventually reach the calorimeter. When hitting the detector material, a shower of secondary particles is created which induces signals in the active detector components. The resulting energy measurements in the detector cells are combined into clusters [156]. First, a set of cluster seeds are formed by finding cells passing a threshold selection based on the significance of the energy deposited in the cell defined by:

$$\left|\zeta_{\mathrm{cell}}^{\mathrm{EM}}\right| = \left|\frac{E_{\mathrm{cell}}^{\mathrm{EM}}}{\sigma_{\mathrm{noise,\,cell}}^{\mathrm{EM}}}\right| > 4,$$

with $E_{\mathrm{cell}}^{\mathrm{EM}}$ the deposited cell energy and $\sigma_{\mathrm{noise,\,cell}}^{\mathrm{EM}}$ the expected period-specific noise. Starting with the highest-energy cluster, neighboring cells in the same and adjacent layers are merged with the seed into a protocluster if the cell passes a relaxed significance criteria of $\left|\zeta_{\mathrm{cell}}^{\mathrm{EM}}\right| > 2$. To improve the resolution of constituents forming overlapping clusters, a splitting algorithm is deployed that allows large clusters with multiple local maxima to be separated. The resulting final set of clusters is used to reconstruct the showers in the calorimeter, left behind by electromagnetically and hadronically interacting particles.

4.2. High-Level Physics Objects

Based on low-level physics objects, high-level objects like electrons and muons are reconstructed. The building process usually follows two steps. In the first step, candidates are defined using low-level objects. In the second step identification algorithms are deployed to separate signatures of genuine true particles from those caused by misreconstruction of other sources. The identification algorithms also define different working points which allows a selection of objects with a desired truth efficiency estimated based on Monte Carlo simulations. On the analysis level, working points can be selected to increase the purity of

the signal signature searched for. The reconstructed objects like electrons or tau jets also require a dedicated energy calibration, scaling the energy of the reconstructed particles to the expected values derived from Monte Carlo simulation and data measurements.

4.2.1. Electrons

When electrons traverse parts of the detector they lose energy due to bremsstrahlung which creates secondary particles like positron-electron pairs, leaving behind tracks in the inner detector and collimated cluster entries in the ECAL. Starting with clusters in the ECAL a seed is formed if a cluster entry geometrically matches to a track in the ID [157]. To compensate for cases where the global track fit fails due to energy loss from bremsstrahlung, tracks are refitted if enough hits are present in the ID using an electron hypothesis that takes bremsstrahlung into account. In the calorimeter, clusters caused by bremsstrahlung in the vicinity of the seed cluster are identified and merged to form superclusters. The tracks are then refitted to superclusters forming electron candidates. The energy resolution of the electron candidates is improved by deploying a multivariate machine learning technique. Corrections on the energy scale and resolution are derived from $Z \to ee$ measurements.

A likelihood (LH) based identification algorithm is used to separate prompt electrons from hadron jets, photon conversions, or non-prompt electron production. The LH score is constructed from probability density functions of calorimeter and track related variables which are generated from $J/\psi \to ee$ and $Z \to ee$ Monte Carlo simulations. Predefined *Loose*, *Medium* and *Tight* working points are available that apply cuts on the LH as well as on track parameters which correspond to a signal efficiency of 93 %, 88 %, 78 % at a reference transverse energy of the electron of $E_T = 40\,\mathrm{GeV}$. In the analysis, electron candidates are only considered in the pseudo-rapidity region of $|\eta| < 2.47$ with $p_\mathrm{T} > 5\,\mathrm{GeV}$.

4.2.2. Muons

Muons are formed from hits in the ID and MS [158] by firstly reconstructing muon tracks in both subdetectors independently and then combining them to create a candidate. While the tracks described in Section 4.1.1 are used for ID tracks, a specialized algorithm is deployed to reconstruct tracks in the MS. Starting with the MDT and CSC segments, hits within a segment are fitted by a straight line. Additional information from the RPC and TGC is used to measure the track position orthogonal to the bending plane of the muon trajectory. The track of the middle segment is then extrapolated to the inner and outer segment layers. If the trajectories of two or more segments are aligned, the seed is considered to be a track candidate with exception of the barrel-end-cap transition region where already one good quality track in the MS is sufficient. Since one segment can be used to reconstruct multiple tracks in the MS, an overlap removal is deployed to mitigate double counting. However, tracks are also allowed to share segments if they are associated with two or more other, not overlapping segments.

The final muon candidates are generated by tracks from the MS and ID. By using different strategies to combine MS and ID tracks to muon candidates, four classes of reconstructed muons are defined by decreasing order of purity. To create a combined track muon candidate (CB) the MS track is extrapolated to the ID where it has to be aligned with an ID track. Segment-tagged muons (ST) are candidates where ID tracks are extrapolated to the MS and match at least one local track within a segment. For the calorimeter-tagged muons (CT), the ID track has to match a calorimeter entry where the energy deposit is consistent with a low ionizing particle hypothesis. The latter allows the recovery of muons with $p_\mathrm{T} < 100\,\mathrm{GeV}$ and $|\eta| < 0.1$ where the other methods show less sufficient recon-

struction efficiencies. Finally, the extrapolated muon candidates (ME) are generated from tracks of the MS that are loosely associated with the interaction point by extending the track trajectory. An overlap removal is deployed to remove double-counted muon candidates where CBs have the highest priority followed by ST, CT, and ME. However, since only muons in the range of $|\eta| < 2.5$ are considered in the analysis, ME muons only play a minor role as they are usually used to extend the reconstruction efficiency to the range of $2.5 < |\eta| < 2.7$.

To suppress QCD background and increase the purity of prompt muons a muon identification is performed. This identification step sets requirements on the number of detector hits, the momentum measured in the ID and MS as well as the quality of the trajectory fit. Four working points are defined with increasing signal purity: *Loose*, *Medium*, *Tight*, and *high-p_T* with signal efficiencies of 98.1 %, 96.1 %, 91.8 %, and 80.4 % respectively.

Prompt muons originating from fully leptonic decays of heavy resonances as well as tau lepton decays, usually create isolated signatures in the detector while muons from non-prompt semi-leptonic decays of hadrons are more likely to be enveloped in hadron jets causing increased activity in the ID and calorimeters. Therefore, an isolation criterion can be applied to separate prompt from non-prompt muon production. Variables used to quantify the isolation are the sum of transverse momenta of tracks and the pile-up corrected energy deposits in the calorimeter in a cone around the muon trajectory. In the analysis, a *Tight* isolation selection, applying cuts in a fixed-size cone around the muon is used. The estimated efficiency for prompt muons is 96 % while a factor 10 reduction of non-prompt processes is observed.

Scale-factors with associated uncertainties are derived from $Z \to \mu\mu$ and $J/\psi \to \mu\mu$ tag and probe measurements. A momentum and energy scale correction of reconstructed muons is determined by extracting weights to reweight simulation to measured data.

4.2.3. Jets

Jets refer to the cone-shaped clusters created by particles interacting with the absorber material of the calorimeters. In ATLAS jets are reconstructed by combining calorimeter clusters using an anti-k_t algorithm provided by the FASTJET software package [159, 160]. The anti-k_t algorithm is a sequential algorithm assigning calorimeter clusters to jets. The algorithm is seeded by calorimeter clusters that have a significant energy deposit above the expected pile-up corrected noise and exceed a threshold of $p_T > 7$ GeV [161, 162]. For seeds i, distance measurements to the surrounding clusters j are calculated by:

$$d_{ij} = \min\left(k_{ti}^{2p}, k_{tj}^{2p}\right) \frac{\Delta_{ij}^2}{R^2},$$
$$d_{iB} = k_{ti},$$

with Δ_{ij} being the angular distance in η and ϕ, k_t denoting the transverse momenta of the clusters, and an exponent p determining the general behavior of the algorithm. In the case of the anti-k_t algorithm, the parameter is set to $p = -1$. The parameter R influences the radius of the generated jets in the η-ϕ plane. The cluster with the smallest distance parameter d_{ij} is recombined with the seed. If the distance of the seed to the beam d_{iB} is smaller than to any of the remaining clusters, the seed i with its combined clusters are called a jet and are removed from the collection. The recombination is repeated until no clusters remain.

Jets selected in the analysis are clustered with a radius parameter of $R = 0.4$. Two independent sets of jets are considered using a different calibration scheme for clusters [156]. By calibrating the clusters to the electromagnetic scale (EM) the energy is weighted to

match the expected energy deposits of electrons in the calorimeter. Jets created from clusters calibrated to the EM scale are called Antik_t4EMTopoJets. To compensate for nonlinear differences in the energy deposits of hadrons compared to electrons, a local calibration weighting scheme (LCW) is used. The LCW scale provides a continuous calibration depending on the probability of clusters being caused by hadronically or electromagnetically interacting particles. Jets constructed using clusters with LCW calibration are called Antik_t4LCTopoJets. The former jets are used as a jet collection in the analysis while the latter serve as seeds for the reconstruction of hadronically decaying tau leptons.

The Antik_t4EMTopoJets are calibrated to the Jet Energy Scale (JES). In the first step, a simulation-based correction is applied by comparing the reconstructed energy with the truth energy of the jet and provide corrections depending on p_T and η. To resolve residual dependencies of the JES a sequential correction on jet observables like the energy fraction in the tile and LAr calorimeters is applied. Finally, an in-situ calibration is conducted by calculating a correction based on a direct comparison of data and simulation in an analysis described in Reference [161].

To account for differences in the Jet Energy Resolution (JER) in data and Monte Carlo simulation, a p_T smearing on jets of simulated events is applied [162]. The η-dependent resolution is extracted from data and Monte Carlo measurements of a di-jet analysis. The measured resolution considers sources from electronic noise and pile-up, statistical fluctuations in the deposited energy, and constant resolution offsets caused by energy deposits in passive detector materials or nonlinear response of the detector.

During reconstruction and calibration, steps are taken to mitigate the impact of pile-up from low p_T jet activity. Additional pile-up suppression is achieved by deploying a Jet Vertex Tagger (JVT) algorithm [163] which calculates a probability that a given jet originates from the primary event vertex.

4.2.4. *b*-Tagging

Jets originating from *b*-hadron decays are of special interest for signals with *b*-quarks in the final state. Bottom mesons, like B^0 with a lifetime of $\tau = 1.52 \times 10^{-12}$ s [25] that have a sufficiently large momentum, live long enough to decay at a distance to the vertex of the hard scatter event, creating a secondary vertex. These special properties are exploited to tag jets from *b*-hadron decays with a two-staged *b*-tagging algorithm [164]. First, low-level algorithms are deployed trying to fit the displaced vertex and reconstruct the decay chain of the *b*-meson by following the trajectory and search for its intermediate decays. Based on kinetic variables and the low-level algorithm results, high-level classifiers are trained to separate *b*-meson decays from those of *c*- and light hadrons. In this analysis, the MV2 tagger is used which provides working points for *b*-tagging efficiencies of 60 %, 70 %, 77 %, and 85 %.

4.2.5. Taus

Tau leptons can decay in both light leptons and hadrons. In the scope of this thesis, the term *tau* refers in an experimental sense to hadronically decaying tau leptons, as leptonically decaying taus are usually reconstructed as prompt muons or electrons. A complete description of the reconstruction and identification of hadronic tau decays is provided in Section 4.3. Due to neutrinos mostly passing through the detector without being measured, kinetic observables of the tau candidates are calculated with respect to the measurable part of the hadronic decay.

Charged hadrons originating from the tau decay create hits in the ID which are reconstructed as tracks. Dedicated algorithms are deployed to identify the tracks caused by the

tau decay products and separate them from tracks coming from other sources. Since the charged hadron multiplicity of the tau decay significantly impacts the shape of the following hadron jet in the calorimeter system, tau candidates are usually treated separately depending on the number of associated charged tracks. The number of reconstructed and identified tau tracks is also called *prongness*. In most analyses, only 1 and 3 prong tau candidates are considered which coincides with the dominant hadronic decay channels of the tau lepton.

4.2.6. Missing Transverse Energy

Hard scatter events produced in the local reference frame of the ATLAS detector usually occur at rest in the transverse plane of the detector since the incoming protons from the beam pipes ideally have no transverse momentum. Thus, the sum of the transverse momentum vectors $\vec{p}_\mathrm{T}$ of all objects produced by the hard scatter process should be zero. However, particles formed in the hard scatter event, like neutrinos, pass through the detector without interacting with any decor material, introducing a loss of transverse energy in the direction of the particle trajectory.

The momentum conservation in the transverse plane can be exploited to reconstruct the missing energy caused by weakly interacting particles. An algorithm is deployed to reconstruct the missing transverse energy $E_\mathrm{T}^\mathrm{miss}$ which calculates its magnitude and polar angle from different reconstructed physics objects [165, 166]. The algorithm differentiates between hard term and soft term contributions, where the former is defined by the final state objects selected in a specific analysis, like electrons, photons, muons, tau leptons, or jets. Therefore, the missing transverse momentum is defined by:

$$\vec{E}_\mathrm{T}^\mathrm{miss} = -\sum \vec{p}_\mathrm{T}^{\,e} - \sum \vec{p}_\mathrm{T}^{\,\gamma} - \sum \vec{p}_\mathrm{T}^{\,\mu} - \sum \vec{p}_\mathrm{T}^{\,\tau} - \sum \vec{p}_\mathrm{T}^{\,\mathrm{jet}} - \vec{E}_\mathrm{T}^{\mathrm{miss,\,soft}}. \qquad (4.1)$$

A dedicated overlap removal is deployed on the physics objects forming the hard term component to reduce the double-counting of energy deposits in the detector. Of particular interest are jets entering the hard term $E_\mathrm{T}^\mathrm{miss}$ calculation as they have a high probability of originating from other processes than the hard scatter event. The algorithm provides a *Loose* and *Tight* working point for the preselection of jets considered in the $E_\mathrm{T}^\mathrm{miss}$ reconstruction. In the analysis, the *Tight* working point is used where jets have to pass a threshold of $p_\mathrm{T} > 30\,\mathrm{GeV}$. Additionally, jets with $p_\mathrm{T} < 60\,\mathrm{GeV}$ have to pass a JVT quality cut that reduces contamination from non-hard scatter events.

The soft term aims at covering the remaining low energy transverse momentum particles from the hard scatter event, such as recoil particles that are not associated with one of the main physics objects included in the hard term. It is constructed purely from tracks in the ID which have to pass a threshold of $p_\mathrm{T} > 400\,\mathrm{MeV}$ and lie within $|\eta| < 2.5$. To reduce the impact of pile-up tracks on the resolution of the missing transverse energy, the tracks used in the soft term need to pass track quality cuts on the impact parameters as well as hits in the SCT and pixel detector [151]. An overlap removal is applied to mitigate double-counting of tracks in the soft term which are already associated with other high-level physics objects included in the hard term component. The final track-based soft term is then the vector sum of the transversal momentum components of the remaining tracks.

Since the missing transverse energy is a vector in the transverse plane, it is usually parameterized using polar coordinates with $E_\mathrm{T}^\mathrm{miss}$ the magnitude and the transversal angle $E_\mathrm{T}^\mathrm{miss}\,\phi$.

4.3. Reconstruction and Identification of Tau Leptons

In the search for neutral Higgs bosons decaying into pairs of tau leptons, the reconstruction and identification of taus are imperative for a high discovery potential. Since tau leptons decay within a mean lifetime of $\tau = 290.3 \times 10^{-15}$ s [25], the tau leptons mostly decay before reaching the inner layer of the detector and thus can only be detected by their decay products. Tau leptons decaying to lighter leptons will be reconstructed as prompt muons or electrons. The main concern here will be the reconstruction of hadronically decaying tau leptons. In Section 2.3 it was shown that tau leptons can decay into an odd number of charged hadrons, accompanied by neutral hadrons and one tau neutrino. Only the charged and neutral hadronic components can be detected by the EM and hadronic calorimeters while neutrinos leave the detector without interacting with any of its components. Additionally, charged particles from the tau decay interact with the components of the pixel, STC, and TRT detector, leaving tracks in the inner detector. Therefore, identification of tracks from tau decays and the association with the calorimeter jets is an important part of the tau reconstruction.

This section covers the default algorithms deployed for the hadronic tau reconstruction and identification. In Chapter 6, improvements to the default procedure of associating tracks from hadronic tau decays are presented. Thus, special emphasis is placed on explaining the tau track identification as well as the algorithm used to match reconstructed tau jets and tracks to truth particles.

4.3.1. Tau Truth Matching

To understand the performance of algorithms used to reconstruct and identify hadronically decaying tau leptons in Monte Carlo simulation, a consistent definition of the underlying truth event is paramount. Therefore, reconstructed tau candidates need to be associated with the true tau decay. The construction of the true tau objects starts by selecting a generated tau particle from the Monte Carlo truth record which serves as a seed [167]. Depending on whether the tau particle decays into lighter leptons or hadrons, such as pions and kaons, the seed is classified as a leptonically or hadronically decaying truth tau where the latter case is of importance for tau reconstruction and identification. A truth matching is performed by comparing the angular separation of the momentum vector between the reconstructed tau jet with the true tau object. If a true tau object is found that fulfills the criteria $\Delta R \left(\tau_{\text{Reco}}, \tau_{\text{Truth}} \right) \leq 0.2$ then the reconstructed tau jet is truth-matched and associated with the true tau object. Truth decay multiplicity, charge, and other variables of the reconstructed tau objects are then taken from the associate truth tau.

Tracks within the jet cone are truth-matched to particles of the truth record by geometrically associating the track hits with the charged truth particles passing the detector, selecting the one with the highest energy deposit in this region [168]. Based on the cluster matches, a track matching probability is calculated by looking at the number of times the particles are associated with the hits used to reconstruct the track. Hits in the pixel layers are given a higher weight in the probability calculation than hits in SCT and TRT. If the probability surpasses a threshold of 0.5 the track is matched to the truth particle.

Since hadronically decaying tau leptons always produce an odd number of charged hadrons, a distinction is made between the actual generated truth charge multiplicity of the decay and the truth prongness. While the truth multiplicity always quotes the number of generated charged hadrons from the tau decay, the truth prongness refers to the number of reconstructed tracks matching these particles. As a consequence of this differentiation, the truth prongness includes inefficiencies of the track reconstruction and track truth matching. Thus, in some cases, the truth prongness can be lower than the

truth multiplicity when tracks are not reconstructed.

As a convention, observables of the truth tau particles are always referred to with the subscript *Truth*, like $p_{\mathrm{T,\,Truth}}$. If not stated otherwise, observables will always refer to the measured value of the reconstructed tau candidate. However, since the ID and calorimeter can not detect neutrinos from the tau decay, truth observables can also be calculated with respect to the visible truth decay products, e.g. $p_{\mathrm{T,\,Truth\text{-}vis}}$.

4.3.2. Jet Seeding

The particle shower from hadronically decaying taus leaves behind a jet-like structure in the calorimeter. This means that the anti-k_t algorithm outlined in Section 4.2.3 will reconstruct the signatures of the hadronic decay products as jets. Hence, Antik_t4LCTopo jets that satisfy $p_{\mathrm{T}} > 10\,\mathrm{GeV}$ are used to seed taus [169]. Furthermore, only candidates within the range of $|\eta| < 2.5$, excluding the barrel-forward transition region $1.37 < |\eta| < 1.52$ are considered.

Since the final state of hadronically decaying taus mainly consists of a few charged and neutral mesons, the decay cone of the tau jets is usually narrower than that of QCD jets. This feature is exploited by defining a core region of $\Delta R < 0.2$ within the set seed. The p_{T} of the reconstructed tau candidate at the local calibration scale is then calculated from the energy deposited in the calorimeter within the core region.

4.3.3. Tau Vertex Association

In events with multiple hard scattering vertices, the selected primary event vertex is not necessarily the same as the tau decay vertex. This is especially the case for taus with high momentum as they tend to travel farther from the hard scatter vertex before decaying. An algorithm is deployed to determine the vertex of the tau decay. By following the trajectory of the core tracks, a set of potential vertices is generated [170,171]. From these vertices, the one with the highest $\sum p_{\mathrm{T}}^2$ of the associated core tracks is selected as the tau vertex. The vertex association aims at reducing the impact of pile-up. After choosing the tau vertex all impact parameters are calculated with respect to this point. After the tau vertex is found, the variables p_{T}, η, and ϕ are recalculated with respect to the axis formed by the vertex and the cluster barycenter in the core region.

4.3.4. Track Selection and Identification

An important part of reconstructing hadronically decaying tau leptons is the determination of the charged track multiplicity of the decay. Within the tau jet cone, the charged hadrons from the tau decay can be accompanied by other tracks from charged particles that are not directly related to the tau decay. In order to calculate the charge and prongness of the tau decay the tracks directly associated with the tau decay need to be identified. The baseline procedure outlined in this section was first described in Reference [172].

In the first step, all tracks are associated with the seed jet if they fall inside a cone of $\Delta R < 0.4$ and passing a transverse momentum threshold of $p_{\mathrm{T}} > 500\,\mathrm{MeV}$. On tracks passing the loose association requirement, multivariate algorithms, called Boosted Decision Tree (BTD), are deployed to classify the tracks into different categories. A BDT is a collection of multiple decision trees combined with a boosting algorithm. Each decision tree categorizes and separates entities as background- or signal-like by applying successive cuts to variables [173]. Based on training data, the datasets are split into two subsets by a cut on the variable that best separates signal and background, with one subset failing and the other passing the cut threshold. This splitting is then repeated until a stop

criterion is reached, for example, the maximum number of branches. The trained decision tree assigns a score between 0 and 1 depending on whether the event is background- or signal-like. After the first decision tree is trained, a boosting algorithm is applied which increases the weights of events that are misclassified by the previous tree, thus raising the classification importance of these events for the next tree [174]. By using this boosting technique, multiple weak classifiers can be combined into one strong classifier. The Toolkit for Multivariate Analysis (TMVA) [175] is used to implement and train the BDT.

In the case of tau track identification four types of tracks are considered which are:

- **Tau Tracks (TT):** Tracks caused by charged particles from the tau decay not including tracks of π^0 conversions.

- **Conversion Tracks (CT):** Secondary tracks caused by electrons and positrons originating from photon conversion[1].

- **Underlying Event Tracks (UT):** Tracks from charged particles generated by the underlying event[2].

- **Other Tracks (OT):** Collection of tracks not belonging to one of the other classes. This category consists mostly of tracks from pile-up events.

The definition presented here as part of the default tau reconstruction differs from the definitions in Reference [172]. Most notably the Secondary Tracks (ST) class that previously contained all tracks with barcodes[3] larger than 200 000 is now replaced by the CT class which adds a requirement that the tracks are also associated with electrons from photon conversions. Tracks that were previously defined as secondary tracks but not contained in the CT class fall under the OT class category.

Classifying tracks in the categories defined above serves the purpose of calculating variables that are important for the identification and classification of hadronically decaying tau jet candidates in downstream algorithms. From the number of tau tracks, the charge and decay multiplicity can be directly deduced. Conversion tracks can be used to reconstruct the momentum fraction of neutral pion components of hadronic tau decays, since π^0 particles predominantly decay into pairs of photons which in turn cause e^+-e^- pair production when interacting with the detector. Classifying tracks from underlying events allows for better separation of tau decays from QCD jets in the identification step. Since QCD jets are created by strongly interacting particles, more tracks are expected in a QCD jet decay cone compared to that of a tau decay.

To classify the tracks into four categories using BDTs with binary classification output, a two-level pyramid strategy is deployed using three independent classifiers as shown in Figure (4.3.1). The BDT in the first layer splits all tracks into subclasses of TT and CT, forming the T-C group as well as UT and OT in the U-O group. In the second layer, these subsets are further split into the disjoint track classes where one BDT splits the T-C group into TT and CT while the second BDT splits the U-O group in UT and OT. After the classification is completed the charge and prongness are recalculated based on the BDT results.

---

[1] In ATLAS simulation, particles creating photon conversion tracks also require to have a barcode larger than 200 000.

[2] This corresponds to tracks created by particles with barcodes smaller than 10 000.

[3] Barcodes are numbers assigned to truth particles by the Monte Carlo generator during event simulation to identify and track the produced objects. Although the barcodes assignment can differ between generators, specific ranges are reserved for certain processes.
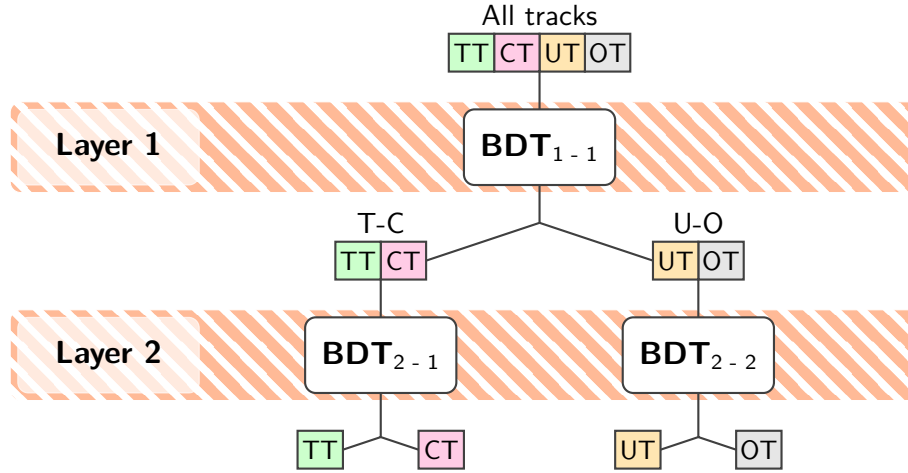
Figure 4.3.1.: Visualization of the BDT based tau track classification. The first layer BDT classifies all tracks into the T-C and U-O subgroups. In the second layer, two BDTs classify tracks from the subgroups in the elementary track classes.

4.3.5. Tau Jet Identification

Reconstructing tau jets from Antik_t4EMTopoJets offers almost no rejection against processes with similar detector signatures. Thus, most of the tau candidates are actual QCD jets. Since in most regions of the phase space QCD processes occur at much higher rates at hadron colliders than processes with tau leptons, the main background comes from the quark- or gluon-initiated jets faking hadronic tau decays. To reject these fakes and to gain a higher purity of true tau decays, a tau identification algorithm is deployed. The algorithm consists of a BDT trained on simulated $Z/\gamma^* \to \tau^+\tau^-$ events as signal and dijet events as background. The BDT takes variables related to the energy deposits in the ECAL and HCAL as well as geometric and kinetic variables of associated tau tracks and underlying event tracks as input. Since the 1 and 3 prong decays create distinct patterns in the detector, two separate classifiers were trained for 1 and 3 prong candidates. Based on the variables a score in the range of 0 to 1 is calculated. Tau candidates with scores close to 0 are considered QCD background like and scores close to 1 are true tau like. The BDT output is then transformed so that the cut value on the transformed score is related to the true tau selection efficiency like:

$$\epsilon_{\text{Tau}} = 1 - \Lambda_{\text{Tau-ID score}}, \tag{4.2}$$

with ϵ_{Tau} being the selection efficiency for true taus evaluated on $Z/\gamma^* \to \tau^+\tau^-$ events and $\Lambda_{\text{Tau-ID score}}$ the tau-ID cut threshold value. By cutting on the tau-ID score the *Loose*, *Medium*, and *Tight* working points are defined corresponding to a signal efficiency of 85 %, 75 %, and 60 % for 1 prong and 75 %, 60 %, and 45 % for 3 prong taus respectively [176]. As shown in Figure (4.3.2) the identification efficiency of each working point is calibrated to be stable over a wide range of tau p_{T} and average interactions per bunch crossing. The background rejection, however, depends on the tau p_{T}, making it a variable to consider when estimating backgrounds from data as described in Sections 7.3.2 and 7.3.3.
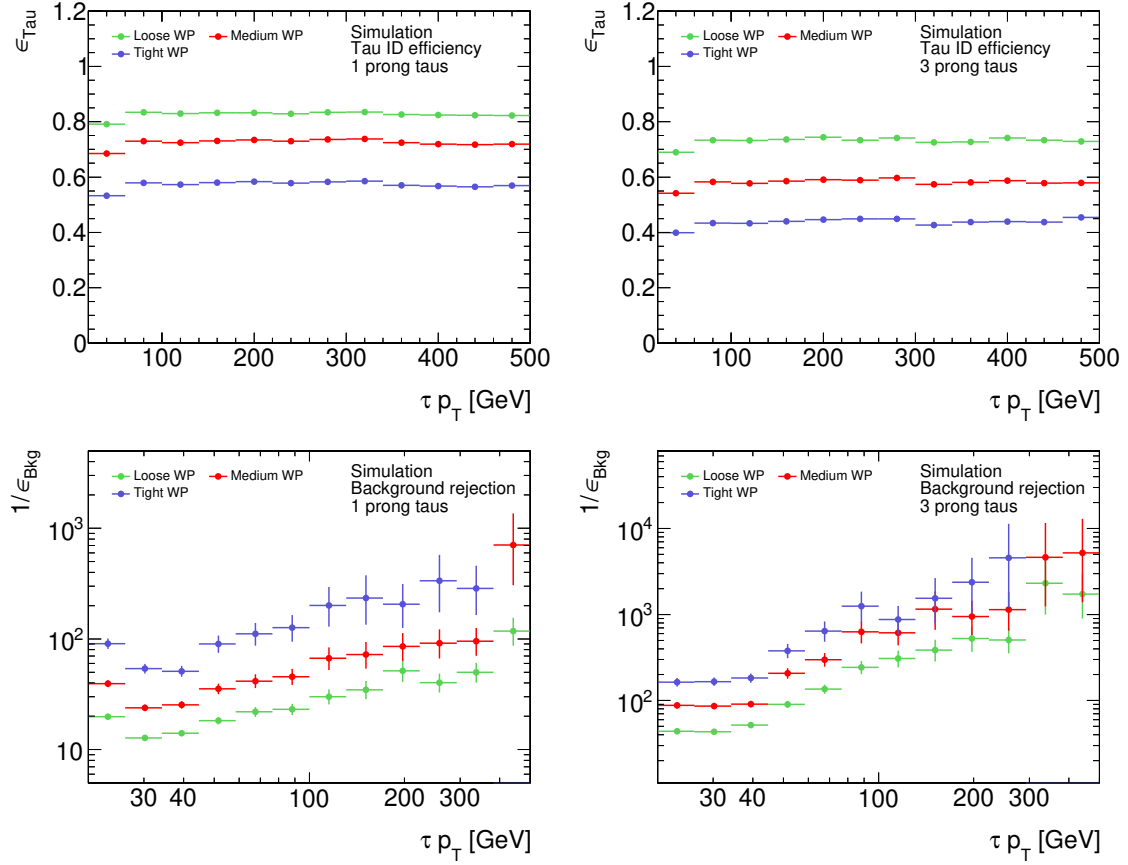
Figure 4.3.2.: Measured tau identification efficiencies and background rejections for different tau-ID working points parameterized in the reconstructed tau p_{T}. The top figures show the efficiency of true hadronic tau decays for the three tau-ID working points for 1 prong (left) and 3 prong (right) tau decays. The corresponding background rejection is given in the lower figures in terms of inverse background efficiency.

5. Introduction to Neural Networks

With a better understanding of the operation of the human brain and the discovery of neurons and their properties of conveying and manipulating electrical signals in the late 19th and early 20th centuries, experimental and theoretical attempts were made to model and artificially recreate the function of brain cells. In the 1940s pioneers like Warren McCulloch and Walter Pitts [177] provided the first models of artificial neurons while Donald Hebb [178] laid the groundwork for understanding how interconnected networks of neurons can learn to solve tasks. The theory of neurons and neural learning has since been the foundation on which artificial neural networks are based. In 1957 Frank Rosenblatt invented the concept of *perceptrons*, the simplest computational cell still in use in modern neural network applications [179]. Neural networks again gained attraction in the 1980s with the introduction of more complex network architectures like simple Recurrent Neural Networks (RNN) [180] which were specifically developed for time sequence applications. With the consolidation of the *backpropagation* algorithm as a method to train multivariate models, it was possible to easily and reliably train larger and increasingly deeper networks [181].

Thanks to improvements in computing power of modern hardware and the quality of data used to train neural networks, complex models like ResNet [182, 183] show incredible image recognition performance [184]. In high-energy physics, it is common to use classification and regression algorithms that are often capable of outperforming the cut-based selections developed by physicists, given the right training strategy. Examples of these multivariate machine learning techniques are BDTs deployed in track classification or identification of tau candidates. However, due to the narrow, predefined shape of BDTs, they usually struggle to adapt to more complex data structures. This can be shown by the use of RNNs for tau identification [176]. Thanks to the flexible architecture of neural networks, the information of tracks and calorimeter clusters could be treated as a sequence input of dynamic size. This change in paradigm and granularity of data resulted in an improvement of approximately a factor of two in background rejection power.

In this chapter the tools and neural network architectures used to improve the tau track selection and identification are presented. In the first section, an explanation is given on how simple neural networks are trained and applied, establishing the backpropagation algorithm as a way to train networks. The second section describes the architecture used in the classification model presented in Chapter 6. It aims at establishing and defining commonly used activation functions, loss functions, and optimization algorithms.

5.1. Dense Networks and the Backpropagation Algorithm

The simplest form of a modern neural network is made out of interconnected layers of perceptrons. A perceptron is a basic neuron that has one or many inputs x_i and one output o. In the first step, all input values are multiplied by weights w_i which are summed up to form the neuron input. The resulting value of the sum *net* is then passed through a predefined activation function $\phi\left(\text{net}\right)$ to compute the output of the neuron. This activation function governs the behavior of the neuron. Frequently used functions are linear functions, the rectifier function [185], or sigmoid functions. Perceptrons can be organized in layers

of arbitrary size N. The perceptrons within a layer are then called nodes. Multiple layers can be stacked by connecting the outputs with the inputs of the adjacent layer. Each connection line is associated with a weight that gets multiplied by the forwarded output. Networks, where successive layers are fully connected with each other by weights, are called dense networks [186]. The first layer is the input layer serving to forward the values of the input variables while the last layer is the output layer returning the result of the network. Layers sandwiched in between are called hidden layers. A sketch of a small dense network is shown in Figure 5.1.1. In the case of the dense network with one hidden layer the lines

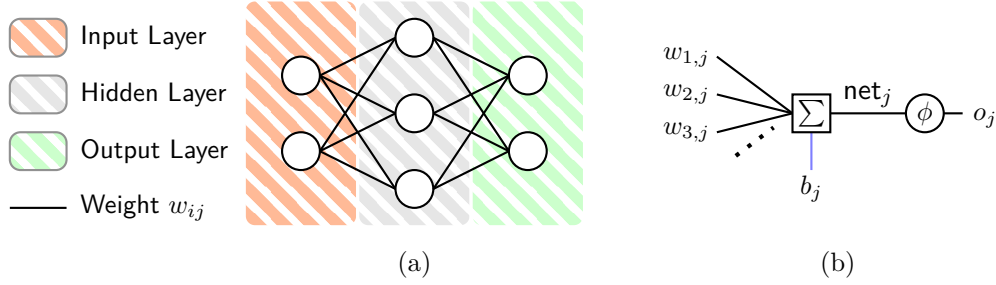(a)   (b)

Figure 5.1.1.: Dense neural network consisting of multiple perceptrons organized in interconnected layers. Figure (a) shows the architecture of the example network with one input, one hidden, and one output layer connected by the weights w_{ij}^1 and w_{jk}^2. The sketch in figure (b) represents the internal construction of nodes used in dense layers.

connecting the input with the hidden layer are associated with weights w_{ij}. Usually, layers also come with a bias node adding a constant offset multiplied with a bias weight b_j. In case the model of Figure 5.1.1, the calculation of the network is equivalent to the matrix multiplication written in index notation, from the input layer to the hidden layer:

$$o_{j,\,\text{hidden}} = \phi \left(\sum_{i=1}^{N_{\text{input}}} w_{ij}^1 \times x_{i,\,\text{input}} + b_j^1 \right) = \phi \left(\text{net}_j^1 \right), \qquad (5.1)$$

with w_{ij}^1 being the weights of the hidden layer, $x_{i\,\text{input}}$ the values feed into the input layer, and net_j the network value of the perceptron j after summation of the inputs[1]. The additional bias weight vector b_i^1 applies a linear shift to the input of the activation function. Adding degrees of freedom in the form of trainable bias vector weights enables layers to solve more complex problems. In conjunction with the perceptron activation function, it acts as a variable activation threshold. Propagating the output of the hidden layer to the output layer yields:

$$o_{k,\,\text{output}} = \phi \left(\sum_{j=0}^{N_{\text{hidden}}} w_{jk}^2 \times o_{j,\,\text{hidden}} + b_k^2 \right) = \phi \left(\text{net}_k^2 \right), \qquad (5.2)$$

with w_{jk}^2 the weights connecting the hidden layer with the output layer. The dimension of the weight matrix from the input to the hidden layer is of size $(N_{\text{input}}, N_{\text{hidden}})$ and $(N_{\text{hidden}}, N_{\text{output}})$ for the hidden layer to the output. In case the activation function is a linear function $\phi(x) = x$ the layer calculation of Equation (5.1) and (5.2) would translate in consecutively executed matrix multiplications of the input vector $\boldsymbol{x}$ with the weight matrices $\boldsymbol{w}$ adding the bias vector $\boldsymbol{b}$. The weights and biases are the free parameters

---

[1]Vector and matrix-like variables can be written in index notation using common indexing rules, e.g. $\boldsymbol{x}^{\text{T}}\boldsymbol{x} = x_i x_i$.

used to tune the network to perform a specific task. Finding and optimizing the weights is done by fitting them using an example dataset. This fitting process is conducted by learning algorithms. The most frequently used learning algorithm is the backpropagation algorithm which describes how the weights of the models are updated given the gradient of a measure of goodness. This measure of goodness with which the gradient is calculated is referred to as *loss function*. In classification problems two primary sets are required to train the network: The input data x_i and the truth data y_i, called labels. Loss functions for classification problems usually assign a distance measure between the network output and the truth labels. One example is the root-mean-square error defined by:

$$\mathcal{L}_{\text{RMS}}\left(\boldsymbol{x}, \boldsymbol{y}\right) = \sqrt{\frac{1}{N} \sum_{i=0}^{N} \left(o_{i,\,\text{NN}}\left(\boldsymbol{x}\right) - y_i\right)^2}, \tag{5.3}$$

with $o_{i,\,\text{NN}}\left(\boldsymbol{x}\right)$ being the response of the network given input $\boldsymbol{x}$. Based on the analytical definition of the loss function the local gradient with respect to a weight w_{ij} of an arbitrary neuron j is calculated by applying the chain rule[2]:

$$\frac{\partial \mathcal{L}}{\partial w_{ij}} = \frac{\partial \mathcal{L}}{\partial o_j} \frac{\partial o_j}{\partial w_{ij}} = \frac{\partial \mathcal{L}}{\partial o_j} \frac{\partial o_j}{\partial \text{net}_j} \frac{\partial \text{net}_j}{\partial w_{ij}}. \tag{5.4}$$

The term $\frac{\partial o_j}{\text{net}_j} \frac{\text{net}_j}{w_{ij}}$ describes the local derivative at the point of node j whose weight will be updated. The first part of this term is the derivative of the activation function with respect to the sum of the inputs while the second part is the derivative of the summation itself. Thus the derivative at node j can be written as:

$$\frac{\partial o_j}{\partial \text{net}_j} \frac{\partial \text{net}_j}{\partial w_{ij}} = \phi'\left(\text{net}_j\right) \frac{\partial}{\partial w_{ij}} \sum_i w_{ij} \times o_i = \phi'\left(\text{net}_j\right) o_i, \tag{5.5}$$

where o_i is the output of the previous layer connected via the weight w_{ij}. In the case of the weights being connected to the input layer, the value of o_i would just be the value of the input data x_i.

The first term of the gradient calculation of Equation (5.4) can be split further using the chain rule:

$$\frac{\partial \mathcal{L}}{\partial o_j} = \frac{\partial \mathcal{L}}{\partial o_{\text{NN}}} \frac{\partial o_{\text{NN}}}{\partial o_j}, \tag{5.6}$$

where the output of the neural network o_{NN} can be scalar, vector-like, or a higher dimensional matrix depending on the model. The first term describes the derivative of the loss function depending on the network output and is loss-specific. The second term is the derivative of the network output with respect to the layer j. If j is the output layer, this derivative becomes equal to one. In case the layer j is a hidden layer or the input layer, the term can be calculated by expanding Equation (5.6) with the partial derivatives of the output functions of the adjacent layers until the output layer is reached. Suppose there is a hidden layer k with weights w_{jk} between the layer j and the network output, then the expansion equates to:

$$\begin{aligned}
\frac{\partial \mathcal{L}}{\partial o_j} &= \frac{\partial \mathcal{L}}{\partial o_{\text{NN}}} \frac{\partial o_{\text{NN}}}{\partial o_k} \frac{\partial o_k}{\partial o_j} = \frac{\partial \mathcal{L}}{\partial o_{\text{NN}}} \sum_k \left(\frac{\partial o_{\text{NN}}}{\partial o_k} \frac{\partial o_k}{\partial o_j} \right) \\
&= \frac{\partial \mathcal{L}}{\partial o_{\text{NN}}} \sum_k \left(\frac{\partial o_{\text{NN}}}{\partial o_k} \frac{\partial o_k}{\partial \text{net}_k} \frac{\partial \text{net}_k}{\partial o_j} \right) = \frac{\partial \mathcal{L}}{\partial o_{\text{NN}}} \sum_k \left(\frac{\partial o_{\text{NN}}}{\partial o_k} \frac{\partial o_k}{\partial \text{net}_k} w_{jk} \right) \\
&= \frac{\partial \mathcal{L}}{\partial o_{\text{NN}}} \sum_k \left(\frac{\partial o_{\text{NN}}}{\partial o_k} \phi'\left(\text{net}_k\right) w_{jk} \right).
\end{aligned} \tag{5.7}$$

---

[2]The Einstein summation convention is used, summing over indices occurring more than once on only one side of the equation.

The last sum contains the derivative of the network output, similar to Equation (5.6), as well as the local derivative of the activation function at node k. This step can be done recursively to calculate the gradient for each weight at each layer in the network.

Substituting Equation (5.4) with (5.5) and (5.7) one can define:

$$\frac{\partial \mathcal{L}}{\partial w_{ij}} = o_i \delta_j, \tag{5.8}$$

with the recursive update function δ_j defined by:

$$\delta_j = \begin{cases} \dfrac{\partial \mathcal{L}}{\partial o_j} \phi' \left(\mathrm{net}_j \right), & \text{if } j \text{ is a ouput node,} \\[2ex] \left(\displaystyle\sum_k \delta_k w_{jk} \right) \phi' \left(\mathrm{net}_j \right), & \text{if } j \text{ is a hidden node.} \end{cases} \tag{5.9}$$

Weights are updated by firstly applying the neural on example data and evaluate the loss function. Then, the recursive update functions δ are calculated for the nodes of each layer by going backward through the network, starting with the output layer. Hence, the update algorithm is called error backpropagation.

Based on the δ of each layer, *optimization algorithm* functions $O(\delta)$ are used to update the weights. An example is a simple gradient descent algorithm with learning rate η:

$$\Delta w_{ij} = -O \left(\delta_j, \, o_i, \, \eta \right) = -\eta \delta_j o_i, \tag{5.10}$$

where the weights are updated according to:

$$w_{ij, \text{new}} = w_{ij, \text{old}} + \Delta w_{ij}. \tag{5.11}$$

The learning rate acts as a factor to control the size of the step that is made in the direction of the gradient. This parameter has to be chosen carefully as too small steps can result in slow convergence. With too large steps, however, the algorithm might not converge to the minimum of the loss function as the gradient is more likely to oscillate, thus being unable to resolve narrow minima. Since the gradient used to update any given weight is only dependent on the local derivative of the activation and the δ of the previous layer, more complex nodes than the perceptrons can be designed and trained using the same algorithm.

5.2. Recurrent Networks and LSTMs

Dense networks consisting of layers of perceptrons can be trained to conduct complex classification tasks in high-dimensional input spaces. However, due to the fixed size of input nodes, a dense network is usually less suited for problems with inputs of variable size. In the case of classifying reconstructed tracks within a tau candidate, the tracks can be treated as an input of variable length per tau candidate. A similar data structure can be found in problems with inputs that change over time like natural language processing. For these purposes, RNNs were developed that allow information to be propagated through time such that previous inputs can affect later results. The simplest RNN node can be created by adding a recurrent connection to a perceptron shown in Figure 5.2.1. The recurrent connection acts as a feedback loop to the perceptron itself which is associated with a trainable weight $w_{j, \text{rec}}$. The feedback loop is then evaluated at each time t using the output at a previous time, $t - 1$. This process allows the node to remember the previous output which in turn can influence the output of later steps. Recurrent neural networks are trained
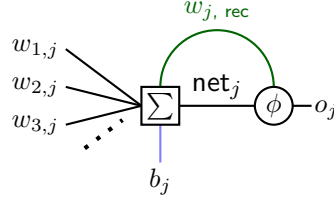
Figure 5.2.1.: Architecture of a simple recurrent neural network node.

by an adaptation of the backpropagation algorithm called backpropagation-through-time [187]. However, simple neural networks tend to perform poorly in resolving long-term dependencies due to vanishing or exploding gradients during error backpropagation through time [188]. This problem is solved by using Long Short-term Memory (LSTM) cells as fundamental building blocks of recurrent neural networks [189].
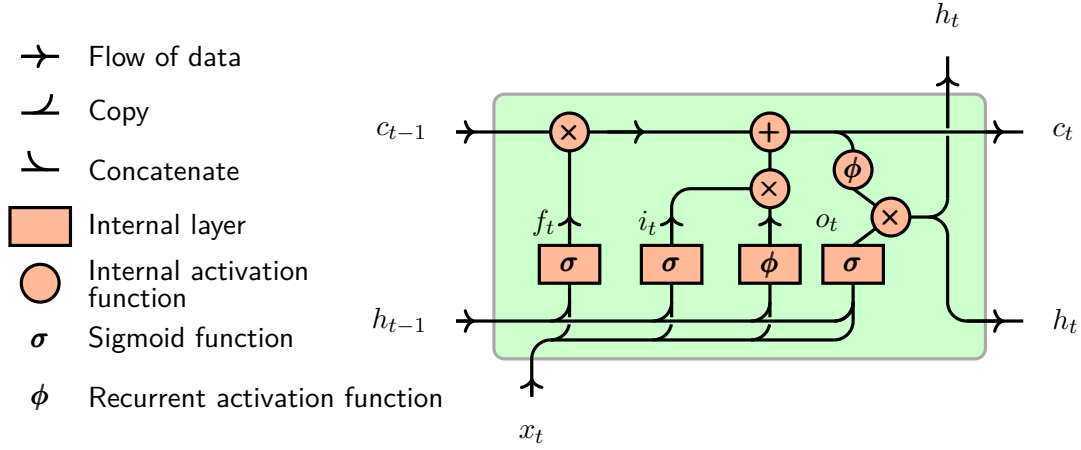

Figure 5.2.2.: Sketch of the structural architecture of an LSTM cell depicted at time step t. At each time step, the cell gets the feature data x_t as well as the previous cell state c_{t-1} and hidden output h_{t-1} as input. The internal layers with trainable weights govern the manipulation of the internal state c_t and the hidden cell output h_t. Three of the layers act as control gates using a sigmoid activation function, the forget gate f_t, the input gate i_t, and the output gate o_t. The fourth layer is the recurrent layer using the recurrent activation function ϕ.

As shown in Figure 5.2.2 the LSTM node expands the recurrent node with an internal state c_t which is used as memory to propagate information through time. Additionally, the internal state acts as a pathway to let the error gradient flow through time during backpropagation without vanishing or exploding. Internal layers with sigmoid activation functions and trainable weights, called gates, are used to learn when to change the internal state. Three gates are present in the LSTM cell. The forget gate f_t controls how much of the information stored in the internal state should be passed to the current time instance. The input gate acts like a valve controlling how much of the new information derived from the recurrent layer is written to the internal state. The cell output is then calculated by passing the updated internal state through the recurrent activation function and multiplying it with the response of the output gate o_t. Multiple LSTM cells are organized in layers that can be connected similar to dense networks in Figure 5.1.1. Given the input with T time steps and an input feature space of X variables, an LSTM layer with N nodes will transform

the input from dimensions (T, X) to (T, N).

Applying the concept of time steps to a list of tracks associated with the hadronic tau decay requires imposing an order on the track sequence, which determines in which order the tracks are classified. Although LSTMs allow previously classified tracks to impact the classification of future ones, the reverse is not possible. This can cause problems in cases where one might want to re-evaluate prior decisions upon being confronted with more tracks of a tau decay. An example would be the correlation between tau tracks in the tau cone. Since taus only decay in odd numbers of charged hadrons, the classification of tau tracks is dependent on the number of tracks already classified as TT as well as the number of tracks that will be classified as TT. To resolve dependencies forward and backward in time simultaneously, two LSTM layers can be combined where one layer goes forward in time starting at $t = 0$ to a point in the track series $t = i$ and the other one backward from $t = T$. This compound layer is called bidirectional LSTM (bLSTM) [190]. For each point i in time of the sequence, the output of the bLSTM layer is a combination of the forward and backward layers. Typical methods of combining the two sub-layers are element-wise addition and multiplication or concatenation of the two outputs. Figure 5.2.3 shows how two layers of LSTMs are forming one bLSTM layer. In the case of track classification, exchanging LSTM layers with bLSTM layers significantly reduces the impact of the order of tracks, which results in classifiers with higher response stability and performance.
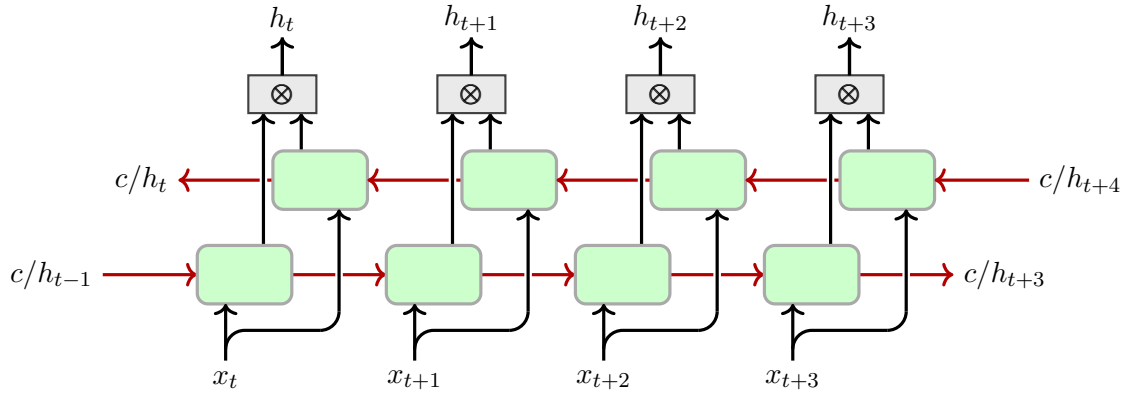

Figure 5.2.3.: Sketch of the structural architecture of a bidirectional LSTM cell depicted at time step t. The two LSTM layers go in the opposite direction in time. The output is calculated by merging the results of the forward and backward layers using a merge function denoted by $\otimes$.

6. Improvements of Tau Reconstruction

Improving the reconstruction and identification performance of hadronically decaying tau leptons is crucial for many analyses performing searches or measurements with taus in the final state. As described in Section 4.3, hadronically decaying tau candidates are built from Antik_t4LCTopo and their associated tracks and secondary vertices. Improvements at the track selection stage can result in more true tau jets being reconstructed and processed in downstream algorithms. However, the track selection and identification not only aims at increasing the reconstruction of 1 and 3 prong taus but also at improving the classification of other tau track classes which serve as inputs for identification algorithms.

Although being generally considered part of the tau reconstruction, the track selection and identification sits somewhere in the middle between reconstruction and identification. It does not explicitly separate tau jets from QCD jets, but by only allowing 1 and 3 prong tau candidates in analysis selections the track identification can have a direct impact on backgrounds containing fake taus. In some cases, a significant reduction in backgrounds caused at the track identification stage might prove problematic for data-driven fake estimations, as they require enough events to pass the reconstruction in order to work reliably.

In the following sections, bLSTM based track classification algorithms are presented delivering significant improvements over the BDT based algorithm. Two strategies are developed resulting in different behavior on the QCD jet background.

6.1. Monte Carlo Samples

The evaluation of the performance of different track identification algorithms is done on Monte Carlo simulated events. True tau jet samples are generated by simulated off-shell $\gamma^* \to \tau^+\tau^-$ events while QCD jets are taken from di-jet simulations. Both processes are simulated with PYTHIA 8.230 [134] at leading order for both ME and PS modeling using the NNPDF2.3LO PDF set [147] with the A14 parameter tune [137]. For the $\gamma^* \to \tau^+\tau^-$ process, one continuous sample is generated covering an off-shell mass spectrum from $60\,\text{GeV}$ to $7\,\text{TeV}$. In order to achieve reasonable coverage over the entire mass spectrum, the event weights are adjusted to oversample the higher mass phase space. To improve the coverage of di-jet events at large jet p_T, six sample slices are generated using a biased phase space sampling method. In each slice, the phase space is oversampled based at a rate of $(\hat{p}_\text{T}/10\,\text{GeV})^4$ where $\hat{p}_\text{T}$ is defined by:

$$\hat{p}_\text{T} = \sqrt{\left(p_{\text{T},1}^2 + m_1^2\right)\left(p_{\text{T},2}^2 + m_2^2\right)}, \tag{6.1}$$

with $p_{\text{T},1/2}$ and $m_{1/2}$ being the transverse momenta and mass of the first and second jet. Thus, the variable $\hat{p}_\text{T}$ describes the geometric mean of the squared transverse energy of the di-jet system at ME level. This slicing procedure is called JZ with the thresholds of the sample slices given in Table 6.1.1. A full list of samples used in this chapter to evaluate and train tau reconstruction and identification algorithms is given in Appendix A.1.

JZ slice	$\min\left(\hat{p}_{\mathrm{T}}\right)$ in GeV
JZ1W	0
JZ2W	15
JZ3W	50
JZ4W	150
JZ5W	350
JZ6W	600

Table 6.1.1.: Values of $\hat{p}_{\mathrm{T}}$ for different JZ slices used in the training and evaluation of tau track selection algorithms.

6.2. Performance of the Baseline Track Classification

The BDT based track classification algorithm described in Section 4.3.4 is the default algorithm used to reconstruct tau candidates. Thus, it serves as the baseline to which the performance of the new algorithms is compared. Two primary measures are used to quantify the performance: the confusion matrix and the tau reconstruction efficiency.

The confusion matrix is a two-dimensional matrix depicting the mapping of the track classes predicted by the classifier to their true values. If the matrix is normalized to the track truth type, the resulting efficiency confusion matrices measure the probability that a track of a given truth type gets classified in the different reconstructed track classes. On the other hand, the matrices normalized by the reconstructed track-type show the relative composition of the reconstructed track classes in terms of the truth types and are therefore called purity confusion matrices. The confusion matrices for the BDT based algorithm are given in Figure 6.2.1.

With tau track identification efficiencies of 94.1 % and 93.4 % for taus with truth multiplicity of 1 and 3 respectively, the BDT based classification algorithm delivers good performance in differentiating tau tracks from other track classes. This is also reflected in the purity matrices as the reconstructed TT class achieves a purity of 86.9 % and 96.2 % for 1 and 3 prong tau candidates. Other track classes like UT and CT show significant differences in purity and efficiency which is due to their relative differences in occurrences visualized in Figure 6.2.2.

With an average of 8 truth-matched tracks per tau decay, the OT class is the dominant track class mostly consisting of pile-up tracks, while the average number of truth TT is dependent on the truth decay multiplicity of the tau decay with a maximum at one or three tracks per tau. Tracks classified as CT or UT are significantly rarer. Due to the large differences between OT and CT or UT classified tracks, already small fractions of misclassified true OT tracks result in high contamination in other reconstructed track classes. This effect is largest for classified CT where 6.7 % (6.5 %) of misclassified truth-matched OT results in a purity contamination of 59.2 % (70 %) for taus with truth multiplicity of 1 (3).

Based on the number of identified TT the charge and track multiplicity of the tau jet candidate is reconstructed. The associated reconstruction efficiency is calculated with respect to a kinematic variable x for truth-matched taus with truth multiplicity 1 or 3:

$$\epsilon\left(x, n_{\mathrm{TT}}\right) = \frac{n_{\tau}^{\mathrm{rec}}\left(x, n_{\mathrm{TT}}\right)}{n_{\tau}^{\mathrm{truth\ gen}}\left(x\right)} \, , \tag{6.2}$$

where $n_{\tau}^{\mathrm{rec}}\left(x, n_{\mathrm{TT}}\right)$ is the number of truth-matched taus reconstructed with n_{TT} of identified tau tracks and $n_{\tau}^{\mathrm{truth\ gen}}\left(x\right)$ is the total number of truth taus associated with reconstructed tau jets. This reconstruction efficiency is an important measure to determine
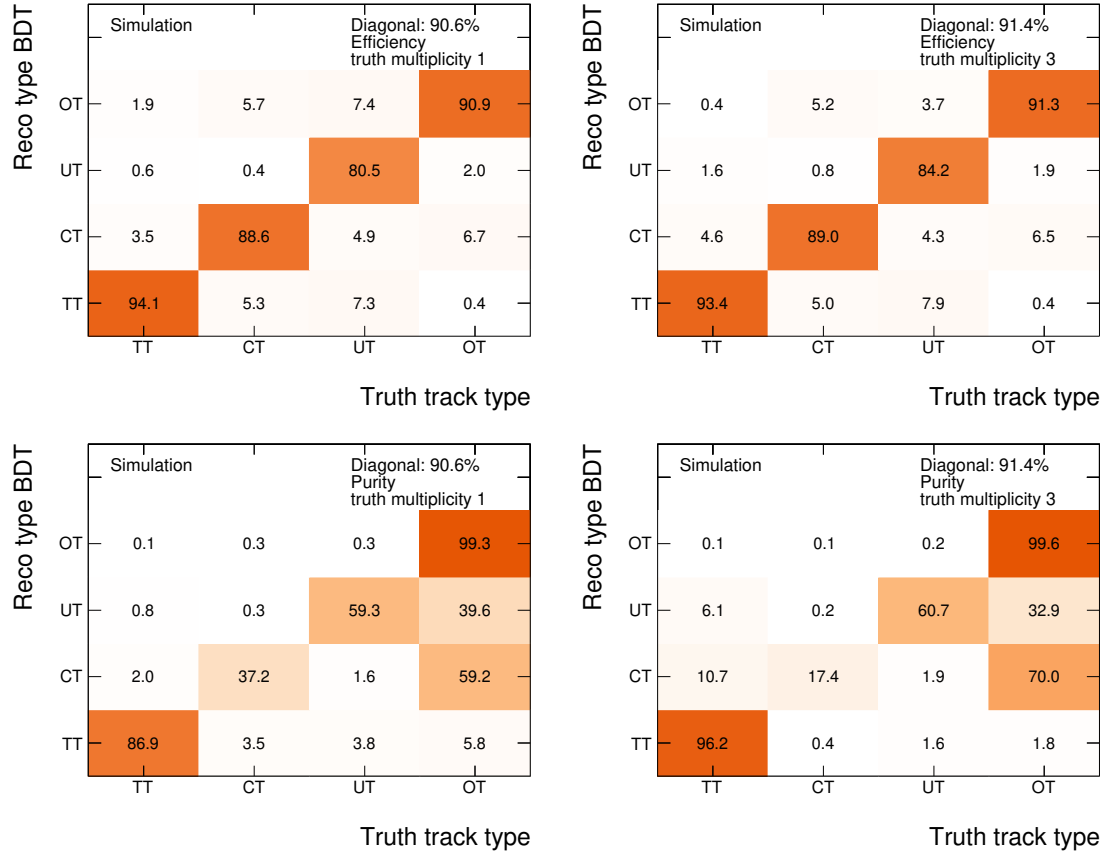
Figure 6.2.1.: Identification efficiency (top) and purity (bottom) confusion matrix of the BDT based track selection for taus with truth multiplicity of 1 (left) and 3 (right).
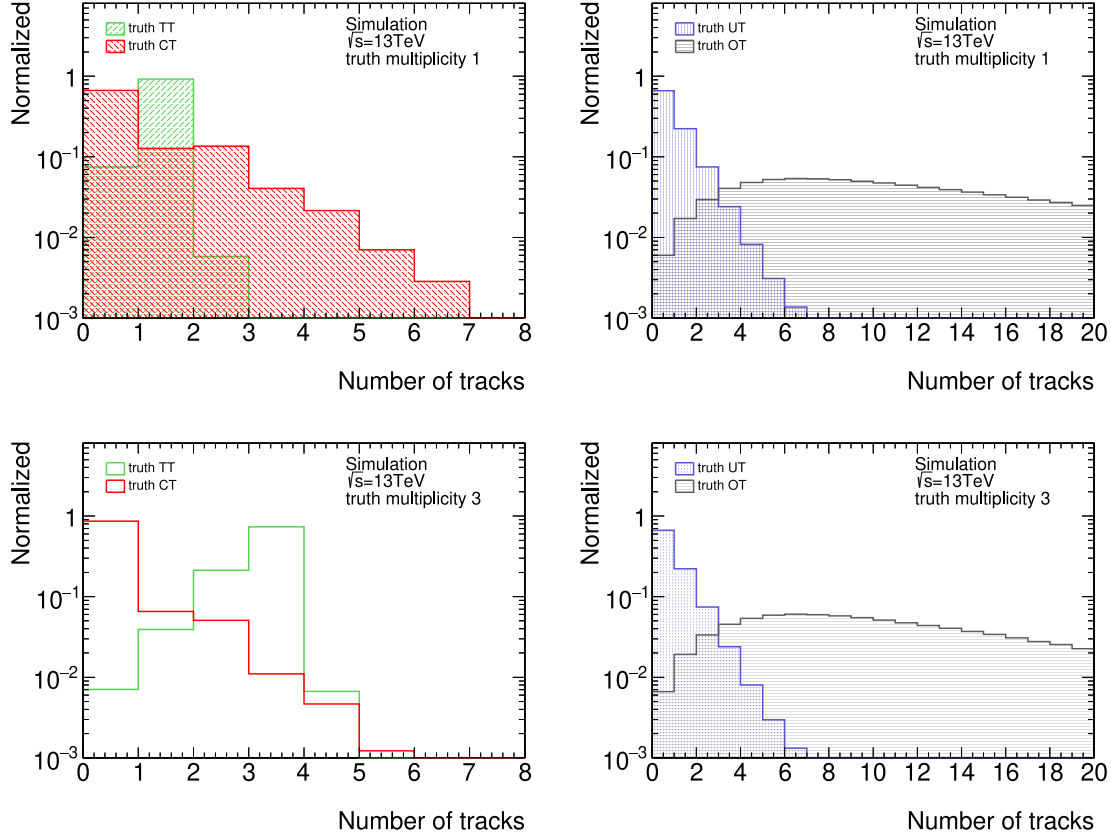
Figure 6.2.2.: Histograms of the number of truth classified reconstructed tracks associated with a tau decay for taus with truth multiplicity of 1 (top) and 3 (bottom). Since only reconstructed tracks are counted, the number of tracks is subject to track reconstruction inefficiencies resulting in a lower number of tau tracks than expected by their truth multiplicity. Conversely, misassociation of reconstructed tracks to the truth particles can result in more truth-matched tau tracks.

the performance of the track classification algorithm. Since the denominator contains all generated taus with a truth multiplicity of 1 or 3, the efficiency also takes into account inefficiencies of the track reconstruction itself, resulting in an efficiency loss observed in Figure 6.2.3. The plots show the reconstruction efficiency for generated truth-matched taus with truth multiplicity of 1 or 3 to be reconstructed with different prongness given an ideal classifier. In this case, the ideal classifier is defined to be a classifier that assigns each reconstructed track the truth label of the associated truth particle.
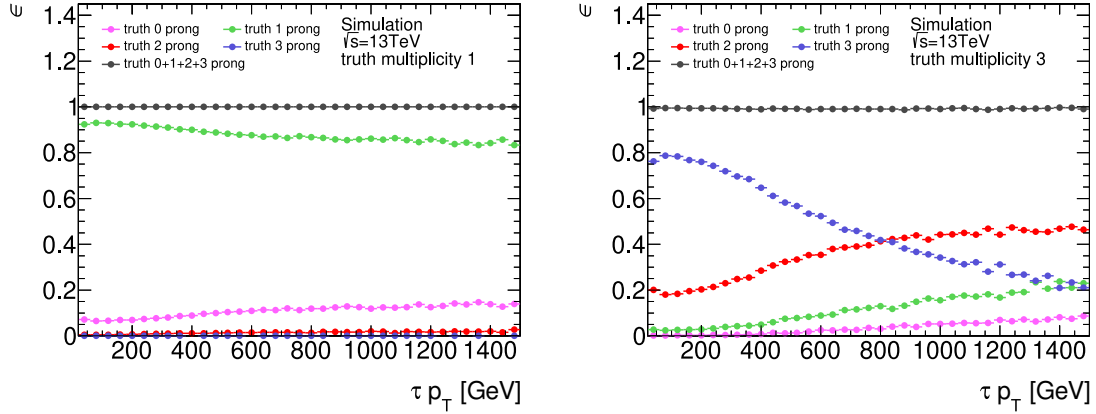

Figure 6.2.3.: Tau reconstruction efficiency of the ideal classifier for different prongness categories. At higher tau jet p_T, taus get reconstructed more often with lower prongness than expected by their truth multiplicity.

Most tau decays with a truth multiplicity of 1 are correctly reconstructed as 1 prong tau by the truth classifier. However, with increasing transverse momenta the fraction of tau jets with no truth-matched tau tracks increases. This is caused by inefficiencies of the track reconstitution algorithm as some tracks might not be properly reconstructed and truth-matched. The fraction of 0 prong taus rises with higher tau p_T due to the more collimated decay products, decreasing the separation between tracks in the decay cone. If tracks get too close they can not be resolved and merge into one track or are misreconstructed and rejected. A similar but much larger effect is observed for taus with a truth multiplicity of 3. Here track merging at high p_T results in tau jets having 2 or 1 truth-matched tau tracks, reducing the fraction of correctly reconstructed truth 3 prong taus. Unfortunately, at the track identification level, the reconstruction efficiency for 1 and 3 prong taus lost to track merging can not be recovered as it would require a higher resolution tracking system or improved track fitting algorithms.

As a reference, classifier efficiencies are compared to the reconstruction efficiency of an ideal classifier as it resembles the best achievable efficiency given the limitation of the track reconstruction algorithm. For the BDT based algorithm, the reconstruction efficiencies over the reconstructed tau p_T and average interactions per bunch crossing $\langle \mu \rangle$ are shown in Figure 6.2.4.

The BDT based track identification algorithms show a stable efficiency over $\langle \mu \rangle$, only declining by less than 7% between $20 < \langle \mu \rangle < 70$. However, the BDT is still 10-20 $\%$ worse than the ideal classifier. While the performance for 1 prong taus is stable over tau p_T, the efficiency gap is largest for 3 prong taus in the range of $200\,\text{GeV} < p_T < 600\,\text{GeV}$.
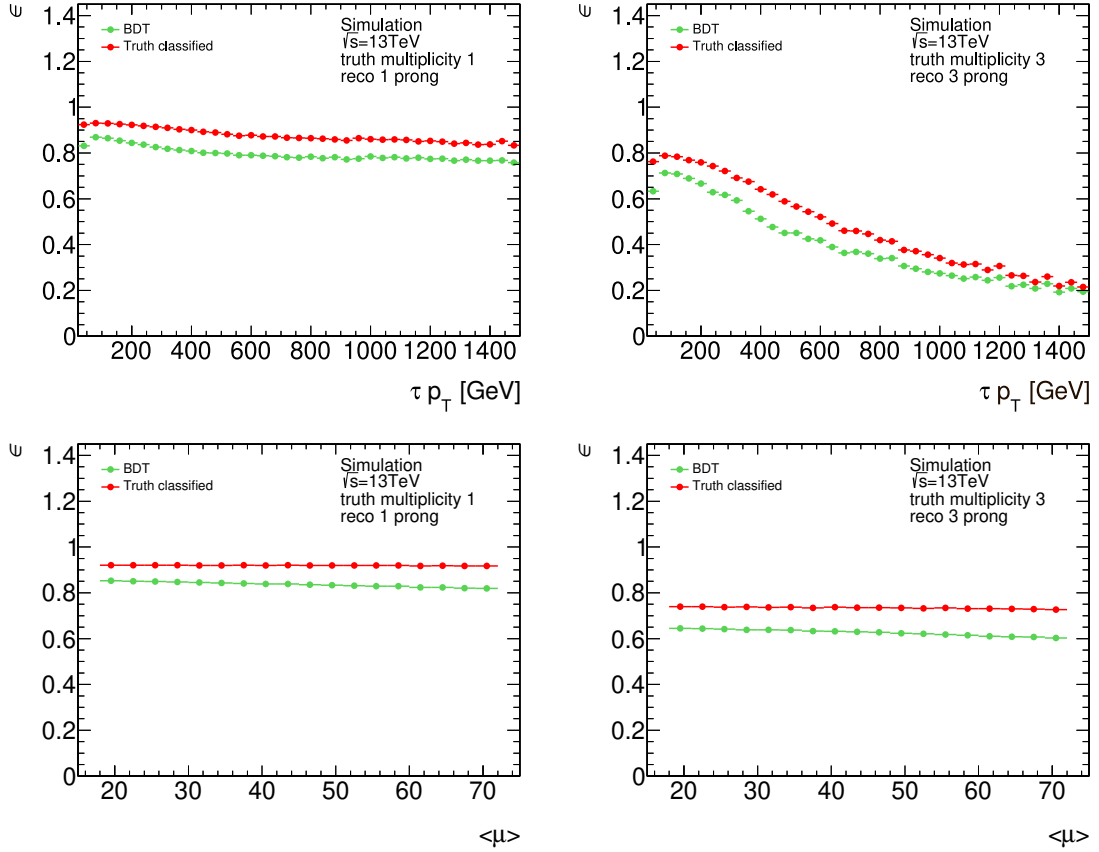
Figure 6.2.4.: Tau reconstruction efficiency of the BDT based track classifier. The plots show the efficiency of taus with truth multiplicity of 1 (left) and 3 (right) being reconstructed as 1 and 3 prong taus over the reconstructed tau p_{T} (top) and $\langle\mu\rangle$ (bottom). The BDT algorithm (green) is compared with the ideal classifier (red).

6.3. LSTM Based Tau Track Selection

Although the BDT based track identification and selection algorithm uses a multivariate technique to achieve good reconstruction efficiencies, it is still only classifying each individual track independently. This approach does not take into account possible residual information inherent in the correlation of tracks within a tau decay. For example, due to charge conservation taus decay into an odd number of charged tracks with $|\sum q_{\text{track}}| = 1$, which implies that after 2 tracks are classified as TT there is a high probability that there is also a third tau track. By deploying bidirectional LSTMs the forward and backward correlation in a sequence of tracks associated with the tau decay can be exploited.

In this section, the training and evaluation of the neural network track classifier are explained and the performance is compared with the BDT based track identification algorithm. Two different training approaches are presented with differing behavior on QCD jets.

6.3.1. Training Strategy

One of the key components to a achieve a good performance of any network training is to understand the structure of the input data upon which the model is built. Special emphasis is put on input data preparation and transformation as well as the parameter configuration of the LSTM network. In the following sections, the input variables, network architecture, and training strategy are outlined.

Input Variable Set

Similar to the BDT based algorithm the bLSTM classifier is trained on a set of variables derived from geometric and kinetic properties as well as detector hits of the tracks. Many variables provide separation power between the track classes like the number of pixel hits and the TRT electron probability. Other variables, however, do not provide direct discrimination power but rather serve to parameterize the network. In the following, a description of the input variables is provided. The distributions shown are derived from $\gamma^* \to \tau\tau$ samples listed in Appendix A.1 and weighted to match a common cross-section of $1\,\text{pb}$. Histograms of the variables of different track classes are normalized to allow for better shape comparison.

Seed jet transverse momenta $p_{\text{T, seed jet}}$:   The transverse momenta of the tau jet candidate is an important variable to parameterize the neural network. Although it provides only little separation power between track classes it allows the network to learn how other variables are depending on the tau momentum. During runtime of the track classification the dedicated tau energy calibration is not yet applied, thus only the momenta of the seed jet can be used. Figure 6.3.1a shows the distribution of $p_{\text{T, seed jet}}$ for generated 1 and 3 prong taus.

Track transverse momenta $p_{\text{T, track}}$:   The $p_{\text{T, track}}$ plotted in Figure 6.3.1b enables the neural network to learn momentum dependencies of other kinetic variables. However, since most of the energy and momentum of tau decays is carried away by charged hadronic decay products and conversion tracks from π^0 decays, this variable has also limited separation power for TT and CT against UT and FT. Since particles from the TT and CT directly originate from the tau decay they tend to have a larger momentum.
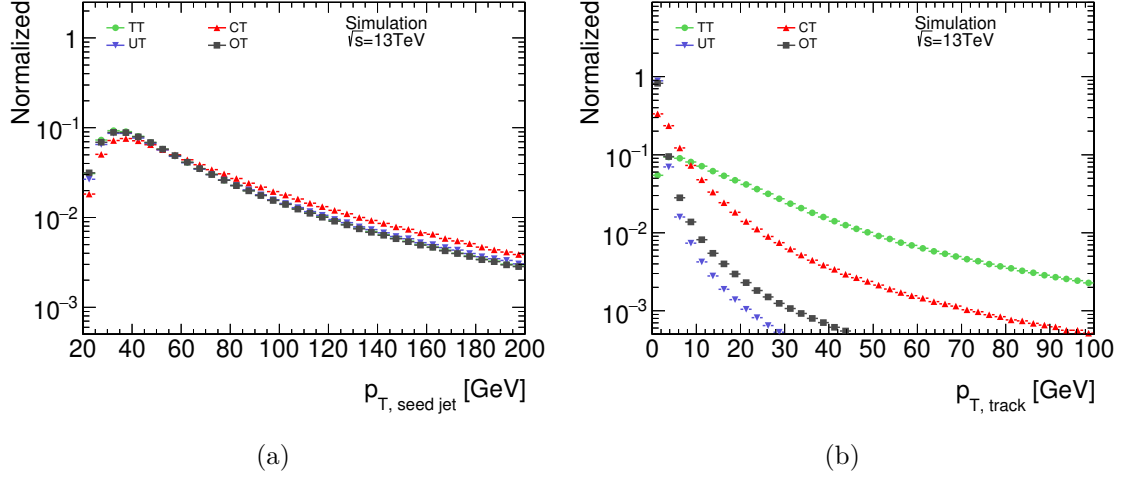
Figure 6.3.1.: Seed jet and track transverse momenta distributions for different track classes.

Track pseudo-rapidity η_{track}: At higher pseudo-rapidity the total amount of active detector material that the particle has to pass increases, which impacts the measurements of other kinetic variables. While the distributions of most track classes are centered around $\eta = 0$, tracks from photon conversions occur more often at higher values of $|\eta|$ due to the increase in the detector material. Adding η_{track} to the training enables the network to adjust to these differences.

$z_0^{\text{TJVA}} \sin(\theta)$: The product of the longitudinal impact parameter z_0^{TJVA}, measured with respect to the tau jet vertex axis, and the sine of the polar angle yields good rejection of OT versus TT class tracks. Tracks that originate from tau decays with large z_0^{TJVA} tend to be boosted in the longitudinal direction resulting in smaller values of $\sin(\theta)$. The OT class tracks, and especially pileup tracks, however, are produced at different vertices and thus show less correlation between these variables relative to the tau vertex. This variable was first derived and used in the BDT based approach described in Reference [172].
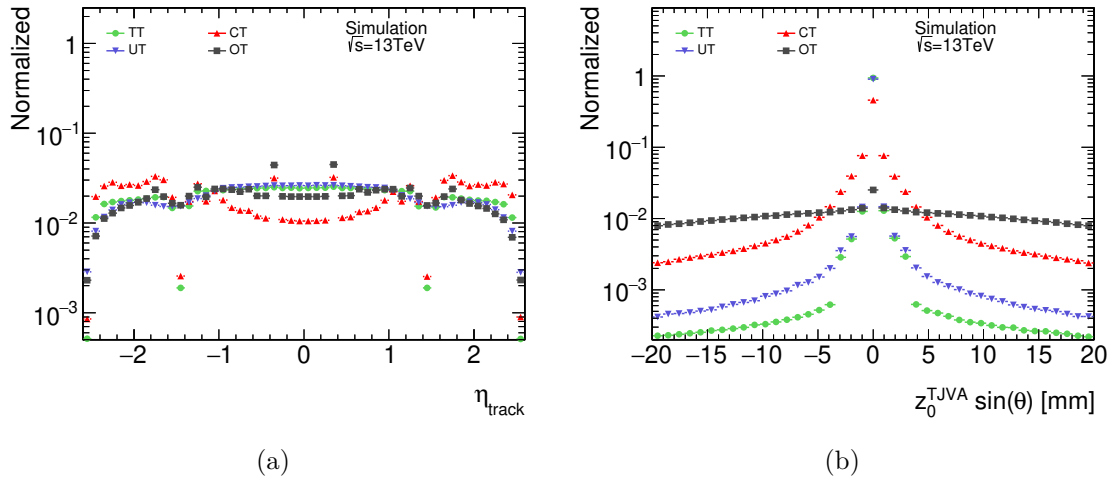

Figure 6.3.2.: Distribution of track η and $z_0^{\text{TJVA}} \sin(\theta)$ for different track classes.

Angular distance to the jet axis $\Delta R_{\text{seed jet axis}}$: The angular distance of the tracks to the seed jet axis as shown in Figure 6.3.3a is an important variable to separate UT and OT from TT and CT. The latter two originate from the tau decay and are subsequently clustered closer around the jet axis. In contrast, the UT and OT track classes are not directly related to the tau decay and originate from secondary processes. Thus they tend to occur at larger distances from the seed jet axis.

Transverse impact parameter d_0: The signed impact parameter d_0 is defined as the closest distance in the r-ϕ plane between the beam axis and the fitted particle trajectory. Tracks from particles coming from the tau decay, like TT and CT, typically tend to follow the tau particle trajectory and thus having smaller values of d_0 compared to tracks from pile-up or the underlying event. The distributions for the different truth classes are shown in Figure 6.3.3b.
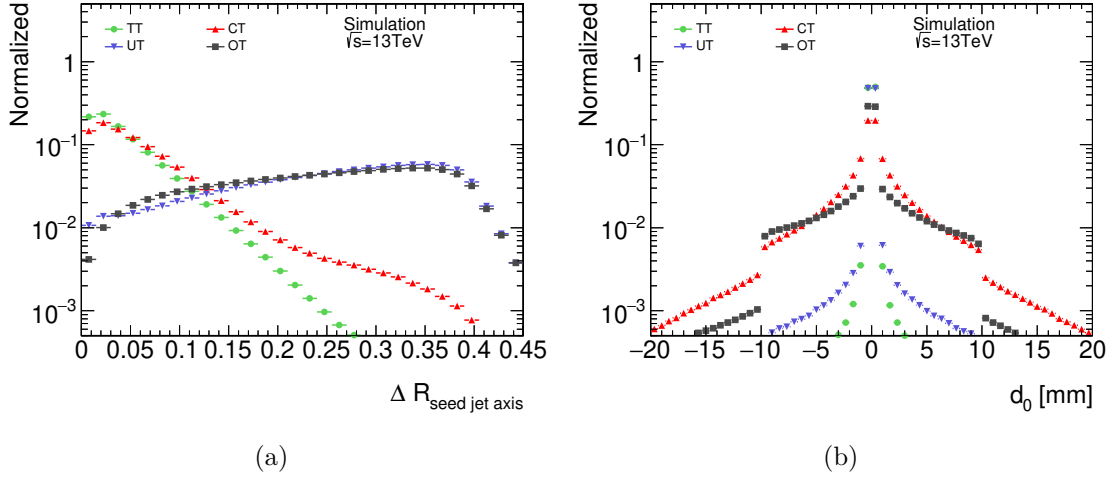

(a) (b)

Figure 6.3.3.: Distributions of the radial distance to the seed jet axis and transverse impact parameter of the tracks.

Conversion radius R_{conv}: Conversions of photons into electron-positron pairs usually occur at a non-zero distance in the transverse plane from the interaction point. This distance from the interaction point is called conversion radius and can be approximated by $R_{\text{conv}} = \sqrt{\frac{|d_0|p_T}{0.15 \cdot B}}$ [191] where B coincides with the magnetic flux density of the inner solenoid magnet. Based on definitions developed for the BDT based algorithm the value of B is set to a dimensionless value of 2, corresponding to a magnetic field of 2 T of the inner detector solenoid magnets. During the development of a cut-based conversion tagger [192], it has been found that for conversion tracks the product $\text{sign}(d_0) \cdot q$ preferably assumes a value of -1 while tracks from other sources are symmetrically distributed at values of ± 1. To exploit this asymmetry a signed conversion radius is defined by $R_{\text{conv}} \cdot \text{sign}(d_0) \cdot q$. Both variables shown in Figure 6.3.4 provide good separation power for TT and CT from OT and UT. Especially the signed conversion radius is well suited to distinguish CT from other track classes.
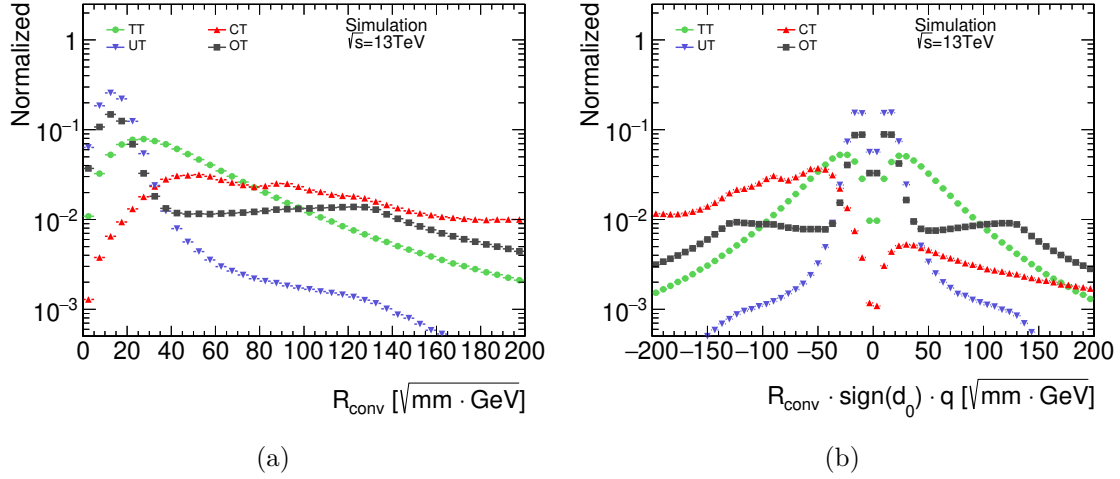
(a) (b)

Figure 6.3.4.: Distribution of the conversion radius R_conv and the signed $R_\mathrm{conv} \cdot \mathrm{sign}\,(d_0) \cdot q$.

Track charge: Based on the direction of the curvature of the reconstructed track in the magnetic field of the inner detector the charge of the particle can be determined. Although Figure 6.3.5a shows that the charge itself does not provide significant separation power, when correlated across all tracks within a tau decay, features can be exploited that are unique to certain track classes. For example, taus decay into an odd number of tau tracks with a charge sum of $\sum q = \pm 1$ while conversion tracks occur in pairs with $\sum q = \pm 0$.

TRT electron probability: From the transition radiation detected by the TRT, a likelihood is constructed to identify electrons from hadronic particle tracks [157, 193]. The probability is calculated by comparing the patterns of high threshold TRT hits with that predicted by the electron hypothesis. The resulting probability distributions for the various track types are shown in Figure 6.3.5b. If the probability could not be calculated, e.g. due to an insufficient number of hits in the TRT, a default value of 0.5 is set. This variable delivers great separation for electron tracks originating from photon conversions and hadronic particles.
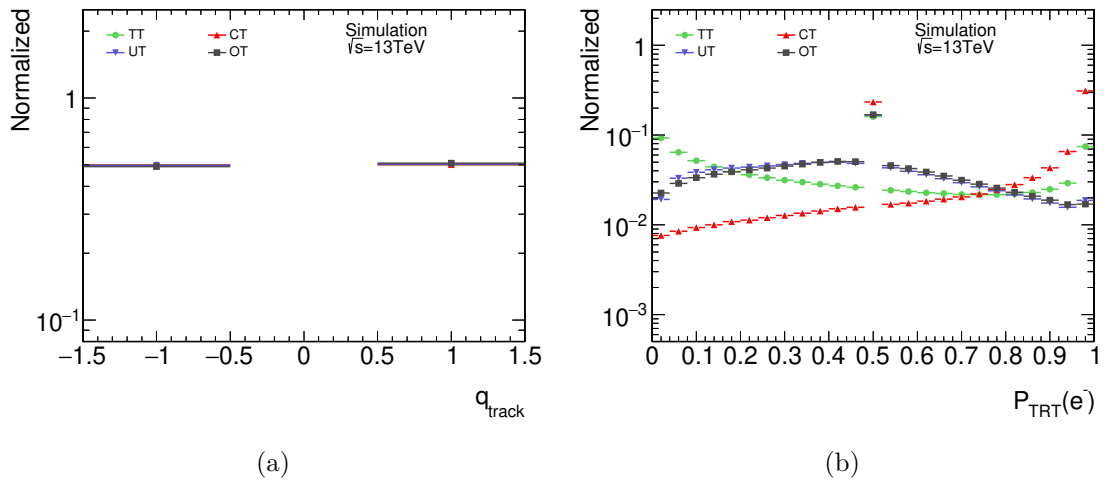

(a) (b)

Figure 6.3.5.: Distribution of the track charge and the TRT electron probability score.

Number of inner detector hits: To further improve the classification performance of the neural network, low-level information from the inner detector in the form of the number of hits in the detector components are used as input. Figure 6.3.6 shows the distributions of the number of hits in the various subdetectors. The number of hits in the IBL serves to isolate conversion tracks. Since pair-production in photon conversions requires the presence of atomic nuclei, they tend to occur farther away from the interaction point in the detector material. Thus more than 80 % of conversion tracks do not cause hits in the innermost layer. The total number of pixel hits is the sum of all hits in the four pixel layers and the number of dead sensors the reconstructed track trajectory crosses. Similarly, the total number of silicon hits is calculated from the hits in the pixel and SCT detectors and potential hits in the dead sensor material. In both cases CT and OT class tracks on average count fewer hits than TT and UT. For CT this is caused by displaced conversion vertices, while pile-up tracks, which dominate the OT class, mainly originate away from the tau decay vertex and are scattered inside the tau decay cone. Also, the number of pixel and SCT hits shared by multiple tracks are considered as input variable. As conversion tracks are created in pairs from photon conversions, they are usually closer to each other and share hits more frequently. Similarly, tau tracks tend to be more collimated as well and are thus more likely to share hits in the inner detector.

Additionally, the input variables of the track and jet momentum as well as R_{conv} and d_0 undergo a variable transformation. The transformation aims to expand the domain of the distributions where distinctive features of the track classes are observed. Ideally, a bijective transformation of variables does not reduce the information and should not impact the results. However, due to the limited numerical resolution during training of the network, it can be helpful to widen the numerical range where distinctive features are observed while shrinking those with lower separation power.

In the case of the momentum variables, the important differentiating features are located over a wide range at low and high momenta. Thus a logarithmic transformation is applied. Using the same reasoning a logarithmic transformation is also applied for the R_{conv} variable. For the distributions of d_0 and $R_{\mathrm{conv}}{\cdot}\mathrm{sign}\,(d_0){\cdot}q$, the interesting features are closely clustered around 0 with large tails that do not yield further separating power. These variables are transformed using a hyperbolic tangent function which acts like a fish-eye lens by widening the center and compressing outer tails.

Besides the variable transformation, two additional variables are calculated by combining the above mentioned variables. Although these variables could be modeled internally by the network during the training process, adding physically interesting combinations of variables reduces the required complexity of the network. The first additional variable is the track momentum fraction calculated with respect to the seed jet momentum. This allows the network to directly access important dimensionless information. A second one is the charge-momentum ratio $\frac{q}{p}$ which has been already successfully used in Reference [172] as the inverse of the momenta allows for good resolution of the low p_{T} range. Figures showing the distributions of the additional and transformed variables are listed in Appendix A.2. In total, a set of 18 variables is used to train the neural network which is summarized in Table 6.3.1.
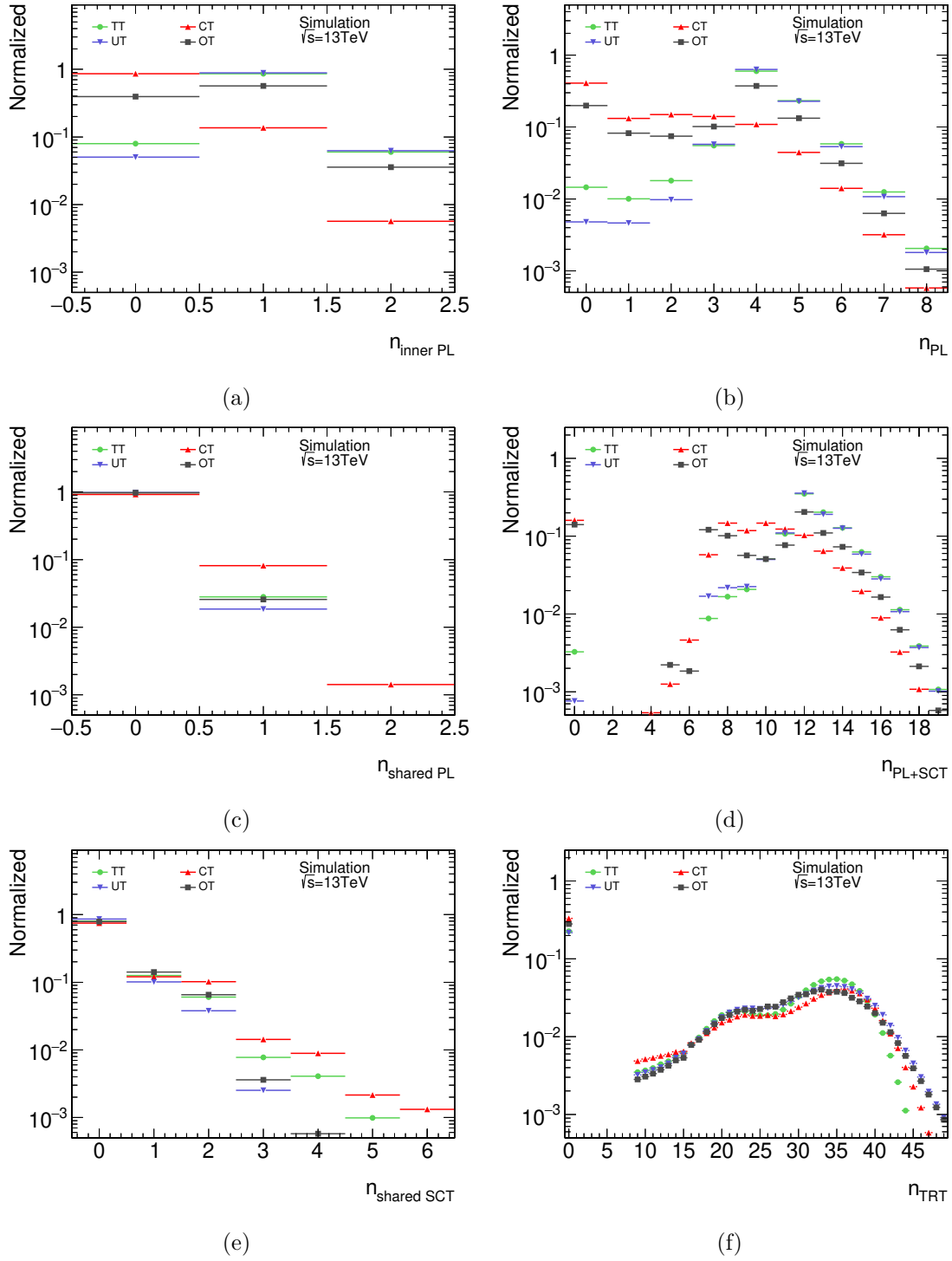
(a)

(b)

(c)

(d)

(e)

(f)

Figure 6.3.6.: Distribution of inner detector hits used for track classification. The hit variables considered are (a) the number of IBL hits, (b) the total number of pixel hits, (c) the number of shared pixel hits, (d) the sum of pixel and SCT hits, (e) the number of shared SCT hits and (f) the number of TRT hits.

Variable	Description
Kinetic and geometric variables	
$\ln\left(p_{\mathrm{T,\,track}}\right)$	Logarithm of the transverse track momentum
$\ln\left(p_{\mathrm{T,\,seed\,jet}}\right)$	Logarithm of the transverse seed jet momentum
$\frac{p_{\mathrm{T,\,track}}}{p_{\mathrm{T,\,seed\,jet}}}$	Transverse momentum balance between track and jet
η_{track}	Track pseudo-rapidity angle
$\Delta R_{\mathrm{seed\,jet\,axis}}$	Radial distance of track w.r.t. jet axis
$z_0^{\mathrm{TJVA}}\sin\left(\theta\right)$	Combination of longitudinal impact parameter and angle of track
$\tanh\left(\frac{d_0}{10}\right)$	With hyperbolic tangent transformed impact parameter in transverse plane
$\ln\left(R_{\mathrm{conv}}\right)$	Logarithm of track conversion radius
$\tanh\left(\frac{R_{\mathrm{conv}}\cdot\mathrm{sign}(d_0)\cdot q}{500}\right)$	With hyperbolic tangent transformed signed conversion radius
q_{track}	Track charge
$\frac{q_{\mathrm{track}}}{p_{\mathrm{T,\,track}}}$	Ratio of track charge and transverse momentum
Detector hit variables	
$n_{\mathrm{inner\,PL}}$	Number of hits in the innermost pixel layer
$n_{\mathrm{shared\,PL}}$	Number of shared hits in the pixel detector
$n_{\mathrm{shared\,SCT}}$	Number of shared hits in the SCT detector
n_{TRT}	Number of hits in the TRT
n_{PL}	Total number of pixel detector hits
$n_{\mathrm{PL+SCT}}$	Total number of pixel and SCT detector hits
$P_{\mathrm{TRT}}\left(e^-\right)$	TRT hits based electron probability

Table 6.3.1.: Track and jet variables used for RNN training and classification.

Network Architecture

The network used as a classifier is configured and trained with the KERAS [194] high-level API framework in conjunction with the TENSORFLOW software package [195] to calculate the matrix operations. The baseline of the network is formed by three fully connected dense layers. The first dense layer is connected to the variable input and serves to expand the hidden state of the network before the information is fed through the recurrent layers. Between the first and the second dense layer, a variable amount of bLSTM layers with varying numbers of nodes are placed. The number of bLSTM layers and the number of cells per layer are variable hyperparameters and are tuned to give the best performance for a given training setup. The second and third dense layers are used to scale down the dimension of the hidden state to match the number of track classes. Contrary to the bLSTM layers the dense layers do not carry information between time steps. Instead, the same weights are used for each step in the time series. By testing different combinations of the number of dense layer nodes it has been found that the network performance is not impacted by the choice of layer size, given the layers are large enough. Thus the number of nodes is fixed to 80 nodes for the first and 25 for the second dense layer. The dimension of the output layer is fixed to 4 nodes, each representing one track class. Figure 6.3.7 shows a sketch of the network architecture with its variable and fixed parts. The neural
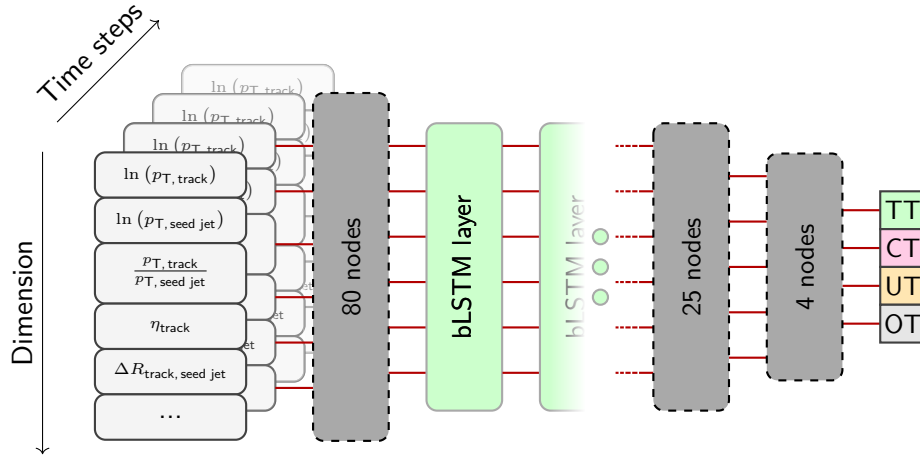

Figure 6.3.7.: Sketch of the track classification RNN architecture going through all tracks associated with a tau decay. While the configuration of the first and second dense layers (gray) is fixed, the number and configuration of the bLSTM layers (green) are variable. The last dense layer maps the network output to a four-dimensional probability for each track class.

network is applied on a sequence of tacks for each tau jet and returns for each track the class probability. Thus the network tries to solve a sequence-to-sequence problem. All layers, with exception of the last dense layer, are configured with Rectified Linear units (ReLu) as an activation function which is given by:

$$\phi_{\mathrm{ReLu}}\left(x\right) = \max\left(0,\,x\right). \tag{6.3}$$

Using the ReLu activation usually allows for a better convergence of deep neural networks during training compared to sigmoid activation functions since the derivative is constant when $x > 0$. This reduces the possibility of vanishing gradients while also being computationally less expensive. The discontinuity of the derivative is numerically not of importance and is manually resolved by setting the value of the derivative at this point to

0. The response returned by the output dense layer is modeled to resemble a confidence probability of the network for classifying a track in a respective class, meaning the output layer activation function must fulfill:

$$\phi_i(x) \geq 0 \qquad \forall x \in \mathbb{R},\, i \in \{1, ..., 4\} \qquad \text{(positive semidefinite)}, \qquad (6.4)$$

$$\sum_{i \in \{1,...,4\}} \phi_i(x) = 1 \qquad\qquad\qquad \text{(unitarity)}. \qquad (6.5)$$

This is achieved by using the softmax activation [196], which is a multidimensional generalized version of the logistic function defined by:

$$\phi_{\text{softmax}}(x_i) = \frac{e^{x_i}}{\sum_{k=1}^{4} e^{x_k}} \qquad i \in \{1, ..., 4\}. \qquad (6.6)$$

The components of the resulting four-dimensional vector output correspond to the track class probability.

All configurations of the network parameters like weight initialization and activation functions of the inner gates of the LSTM cells are summarized in Table 6.3.2.

Layer	Configuration	
Dense layer configurations		
Common	Weight initialization:	Random unifrom acc. Glorot et al. [197]
	Bias initialization:	Zeros
Dense layer 1	Number of Nodes:	80
	Activation:	ReLu
Dense layer 2	Number of Nodes:	25
	Activation:	ReLu
Dense layer 3	Number of Nodes:	4
	Activation:	Softmax
bLSTM layer configurations		
Common	Kernel initialization:	Random unifrom acc. Glorot et al.
	recurrent initialization:	Random othogonal matrix [198]
	Activation:	ReLu
	Recurrent activation:	Sigmoid
Variable hyper-parameters	Number of layers:	$\{1, 2, 3, 4, 5\}$
	Number of cells:	$\{20, 30, 40\,50, 60\}$
	Bidirectional merging:	$\{\text{summation, multiplication}\}$

Table 6.3.2.: Hyperparameter configurations used to train the track classification RNN. Parameters quoted in curly brackets are sets of configurations tested. Using all unique combinations of the variable parameters, a total of 50 networks are trained.

Data Preparation

Based on the hyperparameter configurations outlined in previous sections, a multitude of different networks are trained and evaluated. However, by correlating the information

between tracks in a hadronic tau decay cone the bLSTM network will inevitably learn that taus decay into an odd number of charged hadrons. This behavior is not observed in the BDT based approach as the BDT is insensitive to the total track multiplicity of the tau decay. The bias towards reconstructing 1 and 3 prong taus would also apply to tau candidates reconstructed from QCD jets and increase the background contamination in these categories. Figure 6.3.8 shows the tau track spectra on QCD jets and true taus if the classifier is trained only on tracks from tau candidates. The resulting strong increase in
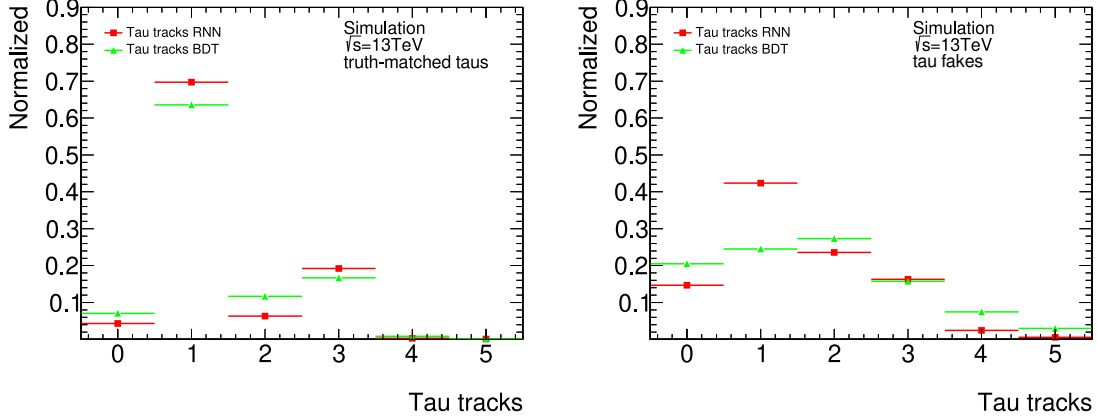

Figure 6.3.8.: Reconstructed tau track spectra on truth taus (left) and taus faked by QCD jets (right) of an RNN only trained on tau decays compared to the BDT based classifier. Although the performance of reconstructing true taus improves when choosing the RNN classifier, this comes at the cost of significantly increased background for 1 prong taus. For this measurement, all Monte Carlo samples are weighted to a common cross-section of 1 pb.

fake taus in the 1 prong category can negatively impact the subsequent tau identification algorithms, potentially leading to worse background rejection performance. To mitigate the bias impact the network is trained on hadronic tau decays and QCD jets containing no tau tracks. The datasets are derived from the Monte Carlo simulation samples listed in Table A.1. To train the neural network and to reduce the over-fitting bias during evaluation, the dataset is split into 3 orthogonal subsamples. The training datasets consist of tracks from about 260 000 tau jet and 200 000 QCD jet decays. A second independent validation set with 10 % of the size of the training set is used to measure accuracy and loss during training. On the last subsets, the evaluation dataset, consisting of 7 million tau jets and 5.5 million QCD jets the efficiency and performance of the classifiers is measured.

For each tau candidate, the associated tracks are sorted by their transverse momentum in descending order. To improve the application and training speed the maximum number of tracks considered for classification is limited to 30 since the vast majority of TT, CT, or UT class tracks in tau jets are contained within this range as shown by Figure 6.3.9. Additional improvements in the stability and speed at which the network converges are achieved by normalizing the truncated training data. Using the standard deviation σ_i and the mean value μ_i measured for each variable on the combined training dataset, each input variable x_i is transformed by the formula:

$$\tilde{x}_i = \frac{x_i - \mu_i}{\sigma_i}. \tag{6.7}$$

Normalizing the input results in significantly improved training stability because the input variables are scaled to a similar numerical magnitude. Especially in the first layers the
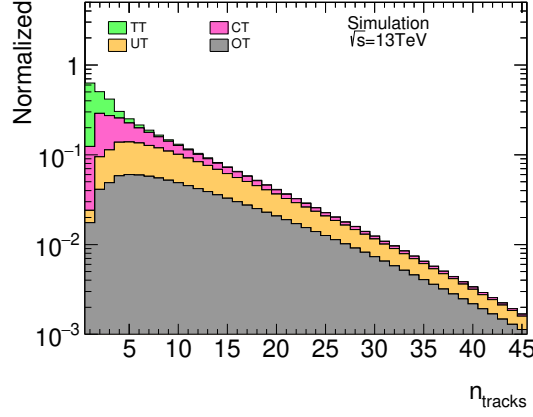
Figure 6.3.9.: This histogram shows the position of different track classes when ordered by the track p_T. The sum of all track categories is normalized to one. With a cutoff set to the first 30 tracks, most of the UT and CT as well as almost all of the TT class tracks are retained while mostly low p_T underlying and pile-up event tracks are discarded.

gradient calculated to update weights during error backpropagation is directly dependent on the numerical values of the input data. Large differences in the scale of the input data can result in large numerical differences of the gradients causing rounding errors due to the limited precision of the calculations and introduce statistical noise. The values of μ_i and σ_i are determined on training data and are then used for data preprocessing throughout training, testing, and inference.

The truth values for each track to which the neural network is fitted, called labels, are calculated based on the truth track category by transforming the four truth track classes to four-dimensional unit vectors, each unit vector corresponding to one track class according to:

$$\mathsf{TT} \to \begin{pmatrix} 1 \\ 0 \\ 0 \\ 0 \end{pmatrix} \qquad \mathsf{CT} \to \begin{pmatrix} 0 \\ 1 \\ 0 \\ 0 \end{pmatrix} \qquad \mathsf{UT} \to \begin{pmatrix} 0 \\ 0 \\ 1 \\ 0 \end{pmatrix} \qquad \mathsf{OT} \to \begin{pmatrix} 0 \\ 0 \\ 0 \\ 1 \end{pmatrix}. \tag{6.8}$$

In conjunction with the softmax layer, the resulting output of the network can be interpreted as a probability that a track is of a certain truth track type. Based on this interpretation, the type with the highest probability is chosen to classify the track.

Training Setup

The network is trained by updating the weights using the backpropagation algorithm while iterating over the training data and truth label set. To calculate the weight updates as outlined in Equation (5.10) the stochastic optimization algorithm *Adam* [199] is used. The Adam optimizer is a gradient descent algorithm based on the running first and second-order derivative of the loss function. Similar to a simple stochastic gradient descent algorithm, the general size of a weight update is controlled by the learning rate η. The loss function best suited for a multi-classification problem with a vectorized representation of the labels is the Categorical Cross Entropy (CCE) defined by [195]:

$$\mathcal{L}_{\mathrm{CCE}}\left(\boldsymbol{x}, \boldsymbol{y}\right) = -\sum_{i=1}^{4} y_i \cdot \log\left(o_{i,\,\mathrm{NN}}\left(\boldsymbol{x}\right)\right), \tag{6.9}$$

with $o_{i,\,\mathrm{NN}}(\boldsymbol{x})$ the prediction of the neural network for class i of one track given the input $\boldsymbol{x}$ and y_i the corresponding truth label.

To stabilize the update procedure, the training dataset is split into disjoint subsets, called *batches*, upon which the error backpropagation is performed resulting in one update per batch. Each full iteration over the dataset equals one *epoch*. The network is trained over a total of 60 to 100 epochs, depending on the size of the network, with batches containing 2000 tau and QCD jet decays each.

While iterating over the datasets the network might reach a stable point in the loss function surface depending on the learning rate that is close to a local minimum. However, if the learning rate is too high, the update step size becomes too big to resolve narrow and steep minima in the loss plane. To achieve a fast and complete convergence the learning rate is decreased over time if no significant reduction in the loss of the validation dataset has been measured over a period of 5 epochs. With this strategy, the learning rate is dynamically adjusted from values starting from $\eta = 5 \cdot 10^{-3}$ to $\eta = 1 \cdot 10^{-5}$.

The setup described so far will lead to fast convergence of the loss function. However, the loss functions and optimization do not take into account the importance of different types of tracks for the reconstruction of tau lepton decays. In fact, due to the overabundance of OT class tracks the network will mostly try to concentrate on identifying the dominant class, resulting in bad differentiation of the other more important track classes. To counteract this behavior and to raise the importance of rarer track classes a balance weight is applied by directly weighting the loss in Equation (6.9) with a balance factor ω_k for each track k:

$$\mathcal{L}_{\mathrm{CCE},\,k}(\boldsymbol{x}, \boldsymbol{y}) = -\omega_k \sum_{i=1}^{4} y_{i,\,k} \cdot \log\left(o_{i,\,k,\,\mathrm{NN}}(\boldsymbol{x})\right). \tag{6.10}$$

Two major sources of imbalances that affect the loss are corrected by deploying a weighting strategy explained in the following.

Different number of tracks in decay cones: The number of tracks in each tau decay cone differs greatly as shown in Figure 6.2.2 in Section 6.2. Additionally, the number of tracks of each class can also vary between tau and QCD jet decays because the latter has no tau tracks but significantly more tracks from particles associated with the underlying event. This difference in class occurrences is corrected by firstly calculating weights for tracks associated with tau candidates from γ^* and QCD samples independently[1] by taking the inverse of the track class fraction:

$$\left.\omega_{k,\,x}^{\mathrm{class}}\right|_{\gamma^*,\,\mathrm{QCD}} = \left.\frac{\sum_{\tilde{x}} n_{\tilde{x}}}{4 n_x}\right|_{\gamma^*,\,\mathrm{QCD}} \qquad x,\,\tilde{x} \in \{\mathsf{TT}, \mathsf{CT}, \mathsf{UT}, \mathsf{OT}\}, \tag{6.11}$$

given that track k is of truth-type x. The factor $\frac{1}{4}$ normalizes the correction factors to values around one. To account for the difference in the total number of tracks in tau candidates between the γ^* and QCD samples, the individual sample weights are rescaled to the mean number of tracks of the two samples:

$$\left.\tilde{\omega}_{k,\,x}^{\mathrm{class}}\right|_{\gamma^*} = \left(\left.\omega_{k,\,x}^{\mathrm{class}}\right|_{\gamma^*} \cdot \frac{n_{\gamma^*} + n_{\mathrm{QCD}}}{2 n_{\gamma^*}}\right), \tag{6.12}$$

$$\left.\tilde{\omega}_{k,\,x}^{\mathrm{class}}\right|_{\mathrm{QCD}} = \left(\left.\omega_{k,\,x}^{\mathrm{class}}\right|_{\mathrm{QCD}} \cdot \frac{n_{\gamma^*} + n_{\mathrm{QCD}}}{2 n_{\mathrm{QCD}}}\right), \tag{6.13}$$

with $n_{\gamma^*/\mathrm{QCD}}$ the total number of tracks in the QCD and tau dataset.

---

[1]As indicated by being evaluated at γ^* and QCD

Different jet momentum profiles: Since the di-jet samples used as sources for tau candidates faked by QCD are sliced in $\hat{p}_\mathrm{T}$ to improve the population of the high p_T phase space, the resulting momentum distribution is uneven and does not have an exponential shape. On the other hand, the γ^* samples are generated without slicing. Thus the p_T distribution of the truth-matched tau jets decays quicker than that of the one faked by QCD jets. The difference in the shape of the tau p_T spectrum will cause the network to focus on the dominant process depending on the jet momenta, diminishing the performance on track classification on truth taus especially in the high tau jet momentum region. To level the importance of both processes, weights $\omega_{k,\,p_\mathrm{T}}$ are calculated by reweighting the p_T distributions of the QCD samples to match that of the γ^* sample. As this weight only depends on the seed jet p_T, each track within a jet cone receives the same weight. Figure 6.3.10 shows the shape of the seed jet momentum distribution before and after applying the weights.
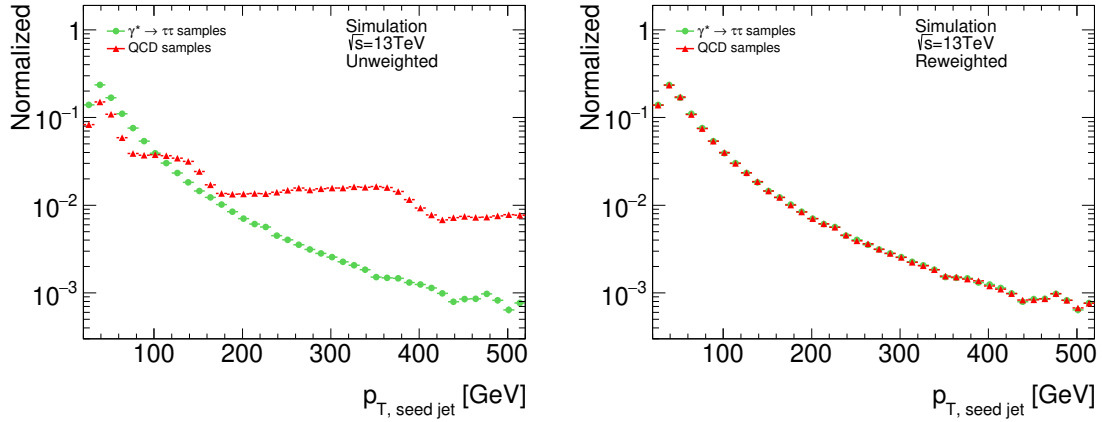

Figure 6.3.10.: Shape of the transverse momentum of the tau seed jet on QCD and γ^* samples before and after reweighting.

The final weight for each track k of truth-type x is then defined by the class balance weight for the γ^* samples and the Hadamard product of the class balance and p_T weights for the QCD samples:

$$\omega_{k,\,x}\bigg|_{\gamma^*} = \hat{\omega}_{k,\,x}^{\mathrm{class}}\bigg|_{\gamma^*}, \tag{6.14}$$

$$\omega_{k,\,x}\bigg|_{\mathrm{QCD}} = \hat{\omega}_{k,\,x}^{\mathrm{class}}\bigg|_{\mathrm{QCD}} \circ \omega_k^{p_\mathrm{T}}. \tag{6.15}$$

6.3.2. Alternative Track Classification

The description of truth classes for tracks in reconstructed tau jet cones as defined in Section 4.3.4 is well suited for true tau decays and is also well defined on tau candidates reconstructed from parton decays. As taus faked by QCD jets do not contain any truth tau tracks the network will try to reconstruct fake tau candidates as 0 prong taus. If the performance is good enough a significant part of the fake taus can be rejected at reconstruction level when cutting on 1 or 3 prong taus. However, strong rejection power at the track classification stage can potentially result in problems for downstream algorithms like tau-ID. Since algorithms used for tau identification are based on results of the track selection, a reduction of fake taus passing the reconstruction for 1 and 3 prong taus might result

in significant depletion of data available to train these algorithms, resulting in reduced performance. Additionally, common data-driven fake estimations frequently rely on jets failing the ID working points. A reduction of the total number of fake taus available before the application of the tau-ID might also significantly increase the statistical uncertainty on the fake estimation measurements. Examples of data-driven fake tau techniques that would be affected negatively by a total decrease of fake tau candidates are the fake-factor and fake-rate techniques explained in Section 7.3 that are used to model backgrounds in the Higgs search analysis.

A possible solution to these problems is to generalize the definition of the tau track class in such a way that the tau track spectrum on fake taus from QCD jets is more continuous. This generalization is supported by the behavior of the BDT based classification on QCD jets. The BDTs are trained only on true tau decays and classify each track independently. The resulting continuous spectra of classified tau tracks on QCD jets shown in Figure 6.3.8 indicate, that a subset of tracks in QCD jets looks similar to tau tracks. To emulate a similar behavior of the neural network on QCD fake tau candidates, a new generalized Direct Tracks (DT) class is proposed which replaces the TT class definition.

Direct tracks are defined at the event generator level by the following recipe. Firstly, for each hadronically decaying tau candidate the highest energy generated quark, gluon, or lepton from the truth record is selected matching the jet within the core region of $\Delta R < 0.2$. This truth particle acts as the truth origin of the jet. Since the origin particle generated on ME level is usually unstable and decays, hadronizes, or undergoes radiative corrections before interacting with the detector, the decay chain of the origin particle is deconstructed by following the branches of the decay chain until reaching the first generation of particles marked as stable by the ME and PS generator. At the generator level, the stability of the particle is determined by the status code assigned by the Monte Carlo event generator where a value of 1 is considered stable or quasi-stable[2] [200]. Further decays of these particles, like photon conversion of π^0, are then treated by the detector simulation. A direct track is defined as a reconstructed track that is truth-matched to one of the first generation stable particles from the deconstructed origin particle decay. The classification of direct tracks is given priority over the classification of the other track classes. After DT classification, the remaining tracks are checked if they match the other class definitions. A sketch visualizing the direct track classification on taus and QCD jets is given in Figure 6.3.11.

To verify that the newly developed DT class is a generalization of the TT class, the overlap and mixing of the new and old track definitions are compared in a confusion matrix shown in Figure 6.3.12. On truth-matched tau candidates, the previously used tau tracks are fully contained within the new DT class while no significant mixing with other track classes is observed, with only around 1.5 % of previous UT type tracks being misclassified as DT. Thus for truth taus, the TT and DT classes are interchangeable without impacting the training of the network. For tau candidates seeded by QCD jets, however, the new DT track-type contains mostly tracks previously classified as underlying event tracks, giving rise to a more continuous track spectrum. The first network setup will be trained with the TT class while a second alternative setup is trained by replacing the TT class with the DT class definition.

---

[2]Status codes and their meaning are generally specific to the Monte Carlo generator and are used to keep track of why and how particles are created. However, status code 1 is generally reserved to mark stable and quasi-stable particles.
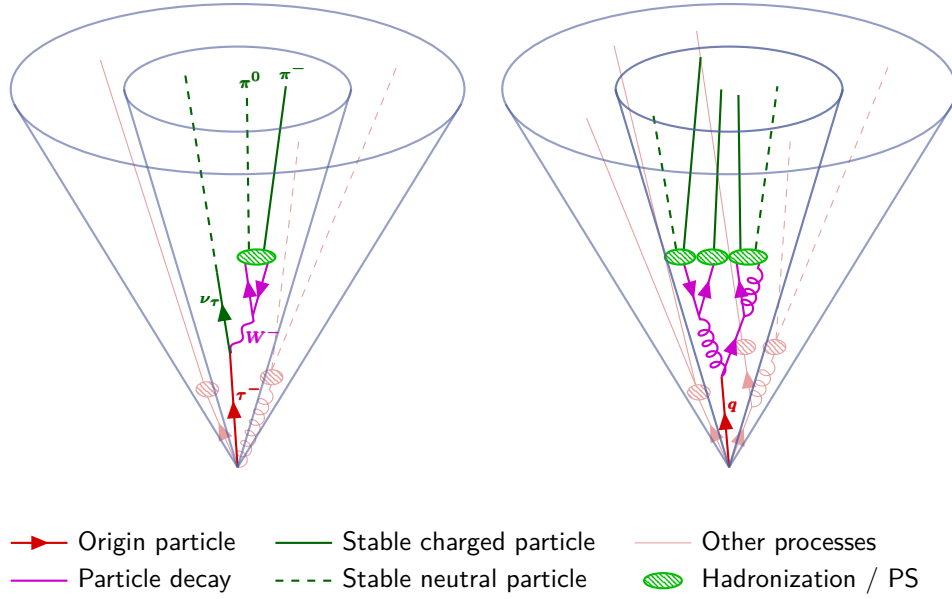
Figure 6.3.11.: Sketch of direct track classification of tracks within a true tau (left) and quark-initiated (right) hadronic tau candidate. The origin of a jet is set to be the highest energy particle in the truth record, overlapping the inner core region of the decay cone. In the case of a true tau initiated candidate, the origin particle is a tau lepton that decays through charged electro-weak interactions into a tau neutrino and hadrons. While in the case of a QCD initiated jet, the highest energy quark or gluon serves as the origin. After following the decay chains, tracks matched to the first generation of stable particles (dark green) are labeled as DT.
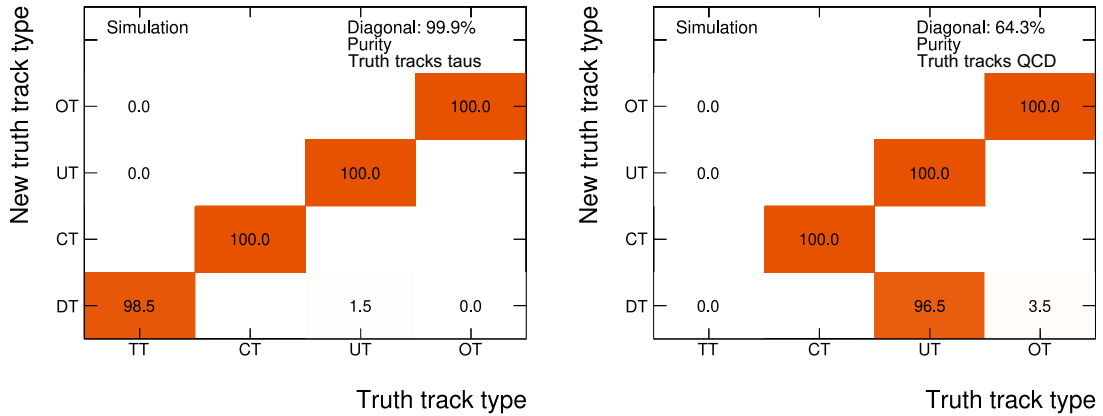

Figure 6.3.12.: Confusion matrix between the nominal and alternative track class definitions for true tau decays (left) and QCD fakes (right). Both definitions are almost identical on true tau decays with more than 98 % overlap between the DT and TT classes. On QCD fakes, the vast majority of DT class tracks were previously classified as UT while the compositions of other track classes are unaffected.

6.3.3. Results: Nominal Setup

The first training setup is conducted using the nominal track classes TT, CT, UT, and OT. By varying the number of bLSTM layers, the merging method as well as the number of nodes in each bLSTM layer a total of 50 networks are trained. A first performance evaluation is made based on the validation loss as well as the difference of the loss on the training and validation dataset. In general, a lower validation loss translates into a better performing network. However, a strong decrease in the training loss while the validation loss is unchanged or worsens might indicate an over-fitting of the classifier. Over-fitting occurs if the network becomes sensitive to statistical fluctuations specific to the training dataset that are not present in the validation dataset. Thus, the network tends to remember the training data instead of learning general structures. This loss of generalization and the tendency towards specialization can introduce performance losses when confronted with new data or even result in unwanted behavior if the new data happens to match the fluctuations on the training data sets. The training and validation loss of the best 4 training configurations using the nominal setup is presented in Figure 6.3.13. In most cases, the training loss is expected to be smaller than the validation loss since the classifier will be slightly biased in favor of the events used to train the model. In general,
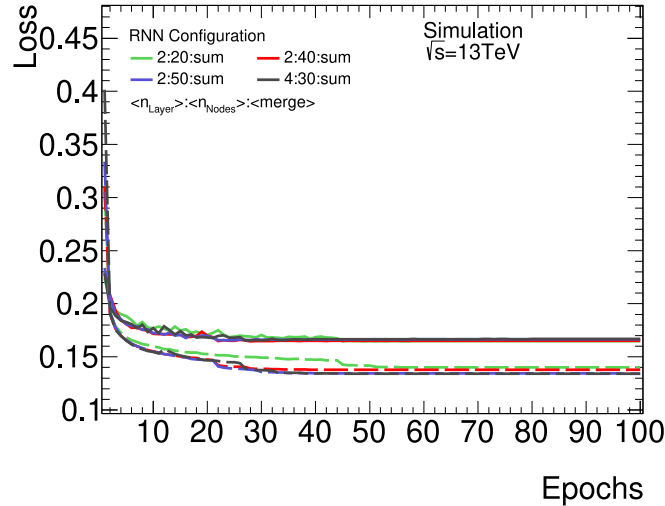

Figure 6.3.13.: Training and validation loss of the 4 best trainings out of the 50 training configurations for the nominal setup, determined by the validation loss. The solid lines represent the loss measured on the validation dataset while the dashed line corresponds to the training data loss. No significant over-fitting is observed.

multiple training configurations converge to similar values of the loss, only showing minute differences. However, the main goal of the track classification is the optimization of the reconstruction efficiency for 1 and 3 prong taus. But the validation loss only gives a general insight into the algorithm performance. Therefore, out of the 4 best training setups the configuration with 4 bLSTM layers and 30 nodes each, using summation as merge function is selected as the final classifier as it shows the best reconstruction efficiency. The track classification efficiency and purity for the selected network configuration are shown in 6.3.14. A major difference compared to the BDT based approach is the additional row for Not Classified tracks (NC). This row includes all tracks that do not pass the 30 track threshold. As shown in the purity migration matrix, this category consists of over 97% of truth OT class tracks. During inference time, unclassified tracks will be treated like OT
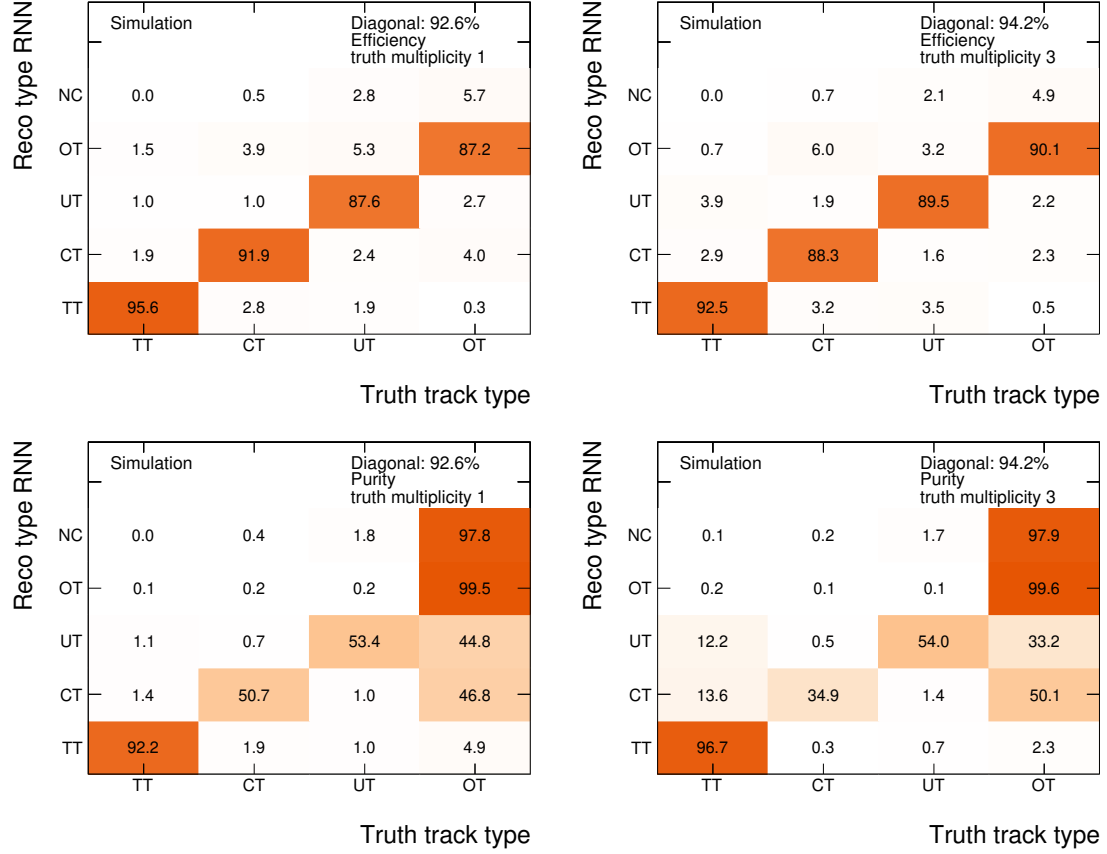
Figure 6.3.14.: Identification efficiency (top) and purity (bottom) confusion matrix for the track selection RNN trained on the nominal setup for taus with truth multiplicity of 1 (left) and 3 (right). The NC class denotes tracks not passing the track cut off of 30 tracks.

class tracks.

Comparing the classification performance of the BDT and bLSTM based track classifiers, the new classifier significantly outperforms the previous approach in terms of classification efficiency. This mostly translates into track categories with higher purities.

For taus with truth multiplicity of 1, the purity of tau tracks and conversion tracks show large improvements. For UT class tracks, despite the classification efficiency increase of 7.1 %, the purity decreased by 5.9 %. This is due to an increase of truth OT tracks being misidentified as UT tracks by 0.7 %. Since the number of OT class tracks in a tau decay cone is usually much larger compared to TT, CT, and UT, a small change in the off-diagonal elements of the OT efficiency will result in significant contamination in the other three track classes.

For tau decays with 3 charged particles, the classification efficiency for tau and conversion tracks is slightly reduced compared with the BDT based algorithm. At the same time, however, the OT off-diagonal efficiency elements of the TT and CT rows are smaller, resulting in higher purities in these track categories. However, the purity of UT class tracks is reduced by 6.7 % due to increased contamination of OT class tracks.

Based on the number of identified tau tracks, the reconstruction efficiency of tau jets being reconstructed as 1 or 3 prong taus is shown in Figure 6.3.15. A significant improvement
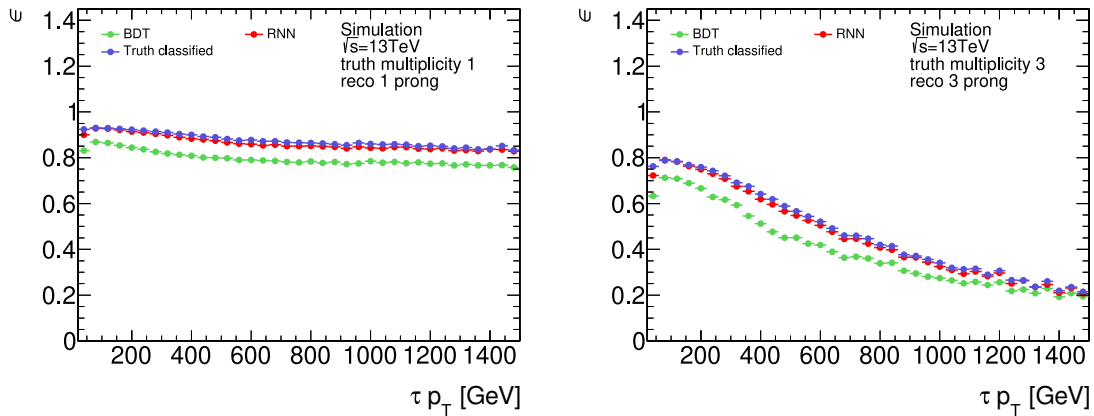

Figure 6.3.15.: Comparison of the reconstruction efficiency for taus with truth multiplicity of 1 (left) and 3 (right) between BDT and RNN based track selection trained with the nominal setup. The two algorithms are compared with the ideal classifier.

in the reconstruction efficiency is achieved by the neural network over the BDT based algorithm, with the new algorithm almost matching the efficiency of the ideal classifier. This shows that the network can utilize the additional information by correlating tracks within the tau decay cone to improve the reconstruction of hadronically decaying tau leptons. Thanks to the addition of tau candidates faked by QCD jets during the training, the tau track spectrum in Figure 6.3.16 on di-jet events does not show an increased background contribution for reconstructed 1 and 3 prong tau candidates compared to the training without QCD jets. Instead, most jets are correctly categorized as 0 prong taus since QCD jets do not contain tau tracks. Therefore, the increase in reconstructed taus of $\sim 10\%$ for 1 prong and $\sim 20\%$ for 3 prong taus is accompanied by a total reduction of expected QCD fakes. An especially strong fake reduction is observed for 3 prong tau candidates, reducing the expected QCD background by 68 %.
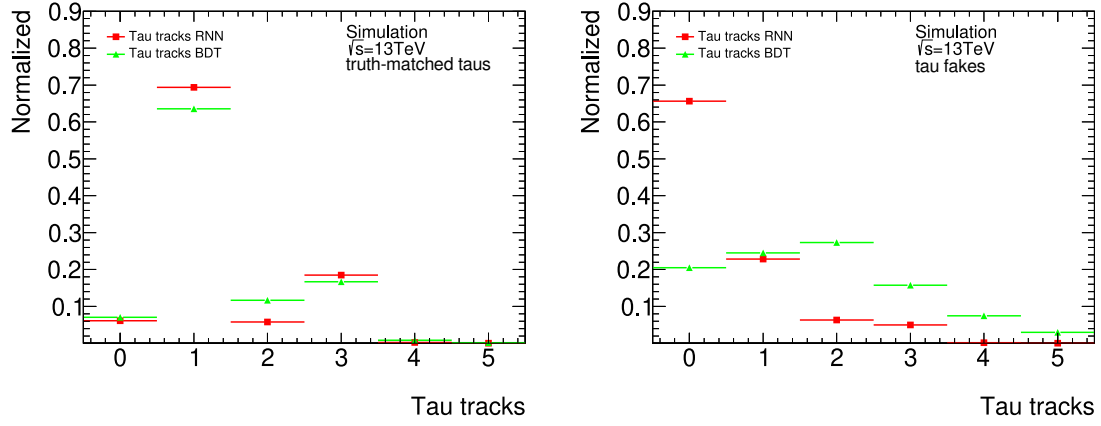
Figure 6.3.16.: Tau track spectra on truth-matched tau jets (left) and QCD fakes (right) of the BDT and RNN based approach trained on the nominal setup. By using the new neural network based classifier, a increase in the total number of reconstructed 1 and 3 prong taus is observed which is accompanied by a total reduction of QCD background in the same prongness categories.

6.3.4. Results: Alternative Setup

Although the performance of the nominal neural network setup shows significant performance gains over the BDT based track classification, the reduced QCD contamination in the 1 and 3 prong category can cause problems for downstream algorithms and data-driven fake estimations. Exchanging the TT class with the DT class during training reduces the bias and the resulting track multiplicity distribution is more continuous on QCD jets. Using the same training setup as for the nominal setup, a preselection is made based on the 4 training setups with the lowest validation loss which are shown in Figure 6.3.17.

From the 4 preselected setups, the one with the best performance on the validation dataset is selected. Based on the tau reconstruction efficiency the model with 4 bLSTM layers, 20 nodes each, and using summation as merge strategy is determined to be the best network setup. The performance measurements of the models trained with the DT class definition are conducted by reverting back to the nominal track class definitions when interpreting the results on the evaluation dataset. This allows for better consistency when comparing the performance of different classifiers. Thus, the DT class tracks identified by the network are treated as TT instead. The classification efficiency and purity are presented in Figure 6.3.18. Similar to the nominal setup significant improvements in the purity of CT and TT class tracks are observed. However, the purity of tracks from the underlying event is worse compared to the nominal setup due to an increase of misidentified truth OT class tracks. The performance loss in the UT category might be caused by the change in track class composition on QCD jets where the new DT track class mainly consists of tracks previously classified as UT class tracks. Since many input distributions for true UT and OT class tracks have similar shapes, like $\Delta R_{\text{seed jet axis}}$ and $p_{\text{T, track}}$, a general loss of identification performance for underlying event tracks is likely to result in a larger overlap with the OT class tracks.

By calculating the prongness of the tau decay from the number of identified direct tracks, the reconstruction efficiencies in Figure 6.3.19 are calculated. Here the efficiency of the network almost matches the ideal classifier. Thus, no significant further improvements in reconstructing tau jets can be expected from the track classification without changes to the track reconstruction itself. Although the alternative setup trained on the DT class
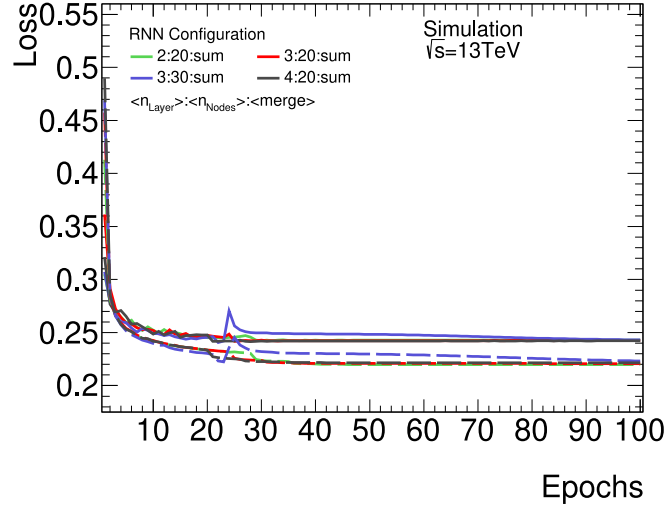
Figure 6.3.17.: Training and validation loss of the 4 best trainings out of the 50 training configurations for the alternative setup, determined by the validation loss. The solid lines represent the training loss measured on the validation dataset while the dashed line corresponds to the training data loss. No significant over-fitting is observed.

performs as well as the nominal setup, a significant difference in the behavior on QCD jets is observed. Figure 6.3.20 shows the number of classified tau tracks for tau candidates from true tau decays and QCD fakes. While the track spectra for true taus look similar to the one observed in the nominal setup, the alternative setup is able to create a continuous distribution on QCD jets.
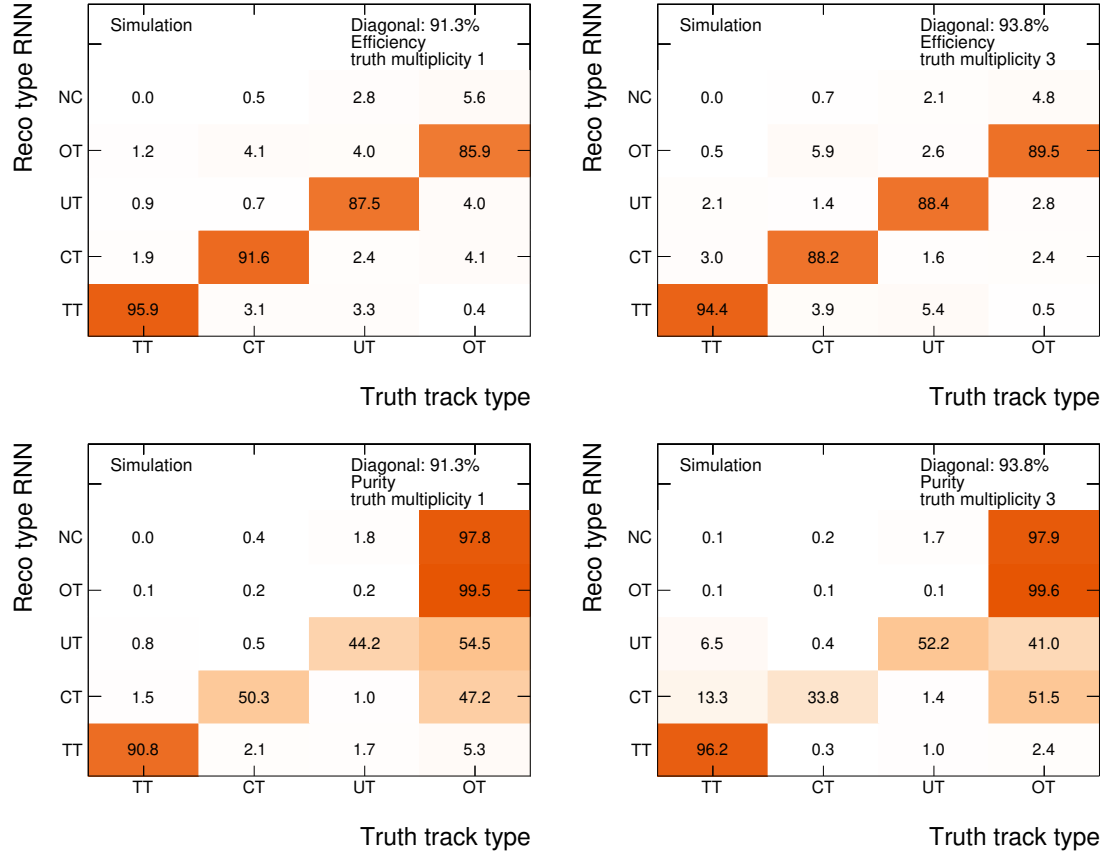
Figure 6.3.18.: Reconstruction efficiency (top) and purity (bottom) confusion matrix for the track selection RNN trained on the alternative track class setup for taus with truth multiplicity of 1 (left) and 3 (right). The NC class denotes tracks not passing the track cut off of 30 tracks. Although the DT class is used during training, the evaluation is conducted by interpreting the DT identified by the neural network as TT classes tracks.
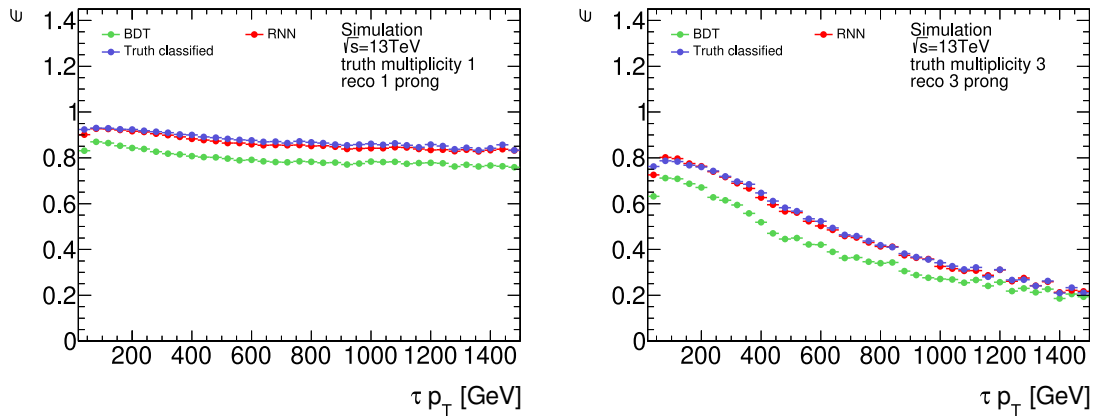
Figure 6.3.19.: Comparison of the reconstruction efficiency for taus with truth multiplicity of 1 (left) and 3 (right) between BDT and RNN based track selection trained with the alternative track class setup. The two algorithms are compared with the ideal classifier.
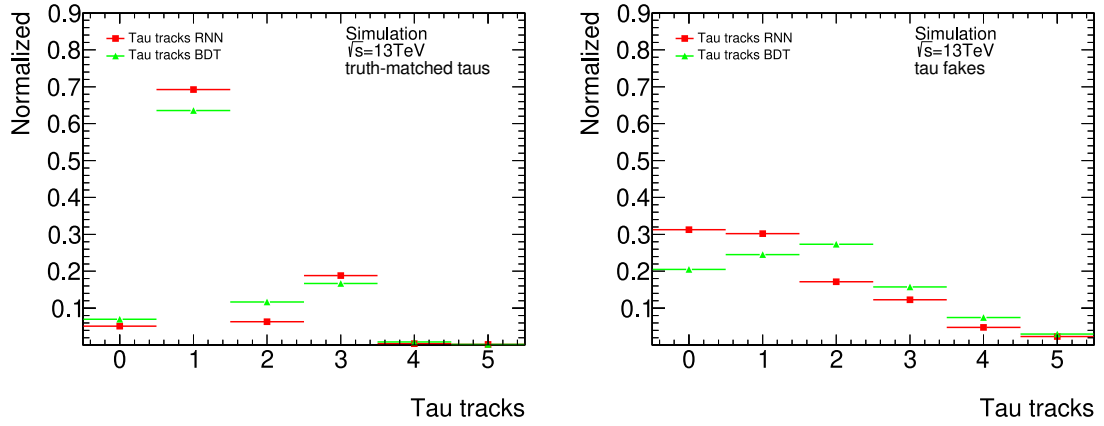
Figure 6.3.20.: Tau track spectra on truth-matched tau jets (left) and QCD fakes (right) of the BDT and RNN based approach trained on the alternative track class setup. Similar to the nominal setup the number of reconstructed truth-matched 1 and 3 prong taus is increased when using the neural network. However, using the DT class during training results in a more continuous track spectrum for tau tracks in tau candidates faked by QCD jets.

7. Search for Neutral Higgs Bosons

In the second part of this thesis, the search for heavy neutral Higgs bosons decaying into pairs of tau leptons is presented. As discussed in Section 2.2 the focus is set on the fully hadronic di-tau $\tau_{\mathrm{had}}\tau_{\mathrm{had}}$ decay channel of the tau pair as it is the dominant decay channel of the tau leptons. The analysis described in this thesis contributes to the results published in Reference [24] together with the search in the semileptonic $\tau_{\mathrm{lep}}\tau_{\mathrm{had}}$ decay channel. However, in the scope of this thesis improvements to the data-driven background estimation and corrections are made, resulting in better background modeling.

An important part of the design of analyses searching for new particles is to select events based on cut criteria to reduce the Standard Model background while retaining as many signal events as possible. In this analysis, an event selection is applied that exploits the kinetic properties of the Higgs boson decay like the back-to-back decay topology of the tau pairs in the transverse plane. To understand the expected background, different SM processes need to be modeled by using Monte Carlo simulation as well as data-driven methods. Especially the latter requires the definition of control and validation regions to measure and study the background modeling before they can be applied in the signal-enriched regions. Finally, the impact of statistic and systematic uncertainties are studied and upper limits are set using a profile likelihood method [201] in the phase space of the theory parameters.

7.1. Higgs Signal Samples

To measure the sensitivity of the analysis to a potential heavy Higgs signal and interpret the results in the different benchmark models presented in Section 2.2.2, template samples of the signal process are required. The models considered in the analysis predict two heavy neutral bosons A and H which differ in mass and CP-eigenstate. Due to the statistical limitations, the analysis is not sensitive to the differences in CP of the two Higgs bosons. Differences in mass between the CP-even and -odd Higgs bosons primarily depend on m_A and $\tan\beta$ but also other SUSY parameters defined within the individual benchmark model. However, for m_{h}^{125} and hMSSM models the mass splitting in the high m_A and high $\tan\beta$ parameter space is typically of the order of $< 10\,\mathrm{GeV}$ which is significantly lower than the mass resolution achieved in the analysis. This is mostly driven by the choice of the final state since decays of taus always involve at least one neutrino which leaves the ATLAS detector without being detected, resulting in a significant reduction of the energy resolution. In general, the differences in mass between A and H bosons can not be resolved in the analysis. Hence, both bosons can be treated as mass degenerate states. Nevertheless, at low values of m_A-$\tan\beta$, the Higgs mass splitting can be significant and exceed the intrinsic mass resolution. In this case, the mass degeneracy assumption is not justified. A detailed study on the mass splitting and the resolution of the analysis is given in Section 7.6.2, testing the validity of the mass degeneracy assumption for each benchmark model and determine exclusion regions where the mass splitting exceeds a predetermined resolution threshold.

As Higgs signal templates serve simulated decays of heavy SM-like Higgs bosons with varying invariant masses. Signal samples are produced for both gluon-gluon fusion and

b-associated production. Samples simulating Higgs production via gluon-gluon fusion are produced with the POWHEG BOX V2 [202–204] as matrix element generator, configured with the CT10 PDF set [205]. The parton shower is calculated by PYTHIA 8.212 [134] using the CTEQ6L1 PDF set [206] and the AZNLO tune [207]. Signal events for the *b*-associated Higgs production are generated at the ME level by the MADGRAPH5_AMC@NLO V2.1.2 [136] using the CT10NLO_NF4 [205] PDF set at NLO accuracy. The events are then showered by PYTHIA V8.212 which is configured with the A14 [137] tune using the NNPDF2.3LO [147] PDF set. For both signal processes, QED corrections in the PS stage are calculated with PHOTOS++ V3.61 [208, 209] while decays of *c*- and *b*-mesons are simulated using EVTGEN V1.6 [210].

Due to a large fraction of negative event weight observed in the *b*-associated signal samples, significantly more events need to be generated to achieve good statistical coverage. Unfortunately, this results in a large increase in computational time needed to simulate the full detector response. Instead, the detector simulation for the *b*-associated signal samples is conducted using the ATLFAST-II simulation of the calorimeter system presented in Section 3.5. Gluon-gluon fusion samples on the other hand are generated using the full detector simulation prescription.

A list of signal samples is provided in Appendix B.2 Tables B.2.18 to B.2.20 for *b*-associated signal samples and Tables B.2.21 to B.2.24 for gluon-gluon fusion. Heavy *A* and *H* bosons are expected to have a narrow decay width which is negligible compared to the intrinsic energy resolution of the reconstructed objects and final discriminating variable. To evaluate the model-dependent results the generated SM-like Higgs signal normalization of the two production processes are scaled to the cross-section times branching ratio of the model prediction.

7.2. Event Selection

In the search for heavy Higgs bosons, the production cross-section of the Higgs signal is usually considered to be much smaller compared to the Standard Model background processes. This requires a dedicated selection procedure to maximize signal yields while reducing background contamination. The selected phase space which is most sensitive to the signal hypothesis is called the *signal region*. Additional phase space regions can be defined which are enriched in a specific SM background while having low signal contamination by altering the signal regions selection criteria. These background enriched regions can be used to validate the background modeling or aid in the background estimation in the signal region. Regions serving the former purpose are called *validation regions* while the latter ones are called *control regions*. In this section, an overview of the baseline selection, signal region and validation region definitions is given.

7.2.1. Baseline Selection

A first selection of the recorded data is applied by vetoing events that do not pass common data quality criteria. Events are only selected if the corresponding luminosity block passes the GRL [128, 129] selection criteria. The GRLs provided for each data-taking period are listed in Appendix B.1. Furthermore, events during which parts of the detector were not fully operational are vetoed. An additional event veto is applied if the recorded event contains jets that originate from non-collision backgrounds, such as cosmic rays or beam-induced backgrounds, as well as jets reconstructed from calorimeter cell noise [211]. After the event quality selection, a set of loose cuts are applied that aim at preselecting events with two hadronically decaying tau candidates:

- at least two hadronic tau candidates with one or three reconstructed tau tracks are required,

- at least one primary event vertex must be detected,

- both tau candidates shall pass the threshold of $p_\mathrm{T} > 45\,\mathrm{GeV}$,

- the event shall be triggered by one of the high-level single-tau trigger or jet triggers (see Appendix B.1).

Based on the loose preselection a tighter event selection is performed to define signal, control, and validation regions.

7.2.2. Signal Region Definition

The signal region is defined by applying an event selection to maximize the purity of the heavy Higgs signal. Firstly, only events triggered by one of the single-tau triggers are selected. The HLT deploys a BDT based algorithm to separate hadronically decaying tau leptons from QCD jets requiring *Medium* online identification criteria [212]. In addition to identification requirements, the tau high-level triggers also deploy varying cuts on the p_T of the L1 seed jet and the reconstructed HLT tau objects. During runs of higher instantaneous luminosity, triggers with lower threshold requirements are prescaled. In this analysis, only events are accepted which pass the active unprescaled trigger with the lowest p_T threshold. During the 2015 to 2016 data-taking periods, three triggers with different momentum thresholds were active and unprescaled at different times, while throughout the 2017 to 2018 periods only one trigger with a threshold of $p_\mathrm{T} > 160\,\mathrm{GeV}$ was unprescaled. A list of active singe tau triggers is given in Table 7.2.1 including their active integrated luminosity in which they were the lowest unprescaled threshold trigger.

Year	Tau trigger	L1 p_T threshold in [GeV]	HLT p_T threshold in [GeV]	Active luminosity in [fb^{-1}]
2015	HLT_tau80	60	80	3.1
	HLT_tau125	60	125	0.1
2016	HLT_tau80	60	80	2.3
	HLT_tau125	60	125	9.2
	HLT_tau160	60	160	21.5
2017	HLT_tau160	60 or 100	160	44.3
2018	HLT_tau160	100	160	58.5

Table 7.2.1.: List of high-level single-tau triggers used to define the signal region including their respective triggered luminosity. The quoted luminosity corresponds to the integrated luminosity during which the trigger was the lowest threshold unprescaled trigger in the respective data-taking period. The trigger names listed here are abbreviations of the full names listed in Appendix B.1.

All reconstructed tau candidates are required to stay within the pseudo-rapidity range of $|\eta| < 2.5$, excluding the transition region between the barrel and end-cap calorimeters $1.37 < |\eta| < 1.52$. Muon candidates considered in the analysis need to be reconstructed within the $|\eta| < 2.5$ region with $p_\mathrm{T} > 7\,\mathrm{GeV}$ and have to pass the *Loose* identification requirement. Reconstructed electron candidates need to pass a threshold of $p_\mathrm{T} > 15\,\mathrm{GeV}$ and fulfill the *Loose* likelihood identification working point, as well as stay within $|\eta| < 2.47$.

Since the reconstruction of different physics objects is done independently, detector signatures can be shared between multiple physics objects. For example, clusters in the EM calorimeter used to seed electron candidates might also contribute to a reconstructed jet. To mitigate double counting of these signatures an overlap removal is deployed removing geometrically overlapping objects by applying a cut on ΔR. Because muons are mainly reconstructed from hits in the MS, other physics objects are rarely misidentified as muon candidates. Thus, the overlap removal procedure eliminates taus and electron candidates from the physics object lists of the event record in favor of identified muons. The pattern is continued by removing objects reconstructed with lower purity against those with higher purity. The following order of removal is applied:

- electrons are removed in favor of muons,

- taus are removed in favor of muons,

- taus are removed in favor of electrons,

- jets are removed in favor of electrons,

- jets are removed in favor of taus.

For all objects, the overlap removal is performed if $\Delta R < 0.2$, except for jets that are removed in favor of electrons where the criterion is relaxed to $\Delta R < 0.4$ since QCD jets produce larger-radius signatures in which the electron can be mistaken as charged pion.

Events containing muons or electrons after overlap removal are vetoed. This allows for cleaner fully hadronic di-tau signatures while also enforcing orthogonality to the $\tau_{\mathrm{lep}}\tau_{\mathrm{had}}$-channel described in Reference [24].

For events passing the selection, the leading and subleading hadronic tau candidates are selected based on their transverse momenta. The leading tau candidate has to match the HLT object that triggered the event within $\Delta R < 0.2$. Depending on the trigger, a cut on the transverse momentum of $5\,\mathrm{GeV}$ above the trigger threshold is applied on the leading tau, which translates into a p_{T} larger than 85, 130, and $165\,\mathrm{GeV}$ for HLT_tau80, HLT_tau125, and HLT_tau160 triggered events respectively. Applying an offline cut above the online trigger threshold is necessary since the online energy calibration is generally less precise than the calibration deployed during offline reconstruction due to the less granular detector information available at the trigger decision stage [212]. Hence, the cut is chosen to be high enough to ensure that the trigger is at the efficiency plateau in order to reduce the impact of the online energy calibration while being as low as possible to achieve a high acceptance for lower mass signals. Additionally, the leading tau candidate must pass the *Medium* identification working point. The subleading tau candidate is required to have $p_{\mathrm{T}} > 65\,\mathrm{GeV}$ and pass the *Loose* tau-ID working point.

To emulate the different trigger thresholds on Monte Carlo simulation, a consecutive luminosity weighing is applied depending on the leading tau p_{T} as well as the Monte Carlo campaign corresponding to the data taking periods. For the MC16a campaign samples matching the 2015-2016 data-taking conditions, the simulated events with a leading tau momentum of $p_{\mathrm{T}} < 130\,\mathrm{GeV}$ are scaled to the combined integrated luminosity of the HLT_tau80 triggers in 2015 and 2016 of $5.4\,\mathrm{fb}^{-1}$. Events with a leading tau momentum between $135\,\mathrm{GeV}$ and $165\,\mathrm{GeV}$ can be triggered by both HLT_tau80 and HLT_tau125 triggers. Thus these events are scaled to the sum of the integrated luminosity exclusively triggered by the two triggers of $14.7\,\mathrm{fb}^{-1}$. Lastly, events with leading tau momentum beyond $165\,\mathrm{GeV}$ can be triggered by all triggers and are subsequently scaled to the total integrated luminosity recorded in 2015 to 2016 of $36.2\,\mathrm{fb}^{-1}$. Since only one trigger was active during the 2017 and 2018 data-taking periods, samples from the corresponding Monte

Carlo campaign MC16d and MC16e are weighted to the integrated luminosity triggered by the HLT_tau160 trigger in the respective periods.

A significant reduction of QCD jet background is achieved by exploiting the conservation of charge by selecting events where the leading and subleading tau candidates are of opposite charge via a cut on the charge product:

$$q_{\tau,1} \times q_{\tau,2} = -1. \tag{7.1}$$

To take advantage of the presence of the additional b-quarks in the final state of the b-associated Higgs production, the MV2 b-tagging algorithm is deployed on jets with $p_T > 20\,\text{GeV}$ within $\eta < 2.5$. This allows splitting of the signal region into two categories: the b-tag category with at least one jet passing the 70 % b-jet tagging efficiency working point, and the b-veto category where no b-tagged jet is found.

Since heavy Higgs bosons would be produced predominantly with small transverse momentum, a cut on the angular distance $\Delta\phi$ between the leading and subleading tau candidate in the transverse plane is applied, selecting a back-to-back decay topology. Distributions of $\Delta\phi(\tau_1, \tau_2)$ are shown in Figure 7.2.1 for backgrounds and different signal hypotheses in the b-veto and b-tag signal regions. A cut of $\Delta\phi(\tau_1, \tau_2) > 2.7$ is chosen because it preserves most of the signal while significantly reducing the background contamination.
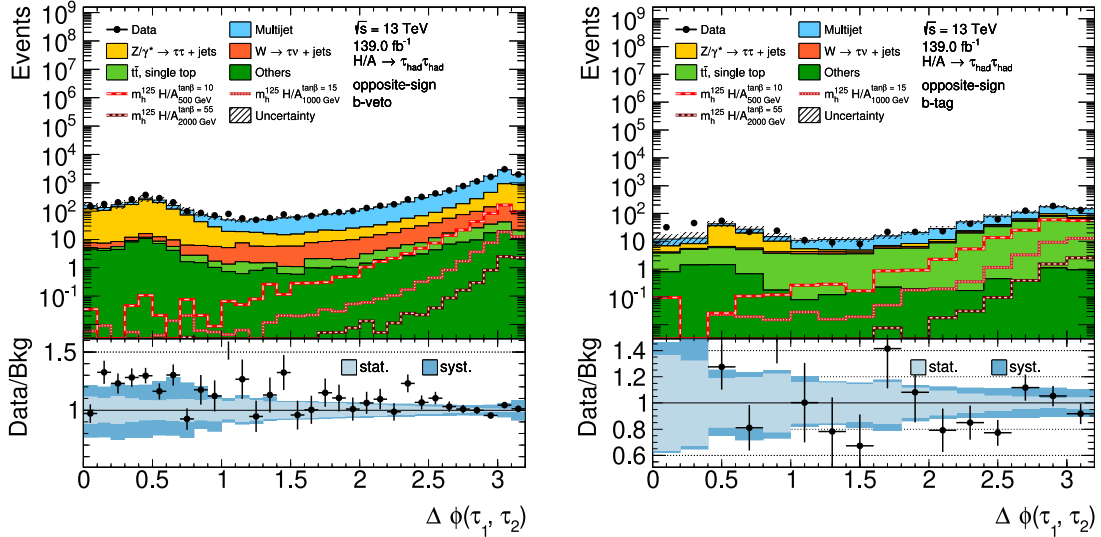

Figure 7.2.1.: Distribution of $\Delta\phi$ between the leading and subleading tau candidate in the b-veto (left) and b-tag (right) category. The backgrounds shown in these plots are estimated following the procedures outlined in Section 7.3. Differences between measured data and estimated background in the b-tag category at $\Delta\phi < 0.5$ are due to limitations in extrapolating multijet background to the low $\Delta\phi$ region since the fake-factors are only calculated for $\Delta\eta > 2.7$. Additionally, the large background contribution of Z/γ^* decays is known to be mismodeled in regions requiring one or more heavy flavor jets [213].

The major backgrounds observed in the signal regions can be differentiated in processes where a QCD jet is misidentified as a tau decay and backgrounds containing true tau decays. The main source of backgrounds where both tau candidates are faked by QCD jets comes from multijet processes. This process is the dominant background background in both the b-veto and b-tag categories. Other leading background processes like $W^\pm \to \tau^\pm \nu_\tau$

in the b-veto category as well as single top and $t\bar{t}$ decays in the b-tag category can contain both, true taus and fake taus. Irreducible background comes from $Z/\gamma^* \to \tau\tau$, mostly present in the b-veto category, resulting in two true tau candidates. The latter process includes heavy off-shell Z/γ^* boson decays which are similar to the heavy Higgs signal processes except for differences in spin and CP state properties. However, due to large statistical uncertainties, the analysis is not sensitive to these differences.

Based on Equation (7.1) one can define a validation region to check the background modeling by inverting the sign requirement to $q_{\tau, 1} \times q_{\tau, 2} = +1$, selecting two tau jets with the same charge. This region is particularly enriched with multijet background and will be referred to as the same-sign validation region.

The expected Standard Model backgrounds and their estimation strategies are explained in the following section. A discussion of the kinetic distributions of the same-sign validation and the signal region is presented in Section 7.4.

7.3. Background Estimation

Backgrounds produced by Standard Model processes significantly contribute to the measured event yields in the signal region. It is therefore a crucial part of the analysis to identify the contributing processes and develop methods to estimate and validate them. All backgrounds, except for multijet events, are estimated using Monte Carlo simulation, where the major backgrounds simulated originate from Z and W boson decay as well as top quark production. Due to the difficult nature of simulating the hadronization of quarks and gluons, backgrounds where one or more QCD jets are misidentified as hadronic tau candidates require a data-driven estimation or correction. The multijet background is fully estimated by a data-driven fake-factor method, while in the case of QCD jets faking tau candidates in Monte Carlo simulated processes data-driven fake-rate corrections are applied on the fake tau candidates. In this section, an overview of simulated Standard Model processes as well as the data-driven methods are presented. Special emphasis is given to the validation of the background estimation.

7.3.1. Monte Carlo Simulated Backgrounds

One of the main backgrounds observed in the b-veto region is caused by the Drell-Yan processes Z/γ^*+jets [214]. Contributions of this process can result in true tau background where the Z boson decays into a pair of hadronically decaying tau leptons as well as fake tau background when electrons or muons from the Z decay are mistaken as tau candidates. The hard scattering process is simulated using the Powheg Box v1 [202–204, 215] generator with the CT10 PDF set [205] at NLO precision. The PS is then computed by Pythia 8.186 [146] configured with the CTEQ6L1 PDF set [206] and the corresponding AZNLO tune [207]. Contributions of QED final-state radiation are calculated with Photos++ [208, 209] while EvtGen v1.2.0 [210] is used to simulate the decay of charm and bottom hadrons. A ME level correction is applied by reweighting the Z/γ^* samples to NNLO precision in α_S by k-factors which depend on the born level mass of the resonance [216, 217].

Background events from W bosons decaying into leptons are simulated with the Sherpa 2.2.1 [135] generator using the NNPDF 3.0nnlo PDF set [218]. The ME calculations are conducted at NLO for up to two jets and LO precision for further two jets with the Comix [219] and OpenLoops [220, 221] packages. The PS handling is done by Sherpa with the internal MEPS@NLO prescription of merging ME and PS [222–226]. The generated $W+$jets boson samples are normalized to analytically calculated NNLO cross-sections [227] with an associated uncertainty of $5\,\%$.

To improve statistical coverage especially at the high invariant mass region, a slicing strategy is applied on the weak boson production samples. The Z boson samples are sliced in the mass of the resonance while for the W samples a slicing in the maximum of the transverse momentum of the boson $(p_T(V))$ or the scalar sum of the parton-level jets (H_T) is applied. The latter slicing is also referred to as max $[H_T, p_T(V)]$ slicing [228].

The second leading background in the b-tag region originates from top quark production. In this analysis, top background is modeled with POWHEG BOX v2 [202–204, 215] in conjunction with the NNPDF 3.0NLO PDF set providing NLO precision at the ME level. Parton showering, underlying event, and hadronization are simulated by PYTHIA 8.230 [134] using the NNPDF 2.3LO [147] set with the A14 tune [137]. Finally, the decay of charm and bottom quarks is done by the EVTGEN 1.6.0 Monte Carlo generator. The top production processes considered are top pair production [229] and single top production, while the latter is further subdivided into the s-, t-, and tW-production channels [230–232]. For $t\bar{t}$ production, the h_{damp} parameter of the POWHEG generator, which governs the high transverse momenta radiation against which the $t\bar{t}$ system recoils, is set to $1.5 \times m_{\mathrm{top}}$ [233] where the top mass is given by $m_{\mathrm{top}} = 172.5\,\mathrm{GeV}$. Higher-order corrections at NNLO for $t\bar{t}$ events are applied by normalizing the production cross-section to the cross-section derived from the TOP++ 2.0 software package [234–240]. During the simulation of single top events in the Wt-channel a diagram removal scheme is applied to suppress interference with $t\bar{t}$ production [241]. The cross-section in this channel is normalized to that calculated at NLO in α_s using next-to-next-to-leading logarithmic soft gluon corrections [242, 243]. For the s- and t-channels the HATOR v2.1 package [244, 245] is used to calculate the corrected production cross-section.

The last background considered simulated by Monte Carlo generators is diboson production. Hard scattered processes with two bosons in the final state are generated using SHERPA v2.2.1 or SHERPA v2.2.2 depending on whether the bosons decay semi- or fully leptonically. The ME calculations are conducted at NLO in α_s for up to one additional parton and to LO for up to three parton emissions. The PS provided by SHERPA is merged with the ME generation using the MEPS@NLO prescription and virtual QCD corrections are calculated with OPENLOOPS. The Sherpa generators are configured with the NNPDF 3.0NNLO PDF set.

A full list of SM background samples and their production parameters is provided in Appendix B.2 in Tables B.2.3 to B.2.17.

7.3.2. Multijet Background Estimation

The production cross-section of QCD jets in hadron colliders like the LHC is typically many orders of magnitudes larger than hard scatter processes with tau leptons. Despite the deployment of dedicated algorithms to distinguish hadronically decaying tau leptons from QCD background, jets faking tau candidates still pose the dominant source of background in the signal regions. Unfortunately, currently available Monte Carlo generators do not model the hadronization of QCD jets well enough, resulting in modeling issues in the tau-ID response. Therefore, a data-driven *fake-factor* method is presented, estimating the multijet background where both tau candidates are misidentified QCD jets.

Di-Jet Control Region Definition

Estimating the number of events where both taus are faked by QCD jets requires the definitions of a control region enriched with multijet background and low true tau contamination. At the same time, the region must be kinetically similar to the signal region to ensure a valid extrapolation from the control region into the signal region. The measurement of the

fake-factors is conducted by a tag-and-probe analysis in the di-jet control region with the leading tau candidate being the tag and the subleading tau candidate the probe object.

The di-jet control region is constructed by inverting the leading tau identification criteria of the signal region, selecting events where the leading tau fails the *Medium* working point. Using single-tau triggers like in the signal region would bias the leading tau candidate as the trigger already deploys an online identification selection. To remove the bias, the single-tau trigger requirement is dropped and instead, events need to be triggered by one of the single-jet triggers with different p_T thresholds between 0 GeV and 420 GeV (HLT_j0, HLT_j15, HLT_j25, HLT_j35, HLT_j45, HLT_j55, HLT_j60, HLT_j85, HLT_j110, HLT_j175, HLT_j260, HLT_j360, HLT_j380, HLT_j400 and HLT_j420) [246–250]. A list of single-jet triggers active during the different data-taking periods is given in Appendix B.1. The statistical sensitivity at low transverse jet momenta is increased by allowing the jet triggers to be prescaled. The prescaling is emulated in Monte Carlo simulation by calculating a correction factor based on the simulated instantaneous luminosity and pile-up that scales events to match the prescale observed in data [150]. To keep the kinetic selection of the di-jet region as close to the signal region as possible, the p_T cut of the leading tau jet is set to $p_T > 85$ GeV. Since the subleading tau serves as probe object, the transverse momentum cut is lowered to $p_T > 50$ GeV to improve the modeling of low-p_T fake-factor measurements. Due to the differences observed in p_T balance of the two tau candidates between the signal region and the di-jet control region shown in Figure 7.3.1, a cut on:

$$p_{T,\,\text{balance}} = \frac{p_{T,\,\text{leading}\,\tau}}{p_{T,\,\text{subleading}\,\tau}} > 0.3 \qquad (7.2)$$
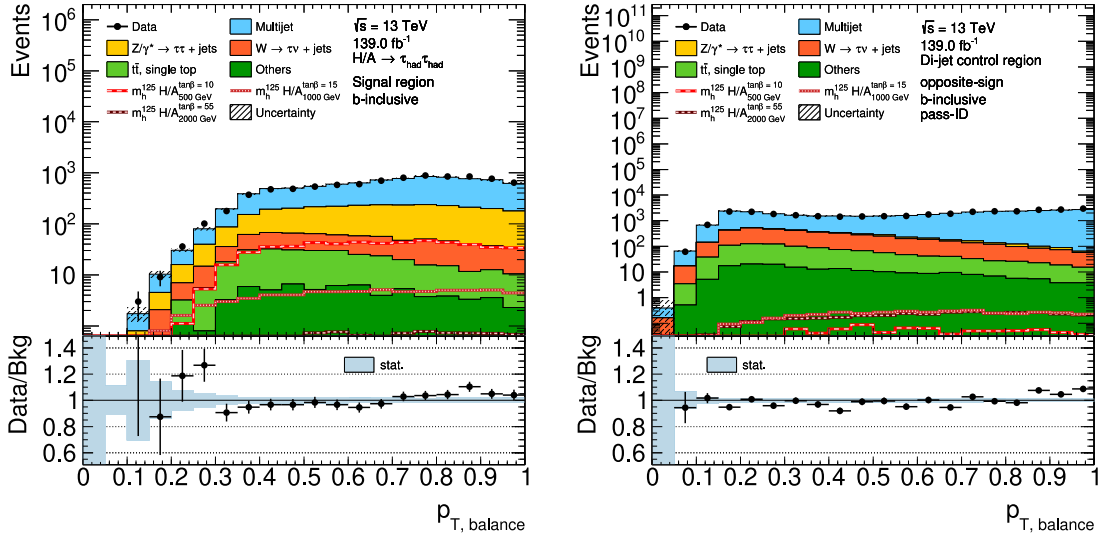
is applied in the di-jet control region.

Figure 7.3.1.: Distribution of the p_T balance of the leading and subleading tau candidate in the signal region (left) and di-jet control region (right). The expected background in the signal region quickly decreases for $p_{T,\,\text{balance}} < 0.3$, while in the di-jet control region the background reaches to significantly lower values of $p_{T,\,\text{balance}}$.

Since fake-factors are measured independently for the opposite-sign, same-sign, the *b*-tag, and *b*-veto category, the di-jet control region is also split into the corresponding subregions.

Fake-Factor Estimation

Fake-factors used to estimate the QCD multijet background are calculated in the di-jet control region. The aim is to measure the change in shape and normalization of the data distribution when inverting the tau identification requirement of the subleading tau candidate. In general, fake-factors are defined via:

$$FF\left(\boldsymbol{x}\right) = \frac{N_{\text{pass-ID}}\left(\boldsymbol{x}\right)}{N_{\text{fail-ID}}\left(\boldsymbol{x}\right)}, \tag{7.3}$$

with $\boldsymbol{x}$ being the set of observables in which the fake-factors are parameterized and $N_{\text{pass-ID}}$ and $N_{\text{fail-ID}}$ being the number of events where the subleading tau candidate passes or fails the tau-ID working point. To measure fake-factors for multijet background in data, all other backgrounds estimated by Monte Carlo simulation need to be subtracted prior to their calculation. Considering the background subtraction, Equation (7.3) is transformed to:

$$FF\left(p_{\text{T}}, N_{\text{Track}}\right) = \frac{N_{\text{data, pass-ID}}\left(p_{\text{T}}, N_{\text{Track}}\right) - N_{\text{MC, pass-ID}}\left(p_{\text{T}}, N_{\text{Track}}\right)}{N_{\text{data, fail-ID}}\left(p_{\text{T}}, N_{\text{Track}}\right) - N_{\text{MC, fail-ID}}\left(p_{\text{T}}, N_{\text{Track}}\right)}, \tag{7.4}$$

where the fake-factors are parameterized in the transverse momenta p_{T} and the number of tau tracks N_{Track} of the subleading tau candidate. The parameterization is chosen to cover the major dependencies of the tau-ID performance, as the background rejection is mostly dependent on the p_{T} and prongness of the tau candidate. Additionally, fake-factors are derived for opposite-sign and same-sign as well as for the *b*-tag, *b*-veto, and *b*-inclusive categories.

To calculate the total multijet background contribution in the signal region, the fake-factors are then reapplied in the *fail-ID signal region*, defined by the same event selection applied in the signal region except that the *Loose* identification requirement on the subleading tau is inverted. Thus, the multijet background yield in the signal region is given by:

$$\begin{aligned} N_{\text{Multijet}}\left(p_{\text{T}}, N_{\text{Track}}\right) = FF\left(p_{\text{T}}, N_{\text{Track}}\right) \times \big[&N_{\text{Data}}\left(p_{\text{T}}, N_{\text{Track}}\right) \\ &- N_{\text{MC}}\left(p_{\text{T}}, N_{\text{Track}}\right)\big]\Big|_{\text{fail-ID}}. \end{aligned} \tag{7.5}$$

Similar to the calculation of the fake-rate itself, Monte Carlo simulated backgrounds are subtracted from data. A sketch visualizing the relation of the regions involved in the multijet estimation is shown in Figure 7.3.2.

In previous searches for heavy Higgs bosons that utilize the fake-factor method, fake taus in Monte Carlo generated backgrounds subtracted from the data yields were directly taken from simulation. However, these fake taus also suffer from the same modeling issues of the tau-ID response as the ones generated in multijet Monte Carlo samples. A new approach to improve the Monte Carlo background modeling and subsequently the multijet estimation is to extend the data-driven fake-rate correction explained in Section 7.3.3 to the di-jet control regions. Previously, this method was only applied to the signal region. The application of fake-rates results in better fake-factor modeling as well as substantially reduced statistical uncertainty on the Monte Carlo background.

Apart from the transverse momentum and the number of charged tracks, the tau identification response also strongly differs depending on the origin of the hadronic jet. Jets initiated by quarks are more likely to fake a hadronic tau decay than jets initiated by gluons. This is caused by the smaller charged track multiplicity expected for quark-initiated jets [251] which are therefore more likely to be misidentified as 1 or 3 prong tau candidates. This behavior is also observed when comparing the tau-ID distributions of simulated
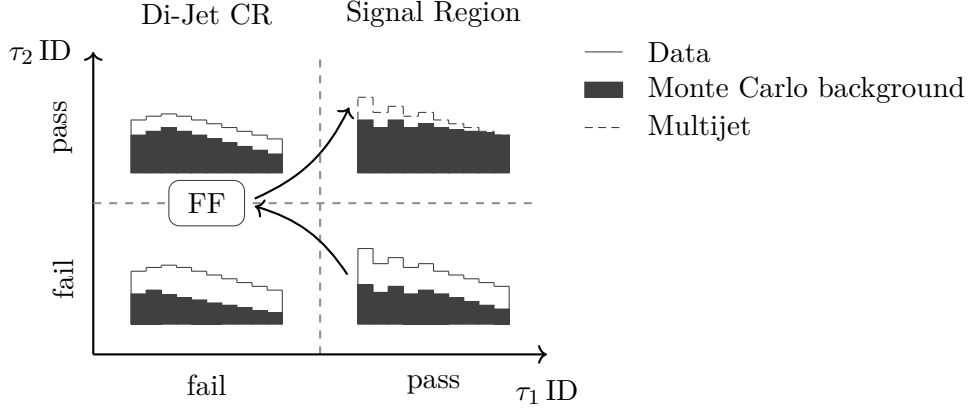
Figure 7.3.2.: Sketch of the regions used in the fake-factor measurement and application. Fake-factors are measured in the di-jet control region by dividing the histograms measured in the subleading tau pass-ID region by those of the fail-ID region. In the signal region, the multijet background is determined by multiplying the data yield in the fail-ID signal region after subtraction of the fake-rate corrected Monte Carlo backgrounds.
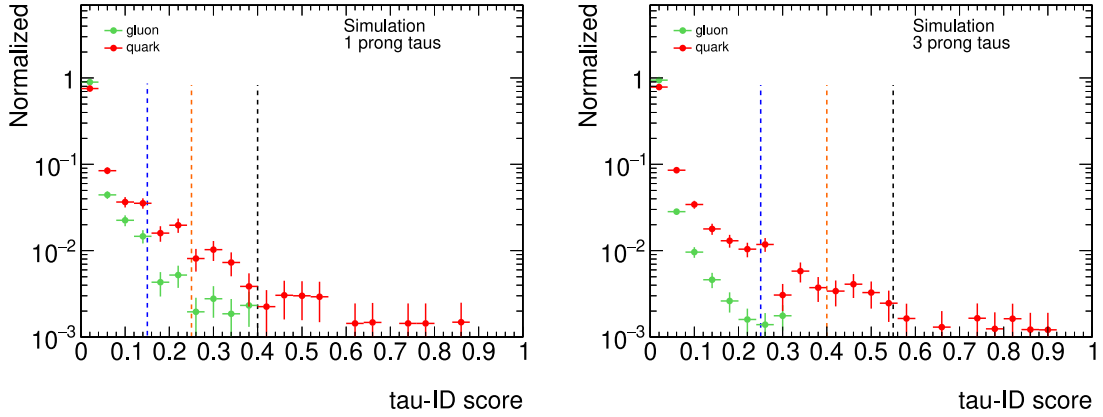

Figure 7.3.3.: Comparison of the tau-ID score between tau candidates faked by gluon-(green) and quark-initiated (red) jets for 1 prong taus (left) and 3 prong taus (right), evaluated on the QCD samples listed in A.1. Dashed lines indicate the score threshold for the *Loose* (blue), *Medium* (orange), and *Tight* (black) working points. All samples are scaled to a common integrated luminosity of $1\,\mathrm{fb}^{-1}$ before being normalized. The distributions of gluon-initiated tau fakes are shifted to lower score values compared to the quark-initiated jets.

quark and gluon-initiated QCD jets reconstructed as tau candidates in Figure 7.3.3. Since the tau-ID response of quark-initiated jets is shifted towards higher values, they have a higher probability to pass the tau-ID working point selection. Unfortunately, the origin of a jet can not be reliably determined in data. Thus, the measured fake-factors in the di-jet control region are a combination of the individual quark and gluon fake-factors and are dependent on the quark-gluon fraction. Although the fake-factors can not be directly parameterized as a function of the quark-gluon fraction, measures can be taken to ensure that all regions involved in the multijet fake estimation have similar quark-gluon composition. As shown in Figure 7.3.3 the largest change in the quark-gluon fraction occurs at low tau-ID score values below 0.1. For higher values above 0.25 fakes from quark initialized jets become dominant, which means only regions where the subleading taus fail the identification requirement need to be corrected.

The quark-gluon fraction is controlled by comparing the normalized distributions of the subleading tau-ID response in data in the fail-ID di-jet and signal regions, separately for different subleading tau prongness as well as for the opposite- and same-sign category. The distributions in Figure 7.3.4 show that the tau-ID score of the probe tau in the di-jet regions is shifted towards smaller values, indicating a higher fraction of gluon-initiated jets. However, above a value of 0.03, the ratio of the di-jet and signal regions are shifted by a constant normalization factor which translates into a similar quark-gluon fraction. Therefore, a threshold cut on the subleading tau-ID score of $\Lambda_{\text{Tau-ID score}} > 0.03$ is applied during the fake-factor measurement and application. Using Equation (4.2), the lower tau-ID cut corresponds to a true tau efficiency of 97 %.

The fake-factors measured in the di-jet control region are shown in Figure 7.3.5, comparing the results of the *b*-tag, *b*-veto, and *b*-inclusive categories. Individual fake-factors are calculated in the opposite-sign and same-sign region, as well as for reconstructed 1 and 3 prong subleading tau candidates.

The fake-factors are calculated in discrete bins of the subleading tau p_{T}. A list of the bin edges for all subcategories is given in Appendix B.3.1 Table B.3.1. The binned fake-factors are then smoothed using a smoothing algorithm described in Reference [252]. The bin centers of the smoothed histogram are then linearly connected allowing for smoother interpolation of the fake-factors between bins. Three types of uncertainties are considered in the fake-factor calculation: the statistical uncertainty on data as well as the statistical and systematic uncertainties on the Monte Carlo estimated backgrounds which are subtracted from data. The third source of uncertainty covers systematic uncertainties related to the identification, reconstruction, and calibration of the selected physics objects in Monte Carlo simulation. These sources of systematic uncertainties are discussed in Section 7.4.4. The statistical uncertainties of the data and the subtracted background are decorrelated for each bin. Since the impact of the systematic uncertainties affecting the Monte Carlo background on the fake-factors is small compared to the statistical uncertainty, all systematic variations are added in quadrature and combined in one single uncertainty. Considering all sources of uncertainty, the comparison in Figure 7.3.5 indicates that the fake-factors measured in *b*-tag and *b*-veto are statistically compatible. This is also supported by the comparison of the tau-ID score distribution in Figure 7.3.6 between the two categories. The shape of the tau-ID score distributions is similar in the *b*-tag and *b*-veto category. This suggests that both categories of the di-jet control region also share a similar quark-gluon fraction. Therefore, only the *b*-inclusive measured fake-factors are used to estimate multijet background. To account for residual differences between the *b*-inclusive and the *b*-tag or *b*-veto category, an additional one-sided uncertainty is calculated by using the difference in the nominal fake-factor distribution between the *b*-inclusive and the corresponding *b*-tag and *b*-veto category. The final fake-factors are presented in Figure 7.3.7 for
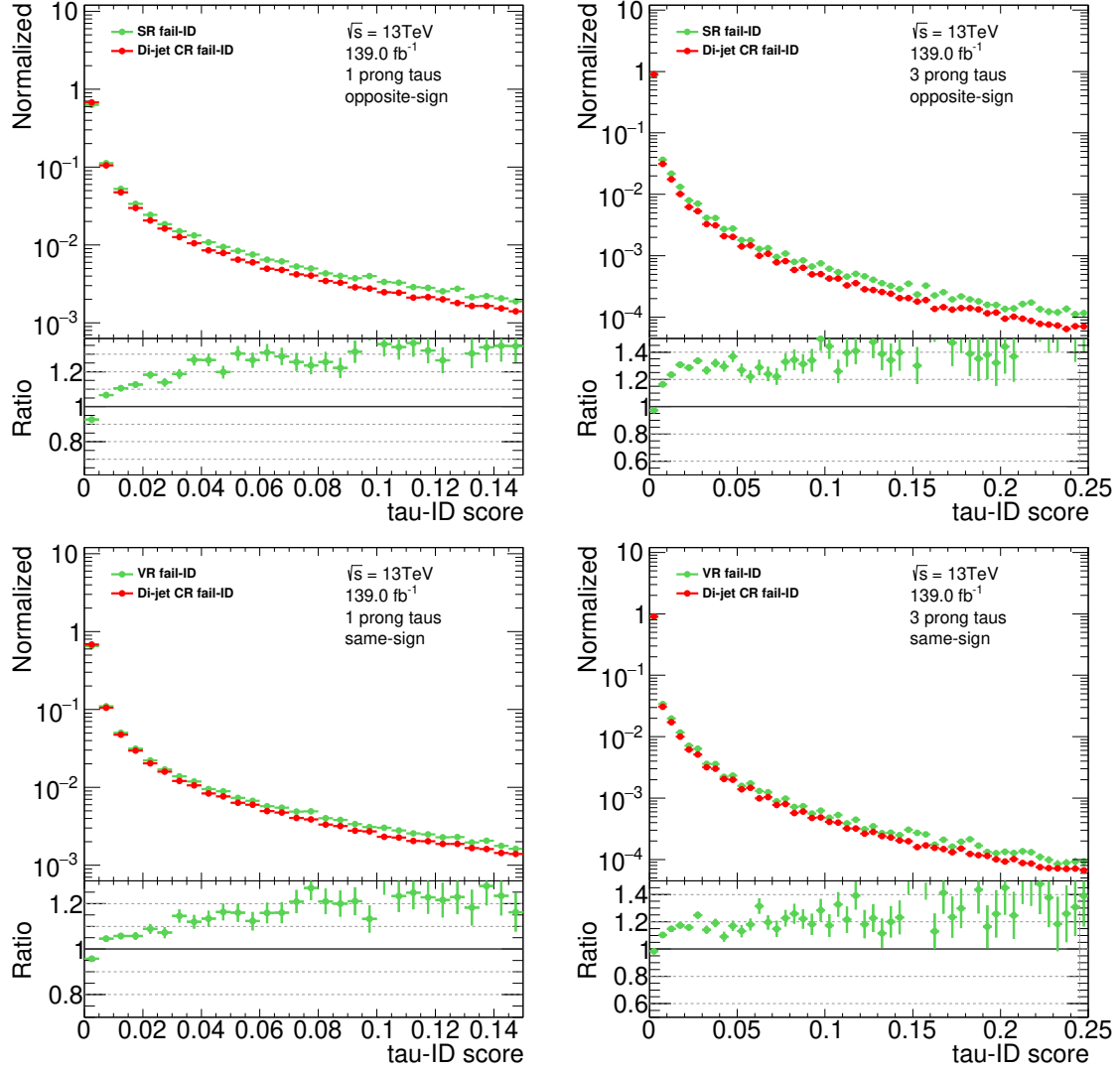
Figure 7.3.4.: Tau-ID distributions of the opposite-sign signal region (top) and the same-sign validation region (bottom) with their respective di-jet control regions. The histograms show the normalized distributions in data after subtraction of all estimated backgrounds not related to multijet production. Above a tau-ID threshold of 0.03, the ratio between the normalized distributions in the di-jet control region and the validation region is constant, indicating a similar quark-gluon fraction between these regions.

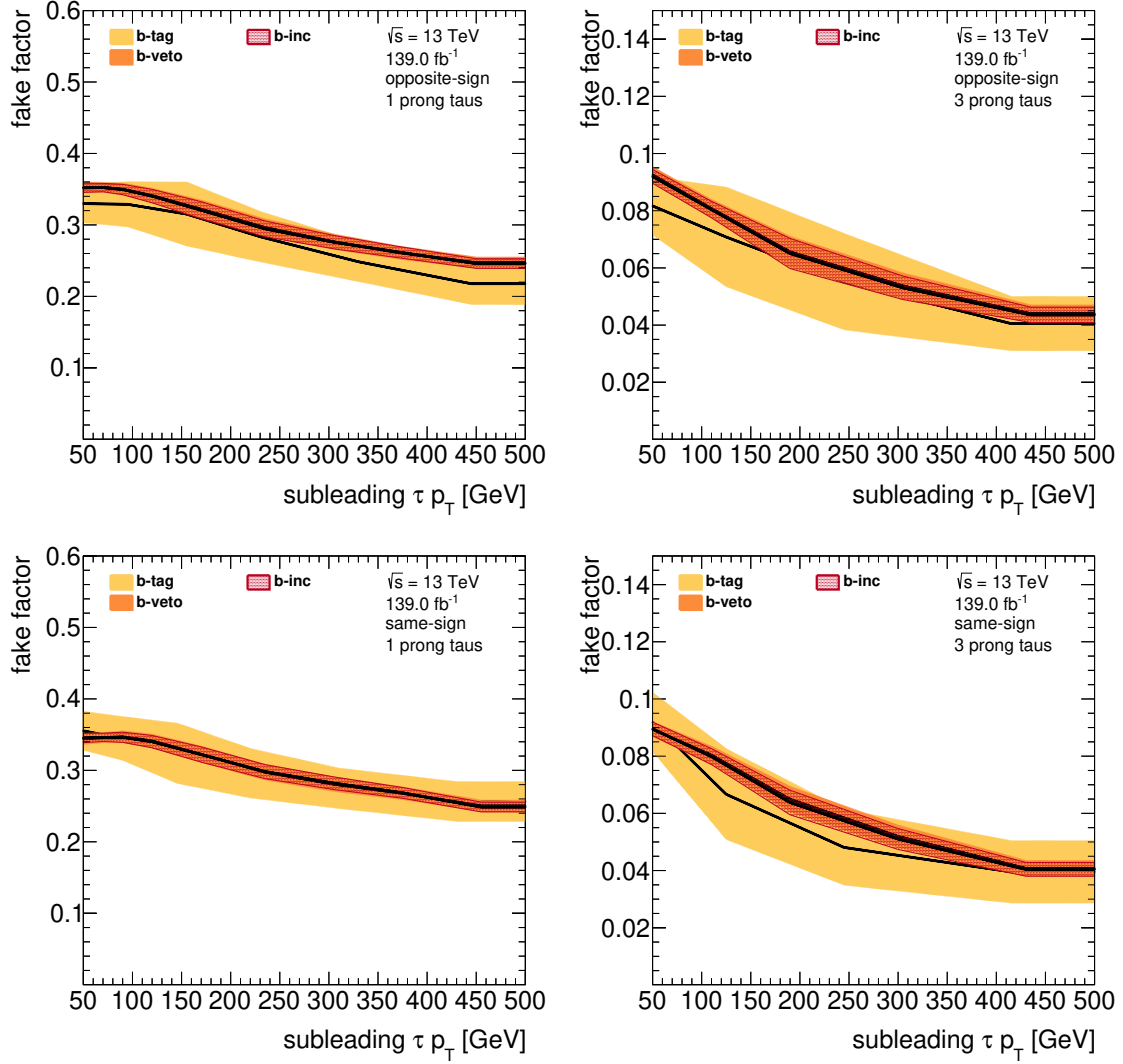Figure 7.3.5.: Fake-factors measured versus the subleading tau p_T in the opposite-sign (top) and same-sign (bottom) di-jet control region for 1 prong (left) and 3 prong (right) subleading tau candidates. The solid lines correspond to the nominal fake-factors measured in the b-tag, b-veto, and b-inclusive categories. The bands around the nominal graphs represent the total uncertainty on the fake-factor measurement.
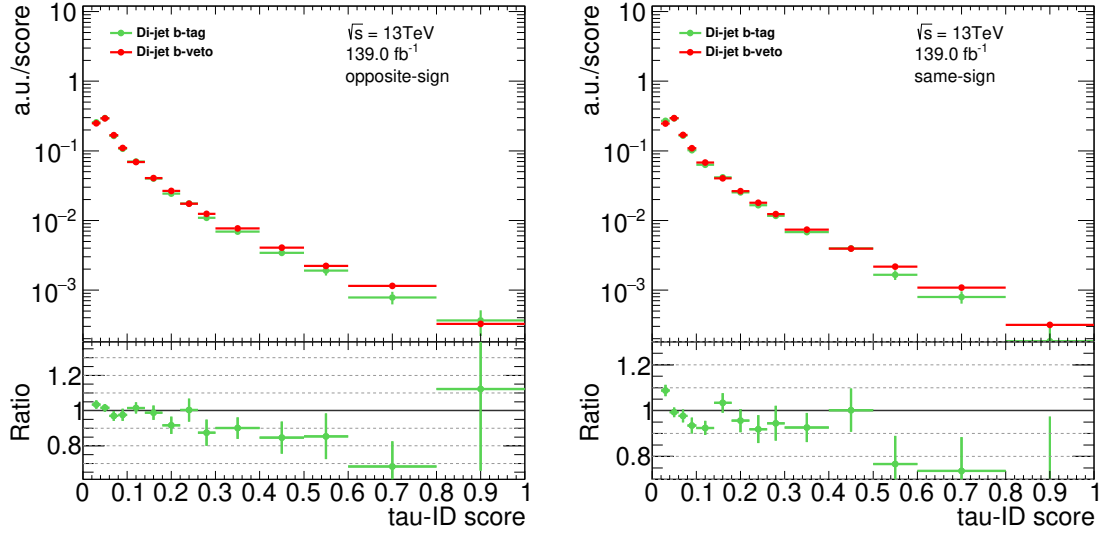
Figure 7.3.6.: Comparison of tau-ID score distribution in the di-jet *b*-tag and *b*-veto control regions used for opposite-sign (left) and same-sign (right) fake-factor calculation. No significant differences in the shape of the normalized distributions are observed.

the opposite-sign signal region and in Figure 7.3.8 for the same-sign validation region.

The validity of the fake-factors is cross-checked in a closure test by reapplying the fake-factors in the di-jet control region. Potential mismodeling when using the *b*-inclusive fake-factors in the *b*-tag and *b*-veto category as well as residual dependencies of the fake-factors on other variables would be visible in the closure test. The modeling of the subleading tau transverse momenta distributions in Figure 7.3.9 show no significant deviation of measured data and estimated background, indicating the *b*-inclusive fake-factors can be used in both *b*-categories. Further distributions of other kinetic variables are listed in Appendix B.3.2.

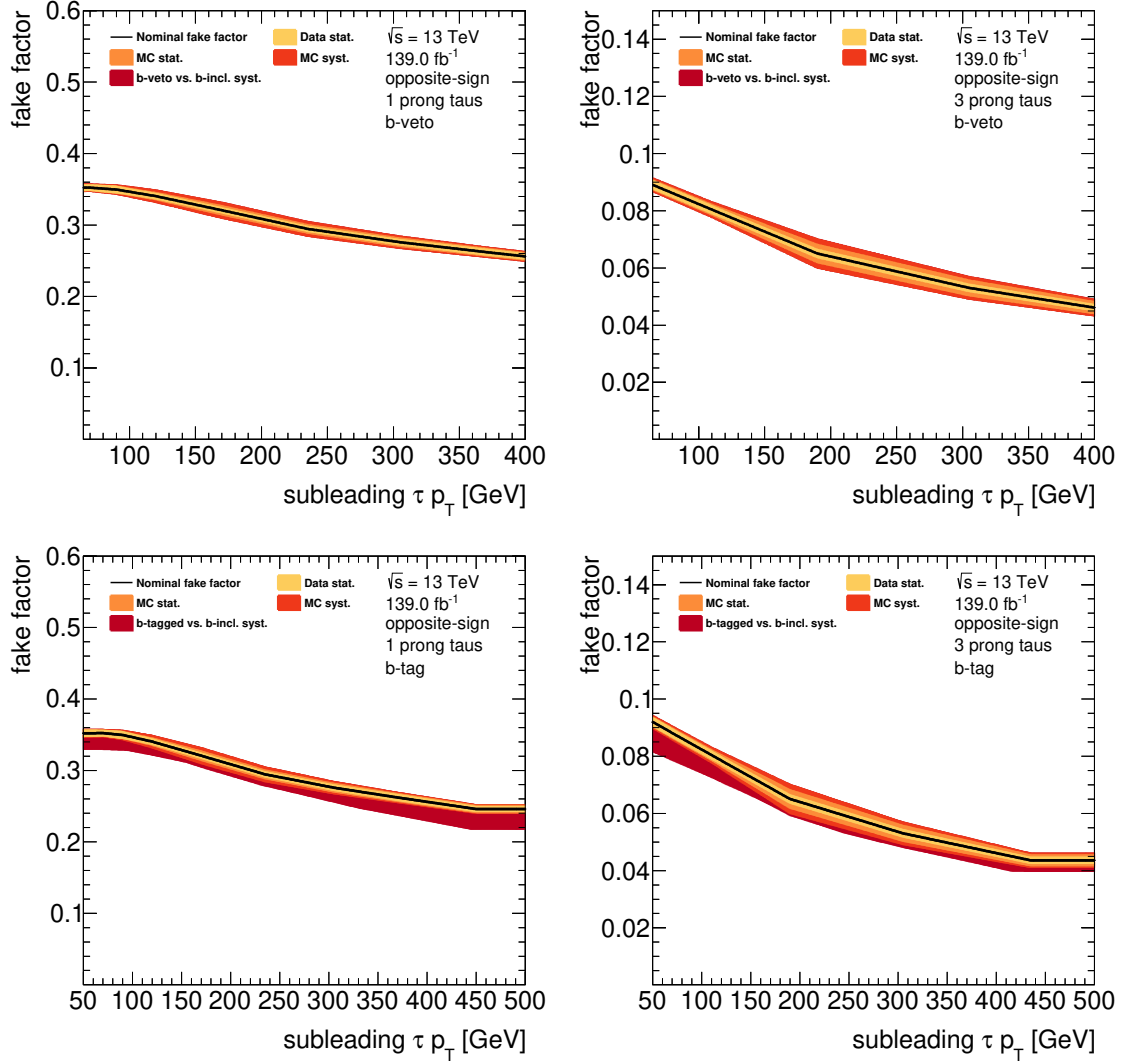Figure 7.3.7.: Fake-factors measured in the opposite-sign di-jet control region for 1 prong (left) and 3 prong (right) subleading tau candidates. The nominal value corresponds to the fake-factors measured in the *b*-inclusive category. Additional uncertainties are introduced to cover the difference between the nominal fake-factors in *b*-inclusive and *b*-veto (top) or *b*-tag (bottom) categories.

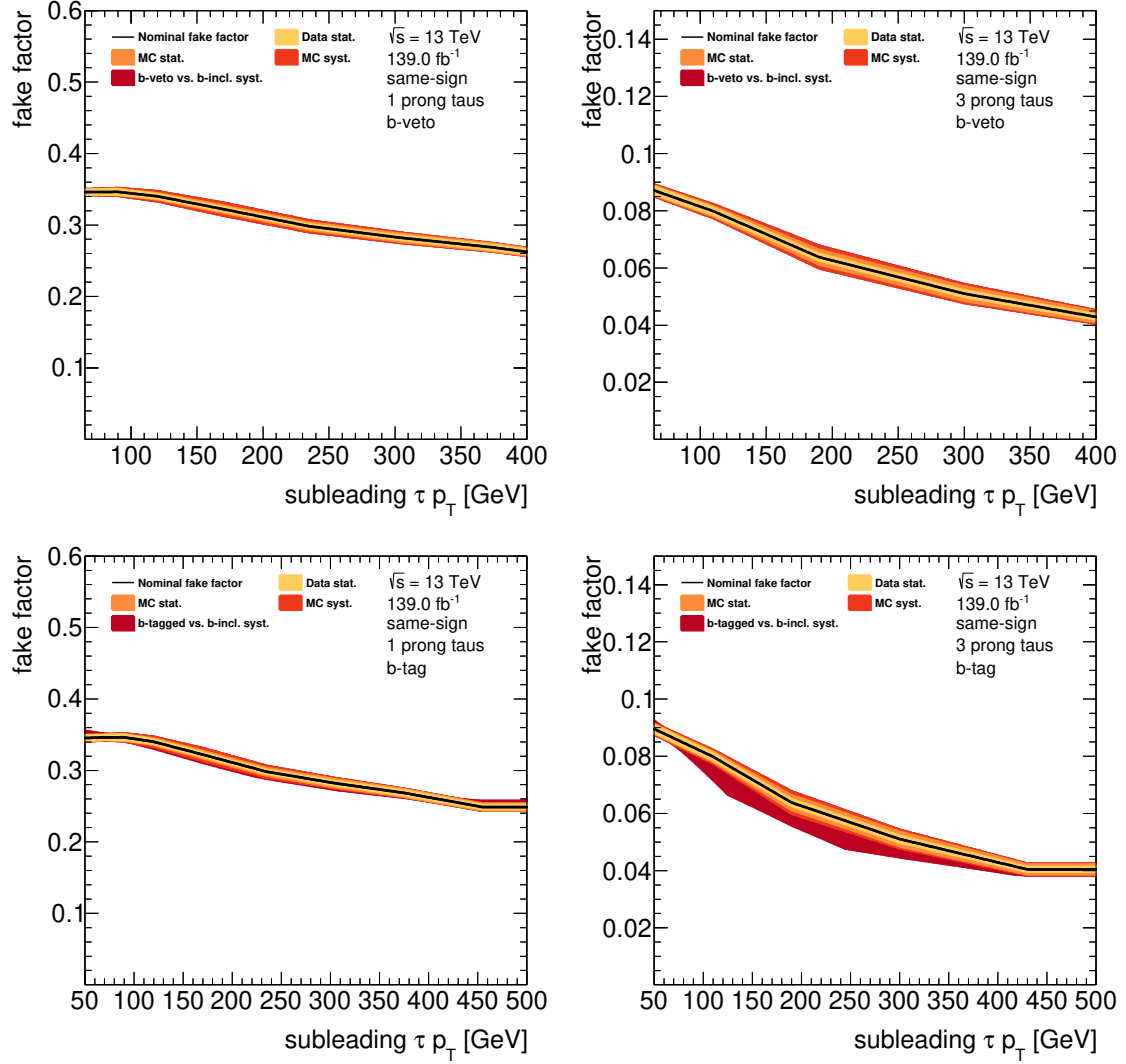Figure 7.3.8.: Fake-factors measured in the same-sign di-jet control region for 1 prong (left) and 3 prong (right) subleading tau candidates. The nominal value corresponds to the fake-factors measured in the *b*-inclusive category. Additional uncertainties are introduced to cover the difference between the nominal fake-factors in the *b*-inclusive and *b*-veto (top) or *b*-tag (bottom) category.
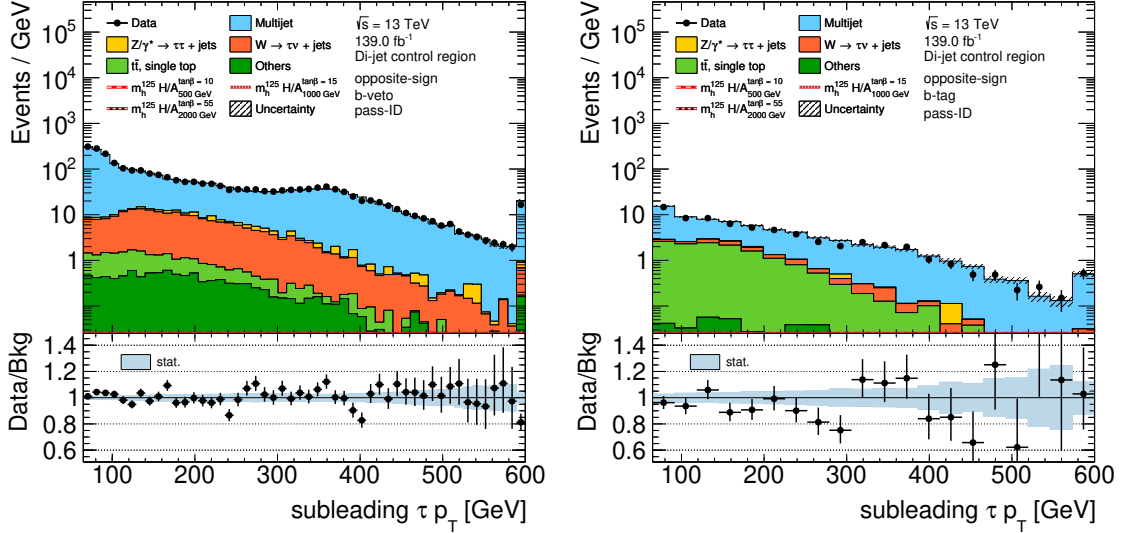
Figure 7.3.9.: Fake-factor closure test in the opposite-sign pass-ID di-jet control region for *b*-veto (left) and *b*-tag (right). The closure test is conducted by reapplying the measured *b*-inclusive fake-factors in the fail-ID region to estimate the multijet background in the pass-ID region. Only statistical uncertainties are considered.

7.3.3. Fake-Rate Method

Although events, where both tau candidates are faked by QCD jet production, are modeled using fake-factors, the Monte Carlo simulated backgrounds outlined in Section 7.3.1 still contain cases where one or both tau candidates are faked by hadronic jets originating from gluons or quarks. The modeling of the tau jet fakes on Monte Carlo simulation is corrected by comparing the probability of a jet faking a hadronic tau decay for a given tau-ID working point between simulation and data. This measurement requires a definition of a control region enriched with fake taus by selecting a topology similar to the signal region. Since a correction is applied on the rate of jets faking taus, the correction factors will be denoted as *fake-rate*. A fake-rate is generally defined by

$$FR\left(\mathbf{x}\right) = \frac{N_{\text{pass-ID}}\left(\mathbf{x}\right)}{N_{\text{pass-ID}}\left(\mathbf{x}\right) + N_{\text{fail-ID}}\left(\mathbf{x}\right)} = \frac{N_{\text{pass-ID}}\left(\mathbf{x}\right)}{N_{\text{all}}\left(\mathbf{x}\right)}, \tag{7.6}$$

where $N_{\text{pass-ID/fail-ID}}$ is the number of events passing or failing the ID working point threshold and $\mathbf{x}$ defines the set of observables used for parameterization.

The fake-rates are measured with a tag-and-probe analysis in the $\mu\nu$+jet control region. This control region was introduced in previous searches for heavy neutral Higgs bosons like in Reference [24], to which this thesis contributes to, or in Reference [83]. However, in the scope of the analysis presented here, improvements were made to the event selection and measurement strategy to increase the statistical coverage and the robustness of the fake-rate correction. Additionally, the application of the fake-rate corrections is extended to all regions used for fake-factor estimation, thus improving the modeling of the multijet background as well. In previous publications of this analysis, the fake-rate application was only applied to tau fakes in the signal region.

The $\mu\nu$+jet control region is defined by selecting an isolated muon as the tag object and a tau candidate that serves as the probe object with both objects located back-to-back in the transverse plane. Events in this region must pass the same preselection criteria on the

GRL and run conditions as in the signal region. Events are triggered by the HLT_mu50 single muon trigger, applying an online threshold cut on the transverse momenta of the muon of $p_T > 50\,\text{GeV}$ [253]. The leading muon has to pass a slightly higher offline threshold of $p_T > 55\,\text{GeV}$ and geometrically match the HLT object. Only events where the leading muon passes the *Medium* identification working point are selected. To reduce background from non-prompt muon production the *Tight Fixed Radius* isolation requirement is applied. Events with additional muons with $p_T > 7\,\text{GeV}$ and electrons with $p_T > 15\,\text{GeV}$ passing the *Loose* ID requirement are rejected. This reduces the contamination of processes with a di-lepton final state. The selection of a medium isolated muon makes the $\mu\nu$+jet control region fully orthogonal to the signal region. Further kinetic event selections that are applied are:

- the leading tau candidate shall pass $p_T > 55\,\text{GeV}$,

- both, leading muon and probe tau are back-to-back in the transverse plane with $\Delta\phi_{\mu,\tau} > 2.4$,

- the transverse mass between muon and E_T^miss shall be greater than $m_\text{T}\left(p_{\text{T},\mu}, E_\text{T}^\text{miss}\right) > 40\,\text{GeV}$,

with the transverse mass defined as [83]:

$$m_\text{T}\left(p_{\text{T},\mu}, E_\text{T}^\text{miss}\right) = \sqrt{2p_{\text{T},\mu} \cdot E_\text{T}^\text{miss} \cdot \left[1 - \cos\Delta\phi\left(p_{\text{T},\mu}, E_\text{T}^\text{miss}\right)\right]}. \qquad (7.7)$$

Compared to the signal region selection the cut on the transverse angle between the two primary objects is relaxed to increase the statistical coverage. A threshold cut on the transverse momentum of the tau candidate is set to $p_\text{T} > 55\,\text{GeV}$, slightly below the signal region threshold to ensure a smooth interpolation of the fake-rates in the low momentum regime.

The cut on $m_\text{T}\left(p_{\text{T},\mu}, E_\text{T}^\text{miss}\right) > 40\,\text{GeV}$ is deployed to achieve orthogonality to the $\tau_\text{lep}\tau_\text{had}$ channel signal region. Since the two largest Mote Carlo simulated backgrounds contributing fake taus are related to the top and W boson decays, the $\mu\nu$+jet control region is split into b-tag and b-veto categories to isolate these background processes. The b-tag control region is enriched with hadronic tau fakes from top decays while in the b-veto category the $W \to \mu\nu$ process is the dominant background. Since both processes are expected to have different probabilities of faking hadronic tau decays, fake-rates are determined separately in the two categories.

Fake-rates are measured for the ID thresholds of both selected tau candidates in the signal region. For the subleading tau candidate, fake-rates are measured with the probe tau passing the *Loose* ID working point while for the leading tau object a combination of the *Medium* working point and the HLT trigger is applied. The latter is realized by requiring that the tau candidate passes the offline *Medium* ID requirement, as well as checking whether the events would also pass a simulated trigger decision of the HLT_tau25 trigger with the probe tau matching the HLT trigger object. The lower threshold tau trigger can be used to emulate the higher threshold triggers applied in the signal region as the triggers only differ in the transverse momentum threshold of the tau candidate [212]. The combination of the *Medium* and HLT threshold is referred to as *Medium+Trigger*.

In addition to the fake-rates applied in the signal region, new ones are developed for the tau fakes in the di-jet control and signal fail-ID region. For the leading tau selected in the di-jet control region, fake-rates are calculated based on the probe tau candidate failing the *Medium* ID working point. Similarly, for the subleading tau fake-rates for failing the *Loose* ID but passing the lower ID cut are derived.

To improve the purity of fake tau backgrounds and reduce contributions from true tau backgrounds, an upper cut on $m_{\mathrm{T}}\left(p_{\mathrm{T},\,\mu},\,E_{\mathrm{T}}^{\mathrm{miss}}\right) < 150\,\mathrm{GeV}$ ($110\,\mathrm{GeV}$) in the b-veto (b-tag) region is introduced. The cuts are chosen based on the *Medium+Trigger* distributions shown in Figure 7.3.10 since here the largest fraction of true tau background is observed. The fake-rates are parameterized in the transverse momentum of the tau candidate and the
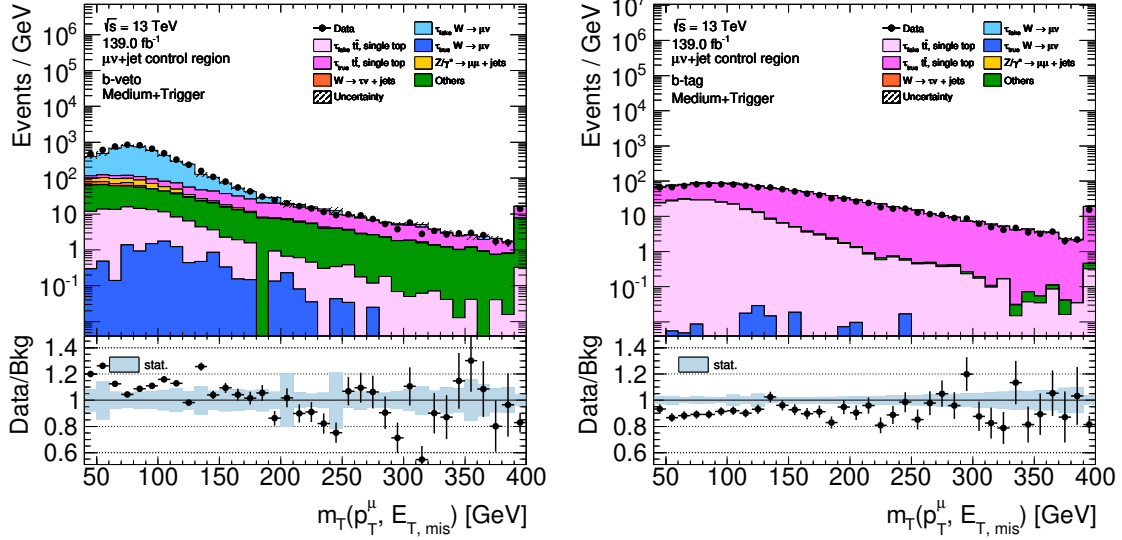

Figure 7.3.10.: Distributions of $m_{\mathrm{T}}\left(p_{\mathrm{T},\,\mu},\,E_{\mathrm{T}}^{\mathrm{miss}}\right)$ in the b-tag (right) and b-veto (left) $\mu\nu$+jet control region passing the *Medium+Trigger* ID threshold. Above the threshold of $150\,\mathrm{GeV}$ in b-veto and $110\,\mathrm{GeV}$ in b-tag, the true tau backgrounds becomes dominant.

reconstructed prongness. Individual sets of fake-rates are determined in the opposite-sign and same-sign $\mu\nu$+jet control region to be applied in the respective signal and validation regions. Additionally, to account for the differences of QCD jets from top and W decay processes, fake-rates are measured in the respective b-tag and b-veto category of the control region. Figure 7.3.11 shows the transverse momentum distribution in the opposite-sign b-tag region for 1 prong probe taus inclusive-ID and passing the *Medium+Trigger* identification criterion. Distributions for the other regions are shown in Appendix B.3.3

The fake-rates are measured in Monte Carlo simulation by evaluating Equation (7.6) for the different identification requirements by selecting events where the tau candidate is not truth-matched to a true tau decay. This yields the following definitions for the fake-rates:

$$FR_{\mathrm{MC}}\left(p_{T,\tau},\,N_{\mathrm{Track}}\right) = \frac{N_{\mathrm{pass\text{-}ID}}^{\mathrm{MC,\,fake}}\left(p_{T,\tau},\,N_{\mathrm{Track}}\right)}{N_{\mathrm{all}}^{\mathrm{MC,\,fake}}\left(p_{T,\tau},\,N_{\mathrm{Track}}\right)}. \tag{7.8}$$

Fake-rates measured on simulated events are then compared to the ones measured on data which are calculated by subtracting all Monte Carlo simulated backgrounds where the probe tau is truth-matched. By integrating the background subtraction into Equation (7.6), the following expression for the data-driven fake-rates is derived:

$$FR_{\mathrm{data}}\left(p_{T,\tau},\,N_{\mathrm{Track}}\right) = \frac{N_{\mathrm{pass\text{-}ID}}^{\mathrm{data}}\left(p_{T,\tau},\,N_{\mathrm{Track}}\right) - N_{\mathrm{pass\text{-}ID}}^{\mathrm{MC,\,true}}\left(p_{T,\tau},\,N_{\mathrm{Track}}\right)}{N_{\mathrm{all}}^{\mathrm{data}}\left(p_{T,\tau},\,N_{\mathrm{Track}}\right) - N_{\mathrm{all}}^{\mathrm{MC,\,true}}\left(p_{T,\tau},\,N_{\mathrm{Track}}\right)}. \tag{7.9}$$

Since the set of events passing the tau-ID thresholds is a subset of all events passing the event selection, the numerator and denominator of Equations (7.8) and (7.9) are highly
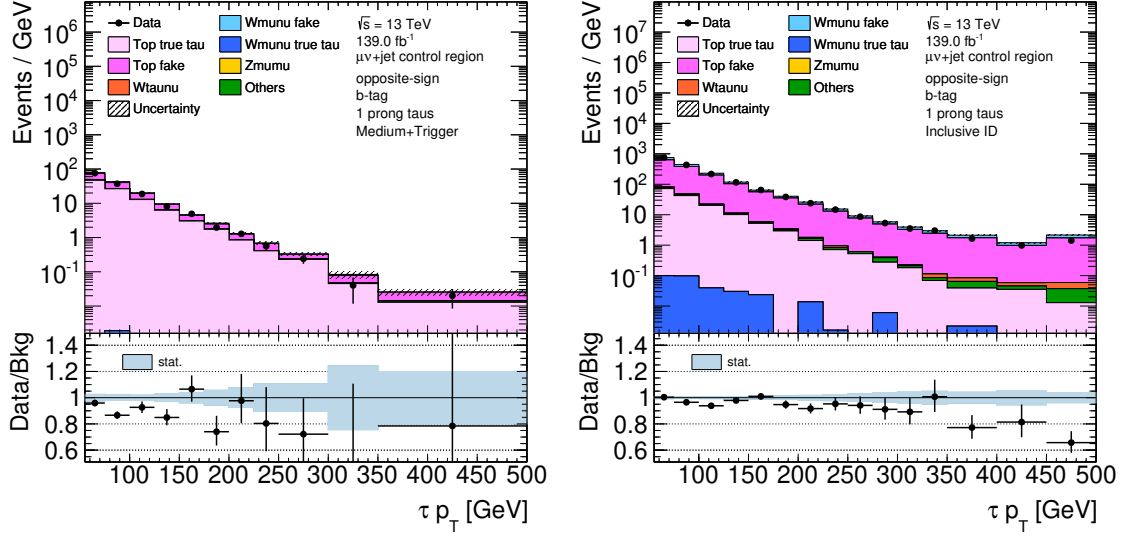
Figure 7.3.11.: Distributions of the probe tau p_T in the $\mu\nu$+jet opposite-sign b-tag control region, with (left) and without (right) the *Medium+Trigger* criterion applied.

correlated. This makes uncertainty calculations using Gaussian error propagation unfeasible. Additional complications occur if the statistical coverage and the frequency of fake taus passing the tau-ID are low, as it can lead to empty bins in the histograms used to calculate the fake-rates [254]. In these cases, the Gaussian error propagation is not suitable to calculate error intervals on the measured fake-rates.

Instead, a reliable error estimation can be achieved by expressing the fake-rate calculation in terms of a binomial model with a probability density for the number of events passing the tau-ID threshold:

$$\mathrm{Pr}\left(k \,|\, FR,\, n\right) = \binom{n}{k} FR^k \left(1 - FR\right)^{n-k}, \tag{7.10}$$

with n the total number of events, k the number of events passing the ID threshold, and FR the fake-rate. Equation (7.6) is then the Maximum Likelihood Estimator (MLE) of $\mathrm{L}\left(FR \,|\, k,\, n\right) = \mathrm{Pr}\left(k \,|\, FR,\, n\right)$. With the help of Bayes' theorem, Equation (7.10) can be used to express the probability density function of the fake-rates:

$$\mathrm{Pr}\left(FR \,|\, k,\, n\right) = N \cdot \mathrm{Pr}\left(k \,|\, FR,\, n\right) \cdot \pi\left(FR\right), \tag{7.11}$$

with N being a normalization constant and $\pi\left(FR\right)$ being the prior fake-rate probability. For the prior, a uniform probability function is used, as it preserves Equation (7.6) as MLE. The measured fake-rate is then determined as the MLE of the posterior probability with uncertainties determined by a confidence interval of 68.3 %, where the upper and lower boundaries of the uncertainty bands are corresponding to the 34.15 % half quantile around the MLE of the probability density function. In the calculation of the fake-rates only statistical uncertainties are considered. The measured fake-rates for the *Medium+Trigger* tau-ID working point are shown in Figure 7.3.12. Fake-rates for the other tau-ID working points are given in Appendix B.3.3, Figures B.3.9 to B.3.15.

Unfortunately, the statistical coverage in the opposite-sign b-tag region for 3 prong taus is not enough to model the slope of the fake-rate in data. In previous publications of the analysis, the fake-rate measured on simulated events is used for this case. However, there
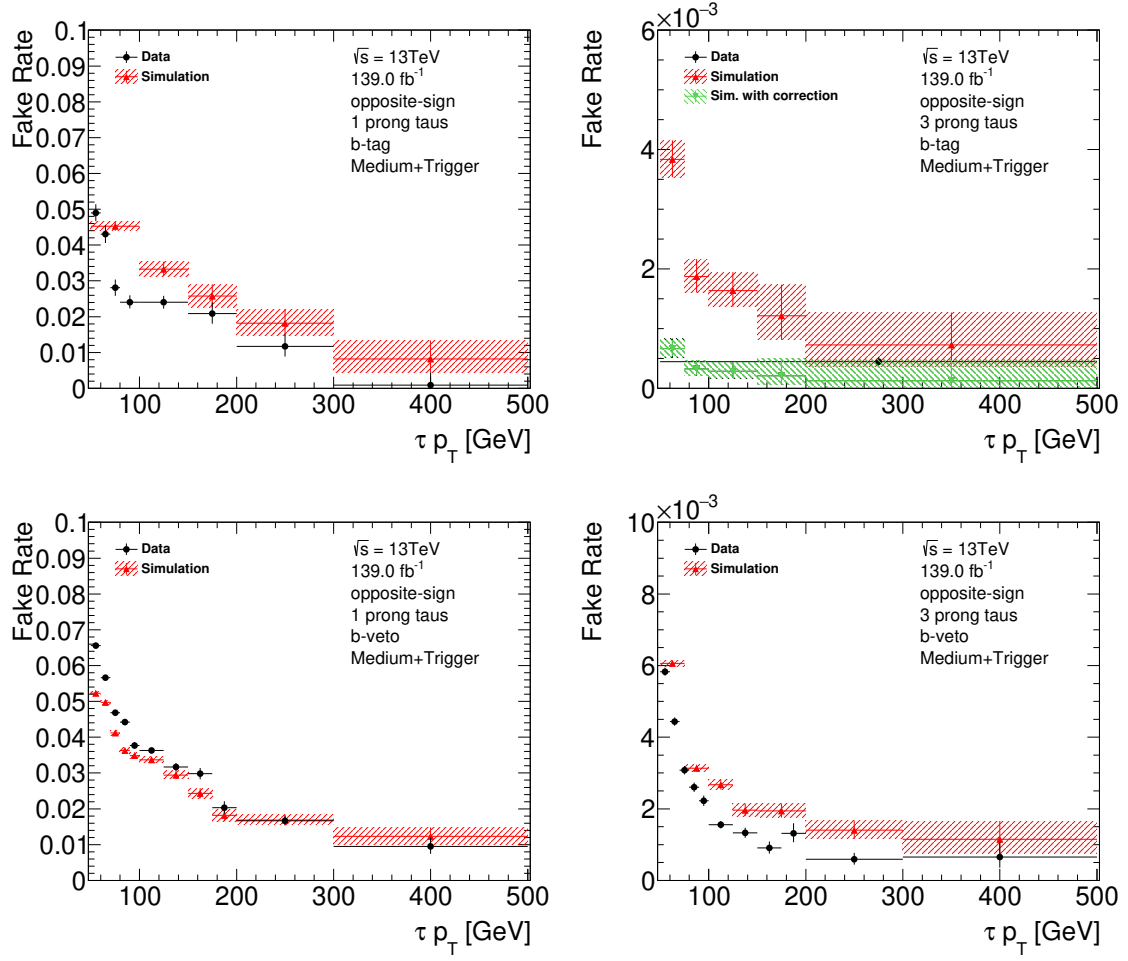
Figure 7.3.12.: Fake-rates for fake tau candidates passing the *Medium+Trigger* working point measured in the opposite-sign *b*-tag (top) and *b*-veto (bottom) $\mu\nu$+jet control region for reconstructed 1 prong (left) and 3 prong (right) fake taus.

is still a significant difference between the measured fake-rates on data and Monte Carlo simulation. To improve the modeling and granularity of the fake-rates in this region, a correction is applied by scaling the normalization of simulated tau fake backgrounds in the pass-ID and inclusive-ID region to match the total data yield. The fake-rates with corrected normalization are then recalculated. An additional uncertainty on the scaling factor of 15 % is determined by considering the statistical uncertainty of both, data and Monte Carlo simulated event yields. This uncertainty is then propagated to the total uncertainty of the fake-rate measurement by varying the event yields and applying the difference of the fake-rate values as uncertainty.

The fake-rates measured in data are applied as event weights to Monte Carlo events for each non-truth-matched tau candidate instead of applying the tau-ID requirements. This allows for correcting mismodeling in the tau-ID response on simulated fake taus but also results in an increase in the statistical coverage as the fake-rates are applied to all events, including those which fail the tau-ID selection. Since the $\mu\nu$+jet b-tag control region is dominated by top decay processes, fake-rates measured in the b-tag category are only applied to fake tau candidates in the top decay background. For all other background processes, the fake-rates measured in the $W \to \mu\nu$+jet dominated b-veto control region are used.

7.4. Analysis Results

Searches for new particles are usually conducted in a *blinded* state [255]. This means the data yields in the signal regions, which are most sensitive to the predicted signal process, are not disclosed until the background modeling is finalized. Otherwise, potential biases can be introduced if the background is modeled by comparing them directly or indirectly with the measured signal region data.

Before the signal region can be unblinded, the SM background modeling is scrutinized in validation regions orthogonal to the signal region which are insensitive to the signal hypothesis. Firstly, a general background modeling check is performed in the same-sign validation region. Additionally, a new dedicated Z validation region is presented in Section 7.4.2 to validate the modeling of background processes containing mostly truth-matched taus.

After validating the background modeling a statistical analysis is conducted based on the results in the signal region. As the final discriminating variable, the total transverse mass is used defined by:

$$m_{\mathrm{T}}^{\mathrm{tot}} = \sqrt{m_T^2\left(E_{\mathrm{T}}^{\mathrm{miss}},\, \tau_1\right) + m_T^2\left(E_{\mathrm{T}}^{\mathrm{miss}},\, \tau_2\right) + m_T^2\left(\tau_1,\, \tau_2\right)}, \tag{7.12}$$

with the transverse mass between two objects:

$$m_T\left(a,\, b\right) = \sqrt{2p_{\mathrm{T}}\left(a\right)p_{\mathrm{T}}\left(b\right)\left[1 - \cos\Delta\left(a,\, b\right)\right]}. \tag{7.13}$$

This variable is particularly well suited as it tends to shift the dominant multijet background towards lower values, creating good separation power to isolate high mass Higgs signals. Although the mass resolution and bias might not be on par with other mass reconstruction algorithms like collinear approximation or the visible mass of the di-tau system, the increased separation power of the total transverse mass is prioritized when searching for new particles.

7.4.1. Background Modeling in the Same-Sign Validation Region

The same-sign validation is designed to be kinetically close to the signal region while also having no significant sensitivity to the signal hypothesis. This is achieved by applying

the same selection criteria as in the signal region and only inverting the sign criteria. Similar to the signal region, the same-sign region is split in *b*-tag and *b*-veto subcategories which are enriched in QCD multijet background and thus are particularly suitable to validate the data-driven fake-factor background estimation. Figures 7.4.1 and 7.4.2 show the distributions of the total transverse mass, the missing transverse energy, and the p_T of the leading and subleading tau candidate in the *b*-veto and *b*-tag validation region. More distributions of variables in the same-sign validation region are presented in Appendix B.4.1.

(a)   (b)

(c)   (d)

Figure 7.4.1.: Distributions of (a) the total transverse mass, (b) the missing transverse energy, as well as the transverse momenta of (c) the leading and (d) subleading tau candidate in the same-sign *b*-veto validation region.

In general, no significant deviation between the measured data and estimated backgrounds is observed. Systematic uncertainties considered in the plots originate from the data-driven fake-factor and fake-rate measurement, physics object calibration, selection
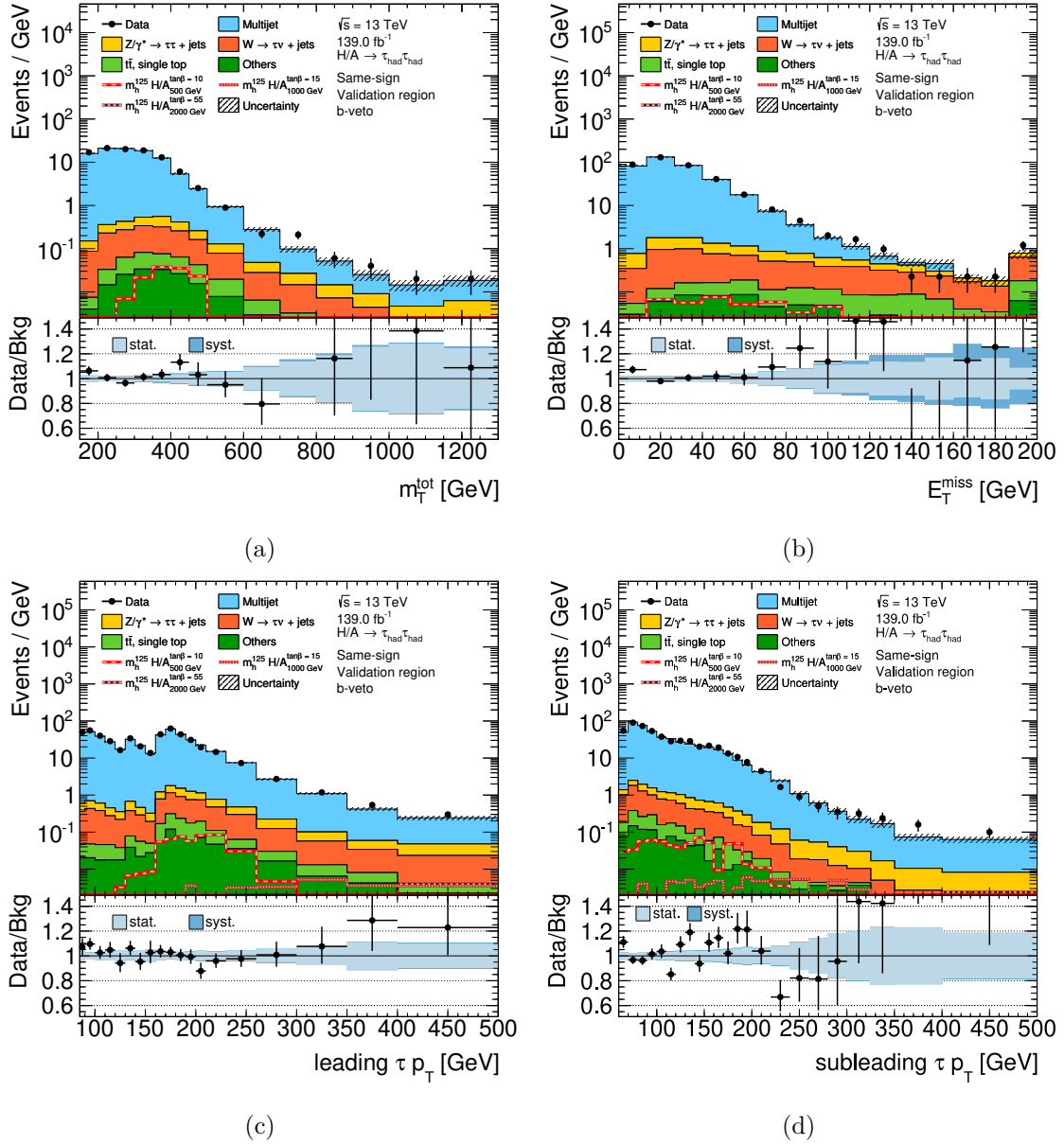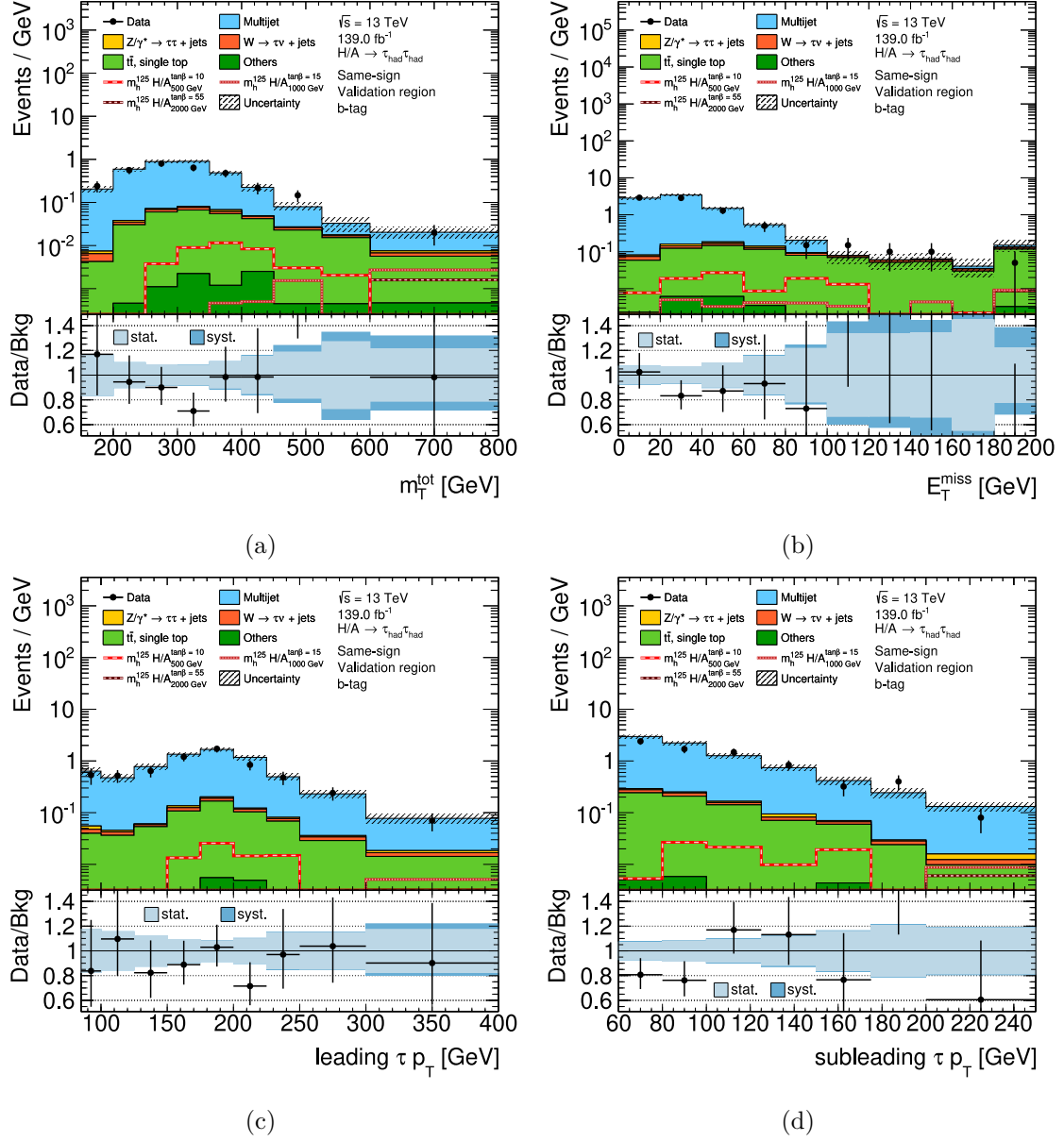
Figure 7.4.2.: Distributions of (a) the total transverse mass, (b) the missing transverse energy, as well as the transverse momenta of (c) the leading and (d) subleading tau candidate in the same-sign *b*-tag validation region.

efficiency scale-factors as well as uncertainties applied to the cross-section of simulated backgrounds. A detailed discussion of the different sources of systematic uncertainties affecting the background estimation is outlined in Section 7.4.4. However, since the QCD multijet process is the main contributing background in the same-sign region, the largest contribution to the systematic uncertainties originates from the fake-factor measurement. Tables 7.4.1 and 7.4.2 list the event yields of the estimated backgrounds and measured data.

Process	Event yield	Statistical unc.	Systematic unc.
Multijet	4830	± 40	$^{+60}_{-60}$
$Z \to \tau\tau$+jet	62.01	± 0.14	$^{+13.60}_{-13.48}$
$W \to \tau\nu$+jet	75.68	± 0.11	$^{+12.59}_{-11.61}$
$t\bar{t}$, single top	12.541	± 0.026	$^{+3.632}_{-2.993}$
Others	8.975	± 0.017	$^{+1.077}_{-1.134}$
m_h^{125} $H/A^{\tan\beta=10}_{500\,\mathrm{GeV}}$	6.42	± 0.10	$^{+1.05}_{-1.27}$
m_h^{125} $H/A^{\tan\beta=15}_{1000\,\mathrm{GeV}}$	1.124	± 0.014	$^{+0.174}_{-0.187}$
m_h^{125} $H/A^{\tan\beta=55}_{2000\,\mathrm{GeV}}$	0.418	± 0.004	$^{+0.074}_{-0.074}$
Background	4990	± 40	$^{+70}_{-70}$
Data	5080	± 70	

Table 7.4.1.: Event yields for the same-sign b-veto validation region including the total statistical and systematic uncertainties. Numbers are rounded according to the PDG recommendations defined in Reference [25] taking the smaller of the two uncertainties as reference.

Process	Event yield	Statistical unc.	Systematic unc.
Multijet	156.8	± 7.0	$^{+2.9}_{-4.3}$
$Z \to \tau\tau$+jet	1.375	± 0.020	$^{+0.463}_{-0.346}$
$W \to \tau\nu$+jet	2.400	± 0.014	$^{+0.431}_{-0.396}$
$t\bar{t}$, single top	16.336	± 0.031	$^{+5.345}_{-4.252}$
Others	0.536	± 0.004	$^{+0.101}_{-0.085}$
m_h^{125} $H/A_{500\,\text{GeV}}^{\tan\beta=10}$	2.01	± 0.05	$^{+0.41}_{-0.51}$
m_h^{125} $H/A_{1000\,\text{GeV}}^{\tan\beta=15}$	0.729	± 0.013	$^{+0.124}_{-0.144}$
m_h^{125} $H/A_{2000\,\text{GeV}}^{\tan\beta=55}$	0.331	± 0.005	$^{+0.059}_{-0.068}$
Background	177	± 7	$^{+6}_{-6}$
Data	162	± 13	

Table 7.4.2.: Event yields for the same-sign b-tag validation region including the total statistical and systematic uncertainties.

7.4.2. Modeling of True Tau Background

Although the same-sign control region provides good insight into the modeling of fake backgrounds, it is not well suited to validate backgrounds with large fractions of true taus like $Z/\gamma^* \to \tau\tau$. The Z/γ^* background measured in the signal region predominantly originates from high mass, off-shell bosons where their decay only differ from that of Higgs bosons in terms of spin and CP states. Unfortunately, due to high statistical uncertainties, the analysis is not sensitive to these differences. Thus, hadronically decaying true taus from off-shell Z/γ^* decays yield an irreducible background contribution.

To still be able to check the high momentum true tau modeling, a new Z validation region is developed by selecting a phase-space region that is dominated by Z boson decays. The region is defined by applying the same selection cuts as in the b-veto signal region except for inverting the angular distance requirement between the two tau candidates to $\Delta\phi\,(\tau_1,\,\tau_2) < 2.7$. This also ensures that the new region is orthogonal to the signal region. To further reduce background from non-Z decay processes as well as signal processes, a cut on the visible mass of the two tau candidate close to the on-shell rest mass of the Z boson of $m_{\text{vis}} < 90\,\text{GeV}$ is applied. In conjunction with the high tau p_T cuts, the collimated event topology predominantly selects boosted on-shell Z boson decays.

Figure 7.4.3 shows the measured data and background distributions in the Z validation region. The event yields are listed in Table 7.4.3. With a purity of 87.4% of $Z \to \tau\tau$ decays and negligible background contamination, this region is well suited to validate the modeling of high p_T true tau candidates.

Good agreement between data and background is observed indicating good modeling of simulated true tau backgrounds in the analysis. Unfortunately, this region can not be used to constrain uncertainties on the Drell-Yan process modeling since the on-shell Z production phase space strongly differs from the off-shell production observed in the signal region. Instead, the Z validation region can only be used to validate the true tau modeling itself.
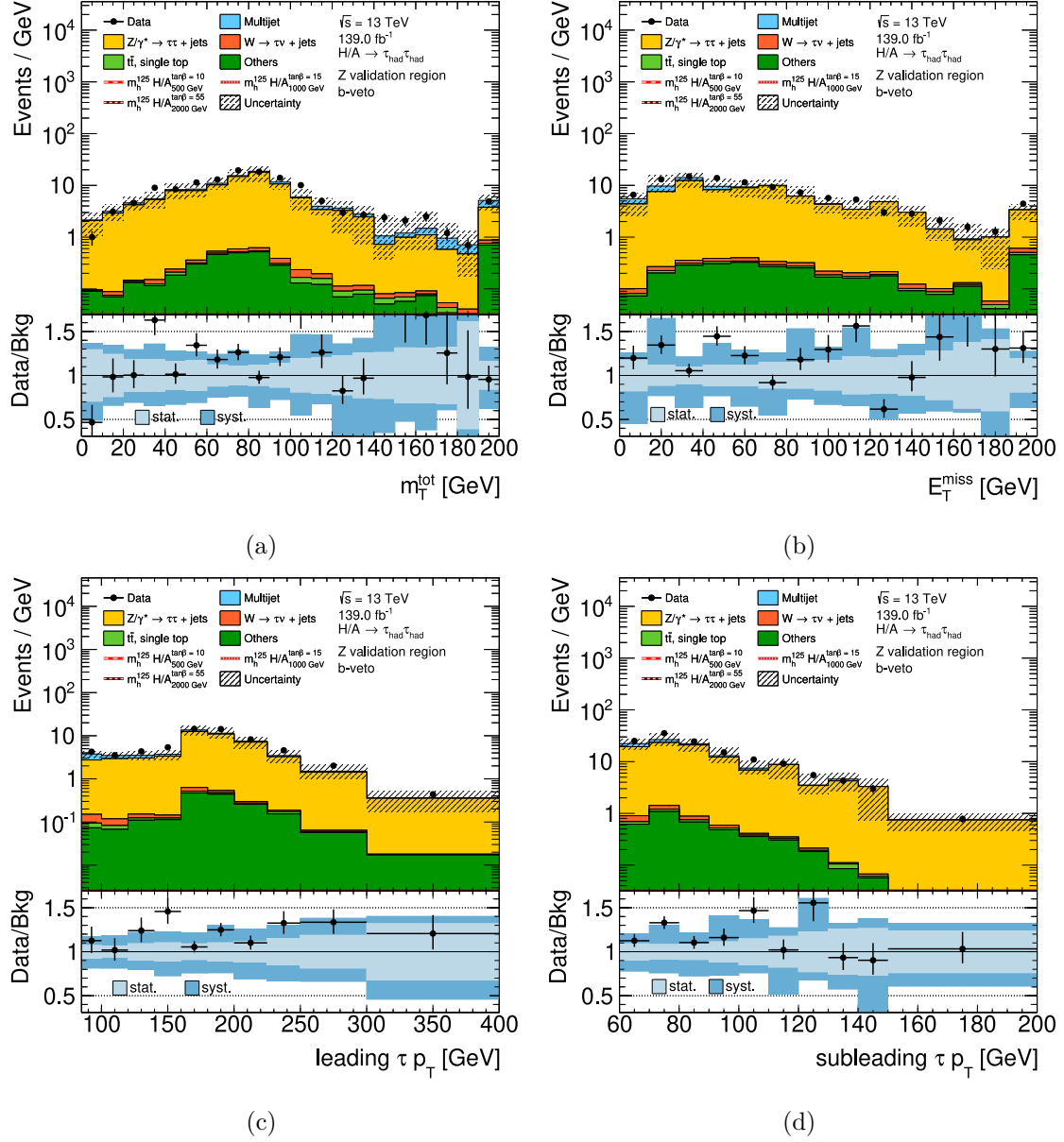
Figure 7.4.3.: Distributions of (a) the total transverse mass, (b) the missing transverse energy, as well as the transverse momenta of (c) the leading and (d) subleading tau candidate in the Z validation region.

Process	Event yield	Statistical unc.	Systematic unc.
Multijet	95	± 8	$^{+7}_{-6}$
$Z \to \tau\tau$+jet	1012	± 29	$^{+244}_{-264}$
$W \to \tau\nu$+jet	7.29	± 0.05	$^{+0.76}_{-0.74}$
$t\bar{t}$, single top	3.783	± 0.019	$^{+0.977}_{-0.831}$
Others	39.96	± 0.27	$^{+5.65}_{-6.82}$
$m_h^{125}\ H/A^{\tan\beta=10}_{500\,\mathrm{GeV}}$	0.0	± 0.00021	$^{+0.00087}_{-0.01567}$
$m_h^{125}\ H/A^{\tan\beta=15}_{1000\,\mathrm{GeV}}$	0.00270	± 0.00028	$^{+0.00257}_{-0.00061}$
$m_h^{125}\ H/A^{\tan\beta=55}_{2000\,\mathrm{GeV}}$	0.00022	± 0.00004	$^{+0.00091}_{-0.00024}$
Background	1158	± 30	$^{+244}_{-264}$
Data	1370	± 40	

Table 7.4.3.: Event yields for the Z validation region including the total statistical and systematic uncertainties.

7.4.3. Signal Region Results

After validating the background modeling in the same-sign and Z validation regions, the data in the signal region can be unblinded and compared with the estimated backgrounds. A summary of the event selections defining the various regions used to estimate and validate backgrounds is given in Table 7.4.4

Figures 7.4.4 and 7.4.5 show the distributions for the final discriminating variable $m_\mathrm{T}^{\mathrm{tot}}$ as well as other kinetic variables in the b-veto and b-tag categories. Further distributions of kinetic variables are presented in Appendix B.4.2.

Uncertainty bars shown in the plots include statistical and systematic uncertainties. The latter uncertainties are explained in Section 7.4.4 where the various sources are discussed and their impact on the signal region is evaluated. The event yields for background and signal processes are listed in Table 7.4.5 for the b-veto and in Table 7.4.6 for the b-tag signal region categories.

No significant excess of data over the estimated backgrounds is observed, meaning that there are no signs of the presence of additional heavy Higgs bosons. Therefore, the results derived from the $m_\mathrm{T}^{\mathrm{tot}}$ distributions are used to calculate upper limits on the production cross-sections for the signal hypotheses.

Region	Event selection	Description
Di-jet control region		
Common selection	• leading tau $p_T > 85\,\mathrm{GeV}$ • subleading tau $p_T > 50\,\mathrm{GeV}$ • triggered by HLT jet trigger • leading tau fails *Medium* tau-ID • $p_{T,\,\mathrm{balance}} > 0.3$ and $\Delta\phi\,(\tau_1,\,\tau_2) > 2.7$ • sub-categories for b-tag, b-veto, opposite- and same-sign	Fake-factor measurement
Fail-ID region	• subleading tau fails *Loose* tau-ID • $\Lambda_{\mathrm{Tau\text{-}ID\ score}} > 0.03$	
Pass-ID region	• subleading tau pass *Loose* tau-ID	
$\mu\nu$+jet control region		
Common selection	• triggered by HLT_mu50 • one *Medium* isolated muon with $p_T > 55\,\mathrm{GeV}$ • hadronic tau candidate with $p_T > 55\,\mathrm{GeV}$ • no further leptons • $\Delta\phi\,(\mu,\,\tau) > 2.4$ • $40\,\mathrm{GeV} > m_T\,(p_{T,\,\mu},\,E_T^{\mathrm{miss}}) > 150\,(110)\,\mathrm{GeV}$ for b-veto (b-tag) • sub-categories for b-tag, b-veto, opposite- and same-sign	Fake-rate measurement
Tau-ID region	• passing/failing tau-ID WP	
Validation and signal regions		
Common selection	• triggered by HLT_tau80, HLT_tau125 or HLT_tau160 • *Medium* ID leading tau with p_T 5 GeV over trigger threshold • *Loose* subleading tau with $p_T > 65\,\mathrm{GeV}$ • no identified light leptons • sub-categories for b-tag and b-veto,	
Z validation region	• opposite-sign taus, b-veto category • $\Delta\phi\,(\tau_1,\,\tau_2) < 2.7$ • $m_{\mathrm{vis}} < 90\,\mathrm{GeV}$	Validate true tau background
Same-sign validation region	• same-sign taus • $\Delta\phi\,(\tau_1,\,\tau_2) > 2.7$	Validate multi-jet background
Signal region	• opposite-sign taus • $\Delta\phi\,(\tau_1,\,\tau_2) > 2.7$	

Table 7.4.4.: List of regions used in the search for heavy neutral Higgs bosons with defining cuts and description.

(a)

(b)

(c)

(d)

Figure 7.4.4.: Distributions of (a) the total transverse mass, (b) the missing transverse energy, as well as the transverse momenta of (c) the leading and (d) subleading tau candidate in the *b*-veto signal region.
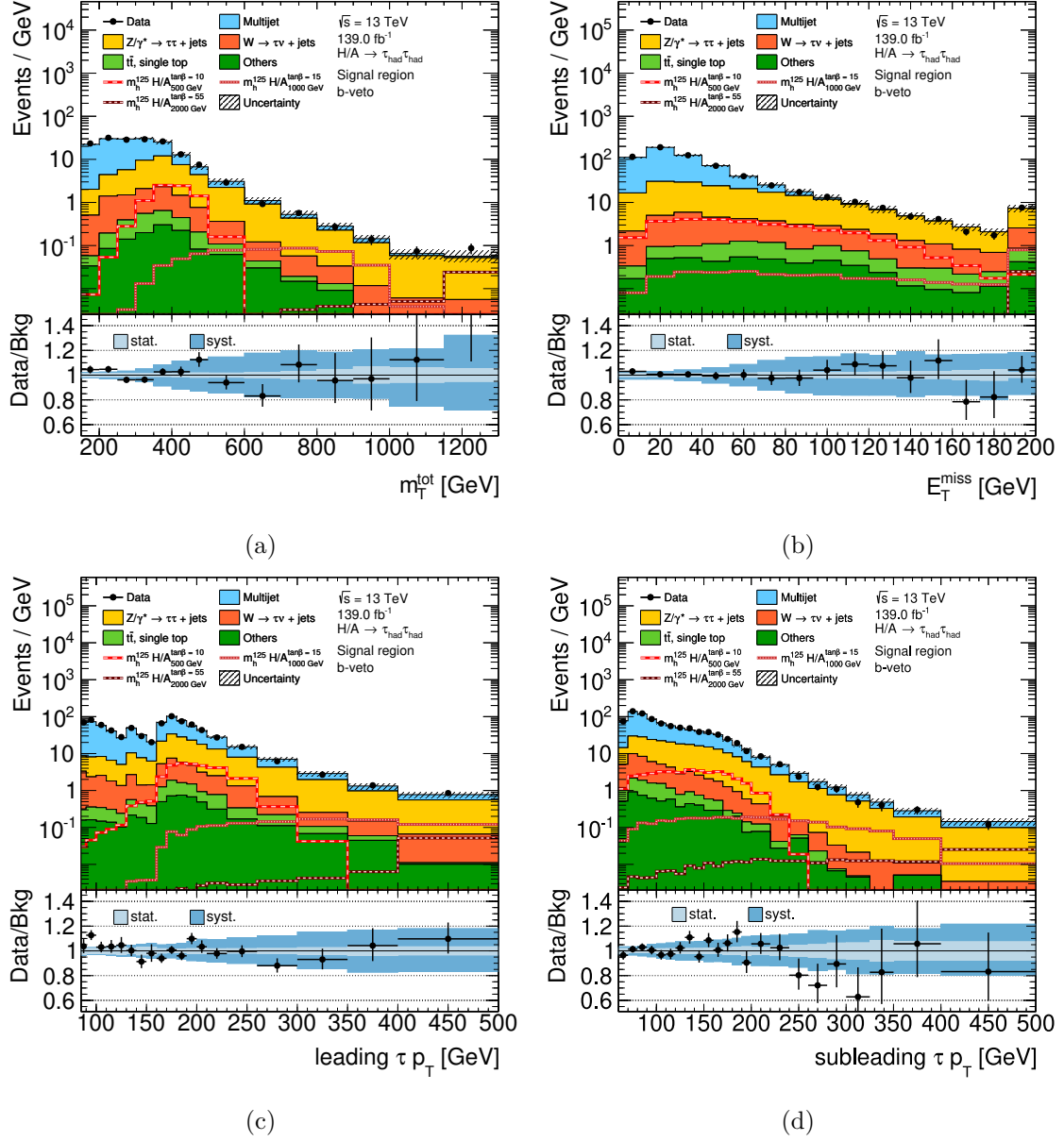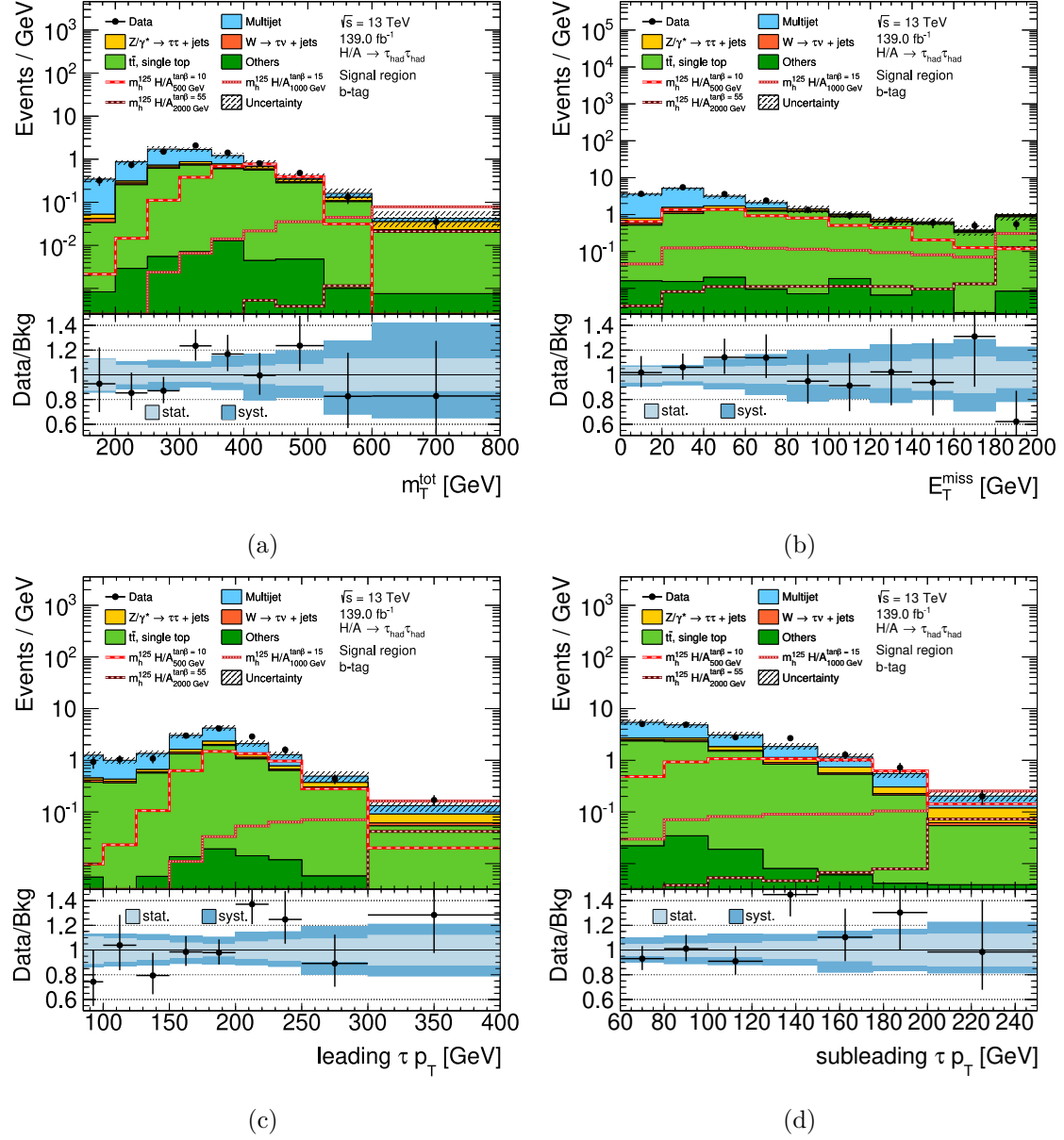
Figure 7.4.5.: Distributions of (a) the total transverse mass, (b) the missing transverse energy, as well as the transverse momenta of (c) the leading and (d) subleading tau candidate in the *b*-tag signal region.

Process	Event yield	Statistical unc.	Systematic unc.
Multijet	5720	± 40	$^{+100}_{-100}$
$Z \to \tau\tau$+jet	2125.6	± 1.7	$^{+439.0}_{-449.9}$
$W \to \tau\nu$+jet	418.3	± 0.5	$^{+48.5}_{-48.7}$
$t\bar{t}$, single top	78.38	± 0.16	$^{+17.21}_{-15.96}$
Others	65.08	± 0.11	$^{+8.02}_{-8.04}$
$m_h^{125} \, H/A_{500\,\mathrm{GeV}}^{\tan\beta=10}$	406.6	± 1.1	$^{+63.7}_{-66.1}$
$m_h^{125} \, H/A_{1000\,\mathrm{GeV}}^{\tan\beta=15}$	44.27	± 0.11	$^{+7.00}_{-6.90}$
$m_h^{125} \, H/A_{2000\,\mathrm{GeV}}^{\tan\beta=55}$	6.068	± 0.019	$^{+1.028}_{-1.015}$
Background	8410	± 40	$^{+450}_{-460}$
Data	8480	± 90	

Table 7.4.5.: Event yields for the *b*-veto signal region including the total statistical and systematic uncertainties.

Process	Event yield	Statistical unc.	Systematic unc.
Multijet	169	± 8	$^{+7}_{-13}$
$Z \to \tau\tau$+jet	29.31	± 0.17	$^{+6.49}_{-6.37}$
$W \to \tau\nu$+jet	11.61	± 0.06	$^{+1.49}_{-1.44}$
$t\bar{t}$, single top	169.84	± 0.30	$^{+38.55}_{-35.30}$
Others	2.249	± 0.016	$^{+0.314}_{-0.301}$
$m_h^{125} \, H/A_{500\,\mathrm{GeV}}^{\tan\beta=10}$	130.1	± 0.6	$^{+23.1}_{-24.4}$
$m_h^{125} \, H/A_{1000\,\mathrm{GeV}}^{\tan\beta=15}$	23.94	± 0.09	$^{+3.97}_{-3.84}$
$m_h^{125} \, H/A_{2000\,\mathrm{GeV}}^{\tan\beta=55}$	4.369	± 0.020	$^{+0.743}_{-0.731}$
Background	382	± 8	$^{+40}_{-38}$
Data	396	± 20	

Table 7.4.6.: Event yields for the *b*-tag signal region including the total statistical and systematic uncertainties.

7.4.4. Systematic Uncertainties

All measurements conducted in the signal, validation, or control regions are subject to many sources of uncertainty. A distinction is made between statistical and systematic uncertainties which are treated independently. Since events passing the selection are assumed to be uncorrelated, the probability behind the event yields follows a Poison distribution around the measured value of n_i. For statistical uncertainties on data yields, the parameter n_i is equivalent to the number of events measured, while for Monte Carlo generated samples it refers to the sum of all event weights for each bin.

Sources of systematic uncertainties are much more diverse. Uncertainties considered arise from corrections on energy and resolution calibrations, as well as identification efficiency corrections for selected physics objects on Mont Carlo simulated events. Also, backgrounds that are estimated via the fake-factor and fake-rates methods are affected by systematic uncertainties associated with the measurements of the data-driven techniques. Further systematic uncertainties considered on simulated events cover the cross-section, luminosity, and generator-specific uncertainty sources. In the following section, the sources of systematic uncertainties are explained and their impact on the signal regions is evaluated.

Uncertainties on Physics Object Reconstruction and Identification

Physics objects generated in Monte Carlo simulated events undergo a variety of corrections to account for differences between simulation and data, each associated with systematic uncertainties. These systematic uncertainties are typically categorized in two sets: normalization uncertainties only vary the total number of events of a given background by a given factor while shape uncertainties also change the shape of the distribution of the final discriminating variable. In this section, an overview is presented on the sources of systematic uncertainties associated with the reconstruction and identification of the physics objects selected in the signal region.

Tau calibration and identification: Uncertainties on calibration and identification corrections of simulated taus are one of the major contributing sources of systematic uncertainties in the signal region.

For the energy calibration of tau leptons, three uncorrelated sources of uncertainties are considered [169, 171]. Two uncertainties are derived by changing the configuration of the GEANT4 detector simulation by varying the material thickness of detector parts as well as changing the physics modeling. The third uncertainty directly comes from the $Z \to \tau_\mu \tau_{\text{had}}$ in-situ measurement of the tau energy scale.

Uncertainties associated with identification and reconstruction efficiencies are only applied on truth-matched taus as fake taus are corrected using fake-rates. Uncertainties on the trigger identification corrections are evaluated for all data-taking periods from 2015 to 2018 independently. In total there are three uncertainties per trigger period, related to the statistical and systematic uncertainties from the trigger scale-factor measurements. The set of uncertainties for tau-ID scale-factors are determined separately for 1 and 3 prong taus as well as for different tau p_{T} regions. These uncertainties are treated independently for the leading and subleading tau. This creates a set of 12 uncorrelated variations. Lastly, corrections on the reconstruction efficiency of tau candidates are associated with one common uncertainty for both tau candidates.

On both tau-ID and reconstruction efficiency corrections an additional high-p_{T} uncertainty is applied for taus with $p_{\text{T}} > 100\,\text{GeV}$. To cover differences in the modeling of the detector response when using the ATLFAST-II simulation framework, dedicated uncertainties are defined for calibration, reconstruction, and identification efficiencies.

Jet calibration and *b*-tagging: The uncertainty set for JER and JES calibrations usually consists of over 100 components, part of which are highly correlated. The main source of the uncertainty comes from the bin-wise calibration in jet p_T as well as from extrapolating the energy scale calibration from the central to the forward η region. Since the analysis selection is insensitive to the high granularity correlation model, a strongly reduced uncertainty set is chosen with six independent uncertainties for JES corrections and eight for JER. An additional uncertainty on the JES is applied on samples generated using the ATLFAST-II detector simulation. The reduced set of jet-related systematic uncertainties are provided as one-sided continuous uncertainties that are mirrored around the nominal distribution of all background processes affecting them. A further jet-related systematic uncertainty is introduced by the JVT correction.

Similar to the jet calibration uncertainties, the set of systematic uncertainties on the *b*-tagging efficiency scale-factor is determined on a wide range of partially correlated jet p_T bins. This set is reduced in size following an eigenvector decomposition described in Reference [164], resulting in a total of 14 decomposed uncertainties, separated into subsets for efficiency scale-factors calculated on *b*, *c*, or light quark-initiated jets.

Missing transverse energy reconstruction: Systematic uncertainties on the missing transverse energy reconstruction are extracted by measuring the longitudinal and perpendicular projection of the track-based soft term of the missing transverse energy along the direction of the hard term contribution in a $Z \to \mu\mu$ analysis in which no E_T^{miss} is expected to be present [165, 166]. From the deviations measured between Monte Carlo simulation and data, an uncertainty on the scale of the soft term is determined by varying the longitudinal component. Uncertainties on the resolution are derived from the variance of the root mean square of the longitudinal and perpendicular components of the soft term. Similar to the continuous jet uncertainties, the E_T^{miss} resolution uncertainties are one-sided and thus are mirrored around the nominal yields of the background processes.

Pile-up reweighting and luminosity: Since Monte Carlo samples are weighted to match the recorded data cross-section of each data-taking period, the simulated background yields are subject to the uncertainty of the measured integrated luminosity. Based on measurements of the LUCID-2 detector the uncertainty of the full Run-2 luminosity measurement is $\pm 1.7\,\%$ [93, 120]. Furthermore, the scale-factor applied by the pile-up reweighting procedure is also associated with one uncertainty variation.

Other sources of uncertainties from muon or electron calibration were investigated but were found to be negligible.

Cross-section and Modeling Uncertainties

Uncertainties on the modeling of the nominal Monte Carlo generators are calculated from higher-order cross-section calculations, choice of generator configurations, or by comparing the nominal generators with alternative generator setups. In the following, a summary of the Monte Carlo generator uncertainties derived for the major backgrounds is given.

$Z/\gamma^* \to \tau\tau$+jets background: As described in Section 7.3.1 a resonance mass dependent higher-order k-factor correction is applied on $Z/\gamma^* \to \tau\tau$ events [216, 217]. Uncertainties on the k-factors are estimated by studying the impact of the uncertainty variation of the CT14NNLO PDF set [256] as well as the choice of the PDF itself. The latter is realized by exchanging the nominal PDF set with the alternative NNPDF 3.0NNLO [218]

and HERAPDF 2.0 [257]. Additional uncertainties are given by the impact of variations on the beam energy, electro-weak, and photon-induced corrections.

A possible bias of the heavy-flavor modeling described in Reference [213] is considered and studied by adding a conservative uncertainty of $50\,\%$ on $Z/\gamma^* \to \tau\tau$ background in the b-tag signal region. This uncertainty only causes a change in the cross-section limits by $1.8\,\%$ and is thus ignored.

$W \to \tau\nu$+jets background: In general, this background only plays a minor role in the signal region. The impact on the statistical analysis is tested by adding a conservative uncertainty of $20\,\%$ causing only a negligible degradation in the cross-section limits of $0.9\,\%$. Thus, for this background process, no further cross-section related uncertainties are considered aside from the uncertainty on the total cross-section normalization.

Di-Boson production: The background from di-boson production accounts for less than $1\,\%$ of background in the signal region. Hence, only a conservative systematic uncertainty of $10\,\%$ on the cross-section is applied.

Top process modeling uncertainty: For single top and $t\bar{t}$ background processes, uncertainties on the higher-order cross-section correction are determined by varying the PDF set as well as the renormalization and factorization scale [240, 245]. The total uncertainty on the top background cross-section is estimated to be $6\,\%$ [237, 238, 243].

Additional uncertainties on the modeling of the generators themselves are estimated by varying the generator configurations, as well as exchanging the ME and PS generators. This procedure follows the general recommendation described in Reference [258]. The resulting distributions are compared to the nominal sample and the difference is taken as uncertainty. Since the main top-related background in the signal region originates from top pair production, the uncertainties are calculated on $t\bar{t}$ samples and applied to all top decay processes. Due to the low acceptance of fully simulated and reconstructed $t\bar{t}$ events in the signal region, the model uncertainty analysis is conducted as a truth-level study.

The truth-level selection aims at emulating the selection of the signal regions on truth-level objects. The two tau leptons with the highest $p_{\mathrm{T,\,Truth\text{-}vis}}$ lying within $|\eta| < 2.5$, excluding the barrel-end-cap region, are selected as the leading and subleading tau candidates. The following event selection is applied:

- the leading tau shall pass $p_{\mathrm{T,\,Truth\text{-}vis}} > 85\,\mathrm{GeV}$,

- the subleading tau shall pass $p_{\mathrm{T,\,Truth\text{-}vis}} > 65\,\mathrm{GeV}$,

- both true taus are located back-to-back within $\Delta\phi_{\mathrm{Truth}} > 2.7$,

- truth electrons must pass $p_{\mathrm{T,\,Truth}} > 15\,\mathrm{GeV}$ and lie within $|\eta_{\mathrm{Truth}}| < 2.47$,

- truth muons have to pass $p_{\mathrm{T,\,Truth}} > 7\,\mathrm{GeV}$ and lie within $|\eta_{\mathrm{Truth}}| < 2.5$,

- both true taus have opposite-sign charges.

Events with one or more light leptons passing the event selection are vetoed in order to emulate the orthogonality to the semi-leptonic search channel applied in the signal region selection. Jets from the Antik_t4TruthJets collection are used which contains jets reconstructed from stable truth particles using the anti-k_t algorithm with radius parameter $R = 0.4$. The truth jets have to pass a threshold of $p_{\mathrm{T,\,Truth}} > 20\,\mathrm{GeV}$ and lie within $|\eta_{\mathrm{Truth}}| < 2.5$. An overlap removal procedure removes jets in the vicinity of $\Delta R < 0.4$ around true taus to reduce double counting of jet constituents.

To simulate the different thresholds of the single-tau triggers used in the signal region, an event weight is applied scaling the p_T regions to the cumulative fraction of the triggered luminosity in each p_T slice. Based on the exclusively triggered luminosity from Table 7.2.1, the scale-factor w_{Trig}, dependent on the $p_{T,\text{Truth-vis}}$ of the leading tau, is calculated by:

$$w_{\text{Trig}} = \begin{cases} \frac{\mathcal{L}_{\text{tau80}}}{\mathcal{L}_{\text{tot}}} = 0.04 & \text{, if } p_{T,\text{Truth-vis}} < 130\,\text{GeV} \\ \frac{\mathcal{L}_{\text{tau80}} + \mathcal{L}_{\text{tau125}}}{\mathcal{L}_{\text{tot}}} = 0.11 & \text{, if } 130\,\text{GeV} < p_{T,\text{Truth-vis}} < 165\,\text{GeV} \\ \frac{\mathcal{L}_{\text{tau80}} + \mathcal{L}_{\text{tau125}} + \mathcal{L}_{\text{tau160}}}{\mathcal{L}_{\text{tot}}} = 1 & \text{, if } p_{T,\text{Truth-vis}} > 165\,\text{GeV} \end{cases} \quad (7.14)$$

with $\mathcal{L}_{\text{tau}}$ being the integrated luminosity exclusively triggered by the HLT trigger and $\mathcal{L}_{\text{tot}} = 139\,\text{fb}^{-1}$ the total integrated luminosity.

A sample of 24 million truth events generated using the same generator configuration as the nominal sample defined in Section 7.3.1 serves as reference. Only the all-had and non-all-had filters are exchanged by a di-lepton filter, selecting for $t\bar{t}$ decays with leptons in the final state. This significantly increases the acceptance of generated events since hadronic top decays are vetoed at the ME level.

The modeling uncertainty of FSR is estimated by varying the renormalization scale of the final state radiation calculation of the ME generator by a factor of two. For uncertainties on the ISR, the down variation is calculated by setting the renormalization and factorization scale to $\mu_R = \mu_F = 0.5$. Additionally, the Var3c up variation of the A14 tune is applied which varies the scale α_S by 10 % [137]. The ISR up variation is derived by setting $\mu_R = \mu_F = 2$ and using the Var3c down variation of the A14 tune in addition to changing the damping parameter to $h_{\text{damp}} = 3 \times m_{\text{top}}$.

The uncertainty on the hard scatter event modeling is calculated by exchanging POWHEG BOX with the MADGRAPH5_AMC@NLO v2.6.0 generator [136, 259], which is configured with the NNPDF 3.0NLO PDF set. To extract the uncertainty on the PS generation the nominal PYTHIA 8 generator is replaced by HERWIG 7.04 [260, 261], using the MMHT2014LO PDF set [262] and the corresponding H7UE tune.

A list of samples used in this truth-level estimation of the top generator uncertainty is given in Table 7.4.7

DSID	Short name	Tags	Events
410472	PhPy8EG_A14_ttbar_hdamp258p75_dil	e6348_e5984	24 M
410482	PhPy8EG_A14_ttbar_hdamp517p5_dil	e6454_e5984	8 M
410465	aMcAtNloPy8EvtGen_MEN30NLO_A14N23LO_ttbar_noShWe_dil	e6762_e5984	24 M
410558	PowhegHerwig7EvtGen_H7UE_tt_hdamp258p75_704_dil	e6366_e5984	24 M

Table 7.4.7.: List of Monte Carlo samples used in top model uncertainty estimations.

By comparing the distributions of the m_T^{tot} variable after applying the truth selections shown in Figure 7.4.6, the respective uncertainties are determined by the difference between the nominal and the systematic variation sample. The uncertainties for FSR and ISR are treated as normalization uncertainty with a measured uncertainty band of $^{+0.1\,\%}_{-4.6\,\%}$ and $^{+13.8\,\%}_{-7.4\,\%}$ respectively. Systematic uncertainties for ME and PS are treated as bin-wise shape uncertainty where the up variation is given by the ratio of the distributions of the nominal and alternative generator setup, while the down variation is derived by mirroring the up variation around the nominal distribution.

Signal Acceptance Uncertainty: Uncertainties on the modeling of the Higgs signal process generators are estimated by varying the scale of the QCD calculations, the recommended tune parameters of the PS, and the systematic uncertainty sets of the PDFs
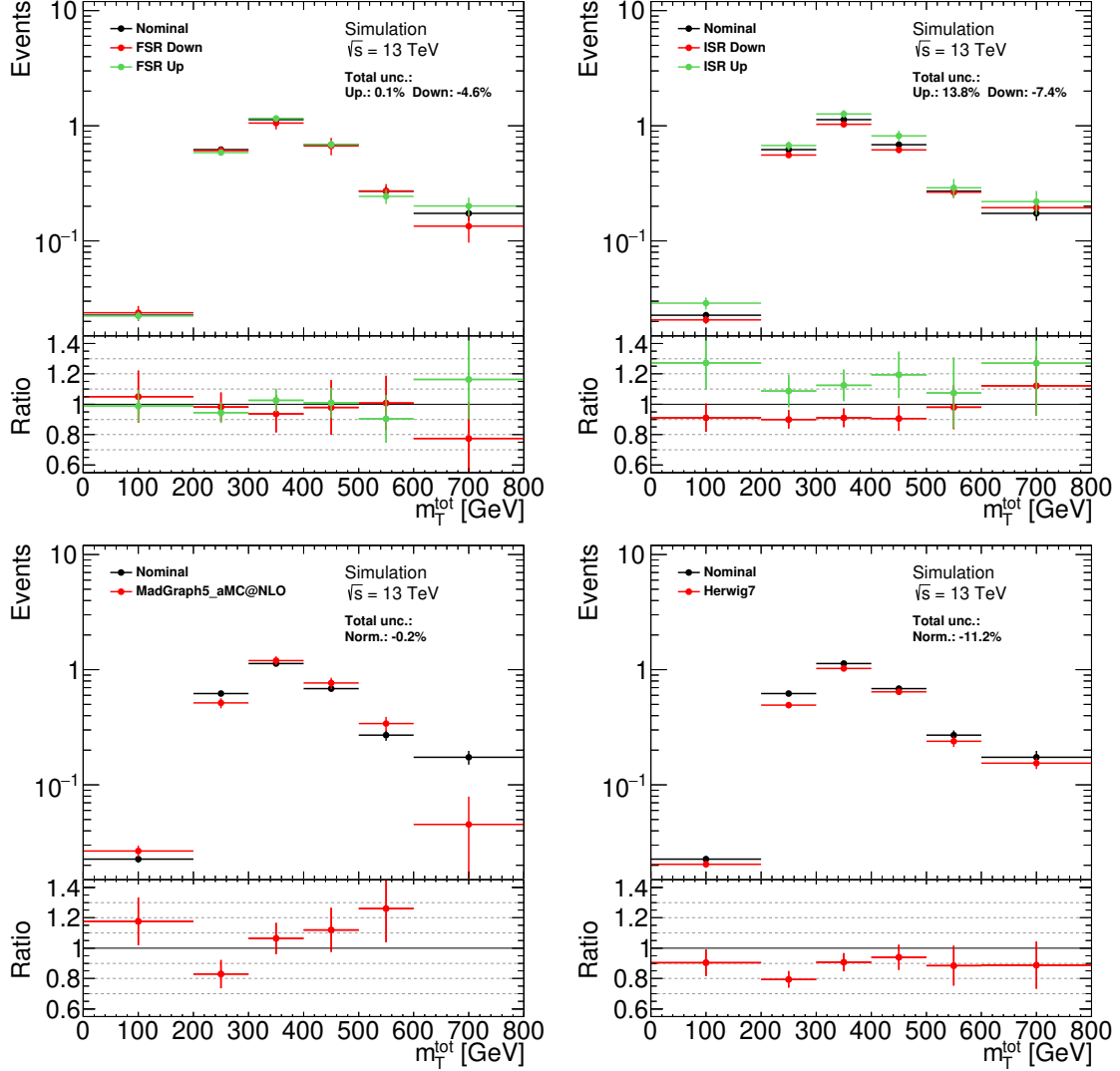
Figure 7.4.6.: Total transverse mass distributions of $t\bar{t}$ events passing the truth-level selection. Generator uncertainties are derived from the differences of the nominal and alternative generator setups.

used during ME generation. Similar to the top-model uncertainty, the signal acceptance uncertainty is evaluated on truth-level by applying the same truth analysis selection and trigger event weighting.

Since the uncertainty for gluon-gluon fusion and *b*-associated signal production has to be evaluated independently for the *b*-tag and *b*-veto category, the *b*-tagging process needs to be emulated at the truth-level. In a first step, the probability for jets not being *b*-tagged is derived from the truth *b*-jet efficiency and light-flavor jet rejection of the MV2 *b*-tagging algorithm, listed in Reference [164]. The *b*-tag and *b*-veto categories in the truth analysis are then created by applying an event weight derived from the *b*-tagging probability of the individual true jets i according to:

$$w_{b\text{-veto}} = \prod_i \begin{cases} 1 - \epsilon_i^b & \text{, for truth } b\text{-jets,} \\ 1/r_i^{\text{bkg}} & \text{, for truth } c\text{- and light jets,} \end{cases} \tag{7.15}$$

$$w_{b-tag} = 1 - w_{b\text{-veto}}, \tag{7.16}$$

with ϵ_i^b being the *b*-tagging efficiency and r_i^{bkg} being the jet-flavor specific rejection efficiency.

In order to decouple and isolate the effect of process modeling from changes in the overall cross-section normalization, the uncertainties are calculated from the difference of the signal acceptance of the uncertainty variation with respect to the nominal sample. The acceptance is defined by:

$$\chi_{\text{acc.}} = \frac{N_{\text{pass}}}{N_{\text{total}}}, \tag{7.17}$$

with N_{total} the weighted number of signal events generated and N_{pass} the number of signal events passing the truth-level selection.

The uncertainties are determined for gluon-gluon fusion and *b*-associated production samples with Higgs masses of $m_{\text{H}} = 200, 400, 600, 800, 1000, 1200, 1750, 2000,$ and $2500\,\text{GeV}$. For each mass point and systematic variation, samples containing $100\,000$ truth events are generated.

The QCD scale uncertainty is calculated by varying the renormalization and factorization scale of the ME generators by a factor of two, considering simultaneous and one-sided up and down variations. The magnitude of the uncertainty is then determined by the scale variations that result in the largest change in the positive or negative direction of the signal acceptance.

Uncertainties on the PS are estimated by varying the configuration of the respective tune. For gluon-gluon fusion samples, the two eigen-variations Var1 and Var2 of the AZNLO tune [207] are applied, which simultaneously vary the primordial transverse momentum of the proton partons and the ISR cut-off scale as well as generator configurations governing the ISR and MPI. On the *b*-associated Higgs production samples the recommended Var1, Var2, and Var3a eigen-variation sets of the A14 tune are used which vary a multitude of internal generator settings as described in Reference [137]. The results are combined by adding the change in acceptance in quadrature from which the up and down variation of the uncertainty is extracted.

An evaluation of PDF uncertainties is conducted by varying the systematic uncertainty sets of the respective PDF used by the ME generator. The CT10NLO_NF4 and CT10 PDF sets used to configure the *b*-associated and gluon-gluon fusion production samples contain eigen-variations [205]. The PDF eigen-variation uncertainty is calculated by adding the changes in signal acceptance in quadrature. The CT10 PDF set also provides variations of the strong coupling parameter ranging from $0.113 < \alpha_S (M_Z) < 0.123$. The systematic uncertainty on α_S is calculated from the envelope in changes on the acceptance. An

additional uncertainty on the choice of the PDF set is derived by exchanging the nominal PDF of the *b*-associated production and gluon-gluon fusion signal sample generators with the PDF4LHC15_NLO_NF4_30 and PDF4LHC15_NLO_30 PDFs respectively [77]. By comparing the results between the nominal and alternative PDF, the up and down variations of the PDF choice uncertainty are calculated by mirroring the difference in signal acceptance around the nominal value.

The combined PDF uncertainty is calculated by adding the uncertainties on PDF eigenvariations, changes in α_S, and PDF choice in quadrature.

Figure 7.4.7 shows the combined QCD scale, PS tune, and PDF uncertainties on the signal acceptance. A listing of the numerical values of the acceptance uncertainty is given in Appendix C.1. The total acceptance uncertainty is derived by adding the various uncer-
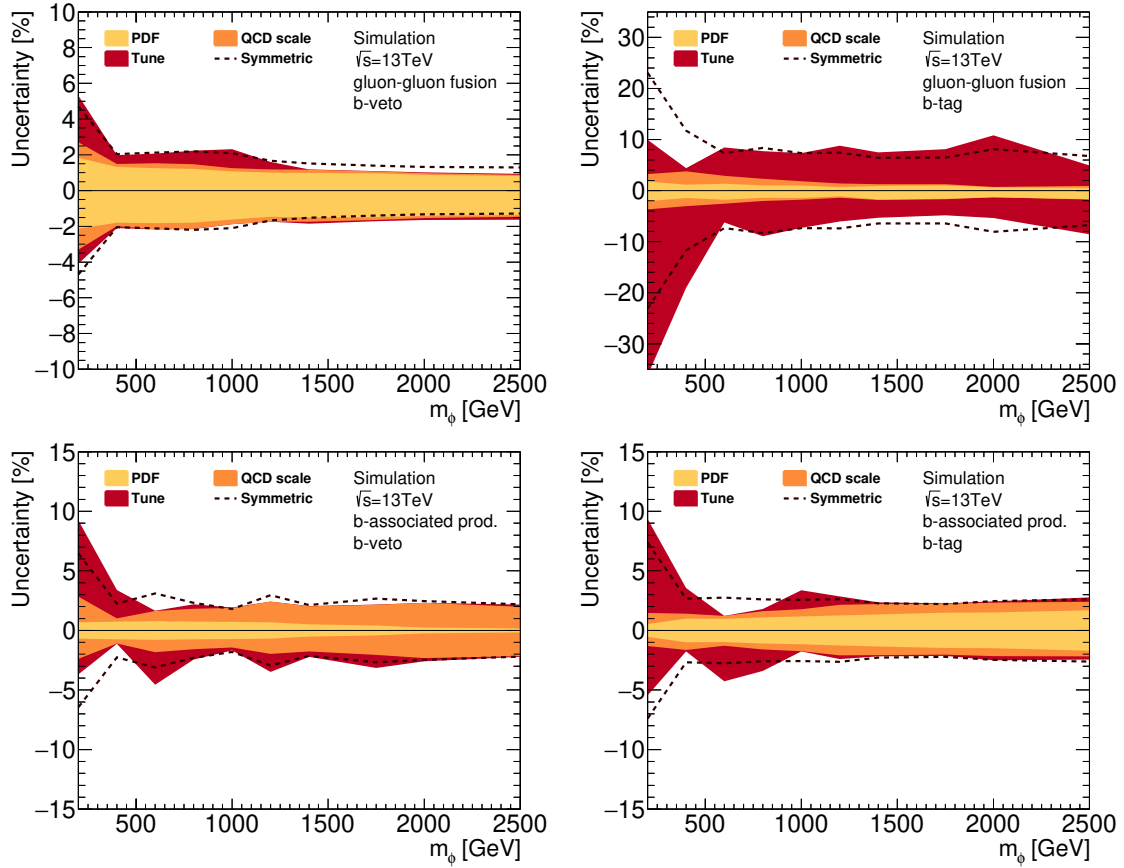

Figure 7.4.7.: Combined acceptance uncertainty for Higgs boson samples produced via gluon-gluon fusion (top) and *b*-associated production (bottom) for signals in the *b*-veto (left) and *b*-tag (right) category.

tainty sources in quadrature. The total acceptance uncertainty is smoothed by symmetrizing the uncertainty bands, reducing the impact of statistical fluctuations. In most cases the acceptance uncertainty stays at about 2 % for Higgs masses above 500 GeV, steeply increasing at lower mass values. This is caused by the lower acceptance for low mass signals due to the high momentum thresholds of the triggers used in the signal region. One exception are the gluon-gluon fusion samples in the *b*-tag region where the total uncertainty ranges from 7 % to 23 %, mostly caused by large generator tuning uncertainties. For gluon-gluon fusion samples, the probability of an event containing a *b*-tagged jet depends on the hadronization of the additional jets in the event record. Hence, the impact of the PS tuning is larger for gluon-gluon fusion samples in this category.

Data-Driven Background uncertainties

The sources of uncertainties for the data-driven background estimation and correction methods are covered in Section 7.3.2 for fake-factors and 7.3.3 for fake-rates. In total there is one systematic variation for fake-rates and 32 variations for fake-factors.

About 30 fake-factor uncertainties originate from the bin-wise decorrelation of the statistical uncertainty components on data and Monte Carlo background in the fake-factor measurement. Since the multijet background is the dominant background in the low-$m_{\mathrm{T}}^{\mathrm{tot}}$ regime, uncertainties on the fake-factors could potentially be constrained by the limit fit. If the statistical uncertainties were correlated, constraints in the low-$m_{\mathrm{T}}^{\mathrm{tot}}$ regions can propagate to the high-$m_{\mathrm{T}}^{\mathrm{tot}}$ regime, causing over-optimistic limit results. Thus, decorrelating the statistical uncertainty components is necessary to avoid over-constraining of the systematic uncertainties of the fake-factors.

7.5. Statistical Evaluation

Results from the measurements in the signal region are interpreted in terms of upper limits on the signal production cross-section using the CL_s method [263, 264] with a 95 % confidence level. From the derived expected and observed limits, it can be deduced whether a signal excess is observed or the background hypothesis holds true. Firstly, the general procedure of calculating limits with the profile likelihood method is presented. The so determined limits are then evaluated and translated into the theory model parameter space by interlacing the measured cross-section limits with the predictions of the benchmark models.

7.5.1. The Statistical Analysis Framework

A limit on a given signal hypothesis is set by testing the nominal signal hypothesis $\mathcal{H}_1$ against the background hypothesis $\mathcal{H}_0$. Introducing a signal strength scale-factor μ enables one to determine upper limits on the potential signal cross-section by testing different values of μ. The statistical test is conducted using the profile likelihood method [201]. This requires the construction of the likelihood ratios of binned variable distributions containing the event yields measured in the signal region. For a given distribution $\mathcal{D}$ with bins $i \in \{1, ..., N\}$ the expected number of events n_i^{exp}, depending on the signal strengths parameter μ is defined by:

$$E_\mu [n_i] = n_i^{\mathrm{exp}} = \mu s_i + b_i, \tag{7.18}$$

with b_i being the expected background yield and s_i the signal yield scaled by μ in bin i. Setting the signal scale parameter to $\mu = 1$ corresponds to the nominal signal hypothesis predicted by the model tested while the case of $\mu = 0$ represents the background-only hypothesis. Thus, fitting μ as the parameter of interest coincides with testing for multiple signal hypotheses with different signal strengths.

The test statistic used in the limit calculation is derived from the likelihood function of the bin yield measurements. Since the uncorrelated events are produced at a constant average rate, the probability of the measured data yields follow a Poisson distribution. Hence, the conditional likelihood for each bin can be expressed by:

$$\mathcal{L}_i \left(\mu \,|\, s_i, \, b_i, \, n_i^{\mathrm{obs}} \right) = \mathrm{Pois} \left(n_i^{\mathrm{obs}}, \, \mu s_i + b_i \right) = \mathrm{Pois} \left(n_i^{\mathrm{obs}}, \, n_i^{\mathrm{exp}} \right), \tag{7.19}$$

with n_i^{obs} being the number of observed events in bin i and the Poisson distribution defined by:

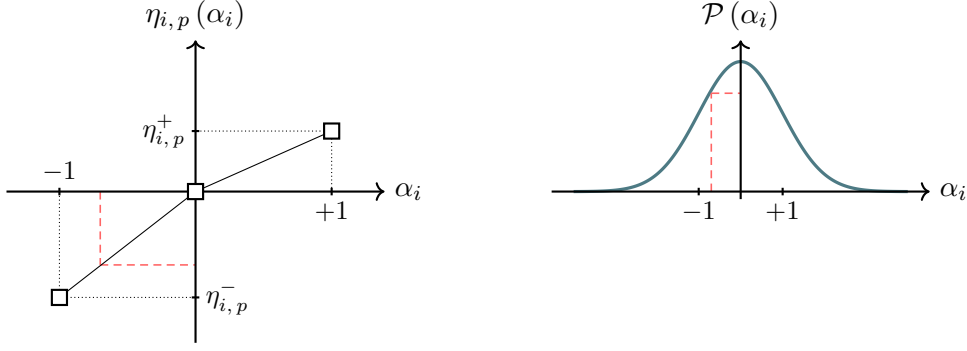$$\mathrm{Pois} \left(m, \, n \right) = \frac{n^m}{m!} e^{-n}. \tag{7.20}$$

Figure 7.5.1.: Visualization of nuisance parameter transformation functions $\eta_{j,p}(\alpha_j)$.

The total likelihood of a distribution $\mathcal{D}$ is then calculated from the product of the binned likelihood $\mathcal{L}_i$:

$$\mathcal{L}_{\mathcal{D}}\left(\mu\,|\,s_i,\,b_i,\,n_i^{\text{obs}}\right) = \mathcal{C}\prod_{i=1}^{N}\mathcal{L}_i\left(\mu\,|\,s_i,\,b_i,\,n_i^{\text{obs}}\right),\qquad(7.21)$$

which is scaled by a normalization constant $\mathcal{C}$. The likelihood constructed in Equation (7.21) only depends on the number of measured data and expected background and signal yields. Both background and signal events, however, are affected by systematic uncertainties. These uncertainties have to be incorporated into the total likelihood by extending the likelihood with additional probability terms. For each source of uncertainty, like tau energy scale or tau-ID scale-factor uncertainties, an associated nuisance parameter α is constructed as a random variable following a Gaussian normal distribution with a mean of 0 and variance of 1. The Nuisance Parameters (NP) are connected to the uncertainties of different background and signal processes by transformation functions.

Suppose there are $j \in \{1, ..., M\}$ nuisance parameters α_j associated with systematic uncertainties acting on background or signal processes p, like $Z \to \tau\tau$ or gluon-gluon fusion production. If the uncertainty is a normalization uncertainty, only shifting the yield by a factor $\eta_{j,p}^{+}$ up and $\eta_{j,p}^{-}$ down, the NP are connected to the change in the event yields of the process by transformation functions $\eta_{j,p}$. The transformation function is a piecewise linear function that fulfills the following criteria:

$$\eta_{j,p}\left(\alpha_j\right) = \begin{cases} \eta_{j,p}^{+} & , \text{if } \alpha_j = +1, \\ 1 & , \text{if } \alpha_j = 0, \\ \eta_{j,p}^{-} & , \text{if } \alpha_j = -1. \end{cases}\qquad(7.22)$$

Figure 7.5.1 shows a visualization of the transformation function.

In case that the magnitude and direction of a given uncertainty vary significantly throughout the variable distribution, the systematic uncertainty is classified as shape uncertainty. In this case, the impact on the background and signal yield has to be calculated for each bin i individually via transformation functions $\zeta_{i,j,p}(\alpha_j)$. These transformation functions are constructed in the same way as the $\eta_{j,p}$ functions. Whether an uncertainty is treated as shape or normalization uncertainty is decided for each background and signal process separately.

All nuisance parameters related to systematic uncertainties are subject to a pruning algorithm. Normalization uncertainties are dropped if their magnitude is smaller than 1 %. To evaluate shape uncertainties, their impact on the change of the overall normalization and shape is separated. If the change in normalization or the residual change in shape in any bin of the distribution is larger than 1 %, the shape uncertainty is kept. A list of all systematic uncertainties passing the pruning algorithm is given in Appendix C.2.

Statistical uncertainties on the background templates are taken into account by using a variation of the Beeston-Barlow method [265]. This method introduces scale-factors γ_i which are applied to each bin i of the combined background distribution. The γ factors are constrained by Poisson distributions, thus allowing the background yield of each bin to float within the statistical uncertainty.

Including the terms of nuisance parameters for systematic uncertainties and statistical uncertainties on the background, the signal and background event yields s_i and b_i from Equation 7.21 transform as follows:

$$b_i \rightarrow \tilde{b}_i = \gamma_i \sum_p b_{i,\,p} \times \left[\prod_{j=1}^{M} \eta_{j,\,p}\left(\alpha_j\right) \zeta_{i,\,j,\,p}\left(\alpha_j\right) \right], \tag{7.23}$$

$$s_i \rightarrow \tilde{s}_i = \sum_p s_{i,\,p} \times \left[\prod_{j=1}^{M} \eta_{j,\,p}\left(\alpha_j\right) \zeta_{i,\,j,\,p}\left(\alpha_j\right) \right], \tag{7.24}$$

with $b_{i,p}$ and $s_{i,p}$ the bin yields of individual background and signal processes p. Substituting $\tilde{b}_i$ and $\tilde{s}_i$ in Equation (7.21) and adding the constraining terms for the NP and γ factors yields the complete likelihood function:

$$\mathcal{L}_{\mathcal{D}}\left(\mu, \boldsymbol{\theta} \,|\, s_i,\, b_i,\, n_i^{\mathrm{obs}}\right) = \mathcal{C} \prod_{i=1}^{N} \mathrm{Pois}\left(n_i^{\mathrm{obs}},\, \mu\tilde{s}_i + \tilde{b}_i\right) \cdot \mathrm{Pois}\left(\gamma_i b_i,\, b_i\right)$$
$$\times \prod_{j=1}^{M} \mathrm{Gauss}\left(\alpha_j,\, 0,\, 1\right), \tag{7.25}$$

with $\boldsymbol{\theta} = \{\alpha_1,\, ...,\, \alpha_M,\, \gamma_1,\, ...,\, \gamma_N\}$ the combined set of nuisance parameters and the Gauss function defined by:

$$\mathrm{Gauss}\left(x,\, \mu,\, \sigma\right) = \frac{1}{\sigma\sqrt{2\pi}} e^{-\frac{1}{2}\frac{(x-\mu)^2}{\sigma^2}}. \tag{7.26}$$

The construction of the likelihood function is performed by the HISTFACTORY software package [266] and is evaluated within the ROOFIT and ROOSTATS framework [267–269].

From the likelihood distribution, the profile likelihood ratio $\tilde{\lambda}\left(\mu\right)$ is constructed according to Reference [270]:[1]

$$\tilde{\lambda}\left(\mu\right) = \begin{cases} \dfrac{\mathcal{L}_{\mathcal{D}}\left(\mu, \hat{\hat{\boldsymbol{\theta}}}(\mu)\right)}{\mathcal{L}_{\mathcal{D}}\left(\hat{\mu}, \hat{\boldsymbol{\theta}}\right)} & , \text{if } \hat{\mu} \geq 0, \\[3ex] \dfrac{\mathcal{L}_{\mathcal{D}}\left(\mu, \hat{\hat{\boldsymbol{\theta}}}(\mu)\right)}{\mathcal{L}_{\mathcal{D}}\left(0, \hat{\hat{\boldsymbol{\theta}}}(0)\right)} & , \text{if } \hat{\mu} < 0. \end{cases} \tag{7.27}$$

The variables $\hat{\mu}$ and $\hat{\boldsymbol{\theta}}$ refer to the MLE of $\mathcal{L}_{\mathcal{D}}$ while $\hat{\hat{\boldsymbol{\theta}}}\left(\mu\right)$ corresponds to the conditional MLE for a given value of μ. As the signal hypothesis tested in this analysis is supposed to only add events to the total event yield, the test statistic $\tilde{\lambda}$ is bound from below. If the data fluctuates below the MLE of $\hat{\mu} < 0$ the likelihood is then evaluated at the nearest possible value of $\hat{\mu} = 0$. For reasons of practicality the logarithm of the profile likelihood ratio is used:

$$\tilde{t}_\mu = -2 \ln \tilde{\lambda}\left(\mu\right), \tag{7.28}$$

---

[1] For convenience, the parameters of the conditional likelihood s_i, b_i, and n_i^{obs} are omitted in further calculations.

resulting in values of μ which are more compatible with data to have smaller $\tilde{t}_\mu$. Upper limits on μ are set with the test statistic $\tilde{q}_\mu$ defined by:

$$
\tilde{q}_\mu = \begin{cases} \tilde{t}_\mu & \text{, if } \hat{\mu} \leq \mu \\ 0 & \text{, if } \hat{\mu} > \mu \end{cases} = \begin{cases} -2\ln \dfrac{\mathcal{L}_\mathcal{D}\left(\mu, \hat{\hat{\boldsymbol{\theta}}}(\mu)\right)}{\mathcal{L}_\mathcal{D}\left(0, \hat{\hat{\boldsymbol{\theta}}}(0)\right)} & \text{, if } \hat{\mu} < 0, \\[2ex] -2\ln \dfrac{\mathcal{L}_\mathcal{D}\left(\mu, \hat{\hat{\boldsymbol{\theta}}}(\mu)\right)}{\mathcal{L}_\mathcal{D}\left(\hat{\mu}, \hat{\boldsymbol{\theta}}\right)} & \text{, if } 0 \leq \hat{\mu} \leq \mu, \\[2ex] 0 & \text{, if } \hat{\mu} > \mu. \end{cases}
\tag{7.29}
$$

Since the test statistic shall be used to calculate upper limits on μ, it is bound from below for $\mu < \hat{\mu}$. This prevents signal hypotheses with a signal strength below the MLE to be less compatible with data than the MLE itself. From the Probability Density Function (p.d.f.) of the test statistic $f\left(\tilde{q}_\mu \mid \mu'\right)$, the p-value for a hypothesized signal strength parameter μ' is derived by:

$$
p_{\mu'} = \int_{\tilde{q}_\mu^{\mathrm{obs}}}^{\infty} f\left(\tilde{q}_\mu \mid \mu'\right) dq_\mu,
\tag{7.30}
$$

where $\tilde{q}_\mu^{\mathrm{obs}}$ is the value of the test statistic evaluated on the measured data. The p-value determines the probability that the observed data could be explained by a statistical fluctuation of the model hypothesis.

The CL_s Method

Based on the p-value in Equation (7.30) one-sided upper limits on μ can be constructed by scanning different values of the signal strength μ. An upper limit is defined at the Confidence Level (CL) of $1 - \alpha$ as the set of all values of μ that fulfill $p_{\mu'} < \alpha$. Given the data observed, the p-values for the signal-plus-background $\mathcal{H}_1$ and the background-only hypothesis $\mathcal{H}_0$ are calculated by evaluating $p_{\mu'}$ at $\mu' = \mu$ and $\mu' = 0$ respectively. The two hypothesis measures are usually also referred to as CL_{s+b} or CL_b:

$$
CL_{s+b} = p_\mu = \int_{\tilde{q}_\mu^{\mathrm{obs}}}^{\infty} f\left(\tilde{q}_\mu \mid \mu\right) dq_\mu,
\tag{7.31}
$$

$$
CL_b = p_0 = \int_{\tilde{q}_\mu^{\mathrm{obs}}}^{\infty} f\left(\tilde{q}_\mu \mid 0\right) dq_\mu.
\tag{7.32}
$$

While CL_b is usually used to quote discoveries, upper limits on μ calculated based on CL_{s+b} tend to set too strong exclusion limits on the signal hypotheses in regions where the analysis is not sensitive [271, 272]. Therefore, a modified CL_s hypothesis is defined by normalizing the CL_{s+b} to the background-only p-value [263, 264]:

$$
CL_s = \frac{CL_{s+b}}{CL_b}.
\tag{7.33}
$$

Values of μ within the upper limit contour of $CL_s < \alpha = 0.05$ are then excluded with a confidence level of $\mathrm{CL} = 1 - \alpha = 95\,\%$. Due to its construction, the CL_s method does not provide true confidence intervals as it is a confidence ratio. However, the true coverage probability is always larger than the target coverage of $1 - \alpha$. Hence, exclusion limits calculated using the CL_s method are always more conservative while not expressing the undesirable properties of the CL_{s+b} method.

In order to evaluate the expected sensitivity of the analysis assuming the data follows the background-only hypothesis, the expected upper limit is calculated by exchanging q_μ^{obs} in Equations (7.31) and (7.32) with the median q_μ of the background-only p.d.f., $\mathrm{med}[q_\mu \mid 0]$.

In practice, the distribution of $f\left(\tilde{q}_\mu \,|\, \mu'\right)$ is calculated by simulating many repetitions of the experiment using toy Monte Carlo data. These toy Monte Carlo measurements are generated by sampling pseudo-data according to the likelihood function in Equation (7.25). From calculating the values of the upper limit on μ many times, the $\pm 1\sigma$ and $\pm 2\sigma$ bands can be derived from the respective quantiles of the resulting distribution of μ.

Asymptotic Approximation

Generating enough pseudo-experiments to sample numerically stable distributions for the p.d.f.s of the test statistics is very computationally expensive. Therefore, approximations investigated in Reference [270] are needed to estimate the p.d.f. functions. By using Wilks' theorem [273] and Wald's approximation [274] the negative logarithmic likelihood function used in Equations (7.27) and (7.28) can be approximated by the asymptotic formula[2]:

$$-2\ln\lambda\left(\mu\right) = -2\ln\frac{\mathcal{L}_{\mathcal{D}}\left(\mu, \hat{\hat{\boldsymbol{\theta}}}\left(\mu\right)\right)}{\mathcal{L}_{\mathcal{D}}\left(\hat{\mu}, \hat{\boldsymbol{\theta}}\right)} = \frac{(\mu - \hat{\mu})^2}{\sigma^2} + \mathcal{O}\left(\frac{1}{\sqrt{N}}\right). \tag{7.34}$$

In this equation the value of $\hat{\mu}$ is thought to follow a normal distribution with a mean around the hypothesized signal strength parameter μ' and standard deviation σ. If the number of expected events is large enough, the second term can be neglected. By applying Equation (7.34) to the test statistic of Equation (7.29), omitting the $\mathcal{O}(1/\sqrt{N})$ term, an approximation for $\tilde{q}_\mu$ can be found, as:

$$\tilde{q}_\mu = \begin{cases} \frac{\mu^2 - 2\mu\hat{\mu}}{\sigma^2} & \text{, if } \hat{\mu} < 0, \\ \frac{(\mu - \hat{\mu})^2}{\sigma^2} & \text{, if } 0 \le \hat{\mu} \le \mu, \\ 0 & \text{, if } \hat{\mu} > \mu. \end{cases} \tag{7.35}$$

The corresponding p.d.f. is given by:

$$f\left(\tilde{q}_\mu \,|\, \mu'\right) = \Phi\left(\frac{\mu' - \mu}{\sigma}\right)$$
$$+ \begin{cases} \frac{1}{2\sqrt{2\pi\tilde{q}_\mu}}\exp\left[-\frac{1}{2}\left(\sqrt{\tilde{q}_\mu} - \frac{\mu - \mu'}{\sigma}\right)\right] & \text{, if } 0 < \tilde{q}_\mu \le \frac{\mu^2}{\sigma^2}, \\ \frac{1}{\sqrt{2\pi}(2\mu/\sigma)}\exp\left[-\frac{1}{2}\frac{\left(\tilde{q}_\mu - (\mu^2 - 2\mu\mu')/\sigma^2\right)^2}{(2\mu/\sigma)^2}\right] & \text{, if } \tilde{q}_\mu > \frac{\mu^2}{\sigma^2}, \end{cases} \tag{7.36}$$

with Φ being the cumulative function of the standard normal distribution. The estimation of the standard deviation σ of $\hat{\mu}$ is conducted by evaluating the test statistic on a specially defined dataset, named Asimov data n_{A}, which is constructed for a specific hypothetical signal strength parameter μ'. The Asimov data yields $n_{\mathrm{A},i}$ are then determined in such a way, that the NP are at their nominal values. By definition of the likelihood function, this is the case when the Asimov data matches the expected data given a signal strength hypothesis:

$$n_{\mathrm{A},i} = E_{\mu'}\left[n_i\right] = \mu'\tilde{s}_i + \tilde{b}_i. \tag{7.37}$$

Evaluating the likelihood function $\lambda\left(\mu\right)$ using the Asimov dataset one can approximate σ by:

$$\sigma_{\mathrm{A}}^2 = \frac{(\mu - \mu')^2}{-2\ln\lambda_{\mathrm{A}}\left(\mu\right)}. \tag{7.38}$$

---

[2]Note that $\lambda(\mu)$ without tilde is similar to the definition in Equation (7.27), only omitting the lower bound for $\hat{\mu} < 0$.

Setting the hypothesized parameter to $\mu' = 0$ or the tested signal strength $\mu' = \mu$ one can construct approximations for the p.d.f.s $f(\tilde{q}_\mu \,|\, 0)$ and $f(\tilde{q}_\mu \,|\, \mu)$ using the asymptotic formula in Equation (7.36). Additionally, as the expected limit is set based on the background-only hypothesis, the Asimov data generated with $\mu' = 0$ can be used to estimate $\mathrm{med}[q_\mu \,|\, 0] \approx \tilde{q}_{\mu,\,\mathrm{A}}$ and therefore the expected upper limit on μ.

To check the validity of asymptotic approximation, a test is performed by comparing the approximation with the results generated using toy Monte Carlo. Two core assumptions are tested: the shape of the p.d.f. from Equation (7.36) and the standard deviation of $\hat{\mu}$ from Equation (7.38). With increasing expected background events the neglected second term in Equation (7.34) gets smaller, thus resulting in a better approximation. However, estimating the minimum amount of events needed for the approximation to hold true is not trivial. The binning of the $m_{\mathrm{T}}^{\mathrm{tot}}$ distribution in the b-tag and b-veto signal region is chosen such that at least 10 expected background events are present in each bin. Exclusion limits suffering the most from low background yields are limits set on the $2500\,\mathrm{GeV}$ signal mass samples as they are mostly concentrated in the highest bins of $m_{\mathrm{T}}^{\mathrm{tot}}$ where the least amount of events are expected. A cross-check is therefore conducted by evaluating the true and the approximated p.d.f. of $\tilde{q}_\mu$ at the point of the expected upper limit on μ. As the total signal is a combination of heavy Higgs bosons produced via gluon-gluon fusion and b-associated production, the signal tested is an equal combination of both signal processes, translating to a b-fraction $f_{b\text{-frac}}$ of 0.5:

$$s_{\mathrm{tot}} = (1 - f_{b\text{-frac}}) \cdot s_{\mathrm{ggH}} + f_{b\text{-frac}} \cdot s_{\mathrm{bbH}}, \tag{7.39}$$

with s_{ggH} being the gluon-gluon fusion and s_{bbH} the b-associated production signal yields. The variable $f_{b\text{-frac}}$ can be thus defined in terms of the total b-associated and gluon-gluon fusion production cross-section by:

$$f_{b\text{-frac}} = \frac{\sigma_{\mathrm{bbH}}}{\sigma_{\mathrm{ggH}} + \sigma_{\mathrm{bbH}}}. \tag{7.40}$$

Figure 7.5.2 shows the distributions of $f(\tilde{q}_\mu \,|\, \mu)$ and $f(\tilde{q}_\mu \,|\, 0)$ derived from pseudo-experiments from toy data and using the asymptotic formula, as well as the standard derivation of $\hat{\mu}$ compared to the approximation derived from the Asimov dataset. At the predicted upper limit of $\mu = 0.0013$, the approximation and toy distribution show good agreement. The $\pm 1\sigma$ bands can be estimated by calculating the upper limit on μ while evaluating the p.d.f. of the test statistic $f(\tilde{q}_\mu \,|\, 0)$ at the $15.9\,\%$ and $84.1\,\%$ quantile respectively. The p.d.f.s for the $\pm 1\sigma$ band evaluation are shown in Figure 7.5.3. In general, the probability distributions estimated by the asymptotic approximation in conjunction with the Asimov data match the ones generated using toy Monte Carlo data. This indicates that the minimum requirement of ~ 10 expected background events per bin is sufficient for the asymptotic approximation to yield valid results within reasonable error margins in the confidence level of $\left| CL_s^{\mathrm{Toy}} - CL_s^{\mathrm{Asymp.}} \right| < 1\,\%$.

7.5.2. Cross-Section Limits

Upper limits on the signal strength parameter μ are calculated at the $95\,\%$ CL using the CL_s method for mass points of 200, 250, 300, 350, 400, 500, 600, 700, 800, 1000, 1200, 1500, 2000, and $2500\,\mathrm{GeV}$. The limits on μ are then presented in terms of upper limits on the cross-section times branching ratio of a Higgs boson decaying into pairs of tau leptons. Upper limits on the cross-section of heavy neutral Higgs bosons produced via gluon-gluon fusion and b-associated production, corresponding to $f_{b\text{-frac}} = 0$ and 1, are shown in Figure 7.5.4. As expected, the limits on gluon-gluon fusion production are mostly driven by the
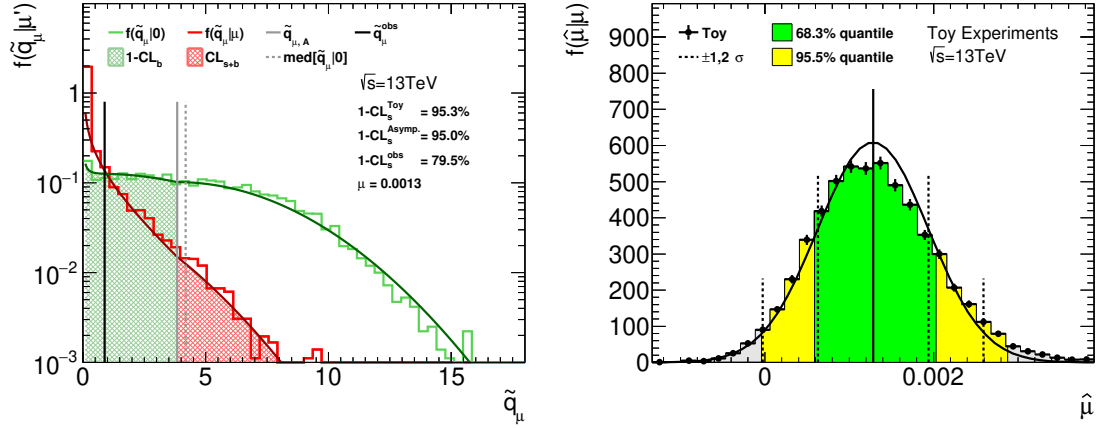
Figure 7.5.2.: Distribution of $f(\tilde{q}_\mu \,|\, \mu')$ (left) and $f(\hat{\mu} \,|\, \mu)$ (right) for the 2500 GeV signal hypothesis with $f_{b\text{-frac}} = 0.5$. The p.d.f.s are evaluated at the expected upper limit derived from the asymptotic approximation. The distributions obtained and the confidence levels derived from toy pseudo-data (histogram) and asymptotic approximations (solid lines) are in good agreement. The p.d.f. of $\hat{\mu}$ is compared with the distribution predicted by the Asimov data.
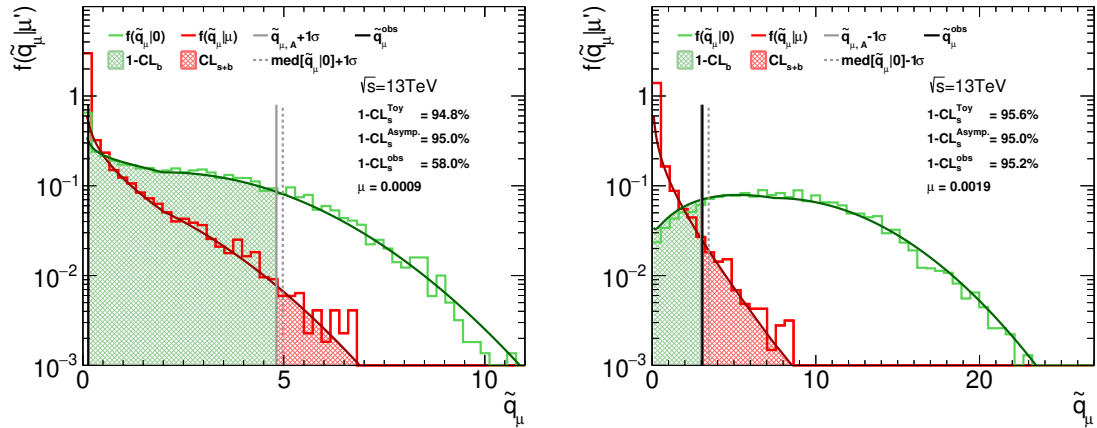

Figure 7.5.3.: Distribution of $f(\tilde{q}_\mu \,|\, \mu')$ evaluated at the $+1\sigma$ (left) and -1σ quantile (right) of $f(\tilde{q}_\mu \,|\, 0)$.
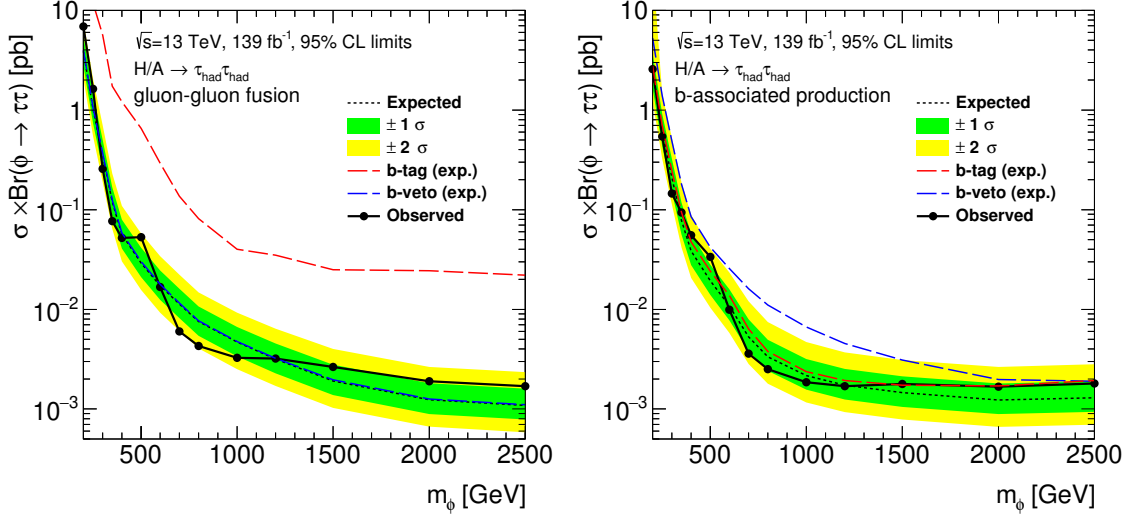
Figure 7.5.4.: Upper limits on the cross-section times branching ratio for Higgs boson production via gluon-gluon fusion (left) and *b*-associated production (right) in the $\tau_{\mathrm{had}}\tau_{\mathrm{had}}$ channel.

results of the *b*-veto signal region since the acceptance of this signal process in the *b*-tag category is very low. Similarly, the upper limit on the *b*-associated production is determined to a large degree by the *b*-tag region. However, at high signal masses, the sensitivity of the *b*-veto region approaches that of the *b*-tag region.

For all mass points considered, the observed limits lie within the $\pm 2\,\sigma$ bands of the expected limit. The largest deviations from the expected limits are observed at Higgs boson mass hypotheses of $500\,\mathrm{GeV}$ and $700\,\mathrm{GeV}$ of $+1.80\,\sigma\,(+1.46\,\sigma)$ and $-2.06\,\sigma\,(-0.95\,\sigma)$ for gluon-gluon fusion (*b*-associated production) respectively. The upward deviation at $500\,\mathrm{GeV}$ in the limits for the gluon-gluon fusion Higgs production coincides with the upward fluctuation of data over the expected background observed in the 450-500 GeV bin of the $m_{\mathrm{T}}^{\mathrm{tot}}$ distribution in the *b*-veto signal region. This data excess is followed by an undershoot of data over the background expectation resulting in a stronger limit on the production cross-section of the 700 and 800 GeV signal mass samples. A similar, yet less significant, shape of the limit fluctuation is observed for the *b*-associated production.

Since the theory models discussed in Section 2.2 predict different fractions of gluon-gluon fusion and *b*-associated Higgs production depending on the theory parameters m_A-$\tan\beta$, limits on the model parameter space can be derived from the model-independent cross-section times branching ratio limits parameterized in m_ϕ and $f_{b\text{-frac}}$ using a procedure discussed in Section 7.6. Figure 7.5.5 shows the observed and expected model-independent upper limits. A list containing the numerical values of the model-independent upper limits including the values of the $\pm 1\sigma$ and $\pm 2\sigma$ bands can be found in Appendix D.2.

In order to judge the goodness of the profile likelihood fits conducted during limit calculation, it is useful to study the impact of the nuisance parameters on the signal strength. From the unconditional MLE fit, the pull of the nuisance parameter α_i with respect to the nominal value is calculated. Additionally, the fit determines whether the uncertainty can be constrained. These constraints are quoted for the postfit results in terms of $\pm 1\sigma$ in α_i relative to the prefit values. A bad fit is usually indicated by large pulls above 2σ on one or more nuisance parameters. Strong constraints are also undesirable as they indicate that uncertainties are over- or underestimated if the postfit uncertainty is smaller or larger than the nominal uncertainty.
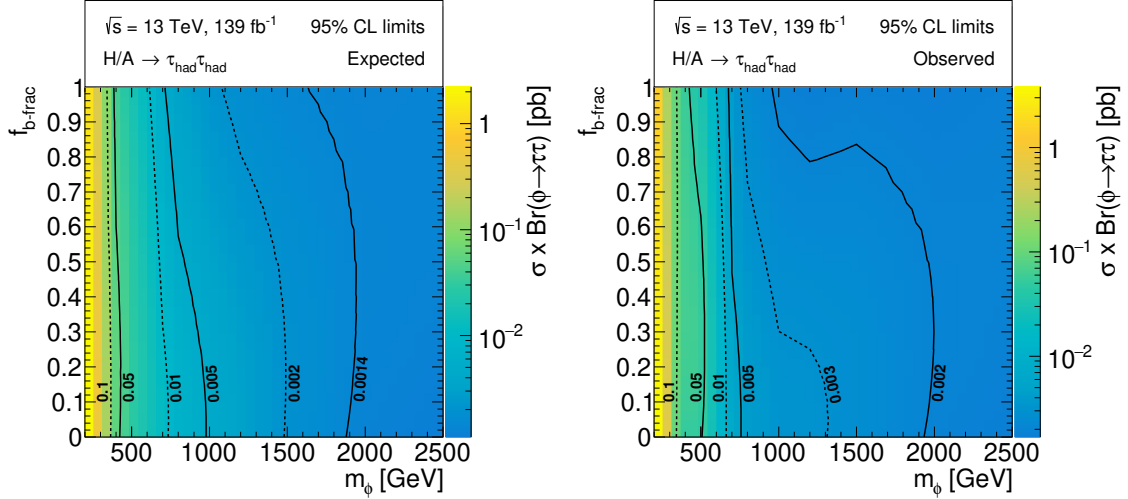
Figure 7.5.5.: Expected (left) and observed (right) model-independent exclusion limits on the cross-section times branching ratio parameterized in the neutral resonance mass m_ϕ and $f_{b\text{-frac}}$.

Figure 7.5.6 lists the first 25 nuisance parameters ordered by their prefit impact for the 500 GeV and 2000 GeV mass points. The nuisance parameter impact is defined as the relative change of $\hat{\mu}$ when setting the NP to their $\pm 1\,\sigma$ value. As expected, top background related uncertainties have a larger impact on the fits in the b-tag category while Z boson production related uncertainties are more important in the b-veto category. In general, the fit shows good behavior as no nuisance parameter is strongly pulled or constrained. The largest pull and constraint is applied on the top ME uncertainty which is pulled by about $+1\,\sigma$ and constrained to about $81\,\%$ of the prefit value. This is caused by the downward fluctuation of the uncertainty estimate shown in Figure 7.4.6 which coincides with the downward fluctuation of measured data in the last bin of the $m_{\text{T}}^{\text{tot}}$ distribution in the b-tag category. Simultaneously, the top ME uncertainty estimation suffers from a high statistical uncertainty component in this bin which is not reflected in the fit, thus resulting in a possible overestimate of the uncertainty. However, the modeling of this uncertainty is not problematic as it is well within the $2\,\sigma$ boundaries.

In addition to the nuisance parameter pulls and constraints the correlation between two nuisance parameters, including the parameter of interest μ, can be calculated by evaluating the covariance of two NP θ_i and θ_j:

$$\text{corr}\,[\theta_i,\,\theta_j] = \frac{\text{cov}\,[\theta_i,\,\theta_j]}{\sqrt{\text{cov}\,[\theta_i,\,\theta_i]\cdot\text{cov}\,[\theta_j,\,\theta_j]}}. \tag{7.41}$$

Figure 7.5.7 shows the correlation matrix of nuisance parameters with correlation coefficients larger than $10\,\%$. No strong correlations between nuisance parameters are observed. Correlation between top PS and ISR is expected as both uncertainties are similar in shape and magnitude and affect the same background process. Similarly, some correlations between uncertainties on the tau energy scale, tau-ID, and higher-order Z boson cross-section corrections are observed, since these uncertainties tend to be leading uncertainties on off-shell $Z/\gamma^* \to \tau\tau$+jet background. Correlations with the parameter of interest μ coincide in terms of magnitude and direction of the pulls observed in Figure 7.5.6. By conducting the likelihood fit with the background-only hypothesis, the postfit background yields are extracted which are listed in Table 7.5.1.
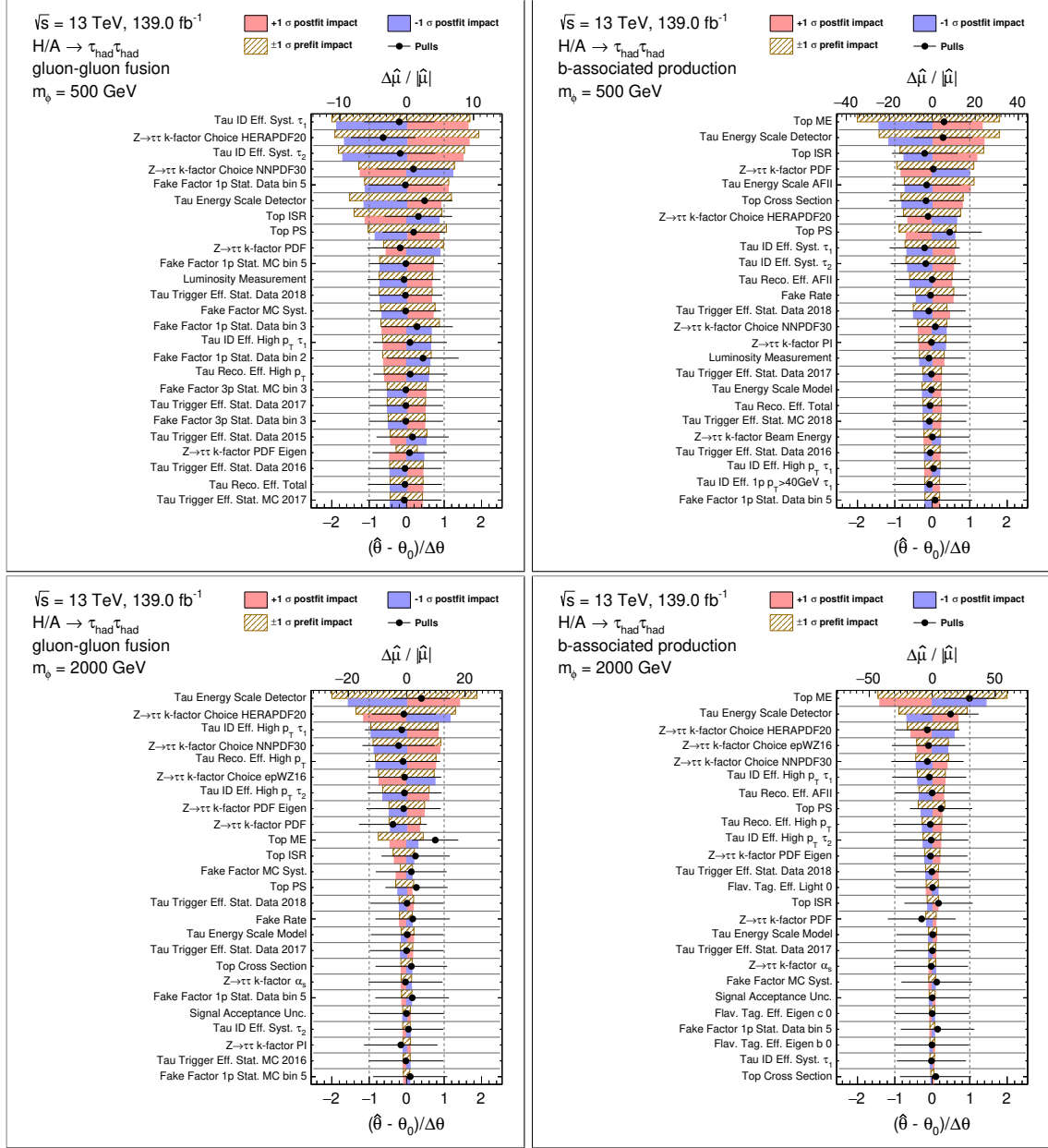
Figure 7.5.6.: First 25 nuisance parameters ordered by the prefit impact for the 500 GeV (top) and 2000 GeV (bottom) signal mass hypothesis produced via gluon-gluon fusion (left) and *b*-associated production (right). The upper x-axis measures the pre- and postfit impact on $\hat{\mu}$ while the lower axis parameterizes the pulls and constraints in terms of standard deviations of its prefit value.
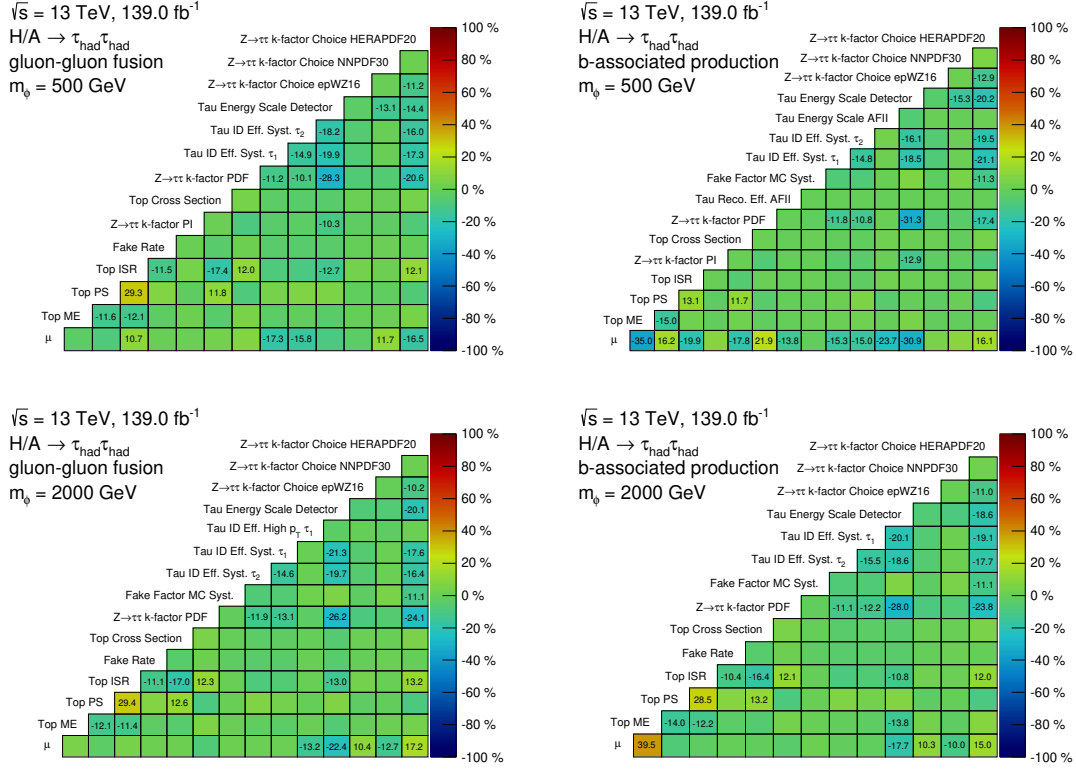
Figure 7.5.7.: Nuisance parameter correlation matrices for the 500 GeV (top) and 2000 GeV (bottom) signal mass hypothesis produced via gluon-gluon fusion (left) and b-associated production (right). Nuisance parameters are omitted if their absolute maximum correlation is below 10 %.

Process	Postfit	
	b-veto Category	b-tag Category
Multijet	5750 ± 80	166 ± 6
$Z/\gamma^* \to \tau\tau$+jets	2120 ± 100	29.3 ± 2.7
$W \to \tau\nu$+jets	440 ± 40	12.3 ± 1.1
$t\bar{t}$, single top	85 ± 9	184 ± 17
Others	68 ± 5	2.38 ± 0.23
Total background	8460 ± 80	394 ± 17
Data	8480	396

Table 7.5.1.: Postfit yield table of the $\tau_{\mathrm{had}}\tau_{\mathrm{had}}$ channel signal regions.

7.6. Results in the Context of the Combined Higgs Search

The analysis presented in this thesis is part of the search for heavy neutral Higgs bosons decaying into two tau leptons published in Reference [24]. In this section, the exclusion limits calculated from the combination of the $\tau_{\text{had}}\tau_{\text{had}}$ and $\tau_{\text{lep}}\tau_{\text{had}}$ categories are presented. Additionally, the impact of the improved background modeling in the limit calculation is assessed by comparing the cross-section limits from the published paper with the results derived by applying the improved fake-rates and fake-factors.

The cross-section limits are then translated into an upper exclusion limit in the theory parameter space of the benchmark models described in Section 2.2.

7.6.1. Model-Independent Limits

Alongside the fully hadronic search channel, the analysis presented in Reference [24] also includes a semi-leptonic search channel where one tau candidate decays hadronically and the other one into an electron or muon as well as lepton neutrinos. Similar to the $\tau_{\text{had}}\tau_{\text{had}}$ search channel, the $\tau_{\text{lep}}\tau_{\text{had}}$ channel uses the total transverse mass distribution measured in the b-tag and b-veto subregions as the final discriminant. An additional top-quark control region, enriched with $t\bar{t}$ events, is defined in the b-tag category of the $\tau_{\text{lep}}\tau_{\text{had}}$ channel by substituting the cut on the transverse mass of the lepton and the missing transverse energy with $m_{\text{T}}\left(p_{\text{T},l}, E_{\text{T}}^{\text{miss}}\right) > 110\,(100)\,\text{GeV}$ for the $\tau_e\tau_{\text{had}}$ ($\tau_\mu\tau_{\text{had}}$) subchannels. Hence, the region is orthogonal to the $\tau_{\text{lep}}\tau_{\text{had}}$ signal region and the $\mu\nu$+jet control region.

In Figure 7.6.1 the signal acceptance times selection efficiency, which measures how many generated signal events pass the reconstruction and signal region selections, is presented for the different decay channels and subcategories. A list with numerical values of the acceptance times efficiency is provided in Appendix D.1. The signal acceptance in the
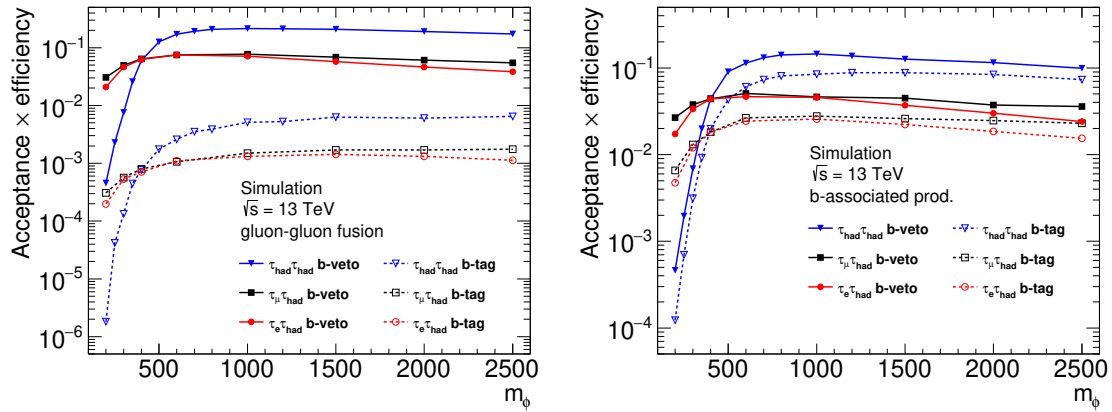

Figure 7.6.1.: Acceptance times efficiency over the signal resonance mass of the $\tau_{\text{had}}\tau_{\text{had}}$ and $\tau_{\text{lep}}\tau_{\text{had}}$ signal regions.

$\tau_{\text{had}}\tau_{\text{had}}$ channel is generally lower than the one in the $\tau_{\text{lep}}\tau_{\text{had}}$ channel for masses of $m_\phi < 400\,\text{GeV}$. This is due to the lower p_{T} thresholds of 24-140 GeV (20-50 GeV) for the single electron (single muon) trigger deployed in the $\tau_{\text{lep}}\tau_{\text{had}}$ channel [253, 275]. Above signal masses of $m_\phi > 700\,\text{GeV}$ the signal acceptance in the $\tau_{\text{had}}\tau_{\text{had}}$ channel surpasses the two $\tau_{\text{lep}}\tau_{\text{had}}$ categories and saturates as the tau jets from the resonance decay have enough momentum to surpass the larger single-tau trigger momentum thresholds.

The combination of both $\tau_{\text{had}}\tau_{\text{had}}$ and $\tau_{\text{lep}}\tau_{\text{had}}$ channels in conjunction with the top-quark control region results in strong limits on the signal production cross-section times

branching ratio over a wide range of possible signal mass hypotheses. Exclusion limits of the combination are presented in Figure 7.6.2. Meeting the expectations of the signal acceptance, the $\tau_{\mathrm{lep}}\tau_{\mathrm{had}}$ channel is more sensitive than the $\tau_{\mathrm{had}}\tau_{\mathrm{had}}$ channel for low resonance masses, while at masses of $m_\phi > 400\,\mathrm{GeV}$ the $\tau_{\mathrm{had}}\tau_{\mathrm{had}}$ channel becomes the dominant channel.
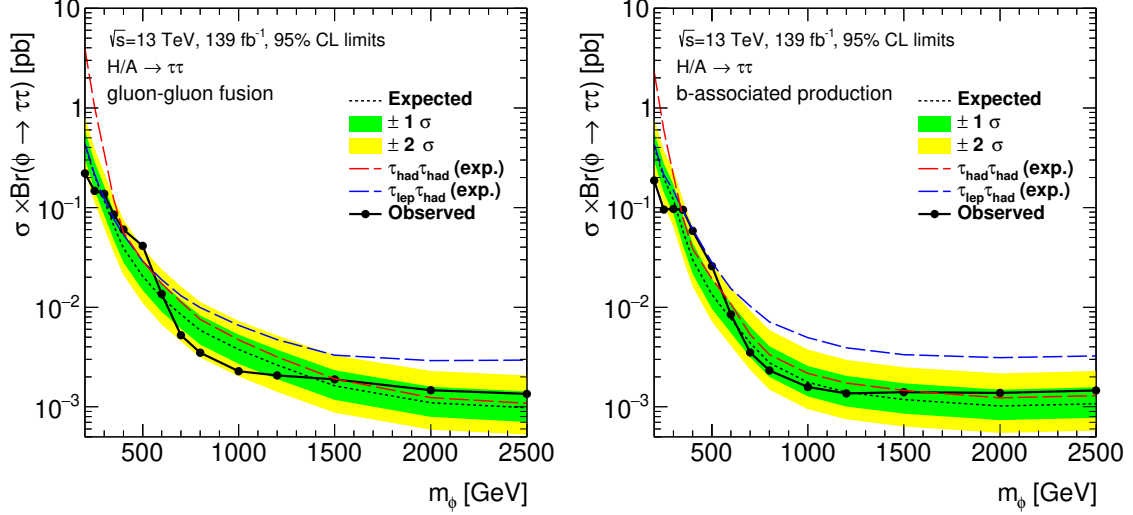

Figure 7.6.2.: Exclusion limits derived from the combination of the $\tau_{\mathrm{had}}\tau_{\mathrm{had}}$ and $\tau_{\mathrm{lep}}\tau_{\mathrm{had}}$ channels as well as the top-quark control region for gluon-gluon fusion and *b*-associated Higgs production.

As part of this thesis, improvements to the background estimates for fake-rates and fake-factors are developed and applied. Thus, the combination of the results presented here with the $\tau_{\mathrm{lep}}\tau_{\mathrm{had}}$ category from Reference [24] differs from the results of the analysis presented in the paper. The differences in the observed and expected upper cross-section limits are shown in Figure 7.6.3.

No significant differences between the expected limits of the paper results and the results of this thesis are observed for the gluon-gluon fusion production. Thus, the sensitivity of a potential new signal is preserved when applying the background modeling improvements. For the *b*-associated production, the modeling improvements yield better expected limits for the signal mass range of $600\,\mathrm{GeV} < m_\phi < 2000\,\mathrm{GeV}$ with a maximum improvement of $21\,\%$ at $m_\phi = 800\,\mathrm{GeV}$. A slight reduction in sensitivity of about $11\,\%$ is observed at the highest resonance mass of $m_\pi = 2500\,\mathrm{GeV}$. This is caused by the reduced number of expected tau fake background events after applying the improved fake-rates in the $\tau_{\mathrm{had}}\tau_{\mathrm{had}}$ *b*-tag signal region. Especially the application of the improved fake-rates for 3 prong leading tau candidates passing the *Medium+Trigger* working point results in a total reduction of expected tau fakes from top decays. The asymptotic formula with which the limits are calculated requires approximately 10 expected background events to yield results that match limits calculated from toy Monte Carlo. Hence, the binning of the $m_{\mathrm{T}}^{\mathrm{tot}}$ distribution in the *b*-tag signal region is shifted slightly to lower values with the last bin starting at $m_{\mathrm{T}}^{\mathrm{tot}} = 600\,\mathrm{GeV}$, compared to $650\,\mathrm{GeV}$ in the paper analysis. Although the coarser binning at large values of the final discriminant results in slightly lower sensitivity at the $m_\phi = 2500\,\mathrm{GeV}$ mass point, the overall background modeling has been improved significantly.

The improved background modeling results in a generally smaller deviation of the observed limit compared to the results of the publication, yielding stronger limits at low
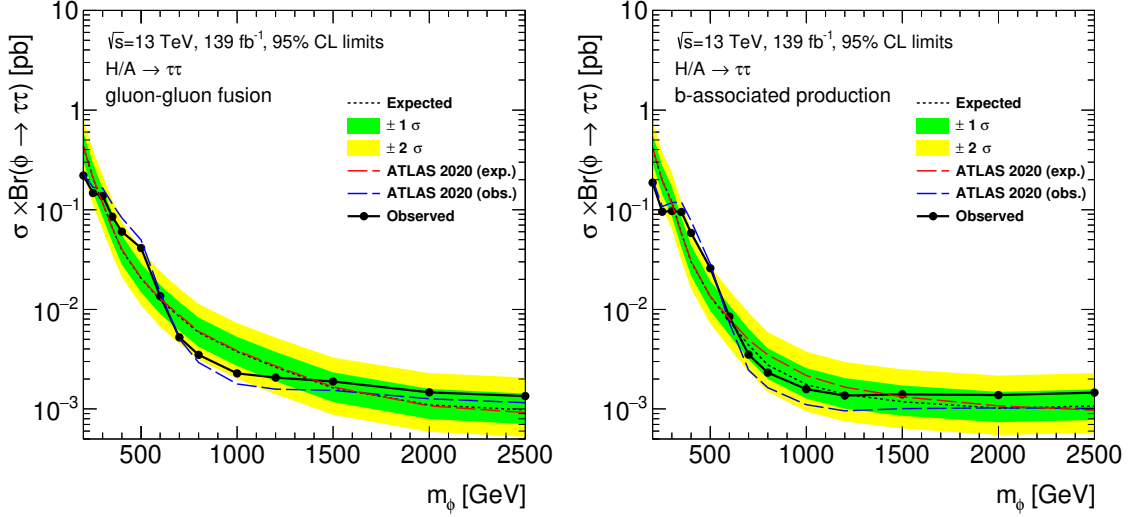
Figure 7.6.3.: Comparison of the upper limits on the cross-section times branching ratio between the results with improved fake background modeling and the results of the published reference [24]. The $\pm 1\sigma$ and $\pm 2\sigma$ bands as well as the solid line correspond to the upper limits derived with fake tau background improvements. Exclusion limits of the reference publication are indicated by the red and blue dashed lines.

masses and weaker ones at higher resonance masses. However, the differences between the observed limits vary only by $\pm 1\,\sigma$ standard deviation of the expected limit and are thus not statistically significant.

The cross-section limits on the combined $\tau_{\mathrm{had}}\tau_{\mathrm{had}}$ and $\tau_{\mathrm{lep}}\tau_{\mathrm{had}}$ search channels are calculated for different values of $f_{b\text{-frac}}$ ranging from 0 to 1 and are presented in Figure 7.6.4. Lists containing the numerical values of the model-independent limits are provided in Appendix D.2.

7.6.2. Model-Dependent Limits

The model-independent upper limits on heavy neutral Higgs boson production cross-section times branching ratio are translated into the parameter space of a specific theory model by transforming the model-independent parameter $f_{b\text{-frac}}$ into the model-dependent parameter $\tan\beta$. By comparing the model prediction with the measured upper limits, the excluded phase space region is derived. Benchmark MSSM models considered in this thesis are the m_{h}^{125}, $m_{\mathrm{h}}^{125}\,(\tilde{\chi})$, $m_{\mathrm{h}}^{125}\,(\tilde{\tau})$, $m_{\mathrm{h}}^{125}\,(\text{alignment})$, and hMSSM models which are discussed in detail in Section 2.2. All models predict the existence of two additional heavy neutral Higgs bosons A and H produced via gluon-gluon fusion and b-associated production and are parameterized at tree level by the model parameters m_A-$\tan\beta$.

For vast regions of the parameter space, both CP-odd and -even sates can be considered mass degenerate as their masses are too close to be resolved by the analysis, due to its limited intrinsic mass-resolution. Additionally, the analysis selection does not apply cuts sensitive to the CP-state of the signal resonance. Hence, the nominal signal samples, derived from heavy SM like Higgs boson production simulations, can be used to represent the combined A and H boson signal contribution.

At small values of m_A-$\tan\beta$ however, the mass splitting $\Delta m = |m_H - m_A|$ can be large enough that the assumption of mass degeneracy is not valid and both neutral Higgs
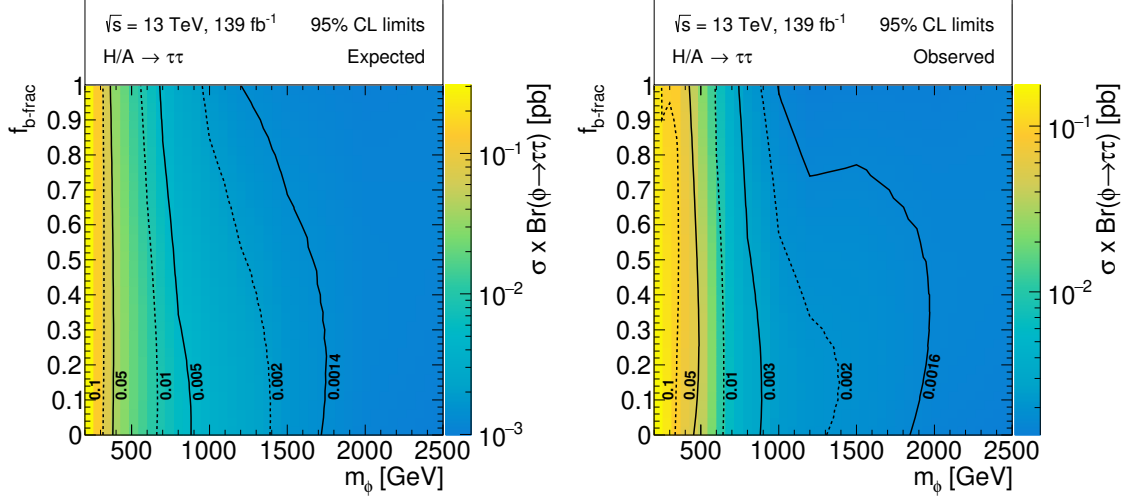
Figure 7.6.4.: Expected (left) and observed (right) model-independent exclusion limits on the cross-section times branching ratio parameterized in the neutral resonance mass m_ϕ and $f_{b\text{-frac}}$. Limits are set based on the combined $\tau_{\text{had}}\tau_{\text{had}}$ and $\tau_{\text{lep}}\tau_{\text{had}}$ channels.

bosons would form distinguishable peaks in the m_T^{tot} mass spectrum. To determine the region in which the assumption is invalid, the width of the gluon-gluon fusion and b-associated production signal samples is determined by calculating the binned standard deviation from the signal histograms in the b-veto and b-tag signal categories of both the $\tau_{\text{had}}\tau_{\text{had}}$ and $\tau_{\text{lep}}\tau_{\text{had}}$ channels. To get the most conservative estimate only the smallest standard deviation of the signal distributions in any of the signal regions is considered. The intrinsic mass resolution is then determined as the average of the standard deviations of the gluon-gluon fusion and b-associated Higgs production samples. A list of the estimated resolutions for each mass point is given in Table 7.6.1.

For each of the four models, the predicted mass difference between the A and H boson is calculated. A conservative exclusion region is determined as the region, where the mass splitting is larger than half of the measured standard deviation of the signal sample distributions. For mass points between the signal sample masses, the signal width is linearly interpolated. Within this region, the calculated upper limits can not be assumed to be correct. Figure 7.6.5 visualizes the predicted mass splitting for the hMSSM and m_h^{125} (alignment) models. Further plots of the mass splitting predicted by the other benchmark models can be found in Appendix D.3. Overall, the hMSSM model predicts negligible mass splitting over a wide range of the theory parameter space, only excluding a small region at low values for m_A-$\tan\beta$ where a significant mass splitting is observed. The increasing difference of the A and H mass at low values of m_A-$\tan\beta$ is shared between all models as the mass splitting in this region is a naturally occurring feature of the EWSB of the MSSM [21]. The m_h^{125} (alignment) model also predicts significant mass splitting for $142 < m_A < 280\,\text{GeV}$ and $\tan\beta > 5$ where the mass splitting rises again above the threshold of $\frac{1}{2}\tilde{\sigma}_{\text{comb.}}$.[3]

To determine whether the regions with significant mass splitting can still be excluded, the upper limit in m_A-$\tan\beta$ is calculated assuming the presence of only one of the heavy neutral Higgs bosons. This is illustrated in Figure 7.6.6 where the predicted cross-section

---

[3]The tilde is applied to distinguish the standard deviation of the signal distribution from the cross-section notation in Equation (7.39)

Signal mass in GeV	$\tilde{\sigma}_{ggH}$ in GeV	$\tilde{\sigma}_{bbH}$ in GeV	$\tilde{\sigma}_{comb.}$ in GeV
200	34	35	34
250	34	35	35
300	43	38	40
350	46	43	44
400	47	46	46
500	63	57	60
600	85	84	84
700	107	104	105
800	131	126	129
1000	197	172	185
1200	466	459	462
1500	771	689	730
2000	479	432	456
2500	415	335	375

Table 7.6.1.: Width of binned *b*-associated and gluon-gluon fusion signal distributions for all mass points considered. Only the smallest width calculated in the *b*-tag or the *b*-veto signal region of both categories is considered. The width $\tilde{\sigma}_{comb.}$[3] used to approximate the resolution is calculated from the arithmetic mean of the standard deviation of the *b*-associated ($\tilde{\sigma}_{bbH}$) and gluon-gluon fusion ($\tilde{\sigma}_{ggH}$) production samples. All measurements are rounded to 1 GeV.
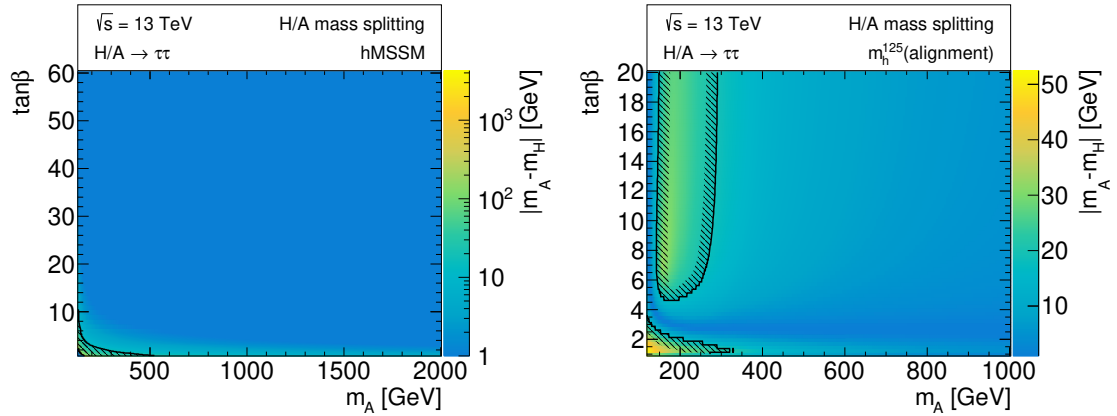

Figure 7.6.5.: Mass splitting between the *A* and *H* boson predicted in the hMSSM and m_h^{125} (alignment) models [40–43, 74]. In the former case, Higgs masses are calculated with HDECAY [71, 72] while in the latter model as well as the other m_h^{125} benchmarks FEYNHIGGS is used [44, 64–70]. The shaded contour line highlights the resolution exclusion region where upper limits are assumed to be not valid.

times branching ratio is overlayed with the exclusion limits for the cases of mass degeneracy of the A and H bosons, as well as for both bosons separately. In all three cases, the region of $142 < m_A < 280\,\text{GeV}$ and $\tan\beta > 5$ is excluded, implicating that the exclusion limits are strong enough that the mass splitting between the bosons would not affect the validity of the upper limit contours. However, the mass splitting in the low-m_A, low-$\tan\beta$ region can not be excluded when considering only the presence of the CP-even H boson. Thus, this region will be highlighted as *Not applicable* in model-dependent limit plots to indicate that the underlying mass degeneracy assumption might be invalid. The same procedure is applied to all remaining benchmark models.

By calculating the intersection between the cross-section times branching ratio values predicted by different benchmark models and the measured limit parameterized in m_A-$\tan\beta$, the model-dependent upper limit is derived by projecting the intersection contour in the m_A-$\tan\beta$ plane, like in Figure 7.6.6a. The parameter phase space above the contour is excluded as the coupling to down-type fermions increases with increasing $\tan\beta$.

Figures 7.6.7 and 7.6.8 show the upper limits translated into the different m_h^{125}-type benchmark models. In these limits, the model-dependent uncertainties on the production cross-section discussed in Section 2.2 are implemented through additional nuisance parameters in the likelihood.

The observed and expected limit contour lines show arc-like structures at values of $m_A < 700\,\text{GeV}$ which are caused by the shallow angle between the intersecting upper limit plane and the $\sigma \times \text{Br}\,(A/H \to \tau\tau)$ plane predicted by theory when translating model-independent to model-dependent limits. An example is shown in Figure 7.6.6a for the m_h^{125} (alignment) benchmark model. Since the limits for values of m_A in between the measured resonance mass points are estimated by a linear interpolation function, the resulting discontinuous surface creates the arc-like structures at the line of the intersection when overlayed with the smooth surface of the $\sigma \times \text{Br}\,(A/H \to \tau\tau)$ plane predicted by the model.

Overall the observed limits are compatible within $\pm 1\,\sigma$ of the expected limit for $m_A > 600\,\text{GeV}$. The largest deviation of the observed from the expected limit is measured at $m_A = 500\,\text{GeV}$ ranging from $2.1\,\sigma$ to $2.4\,\sigma$ depending on the benchmark model. The deviation coincides with the excess observed in the cross-section limits of the combined $\tau_{\text{lep}}\tau_{\text{had}}$ and $\tau_{\text{had}}\tau_{\text{had}}$ channels in Figure 7.6.2. None of the observed excesses passes the discovery threshold $5\,\sigma$. However, large parts of the phase space of the different benchmark models can be excluded. The limits in Figures 7.6.7 and 7.6.8 also show the contour line for different values of m_h predicted by theory calculations. Since the calculations of the SM like Higgs boson mass is usually associated with a theory uncertainty of $\pm 3\,\text{GeV}$ [44, 45] it can be deduced, that the regions where the limits are not applicable due to large mass splitting are already excluded based on the properties of the SM like Higgs boson. In the case of the m_h^{125} (alignment) model, the constraints on the SM like Higgs mass of $m_h = 125\,\text{GeV}$ already confine the possible values of m_A-$\tan\beta$ to a narrow band within $10 \leq \tan\beta \leq 4$ when considering the theory uncertainty [74]. Especially the region with $m_h = 125\,\text{GeV}$ is ruled out by the observed limit.

Another benchmark model which is frequently used in searches for additional Higgs bosons is the hMSSM model. As discussed in Section 2.2 here the mass of the SM like Higgs boson is taken as an input parameter, enforcing a value of $m_h = 125\,\text{GeV}$ [42]. This model was also used in previous publications from ATLAS and CMS searching for heavy neutral Higgs bosons in the di-tau final state, allowing them to be compared to the results presented in this thesis. Figure 7.6.9 shows the limits calculated based on the full Run-2 dataset with previously observed limits presented by the ATLAS collaboration in Reference [83] and the CMS collaboration in Reference [84] which are derived from $36.1\,\text{fb}^{-1}$ and $35.9\,\text{fb}^{-1}$ of
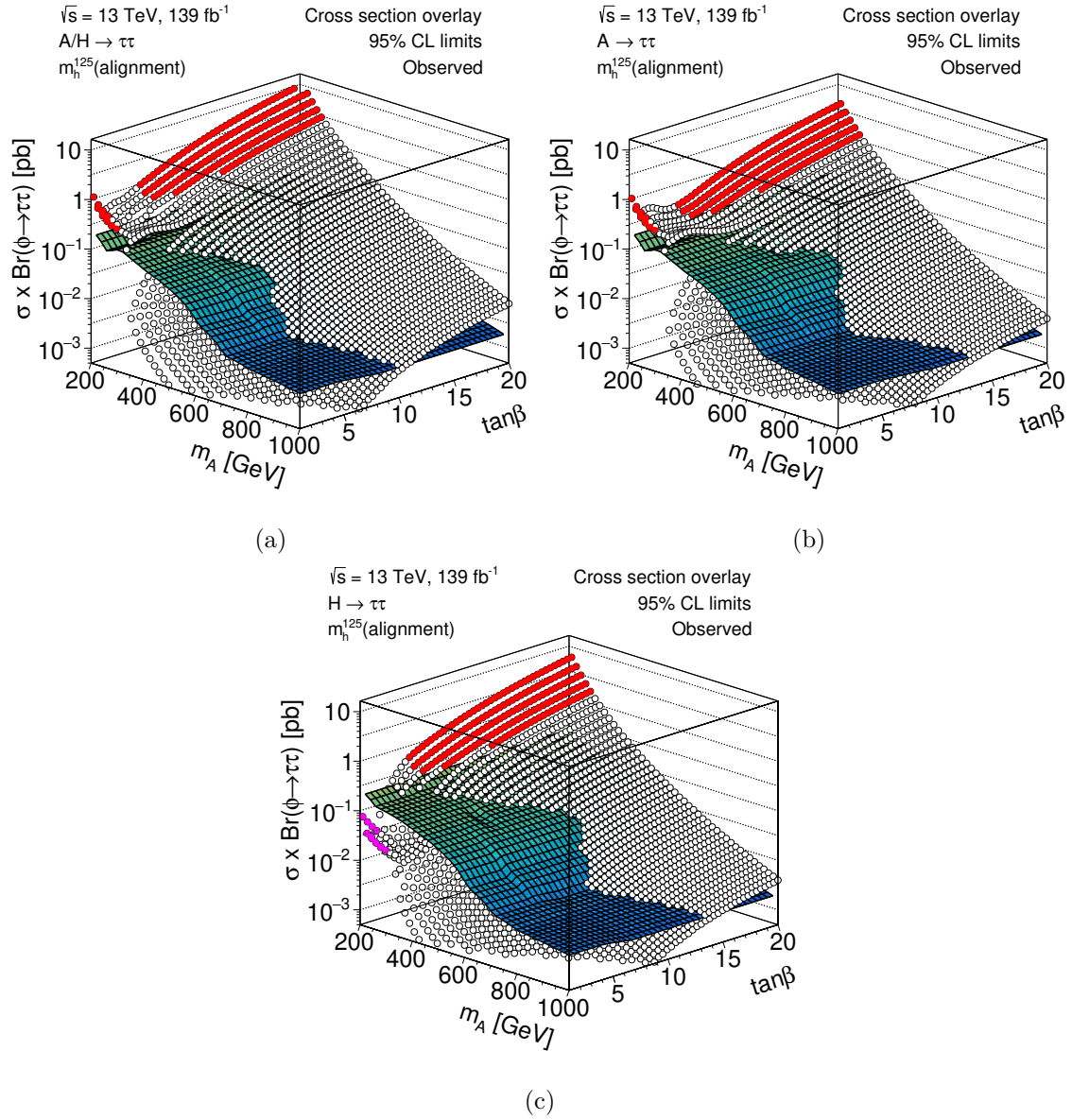
(a)

(b)

(c)

Figure 7.6.6.: Overlay of observed exclusion limit and the predicted cross-section times branching ratio parameterized in the m_A- $\tan\beta$ plane of the m_h^{125} (alignment) model. The colored plane represents the observed 95 % CL upper limit on the signal cross-section transformed from $f_{b\text{-frac}}$ to the $\tan\beta$ parameter space. The surface indicated by white dotted points represents the signal cross-section predicted by the benchmark model. If the prediction is above the limit surface then the parameter phase space is excluded. Figure (a) shows the limit and prediction of the combined A and H boson production while Figure (b) and (c) show the overlay derived when only one of the bosons is considered. The limit plane in (a) assumes mass degeneracy $m_\phi = m_A \approx m_H$ while in (b) and (c) limits are derived by setting $m_\phi = m_A$ and $m_\phi = m_H$ respectively. The red-colored surface indicates the excluded m_A- $\tan\beta$ region where the mass splitting between H and A exceeds $\frac{1}{2}\tilde{\sigma}_{\text{comb.}}$. In contrast, the purple-colored phase space represents the region with significant mass splitting which is not excluded by the observed limit.
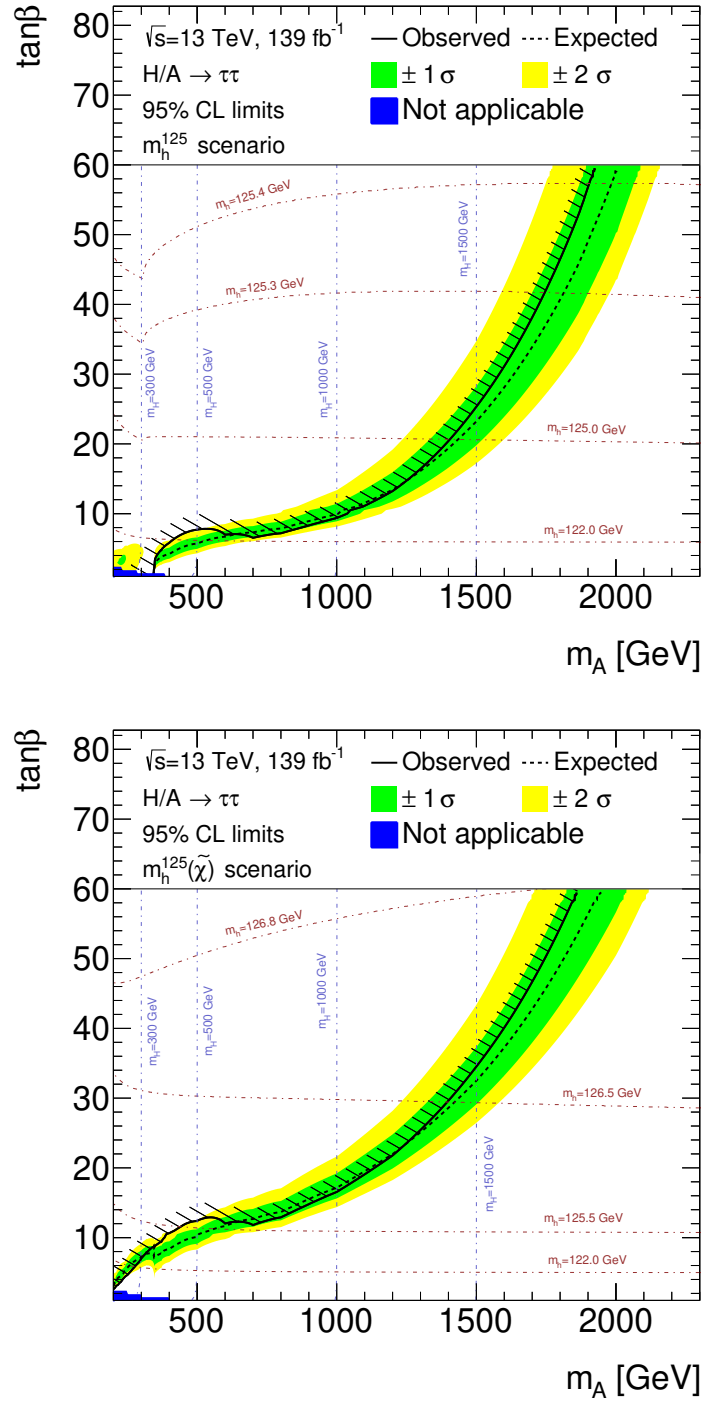
Figure 7.6.7.: Model-dependent upper limits of the combined $\tau_{\mathrm{had}}\tau_{\mathrm{had}}$ and $\tau_{\mathrm{lep}}\tau_{\mathrm{had}}$ channel for the m_{h}^{125} and $m_{\mathrm{h}}^{125}(\tilde{\chi})$ benchmark models as described in Reference [74]. The blue-colored region indicates the phase space in m_A-$\tan\beta$ where significant mass splitting between the A and H boson occurs. Limits set in this region should not be considered excluded at 95 % CL. Profile lines show the contours in the m_A-$\tan\beta$ plane of the masses of the CP-even heavy H and SM-like h Higgs boson. The predicted value of m_h is associated with a theoretical uncertainty of around ± 3 GeV [44, 45].
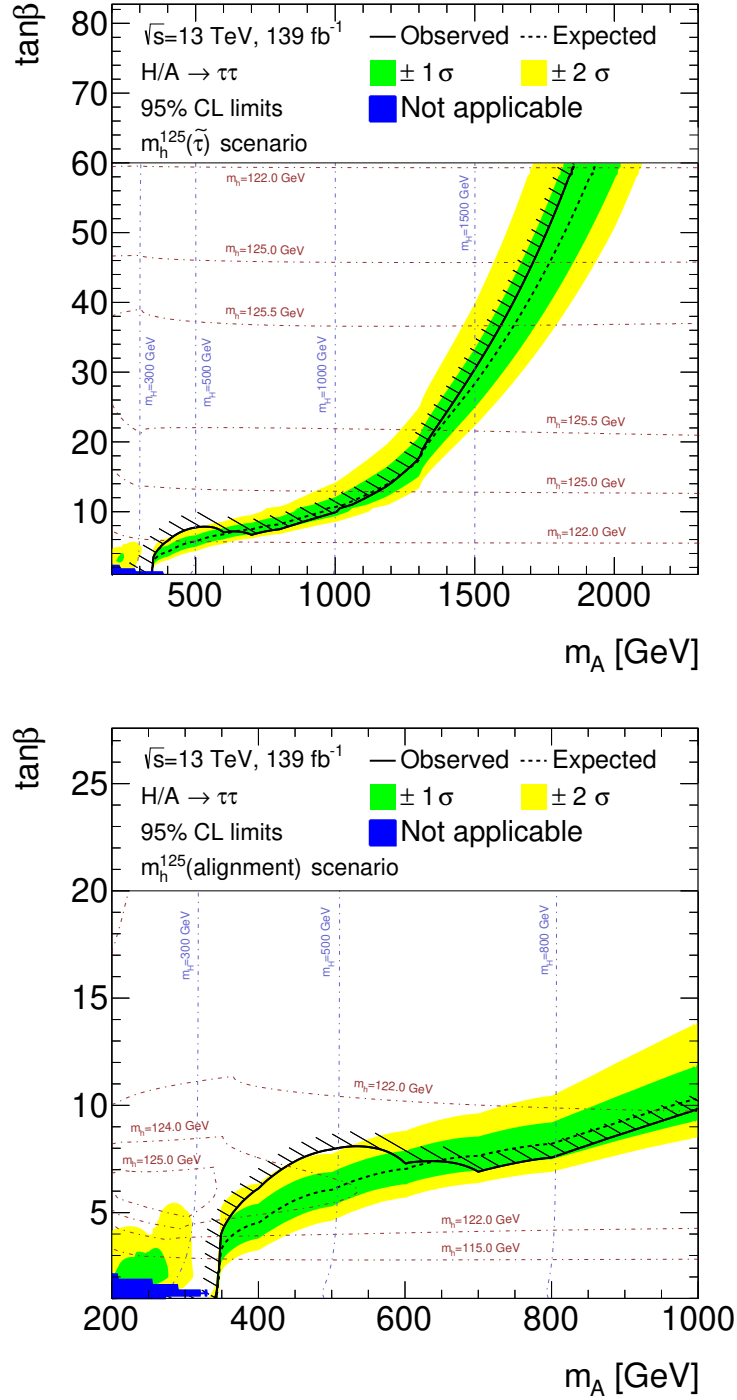
Figure 7.6.8.: Model-dependent upper limits of the combined $\tau_{\mathrm{had}}\tau_{\mathrm{had}}$ and $\tau_{\mathrm{lep}}\tau_{\mathrm{had}}$ channel for the $m_{\mathrm{h}}^{125}\,(\tilde{\tau})$ and m_{h}^{125} (alignment) benchmark models as described in Reference [74]. The blue-colored region indicates the phase space in m_A-$\tan\beta$ where significant mass splitting between the A and H boson occurs. Limits set in this region should not be considered excluded at 95 % CL. Profile lines show the contours in the m_A-$\tan\beta$ plane of the masses of the CP-even heavy H and SM-like h Higgs boson. The predicted value of m_h is associated with a theoretical uncertainty of around $\pm 3\,\mathrm{GeV}$ [44, 45].

data from the 2015-2016 data-taking period respectively. Significant improvements in the
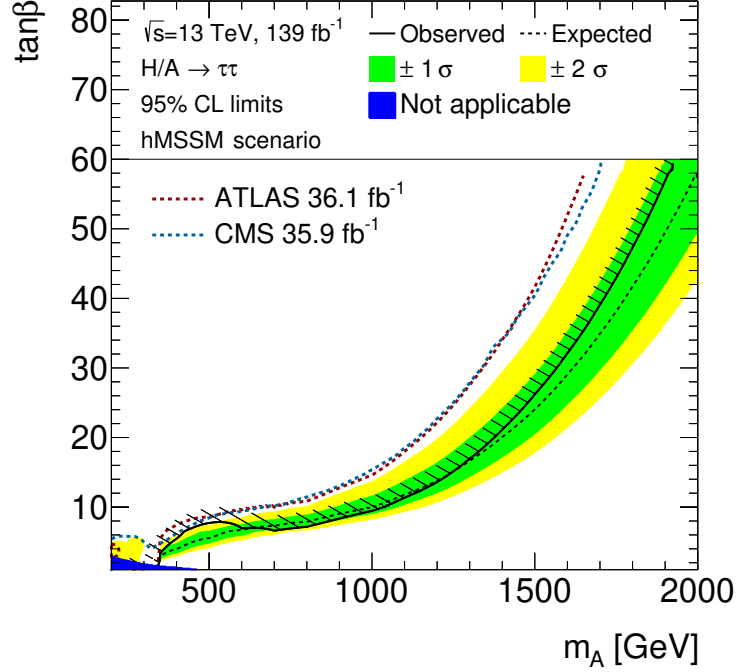

Figure 7.6.9.: Upper limits set in the hMSSM benchmark model parameter space based on the combination of the $\tau_{\mathrm{had}}\tau_{\mathrm{had}}$ results presented in Section 7.4 and the $\tau_{\mathrm{lep}}\tau_{\mathrm{had}}$ results taken from Reference [24]. The limits are compared to previous publications of CMS [84] and ATLAS [83] derived from early Run-2 data of the 2015 to 2016 data taking periods.

observed exclusion limit of the hMSSM benchmark model are achieved, ranging from 11 % (10 %) at $m_A = 500\,\mathrm{GeV}$ up to 63 % (67 %) at $m_A = 1200\,\mathrm{GeV}$ compared to the previously published ATLAS (CMS) result.

In the context of all analyses published by ATLAS that set limits in the m_A-$\tan\beta$ parameter space of the hMSSM scenario, the $A/H \to \tau\tau$ search presented here provides the strongest upper exclusion limits as shown in Figure 7.6.10a. In fact, for $\tan\beta \gtrsim 4$ it is currently the most sensitive search channel providing the most competitive upper limits. As expected, the results derived in this thesis closely match the results presented in Reference [24].

Additionally, Figure 7.6.10b compares the exclusion limits measured using $139\,\mathrm{fb}^{-1}$ of data in the hMSSM scenario with the predicted 2σ sensitivity exclusion region from Reference [43] based on a projection of the Run-1 results measured at a CME of $\sqrt{s} = 7, 8\,\mathrm{TeV}$ projected to $300\,\mathrm{fb}^{-1}$ at $\sqrt{s} = 14\,\mathrm{TeV}$. The current expected limit results already come close to the projection for $m_A < 600\,\mathrm{GeV}$ and exceeds it for higher masses. This indicates that the improvements of the identification algorithms paired with lower systematic uncertainties on backgrounds, as well as improvements on the analysis strategy itself are exceeding the expectations set prior to the beginning of Run-2.
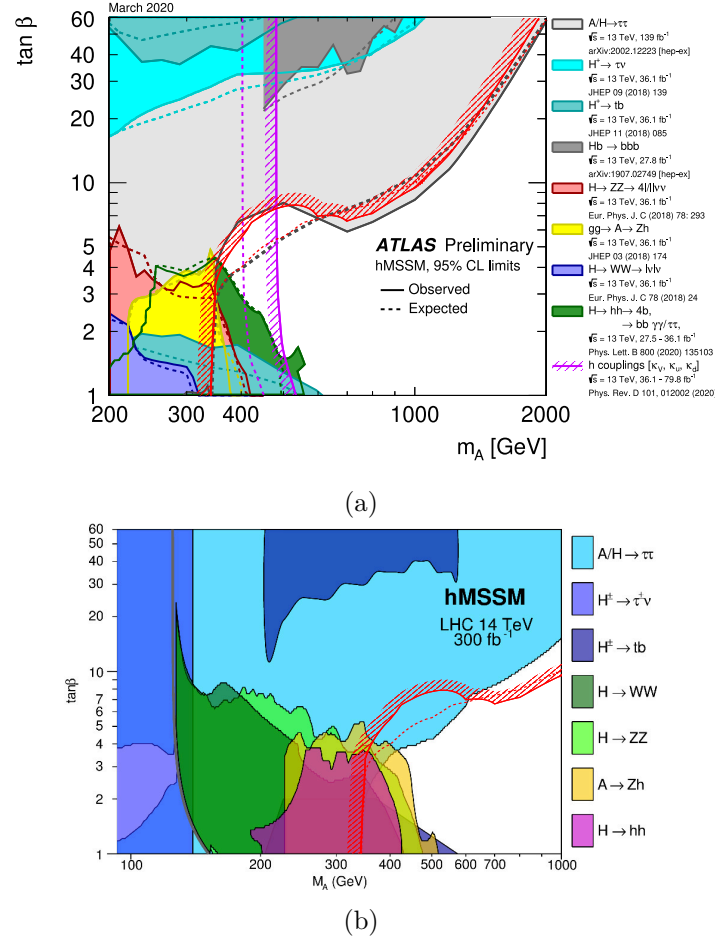
(a)

(b)

Figure 7.6.10.: Upper limit results in the hMSSM model parameters in comparison with other search channels. Figure (a) compares the observed (red shaded line) and expected (red dashed line) upper limit derived from the results presented in this thesis with the paper results from Reference [24] as well as other analyses searching for heavy Higgs bosons. The summary of the upper limits in Figure (a) published in Reference [80]. Figure (b) compares the 95 % CL upper limit with the 2σ sensitivity exclusion region presented in Reference [43] which predicts the exclusion contours by extrapolating the Run-1 results to $300\,\text{fb}^{-1}$ of data taking with a CME of 14 TeV.

8. Summary and Outlook

In the first part of this thesis improvements to the tau track identification and selection are presented. The new approach using recurrent neural networks based on bidirectional LSTMs resulted in significant improvements in the reconstruction efficiency of 1 and 3 prong taus of around 10 % and 20 % respectively compared to the previously used BTD based algorithm. In fact, the selected neural networks achieve a reconstruction efficiency close to that of the ideal classifier. In addition, the reconstruction efficiency and purity for tracks from photon conversion significantly improved while those for the other track classes are preserved.

By developing a new direct track class, the network can be trained to perform differently on tau candidates reconstructed from QCD jets. Two setups are presented. The nominal setup is trained on the nominal track class definition which results in an exponentially decaying tau track spectra on the QCD background, correctly classifying most QCD jets as 0 prong taus. This behavior is particularly interesting for track identification and reconstruction during the online trigger decisions. In this scenario a significant amount of background can be rejected by preselecting reconstructed online 1 and 3 prong taus, thus potentially resulting in reduced trigger bandwidth usage. In the alternative setup, the tau track class is replaced by the newly developed direct track class during training. Neural networks trained with this setup produce a more continuous tau track spectrum on the QCD background. This property might be preferable for offline reconstruction since a reduction in the fake background before the tau identification algorithm is applied can statistically limit the application of data-driven fake background estimates such as the fake-factor method.

In the future, the neural networks can be implemented in the default tau reconstruction and identification toolchain. However, downstream algorithms like the tau-ID have to be retained on top of the new track selection. The decision to choose the nominal or alternative training setup should be made on a case-by-case basis depending on the performance of the downstream algorithms. Potential improvements caused by the bLSTM based track selection might not only significantly improve the search for Higgs bosons presented in this thesis but also many other measurements and searches with hadronically decaying tau leptons in their final state. When deployed in the trigger decision toolchain the algorithm is likely to improve reconstruction efficiencies of true tau decays while also decreasing background from QCD events. This might result in lower bandwidth usage of the HLT tau trigger which in turn can contribute to lower sustained trigger thresholds.

In the second part of the thesis, the search for heavy neutral Higgs bosons decaying in the fully hadronic di-tau final state based on the full Run-2 dataset is presented. This analysis contributed to the paper published in Reference [24] together with the $\tau_{\mathrm{lep}}\tau_{\mathrm{had}}$ channel results. Additional improvements of the multijet background estimation are deployed by extending the fake-rate corrections to all regions involved in the multijet background estimation. The improvements resulted in generally better background modeling in the validation and signal region. By changing the background modeling, an improvement in the sensitivity of the analysis for the b-associated signal production is observed where expected limits improve by about 20 % for $m_\phi = 800\,\mathrm{GeV}$ compared to the paper results. At the same time, only a minor sensitivity reduction of around 11 % is observed

at the $m_\phi = 2500\,\text{GeV}$ mass point. This is caused by the slightly coarser binning at high values of the m_T^tot distribution which is necessary to ensure the validity of the asymptotic approximation deployed during the limit calculation. Despite the small decrease in sensitivity for high mass signals, the improved background modeling results in more trustworthy exclusion limits.

Furthermore, a new Z validation region is developed which allows verifying the modeling of the hadronic tau decay simulation. Using the full Run-2 dataset, the Z validation region provided enough statistical coverage to validate the modeling of simulated hadronic true tau decays up to a transverse momentum of about $350\,\text{GeV}$. Currently, no significant mismodeling is observed.

Exclusion limits are calculated based on the signal region results of the $\tau_\text{had}\tau_\text{had}$ channel and are combined with the $\tau_\text{lep}\tau_\text{had}$ channel measurements from Reference [24]. The limits are translated in the m_A-$\tan\beta$ parameter space of the hMSSM benchmark model and compared to previous publications from CMS and ATLAS based on early Run-2 data. Significant improvements of the exclusion limits ranging between $11\,\%$ ($10\,\%$) and $63\,\%$ ($67\,\%$) are observed compared to previous ATLAS (CMS) results. The measured exclusion limits also exceed the projection for $300\,\text{fb}^{-1}$ predicted prior to the start of Run-2 based on measurements using Run-1 data. The increase in sensitivity is due to improved reconstruction and identification algorithms as well as improvements in the estimation of systematic uncertainties, background modeling, and signal region selection.

The upper limits are also provided for the newly available m_h^{125} model scenarios and as model-independent limits parameterized in m_ϕ and $f_{b\text{-frac}}$. For all benchmark models considered in this analysis, the validity of the mass degeneracy between the CP-even and CP-odd neutral Higgs bosons is studied. In general, the mass splitting for high values of m_A and $\tan\beta$ is found to be negligible. However, regions, where the mass splitting is found to be larger than acceptable, are indicated.

The upper limits presented in this thesis place the currently strongest exclusion limits in the m_A-$\tan\beta$ space. Compared to other searches in ATLAS which set limits on the m_A-$\tan\beta$ parameter space of the hMSSM model, the search for heavy neutral Higgs bosons decaying in the di-tau final state provides the strongest upper exclusion boundaries on $\tan\beta$. By interpreting the limit results in various benchmark models, the analysis also contributes to constraining the vast parameter space of SUSY models and indirectly excluding commonly considered parameter choices. Additionally, some of the benchmark models predict light, uncolored super particles like the $m_\text{h}^{125}(\tilde{\tau})$ and $m_\text{h}^{125}(\tilde{\chi})$ benchmark models. It is known that contributions of these light super particles can help resolving the discrepancy observed between the Standard Model prediction and measurement of the anomalous magnetic moment of the muon [74, 78, 79]. Thus, constraining the parameter space helps to understand the viability of these SUSY models as a potential explanation of the $(g-2)$ measurements.

The search for additional Higgs bosons will significantly profit from the increase in integrated luminosity recorded in future runs of the LHC. During Run-3 the LHC is currently planned to deliver an integrated luminosity of $300\,\text{fb}^{-1}$ to the experiments, resulting in more than three times the available data at the end of Run-3 compared to Run-2 [276]. However, the search results already come close or exceed the expectations based on Run-1 results extrapolated to $300\,\text{fb}^{-1}$. Hence, future results based on Run-3 data will likely access more phase space then previously conceived and will be more sensitive to new potential physics processes. It is also planned to increase the center of mass energy of the proton beams to their design value of $\sqrt{s} = 14\,\text{TeV}$ which also increases the cross-section for heavy Higgs boson production [73]. After Run-3, the LHC is planned to undergo the upgrade to the High-Luminosity LHC (HL-LHC) and is expected to deliver a total of $3000\,\text{fb}^{-1}$ of

data over a period of 12 years. With the current center-of-mass energy of 13 TeV-14 TeV at the LHC, it is expected that the search for neutral Higgs bosons in the di-tau final state reach masses of $m_A \approx 3$ TeV or $m_A \approx 4$ TeV in the relevant benchmark models at the end of the HL-LHC operation [277]. Extending the sensitivity of the analysis to even higher masses, however, requires higher center-of-mass energy particle collision. This long-term goal could be achieved by the Future Circular Collider project which aims at building a particle accelerator at the CERN accelerator complex capable of achieving proton-proton collisions at a center-of-mass energy of 100 TeV [278].

Future analysis might also deploy sophisticated multivariate analysis techniques, such as neural networks, to improve the sensitivity of the analysis. With the increasing amount of data and better statistical coverage, it might also become feasible to exploit the differences in spin and CP-eigenstates between the Higgs bosons and the main irreducible Z/γ^* background to further improve background rejection.

Bibliography

[1] J. J. Thomson, "XL. Cathode Rays", *The London, Edinburgh, and Dublin Philosophical Magazine and Journal of Science* **44** no. 269, (1897) 293–316. https://doi.org/10.1080/14786449708621070.

[2] S. Tomonaga, "On a Relativistically Invariant Formulation of the Quantum Theory of Wave Fields", *Progress of Theoretical Physics* **1** no. 2, (08, 1946) 27–42. https://doi.org/10.1143/PTP.1.27.

[3] J. Schwinger, "Quantum electrodynamics. i. a covariant formulation", *Phys. Rev.* **74** (Nov, 1948) 1439–1461. https://link.aps.org/doi/10.1103/PhysRev.74.1439.

[4] R. P. Feynman, "Space-time approach to quantum electrodynamics", *Phys. Rev.* **76** (Sep, 1949) 769–789. https://link.aps.org/doi/10.1103/PhysRev.76.769.

[5] R. P. Feynman, "Mathematical formulation of the quantum theory of electromagnetic interaction", *Phys. Rev.* **80** (Nov, 1950) 440–457. https://link.aps.org/doi/10.1103/PhysRev.80.440.

[6] F. J. Dyson, "The radiation theories of tomonaga, schwinger, and feynman", *Phys. Rev.* **75** (Feb, 1949) 486–502. https://link.aps.org/doi/10.1103/PhysRev.75.486.

[7] F. J. Dyson, "The s matrix in quantum electrodynamics", *Phys. Rev.* **75** (Jun, 1949) 1736–1755. https://link.aps.org/doi/10.1103/PhysRev.75.1736.

[8] D. Griffiths, "Introduction to elementary particles". Wiley-VCH, second ed., 2008.

[9] H. Fritzsch, M. Gell-Mann, and H. Leutwyler, "Advantages of the Color Octet Gluon Picture", *Phys. Lett. B* **47** (1973) 365–368.

[10] S. L. Glashow, "Partial Symmetries of Weak Interactions", *Nucl. Phys.* **22** (1961) 579–588.

[11] A. Salam, "Weak and Electromagnetic Interactions", *Conf. Proc. C* **680519** (1968) 367–377.

[12] S. Weinberg, "A Model of Leptons", *Phys. Rev. Lett.* **19** (1967) 1264–1266.

[13] P. W. Higgs, "Broken Symmetries and the Masses of Gauge Bosons", *Phys. Rev. Lett.* **13** (1964) 508–509.

[14] F. Englert and R. Brout, "Broken Symmetry and the Mass of Gauge Vector Mesons", *Phys. Rev. Lett.* **13** (1964) 321–323.

[15] G. S. Guralnik, C. R. Hagen, and T. W. B. Kibble, "Global Conservation Laws and Massless Particles", *Phys. Rev. Lett.* **13** (1964) 585–587.

[16] F. Zwicky, "Die Rotverschiebung von extragalaktischen Nebeln", *Helv. Phys. Acta* **6** (1933) 110–127.

[17] **Planck** Collaboration, N. Aghanim *et al.*, "Planck 2018 results - i. overview and the cosmological legacy of planck", *A&A* **641** (2020) A1. https://doi.org/10.1051/0004-6361/201833880.

[18] **Muon g-2** Collaboration, G. W. Bennett *et al.*, "Final report of the e821 muon anomalous magnetic moment measurement at bnl", *Phys. Rev. D* **73** (Apr, 2006) 072003. https://link.aps.org/doi/10.1103/PhysRevD.73.072003.

[19] **Muon g-2** Collaboration, B. Abi *et al.*, "Measurement of the positive muon anomalous magnetic moment to 0.46 ppm", *Phys. Rev. Lett.* **126** (Apr, 2021) 141801. https://link.aps.org/doi/10.1103/PhysRevLett.126.141801.

[20] S. P. Martin, "A Supersymmetry primer", *Adv. Ser. Direct. High Energy Phys.* **18** (1998) 1–98, arXiv:hep-ph/9709356.

[21] A. Djouadi, "The Anatomy of electro-weak symmetry breaking. II. The Higgs bosons in the minimal supersymmetric model", *Phys. Rept.* **459** (2008) 1–241, arXiv:hep-ph/0503173.

[22] "LEP design report". CERN, Geneva, 1984. https://cds.cern.ch/record/102083.

[23] "Design Report Tevatron 1 project", tech. rep., 1984. https://cds.cern.ch/record/1478620.

[24] **ATLAS** Collaboration, G. Aad *et al.*, "Search for heavy Higgs bosons decaying into two tau leptons with the ATLAS detector using pp collisions at $\sqrt{s} = 13$ TeV", *Phys. Rev. Lett.* **125** no. 5, (2020) 051801, arXiv:2002.12223 [hep-ex].

[25] **Particle Data Group** Collaboration, P. Zyla *et al.*, "Review of Particle Physics", *PTEP* **2020** no. 8, (2020) 083C01.

[26] M. E. Peskin and D. V. Schroeder, "An Introduction to quantum field theory". Addison-Wesley, Reading, USA, 1995.

[27] A. Djouadi, "The Anatomy of electro-weak symmetry breaking. I: The Higgs boson in the standard model", *Phys. Rept.* **457** (2008) 1–216, arXiv:hep-ph/0503172.

[28] **Super-Kamiokande** Collaboration, Y. Fukuda *et al.*, "Evidence for oscillation of atmospheric neutrinos", *Phys. Rev. Lett.* **81** (1998) 1562–1567, arXiv:hep-ex/9807003.

[29] **SNO** Collaboration, Q. R. Ahmad *et al.*, "Direct evidence for neutrino flavor transformation from neutral current interactions in the Sudbury Neutrino Observatory", *Phys. Rev. Lett.* **89** (2002) 011301, arXiv:nucl-ex/0204008.

[30] **ATLAS** Collaboration, G. Aad *et al.*, "Observation of a new particle in the search for the Standard Model Higgs boson with the ATLAS detector at the LHC", *Phys. Lett. B* **716** (2012) 1–29, arXiv:1207.7214 [hep-ex].

[31] **CMS** Collaboration, S. Chatrchyan *et al.*, "Observation of a New Boson at a Mass of 125 GeV with the CMS Experiment at the LHC", *Phys. Lett. B* **716** (2012) 30–61, arXiv:1207.7235 [hep-ex].

[32] **CMS** Collaboration, "Combined Higgs boson production and decay measurements with up to 137 fb-1 of proton-proton collision data at sqrts = 13 TeV", 2020. https://cds.cern.ch/record/2706103.

[33] **ATLAS** Collaboration, "A combination of measurements of Higgs boson production and decay using up to 139 fb^{-1} of proton–proton collision data at $\sqrt{s} = 13$ TeV collected with the ATLAS experiment", Aug, 2020. http://cds.cern.ch/record/2725733.

[34] A. Nisati and V. Sharma, eds., "Discovery of the Higgs Boson". World Scientific, 2017.

[35] **ATLAS** Collaboration, "Standard Model Summary Plots March 2021", tech. rep., CERN, Geneva, Mar, 2021. http://cds.cern.ch/record/2758261. All figures including auxiliary figures are available at https://atlas.web.cern.ch/Atlas/GROUPS/PHYSICS/PUBNOTES/ATL-PHYS-PUB-2021-005.

[36] **CMS** Collaboration, "Summaries of CMS cross section measurements", https://twiki.cern.ch/twiki/bin/view/CMSPublic/PhysicsResultsCombined?rev=93. Webpage. Revision 93, last visited 19.04.2021.

[37] J. Terning, "Modern supersymmetry: Dynamics and duality". 2006.

[38] **ATLAS** Collaboration, "SUSY March 2021 Summary Plot Update", tech. rep., CERN, Geneva, Mar, 2021. http://cds.cern.ch/record/2758782.

[39] **CMS** Collaboration, "CMS Supersymmetry Physics Results", https://twiki.cern.ch/twiki/bin/view/CMSPublic/PhysicsResultsSUS?rev=34. Webpage. Revision 34, last visited 23.04.2021.

[40] A. Djouadi and J. Quevillon, "The MSSM Higgs sector at a high M_{SUSY}: reopening the low tanβ regime and heavy Higgs searches", *JHEP* **10** (2013) 028, arXiv:1304.1787 [hep-ph].

[41] L. Maiani, A. D. Polosa, and V. Riquer, "Bounds to the Higgs Sector Masses in Minimal Supersymmetry from LHC Data", *Phys. Lett. B* **724** (2013) 274–277, arXiv:1305.2172 [hep-ph].

[42] A. Djouadi, L. Maiani, G. Moreau, A. Polosa, J. Quevillon, and V. Riquer, "The post-Higgs MSSM scenario: Habemus MSSM?", *Eur. Phys. J. C* **73** (2013) 2650, arXiv:1307.5205 [hep-ph].

[43] A. Djouadi, L. Maiani, A. Polosa, J. Quevillon, and V. Riquer, "Fully covering the MSSM Higgs sector at the LHC", *JHEP* **06** (2015) 168, arXiv:1502.05653 [hep-ph].

[44] G. Degrassi, S. Heinemeyer, W. Hollik, P. Slavich, and G. Weiglein, "Towards high precision predictions for the MSSM Higgs sector", *Eur. Phys. J. C* **28** (2003) 133–143, arXiv:hep-ph/0212020.

[45] B. C. Allanach, A. Djouadi, J. L. Kneur, W. Porod, and P. Slavich, "Precise determination of the neutral Higgs boson masses in the MSSM", *JHEP* **09** (2004) 044, arXiv:hep-ph/0406166.

[46] E. Bagnaschi, F. Frensch, S. Heinemeyer, G. Lee, S. R. Liebler, M. Muhlleitner, A. R. Mc Carn, J. Quevillon, N. Rompotis, P. Slavich, M. Spira, C. Wagner, and R. Wolf, "Benchmark scenarios for low tan β in the MSSM", Aug, 2015. https://cds.cern.ch/record/2039911.

[47] R. V. Harlander, S. Liebler, and H. Mantler, "SusHi: A program for the calculation of Higgs production in gluon fusion and bottom-quark annihilation in the Standard Model and the MSSM", *Comput. Phys. Commun.* **184** (2013) 1605–1617, `arXiv:1212.3249 [hep-ph]`.

[48] R. V. Harlander, S. Liebler, and H. Mantler, "SusHi Bento: Beyond NNLO and the heavy-top limit", *Comput. Phys. Commun.* **212** (2017) 239–257, `arXiv:1605.03190 [hep-ph]`.

[49] M. Spira, A. Djouadi, D. Graudenz, and P. M. Zerwas, "Higgs boson production at the LHC", *Nucl. Phys. B* **453** (1995) 17–82, `arXiv:hep-ph/9504378`.

[50] R. V. Harlander and W. B. Kilgore, "Next-to-next-to-leading order Higgs production at hadron colliders", *Phys. Rev. Lett.* **88** (2002) 201801, `arXiv:hep-ph/0201206`.

[51] C. Anastasiou and K. Melnikov, "Higgs boson production at hadron colliders in NNLO QCD", *Nucl. Phys. B* **646** (2002) 220–256, `arXiv:hep-ph/0207004`.

[52] V. Ravindran, J. Smith, and W. L. van Neerven, "NNLO corrections to the total cross-section for Higgs boson production in hadron hadron collisions", *Nucl. Phys. B* **665** (2003) 325–366, `arXiv:hep-ph/0302135`.

[53] U. Aglietti, R. Bonciani, G. Degrassi, and A. Vicini, "Two loop light fermion contribution to Higgs production and decays", *Phys. Lett. B* **595** (2004) 432–441, `arXiv:hep-ph/0404071`.

[54] R. Bonciani, G. Degrassi, and A. Vicini, "On the Generalized Harmonic Polylogarithms of One Complex Variable", *Comput. Phys. Commun.* **182** (2011) 1253–1264, `arXiv:1007.1891 [hep-ph]`.

[55] S. Dittmaier, M. Krämer, and M. Spira, "Higgs radiation off bottom quarks at the Tevatron and the CERN LHC", *Phys. Rev. D* **70** (2004) 074010, `arXiv:hep-ph/0309204`.

[56] S. Dawson, C. B. Jackson, L. Reina, and D. Wackeroth, "Exclusive Higgs boson production with bottom quarks at hadron colliders", *Phys. Rev. D* **69** (2004) 074027, `arXiv:hep-ph/0311067`.

[57] R. V. Harlander and W. B. Kilgore, "Higgs boson production in bottom quark fusion at next-to-next-to leading order", *Phys. Rev. D* **68** (2003) 013001, `arXiv:hep-ph/0304035`.

[58] R. Harlander, M. Kramer, and M. Schumacher, "Bottom-quark associated Higgs-boson production: reconciling the four- and five-flavour scheme approach", `arXiv:1112.3478 [hep-ph]`, 12, 2011.

[59] S. Forte, D. Napoletano, and M. Ubiali, "Higgs production in bottom-quark fusion in a matched scheme", *Phys. Lett. B* **751** (2015) 331–337, `arXiv:1508.01529 [hep-ph]`.

[60] M. Bonvini, A. S. Papanastasiou, and F. J. Tackmann, "Resummation and matching of b-quark mass effects in $b\bar{b}H$ production", *JHEP* **11** (2015) 196, `arXiv:1508.03288 [hep-ph]`.

[61] S. Forte, D. Napoletano, and M. Ubiali, "Higgs production in bottom-quark fusion: matching beyond leading order", *Phys. Lett. B* **763** (2016) 190–196, `arXiv:1607.00389 [hep-ph]`.

[62] M. Bonvini, A. S. Papanastasiou, and F. J. Tackmann, "Matched predictions for the $b\bar{b}H$ cross section at the 13 TeV LHC", *JHEP* **10** (2016) 053, `arXiv:1605.01733 [hep-ph]`.

[63] A. D. Martin, W. J. Stirling, R. S. Thorne, and G. Watt, "Parton distributions for the LHC", *Eur. Phys. J. C* **63** (2009) 189–285, `arXiv:0901.0002 [hep-ph]`.

[64] S. Heinemeyer, W. Hollik, and G. Weiglein, "FeynHiggs: A Program for the calculation of the masses of the neutral CP even Higgs bosons in the MSSM", *Comput. Phys. Commun.* **124** (2000) 76–89, `arXiv:hep-ph/9812320`.

[65] S. Heinemeyer, W. Hollik, and G. Weiglein, "The Masses of the neutral CP - even Higgs bosons in the MSSM: Accurate analysis at the two loop level", *Eur. Phys. J. C* **9** (1999) 343–366, `arXiv:hep-ph/9812472`.

[66] M. Frank, T. Hahn, S. Heinemeyer, W. Hollik, H. Rzehak, and G. Weiglein, "The Higgs Boson Masses and Mixings of the Complex MSSM in the Feynman-Diagrammatic Approach", *JHEP* **02** (2007) 047, `arXiv:hep-ph/0611326`.

[67] T. Hahn, S. Heinemeyer, W. Hollik, H. Rzehak, and G. Weiglein, "High-Precision Predictions for the Light CP -Even Higgs Boson Mass of the Minimal Supersymmetric Standard Model", *Phys. Rev. Lett.* **112** no. 14, (2014) 141801, `arXiv:1312.4937 [hep-ph]`.

[68] H. Bahl and W. Hollik, "Precise prediction for the light MSSM Higgs boson mass combining effective field theory and fixed-order calculations", *Eur. Phys. J. C* **76** no. 9, (2016) 499, `arXiv:1608.01880 [hep-ph]`.

[69] H. Bahl, S. Heinemeyer, W. Hollik, and G. Weiglein, "Reconciling EFT and hybrid calculations of the light MSSM Higgs-boson mass", *Eur. Phys. J. C* **78** no. 1, (2018) 57, `arXiv:1706.00346 [hep-ph]`.

[70] H. Bahl, T. Hahn, S. Heinemeyer, W. Hollik, S. Paßehr, H. Rzehak, and G. Weiglein, "Precision calculations in the MSSM Higgs-boson sector with FeynHiggs 2.14", *Comput. Phys. Commun.* **249** (2020) 107099, `arXiv:1811.09073 [hep-ph]`.

[71] A. Djouadi, J. Kalinowski, and M. Spira, "HDECAY: A Program for Higgs boson decays in the standard model and its supersymmetric extension", *Comput. Phys. Commun.* **108** (1998) 56–74, `arXiv:hep-ph/9704448`.

[72] A. Djouadi, J. Kalinowski, M. Muehlleitner, and M. Spira, "HDECAY: Twenty$_{++}$ years after", *Comput. Phys. Commun.* **238** (2019) 214–231, `arXiv:1801.09506 [hep-ph]`.

[73] **LHC Higgs Cross Section Working Group** Collaboration, D. de Florian *et al.*, "Handbook of LHC Higgs Cross Sections: 4. Deciphering the Nature of the Higgs Sector". CERN Yellow Reports: Monographs. CERN, Geneva, Oct, 2016. `https://cds.cern.ch/record/2227475`.

[74] E. Bagnaschi *et al.*, "MSSM Higgs Boson Searches at the LHC: Benchmark Scenarios for Run 2 and Beyond", *Eur. Phys. J. C* **79** no. 7, (2019) 617, `arXiv:1808.07542 [hep-ph]`.

[75] A. Bredenstein, A. Denner, S. Dittmaier, and M. M. Weber, "Precise predictions for the Higgs-boson decay H —> WW/ZZ —> 4 leptons", *Phys. Rev. D* **74** (2006) 013004, `arXiv:hep-ph/0604011`.

[76] A. Bredenstein, A. Denner, S. Dittmaier, and M. M. Weber, "Radiative corrections to the semileptonic and hadronic Higgs-boson decays H —> W W / Z Z —> 4 fermions", *JHEP* **02** (2007) 080, `arXiv:hep-ph/0611234`.

[77] J. Butterworth *et al.*, "PDF4LHC recommendations for LHC Run II", *J. Phys. G* **43** (2016) 023001, `arXiv:1510.03865 [hep-ph]`.

[78] K. J. de Vries *et al.*, "The pMSSM10 after LHC Run 1", *Eur. Phys. J. C* **75** no. 9, (2015) 422, `arXiv:1504.03260 [hep-ph]`.

[79] P. Bechtle, H. E. Haber, S. Heinemeyer, O. Stål, T. Stefaniak, G. Weiglein, and L. Zeune, "The Light and Heavy Higgs Interpretation of the MSSM", *Eur. Phys. J. C* **77** no. 2, (2017) 67, `arXiv:1608.00638 [hep-ph]`.

[80] **ATLAS** Collaboration, "hMSSM summary plots from direct and indirect searches", tech. rep., CERN, Geneva, Mar, 2020. `https://cds.cern.ch/record/2713580`. All figures including auxiliary figures are available at https://atlas.web.cern.ch/Atlas/GROUPS/PHYSICS/PUBNOTES/ATL-PHYS-PUB-2020-006.

[81] **ATLAS** Collaboration, G. Aad *et al.*, "Combination of searches for Higgs boson pairs in *pp* collisions at $\sqrt{s}$ =13 TeV with the ATLAS detector", *Phys. Lett. B* **800** (2020) 135103, `arXiv:1906.02025 [hep-ex]`.

[82] **ATLAS** Collaboration, M. Aaboud *et al.*, "Search for heavy ZZ resonances in the $\ell^+\ell^-\ell^+\ell^-$ and $\ell^+\ell^-\nu\bar{\nu}$ final states using proton–proton collisions at $\sqrt{s} = 13$ TeV with the ATLAS detector", *Eur. Phys. J. C* **78** no. 4, (2018) 293, `arXiv:1712.06386 [hep-ex]`.

[83] **ATLAS** Collaboration, M. Aaboud *et al.*, "Search for additional heavy neutral Higgs and gauge bosons in the ditau final state produced in 36 fb^{-1} of pp collisions at $\sqrt{s} = 13$ TeV with the ATLAS detector", *JHEP* **01** (2018) 055, `arXiv:1709.07242 [hep-ex]`.

[84] **CMS** Collaboration, A. M. Sirunyan *et al.*, "Search for additional neutral MSSM Higgs bosons in the $\tau\tau$ final state in proton-proton collisions at $\sqrt{s} = 13$ TeV", *JHEP* **09** (2018) 007, `arXiv:1803.06553 [hep-ex]`.

[85] P. Bechtle, S. Heinemeyer, O. Stål, T. Stefaniak, and G. Weiglein, "*HiggsSignals*: Confronting arbitrary Higgs sectors with measurements at the Tevatron and the LHC", *Eur. Phys. J. C* **74** no. 2, (2014) 2711, `arXiv:1305.1933 [hep-ph]`.

[86] P. Bechtle, O. Brein, S. Heinemeyer, G. Weiglein, and K. E. Williams, "HiggsBounds: Confronting Arbitrary Higgs Sectors with Exclusion Bounds from LEP and the Tevatron", *Comput. Phys. Commun.* **181** (2010) 138–167, `arXiv:0811.4169 [hep-ph]`.

[87] P. Bechtle, O. Brein, S. Heinemeyer, G. Weiglein, and K. E. Williams, "HiggsBounds 2.0.0: Confronting Neutral and Charged Higgs Sector Predictions with Exclusion Bounds from LEP and the Tevatron", *Comput. Phys. Commun.* **182** (2011) 2605–2631, `arXiv:1102.1898 [hep-ph]`.

[88] P. Bechtle, O. Brein, S. Heinemeyer, O. Stål, T. Stefaniak, G. Weiglein, and K. E. Williams, "HiggsBounds − 4: Improved Tests of Extended Higgs Sectors against Exclusion Bounds from LEP, the Tevatron and the LHC", *Eur. Phys. J. C* **74** no. 3, (2014) 2693, `arXiv:1311.0055 [hep-ph]`.

[89] P. Bechtle, S. Heinemeyer, O. Stal, T. Stefaniak, and G. Weiglein, "Applying Exclusion Likelihoods from LHC Searches to Extended Higgs Sectors", *Eur. Phys. J. C* **75** no. 9, (2015) 421, `arXiv:1507.06706 [hep-ph]`.

[90] A. Pich, "Precision Tau Physics", *Prog. Part. Nucl. Phys.* **75** (2014) 41–85, `arXiv:1310.7922 [hep-ph]`.

[91] "LHC Machine", *JINST* **3** (2008) S08001.

[92] R. Bruce *et al.*, "LHC Run 2: Results and challenges", in *57th ICFA Advanced Beam Dynamics Workshop on High-Intensity and High-Brightness Hadron Beams*. 8, 2016.

[93] **ATLAS** Collaboration, "Luminosity determination in pp collisions at $\sqrt{s} = 13$ TeV using the ATLAS detector at the LHC", Jun, 2019. `https://cds.cern.ch/record/2677054`.

[94] **ATLAS** Collaboration, G. Aad *et al.*, "The ATLAS Experiment at the CERN Large Hadron Collider", *JINST* **3** (2008) S08003.

[95] **CMS** Collaboration, S. Chatrchyan *et al.*, "The CMS Experiment at the CERN LHC", *JINST* **3** (2008) S08004.

[96] **ALICE** Collaboration, K. Aamodt *et al.*, "The ALICE experiment at the CERN LHC", *JINST* **3** (2008) S08002.

[97] **LHCb** Collaboration, A. A. Alves, Jr. *et al.*, "The LHCb Detector at the LHC", *JINST* **3** (2008) S08005.

[98] **LHCf** Collaboration, O. Adriani *et al.*, "The LHCf detector at the CERN Large Hadron Collider", *JINST* **3** (2008) S08006.

[99] **TOTEM** Collaboration, G. Anelli *et al.*, "The TOTEM experiment at the CERN Large Hadron Collider", *JINST* **3** (2008) S08007.

[100] **MoEDAL** Collaboration, J. Pinfold *et al.*, "Technical Design Report of the MoEDAL Experiment", 6, 2009. `https://cds.cern.ch/record/1181486`.

[101] C. Lefèvre, "The CERN accelerator complex. Complexe des accélérateurs du CERN", Dec, 2008.

[102] **ATLAS** Collaboration, G. Aad *et al.*, "The ATLAS Inner Detector commissioning and calibration", *Eur. Phys. J. C* **70** (2010) 787–821, `arXiv:1004.5293 [physics.ins-det]`.

[103] **ATLAS** Collaboration, G. Aad *et al.*, "Alignment of the ATLAS Inner Detector in Run-2", *Eur. Phys. J. C* **80** no. 12, (2020) 1194, `arXiv:2007.07624 [hep-ex]`.

[104] G. Aad *et al.*, "ATLAS pixel detector electronics and sensors", *JINST* **3** (2008) P07007.

[105] **ATLAS** Collaboration, H. Oide, "The Pixel Detector of the ATLAS experiment for Run 2 of the Large Hadron Collider", *JINST* **9** no. 12, (2014) C12034.

[106] **ATLAS** Collaboration, M. Capeans, G. Darbo, K. Einsweiler, M. Elsing, T. Flick, M. Garcia-Sciveres, C. Gemme, H. Pernegger, O. Rohne, and R. Vuillermet, "ATLAS Insertable B-Layer Technical Design Report", 9, 2010. `https://cds.cern.ch/record/1291633`.

[107] **ATLAS IBL** Collaboration, B. Abbott *et al.*, "Production and Integration of the ATLAS Insertable B-Layer", *JINST* **13** no. 05, (2018) T05008, `arXiv:1803.00844 [physics.ins-det]`.

[108] **ATLAS** Collaboration, G. Aad *et al.*, "Operation and performance of the ATLAS semiconductor tracker", *JINST* **9** (2014) P08009, `arXiv:1404.7473 [hep-ex]`.

[109] A. Ahmad *et al.*, "The Silicon microstrip sensors of the ATLAS semiconductor tracker", *Nucl. Instrum. Meth. A* **578** (2007) 98–118.

[110] **ATLAS TRT** Collaboration, E. Abat *et al.*, "The ATLAS Transition Radiation Tracker (TRT) proportional drift tube: Design and performance", *JINST* **3** (2008) P02013.

[111] **ATLAS** Collaboration, B. Mindur, "ATLAS Transition Radiation Tracker (TRT): Straw tubes for tracking and particle identification at the Large Hadron Collider", *Nucl. Instrum. Meth. A* **845** (2017) 257–261.

[112] **ATLAS TRT** Collaboration, E. Abat *et al.*, "The ATLAS TRT barrel detector", *JINST* **3** (2008) P02014.

[113] E. Abat *et al.*, "The ATLAS TRT end-cap detectors", *JINST* **3** (2008) P10003.

[114] **ATLAS** Collaboration, M. Aaboud *et al.*, "Performance of the ATLAS Transition Radiation Tracker in Run 1 of the LHC: tracker properties", *JINST* **12** no. 05, (2017) P05002, `arXiv:1702.06473 [hep-ex]`.

[115] **ATLAS** Collaboration, "ATLAS liquid-argon calorimeter: Technical Design Report", 1996. `https://cds.cern.ch/record/331061`.

[116] **ATLAS** Collaboration, "ATLAS tile calorimeter: Technical Design Report". Technical design report. ATLAS. CERN, Geneva, 1996. `https://cds.cern.ch/record/331062`.

[117] **ATLAS** Collaboration, M. Aaboud *et al.*, "Operation and performance of the ATLAS Tile Calorimeter in Run 1", *Eur. Phys. J. C* **78** no. 12, (2018) 987, `arXiv:1806.02129 [hep-ex]`.

[118] D. M. Gingrich *et al.*, "Construction, assembly and testing of the ATLAS hadronic end-cap calorimeter", *JINST* **2** (2007) P05005.

[119] **ATLAS** Collaboration, "ATLAS muon spectrometer: Technical Design Report", 1997. `https://cds.cern.ch/record/331068`.

[120] G. Avoni *et al.*, "The new lucid-2 detector for luminosity measurement and monitoring in atlas", *JINST* **13** no. 07, (2018) P07017.

[121] **ATLAS** Collaboration, P. Jenni, M. Nessi, and M. Nordberg, "Zero Degree Calorimeters for ATLAS", Jan, 2007. `https://cds.cern.ch/record/1009649`.

[122] S. Abdel Khalek *et al.*, "The ALFA Roman Pot Detectors of ATLAS", *JINST* **11** no. 11, (2016) P11013, `arXiv:1609.00249 [physics.ins-det]`.

[123] L. Adamczyk *et al.*, "Technical Design Report for the ATLAS Forward Proton Detector", May, 2015. `https://cds.cern.ch/record/2017378`.

[124] **ATLAS** Collaboration, A. R. Martínez, "The Run-2 ATLAS Trigger System", *J. Phys. Conf. Ser.* **762** no. 1, (2016) 012003.

[125] **ATLAS** Collaboration, G. Aad *et al.*, "Operation of the ATLAS trigger system in Run 2", *JINST* **15** no. 10, (2020) P10004, `arXiv:2007.12539 [physics.ins-det]`.

[126] M. Shochet, L. Tompkins, V. Cavaliere, P. Giannetti, A. Annovi, and G. Volpi, "Fast TracKer (FTK) Technical Design Report", Jun, 2013. `http://cds.cern.ch/record/1552953`. ATLAS Fast Tracker Technical Design Report.

[127] **ATLAS** Collaboration, "Luminosity Public Results Run 2", `https://twiki.cern.ch/twiki/bin/view/AtlasPublic/LuminosityPublicResultsRun2?rev=73`. Webpage. Revision 73, last visited 08.06.2021.

[128] T. Golling, H. S. Hayward, P. U. E. Onyisi, H. J. Stelzer, and P. Waller, "The ATLAS Data Quality Defect Database System", *Eur. Phys. J. C* **72** (2012) 1960, `arXiv:1110.6119 [physics.ins-det]`.

[129] **ATLAS** Collaboration, P. J. Laycock, M. A. Chelstowska, T. C. Donszelmann, J. Guenther, A. Nairz, R. Nikolaidou, E. Shabalina, J. Strandberg, A. Taffard, and S. Wang, "ATLAS data preparation in run 2", *J. Phys. Conf. Ser.* **898** no. 4, (2017) 042050.

[130] T. Sjöstrand, "Monte Carlo Generators", Nov, 2006. `https://cds.cern.ch/record/999717`.

[131] **ATLAS** Collaboration, "ATLAS Computing: technical design report". Technical design report. ATLAS. CERN, Geneva, 2005. `http://cds.cern.ch/record/837738`.

[132] **ATLAS** Collaboration, "Athena", April, 2019. `https://doi.org/10.5281/zenodo.2641997`.

[133] **ATLAS** Collaboration, G. Aad *et al.*, "The ATLAS Simulation Infrastructure", *Eur. Phys. J. C* **70** (2010) 823–874, `arXiv:1005.4568 [physics.ins-det]`.

[134] T. Sjöstrand, S. Ask, J. R. Christiansen, R. Corke, N. Desai, P. Ilten, S. Mrenna, S. Prestel, C. O. Rasmussen, and P. Z. Skands, "An Introduction to PYTHIA 8.2", *Comput. Phys. Commun.* **191** (2015) 159–177, `arXiv:1410.3012 [hep-ph]`.

[135] **Sherpa** Collaboration, E. Bothmann *et al.*, "Event Generation with Sherpa 2.2", *SciPost Phys.* **7** no. 3, (2019) 034, `arXiv:1905.09127 [hep-ph]`.

[136] J. Alwall, R. Frederix, S. Frixione, V. Hirschi, F. Maltoni, O. Mattelaer, H. S. Shao, T. Stelzer, P. Torrielli, and M. Zaro, "The automated computation of tree-level and next-to-leading order differential cross sections, and their matching to parton shower simulations", *JHEP* **07** (2014) 079, `arXiv:1405.0301 [hep-ph]`.

[137] "ATLAS Pythia 8 tunes to 7 TeV datas", Tech. Rep. ATL-PHYS-PUB-2014-021, CERN, Geneva, Nov, 2014. `https://cds.cern.ch/record/1966419`.

[138] T. Gleisberg, S. Hoeche, F. Krauss, M. Schonherr, S. Schumann, F. Siegert, and J. Winter, "Event generation with SHERPA 1.1", *JHEP* **02** (2009) 007, `arXiv:0811.4622 [hep-ph]`.

[139] J. Boudreau and V. Tsulaia, "The GeoModel Toolkit for Detector Description", 2005. `https://cds.cern.ch/record/865601`.

[140] R. M. Bianchi, J. Boudreau, and I. Vukotic, "A new experiment-independent mechanism to persistify and serve the detector geometry of ATLAS", *Journal of Physics: Conference Series* **898** (Oct, 2017) 072015. `https://doi.org/10.1088/1742-6596/898/7/072015`.

[141] **GEANT4** Collaboration, S. Agostinelli *et al.*, "GEANT4–a simulation toolkit", *Nucl. Instrum. Meth. A* **506** (2003) 250–303.

[142] J. Allison *et al.*, "Geant4 developments and applications", *IEEE Trans. Nucl. Sci.* **53** (2006) 270.

[143] J. Allison *et al.*, "Recent developments in Geant4", *Nucl. Instrum. Meth. A* **835** (2016) 186–225.

[144] C. ATLAS *et al.*, "The simulation principle and performance of the ATLAS fast calorimeter simulation FastCaloSim", Oct, 2010. `https://cds.cern.ch/record/1300517`.

[145] **ATLAS** Collaboration, Z. Marshall, "Simulation of Pile-up in the ATLAS Experiment", *J. Phys. Conf. Ser.* **513** (2014) 022024.

[146] T. Sjostrand, S. Mrenna, and P. Z. Skands, "A Brief Introduction to PYTHIA 8.1", *Comput. Phys. Commun.* **178** (2008) 852–867, `arXiv:0710.3820 [hep-ph]`.

[147] R. D. Ball *et al.*, "Parton distributions with LHC data", *Nucl. Phys. B* **867** (2013) 244–289, `arXiv:1207.1303 [hep-ph]`.

[148] **ATLAS** Collaboration, "The Pythia 8 A3 tune description of ATLAS minimum bias and inelastic measurements incorporating the Donnachie-Landshoff diffractive model", 8, 2016. `https://cds.cern.ch/record/2206965`.

[149] **ATLAS** Collaboration, G. Aad *et al.*, "Emulating the impact of additional proton-proton interactions in the ATLAS simulation by pre-sampling sets of inelastic Monte Carlo events", `arXiv:2102.09495 [hep-ex]`, 2, 2021.

[150] W. Buttinger, "Using Event Weights to account for differences in Instantaneous Luminosity and Trigger Prescale in Monte Carlo and Data", Tech. Rep. ATL-COM-SOFT-2015-119, CERN, Geneva, May, 2015. `https://cds.cern.ch/record/2014726`. ATLAS Internal Note.

[151] **ATLAS** Collaboration, M. Aaboud *et al.*, "Performance of the ATLAS Track Reconstruction Algorithms in Dense Environments in LHC Run 2", *Eur. Phys. J.* **C77** no. 10, (2017) 673, `arXiv:1704.07983 [hep-ex]`.

[152] A. Rosenfeld and J. Pfaltz, "Pfalz, j.l.: Sequential operations in digital picture processing. journal of the acm 13(4), 471-494", *J. ACM* **13** (10, 1966) 471–494.

[153] R. Fruhwirth, "Application of Kalman filtering to track and vertex fitting", *Nucl. Instrum. Meth.* **A262** (1987) 444–450.

[154] T. G. Cornelissen, M. Elsing, I. Gavrilenko, J.-F. Laporte, W. Liebig, M. Limper, K. Nikolopoulos, A. Poppleton, and A. Salzburge Jul, 2008. `https://doi.org/10.1088%2F1742-6596%2F119%2F3%2F032013`.

[155] **ATLAS** Collaboration, M. Aaboud *et al.*, "Reconstruction of primary vertices at the ATLAS experiment in Run 1 proton–proton collisions at the LHC", *Eur. Phys. J.* **C77** no. 5, (2017) 332, `arXiv:1611.10235 [physics.ins-det]`.

[156] **ATLAS** Collaboration, G. Aad *et al.*, "Topological cell clustering in the ATLAS calorimeters and its performance in LHC Run 1", *Eur. Phys. J.* **C77** (2017) 490, `arXiv:1603.02934 [hep-ex]`.

[157] **ATLAS** Collaboration, M. Aaboud *et al.*, "Electron reconstruction and identification in the ATLAS experiment using the 2015 and 2016 LHC proton-proton collision data at $\sqrt{s} = 13$ TeV", *Eur. Phys. J.* **C79** no. 8, (2019) 639, `arXiv:1902.04655 [physics.ins-det]`.

[158] **ATLAS** Collaboration, G. Aad *et al.*, "Muon reconstruction performance of the ATLAS detector in proton–proton collision data at $\sqrt{s} =$13 TeV", *Eur. Phys. J.* **C76** no. 5, (2016) 292, `arXiv:1603.05598 [hep-ex]`.

[159] M. Cacciari, G. P. Salam, and G. Soyez, "The anti-k_t jet clustering algorithm", *JHEP* **04** (2008) 063, `arXiv:0802.1189 [hep-ph]`.

[160] M. Cacciari, G. P. Salam, and G. Soyez, "FastJet User Manual", *Eur. Phys. J.* **C72** (2012) 1896, `arXiv:1111.6097 [hep-ph]`.

[161] **ATLAS** Collaboration, M. Aaboud *et al.*, "Jet energy scale measurements and their systematic uncertainties in proton-proton collisions at $\sqrt{s} = 13$ TeV with the ATLAS detector", *Phys. Rev.* **D96** no. 7, (2017) 072002, `arXiv:1703.09665 [hep-ex]`.

[162] **ATLAS** Collaboration, G. Aad *et al.*, "Jet energy scale and resolution measured in proton-proton collisions at $\sqrt{s} = 13$ TeV with the ATLAS detector", `arXiv:2007.02645 [hep-ex]`, 7, 2020.

[163] **ATLAS** Collaboration, G. Aad *et al.*, "Performance of pile-up mitigation techniques for jets in pp collisions at $\sqrt{s} = 8$ TeV using the ATLAS detector", *Eur. Phys. J.* **C76** no. 11, (2016) 581, `arXiv:1510.03823 [hep-ex]`.

[164] **ATLAS** Collaboration, G. Aad *et al.*, "ATLAS b-jet identification performance and efficiency measurement with $t\bar{t}$ events in pp collisions at $\sqrt{s} = 13$ TeV", *Eur. Phys. J.* **C79** no. 11, (2019) 970, `arXiv:1907.05120 [hep-ex]`.

[165] **ATLAS** Collaboration, M. Aaboud *et al.*, "Performance of missing transverse momentum reconstruction with the ATLAS detector using proton-proton collisions at $\sqrt{s} = 13$ TeV", *Eur. Phys. J.* **C78** no. 11, (2018) 903, `arXiv:1802.08168 [hep-ex]`.

[166] **ATLAS** Collaboration, "E_T^{miss} performance in the ATLAS detector using 2015-2016 LHC p-p collisions", Tech. Rep. ATLAS-CONF-2018-023, CERN, Geneva, Jun, 2018. `https://cds.cern.ch/record/2625233`.

[167] **ATLAS** Collaboration, G. Aad *et al.*, "Identification and energy calibration of hadronically decaying tau leptons with the ATLAS experiment in *pp* collisions at $\sqrt{s}$=8 TeV", *Eur. Phys. J. C* **75** no. 7, (2015) 303, `arXiv:1412.7086 [hep-ex]`.

[168] "Early Inner Detector Tracking Performance in the 2015 data at $\sqrt{s} = 13$ TeV", Tech. Rep. ATL-PHYS-PUB-2015-051, CERN, Geneva, Dec, 2015. `https://cds.cern.ch/record/2110140`.

[169] **ATLAS** Collaboration, "Reconstruction, Energy Calibration, and Identification of Hadronically Decaying Tau Leptons in the ATLAS Experiment for Run-2 of the LHC", Tech. Rep. ATL-PHYS-PUB-2015-045, CERN, Geneva, Nov, 2015. `https://cds.cern.ch/record/2064383`.

[170] "Tagging and suppression of pileup jets with the ATLAS detector", Tech. Rep. ATLAS-CONF-2014-018, CERN, Geneva, May, 2014. `http://cds.cern.ch/record/1700870`.

[171] **ATLAS** Collaboration, "Measurement of the tau lepton reconstruction and identification performance in the ATLAS experiment using *pp* collisions at $\sqrt{s} = 13$ TeV", Tech. Rep. ATLAS-CONF-2017-029, CERN, Geneva, May, 2017. `https://cds.cern.ch/record/2261772`.

[172] D. U. Duschinger, "Search for neutral bosons decaying into the fully hadronic di-tau final state with the ATLAS detector at the LHC", Sep, 2018. `https://cds.cern.ch/record/2673361`. Presented 07 Feb 2019.

[173] L. Breiman, J. Friedman, C. J. Stone, and R. A. Olshen, "Classification and regression trees". New York: Chapman and Hall, 1993.

[174] Y. Freund and R. E. Schapire, "A decision-theoretic generalization of on-line learning and an application to boosting", *Journal of Computer and System Sciences* **55** no. 1, (1997) 119–139. `https://www.sciencedirect.com/science/article/pii/S002200009791504X`.

[175] A. Hoecker *et al.*, "TMVA - Toolkit for Multivariate Data Analysis", *ArXiv Physics e-prints* (2007) , `arXiv:physics/0703039 [physics]`.

[176] **ATLAS** Collaboration, "Identification of hadronic tau lepton decays using neural networks in the ATLAS experiment", Tech. Rep. ATL-PHYS-PUB-2019-033, CERN, Geneva, Aug, 2019. `https://cds.cern.ch/record/2688062`.

[177] W. S. McCulloch and W. Pitts, "A logical calculus of the ideas immanent in nervous activity", *The bulletin of mathematical biophysics* **5** (1943) 115–133. `https://doi.org/10.1007/BF02478259`.

[178] D. Hebb, "The organization of behavior: A neuropsychological theory". Neuropsychological Theory. Wiley, 1950. `https://onlinelibrary.wiley.com/doi/pdf/10.1002/sce.37303405110`.

[179] F. Rosenblatt, "The perceptron: A probabilistic model for information storage and organization in the brain.", *Psychological Review* **65** (1958) 386–408. `https://doi.org/10.1037/h0042519`.

[180] D. E. Rumelhart, G. E. Hinton, and R. J. Williams, "Learning representations by back-propagating errors", *Nature* **323** no. 6088, (Oct., 1986) 533–536.

[181] S. Linnainmaa, "Taylor expansion of the accumulated rounding error", *BIT Numerical Mathematics* **16** (1976) 146–160.
`https://doi.org/10.1007/BF01931367`.

[182] K. He, X. Zhang, S. Ren, and J. Sun, "Deep residual learning for image recognition", *CoRR* **abs/1512.03385** (2015) , `arXiv:1512.03385`.
`http://arxiv.org/abs/1512.03385`.

[183] C. Szegedy, S. Ioffe, and V. Vanhoucke, "Inception-v4, inception-resnet and the impact of residual connections on learning", *CoRR* **abs/1602.07261** (2016) , `arXiv:1602.07261`. `http://arxiv.org/abs/1602.07261`.

[184] S. Bianco, R. Cadène, L. Celona, and P. Napoletano, "Benchmark analysis of representative deep neural network architectures", *CoRR* **abs/1810.00736** (2018) , `arXiv:1810.00736`. `http://arxiv.org/abs/1810.00736`.

[185] X. Glorot, A. Bordes, and Y. Bengio, "Deep sparse rectifier neural networks", in *Proceedings of the Fourteenth International Conference on Artificial Intelligence and Statistics*, G. Gordon, D. Dunson, and M. Dudík, eds., vol. 15 of *Proceedings of Machine Learning Research*, pp. 315–323. PMLR, 11–13 apr, 2011.
`http://proceedings.mlr.press/v15/glorot11a.html`.

[186] C. C. Aggarwal, "Neural networks and deep learning". Springer International Publishing, January, 2018.

[187] R. J. Williams and D. Zipser, "Gradient-based learning algorithms for recurrent networks and their computational complexity", p. 433–486. L. Erlbaum Associates Inc., USA, 1995.

[188] Y. Bengio, P. Simard, and P. Frasconi, "Learning long-term dependencies with gradient descent is difficult", *IEEE Transactions on Neural Networks* **5** no. 2, (1994) 157–166.

[189] S. Hochreiter and J. Schmidhuber, "Long short-term memory", *Neural computation* **9** (12, 1997) 1735–80.

[190] M. Schuster and K. K. Paliwal, "Bidirectional recurrent neural networks", *IEEE Transactions on Signal Processing* **45** no. 11, (1997) 2673–2681.

[191] **CDF** Collaboration, T. Aaltonen *et al.*, "Two-Particle Momentum Correlations in Jets Produced in $p\bar{p}$ Collisions at $\sqrt{s} = 1.96$-TeV", *Phys. Rev. D* **77** (2008) 092001, `arXiv:0802.3182 [hep-ex]`.

[192] M. K. Ayoub, "Search of the Standard Model Higgs boson decaying into two lepton taus with the Run2 data of ATLAS detector in LHC", 2016.
`http://cds.cern.ch/record/2317007`. 2016.

[193] **ATLAS** Collaboration, "Particle Identification Performance of the ATLAS Transition Radiation Tracker", Tech. Rep. ATLAS-CONF-2011-128, CERN, Geneva, Sep, 2011. `https://cds.cern.ch/record/1383793`.

[194] F. Chollet *et al.*, "Keras", `https://keras.io`, 2015.

[195] M. Abadi *et al.*, "TensorFlow: Large-scale machine learning on heterogeneous systems", 2015. `https://www.tensorflow.org/`. Software available from tensorflow.org.

[196] J. S. Bridle, "Probabilistic interpretation of feedforward classification network outputs, with relationships to statistical pattern recognition", in *Neurocomputing*, F. F. Soulié and J. Hérault, eds., pp. 227–236. Springer Berlin Heidelberg, Berlin, Heidelberg, 1990.

[197] X. Glorot and Y. Bengio, "Understanding the difficulty of training deep feedforward neural networks", vol. 9 of *Proceedings of Machine Learning Research*, pp. 249–256. JMLR Workshop and Conference Proceedings, Chia Laguna Resort, Sardinia, Italy, 13–15 may, 2010. `http://proceedings.mlr.press/v9/glorot10a.html`.

[198] A. M. Saxe, J. L. McClelland, and S. Ganguli, "Exact solutions to the nonlinear dynamics of learning in deep linear neural networks", `arXiv:1312.6120 [cs.NE]`, 2014.

[199] D. Kingma and J. Ba, "Adam: A method for stochastic optimization", *International Conference on Learning Representations* (2014) , `arXiv:1412.6980`.

[200] A. Buckley *et al.*, "The HepMC3 Event Record Library for Monte Carlo Event Generators", `arXiv:1912.08005 [hep-ph]`, 12, 2019.

[201] R. J. Barlow, "Practical Statistics for Particle Physics", *CERN Yellow Rep. School Proc.* **5** (2020) 149–197, `arXiv:1905.12362 [physics.data-an]`.

[202] P. Nason, "A New method for combining NLO QCD with shower Monte Carlo algorithms", *JHEP* **11** (2004) 040, `arXiv:hep-ph/0409146`.

[203] S. Frixione, P. Nason, and C. Oleari, "Matching NLO QCD computations with Parton Shower simulations: the POWHEG method", *JHEP* **11** (2007) 070, `arXiv:0709.2092 [hep-ph]`.

[204] S. Alioli, P. Nason, C. Oleari, and E. Re, "A general framework for implementing NLO calculations in shower Monte Carlo programs: the POWHEG BOX", *JHEP* **06** (2010) 043, `arXiv:1002.2581 [hep-ph]`.

[205] H.-L. Lai, M. Guzzi, J. Huston, Z. Li, P. M. Nadolsky, J. Pumplin, and C.-P. Yuan, "New parton distributions for collider physics", *Phys. Rev. D* **82** (2010) 074024, `arXiv:1007.2241 [hep-ph]`.

[206] J. Pumplin, D. Stump, J. Huston, H. Lai, P. M. Nadolsky, and W. Tung, "New generation of parton distributions with uncertainties from global QCD analysis", *JHEP* **07** (2002) 012, `arXiv:hep-ph/0201195`.

[207] **ATLAS** Collaboration, G. Aad *et al.*, "Measurement of the Z/γ^* boson transverse momentum distribution in pp collisions at $\sqrt{s} = 7$ TeV with the ATLAS detector", *JHEP* **09** (2014) 145, `arXiv:1406.3660 [hep-ex]`.

[208] P. Golonka and Z. Was, "PHOTOS Monte Carlo: A Precision tool for QED corrections in Z and W decays", *Eur. Phys. J. C* **45** (2006) 97–107, `arXiv:hep-ph/0506026`.

[209] N. Davidson, T. Przedzinski, and Z. Was, "PHOTOS interface in C++: Technical and Physics Documentation", *Comput. Phys. Commun.* **199** (2016) 86–101, `arXiv:1011.0937 [hep-ph]`.

[210] D. J. Lange, "The evtgen particle decay simulation package", *Nuclear Instruments and Methods in Physics Research Section A: Accelerators, Spectrometers, Detectors and Associated Equipment* **462** no. 1, (2001) 152 – 155. http://www.sciencedirect.com/science/article/pii/S0168900201000894. BEAUTY2000, Proceedings of the 7th Int. Conf. on B-Physics at Hadron Machines.

[211] "Selection of jets produced in 13TeV proton-proton collisions with the ATLAS detector", 7, 2015.

[212] **ATLAS** Collaboration, "The ATLAS Tau Trigger in Run 2", Tech. Rep. ATLAS-CONF-2017-061, CERN, Geneva, Jul, 2017. https://cds.cern.ch/record/2274201.

[213] **ATLAS** Collaboration, "ATLAS simulation of boson plus jets processes in Run 2", May, 2017. https://cds.cern.ch/record/2261937.

[214] S. D. Drell and T.-M. Yan, "Massive lepton-pair production in hadron-hadron collisions at high energies", *Phys. Rev. Lett.* **25** (Aug, 1970) 316–320. https://link.aps.org/doi/10.1103/PhysRevLett.25.316.

[215] S. Alioli, P. Nason, C. Oleari, and E. Re, "NLO vector-boson production matched with shower in POWHEG", *JHEP* **07** (2008) 060, arXiv:0805.4802 [hep-ph].

[216] U. Klein, "Nnlo qcd and nlo ew drell yan background predictions for new gauge boson searches", *Les Houches 2013: Physics at TeV Colliders: Standard Model Working Group Report* (5, 2014) 80 – 90, arXiv:1405.1067 [hep-ph].

[217] **ATLAS** Collaboration, M. Aaboud *et al.*, "Search for high-mass new phenomena in the dilepton final state using proton-proton collisions at $\sqrt{s} = 13$ TeV with the ATLAS detector", *Phys. Lett. B* **761** (2016) 372–392, arXiv:1607.03669 [hep-ex].

[218] **NNPDF** Collaboration, R. D. Ball *et al.*, "Parton distributions for the LHC Run II", *JHEP* **04** (2015) 040, arXiv:1410.8849 [hep-ph].

[219] T. Gleisberg and S. Hoeche, "Comix, a new matrix element generator", *JHEP* **12** (2008) 039, arXiv:0808.3674 [hep-ph].

[220] F. Cascioli, P. Maierhofer, and S. Pozzorini, "Scattering Amplitudes with Open Loops", *Phys. Rev. Lett.* **108** (2012) 111601, arXiv:1111.5206 [hep-ph].

[221] A. Denner, S. Dittmaier, and L. Hofer, "Collier: a fortran-based Complex One-Loop LIbrary in Extended Regularizations", *Comput. Phys. Commun.* **212** (2017) 220–238, arXiv:1604.06792 [hep-ph].

[222] S. Schumann and F. Krauss, "A Parton shower algorithm based on Catani-Seymour dipole factorisation", *JHEP* **03** (2008) 038, arXiv:0709.1027 [hep-ph].

[223] S. Hoeche, F. Krauss, M. Schonherr, and F. Siegert, "A critical appraisal of NLO+PS matching methods", *JHEP* **09** (2012) 049, arXiv:1111.1220 [hep-ph].

[224] S. Hoeche, F. Krauss, M. Schonherr, and F. Siegert, "QCD matrix elements + parton showers: The NLO case", *JHEP* **04** (2013) 027, arXiv:1207.5030 [hep-ph].

[225] S. Catani, F. Krauss, R. Kuhn, and B. Webber, "QCD matrix elements + parton showers", *JHEP* **11** (2001) 063, `arXiv:hep-ph/0109231`.

[226] S. Hoeche, F. Krauss, S. Schumann, and F. Siegert, "QCD matrix elements and truncated showers", *JHEP* **05** (2009) 053, `arXiv:0903.1219 [hep-ph]`.

[227] C. Anastasiou, L. J. Dixon, K. Melnikov, and F. Petriello, "High precision QCD at hadron colliders: Electroweak gauge boson rapidity distributions at NNLO", *Phys. Rev. D* **69** (2004) 094008, `arXiv:hep-ph/0312266`.

[228] **ATLAS** Collaboration, "ATLAS simulation of boson plus jets processes in Run 2", May, 2017. `https://cds.cern.ch/record/2261937`.

[229] S. Frixione, P. Nason, and G. Ridolfi, "A Positive-weight next-to-leading-order Monte Carlo for heavy flavour hadroproduction", *JHEP* **09** (2007) 126, `arXiv:0707.3088 [hep-ph]`.

[230] S. Alioli, P. Nason, C. Oleari, and E. Re, "NLO single-top production matched with shower in POWHEG: s- and t-channel contributions", *JHEP* **09** (2009) 111, `arXiv:0907.4076 [hep-ph]`. [Erratum: JHEP 02, 011 (2010)].

[231] R. Frederix, E. Re, and P. Torrielli, "Single-top t-channel hadroproduction in the four-flavour scheme with POWHEG and aMC@NLO", *JHEP* **09** (2012) 130, `arXiv:1207.5391 [hep-ph]`.

[232] E. Re, "Single-top Wt-channel production matched with parton showers using the POWHEG method", *Eur. Phys. J. C* **71** (2011) 1547, `arXiv:1009.2450 [hep-ph]`.

[233] **ATLAS** Collaboration, "Studies on top-quark Monte Carlo modelling for Top2016", Tech. Rep. ATL-PHYS-PUB-2016-020, CERN, Geneva, Sep, 2016. `https://cds.cern.ch/record/2216168`.

[234] M. Beneke, P. Falgari, S. Klein, and C. Schwinn, "Hadronic top-quark pair production with NNLL threshold resummation", *Nucl. Phys. B* **855** (2012) 695–741, `arXiv:1109.1536 [hep-ph]`.

[235] M. Cacciari, M. Czakon, M. Mangano, A. Mitov, and P. Nason, "Top-pair production at hadron colliders with next-to-next-to-leading logarithmic soft-gluon resummation", *Phys. Lett. B* **710** (2012) 612–622, `arXiv:1111.5869 [hep-ph]`.

[236] P. Bärnreuther, M. Czakon, and A. Mitov, "Percent Level Precision Physics at the Tevatron: First Genuine NNLO QCD Corrections to $q\bar{q} \to t\bar{t} + X$", *Phys. Rev. Lett.* **109** (2012) 132001, `arXiv:1204.5201 [hep-ph]`.

[237] M. Czakon and A. Mitov, "NNLO corrections to top-pair production at hadron colliders: the all-fermionic scattering channels", *JHEP* **12** (2012) 054, `arXiv:1207.0236 [hep-ph]`.

[238] M. Czakon and A. Mitov, "NNLO corrections to top pair production at hadron colliders: the quark-gluon reaction", *JHEP* **01** (2013) 080, `arXiv:1210.6832 [hep-ph]`.

[239] M. Czakon, P. Fiedler, and A. Mitov, "Total Top-Quark Pair-Production Cross Section at Hadron Colliders Through $O(\alpha_S^4)$", *Phys. Rev. Lett.* **110** (2013) 252004, `arXiv:1303.6254 [hep-ph]`.

[240] M. Czakon and A. Mitov, "Top++: A Program for the Calculation of the Top-Pair Cross-Section at Hadron Colliders", *Comput. Phys. Commun.* **185** (2014) 2930, `arXiv:1112.5675 [hep-ph]`.

[241] S. Frixione, E. Laenen, P. Motylinski, B. R. Webber, and C. D. White, "Single-top hadroproduction in association with a W boson", *JHEP* **07** (2008) 029, `arXiv:0805.3067 [hep-ph]`.

[242] N. Kidonakis, "Two-loop soft anomalous dimensions for single top quark associated production with a W- or H-", *Phys. Rev. D* **82** (2010) 054018, `arXiv:1005.4451 [hep-ph]`.

[243] N. Kidonakis, "Top Quark Production", in *Helmholtz International Summer School on Physics of Heavy Quarks and Hadrons*, pp. 139–168. 2014. `arXiv:1311.0283 [hep-ph]`.

[244] M. Aliev, H. Lacker, U. Langenfeld, S. Moch, P. Uwer, and M. Wiedermann, "HATHOR: HAdronic Top and Heavy quarks crOss section calculatoR", *Comput. Phys. Commun.* **182** (2011) 1034–1046, `arXiv:1007.1327 [hep-ph]`.

[245] P. Kant, O. Kind, T. Kintscher, T. Lohse, T. Martini, S. Mölbitz, P. Rieck, and P. Uwer, "HatHor for single top-quark production: Updated predictions and uncertainty estimates for single top-quark production in hadronic collisions", *Comput. Phys. Commun.* **191** (2015) 74–89, `arXiv:1406.4403 [hep-ph]`.

[246] **ATLAS** Collaboration, G. Aad *et al.*, "The performance of the jet trigger for the ATLAS detector during 2011 data taking", *Eur. Phys. J. C* **76** no. 10, (2016) 526, `arXiv:1606.07759 [hep-ex]`.

[247] "2015 start-up trigger menu and initial performance assessment of the ATLAS trigger using Run-2 data", Tech. Rep. ATL-DAQ-PUB-2016-001, CERN, Geneva, Mar, 2016. `https://cds.cern.ch/record/2136007`.

[248] **ATLAS** Collaboration, "Trigger Menu in 2016", Tech. Rep. ATL-DAQ-PUB-2017-001, CERN, Geneva, Jan, 2017. `https://cds.cern.ch/record/2242069`.

[249] **ATLAS** Collaboration, "Trigger Menu in 2017", Tech. Rep. ATL-DAQ-PUB-2018-002, CERN, Geneva, Jun, 2018. `https://cds.cern.ch/record/2625986`.

[250] **ATLAS** Collaboration, "Trigger menu in 2018", Tech. Rep. ATL-DAQ-PUB-2019-001, CERN, Geneva, Oct, 2019. `https://cds.cern.ch/record/2693402`.

[251] **ATLAS** Collaboration, G. Aad *et al.*, "Properties of jet fragmentation using charged particles measured with the ATLAS detector in pp collisions at $\sqrt{s} = 13$ TeV", *Phys. Rev. D* **100** no. 5, (2019) 052011, `arXiv:1906.09254 [hep-ex]`.

[252] J. H. Friedman, "Data analysis techniques for high energy particle physics", Oct, 1974. `https://cds.cern.ch/record/695770`.

[253] **ATLAS** Collaboration, G. Aad *et al.*, "Performance of the ATLAS muon triggers in Run 2", *JINST* **15** no. 09, (2020) P09015, `arXiv:2004.13447 [physics.ins-det]`.

[254] D. Casadei, "Estimating the selection efficiency", *JINST* **7** (2012) P08021, `arXiv:0908.0130 [physics.data-an]`.

[255] J. R. Klein and A. Roodman, "Blind analysis in nuclear and particle physics", *Annual Review of Nuclear and Particle Science* **55** no. 1, (2005) 141–163, `https://doi.org/10.1146/annurev.nucl.55.090704.151521`.

[256] S. Dulat *et al.*, "New parton distribution functions from a global analysis of quantum chromodynamics", *Phys. Rev. D* **93** no. 3, (2016) 033006, `arXiv:1506.07443 [hep-ph]`.

[257] **H1, ZEUS** Collaboration, H. Abramowicz *et al.*, "Combination of measurements of inclusive deep inelastic $e^{\pm}p$ scattering cross sections and QCD analysis of HERA data", *Eur. Phys. J. C* **75** no. 12, (2015) 580, `arXiv:1506.06042 [hep-ex]`.

[258] **ATLAS** Collaboration, "Improvements in $t\bar{t}$ modelling using NLO+PS Monte Carlo generators for Run2", Jul, 2018. `https://cds.cern.ch/record/2630327`.

[259] R. Frederix, S. Frixione, V. Hirschi, D. Pagani, H. S. Shao, and M. Zaro, "The automation of next-to-leading order electroweak calculations", *JHEP* **07** (2018) 185, `arXiv:1804.10017 [hep-ph]`.

[260] M. Bahr *et al.*, "Herwig++ Physics and Manual", *Eur. Phys. J. C* **58** (2008) 639–707, `arXiv:0803.0883 [hep-ph]`.

[261] J. Bellm *et al.*, "Herwig 7.0/Herwig++ 3.0 release note", *Eur. Phys. J. C* **76** no. 4, (2016) 196, `arXiv:1512.01178 [hep-ph]`.

[262] L. A. Harland-Lang, A. D. Martin, P. Motylinski, and R. S. Thorne, "Parton distributions in the LHC era: MMHT 2014 PDFs", *Eur. Phys. J. C* **75** no. 5, (2015) 204, `arXiv:1412.3989 [hep-ph]`.

[263] T. Junk, "Confidence level computation for combining searches with small statistics", *Nucl. Instrum. Meth. A* **434** (1999) 435–443, `arXiv:hep-ex/9902006`.

[264] **LEP Working Group for Higgs boson searches, ALEPH, DELPHI, L3, OPAL** Collaboration, R. Barate *et al.*, "Search for the standard model Higgs boson at LEP", *Phys. Lett. B* **565** (2003) 61–75, `arXiv:hep-ex/0306033`.

[265] R. J. Barlow and C. Beeston, "Fitting using finite Monte Carlo samples", *Comput. Phys. Commun.* **77** (1993) 219–228.

[266] **ROOT** Collaboration, K. Cranmer, G. Lewis, L. Moneta, A. Shibata, and W. Verkerke, "HistFactory: A tool for creating statistical models for use with RooFit and RooStats", Tech. Rep. CERN-OPEN-2012-016, New York U., New York, Jan, 2012. `https://cds.cern.ch/record/1456844`.

[267] W. Verkerke and D. P. Kirkby, "The RooFit toolkit for data modeling", *eConf* **C0303241** (2003) MOLT007, `arXiv:physics/0306116`.

[268] L. Moneta, K. Cranmer, G. Schott, and W. Verkerke, "The RooStats project", in *Proceedings of the 13th International Workshop on Advanced Computing and Analysis Techniques in Physics Research. February 22-27*, p. 57. Jan., 2010. `arXiv:1009.1003 [physics.data-an]`.

[269] **RooStats Team** Collaboration, G. Schott, "RooStats for Searches", in *PHYSTAT 2011*, pp. 199–208. CERN, Geneva, 2011. `arXiv:1203.1547 [physics.data-an]`.

[270] G. Cowan, K. Cranmer, E. Gross, and O. Vitells, "Asymptotic formulae for likelihood-based tests of new physics", *Eur. Phys. J. C* **71** (2011) 1554, `arXiv:1007.1727 [physics.data-an]`. [Erratum: Eur.Phys.J.C 73, 2501 (2013)].

[271] E. Gross, "LHC Statistics for Pedestrians", 2008. `https://cds.cern.ch/record/1099994`.

[272] A. L. Read, "Modified frequentist analysis of search results (The CL(s) method)", in *Workshop on Confidence Limits*. 8, 2000.

[273] S. S. Wilks, "The large-sample distribution of the likelihood ratio for testing composite hypotheses", *The Annals of Mathematical Statistics* **9** no. 1, (1938) 60–62. `http://www.jstor.org/stable/2957648`.

[274] A. Wald, "Tests of statistical hypotheses concerning several parameters when the number of observations is large", *Transactions of the American Mathematical Society* **54** no. 3, (1943) 426–482. `http://www.jstor.org/stable/1990256`.

[275] **ATLAS** Collaboration, G. Aad *et al.*, "Performance of electron and photon triggers in ATLAS during LHC Run 2", *Eur. Phys. J. C* **80** no. 1, (2020) 47, `arXiv:1909.00761 [hep-ex]`.

[276] "High-Luminosity Large Hadron Collider (HL-LHC): Technical Design Report V. 0.1", 2017.

[277] **ATLAS** Collaboration, "Prospects for the search for additional Higgs bosons in the ditau final state with the ATLAS detector at HL-LHC", Dec, 2018. `https://cds.cern.ch/record/2652284`.

[278] **FCC** Collaboration, A. Abada *et al.*, "FCC-hh: The Hadron Collider: Future Circular Collider Conceptual Design Report Volume 3", *Eur. Phys. J. ST* **228** no. 4, (2019) 755–1107.

[279] S. Albrand, J. Fulachier, and F. Lambert, "The ATLAS metadata interface", *J. Phys. Conf. Ser.* **219** (2010) 042030.

[280] **ATLAS** Collaboration, G. Aad *et al.*, "ATLAS data quality operations and performance for 2015–2018 data-taking", *JINST* **15** no. 04, (2020) P04003, `arXiv:1911.04632 [physics.ins-det]`.

Appendices

A. Tau Track Selection

A.1. Track Selection Samples

To train and validate the RNN based track classification algorithms, two sets of samples are used. True tau jets are extracted from Drell-Yan processes simulated by the decay of off-shell γ^* decays in pairs of taus, while QCD jets faking hadronic tau decays are taken from di-jet samples. A list of samples is provided in Table A.1.1.

DSID	Sample Name	Production Tags
Drell-Yan $\gamma^* \to \tau\tau$		
425200	Pythia8EvtGen_A14NNPDF23LO_Gammatautau_MassWeight	e5468_s3126_r10376
Di-jet		
361021	Pythia8EvtGen_A14NNPDF23LO_jetjet_JZ1W	e3569_s3126_r10376
361022	Pythia8EvtGen_A14NNPDF23LO_jetjet_JZ2W	e3668_s3126_r10376
361023	Pythia8EvtGen_A14NNPDF23LO_jetjet_JZ3W	e3668_s3126_r10376
361025	Pythia8EvtGen_A14NNPDF23LO_jetjet_JZ5W	e3668_s3126_r10397
361024	Pythia8EvtGen_A14NNPDF23LO_jetjet_JZ4W	e3668_s3126_r10397
361026	Pythia8EvtGen_A14NNPDF23LO_jetjet_JZ6W	e3569_s3126_r10397

Table A.1.1.: List of samples used in track selection studies. The string of tags in the last column encode the specific configuration used for event generation (e-tag), simulation (s-tag) and event reconstruction (r-tag) [279].

A.2. Additional Track Selection Input Variables

Figure A.2.1 shows the distributions of transformed input variables that are used to train the RNNs for track classification and selection.
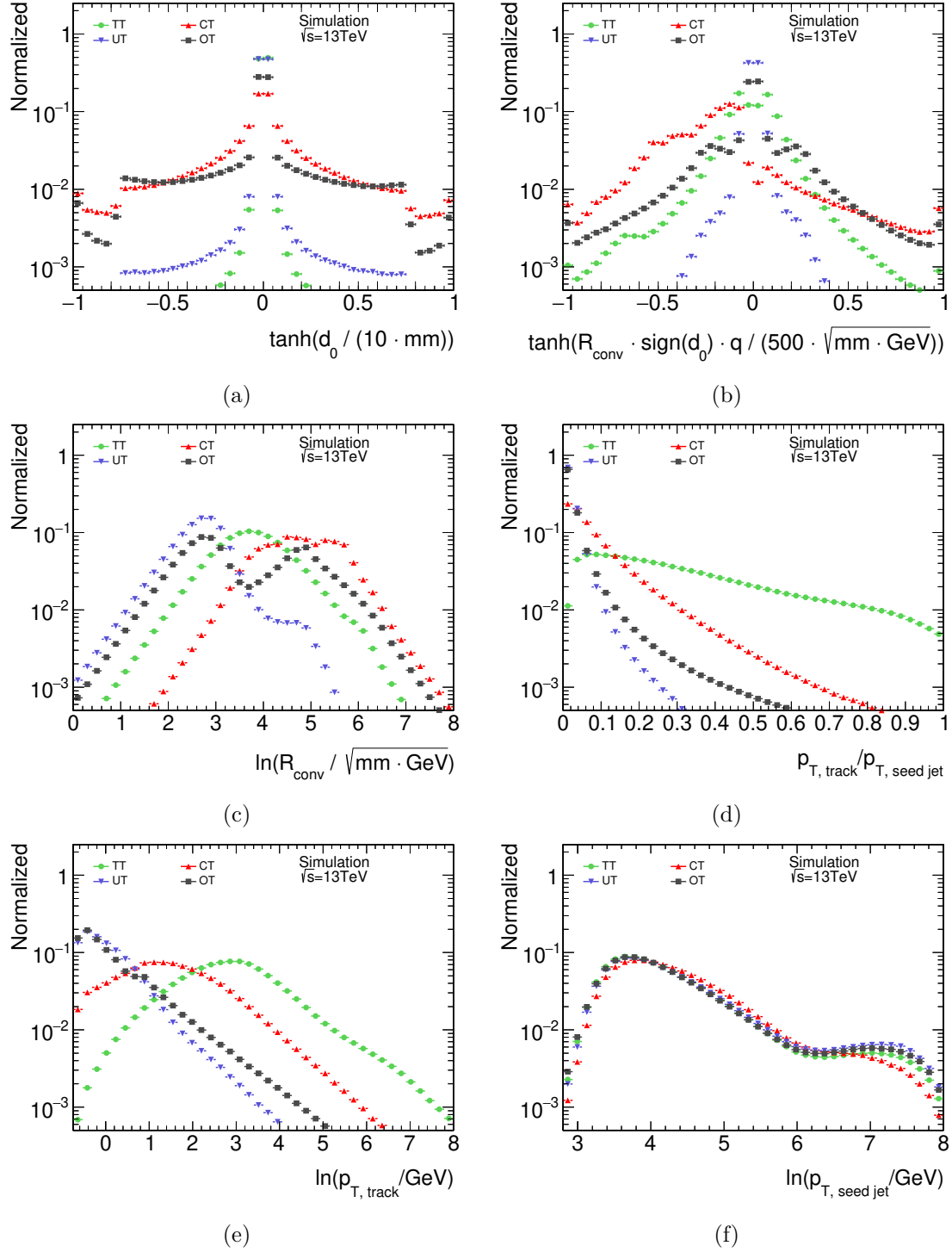
Figure A.2.1.: Distributions of transformed input variables for track selection RNN train-ing. Figure (a) and (b) shows d_0 and $R_{conv} \cdot \text{sign}(d_0) \cdot q$ scaled and trans-formed via a hyperbolic tangent function, while R_{conv}, $p_{T,\text{track}}$, and $p_{T,\text{seed jet}}$ in Figure (c), (e), and (f) are transformed by taking the logarithm. An addi-tional input variable is derived from the ratio of the transverse momentum of the track and seed jet, shown in Figure (d).

B. Higgs Boson Search

B.1. Analysis Setup and Configurations

This section provides an overview of the tool configurations applied in the Higgs search analysis according to the nomenclature used at ATLAS. Below are lists containing the full names of the GRLs, single tau, and di-jet triggers used throughout the analysis.

Good Run Lists: For each data-taking period, a specific GRL in XML format is provided with the following full names according to the ATLAS naming conventions:

- 2015:
  data15_13TeV.periodAllYear_DetStatus-v89-pro21-02
  _Unknown_PHYS_StandardGRL_All_Good_25ns.xml

- 2016:
  data16_13TeV.periodAllYear_DetStatus-v89-pro21-01
  _DQDefects-00-02-04_PHYS_StandardGRL_All_Good_25ns.xml

- 2017:
  data17_13TeV.periodAllYear_DetStatus-v99-pro22-01
  _Unknown_PHYS_StandardGRL_All_Good_25ns_Triggerno17e33prim.xml

- 2018:
  data18_13TeV.periodAllYear_DetStatus-v102-pro22-04
  _Unknown_PHYS_StandardGRL_All_Good_25ns_Triggerno17e33prim.xml

Triggers used in the Analysis: The pre-selection applied in the analysis requires that the events were triggered by one of the single tau (applied in signal and validation regions) or single-jet triggers (applied in di-jet control region). Trigger names and transverse momentum thresholds applied on the selected trigger objects vary for different data-taking periods. Tables B.1.1 and B.1.2 lists the full names according to the ATLAS naming conventions of the singe tau and jet triggers which were active during the data-taking periods.

Period	ATLAS single-tau trigger name
2015-2016	HLT_tau80_medium1_tracktwo_L1TAU60
	HLT_tau125_medium1_tracktwo
	HLT_tau160_medium1_tracktwo
2017	HLT_tau160_medium1_tracktwo
	HLT_tau160_medium1_tracktwo_L1TAU100
2018	HLT_tau160_medium1_tracktwoEF_L1TAU100

Table B.1.1.: List of single-tau triggers with full ATLAS trigger names. Some of the high-level triggers share the same threshold at the HLT stage but differ in track requirements or L1 trigger selections.

Period	ATLAS jet trigger name
2015-2016	HLT_j380, HLT_j360, HLT_j260, HLT_j175, HLT_j110, HLT_j85, HLT_j60, HLT_j55, HLT_j45, HLT_j35, HLT_j25, HLT_j15, HLT_j0_perf_L1RD0_FILLED
2017-2018	HLT_j420, HLT_j400, HLT_j380, HLT_j360, HLT_j260, HLT_j175, HLT_j110, HLT_j85, HLT_j60, HLT_j45, HLT_j35, HLT_j25, HLT_j15, HLT_j0_perf_L1RD0_FILLED

Table B.1.2.: List of jet triggers with full ATLAS trigger names. The list of triggers active during 2015-2016 and 2017-2018 significantly overlap. However, due to the higher instantaneous luminosity achieved in later runs, more high p_T threshold triggers were active during the second half of Run-2 data-taking.

B.2. List of Data and Monte Carlo Samples

A list of data runs from the full Run-2 are given in Tables B.2.1 and B.2.1. The runs are listed in ascending order and clustered according to the different production tags used during event reconstruction (r- and f-tag) and derivation (p-tag). Sets of data samples are identified by the unique run number. All data samples are derived from the main physics stream of the data processing pipeline [280].

The Monte Carlo simulated samples are split into three statistically independent campaigns with configurations corresponding to different data-taking periods. Tables B.2.3 to B.2.17 list all Monte Carlo samples used for background estimation, their respective production cross-section, generator filter efficiencies, and higher-order k-factor corrections. Samples used as signal templates in the search for additional Higgs bosons are listed in Tables B.2.18 to B.2.20 for Higgs bosons produced via *b*-associated production and in Tables B.2.21 to B.2.24 for gluon-gluon fusion production.

The production tags listed in the tables encode specific configurations of the algorithms deployed during the event generation (e-tag), detector simulation (s-tag), event reconstruction (r-tag), and derivation (p-tag) step [279]. Individual simulated processes are associated with a unique 6 digit DSID number.

Data Taking Period	Run Number Range	Production Tags
2015	266904 - 276161	r9264_p3083_p3760
	276176, 276181	r9412_p3083_p3760
	276183 - 284484	r9264_p3083_p3760
2016	297730 - 311481	r9264_p3083_p3760
2017	325713	r10260_p3399_p3760
	325789 - 327265	r10250_p3399_p3760
	327342 - 328393	r10203_p3399_p3760
	329385	r10202_p3399_p3760
	329484 - 330470	r10203_p3399_p3760
	330857	r10202_p3399_p3760
	330874 - 332304	r10203_p3399_p3760
	332720	r10202_p3399_p3760
	332896 - 334779	r10203_p3399_p3760
	334842, 334849	r10258_p3399_p3760
	334878	r10259_p3399_p3760
	334890 - 334960	r10258_p3399_p3760
	334993	r10259_p3399_p3760
	335016 - 336506	r10258_p3399_p3760
	336548	r10259_p3399_p3760
	336567	r10258_p3399_p3760
	336630	r10259_p3399_p3760
	336678 - 336782	r10258_p3399_p3760
	336832	r10259_p3399_p3760
	336852 - 337451	r10258_p3399_p3760
	337491	r10259_p3399_p3760
	337542 - 338183	r10258_p3399_p3760
	338220	r10259_p3399_p3760
	338259 - 338834	r10258_p3399_p3760
	338846	r10250_p3399_p3760
	338897 - 339346	r10258_p3399_p3760
	339387	r10259_p3399_p3760
	339396 - 339957	r10258_p3399_p3760
	340030 - 340453	r10426_p3399_p3760
	341294 - 341649	r10803_p3630_p3760

Table B.2.1.: List of data runs from the 2015 - 2017 data-taking period analyzed in the Higgs search. Run ranges are given for the different production tags used during the event reconstruction and derivation.

Data Taking Period	Run Number Range	Production Tags
2018	348885 - 349592	f937_m1972_p3757
	349637 - 349842	f937_m1979_p3757
	349944 - 350144	f933_m1960_p3757
	350160 - 350531	f934_m1960_p3757
	350682 - 350848	f936_m1972_p3757
	350880 - 351628	f937_m1972_p3757
	351636 - 352514	f938_m1979_p3757
	354124 - 354944	f947_m1993_p3757
	355008 - 355273	f943_m1993_p3757
	355331 - 355468	f948_m1993_p3757
	355529	f948_m1999_p3757
	355544 - 355848	f950_m1999_p3757
	355861 - 356124	f950_m2004_p3757
	356177 - 357077	f956_m2004_p3757
	357193 - 357293	f958_m2010_p3757
	357355	f960_m2015_p3757
	357409 - 357620	f958_m2010_p3757
	357679 - 357772	f958_m2015_p3757
	357821 - 358031	f961_m2015_p3757
	358096 - 358215	f966_m2020_p3757
	358233	f961_m2015_p3757
	358300	f966_m2020_p3757
	358325 - 358577	f961_m2015_p3757
	358615, 358656	f961_m2020_p3757
	358985 - 359823	f964_m2020_p3757
	359872 - 360402	f969_m2020_p3757
	360414	f971_m2020_p3757
	361635 - 361696	f979_m2025_p3757
	361738 - 361862	f988_m2025_p3757
	362204 - 362345	f988_m2032_p3757
	362354 - 363033	f993_m2032_p3757
	363096	f1005_m2037_p3757
	363129	f993_m2032_p3757
	363198 - 363400	f997_m2032_p3757
	363664, 363710	f1001_m2037_p3757
	363738	f1006_m2037_p3757
	363830 - 364214	f1002_m2037_p3757

Table B.2.2.: List of data runs from the 2018 data-taking period analyzed in the Higgs search. Run ranges are given for the different production tags used during the event reconstruction and derivation.

DSID	Campaign	ATLAS Sample Name	Production Tags	σ [pb]	ϵ_{Filter}	k-Factor	N_{Events}
Drell-Yan $Z/\gamma^* \to e^+e^-$ mass sliced							
301000	MC16a	PowhegPythia8EvtGen_AZNLOCTEQ6L1_DYee_120M180	e3649_s3126_r9364_p3749				1496000
	MC16d		e3649_s3126_r10201_p3749	17.5	1.00	1.00	1615000
	MC16e		e3649_s3126_r10724_p3759				2482000
301001	MC16a	PowhegPythia8EvtGen_AZNLOCTEQ6L1_DYee_180M250	e3649_s3126_r9364_p3759				900000
	MC16d		e3649_s3126_r10201_p3749	2.92	1.00	1.00	957000
	MC16e		e3649_s3126_r10724_p3759				1500000
301002	MC16a	PowhegPythia8EvtGen_AZNLOCTEQ6L1_DYee_250M400	e3649_s3126_r9364_p3759				1200000
	MC16d		e3649_s3126_r10201_p3749	1.08	1.00	1.00	1240000
	MC16e		e3649_s3126_r10724_p3759				1998000
301003	MC16a	PowhegPythia8EvtGen_AZNLOCTEQ6L1_DYee_400M600	e3649_s3126_r9364_p3749				900000
	MC16d		e3649_s3126_r10201_p3749	0.196	1.00	1.00	925000
	MC16e		e3649_s3126_r10724_p3759				1495000
301004	MC16a	PowhegPythia8EvtGen_AZNLOCTEQ6L1_DYee_600M800	e3649_s3126_r9364_p3749				510000
	MC16d		e3649_s3126_r10201_p3749	3.74×10^{-2}	1.00	1.00	536000
	MC16e		e3649_s3126_r10724_p3759				850000
301005	MC16a	PowhegPythia8EvtGen_AZNLOCTEQ6L1_DYee_800M1000	e3649_s3126_r9364_p3749				250000
	MC16d		e3649_s3126_r10201_p3749	1.06×10^{-2}	1.00	1.00	262000
	MC16e		e3649_s3126_r10724_p3759				420000
301006	MC16a	PowhegPythia8EvtGen_AZNLOCTEQ6L1_DYee_1000M1250	e3649_s3126_r9364_p3749				100000
	MC16d		e3649_s3126_r10201_p3749	4.26×10^{-3}	1.00	1.00	112000
	MC16e		e3649_s3126_r10724_p3759				100000
301007	MC16a	PowhegPythia8EvtGen_AZNLOCTEQ6L1_DYee_1250M1500	e3649_s3126_r9364_p3749				50000
	MC16d		e3649_s3126_r10201_p3749	1.42×10^{-3}	1.00	1.00	62000
	MC16e		e3649_s3126_r10724_p3759				90000

Table B.2.3.: List of simulated Monte Carlo samples used in the search for additional Higgs bosons.

DSID	Campaign	ATLAS Sample Name	Production Tags	σ [pb]	ϵ_{Filter}	k-Factor	N_{Events}
Drell-Yan $Z/\gamma^* \to e^+e^-$ mass sliced							
301008	MC16a		e3649_s3126_r9364_p3749				50000
	MC16d	PowhegPythia8EvtGen_AZNLOCTEQ6L1_DYee_1500M1750	e3649_s3126_r10201_p3749	5.45×10^{-4}	1.00	1.00	62000
	MC16e		e3649_s3126_r10724_p3759				90000
301009	MC16a		e3649_s3126_r9364_p3749				100000
	MC16d	PowhegPythia8EvtGen_AZNLOCTEQ6L1_DYee_1750M2000	e3649_s3126_r10201_p3749	2.30×10^{-4}	1.00	1.00	125000
	MC16e		e3649_s3126_r10724_p3759				170000
301010	MC16a		e3649_s3126_r9364_p3749				50000
	MC16d	PowhegPythia8EvtGen_AZNLOCTEQ6L1_DYee_2000M2250	e3649_s3126_r10201_p3749	1.04×10^{-4}	1.00	1.00	62000
	MC16e		e3649_s3126_r10724_p3759				90000
301011	MC16a		e3649_s3126_r9364_p3749				50000
	MC16d	PowhegPythia8EvtGen_AZNLOCTEQ6L1_DYee_2250M2500	e3649_s3126_r10201_p3749	4.94×10^{-5}	1.00	1.00	62000
	MC16e		e3649_s3126_r10724_p3759				90000
301012	MC16a		e3649_s3126_r9364_p3749				50000
	MC16d	PowhegPythia8EvtGen_AZNLOCTEQ6L1_DYee_2500M2750	e3649_s3126_r10201_p3749	2.45×10^{-5}	1.00	1.00	62000
	MC16e		e3649_s3126_r10724_p3759				90000
301013	MC16a		e3649_s3126_r9364_p3749				50000
	MC16d	PowhegPythia8EvtGen_AZNLOCTEQ6L1_DYee_2750M3000	e3649_s3126_r10201_p3749	1.25×10^{-5}	1.00	1.00	62000
	MC16e		e3649_s3126_r10724_p3759				90000
301014	MC16a		e3649_s3126_r9364_p3749				50000
	MC16d	PowhegPythia8EvtGen_AZNLOCTEQ6L1_DYee_3000M3500	e3649_s3126_r10201_p3749	1.00×10^{-5}	1.00	1.00	50000
	MC16e		e3649_s3126_r10724_p3759				90000
301015	MC16a		e3649_s3126_r9364_p3749				50000
	MC16d	PowhegPythia8EvtGen_AZNLOCTEQ6L1_DYee_3500M4000	e3649_s3126_r10201_p3749	2.93×10^{-6}	1.00	1.00	56000
	MC16e		e3649_s3126_r10724_p3759				90000

Table B.2.4.: List of simulated Monte Carlo samples used in the search for additional Higgs bosons.

DSID	Campaign	ATLAS Sample Name	Production Tags	σ [pb]	ϵ_Filter	k-Factor	N_Events
Drell-Yan $Z/\gamma^* \to e^+e^-$ mass sliced							
301016	MC16a		e3649_s3126_r9364_p3749				50000
	MC16d	PowhegPythia8EvtGen_AZNLOCTEQ6L1_DYee_4000M4500	e3649_s3126_r10201_p3749	8.98×10^{-7}	1.00	1.00	58000
	MC16e		e3649_s3126_r10724_p3759				90000
301017	MC16a		e3649_s3126_r9364_p3749				50000
	MC16d	PowhegPythia8EvtGen_AZNLOCTEQ6L1_DYee_4500M5000	e3649_s3126_r10201_p3749	2.81×10^{-7}	1.00	1.00	61000
	MC16e		e3649_s3126_r10724_p3759				90000
301018	MC16a		e3649_s3126_r9364_p3749				50000
	MC16d	PowhegPythia8EvtGen_AZNLOCTEQ6L1_DYee_5000M	e3649_s3126_r10201_p3749	1.26×10^{-7}	1.00	1.00	62000
	MC16e		e3649_s3126_r10724_p3759				90000
Drell-Yan $Z/\gamma^* \to \mu^+\mu^-$ mass sliced							
301020	MC16a		e3649_s3126_r9364_p3749				2000000
	MC16d	PowhegPythia8EvtGen_AZNLOCTEQ6L1_DYmumu_120M180	e3649_s3126_r10201_p3749	17.5	1.00	1.00	1486000
	MC16e		e3649_s3126_r10724_p3759				3318000
301021	MC16a		e3649_s3126_r9364_p3749				1150000
	MC16d	PowhegPythia8EvtGen_AZNLOCTEQ6L1_DYmumu_180M250	e3649_s3126_r10201_p3749	2.92	1.00	1.00	898000
	MC16e		e3649_s3126_r10724_p3759				1899000
301022	MC16a		e3649_s3126_r9364_p3749				1345000
	MC16d	PowhegPythia8EvtGen_AZNLOCTEQ6L1_DYmumu_250M400	e3649_s3126_r10201_p3749	1.08	1.00	1.00	1195000
	MC16e		e3649_s3126_r10724_p3759				2249000
301023	MC16a		e3649_s3126_r9364_p3749				1000000
	MC16d	PowhegPythia8EvtGen_AZNLOCTEQ6L1_DYmumu_400M600	e3649_s3126_r10201_p3749	0.196	1.00	1.00	900000
	MC16e		e3649_s3126_r10724_p3759				1660000
301024	MC16a		e3649_s3126_r9364_p3749				600000
	MC16d	PowhegPythia8EvtGen_AZNLOCTEQ6L1_DYmumu_600M800	e3649_s3126_r10201_p3749	3.74×10^{-2}	1.00	1.00	495000
	MC16e		e3649_s3126_r10724_p3759				1000000

Table B.2.5.: List of simulated Monte Carlo samples used in the search for additional Higgs bosons.

DSID	Campaign	ATLAS Sample Name	Production Tags	σ [pb]	ϵ_{Filter}	k-Factor	N_{Events}
Drell-Yan $Z/\gamma^* \to \mu^+\mu^-$ mass sliced							
301025	MC16a	PowhegPythia8EvtGen_AZNLOCTEQ6L1_DYmumu_800M1000	e3649_s3126_r9364_p3749				300000
	MC16d		e3649_s3126_r10201_p3749	1.06×10^{-2}	1.00	1.00	250000
	MC16e		e3649_s3126_r10724_p3759				495000
301026	MC16a	PowhegPythia8EvtGen_AZNLOCTEQ6L1_DYmumu_1000M1250	e3649_s3126_r9364_p3749				150000
	MC16d		e3649_s3126_r10201_p3749	4.26×10^{-3}	1.00	1.00	100000
	MC16e		e3649_s3126_r10724_p3759				250000
301027	MC16a	PowhegPythia8EvtGen_AZNLOCTEQ6L1_DYmumu_1250M1500	e3649_s3126_r9364_p3749				100000
	MC16d		e3649_s3126_r10201_p3749	1.42×10^{-3}	1.00	1.00	50000
	MC16e		e3649_s3126_r10724_p3759				170000
301028	MC16a	PowhegPythia8EvtGen_AZNLOCTEQ6L1_DYmumu_1500M1750	e3649_s3126_r9364_p3749				100000
	MC16d		e3649_s3126_r10201_p3749	5.45×10^{-4}	1.00	1.00	50000
	MC16e		e3649_s3126_r10724_p3759				170000
301029	MC16a	PowhegPythia8EvtGen_AZNLOCTEQ6L1_DYmumu_1750M2000	e3649_s3126_r9364_p3749				100000
	MC16d		e3649_s3126_r10201_p3749	2.30×10^{-4}	1.00	1.00	50000
	MC16e		e3649_s3126_r10724_p3759				170000
301030	MC16a	PowhegPythia8EvtGen_AZNLOCTEQ6L1_DYmumu_2000M2250	e3649_s3126_r9364_p3749				100000
	MC16d		e3649_s3126_r10201_p3749	1.04×10^{-4}	1.00	1.00	50000
	MC16e		e3649_s3126_r10724_p3759				170000
301031	MC16a	PowhegPythia8EvtGen_AZNLOCTEQ6L1_DYmumu_2250M2500	e3649_s3126_r9364_p3749				100000
	MC16d		e3649_s3126_r10201_p3749	4.94×10^{-5}	1.00	1.00	50000
	MC16e		e3649_s3126_r10724_p3759				170000
301032	MC16a	PowhegPythia8EvtGen_AZNLOCTEQ6L1_DYmumu_2500M2750	e3649_s3126_r9364_p3749				100000
	MC16d		e3649_s3126_r10201_p3749	2.45×10^{-5}	1.00	1.00	50000
	MC16e		e3649_s3126_r10724_p3759				170000

Table B.2.6.: List of simulated Monte Carlo samples used in the search for additional Higgs bosons.

DSID	Campaign	ATLAS Sample Name	Production Tags	σ [pb]	ϵ_{Filter}	k-Factor	N_{Events}
Drell-Yan $Z/\gamma^* \to \mu^+\mu^-$ mass sliced							
	MC16a	PowhegPythia8EvtGen_AZNLOCTEQ6L1_DYmumu_2750M3000	e3649_s3126_r9364_p3749				100000
301033	MC16d		e3649_s3126_r10201_p3749	1.25×10^{-5}	1.00	1.00	50000
	MC16e		e3649_s3126_r10724_p3759				170000
	MC16a	PowhegPythia8EvtGen_AZNLOCTEQ6L1_DYmumu_3000M3500	e3649_s3126_r9364_p3749				100000
301034	MC16d		e3649_s3126_r10201_p3749	1.00×10^{-5}	1.00	1.00	50000
	MC16e		e3649_s3126_r10724_p3759				170000
	MC16a	PowhegPythia8EvtGen_AZNLOCTEQ6L1_DYmumu_3500M4000	e3649_s3126_r9364_p3749				100000
301035	MC16d		e3649_s3126_r10201_p3749	2.93×10^{-6}	1.00	1.00	50000
	MC16e		e3649_s3126_r10724_p3759				170000
	MC16a	PowhegPythia8EvtGen_AZNLOCTEQ6L1_DYmumu_4000M4500	e3649_s3126_r9364_p3759				100000
301036	MC16d		e3649_s3126_r10201_p3749	8.98×10^{-7}	1.00	1.00	50000
	MC16e		e3649_s3126_r10724_p3759				170000
	MC16a	PowhegPythia8EvtGen_AZNLOCTEQ6L1_DYmumu_4500M5000	e3649_s3126_r9364_p3749				100000
301037	MC16d		e3649_s3126_r10201_p3749	2.81×10^{-7}	1.00	1.00	50000
	MC16e		e3649_s3126_r10724_p3759				170000
	MC16a	PowhegPythia8EvtGen_AZNLOCTEQ6L1_DYmumu_5000M	e3649_s3126_r9364_p3749				100000
301038	MC16d		e3649_s3126_r10201_p3749	1.26×10^{-7}	1.00	1.00	50000
	MC16e		e3649_s3126_r10724_p3759				170000
Drell-Yan $Z/\gamma^* \to \tau^+\tau^-$ mass sliced							
	MC16a	PowhegPythia8EvtGen_AZNLOCTEQ6L1_DYtautau_120M180	e3649_s3126_r9364_p3749				450000
301040	MC16d		e3649_s3126_r10201_p3749	17.5	1.00	1.00	450000
	MC16e		e3649_s3126_r10724_p3759				750000
	MC16a	PowhegPythia8EvtGen_AZNLOCTEQ6L1_DYtautau_180M250	e3649_s3126_r9364_p3749				423200
301041	MC16d		e3649_s3126_r10201_p3759	2.92	1.00	1.00	450000
	MC16e		e3649_s3126_r10724_p3759				750000

Table B.2.7.: List of simulated Monte Carlo samples used in the search for additional Higgs bosons.

DSID	Campaign	ATLAS Sample Name	Production Tags	σ [pb]	ϵ_{Filter}	k-Factor	N_{Events}
Drell-Yan $Z/\gamma^* \to \tau^+\tau^-$ mass sliced							
301042	MC16a		e3649_s3126_r9364_p3749				444000
	MC16d	PowhegPythia8EvtGen_AZNLOCTEQ6L1_DYtautau_250M400	e3649_s3126_r10201_p3749	1.08	1.00	1.00	450000
	MC16e		e3649_s3126_r10724_p3759				750000
301043	MC16a		e3649_s3126_r9364_p3749				599800
	MC16d	PowhegPythia8EvtGen_AZNLOCTEQ6L1_DYtautau_400M600	e3649_s3126_r10201_p3749	0.196	1.00	1.00	450000
	MC16e		e3649_s3126_r10724_p3759				750000
301044	MC16a		e3649_s3126_r9364_p3749				450000
	MC16d	PowhegPythia8EvtGen_AZNLOCTEQ6L1_DYtautau_600M800	e3649_s3126_r10201_p3749	3.74×10^{-2}	1.00	1.00	450000
	MC16e		e3649_s3126_r10724_p3759				750000
301045	MC16a		e3649_s3126_r9364_p3749				450000
	MC16d	PowhegPythia8EvtGen_AZNLOCTEQ6L1_DYtautau_800M1000	e3649_s3126_r10201_p3759	1.06×10^{-2}	1.00	1.00	450000
	MC16e		e3649_s3126_r10724_p3759				750000
301046	MC16a		e3649_s3126_r9364_p3759				450000
	MC16d	PowhegPythia8EvtGen_AZNLOCTEQ6L1_DYtautau_1000M1250	e3649_s3126_r10201_p3749	4.26×10^{-3}	1.00	1.00	450000
	MC16e		e3649_s3126_r10724_p3759				750000
301047	MC16a		e3649_s3126_r9364_p3749				450000
	MC16d	PowhegPythia8EvtGen_AZNLOCTEQ6L1_DYtautau_1250M1500	e3649_s3126_r10201_p3749	1.42×10^{-3}	1.00	1.00	450000
	MC16e		e3649_s3126_r10724_p3759				580000
301048	MC16a		e3649_s3126_r9364_p3749				350000
	MC16d	PowhegPythia8EvtGen_AZNLOCTEQ6L1_DYtautau_1500M1750	e3649_s3126_r10201_p3749	5.45×10^{-4}	1.00	1.00	350000
	MC16e		e3649_s3126_r10724_p3759				588000
301049	MC16a		e3649_s3126_r9364_p3749				235000
	MC16d	PowhegPythia8EvtGen_AZNLOCTEQ6L1_DYtautau_1750M2000	e3649_s3126_r10201_p3759	2.30×10^{-4}	1.00	1.00	235000
	MC16e		e3649_s3126_r10724_p3759				400000

Table B.2.8.: List of simulated Monte Carlo samples used in the search for additional Higgs bosons.

DSID	Campaign	ATLAS Sample Name	Production Tags	σ [pb]	ϵ_{Filter}	k-Factor	N_{Events}
		Drell-Yan $Z/\gamma^* \to \tau^+\tau^-$ mass sliced					
301050	MC16a		e3649_s3126_r9364_p3749				450000
	MC16d	PowhegPythia8EvtGen_AZNLOCTEQ6L1_DYtautau_2000M2250	e3649_s3126_r10201_p3749	1.04×10^{-4}	1.00	1.00	450000
	MC16e		e3649_s3126_r10724_p3759				750000
301051	MC16a		e3649_s3126_r9364_p3749				350000
	MC16d	PowhegPythia8EvtGen_AZNLOCTEQ6L1_DYtautau_2250M2500	e3649_s3126_r10201_p3749	4.94×10^{-5}	1.00	1.00	350000
	MC16e		e3649_s3126_r10724_p3759				590000
301052	MC16a		e3649_s3126_r9364_p3749				350000
	MC16d	PowhegPythia8EvtGen_AZNLOCTEQ6L1_DYtautau_2500M2750	e3649_s3126_r10201_p3749	2.45×10^{-5}	1.00	1.00	350000
	MC16e		e3649_s3126_r10724_p3759				590000
301053	MC16a		e3649_s3126_r9364_p3749				350000
	MC16d	PowhegPythia8EvtGen_AZNLOCTEQ6L1_DYtautau_2750M3000	e3649_s3126_r10201_p3749	1.25×10^{-5}	1.00	1.00	350000
	MC16e		e3649_s3126_r10724_p3759				590000
301054	MC16a		e3649_s3126_r9364_p3749				350000
	MC16d	PowhegPythia8EvtGen_AZNLOCTEQ6L1_DYtautau_3000M3500	e3649_s3126_r10201_p3749	1.00×10^{-5}	1.00	1.00	350000
	MC16e		e3649_s3126_r10724_p3759				590000
301055	MC16a		e3649_s3126_r9364_p3759				400000
	MC16d	PowhegPythia8EvtGen_AZNLOCTEQ6L1_DYtautau_3500M4000	e3649_s3126_r10201_p3749	2.93×10^{-6}	1.00	1.00	400000
	MC16e		e3649_s3126_r10724_p3759				670000
301056	MC16a		e3649_s3126_r9364_p3749				315000
	MC16d	PowhegPythia8EvtGen_AZNLOCTEQ6L1_DYtautau_4000M4500	e3649_s3126_r10201_p3749	8.98×10^{-7}	1.00	1.00	315000
	MC16e		e3649_s3126_r10724_p3759				540000
301057	MC16a		e3649_s3126_r9364_p3749				350000
	MC16d	PowhegPythia8EvtGen_AZNLOCTEQ6L1_DYtautau_4500M5000	e3649_s3126_r10201_p3749	2.81×10^{-7}	1.00	1.00	350000
	MC16e		e3649_s3126_r10724_p3759				590000
301058	MC16a		e3649_s3126_r9364_p3749				350000
	MC16d	PowhegPythia8EvtGen_AZNLOCTEQ6L1_DYtautau_5000M	e3649_s3126_r10201_p3749	1.26×10^{-7}	1.00	1.00	350000
	MC16e		e3649_s3126_r10724_p3759				590000

Table B.2.9.: List of simulated Monte Carlo samples used in the search for additional Higgs bosons.

DSID	Campaign	ATLAS Sample Name	Production Tags	σ [pb]	ε_Filter	k-Factor	N_Events
Drell-Yan $Z/\gamma^* \to ll$ inclusive							
	MC16a		e3601_s3126_r9364_p3749				7942000
361106	MC16d	PowhegPythia8EvtGen_AZNLOCTEQ6l1_Zee	e3601_s3126_r10201_p3749	1.90×10^3	1.00	1.03	9932000
	MC16e		e3601_s3126_r10724_p3759				13061300
	MC16a		e3601_s3126_r9364_p3749				7987400
361107	MC16d	PowhegPythia8EvtGen_AZNLOCTEQ6l1_Zmumu	e3601_s3126_r10201_p3749	1.89×10^3	1.00	1.03	100666000
	MC16e		e3601_s3126_r10724_p3759				132536000
	MC16a		e3601_s3126_r9364_p3749				39495000
361108	MC16d	PowhegPythia8EvtGen_AZNLOCTEQ6l1_Ztautau	e3601_s3126_r10201_p3749	1.90×10^3	1.00	1.00	46082000
	MC16e		e3601_s3126_r10724_p3759				64740600
Diboson production with semi leptonic final state							
	MC16a		e5525_s3126_r9364_p3749				5400000
363355	MC16d	Sherpa_221_NNPDF30NNLO_ZqqZvv	e5525_s3126_r10201_p3749	15.6	0.277	1.00	5399000
	MC16e		e5525_s3126_r10724_p3759				8965000
	MC16a		e5525_s3126_r9364_p3749				5400000
363356	MC16d	Sherpa_221_NNPDF30NNLO_ZqqZll	e5525_s3126_r10201_p3749	15.6	0.141	1.00	5400000
	MC16e		e5525_s3126_r10724_p3759				8954000
	MC16a		e5525_s3126_r9364_p3749				6000000
363357	MC16d	Sherpa_221_NNPDF30NNLO_WqqZvv	e5525_s3126_r10201_p3759	6.8	1.00	1.00	5998800
	MC16e		e5525_s3126_r10724_p3759				9952000
	MC16a		e5525_s3126_r9364_p3749				5400000
363358	MC16d	Sherpa_221_NNPDF30NNLO_WqqZll	e5525_s3126_r10201_p3759	3.43	1.00	1.00	26911000
	MC16e		e5525_s3126_r10724_p3759				8964000
	MC16a		e5583_s3126_r9364_p3749				7194000
363359	MC16d	Sherpa_221_NNPDF30NNLO_WpqqWmlv	e5583_s3126_r10201_p3749	24.7	1.00	1.00	35904000
	MC16e		e5583_s3126_r10724_p3759				11946000
	MC16a		e5983_s3126_r9364_p3749				7188000
363360	MC16d	Sherpa_221_NNPDF30NNLO_WplvWmqq	e5983_s3126_r10201_p3749	24.7	1.00	1.00	14372000
	MC16e		e5983_s3126_r10724_p3759				11941000

Table B.2.10.: List of simulated Monte Carlo samples used in the search for additional Higgs bosons.

DSID	Campaign	ATLAS Sample Name	Production Tags	σ [pb]	ϵ_{Filter}	k-Factor	N_{Events}
Diboson production with semi leptonic final state							
363489	MC16a		e5525_s3126_r9364_p3749				7180000
	MC16d	Sherpa_221_NNPDF30NNLO_WlvZqq	e5525_s3126_r10201_p3749	11.4	1.00	1.00	35925000
	MC16e		e5525_s3126_r10724_p3759				11955000
Diboson production with fully leptonic final state							
364250	MC16a		e5894_s3126_r9364_p3749				17842900
	MC16d	Sherpa_222_NNPDF30NNLO_llll	e5894_s3126_r10201_p3749	1.25	1.00	1.00	35995900
	MC16e		e5894_s3126_r10724_p3759				25683900
Diboson production with fully leptonic final state							
364253	MC16a		e5916_s3126_r9364_p3749				15537900
	MC16d	Sherpa_222_NNPDF30NNLO_lllv	e5916_s3126_r10201_p3749	4.58	1.00	1.00	32113800
	MC16e		e5916_s3126_r10724_p3759				26789600
364254	MC16a		e5916_s3126_r9364_p3749				14996000
	MC16d	Sherpa_222_NNPDF30NNLO_llvv	e5916_s3126_r10201_p3749	12.5	1.00	1.00	29975000
	MC16e		e5916_s3126_r10724_p3759				24889000
364255	MC16a		e5916_s3126_r9364_p3749				5999000
	MC16d	Sherpa_222_NNPDF30NNLO_lvvv	e5916_s3126_r10201_p3749	3.23	1.00	1.00	11995000
	MC16e		e5916_s3126_r10724_p3759				9957000
$W^{\pm} \to \mu^{\pm}\nu_{\mu}$							
364156	MC16a		e5340_s3126_r9364_p3749				24950000
	MC16d	Sherpa_221_NNPDF30NNLO_Wmunu_MAXHTPTV0_70_CVetoBVeto	e5340_s3126_r10201_p3749	1.91×10^4	0.825	0.97	31111850
	MC16e		e5340_s3126_r10724_p3759				41275000
364157	MC16a		e5340_s3126_r9364_p3749				9993000
	MC16d	Sherpa_221_NNPDF30NNLO_Wmunu_MAXHTPTV0_70_CFilterBVeto	e5340_s3126_r10201_p3749	1.91×10^4	0.131	0.97	12252700
	MC16e		e5340_s3126_r10724_p3759				16542000

Table B.2.11.: List of simulated Monte Carlo samples used in the search for additional Higgs bosons.

DSID	Campaign	ATLAS Sample Name	Production Tags	σ [pb]	$\epsilon_{\mathrm{Filter}}$	k-Factor	N_{Events}
$W^\pm \to \mu^\pm \nu_\mu$							
	MC16a		e5340_s3126_r9364_p3749				17479200
364158	MC16d	Sherpa_221_NNPDF30NNLO_Wmunu_MAXHTPTV0_70_BFilter	e5340_s3126_r10201_p3749	1.91×10^4	4.46×10^{-2}	0.97	21655000
	MC16e		e5340_s3126_r10724_p3759				28985800
	MC16a		e5340_s3126_r9364_p3749				14964000
364159	MC16d	Sherpa_221_NNPDF30NNLO_Wmunu_MAXHTPTV70_140_CVetoBVeto	e5340_s3126_r10201_p3749	9.46×10^2	0.674	0.97	18620000
	MC16e		e5340_s3126_r10724_p3759				24839900
	MC16a		e5340_s3126_r9364_p3749				9975200
364160	MC16d	Sherpa_221_NNPDF30NNLO_Wmunu_MAXHTPTV70_140_CFilterBVeto	e5340_s3126_r10201_p3749	9.45×10^2	0.244	0.97	12459400
	MC16e		e5340_s3126_r10724_p3759				16538500
	MC16a		e5340_s3126_r9364_p3749				19915000
364161	MC16d	Sherpa_221_NNPDF30NNLO_Wmunu_MAXHTPTV70_140_BFilter	e5340_s3126_r10201_p3749	9.44×10^2	8.37×10^{-2}	0.97	25148250
	MC16e		e5340_s3126_r10724_p3759				33016200
	MC16a		e5340_s3126_r9364_p3749				10000000
364162	MC16d	Sherpa_221_NNPDF30NNLO_Wmunu_MAXHTPTV140_280_CVetoBVeto	e5340_s3126_r10201_p3749	3.40×10^2	0.6	0.97	12324250
	MC16e		e5340_s3126_r10724_p3759				16761000
	MC16a		e5340_s3126_r9364_p3749				13387300
364163	MC16d	Sherpa_221_NNPDF30NNLO_Wmunu_MAXHTPTV140_280_CFilterBVeto	e5340_s3126_r10201_p3749	3.40×10^2	0.293	0.97	16839250
	MC16e		e5340_s3126_r10724_p3759				22432300
	MC16a		e5340_s3126_r9364_p3749				25000000
364164	MC16d	Sherpa_221_NNPDF30NNLO_Wmunu_MAXHTPTV140_280_BFilter	e5340_s3126_r10201_p3749	3.40×10^2	0.11	0.97	26415600
	MC16e		e5340_s3126_r10724_p3759				41501000
	MC16a		e5340_s3126_r9364_p3749				4999000
364165	MC16d	Sherpa_221_NNPDF30NNLO_Wmunu_MAXHTPTV280_500_CVetoBVeto	e5340_s3126_r10201_p3749	72.1	0.548	0.97	6228500
	MC16e		e5340_s3126_r10724_p3759				8304800

Table B.2.12.: List of simulated Monte Carlo samples used in the search for additional Higgs bosons.

DSID	Campaign	ATLAS Sample Name	Production Tags	σ [pb]	ϵ_{Filter}	k-Factor	N_{Events}
$W^{\pm} \rightarrow \mu^{\pm}\nu_{\mu}$							
364166	MC16a		e5340_s3126_r9364_p3749				2989000
	MC16d	Sherpa_221_NNPDF30NNLO_Wmunu_MAXHTPTV280_500_CFilterBVeto	e5340_s3126_r10201_p3749	72.1	0.32	0.97	3747350
	MC16e		e5340_s3126_r10724_p3759				4987550
364167	MC16a		e5340_s3126_r9364_p3749				2939500
	MC16d	Sherpa_221_NNPDF30NNLO_Wmunu_MAXHTPTV280_500_BFilter	e5340_s3126_r10201_p3749	72.1	0.125	0.97	3746850
	MC16e		e5340_s3126_r10724_p3759				4983350
364168	MC16a		e5340_s3126_r9364_p3749				5997500
	MC16d	Sherpa_221_NNPDF30NNLO_Wmunu_MAXHTPTV500_1000	e5340_s3126_r10201_p3749	15	1.00	0.97	7498000
	MC16e		e5340_s3126_r10724_p3759				9944990
364169	MC16a		e5340_s3126_r9364_p3749				3998000
	MC16d	Sherpa_221_NNPDF30NNLO_Wmunu_MAXHTPTV1000_E_CMS	e5340_s3126_r10201_p3749	1.23	1.00	0.97	5000000
	MC16e		e5340_s3126_r10724_p3759				6645300
$W^{\pm} \rightarrow e^{\pm}\nu_{e}$							
364170	MC16a		e5340_s3126_r9364_p3749				24997000
	MC16d	Sherpa_221_NNPDF30NNLO_Wenu_MAXHTPTV0_70_CVetoBVeto	e5340_s3126_r10201_p3749	1.92×10^4	0.825	0.97	30822900
	MC16e		e5340_s3126_r10724_p3759				41480000
364171	MC16a		e5340_s3126_r9364_p3749				9910500
	MC16d	Sherpa_221_NNPDF30NNLO_Wenu_MAXHTPTV0_70_CFilterBVeto	e5340_s3126_r10201_p3749	1.91×10^4	0.131	0.97	12486200
	MC16e		e5340_s3126_r10724_p3759				16601500
364172	MC16a		e5340_s3126_r9364_p3749				17478400
	MC16d	Sherpa_221_NNPDF30NNLO_Wenu_MAXHTPTV0_70_BFilter	e5340_s3126_r10201_p3749	1.91×10^4	4.48×10^{-2}	0.97	21838300
	MC16e		e5340_s3126_r10724_p3759				29377800
364173	MC16a		e5340_s3126_r9364_p3749				14815500
	MC16d	Sherpa_221_NNPDF30NNLO_Wenu_MAXHTPTV70_140_CVetoBVeto	e5340_s3126_r10201_p3749	9.45×10^2	0.675	0.97	18480000
	MC16e		e5340_s3126_r10724_p3759				24588700

Table B.2.13.: List of simulated Monte Carlo samples used in the search for additional Higgs bosons.

DSID	Campaign	ATLAS Sample Name	Production Tags	σ [pb]	ϵ_{Filter}	k-Factor	N_{Events}
$W^{\pm} \rightarrow e^{\pm}\nu_e$							
364174	MC16a		e5340_s3126_r9364_p3749				9940400
	MC16d	Sherpa_221_NNPDF30NNLO_Wenu_MAXHTPTV70_140_CFilterBVeto	e5340_s3126_r10201_p3749	9.46×10^2	0.244	0.97	12402800
	MC16e		e5340_s3126_r10724_p3759				16583300
364175	MC16a		e5340_s3126_r9364_p3749				19801100
	MC16d	Sherpa_221_NNPDF30NNLO_Wenu_MAXHTPTV70_140_BFilter	e5340_s3126_r10201_p3749	9.46×10^2	0.103	0.97	24716100
	MC16e		e5340_s3126_r10724_p3759				30699150
364176	MC16a		e5340_s3126_r9364_p3749				10000000
	MC16d	Sherpa_221_NNPDF30NNLO_Wenu_MAXHTPTV140_280_CVetoBVeto	e5340_s3126_r10201_p3749	3.40×10^2	0.599	0.97	12479750
	MC16e		e5340_s3126_r10724_p3759				16742000
364177	MC16a		e5340_s3126_r9364_p3749				13411500
	MC16d	Sherpa_221_NNPDF30NNLO_Wenu_MAXHTPTV140_280_CFilterBVeto	e5340_s3126_r10201_p3749	3.40×10^2	0.288	0.97	16872750
	MC16e		e5340_s3126_r10724_p3759				20817950
364178	MC16a		e5340_s3126_r9364_p3749				24860800
	MC16d	Sherpa_221_NNPDF30NNLO_Wenu_MAXHTPTV140_280_BFilter	e5340_s3126_r10201_p3749	3.40×10^2	0.109	0.97	31859000
	MC16e		e5340_s3126_r10724_p3759				41557000
364179	MC16a		e5340_s3126_r9364_p3749				4998800
	MC16d	Sherpa_221_NNPDF30NNLO_Wenu_MAXHTPTV280_500_CVetoBVeto	e5340_s3126_r10201_p3749	72.1	0.548	0.97	6007600
	MC16e		e5340_s3126_r10724_p3759				8296050
364180	MC16a		e5340_s3126_r9364_p3749				2999400
	MC16d	Sherpa_221_NNPDF30NNLO_Wenu_MAXHTPTV280_500_CFilterBVeto	e5340_s3126_r10201_p3749	72.1	0.32	0.97	3743700
	MC16e		e5340_s3126_r10724_p3759				4984050
364181	MC16a		e5340_s3126_r9364_p3749				2998000
	MC16d	Sherpa_221_NNPDF30NNLO_Wenu_MAXHTPTV280_500_BFilter	e5340_s3126_r10201_p3749	72.1	0.137	0.97	3693850
	MC16e		e5340_s3126_r10724_p3759				4983450

Table B.2.14.: List of simulated Monte Carlo samples used in the search for additional Higgs bosons.

DSID	Campaign	ATLAS Sample Name	Production Tags	σ [pb]	ϵ_{Filter}	k-Factor	N_{Events}
$W^{\pm} \to e^{\pm}\nu_e$							
364182	MC16a	Sherpa_221_NNPDF30NNLO_Wenu_MAXHTPTV500_1000	e5340_s3126_r9364_p3749				5998600
	MC16d		e5340_s3126_r10201_p3749	15	1.00	0.97	7494700
	MC16e		e5340_s3126_r10724_p3759				9954050
364183	MC16a	Sherpa_221_NNPDF30NNLO_Wenu_MAXHTPTV1000_E_CMS	e5340_s3126_r9364_p3749				3999000
	MC16d		e5340_s3126_r10201_p3749	1.23	1.00	0.97	8893000
	MC16e		e5340_s3126_r10724_p3759				6643950
$W^{\pm} \to \tau^{\pm}\nu_{\tau}$							
364184	MC16a	Sherpa_221_NNPDF30NNLO_Wtaunu_MAXHTPTV0_70_CVetoBVeto	e5340_s3126_r9364_p3749				24921000
	MC16d		e5340_s3126_r10201_p3749	1.92×10^4	0.825	0.97	31110000
	MC16e		e5340_s3126_r10724_p3759				41425000
364185	MC16a	Sherpa_221_NNPDF30NNLO_Wtaunu_MAXHTPTV0_70_CFilterBVeto	e5340_s3126_r9364_p3759				9994600
	MC16d		e5340_s3126_r10201_p3749	1.91×10^4	0.132	0.97	12443600
	MC16e		e5340_s3126_r10724_p3759				16593800
364186	MC16a	Sherpa_221_NNPDF30NNLO_Wtaunu_MAXHTPTV0_70_BFilter	e5340_s3126_r9364_p3749				17483200
	MC16d		e5340_s3126_r10201_p3749	1.91×10^4	4.51×10^{-2}	0.97	21824500
	MC16e		e5340_s3126_r10724_p3759				29019700
364187	MC16a	Sherpa_221_NNPDF30NNLO_Wtaunu_MAXHTPTV70_140_CVetoBVeto	e5340_s3126_r9364_p3749				14998500
	MC16d		e5340_s3126_r10201_p3749	9.45×10^2	0.676	0.97	18721000
	MC16e		e5340_s3126_r10724_p3759				24901000
364188	MC16a	Sherpa_221_NNPDF30NNLO_Wtaunu_MAXHTPTV70_140_CFilterBVeto	e5340_s3126_r9364_p3749				9999000
	MC16d		e5340_s3126_r10201_p3749	9.46×10^2	0.242	0.97	12389000
	MC16e		e5340_s3126_r10724_p3759				16576000
364189	MC16a	Sherpa_221_NNPDF30NNLO_Wtaunu_MAXHTPTV70_140_BFilter	e5340_s3126_r9364_p3749				9999000
	MC16d		e5340_s3126_r10201_p3749	9.46×10^2	0.104	0.97	12477850
	MC16e		e5340_s3126_r10724_p3759				24946250

Table B.2.15.: List of simulated Monte Carlo samples used in the search for additional Higgs bosons.

DSID	Campaign	ATLAS Sample Name	Production Tags	σ [pb]	ϵ_{Filter}	k-Factor	N_{Events}
$W^{\pm} \rightarrow \tau^{\pm}\nu_{\tau}$							
	MC16a		e5340_s3126_r9364_p3749				19913000
364190	MC16d	Sherpa_221_NNPDF30NNLO_Wtaunu_MAXHTPTV140_280_CVetoBVeto	e5340_s3126_r10201_p3749	3.40×10^2	0.599	0.97	24974000
	MC16e		e5340_s3126_r10724_p3759				33215800
	MC16a		e5340_s3126_r9364_p3749				11299200
364191	MC16d	Sherpa_221_NNPDF30NNLO_Wtaunu_MAXHTPTV140_280_CFilterBVeto	e5340_s3126_r10201_p3749	3.40×10^2	0.285	0.97	14067150
	MC16e		e5340_s3126_r10724_p3759				16629600
	MC16a		e5340_s3126_r9364_p3749				24999900
364192	MC16d	Sherpa_221_NNPDF30NNLO_Wtaunu_MAXHTPTV140_280_BFilter	e5340_s3126_r10201_p3749	3.39×10^2	0.106	0.97	31843100
	MC16e		e5340_s3126_r10724_p3759				41681700
	MC16a		e5340_s3126_r9364_p3749				7498200
364193	MC16d	Sherpa_221_NNPDF30NNLO_Wtaunu_MAXHTPTV280_500_CVetoBVeto	e5340_s3126_r10201_p3749	72.1	0.562	0.97	93380000
	MC16e		e5340_s3126_r10724_p3759				12462150
	MC16a		e5340_s3126_r9364_p3749				3797000
364194	MC16d	Sherpa_221_NNPDF30NNLO_Wtaunu_MAXHTPTV280_500_CFilterBVeto	e5340_s3126_r10201_p3749	72	0.319	0.97	5627000
	MC16e		e5340_s3126_r10724_p3759				7485000
	MC16a		e5340_s3126_r9364_p3749				2998100
364195	MC16d	Sherpa_221_NNPDF30NNLO_Wtaunu_MAXHTPTV280_500_BFilter	e5340_s3126_r10201_p3749	71.9	0.136	0.97	3742500
	MC16e		e5340_s3126_r10724_p3759				4983000
	MC16a		e5340_s3126_r9364_p3749				5960000
364196	MC16d	Sherpa_221_NNPDF30NNLO_Wtaunu_MAXHTPTV500_1000	e5340_s3126_r10201_p3749	15.1	1.00	0.97	7495450
	MC16e		e5340_s3126_r10724_p3759				9962000
	MC16a		e5340_s3126_r9364_p3749				4000000
364197	MC16d	Sherpa_221_NNPDF30NNLO_Wtaunu_MAXHTPTV1000_E_CMS	e5340_s3126_r10201_p3749	1.23	1.00	0.97	4989800
	MC16e		e5340_s3126_r10724_p3759				6634000

Table B.2.16.: List of simulated Monte Carlo samples used in the search for additional Higgs bosons.

DSID	Campaign	ATLAS Sample Name	Production Tags	σ [pb]	ϵ_{Filter}	k-Factor	N_{Events}
$t\bar{t}$ and single top							
410470	MC16a	PhPy8EG_A14_ttbar_hdamp258p75_nonallhad	e6337_s3126_r9364_p3749				119432000
	MC16d		e6337_s3126_r10201_p3759	7.30×10^2	0.544	1.14	149327000
	MC16e		e6337_s3126_r10724_p3759				199153000
410471	MC16a	PhPy8EG_A14_ttbar_hdamp258p75_allhad	e6337_s3126_r9364_p3749				39885000
	MC16d		e6337_s3126_r10201_p3749	7.30×10^2	0.456	1.14	24714000
	MC16e		e6337_s3126_r10724_p3759				65325000
410644	MC16a	PowhegPythia8EvtGen_A14_singletop_schan_lept_top	e6527_s3126_r9364_p3749				2000000
	MC16d		e6527_s3126_r10201_p3749	2.03	1.00	1.02	2498000
	MC16e		e6527_s3126_r10724_p3759				2796000
410645	MC16a	PowhegPythia8EvtGen_A14_singletop_schan_lept_antitop	e6527_s3126_r9364_p3749				2000000
	MC16d		e6527_s3126_r10201_p3749	1.27	1.00	1.02	2500000
	MC16e		e6527_s3126_r10724_p3759				3317000
410646	MC16a	PowhegPythia8EvtGen_A14_Wt_DR_inclusive_top	e6552_s3126_r9364_p3749				4996000
	MC16d		e6552_s3126_r10201_p3749	37.9	1.00	0.945	6243000
	MC16e		e6552_s3126_r10724_p3759				8300000
410647	MC16a	PowhegPythia8EvtGen_A14_Wt_DR_inclusive_antitop	e6552_s3126_r9364_p3749				4999000
	MC16d		e6552_s3126_r10201_p3749	37.9	1.00	0.946	6240000
	MC16e		e6552_s3126_r10724_p3759				8272000
410658	MC16a	PhPy8EG_A14_tchan_BW50_lept_top	e6671_s3126_r9364_p3749				4790500
	MC16d		e6671_s3126_r10201_p3749	37	1.00	1.19	6226000
	MC16e		e6671_s3126_r10724_p3759				8290900
410659	MC16a	PhPy8EG_A14_tchan_BW50_lept_antitop	e6671_s3126_r9364_p3749				4761500
	MC16d		e6671_s3126_r10201_p3749	22.2	1.00	1.18	5968000
	MC16e		e6671_s3126_r10724_p3759				8298850

Table B.2.17.: List of simulated Monte Carlo samples used in the search for additional Higgs bosons.

Higgs signal samples produced via b-associated production

DSID	Campaign	ATLAS Sample Name	Production Tags	Mass [GeV]	ϵ_{Filter}	N_{Events}
341858	MC16a	aMcAtNloPythia8EvtGen_A14NNPDF23LO_bbH200_yb2_tautaulh	e4482_a875_r9364_p3749	200	0.456	400000
	MC16d		e4482_a875_r10201_p3749			500000
	MC16e		e4482_a875_r10724_p3759			670000
341860	MC16a	aMcAtNloPythia8EvtGen_A14NNPDF23LO_bbH300_yb2_tautaulh	e4482_a875_r9364_p3749	300	0.454	300000
	MC16d		e4482_a875_r10201_p3759			380000
	MC16e		e4482_a875_r10724_p3759			510000
341862	MC16a	aMcAtNloPythia8EvtGen_A14NNPDF23LO_bbH400_yb2_tautaulh	e4298_a875_r9364_p3749	400	0.457	300000
	MC16d		e4298_a875_r10201_p3749			376000
	MC16e		e4298_a875_r10724_p3759			510000
341864	MC16a	aMcAtNloPythia8EvtGen_A14NNPDF23LO_bbH600_yb2_tautaulh	e4482_a875_r9364_p3749	600	0.456	250000
	MC16d		e4482_a875_r10201_p3749			320000
	MC16e		e4298_a875_r10724_p3759			420000
341868	MC16a	aMcAtNloPythia8EvtGen_A14NNPDF23LO_bbH1000_yb2_tautaulh	e4298_a875_r9364_p3749	1000	0.46	250000
	MC16d		e4298_a875_r10201_p3749			320000
	MC16e		e4298_a875_r10724_p3759			420000
341873	MC16a	aMcAtNloPythia8EvtGen_A14NNPDF23LO_bbH1500_yb2_tautaulh	e5314_a875_r9364_p3749	1500	0.456	150000
	MC16d		e5314_a875_r10201_p3749			190000
	MC16e		e5314_a875_r10724_p3759			260000
341875	MC16a	aMcAtNloPythia8EvtGen_A14NNPDF23LO_bbH200_yb2_tautauhh	e4482_a875_r9364_p3749	200	0.421	400000
	MC16d		e4482_a875_r10201_p3749			500000
	MC16e		e4482_a875_r10724_p3759			654000
341876	MC16a	aMcAtNloPythia8EvtGen_A14NNPDF23LO_bbH250_yb2_tautauhh	e5686_a875_r9364_p3749	2500	0.422	300000
	MC16d		e5686_a875_r10201_p3749			380000
	MC16e		e5686_a875_r10724_p3749			510000

Table B.2.18.: List of signal samples produced via b-associated production.

DSID	Campaign	ATLAS Sample Name	Production Tags	Mass [GeV]	ϵ_{Filter}	N_{Events}
Higgs signal samples produced via *b*-associated production						
341877	MC16a		e4482_a875_r9364_p3749			300000
	MC16d	aMcAtNloPythia8EvtGen_A14NNPDF23LO_bbH300_yb2_tautauhh	e4482_a875_r10201_p3749	300	0.422	380000
	MC16e		e4482_a875_r10724_p3759			510000
341878	MC16a		e4482_a875_r9364_p3749			300000
	MC16d	aMcAtNloPythia8EvtGen_A14NNPDF23LO_bbH350_yb2_tautauhh	e4482_a875_r10201_p3749	350	0.422	380000
	MC16e		e4482_a875_r10724_p3749			510000
341879	MC16a		e4298_a875_r9364_p3749			300000
	MC16d	aMcAtNloPythia8EvtGen_A14NNPDF23LO_bbH400_yb2_tautauhh	e4298_a875_r10201_p3749	400	0.423	380000
	MC16e		e4298_a875_r10724_p3759			510000
341880	MC16a		e4482_a875_r9364_p3749			300000
	MC16d	aMcAtNloPythia8EvtGen_A14NNPDF23LO_bbH500_yb2_tautauhh	e4482_a875_r10201_p3749	500	0.422	370000
	MC16e		e4482_a875_r10724_p3749			510000
341881	MC16a		e4482_a875_r9364_p3749			250000
	MC16d	aMcAtNloPythia8EvtGen_A14NNPDF23LO_bbH600_yb2_tautauhh	e4482_a875_r10201_p3749	600	0.42	320000
	MC16e		e4482_a875_r10724_p3759			420000
341882	MC16a		e4482_a875_r9364_p3749			250000
	MC16d	aMcAtNloPythia8EvtGen_A14NNPDF23LO_bbH700_yb2_tautauhh	e4482_a875_r10201_p3749	700	0.42	320000
	MC16e		e4482_a875_r10724_p3749			420000
341883	MC16a		e4482_a875_r9364_p3749			250000
	MC16d	aMcAtNloPythia8EvtGen_A14NNPDF23LO_bbH800_yb2_tautauhh	e4482_a875_r10201_p3749	800	0.421	320000
	MC16e		e4482_a875_r10724_p3749			420000

Table B.2.19.: List of signal samples produced via *b*-associated production.

Higgs signal samples produced via b-associated production

DSID	Campaign	ATLAS Sample Name	Production Tags	Mass [GeV]	ϵ_{Filter}	N_{Events}
341885	MC16a		e4298_a875_r9364_p3749			250000
	MC16d	aMcAtNloPythia8EvtGen_A14NNPDF23LO_bbH1000_yb2_tautauhh	e4298_a875_r10201_p3749	1000	0.424	320000
	MC16e		e4298_a875_r10724_p3759			420000
341917	MC16a		e4482_a875_r9364_p3749			200000
	MC16d	aMcAtNloPythia8EvtGen_A14NNPDF23LO_bbH1200_yb2_tautauhh	e4482_a875_r10201_p3749	1200	0.422	250000
	MC16e		e4482_a875_r10724_p3749			330000
341920	MC16a		e5314_a875_r9364_p3749			150000
	MC16d	aMcAtNloPythia8EvtGen_A14NNPDF23LO_bbH1500_yb2_tautauhh	e5314_a875_r10201_p3749	1500	0.421	190000
	MC16e		e5314_a875_r10724_p3759			260000
345288	MC16a		e5686_a875_r9364_p3749			125000
	MC16d	aMcAtNloPythia8EvtGen_A14NNPDF23LO_bbH2000_yb2_tautauhh	e5686_a875_r10201_p3749	2000	0.422	190000
	MC16e		e5686_a875_r10724_p3759			260000
345289	MC16a		e5686_a875_r9364_p3749			150000
	MC16d	aMcAtNloPythia8EvtGen_A14NNPDF23LO_bbH2000_yb2_tautaulh	e5686_a875_r10201_p3749	2000	0.455	190000
	MC16e		e5686_a875_r10724_p3759			260000
345292	MC16a		e5686_a875_r9364_p3749			125000
	MC16d	aMcAtNloPythia8EvtGen_A14NNPDF23LO_bbH2500_yb2_tautauhh	e5686_a875_r10201_p3749	2500	0.421	190000
	MC16e		e5686_a875_r10724_p3759			260000
345293	MC16a		e5686_a875_r9364_p3749			150000
	MC16d	aMcAtNloPythia8EvtGen_A14NNPDF23LO_bbH2500_yb2_tautaulh	e5686_a875_r10201_p3759	2500	0.457	190000
	MC16e		e5686_a875_r10724_p3759			250000

Table B.2.20.: List of signal samples produced via b-associated production.

Higgs signal samples produced via gluon-gluon fusion

DSID	Campaign	ATLAS Sample Name	Production Tags	Mass [GeV]	Width [GeV]	ϵ_{Filter}	N_{Events}
342305	MC16a		e4284_s3126_r9364_p3749				50000
	MC16d	PowhegPythia8EvtGen_CT10_AZNLOCTEQ6L1_ggH200W1_tautaulh	e4284_s3126_r10201_p3749	200	1	0.455	130000
	MC16e		e4284_s3126_r10724_p3759				170000
342306	MC16a		e4284_s3126_r9364_p3749				50000
	MC16d	PowhegPythia8EvtGen_CT10_AZNLOCTEQ6L1_ggH200W1_tautauhh	e4284_s3126_r10201_p3749	200	1	0.422	130000
	MC16e		e4284_s3126_r10724_p3759				170000
342308	MC16a		e4284_s3126_r9364_p3749				50000
	MC16d	PowhegPythia8EvtGen_CT10_AZNLOCTEQ6L1_ggH250W1_tautaulh	e4284_s3126_r10201_p3749	250	1	0.455	129000
	MC16e		e4284_s3126_r10724_p3759				170000
342309	MC16a		e4284_s3126_r9364_p3749				50000
	MC16d	PowhegPythia8EvtGen_CT10_AZNLOCTEQ6L1_ggH250W1_tautauhh	e4284_s3126_r10201_p3749	250	1	0.422	130000
	MC16e		e4284_s3126_r10724_p3759				170000
342310	MC16a		e4284_s3126_r9364_p3749				50000
	MC16d	PowhegPythia8EvtGen_CT10_AZNLOCTEQ6L1_ggH300W2_tautaulh	e4284_s3126_r10201_p3749	300	2	0.456	130000
	MC16e		e4284_s3126_r10724_p3759				170000
342311	MC16a		e4284_s3126_r9364_p3749				50000
	MC16d	PowhegPythia8EvtGen_CT10_AZNLOCTEQ6L1_ggH300W2_tautauhh	e4284_s3126_r10201_p3749	300	2	0.422	130000
	MC16e		e4284_s3126_r10724_p3759				170000
342312	MC16a		e4284_s3126_r9364_p3749				49000
	MC16d	PowhegPythia8EvtGen_CT10_AZNLOCTEQ6L1_ggH350W3_tautaulh	e4284_s3126_r10201_p3749	350	3	0.455	129000
	MC16e		e4284_s3126_r10724_p3759				170000
342313	MC16a		e4284_s3126_r9364_p3749				49000
	MC16d	PowhegPythia8EvtGen_CT10_AZNLOCTEQ6L1_ggH350W3_tautauhh	e4284_s3126_r10201_p3749	350	3	0.422	130000
	MC16e		e4284_s3126_r10724_p3759				170000

Table B.2.21.: List signal samples produced via gluon-gluon fusion.

Higgs signal samples produced via gluon-gluon fusion

DSID	Campaign	ATLAS Sample Name	Production Tags	Mass [GeV]	Width [GeV]	ϵ_{Filter}	N_{Events}
342314	MC16a		e4284_s3126_r9364_p3749				50000
	MC16d	PowhegPythia8EvtGen_CT10_AZNLOCTEQ6L1_ggH400W5_tautaulh	e4284_s3126_r10201_p3749	400	5	0.455	130000
	MC16e		e4284_s3126_r10724_p3759				169000
342315	MC16a		e4284_s3126_r9364_p3749				50000
	MC16d	PowhegPythia8EvtGen_CT10_AZNLOCTEQ6L1_ggH400W5_tautauhh	e4284_s3126_r10201_p3759	400	5	0.421	130000
	MC16e		e4284_s3126_r10724_p3759				170000
342316	MC16a		e4284_s3126_r9364_p3749				49000
	MC16d	PowhegPythia8EvtGen_CT10_AZNLOCTEQ6L1_ggH500W5_tautaulh	e4284_s3126_r10201_p3749	500	5	0.455	130000
	MC16e		e4284_s3126_r10724_p3759				170000
342317	MC16a		e4284_s3126_r9364_p3749				50000
	MC16d	PowhegPythia8EvtGen_CT10_AZNLOCTEQ6L1_ggH500W5_tautauhh	e4284_s3126_r10201_p3759	500	5	0.422	130000
	MC16e		e4284_s3126_r10724_p3759				170000
342318	MC16a		e4284_s3126_r9364_p3749				40000
	MC16d	PowhegPythia8EvtGen_CT10_AZNLOCTEQ6L1_ggH600W10_tautaulh	e4284_s3126_r10201_p3749	600	10	0.455	66000
	MC16e		e4284_s3126_r10724_p3759				170000
342319	MC16a		e4284_s3126_r9364_p3749				40000
	MC16d	PowhegPythia8EvtGen_CT10_AZNLOCTEQ6L1_ggH600W10_tautauhh	e4284_s3126_r10201_p3749	600	10	0.422	70000
	MC16e		e4284_s3126_r10724_p3759				90000
342320	MC16a		e4284_s3126_r9364_p3749				40000
	MC16d	PowhegPythia8EvtGen_CT10_AZNLOCTEQ6L1_ggH700W20_tautaulh	e4284_s3126_r10201_p3749	700	20	0.456	70000
	MC16e		e4284_s3126_r10724_p3759				90000
342321	MC16a		e4284_s3126_r9364_p3749				40000
	MC16d	PowhegPythia8EvtGen_CT10_AZNLOCTEQ6L1_ggH700W20_tautauhh	e4284_s3126_r10201_p3749	700	20	0.422	70000
	MC16e		e4284_s3126_r10724_p3759				90000

Table B.2.22.: List signal samples produced via gluon-gluon fusion.

DSID	Campaign	ATLAS Sample Name	Production Tags	Mass [GeV]	Width [GeV]	ϵ_{Filter}	N_{Events}
Higgs signal samples produced via gluon-gluon fusion							
342322	MC16a		e4284_s3126_r9364_p3749				40000
	MC16d	PowhegPythia8EvtGen_CT10_AZNLOCTEQ6L1_ggH800W20_tautaulh	e4284_s3126_r10201_p3749	800	20	0.456	70000
	MC16e		e4284_s3126_r10724_p3759				89000
342323	MC16a		e4284_s3126_r9364_p3749				40000
	MC16d	PowhegPythia8EvtGen_CT10_AZNLOCTEQ6L1_ggH800W20_tautauhh	e4284_s3126_r10201_p3749	800	20	0.422	70000
	MC16e		e4284_s3126_r10724_p3759				89000
342326	MC16a		e4284_s3126_r9364_p3749				40000
	MC16d	PowhegPythia8EvtGen_CT10_AZNLOCTEQ6L1_ggH1000W30_tautaulh	e4284_s3126_r10201_p3749	1000	30	0.456	40000
	MC16e		e4284_s3126_r10724_p3759				70000
342327	MC16a		e4284_s3126_r9364_p3749				40000
	MC16d	PowhegPythia8EvtGen_CT10_AZNLOCTEQ6L1_ggH1000W30_tautauhh	e4284_s3126_r10201_p3749	1000	30	0.422	40000
	MC16e		e4284_s3126_r10724_p3759				70000
342330	MC16a		e4284_s3126_r9364_p3749				40000
	MC16d	PowhegPythia8EvtGen_CT10_AZNLOCTEQ6L1_ggH1200W40_tautaulh	e4284_s3126_r10201_p3759	1200	40	0.456	70000
	MC16e		e4284_s3126_r10724_p3759				90000
342331	MC16a		e4284_s3126_r9364_p3759				40000
	MC16d	PowhegPythia8EvtGen_CT10_AZNLOCTEQ6L1_ggH1200W40_tautauhh	e4284_s3126_r10201_p3749	1200	40	0.422	70000
	MC16e		e4284_s3126_r10724_p3759				89000
342336	MC16a		e4284_s3126_r9364_p3749				50000
	MC16d	PowhegPythia8EvtGen_CT10_AZNLOCTEQ6L1_ggH1500W60_tautaulh	e4284_s3126_r10201_p3749	1500	60	0.456	70000
	MC16e		e4284_s3126_r10724_p3759				89000
342337	MC16a		e4284_s3126_r9364_p3759				50000
	MC16d	PowhegPythia8EvtGen_CT10_AZNLOCTEQ6L1_ggH1500W60_tautauhh	e4284_s3126_r10201_p3749	1500	60	0.422	70000
	MC16e		e4284_s3126_r10724_p3759				90000

Table B.2.23.: List signal samples produced via gluon-gluon fusion.

197

Higgs signal samples produced via gluon-gluon fusion

DSID	Campaign	ATLAS Sample Name	Production Tags	Mass [GeV]	Width [GeV]	ϵ_{Filter}	N_{Events}
345296	MC16a		e5685_s3126_r9364_p3749				50000
	MC16d	PowhegPythia8EvtGen_CT10_AZNLOCTEQ6L1_ggH2000W80_tautauhh	e5685_s3126_r10201_p3749	2000	80	0.422	70000
	MC16e		e5685_s3126_r10724_p3759				90000
345297	MC16a		e5685_s3126_r9364_p3749				50000
	MC16d	PowhegPythia8EvtGen_CT10_AZNLOCTEQ6L1_ggH2000W80_tautaulh	e5685_s3126_r10201_p3759	2000	80	0.455	70000
	MC16e		e5685_s3126_r10724_p3759				90000
345300	MC16a		e5685_s3126_r9364_p3749				50000
	MC16d	PowhegPythia8EvtGen_CT10_AZNLOCTEQ6L1_ggH2500W100_tautauhh	e5685_s3126_r10201_p3749	2500	100	0.423	70000
	MC16e		e5685_s3126_r10724_p3759				90000
345301	MC16a		e5685_s3126_r9364_p3749				50000
	MC16d	PowhegPythia8EvtGen_CT10_AZNLOCTEQ6L1_ggH2500W100_tautaulh	e5685_s3126_r10201_p3749	2500	100	0.456	70000
	MC16e		e5685_s3126_r10724_p3759				90000

Table B.2.24.: List signal samples produced via gluon-gluon fusion.

B.3. Additional Plots for Data-Driven Background Estimations

B.3.1. Fake-Factor Measurements

In this section auxiliary information about the fake-factor measurement is provided. Fake-factors are determined based on a binned measurement in the di-jet pass-ID and fail-ID regions. Table B.3.1 lists the bin edges of the histograms from which the fake-factors are derived.

Subleading tau prongness	Sign	b-region	Bin edges in [GeV]
1 prong	OS	b-tag	{50, 70, 120, 190, 270, 390, 500}
		b-veto	{50, 60, 80, 100, 140, 200, 270, 340, 400, 500}
		b-inc.	{50, 60, 80, 100, 140, 200, 270, 340, 400, 500}
	SS	b-tag	{50, 70, 110, 180, 260, 360, 500}
		b-veto	{50, 60, 80, 100, 140, 200, 270, 340, 410, 500}
		b-inc.	{50, 60, 80, 100, 140, 200, 270, 340, 410, 500}
3 prong	OS	b-tag	{50, 90, 160, 330, 500}
		b-veto	{50, 80, 140, 240, 370, 500}
		b-inc.	{50, 80, 140, 240, 370, 500}
	SS	b-tag	{50, 90, 160, 330, 500}
		b-veto	{50, 80, 140, 240, 360, 500}
		b-inc.	{50, 80, 140, 240, 360, 500}

Table B.3.1.: Bin edges of the distributions involved in fake-factor estimation.

B.3.2. Auxiliary Fake-Factor Closure Test Distributions

The modeling of the fake-factors measured in the b-inclusive category of the di-jet control region is validated by a closure test. In this test, the fake-factors are reapplied in the di-jet fail-ID control region to estimate the QCD multijet background in the pass-ID region. Figures B.3.1 and B.3.2 provide closure measurements in auxiliary variables in the b-veto and b-tag categories of the opposite-sign and same-sign control region. No significant mismodeling of the multijet background is observed.
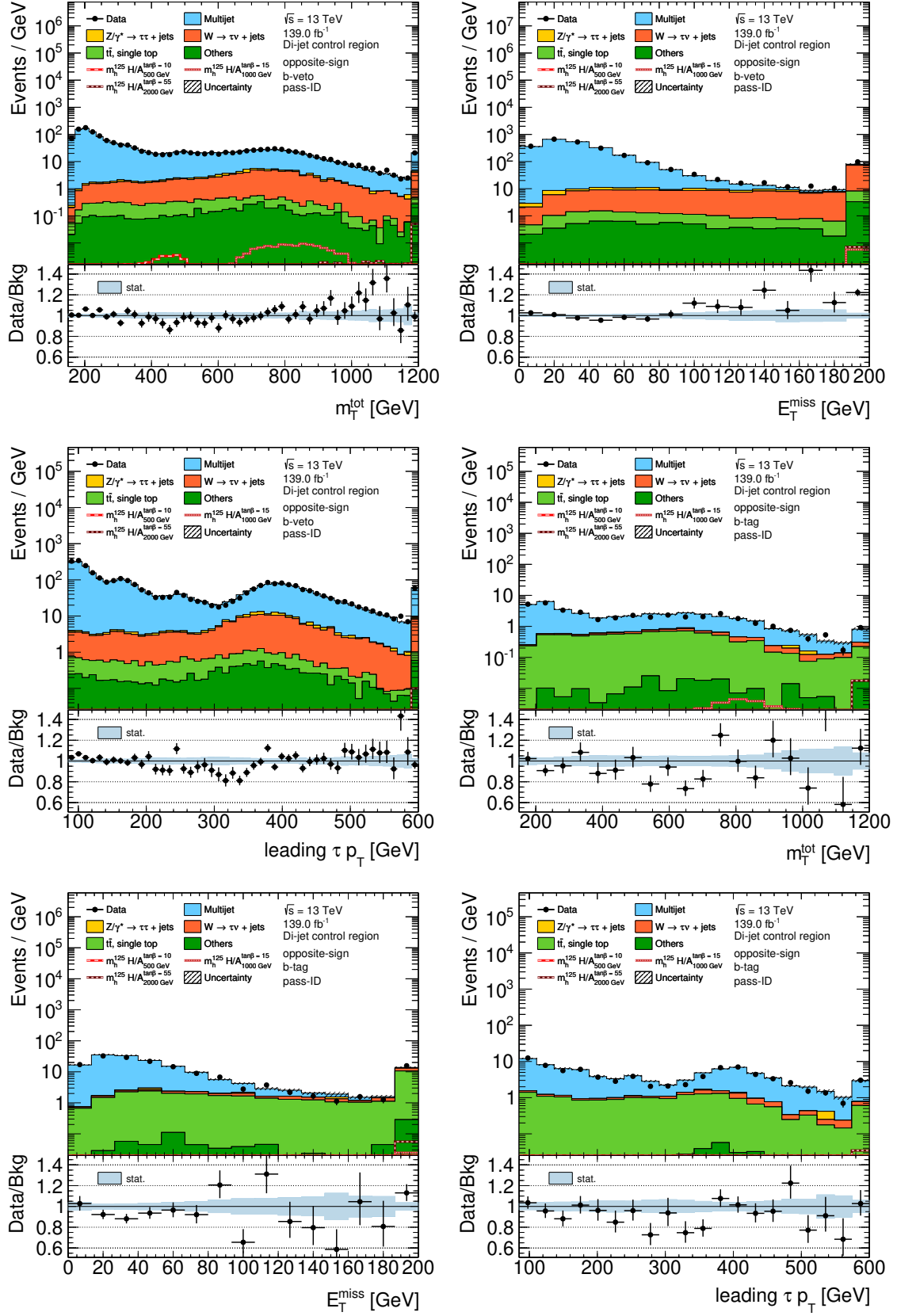
Figure B.3.1.: Auxiliary fake-factor closure test distributions in the opposite-sign di-jet control region.
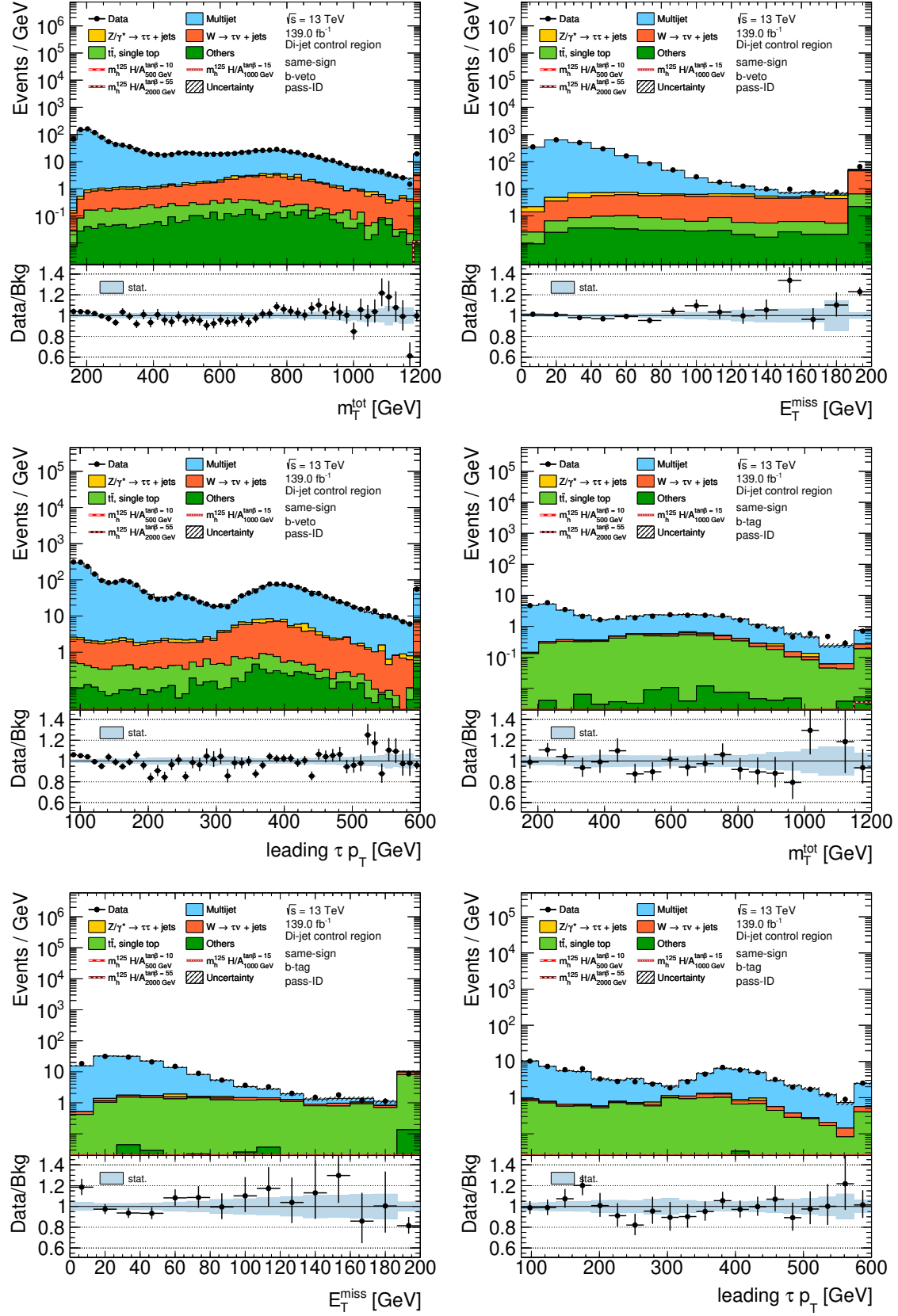
Figure B.3.2.: Auxiliary fake-factor closure test distributions in the same-sign di-jet control region.

B.3.3. Fake-Rate Measurements

In this section, a list of auxiliary plots and fake-rate measurements is presented. The distributions of the probe tau p_T in the $\mu\nu$+jet control region from which the fake-rates are calculated are shown in Figures B.3.3 to B.3.8 for the various tau-ID working points and b-tagging subcategories as well as for 1 and 3 prong taus. Based on the plots, Figures B.3.9 to B.3.15 show the measured fake-rates calculated for the various tau-ID working points used throughout the signal- and validation-region as well as di-jet control region selection.
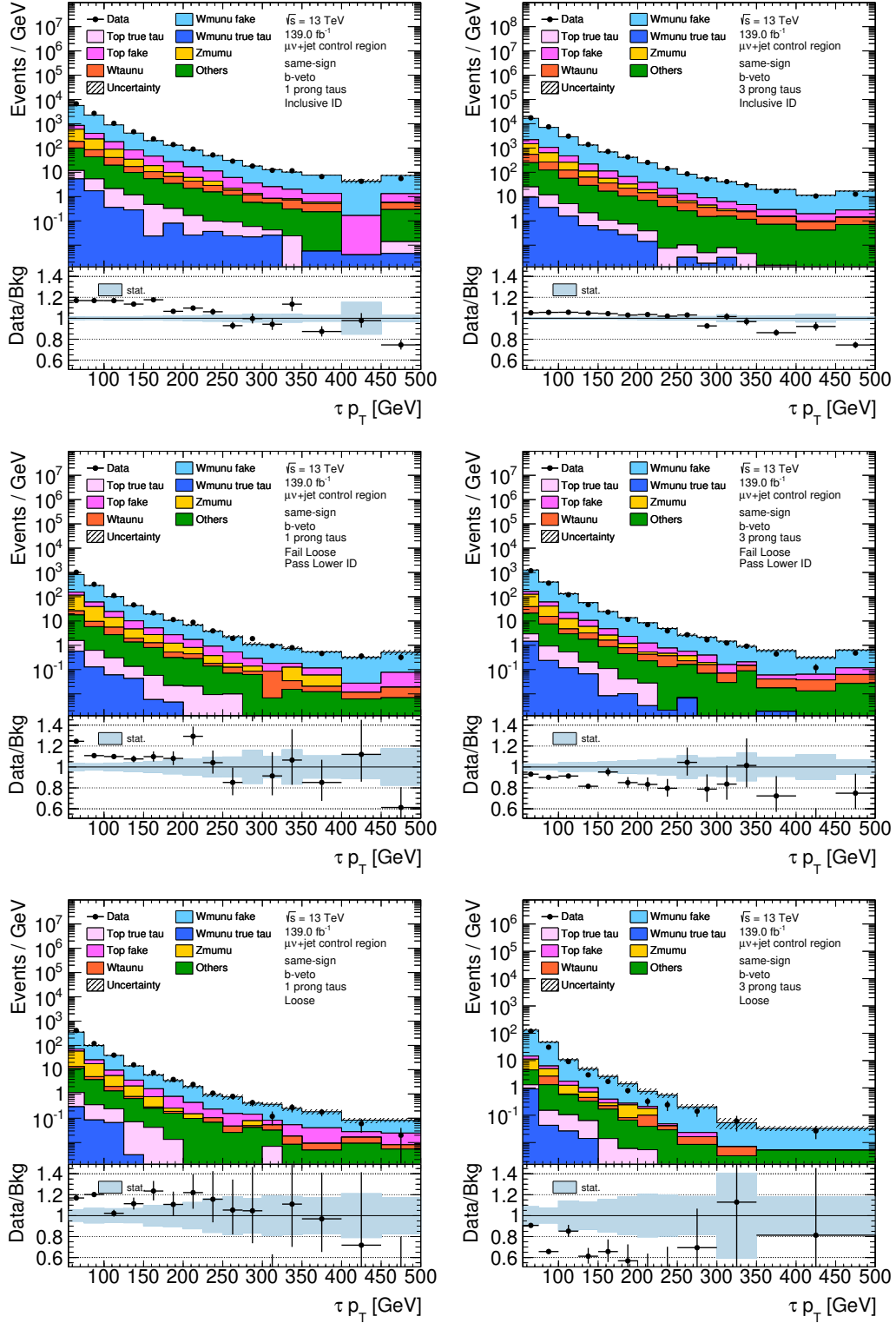
Figure B.3.3.: Distributions of the probe tau p_T in the $\mu\nu$+jet same-sign b-veto control region for various tau-ID working points.
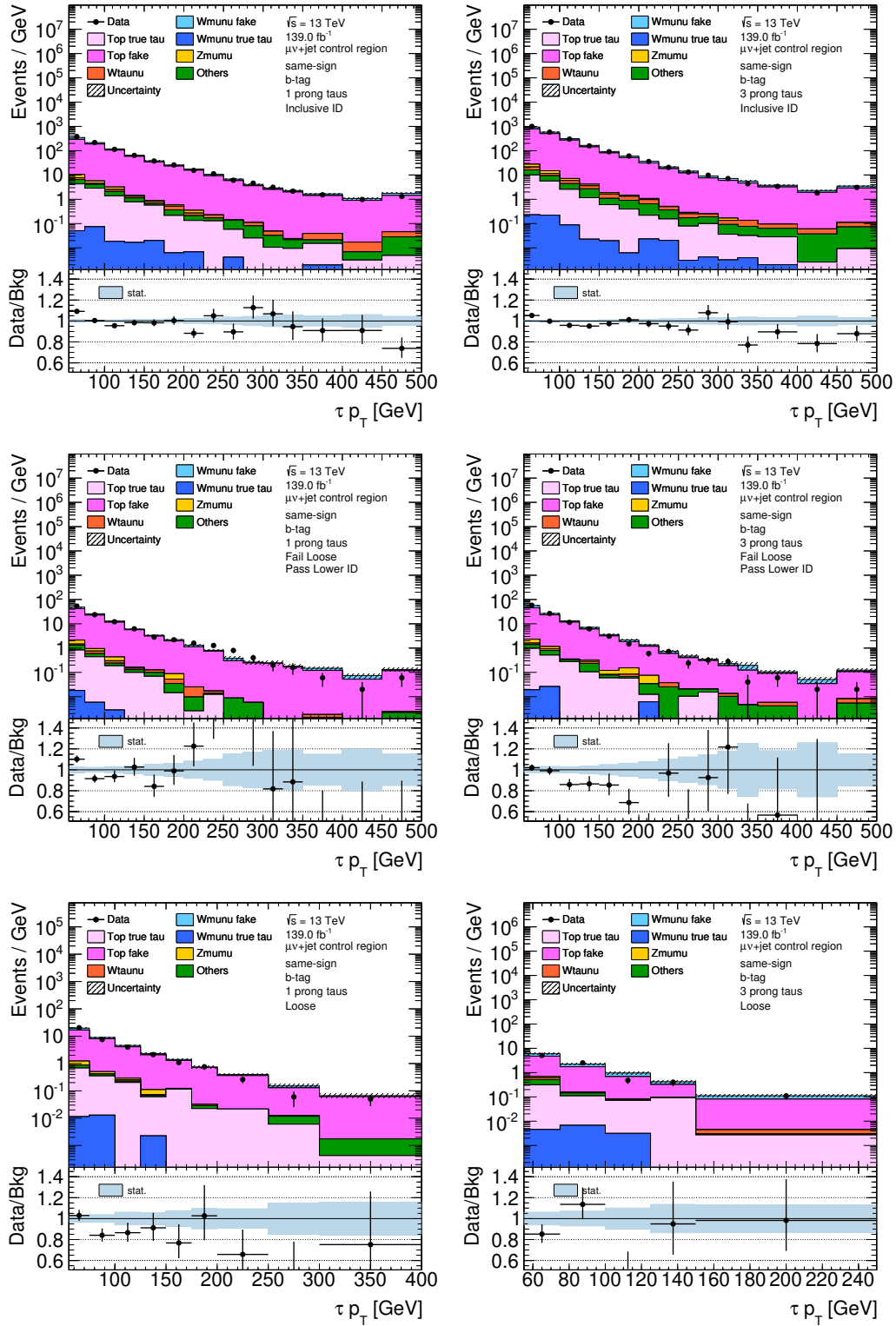
Figure B.3.4.: Distributions of the probe tau p_T in the $\mu\nu$+jet same-sign b-tag control region for various tau-ID working points.
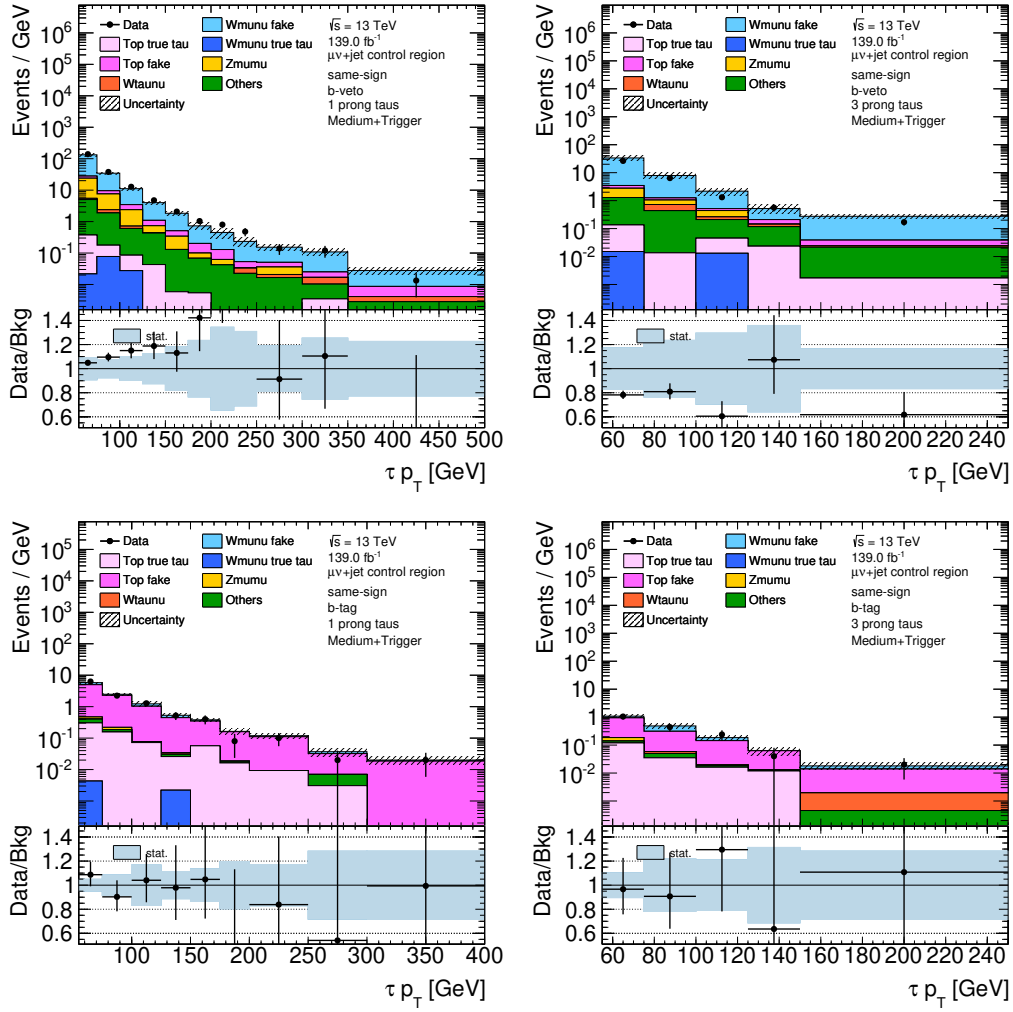
Figure B.3.5.: Distributions of the probe tau p_T in the $\mu\nu$+jet same-sign, b-veto and b-tag control region, with *Medium+Trigger* criterion applied.
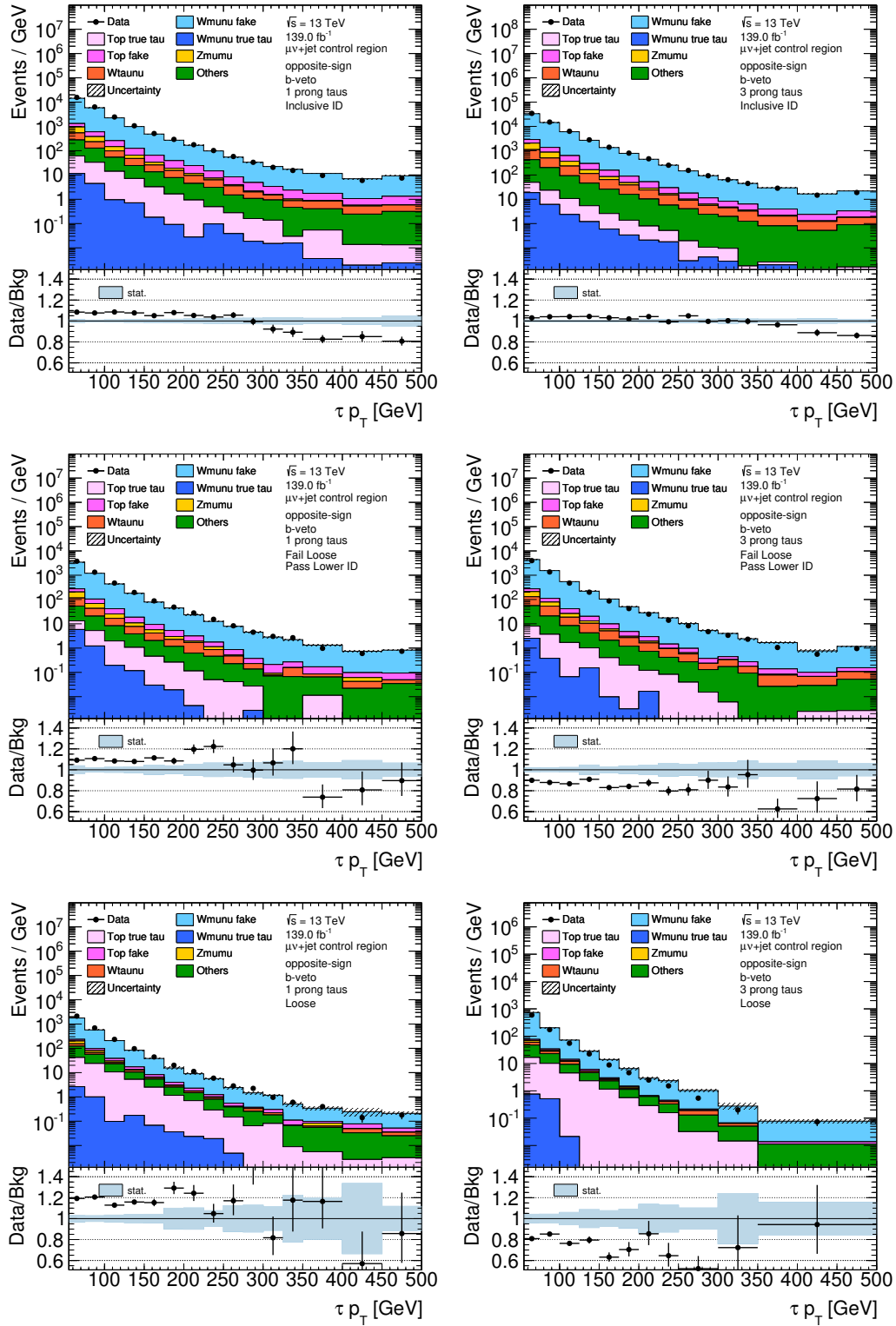
Figure B.3.6.: Distributions of the probe tau p_T in the $\mu\nu$+jet opposite-sign b-veto control region for various tau-ID working points.
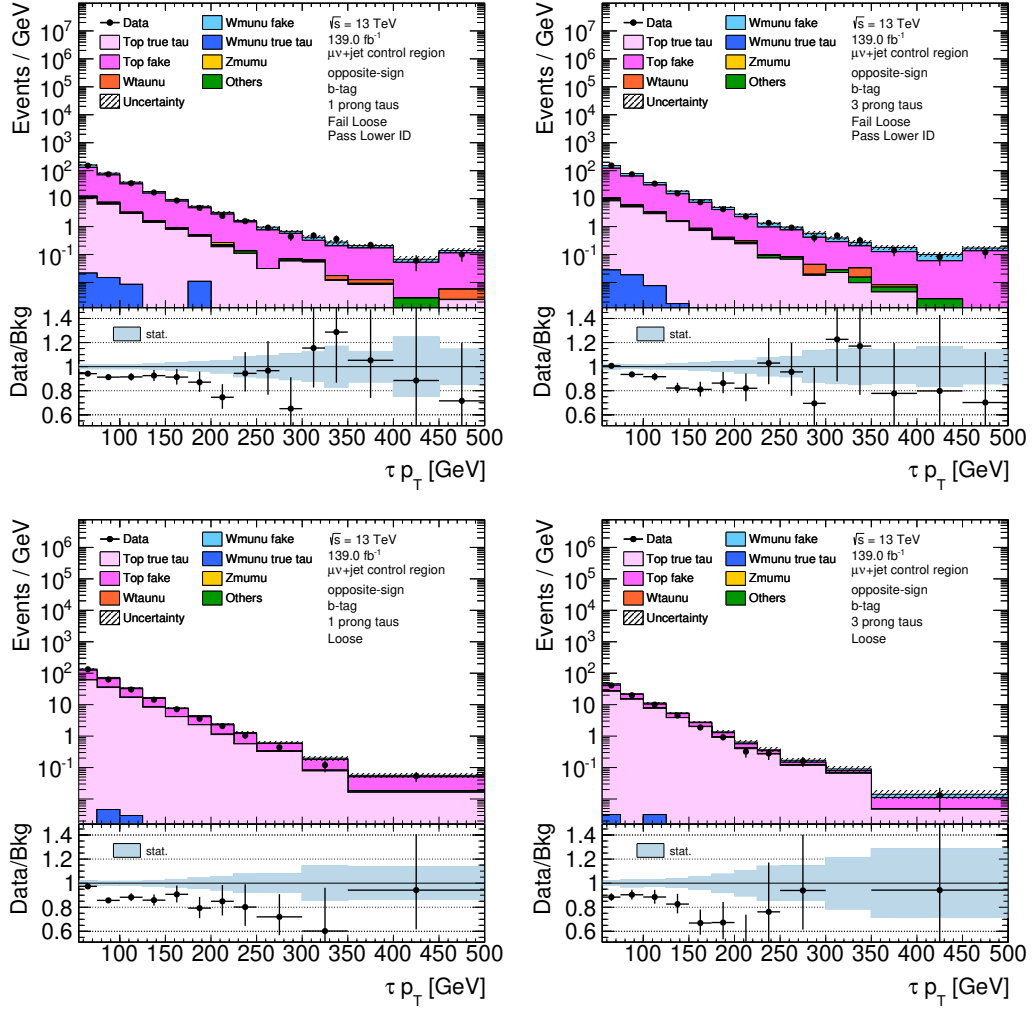
Figure B.3.7.: Distributions of the probe tau p_T in the $\mu\nu$+jet opposite-sign b-tag control region for various tau-ID working points.
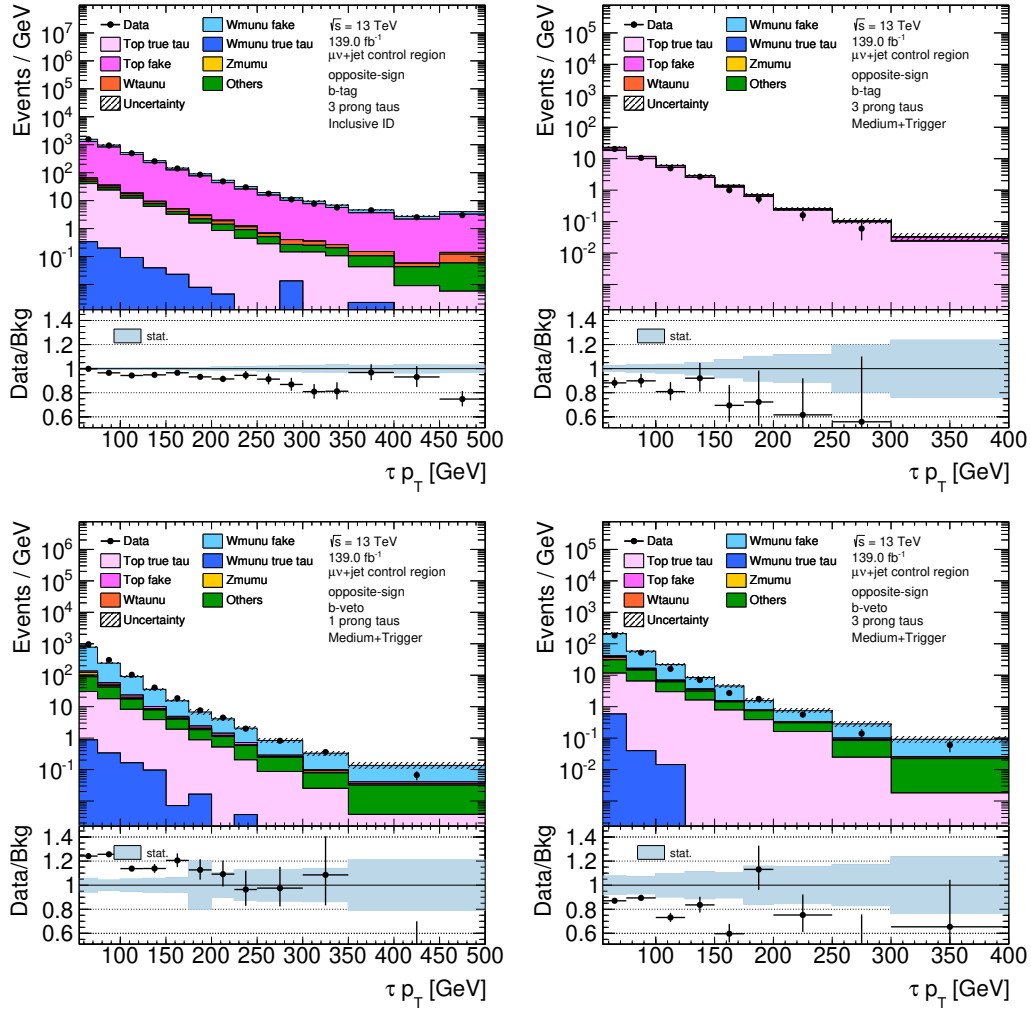
Figure B.3.8.: Distributions of the probe tau p_T in the $\mu\nu$+jet opposite-sign b-tag and b-veto control region for various tau-ID working points.
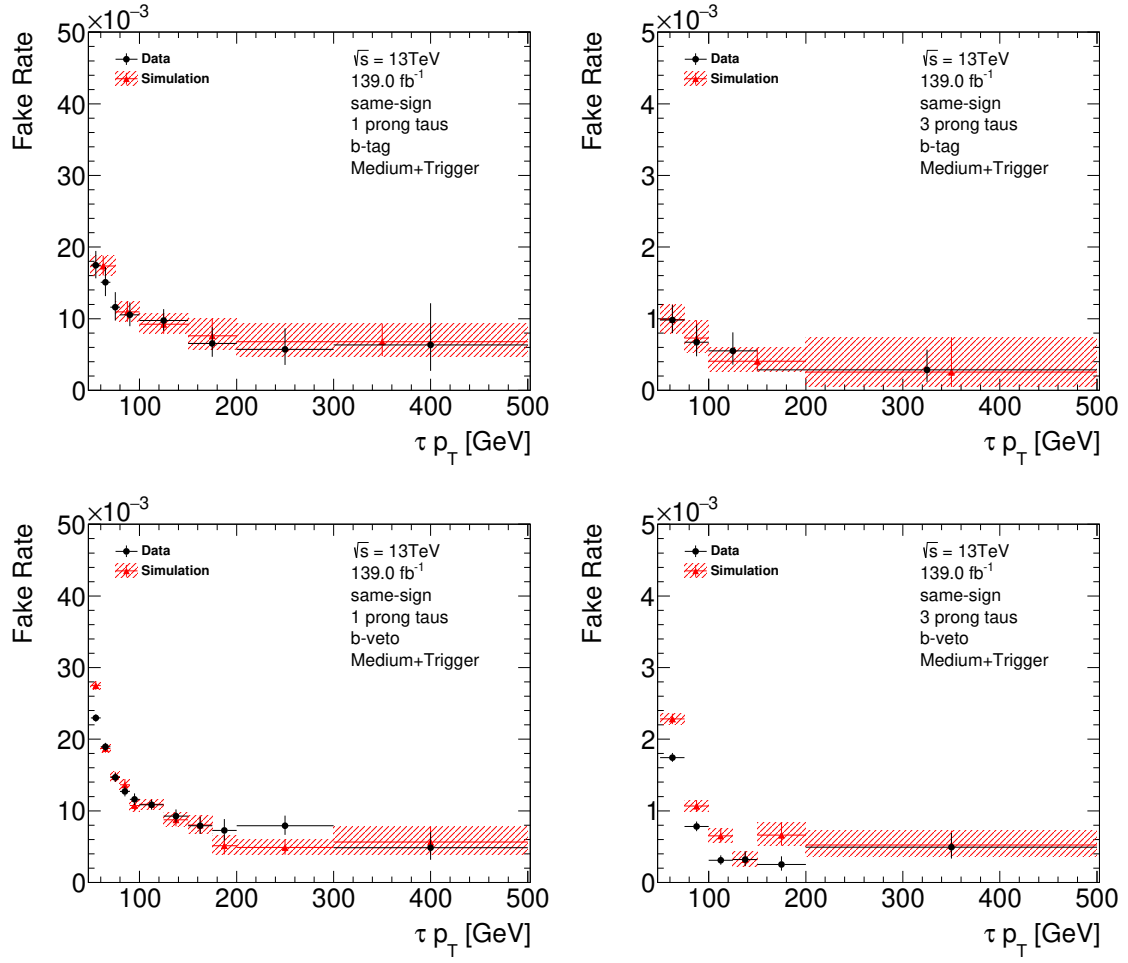
Figure B.3.9.: Fake-rates for fake tau candidates passing the *Medium+Trigger* working point measured in the same-sign *b*-tag (top) and *b*-veto (bottom) $\mu\nu$+jet control region for reconstructed 1 prong (left) and 3 prong (right) fake taus.
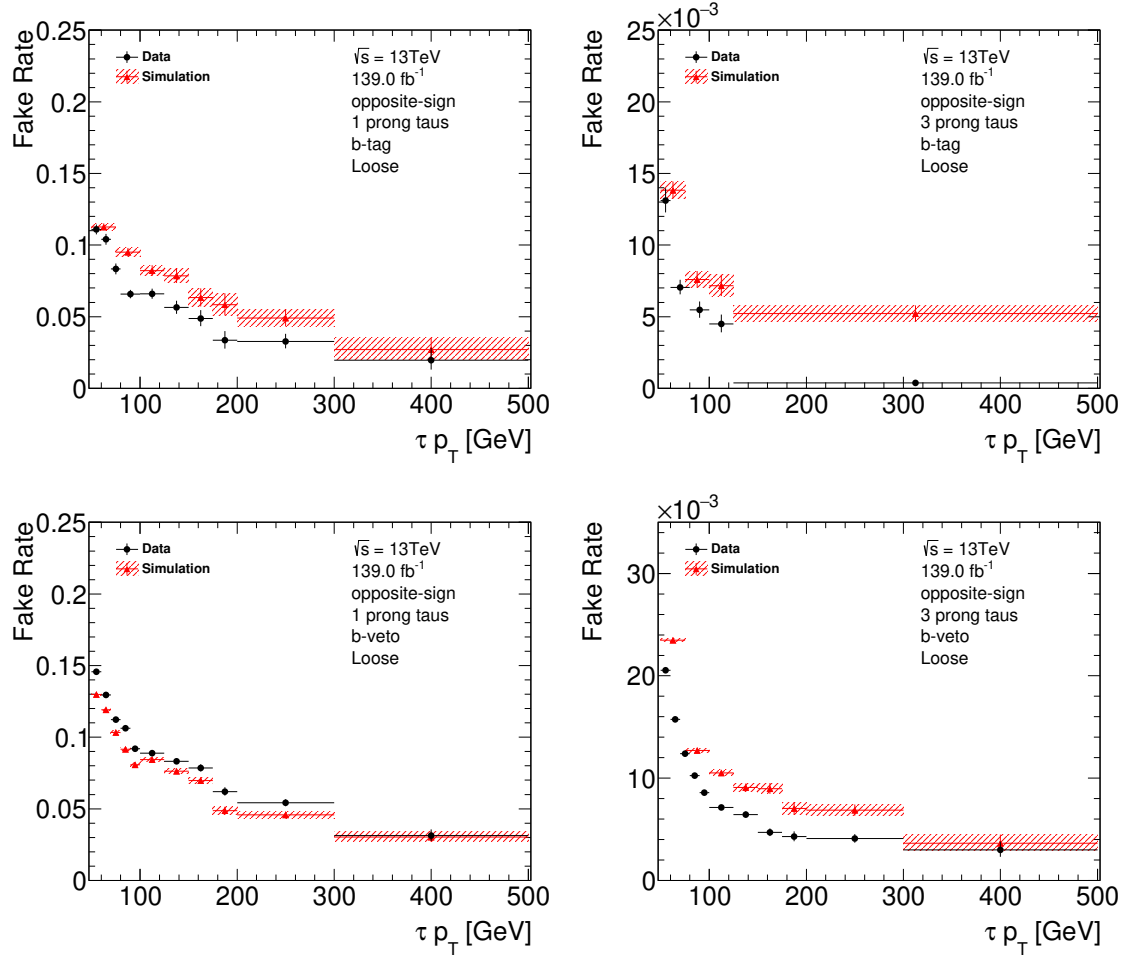
Figure B.3.10.: Fake-rates for fake tau candidates passing the *Loose* working point measured in the opposite-sign *b*-tag (top) and *b*-veto (bottom) $\mu\nu$+jet control region for reconstructed 1 prong (left) and 3 prong (right) fake taus.
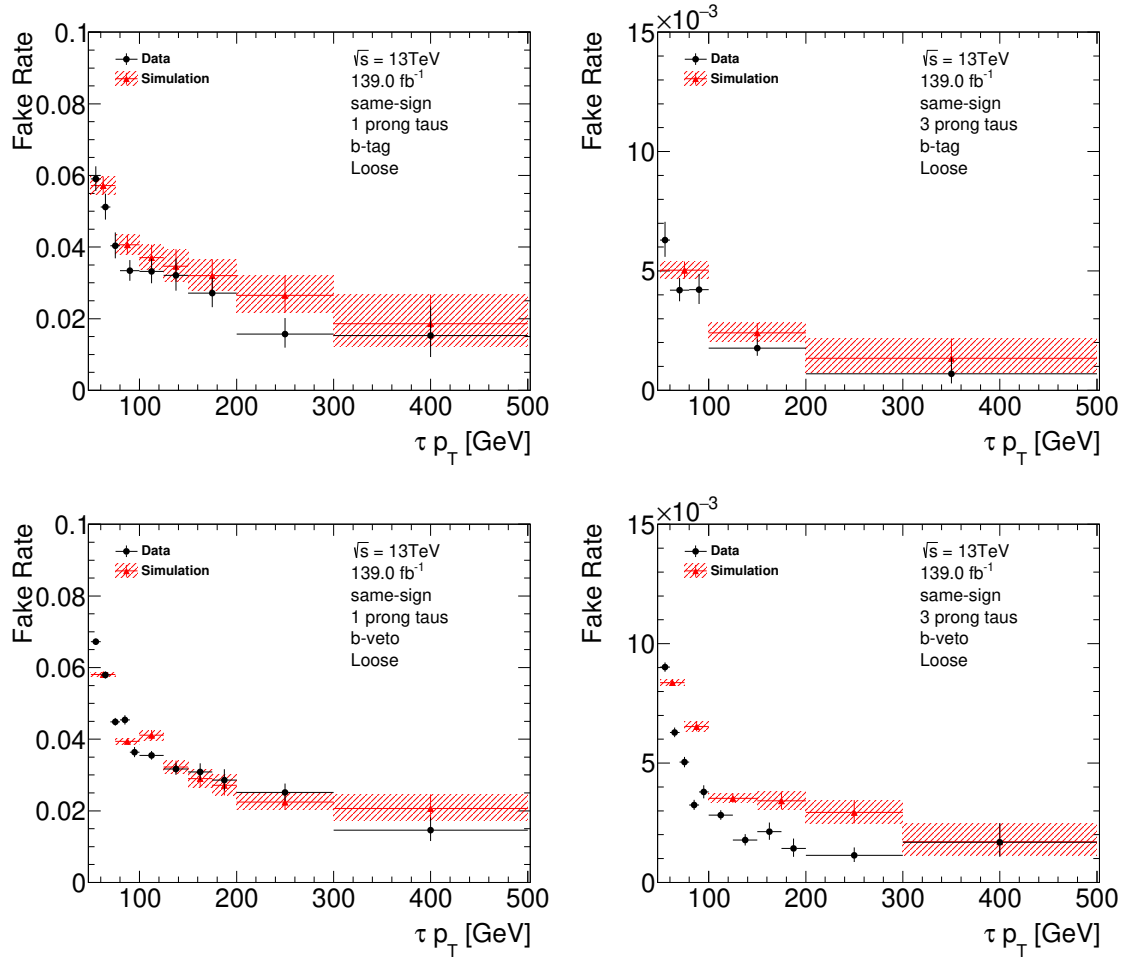
Figure B.3.11.: Fake-rates for fake tau candidates passing the *Loose* working point measured in the same-sign *b*-tag (top) and *b*-veto (bottom) $\mu\nu$+jet control region for reconstructed 1 prong (left) and 3 prong (right) fake taus.
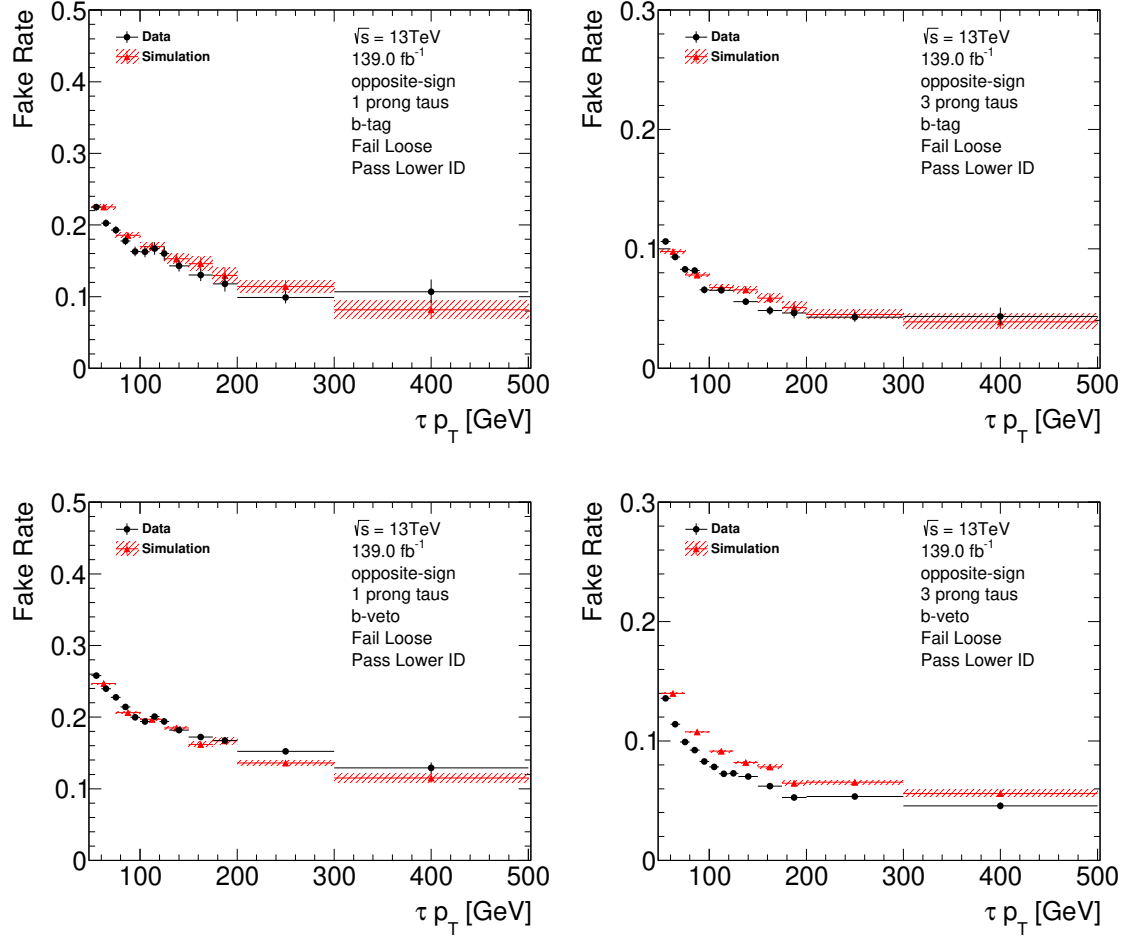
Figure B.3.12.: Fake-rates for fake tau candidates failing the *Loose* working point but passing the lower ID cut measured in the opposite-sign *b*-tag (top) and *b*-veto (bottom) $\mu\nu$+jet control region for reconstructed 1 prong (left) and 3 prong (right) fake taus.
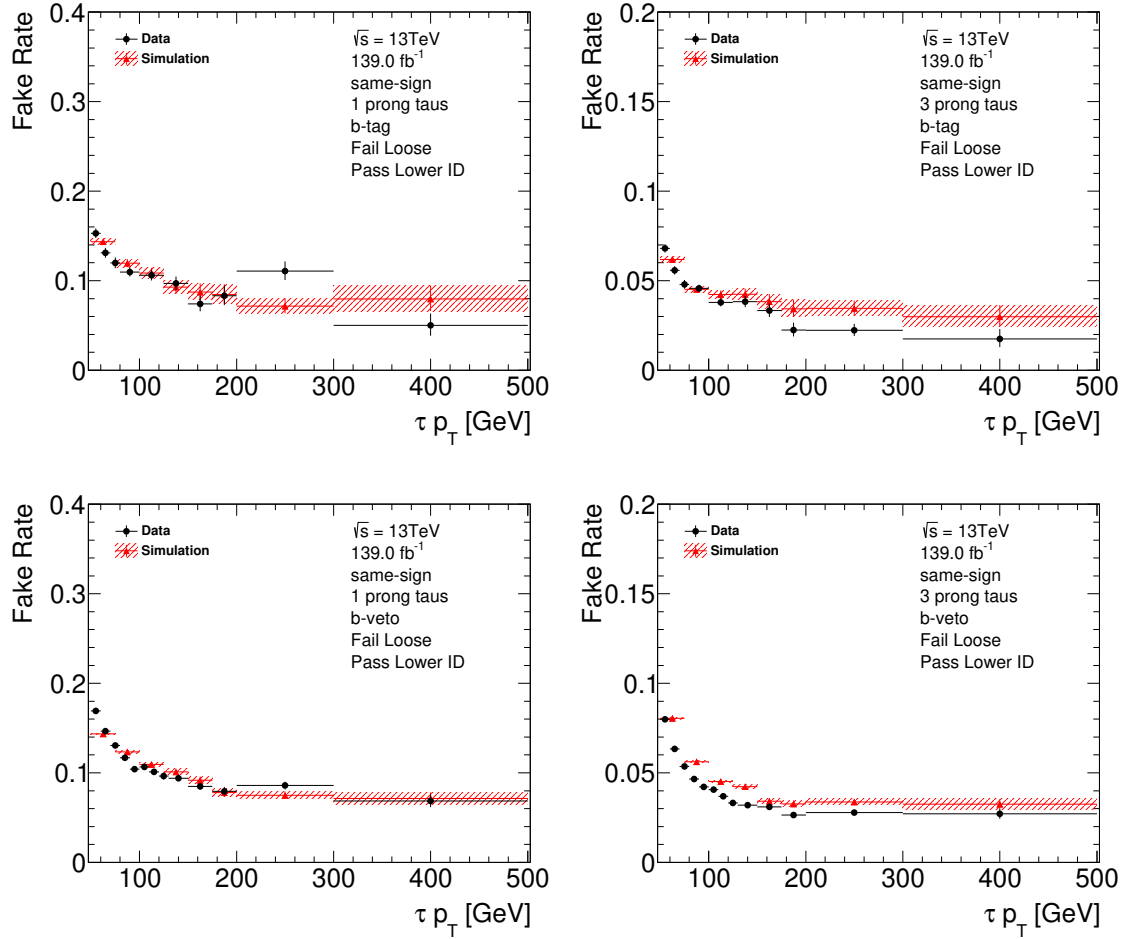
Figure B.3.13.: Fake-rates for fake tau candidates failing the *Loose* working point but passing the lower ID cut measured in the same-sign *b*-tag (top) and *b*-veto (bottom) $\mu\nu$+jet control region for reconstructed 1 prong (left) and 3 prong (right) fake taus.
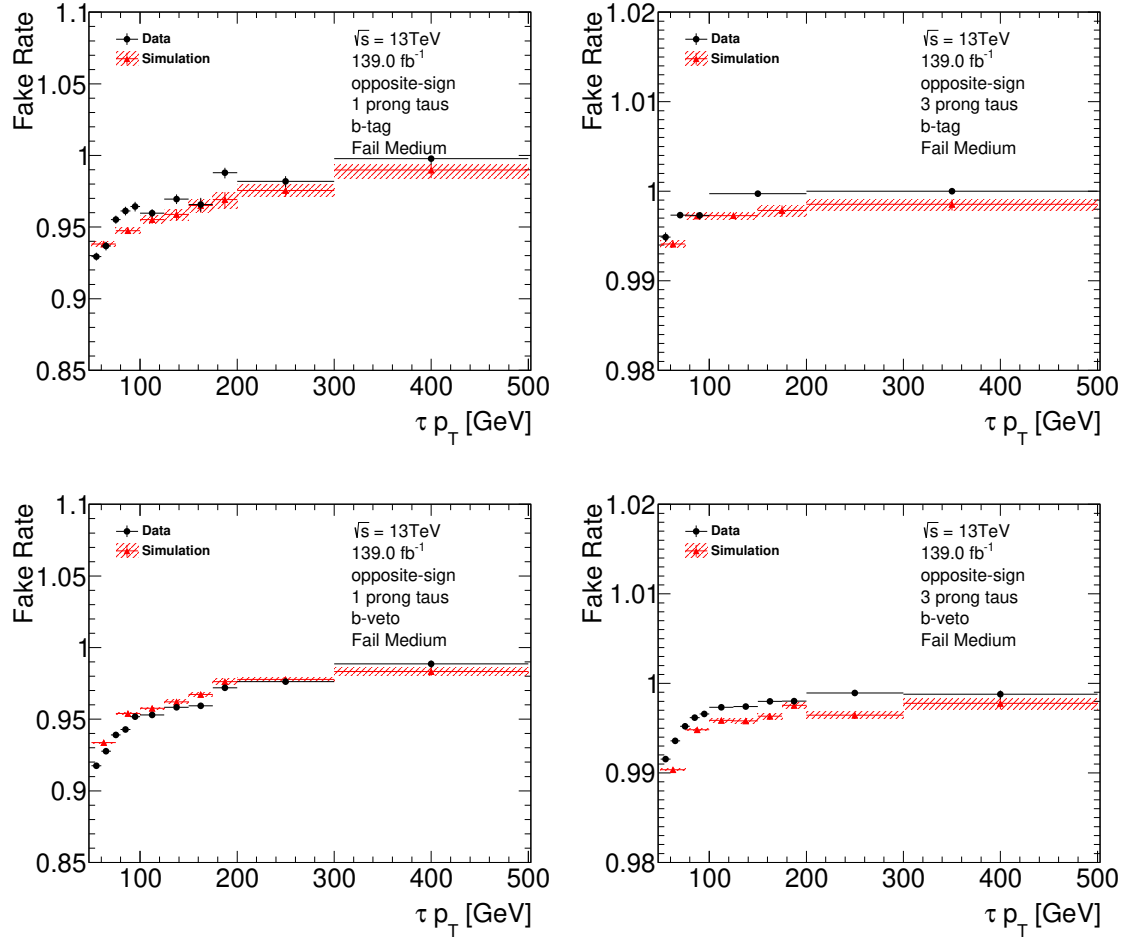
Figure B.3.14.: Fake-rates for fake tau candidates failing the *Medium* working point measured in the opposite-sign *b*-tag (top) and *b*-veto (bottom) $\mu\nu$+jet control region for reconstructed 1 prong (left) and 3 prong (right) fake taus.
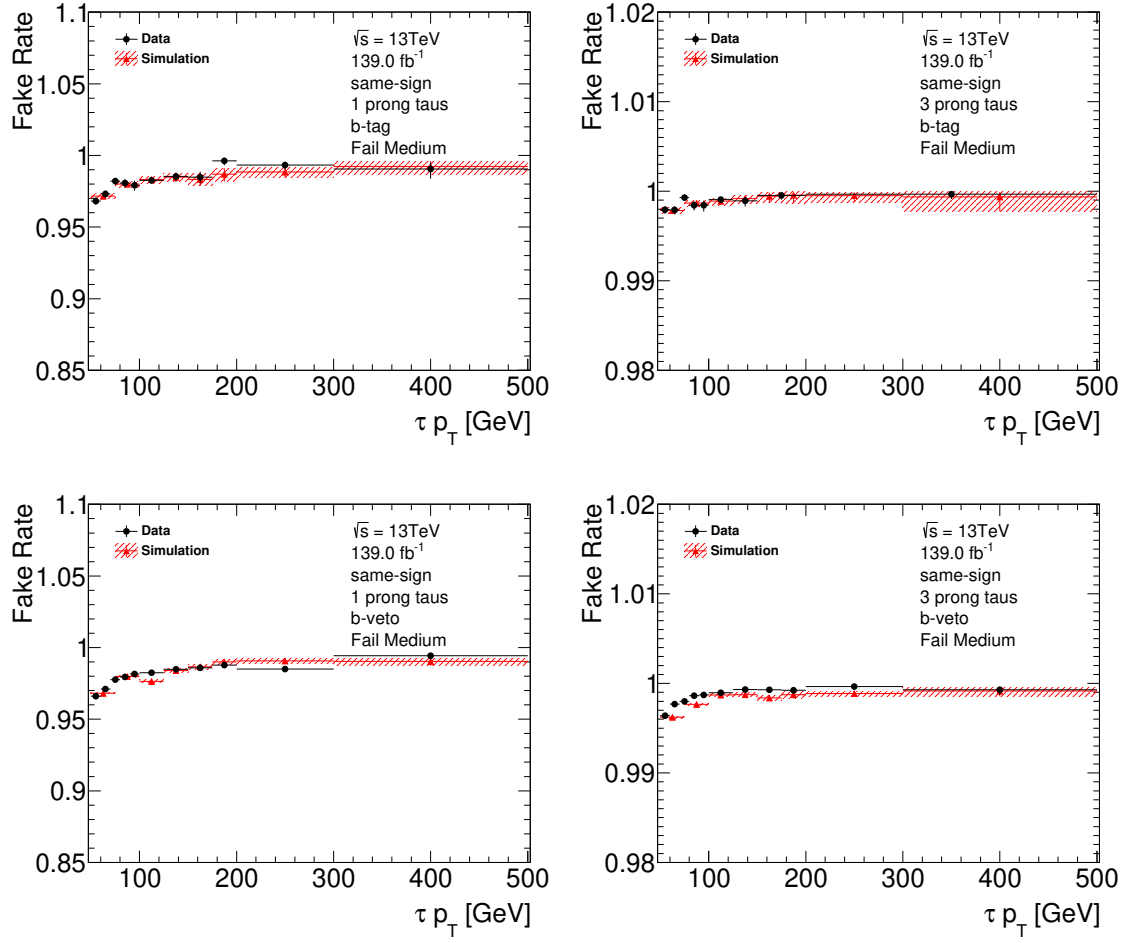
Figure B.3.15.: Fake-rates for fake tau candidates failing the *Medium* working point measured in the same-sign *b*-tag (top) and *b*-veto (bottom) $\mu\nu$+jet control region for reconstructed 1 prong (left) and 3 prong (right) fake taus.

B.4. Signal and Validation Region Variable Distributions

B.4.1. Same-Sign Validation Region

Additional same-sign validation region plots are shown in Figure B.4.1 for distributions in the *b*-veto category and Figure B.4.2 for the *b*-tag category.

B.4.2. Signal Region

Additional signal region variable plots are shown in Figures B.4.3 for distributions in the *b*-veto category and Figure B.4.4 for the *b*-tag category.

Figure B.4.1.: Additional same-sign validation region plots in the *b*-veto category.
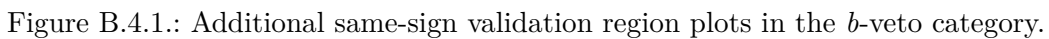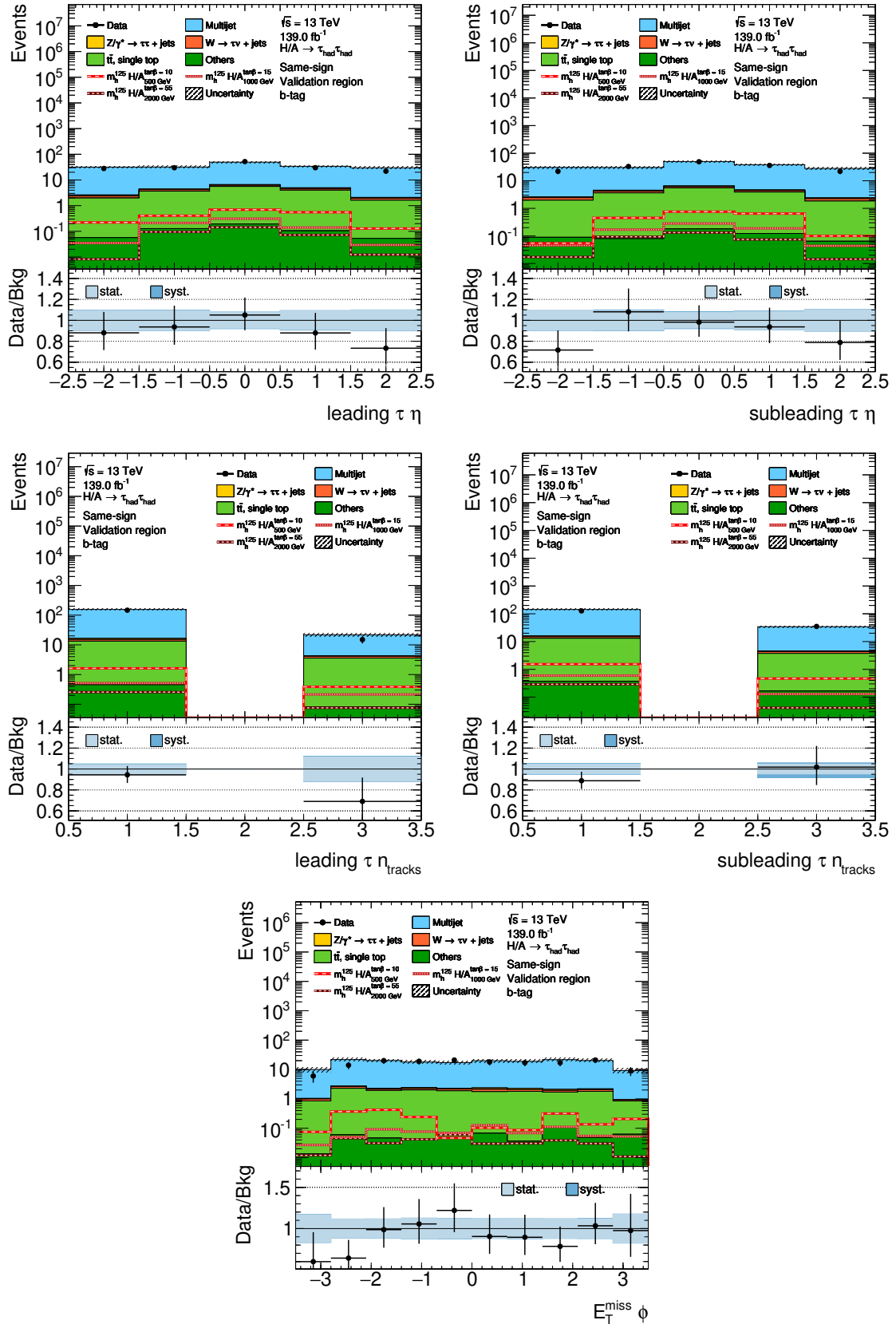
Figure B.4.2.: Additional same-sign validation region plots in the *b*-tag category.
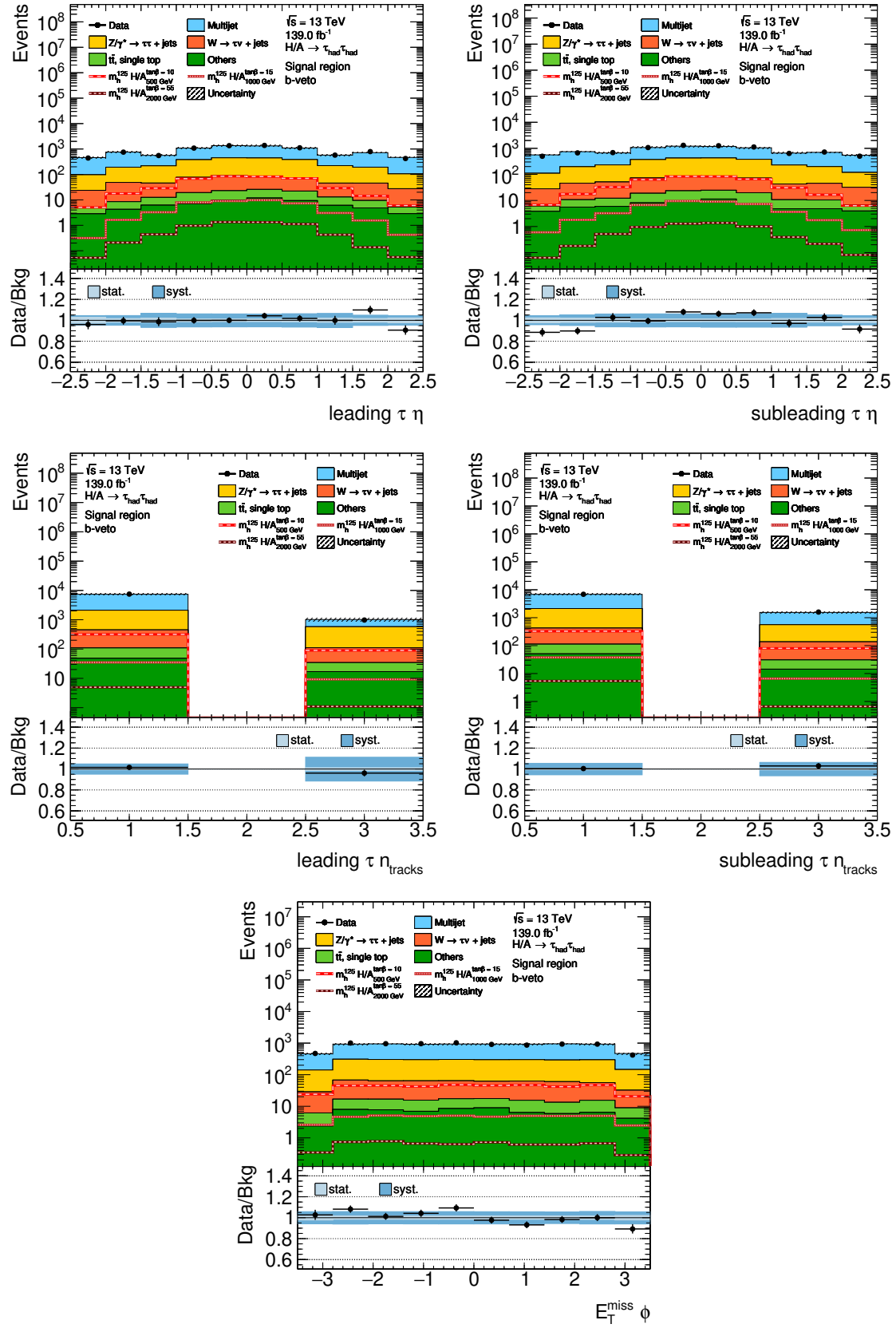
Figure B.4.3.: Additional signal region plots in the *b*-veto category.
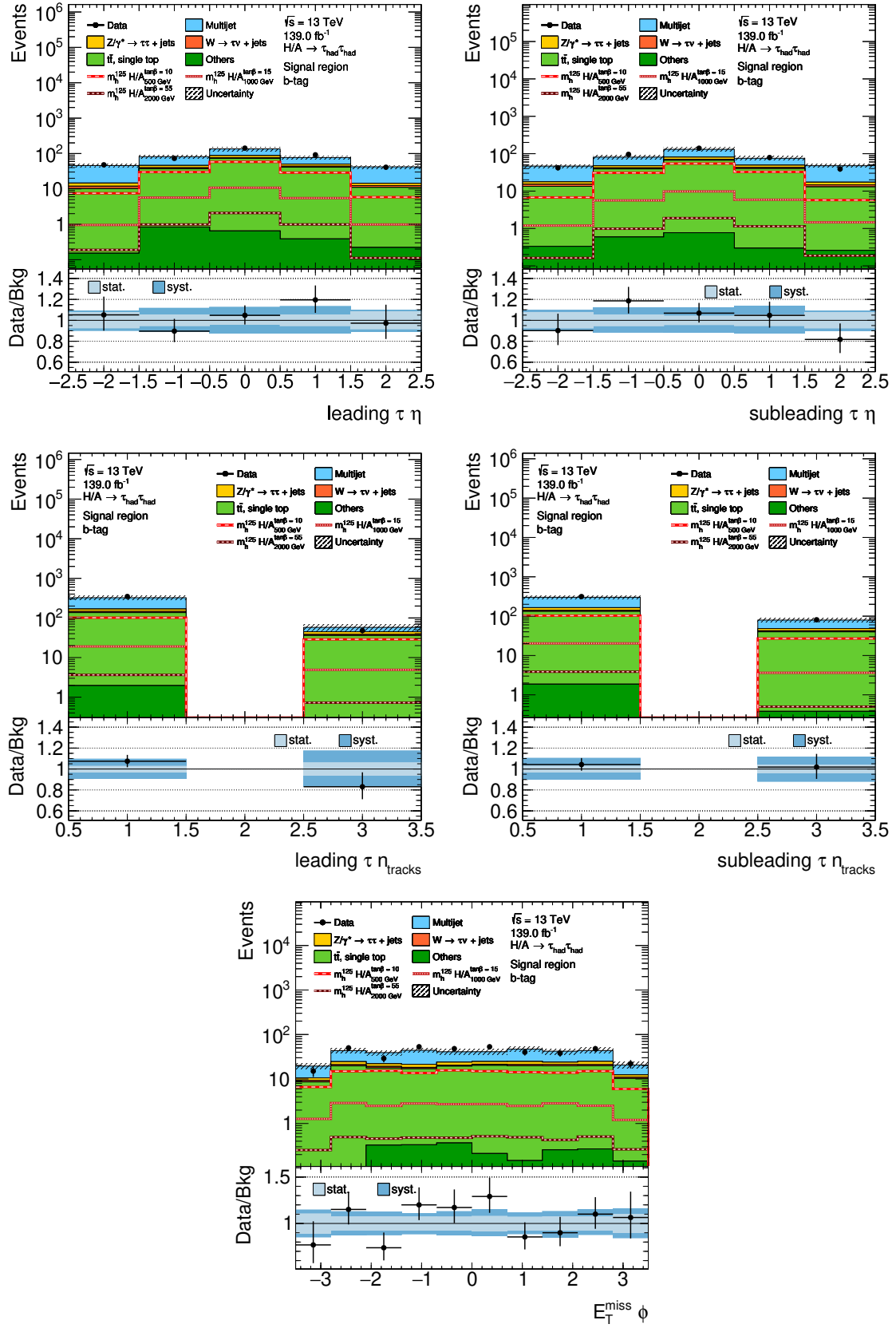
Figure B.4.4.: Additional signal region plots in the *b*-tag category.

C. Systematic Uncertainties

C.1. Breakdown of Signal Acceptance Uncertainties

Tables C.1.1 to C.1.4 list the numerical values of the signal acceptance uncertainty broken down into the different uncertainty sources for the gluon-gluon fusion and b-associated production signal samples. The corresponding visual representation can be found in Figure 7.4.7.

m_ϕ in [GeV]	QCD scale	PDF	Tune	Total	Symmetric
200	$+1.99\,\%$ $-2.52\,\%$	$+4.57\,\%$ $-2.41\,\%$	$+1.84\,\%$ $-2.13\,\%$	$+5.32\,\%$ $-4.09\,\%$	$\pm 4.7\,\%$
400	$+0.67\,\%$ $-0.88\,\%$	$+1.32\,\%$ $-0.66\,\%$	$+1.33\,\%$ $-1.79\,\%$	$+1.98\,\%$ $-2.1\,\%$	$\pm 2.04\,\%$
600	$+0.88\,\%$ $-1.19\,\%$	$+1.39\,\%$ $-0.0\,\%$	$+1.26\,\%$ $-1.82\,\%$	$+2.07\,\%$ $-2.17\,\%$	$\pm 2.12\,\%$
800	$+0.84\,\%$ $-1.17\,\%$	$+1.67\,\%$ $-0.16\,\%$	$+1.22\,\%$ $-1.8\,\%$	$+2.23\,\%$ $-2.15\,\%$	$\pm 2.19\,\%$
1000	$+0.65\,\%$ $-0.94\,\%$	$+1.95\,\%$ $-0.0\,\%$	$+1.07\,\%$ $-1.62\,\%$	$+2.32\,\%$ $-1.88\,\%$	$\pm 2.1\,\%$
1200	$+0.65\,\%$ $-0.95\,\%$	$+1.07\,\%$ $-0.0\,\%$	$+1.0\,\%$ $-1.46\,\%$	$+1.6\,\%$ $-1.74\,\%$	$\pm 1.67\,\%$
1400	$+0.62\,\%$ $-0.88\,\%$	$+0.24\,\%$ $-0.61\,\%$	$+0.99\,\%$ $-1.51\,\%$	$+1.2\,\%$ $-1.85\,\%$	$\pm 1.52\,\%$
1750	$+0.49\,\%$ $-0.69\,\%$	$+0.1\,\%$ $-0.48\,\%$	$+0.96\,\%$ $-1.49\,\%$	$+1.08\,\%$ $-1.71\,\%$	$\pm 1.39\,\%$
2000	$+0.43\,\%$ $-0.62\,\%$	$+0.27\,\%$ $-0.56\,\%$	$+0.88\,\%$ $-1.41\,\%$	$+1.02\,\%$ $-1.64\,\%$	$\pm 1.33\,\%$
2500	$+0.34\,\%$ $-0.5\,\%$	$+0.33\,\%$ $-0.74\,\%$	$+0.81\,\%$ $-1.37\,\%$	$+0.94\,\%$ $-1.64\,\%$	$\pm 1.29\,\%$

Table C.1.1.: Break down of the acceptance uncertainty for gluon-gluon fusion signal samples in b-veto.

m_ϕ in [GeV]	QCD scale	PDF	Tune	Total	Symmetric
200	+2.67 % −3.03 %	+9.42 % −36.04 %	+1.78 % −2.09 %	+9.95 % −36.23 %	±23.09 %
400	+3.59 % −2.7 %	+2.21 % −18.81 %	+1.15 % −1.44 %	+4.37 % −19.06 %	±11.72 %
600	+2.58 % −1.87 %	+7.92 % −5.68 %	+1.34 % −1.77 %	+8.43 % −6.24 %	±7.34 %
800	+2.08 % −1.45 %	+7.39 % −8.7 %	+1.0 % −1.42 %	+7.74 % −8.94 %	±8.34 %
1000	+1.52 % −1.06 %	+7.13 % −7.07 %	+1.0 % −1.47 %	+7.36 % −7.29 %	±7.33 %
1200	+1.22 % −0.87 %	+8.67 % −5.89 %	+0.68 % −1.11 %	+8.79 % −6.06 %	±7.42 %
1400	+0.87 % −0.57 %	+7.39 % −5.02 %	+0.93 % −1.73 %	+7.5 % −5.34 %	±6.42 %
1750	+0.8 % −0.51 %	+7.99 % −4.51 %	+0.99 % −1.62 %	+8.09 % −4.82 %	±6.45 %
2000	+0.31 % −0.19 %	+10.81 % −5.19 %	+0.64 % −1.32 %	+10.83 % −5.36 %	±8.09 %
2500	+0.74 % −0.48 %	+4.86 % −8.37 %	+0.52 % −1.69 %	+4.94 % −8.55 %	±6.75 %

Table C.1.2.: Break down of the acceptance uncertainty for gluon-gluon fusion signal samples in *b*-tag.

m_ϕ in [GeV]	QCD scale	PDF	Tune	Total	Symmetric
200	+2.76 % −2.28 %	+8.78 % −2.81 %	+0.68 % −0.68 %	+9.23 % −3.68 %	±6.45 %
400	+0.7 % −0.82 %	+3.23 % −0.2 %	+0.74 % −0.74 %	+3.38 % −1.12 %	±2.25 %
600	+1.44 % −1.65 %	+0.18 % −4.18 %	+0.79 % −0.79 %	+1.65 % −4.56 %	±3.1 %
800	+1.67 % −1.39 %	+1.2 % −1.86 %	+0.74 % −0.74 %	+2.19 % −2.43 %	±2.31 %
1000	+1.74 % −1.22 %	+0.41 % −0.9 %	+0.73 % −0.73 %	+1.93 % −1.68 %	±1.8 %
1200	+2.31 % −1.85 %	+0.12 % −2.87 %	+0.69 % −0.69 %	+2.42 % −3.48 %	±2.95 %
1400	+1.97 % −1.68 %	+0.3 % −1.34 %	+0.51 % −0.51 %	+2.06 % −2.21 %	±2.13 %
1750	+2.11 % −2.01 %	+0.29 % −2.4 %	+0.42 % −0.42 %	+2.17 % −3.16 %	±2.67 %
2000	+2.3 % −2.31 %	+0.23 % −1.14 %	+0.25 % −0.25 %	+2.33 % −2.59 %	±2.46 %
2500	+1.98 % −2.15 %	+0.86 % −0.49 %	+0.17 % −0.17 %	+2.16 % −2.21 %	±2.19 %

Table C.1.3.: Break down of the acceptance uncertainty for *b*-associated production signal samples in *b*-veto.

m_ϕ in [GeV]	QCD scale	PDF	Tune	Total	Symmetric
200	$+1.36\%$ -1.19%	$+9.25\%$ -5.28%	$+0.54\%$ -0.54%	$+9.37\%$ -5.43%	$\pm 7.4\%$
400	$+0.99\%$ -1.3%	$+3.28\%$ -0.67%	$+0.99\%$ -0.99%	$+3.57\%$ -1.76%	$\pm 2.67\%$
600	$+0.75\%$ -0.84%	$+0.08\%$ -4.08%	$+0.97\%$ -0.97%	$+1.23\%$ -4.28%	$\pm 2.76\%$
800	$+1.19\%$ -1.17%	$+0.8\%$ -3.0%	$+1.09\%$ -1.09%	$+1.8\%$ -3.4%	$\pm 2.6\%$
1000	$+1.33\%$ -1.29%	$+2.86\%$ -0.27%	$+1.17\%$ -1.17%	$+3.37\%$ -1.76%	$\pm 2.57\%$
1200	$+1.75\%$ -1.68%	$+1.86\%$ -1.18%	$+1.26\%$ -1.26%	$+2.84\%$ -2.41%	$\pm 2.63\%$
1400	$+1.75\%$ -1.56%	$+0.8\%$ -0.7%	$+1.35\%$ -1.35%	$+2.35\%$ -2.18%	$\pm 2.27\%$
1750	$+1.68\%$ -1.39%	$+0.46\%$ -0.64%	$+1.48\%$ -1.48%	$+2.28\%$ -2.13%	$\pm 2.21\%$
2000	$+1.78\%$ -1.56%	$+0.73\%$ -1.26%	$+1.5\%$ -1.5%	$+2.44\%$ -2.5%	$\pm 2.47\%$
2500	$+1.68\%$ -1.37%	$+1.4\%$ -1.09%	$+1.7\%$ -1.7%	$+2.78\%$ -2.44%	$\pm 2.61\%$

Table C.1.4.: Break down of the acceptance uncertainty for *b*-associated production signal samples in *b*-tag.

C.2. List of Uncertainties Affecting the Signal Region

Tables C.2.1 to C.2.6 list the scale of the uncertainties affecting the $\tau_\text{had}\tau_\text{had}$ signal-region fit in *b*-tag and *b*-veto for the different backgrounds. The impact is quoted in terms of the relative uncertainty factor $\eta^\pm$ which determines the scale of the normalization uncertainty. In the last column it is noted if the uncertainty is treated as shape uncertainty. Normalization uncertainties with a magnitude below 1% are removed by the pruning algorithm. However, the shape uncertainty component is kept if the magnitude of the shape is significant enough.

Systematic Unc.	η^+	η^-	Shape unc.	Systematic Unc.	η^+	η^-	Shape unc.
Multijet				**$t\bar{t}$, single top**			
Fake Factor 1p Stat. Data bin 1	1.000	1.000	✓	Tau ID Eff. Syst. τ_2	1.054	0.946	·
Fake Factor 1p Stat. Data bin 2	1.004	0.996	✓	Tau Reco. Eff. Total	1.015	0.985	·
Fake Factor 1p Stat. Data bin 3	1.005	0.995	✓	Tau Energy Scale Detector	0.993	1.007	✓
Fake Factor 1p Stat. Data bin 4	1.004	0.996	✓	Tau Trigger Eff. Stat. Data 2016	1.016	0.984	·
Fake Factor 1p Stat. Data bin 5	1.003	0.997	✓	Tau Trigger Eff. Stat. Data 2017	1.015	0.985	·
Fake Factor 1p Stat. Data bin 6	1.001	0.999	✓	Tau Trigger Eff. Stat. Data 2018	1.020	0.980	·
Fake Factor 1p Stat. Data bin 7	1.000	1.000	✓	Tau Trigger Eff. Stat. MC 2016	1.011	0.989	·
Fake Factor 1p Stat. Data bin 8	1.000	1.000	✓	Tau Trigger Eff. Stat. MC 2017	1.010	0.990	·
Fake Factor 1p Stat. Data bin 9	1.000	1.000	✓	Tau Trigger Eff. Stat. MC 2018	1.014	0.986	·
Fake Factor 1p Stat. MC bin 1	1.000	1.000	✓	Top Cross Section	1.060	0.940	·
Fake Factor 1p Stat. MC bin 2	1.000	1.000	✓	Top ISR	1.109	0.941	✓
Fake Factor 1p Stat. MC bin 3	1.000	1.000	✓	Top ME	1.010	0.990	✓
Fake Factor 1p Stat. MC bin 4	1.001	0.999	✓	Top PS	0.909	1.091	✓
Fake Factor 1p Stat. MC bin 5	1.002	0.998	✓	**$Z/\gamma^* \to \tau\tau$ + jets**			
Fake Factor 1p Stat. MC bin 6	1.000	1.000	✓	$Z \to \tau\tau$ k-factor α_s	1.020	0.979	·
Fake Factor 1p Stat. MC bin 7	1.000	1.000	✓	$Z \to \tau\tau$ k-factor Beam Energy	1.020	0.980	✓
Fake Factor 1p Stat. MC bin 8	1.000	1.000	✓	$Z \to \tau\tau$ k-factor Choice HERAPDF20	1.103	0.897	✓
Fake Factor 1p Stat. MC bin 9	1.000	1.000	✓	$Z \to \tau\tau$ k-factor Choice NNPDF30	0.992	1.008	✓
Fake Factor 3p Stat. Data bin 1	1.001	0.999	✓	$Z \to \tau\tau$ k-factor Choice epWZ16	1.038	0.962	✓
Fake Factor 3p Stat. Data bin 2	1.003	0.997	✓	$Z \to \tau\tau$ k-factor PDF	1.075	0.917	✓
Fake Factor 3p Stat. Data bin 3	1.001	0.999	✓	$Z \to \tau\tau$ k-factor PDF Eigen	1.006	0.994	✓
Fake Factor 3p Stat. Data bin 4	1.000	1.000	✓	$Z \to \tau\tau$ k-factor PI	1.031	0.970	✓
Fake Factor 3p Stat. Data bin 5	1.000	1.000	✓	Luminosity Measurement	1.032	0.968	·
Fake Factor 3p Stat. MC bin 1	1.000	1.000	✓	Tau Energy Scale Detector	1.094	0.897	✓
Fake Factor 3p Stat. MC bin 2	1.001	0.999	✓	Tau Energy Scale Model	1.008	0.990	✓
Fake Factor 3p Stat. MC bin 3	1.001	0.999	✓	Tau ID Eff. 1p p_T>40GeV τ_1	1.022	0.978	·
Fake Factor 3p Stat. MC bin 4	1.000	1.000	✓	Tau ID Eff. 1p p_T>40GeV τ_2	1.020	0.980	·
Fake Factor 3p Stat. MC bin 5	1.000	1.000	✓	Tau ID Eff. High p_T τ_1	1.009	0.991	✓
Fake Factor MC Syst.	1.012	0.988	✓	Tau ID Eff. High p_T τ_2	1.004	0.996	✓
Tau Energy Scale Detector	0.993	1.007	✓	Tau ID Eff. Syst. τ_1	1.073	0.927	·
$t\bar{t}$, single top				Tau ID Eff. Syst. τ_2	1.067	0.933	·
Fake Rate	1.055	0.957	·	Tau Reco. Eff. High p_T	1.004	0.996	✓
Flav. Tag. Eff. Eigen B 0	0.964	1.037	·	Tau Reco. Eff. Total	1.017	0.983	·
Flav. Tag. Eff. Eigen B 2	0.985	1.015	·	Tau Trigger Eff. Stat. Data 2015	1.006	0.992	✓
Luminosity Measurement	1.032	0.968	·	Tau Trigger Eff. Stat. Data 2016	1.016	0.984	·
Tau Energy Scale Detector	1.114	0.873	·	Tau Trigger Eff. Stat. Data 2017	1.018	0.982	✓
Tau Energy Scale Model	1.010	0.989	·	Tau Trigger Eff. Stat. Data 2018	1.030	0.970	✓
Tau ID Eff. 1p p_T>40GeV τ_1	1.017	0.983	·	Tau Trigger Eff. Stat. MC 2016	1.011	0.989	·
Tau ID Eff. 1p p_T>40GeV τ_2	1.015	0.985	·	Tau Trigger Eff. Stat. MC 2017	1.012	0.988	·
Tau ID Eff. Syst. τ_1	1.060	0.940	·	Tau Trigger Eff. Stat. MC 2018	1.020	0.980	·
				Tau Trigger Eff. Syst. 2015	1.003	0.997	✓

Table C.2.1.: List of systematic uncertainties affecting the *b*-veto signal region. The magnitude is quoted in terms of the relative uncertainty factor $\eta^\pm$ from Equation (7.22). The last column indicates if the nuisance parameter is implemented as shape uncertainty.

Systematic Unc.	η^+	η^-	Shape unc.
$W \to \tau\nu$ + jets			
Fake Rate	1.062	0.944	·
Luminosity Measurement	1.032	0.968	·
Tau Energy Scale Detector	1.080	0.915	·
Tau ID Eff. 1p p_T>40GeV τ_2	1.011	0.989	·
Tau ID Eff. Syst. τ_1	1.029	0.971	·
Tau ID Eff. Syst. τ_2	1.041	0.959	·
Tau Trigger Eff. Stat. Data 2015	1.005	0.994	✓
Others			
Fake Rate	1.020	0.981	·
Luminosity Measurement	1.032	0.968	·
Tau Energy Scale Detector	1.072	0.926	·
Tau ID Eff. 1p p_T>40GeV τ_1	1.016	0.984	·
Tau ID Eff. 1p p_T>40GeV τ_2	1.015	0.985	·
Tau ID Eff. Syst. τ_1	1.060	0.940	·
Tau ID Eff. Syst. τ_2	1.052	0.948	·
Tau Reco. Eff. Total	1.015	0.985	·
Tau Trigger Eff. Stat. Data 2016	1.013	0.987	·
Tau Trigger Eff. Stat. Data 2017	1.016	0.984	·
Tau Trigger Eff. Stat. Data 2018	1.032	0.968	·
Tau Trigger Eff. Stat. MC 2017	1.011	0.989	·
Tau Trigger Eff. Stat. MC 2018	1.021	0.979	·
ggH500			
Luminosity Measurement	1.032	0.968	·
Signal Acceptance Unc.	1.021	0.979	·
Tau Energy Scale Detector	1.055	0.926	·
Tau ID Eff. 1p p_T>40GeV τ_1	1.022	0.978	·
Tau ID Eff. 1p p_T>40GeV τ_2	1.020	0.980	·
Tau ID Eff. Syst. τ_1	1.074	0.926	·
Tau ID Eff. Syst. τ_2	1.068	0.932	·
Tau Reco. Eff. Total	1.017	0.983	·
Tau Trigger Eff. Stat. Data 2015	1.003	0.996	✓
Tau Trigger Eff. Stat. Data 2016	1.017	0.983	·
Tau Trigger Eff. Stat. Data 2017	1.021	0.979	·
Tau Trigger Eff. Stat. Data 2018	1.036	0.964	·
Tau Trigger Eff. Stat. MC 2016	1.011	0.989	·
Tau Trigger Eff. Stat. MC 2017	1.014	0.986	·
Tau Trigger Eff. Stat. MC 2018	1.024	0.976	·
Tau Trigger Eff. Syst. 2015	1.001	0.999	✓

Systematic Unc.	η^+	η^-	Shape unc.
bbH500			
Flav. Tag. Eff. Eigen B 0	0.984	1.016	·
Luminosity Measurement	1.032	0.968	·
Signal Acceptance Unc.	1.027	0.973	·
Tau Energy Scale AFII	1.068	0.922	·
Tau Energy Scale Detector	1.057	0.932	·
Tau ID Eff. 1p p_T>40GeV τ_1	1.023	0.977	·
Tau ID Eff. 1p p_T>40GeV τ_2	1.020	0.980	·
Tau ID Eff. AFII τ_1	1.012	0.988	·
Tau ID Eff. Syst. τ_1	1.074	0.926	·
Tau ID Eff. Syst. τ_2	1.068	0.932	·
Tau Reco. Eff. AFII	1.102	0.903	·
Tau Reco. Eff. Total	1.017	0.983	·
Tau Trigger Eff. Stat. Data 2016	1.016	0.984	·
Tau Trigger Eff. Stat. Data 2017	1.022	0.978	·
Tau Trigger Eff. Stat. Data 2018	1.036	0.964	·
Tau Trigger Eff. Stat. MC 2016	1.011	0.989	·
Tau Trigger Eff. Stat. MC 2017	1.015	0.985	·
Tau Trigger Eff. Stat. MC 2018	1.024	0.976	·
ggH2000			
Luminosity Measurement	1.032	0.968	·
Signal Acceptance Unc.	1.013	0.987	·
Tau Energy Scale Detector	1.002	0.996	✓
Tau ID Eff. 1p p_T>40GeV τ_1	1.024	0.976	·
Tau ID Eff. 1p p_T>40GeV τ_2	1.022	0.978	·
Tau ID Eff. High p_T τ_1	1.045	0.955	✓
Tau ID Eff. High p_T τ_2	1.025	0.975	✓
Tau ID Eff. Syst. τ_1	1.073	0.927	·
Tau ID Eff. Syst. τ_2	1.068	0.932	·
Tau Reco. Eff. High p_T	1.027	0.974	✓
Tau Reco. Eff. Total	1.019	0.981	·
Tau Trigger Eff. Stat. Data 2016	1.015	0.985	·
Tau Trigger Eff. Stat. Data 2017	1.025	0.975	·
Tau Trigger Eff. Stat. Data 2018	1.037	0.963	✓
Tau Trigger Eff. Stat. MC 2017	1.015	0.985	·
Tau Trigger Eff. Stat. MC 2018	1.022	0.978	·

Table C.2.2.: List of systematic uncertainties affecting the *b*-veto signal region. The magnitude is quoted in terms of the relative uncertainty factor $\eta^\pm$ from Equation (7.22). The last column indicates if the nuisance parameter is implemented as shape uncertainty.

Systematic Unc.	η^+	η^-	Shape unc.
bbH2000			
Flav. Tag. Eff. Eigen B 0	0.989	1.011	·
Luminosity Measurement	1.032	0.968	·
Pile-up Reweighting	0.984	1.002	✓
Signal Acceptance Unc.	1.025	0.975	·
Tau Energy Scale AFII	1.004	0.996	✓
Tau Energy Scale Detector	1.002	0.997	✓
Tau ID Eff. 1p p_T>40GeV τ_1	1.024	0.976	·
Tau ID Eff. 1p p_T>40GeV τ_2	1.022	0.978	·
Tau ID Eff. AFII τ_1	1.012	0.988	·
Tau ID Eff. High p_T τ_1	1.047	0.953	✓
Tau ID Eff. High p_T τ_2	1.026	0.974	✓
Tau ID Eff. Syst. τ_1	1.073	0.927	·
Tau ID Eff. Syst. τ_2	1.067	0.933	·
Tau Reco. Eff. AFII	1.102	0.903	·
Tau Reco. Eff. High p_T	1.029	0.971	✓
Tau Reco. Eff. Total	1.019	0.981	·
Tau Trigger Eff. Stat. Data 2016	1.014	0.985	·
Tau Trigger Eff. Stat. Data 2017	1.024	0.976	✓
Tau Trigger Eff. Stat. Data 2018	1.038	0.962	·
Tau Trigger Eff. Stat. MC 2017	1.015	0.985	·
Tau Trigger Eff. Stat. MC 2018	1.023	0.977	·

Table C.2.3.: List of systematic uncertainties affecting the *b*-veto signal region. The magnitude is quoted in terms of the relative uncertainty factor $\eta^\pm$ from Equation (7.22). The last column indicates if the nuisance parameter is implemented as shape uncertainty.

Systematic Unc.	η^+	η^-	Shape unc.	Systematic Unc.	η^+	η^-	Shape unc.
Multijet				$t\bar{t}$, single top			
Fake Factor 1p Stat. Data bin 1	1.000	1.000	✓	Tau Reco. Eff. Total	1.016	0.984	·
Fake Factor 1p Stat. Data bin 2	1.004	0.996	✓	Tau Trigger Eff. Stat. Data 2015	1.005	0.993	✓
Fake Factor 1p Stat. Data bin 3	1.005	0.995	✓	Tau Trigger Eff. Stat. Data 2016	1.012	0.988	·
Fake Factor 1p Stat. Data bin 4	1.004	0.996	✓	Tau Trigger Eff. Stat. Data 2017	1.014	0.986	·
Fake Factor 1p Stat. Data bin 5	1.002	0.998	✓	Tau Trigger Eff. Stat. Data 2018	1.029	0.971	·
Fake Factor 1p Stat. Data bin 6	1.000	1.000	✓	Tau Trigger Eff. Stat. MC 2018	1.020	0.980	·
Fake Factor 1p Stat. Data bin 7	1.000	1.000	✓	Top Cross Section	1.060	0.940	·
Fake Factor 1p Stat. Data bin 8	1.000	1.000	✓	Top ISR	1.122	0.935	·
Fake Factor 1p Stat. Data bin 9	1.000	1.000	✓	Top ME	1.013	0.987	✓
Fake Factor 1p Stat. MC bin 1	1.000	1.000	✓	Top PS	0.898	1.102	✓
Fake Factor 1p Stat. MC bin 2	1.000	1.000	✓	$Z/\gamma^* \to \tau\tau$ + jets			
Fake Factor 1p Stat. MC bin 3	1.000	1.000	✓	$Z \to \tau\tau$ k-factor α_s	1.024	0.975	✓
Fake Factor 1p Stat. MC bin 4	1.001	0.999	✓	$Z \to \tau\tau$ k-factor Beam Energy	1.020	0.980	·
Fake Factor 1p Stat. MC bin 5	1.001	0.999	✓	$Z \to \tau\tau$ k-factor Choice HERAPDF20	1.105	0.895	✓
Fake Factor 1p Stat. MC bin 6	1.000	1.000	✓	$Z \to \tau\tau$ k-factor Choice NNPDF30	0.991	1.009	✓
Fake Factor 1p Stat. MC bin 7	1.000	1.000	✓	$Z \to \tau\tau$ k-factor Choice epWZ16	1.047	0.953	✓
Fake Factor 1p Stat. MC bin 8	1.000	1.000	✓	$Z \to \tau\tau$ k-factor PDF	1.078	0.914	✓
Fake Factor 1p Stat. MC bin 9	1.000	1.000	✓	$Z \to \tau\tau$ k-factor PDF Eigen	1.006	0.994	✓
Fake Factor 3p Stat. Data bin 1	1.001	0.999	✓	$Z \to \tau\tau$ k-factor PI	1.028	0.972	✓
Fake Factor 3p Stat. Data bin 2	1.003	0.997	✓	E_T^{miss} Soft Track ResoPara	1.000	1.000	✓
Fake Factor 3p Stat. Data bin 3	1.001	0.999	✓	Flav. Tag. Eff. Eigen B 0	1.011	0.988	·
Fake Factor 3p Stat. Data bin 4	1.000	1.000	✓	Flav. Tag. Eff. Eigen C 0	0.960	1.040	✓
Fake Factor 3p Stat. Data bin 5	1.000	1.000	✓	Flav. Tag. Eff. Light 0	0.943	1.057	✓
Fake Factor 3p Stat. MC bin 1	1.000	1.000	✓	Flav. Tag. Eff. Light 1	1.015	0.985	·
Fake Factor 3p Stat. MC bin 2	1.001	0.999	✓	Flav. Tag. Eff. Rxtrapol. from Charm	1.013	0.987	✓
Fake Factor 3p Stat. MC bin 3	1.001	0.999	✓	Luminosity Measurement	1.032	0.968	·
Fake Factor 3p Stat. MC bin 4	1.000	1.000	✓	Tau Energy Scale Detector	1.095	0.917	✓
Fake Factor 3p Stat. MC bin 5	1.000	1.000	✓	Tau Energy Scale Model	1.015	0.988	·
Fake Factor MC Syst.	1.011	0.989	✓	Tau ID Eff. 1p p_T>40GeV τ_1	1.021	0.979	·
Tau Energy Scale Detector	0.972	1.028	·	Tau ID Eff. 1p p_T>40GeV τ_2	1.018	0.982	·
Tau ID Eff. Syst. τ_1	0.984	1.016	·	Tau ID Eff. High p_T τ_1	1.010	0.990	✓
$t\bar{t}$, single top				Tau ID Eff. Syst. τ_1	1.070	0.930	·
Fake Rate	1.042	0.968	·	Tau ID Eff. Syst. τ_2	1.064	0.936	✓
Luminosity Measurement	1.032	0.968	·	Tau Reco. Eff. High p_T	1.004	0.996	✓
Tau Energy Scale Detector	1.116	0.877	·	Tau Reco. Eff. Total	1.017	0.983	·
Tau Energy Scale In-situ	1.003	0.997	✓	Tau Trigger Eff. Stat. Data 2016	1.016	0.984	·
Tau Energy Scale Model	1.011	0.984	·	Tau Trigger Eff. Stat. Data 2017	1.018	0.982	·
Tau ID Eff. 1p p_T>40GeV τ_1	1.019	0.981	·	Tau Trigger Eff. Stat. Data 2018	1.030	0.970	✓
Tau ID Eff. 1p p_T>40GeV τ_2	1.016	0.984	·	Tau Trigger Eff. Stat. MC 2016	1.011	0.989	·
Tau ID Eff. Syst. τ_1	1.064	0.936	·	Tau Trigger Eff. Stat. MC 2017	1.012	0.988	·
Tau ID Eff. Syst. τ_2	1.057	0.943	·	Tau Trigger Eff. Stat. MC 2018	1.020	0.980	·

Table C.2.4.: List of systematic uncertainties affecting the *b*-tag signal region. The magnitude is quoted in terms of the relative uncertainty factor $\eta^\pm$ from Equation (7.22). The last column indicates if the nuisance parameter is implemented as shape uncertainty.

Left panel:

Systematic Unc.	η^+	η^-	Shape unc.
$W \to \tau\nu$ + jets			
Fake Rate	1.059	0.947	✓
Flav. Tag. Eff. Eigen B 0	1.013	0.987	·
Flav. Tag. Eff. Eigen C 0	0.975	1.025	·
Flav. Tag. Eff. Light 0	0.966	1.034	·
Luminosity Measurement	1.032	0.968	·
Tau Energy Scale Detector	1.086	0.918	·
Tau ID Eff. 1p p_T>40GeV τ_1	1.011	0.989	·
Tau ID Eff. Syst. τ_1	1.039	0.961	✓
Tau ID Eff. Syst. τ_2	1.032	0.968	✓
Tau Trigger Eff. Stat. Data 2018	1.017	0.983	·
Tau Trigger Eff. Stat. MC 2018	1.012	0.988	·
Others			
Fake Rate	1.029	0.974	·
Flav. Tag. Eff. Eigen C 0	0.964	1.036	·
Flav. Tag. Eff. Light 0	0.944	1.056	·
Luminosity Measurement	1.032	0.968	·
Tau Energy Scale Detector	1.080	0.925	·
Tau ID Eff. 1p p_T>40GeV τ_1	1.019	0.981	·
Tau ID Eff. 1p p_T>40GeV τ_2	1.014	0.986	·
Tau ID Eff. Syst. τ_1	1.055	0.945	·
Tau ID Eff. Syst. τ_2	1.045	0.955	·
Tau Reco. Eff. Total	1.012	0.988	·
Tau Trigger Eff. Stat. Data 2016	1.015	0.985	·
Tau Trigger Eff. Stat. Data 2017	1.011	0.989	·
Tau Trigger Eff. Stat. Data 2018	1.017	0.983	·
Tau Trigger Eff. Stat. MC 2016	1.011	0.989	·
Tau Trigger Eff. Stat. MC 2018	1.011	0.989	·
ggH500			
Flav. Tag. Eff. Eigen B 0	1.010	0.990	✓
Flav. Tag. Eff. Eigen C 0	0.970	1.030	·
Flav. Tag. Eff. Light 0	0.930	1.069	·
Flav. Tag. Eff. Light 1	1.018	0.982	·
Luminosity Measurement	1.032	0.968	·
Pile-up reweighting	1.012	0.977	·

Right panel:

Systematic Unc.	η^+	η^-	Shape unc.
ggH500			
Signal Acceptance Unc.	1.095	0.905	·
Tau Energy Scale Detector	1.047	0.935	·
Tau ID Eff. 1p p_T>40GeV τ_1	1.022	0.978	·
Tau ID Eff. 1p p_T>40GeV τ_2	1.020	0.980	·
Tau ID Eff. Syst. τ_1	1.074	0.926	·
Tau ID Eff. Syst. τ_2	1.068	0.932	·
Tau Reco. Eff. Total	1.017	0.983	·
Tau Trigger Eff. Stat. Data 2015	1.003	0.996	✓
Tau Trigger Eff. Stat. Data 2016	1.016	0.984	·
Tau Trigger Eff. Stat. Data 2017	1.021	0.979	✓
Tau Trigger Eff. Stat. Data 2018	1.040	0.960	·
Tau Trigger Eff. Stat. MC 2016	1.010	0.990	·
Tau Trigger Eff. Stat. MC 2017	1.015	0.985	·
Tau Trigger Eff. Stat. MC 2018	1.026	0.974	·
bbH500			
Flav. Tag. Eff. Eigen B 0	1.019	0.981	·
Luminosity Measurement	1.032	0.968	·
Signal Acceptance Unc.	1.027	0.973	·
Tau Energy Scale AFII	1.059	0.920	✓
Tau Energy Scale Detector	1.051	0.933	✓
Tau Energy Scale Model	1.004	0.996	✓
Tau ID Eff. 1p p_T>40GeV τ_1	1.023	0.977	·
Tau ID Eff. 1p p_T>40GeV τ_2	1.020	0.980	·
Tau ID Eff. AFII τ_1	1.012	0.988	·
Tau ID Eff. Syst. τ_1	1.074	0.926	·
Tau ID Eff. Syst. τ_2	1.068	0.932	·
Tau Reco. Eff. AFII	1.102	0.903	·
Tau Reco. Eff. Total	1.017	0.983	·
Tau Trigger Eff. Stat. Data 2016	1.017	0.983	·
Tau Trigger Eff. Stat. Data 2017	1.021	0.979	·
Tau Trigger Eff. Stat. Data 2018	1.036	0.964	✓
Tau Trigger Eff. Stat. MC 2016	1.011	0.989	·
Tau Trigger Eff. Stat. MC 2017	1.014	0.986	·
Tau Trigger Eff. Stat. MC 2018	1.024	0.976	·

Table C.2.5.: List of systematic uncertainties affecting the *b*-tag signal region. The magnitude is quoted in terms of the relative uncertainty factor $\eta^\pm$ from Equation (7.22). The last column indicates if the nuisance parameter is implemented as shape uncertainty.

Systematic Unc.	η^+	η^-	Shape unc.	Systematic Unc.	η^+	η^-	Shape unc.
ggH2000				bbH2000			
E_T^{miss} Soft Track ResoPara	1.000	1.000	✓	Flav. Tag. Eff. Eigen B 0	1.010	0.990	✓
E_T^{miss} Soft Track ResoPerp	1.000	1.000	✓	Luminosity Measurement	1.032	0.968	·
Flav. Tag. Eff. Eigen C 0	0.977	1.023	·	Pile-up Reweighting	0.988	0.997	✓
Flav. Tag. Eff. Light 0	0.938	1.061	·	Signal Acceptance Unc.	1.025	0.975	·
Flav. Tag. Eff. Light 1	1.009	0.991	✓	Tau Energy Scale AFII	1.007	0.995	✓
Luminosity Measurement	1.032	0.968	·	Tau Energy Scale Detector	1.004	0.995	✓
Signal Acceptance Unc.	1.081	0.919	·	Tau Energy Scale Model	1.000	0.999	✓
Tau Energy Scale Detector	1.003	0.997	✓	Tau ID Eff. 1p p_T>40GeV τ_1	1.024	0.976	·
Tau ID Eff. 1p p_T>40GeV τ_1	1.025	0.975	·	Tau ID Eff. 1p p_T>40GeV τ_2	1.022	0.978	·
Tau ID Eff. 1p p_T>40GeV τ_2	1.022	0.978	·	Tau ID Eff. AFII τ_1	1.012	0.988	·
Tau ID Eff. High p_T τ_1	1.046	0.954	✓	Tau ID Eff. High p_T τ_1	1.048	0.952	✓
Tau ID Eff. High p_T τ_2	1.024	0.976	✓	Tau ID Eff. High p_T τ_2	1.026	0.974	✓
Tau ID Eff. Syst. τ_1	1.072	0.928	·	Tau ID Eff. Syst. τ_1	1.073	0.927	·
Tau ID Eff. Syst. τ_2	1.067	0.933	·	Tau ID Eff. Syst. τ_2	1.068	0.932	·
Tau Reco. Eff. High p_T	1.025	0.975	✓	Tau Reco. Eff. AFII	1.102	0.903	·
Tau Reco. Eff. Total	1.019	0.981	·	Tau Reco. Eff. High p_T	1.028	0.973	✓
Tau Trigger Eff. Stat. Data 2016	1.011	0.989	·	Tau Reco. Eff. Total	1.019	0.981	·
Tau Trigger Eff. Stat. Data 2017	1.027	0.973	·	Tau Trigger Eff. Stat. Data 2016	1.014	0.986	·
Tau Trigger Eff. Stat. Data 2018	1.035	0.965	·	Tau Trigger Eff. Stat. Data 2017	1.023	0.977	·
Tau Trigger Eff. Stat. MC 2017	1.016	0.984	·	Tau Trigger Eff. Stat. Data 2018	1.038	0.962	·
Tau Trigger Eff. Stat. MC 2018	1.021	0.979	·	Tau Trigger Eff. Stat. MC 2017	1.014	0.986	·
				Tau Trigger Eff. Stat. MC 2018	1.022	0.978	·

Table C.2.6.: List of systematic uncertainties affecting the *b*-tag signal region. The magnitude is quoted in terms of the relative uncertainty factor $\eta^{\pm}$ from Equation (7.22). The last column indicates if the nuisance parameter is implemented as shape uncertainty.

D. Statistical Analysis

D.1. Signal Acceptance Efficiency Tables

Tables D.1.1 and D.1.2 lists the acceptance times efficiency of the Higgs signals produced via gluon-gluon fusion and b-associated production in the $\tau_{\mathrm{had}}\tau_{\mathrm{had}}$ and $\tau_{\mathrm{lep}}\tau_{\mathrm{had}}$ signal regions. The $\tau_{\mathrm{had}}\tau_{\mathrm{had}}$ channel values are derived from measurements of the results presented in this thesis. The $\tau_{\mathrm{lep}}\tau_{\mathrm{had}}$ channel measurements are taken from Reference [24] which only lists values for the masses $m_\phi = 200, 300, 400, 600, 1000, 1500, 2000,$ and $2500\,\mathrm{GeV}$.

m_ϕ [GeV]	$\tau_{\mathrm{had}}\tau_{\mathrm{had}}$		$\tau_e\tau_{\mathrm{had}}$		$\tau_\mu\tau_{\mathrm{had}}$	
	b-veto	b-tag	b-veto	b-tag	b-veto	b-tag
200	4.54×10^{-4}	1.82×10^{-6}	2.09×10^{-2}	1.98×10^{-4}	3.08×10^{-2}	3.09×10^{-4}
250	2.29×10^{-3}	4.17×10^{-5}	-	-	-	-
300	7.61×10^{-3}	1.34×10^{-4}	4.65×10^{-2}	5.33×10^{-4}	4.97×10^{-2}	5.64×10^{-4}
350	2.59×10^{-2}	4.46×10^{-4}	-	-	-	-
400	6.06×10^{-2}	7.68×10^{-4}	6.28×10^{-2}	7.12×10^{-4}	6.40×10^{-2}	7.99×10^{-4}
500	0.127	1.75×10^{-3}	-	-	-	-
600	0.171	2.59×10^{-3}	7.48×10^{-2}	1.10×10^{-3}	7.47×10^{-2}	1.06×10^{-3}
700	0.193	3.52×10^{-3}	-	-	-	-
800	0.209	3.88×10^{-3}	-	-	-	-
1000	0.215	5.10×10^{-3}	7.13×10^{-2}	1.32×10^{-3}	7.71×10^{-2}	1.50×10^{-3}
1200	0.213	5.26×10^{-3}	-	-	-	-
1500	0.209	6.27×10^{-3}	5.76×10^{-2}	1.43×10^{-3}	6.86×10^{-2}	1.71×10^{-3}
2000	0.19	6.04×10^{-3}	4.61×10^{-2}	1.32×10^{-3}	6.10×10^{-2}	1.71×10^{-3}
2500	0.172	6.50×10^{-3}	3.85×10^{-2}	1.13×10^{-3}	5.45×10^{-2}	1.76×10^{-3}

Table D.1.1.: List of acceptance times efficiency values measured in the $\tau_{\mathrm{had}}\tau_{\mathrm{had}}$ and $\tau_{\mathrm{lep}}\tau_{\mathrm{had}}$ signal regions for Higgs samples produced via gluon-gluon fusion.

m_ϕ [GeV]	$\tau_{\text{had}}\tau_{\text{had}}$		$\tau_e\tau_{\text{had}}$		$\tau_\mu\tau_{\text{had}}$	
	b-veto	b-tag	b-veto	b-tag	b-veto	b-tag
200	4.61×10^{-4}	1.23×10^{-4}	1.73×10^{-2}	4.73×10^{-3}	2.68×10^{-2}	6.58×10^{-3}
250	1.96×10^{-3}	7.01×10^{-4}	-	-	-	-
300	6.88×10^{-3}	3.14×10^{-3}	3.37×10^{-2}	1.20×10^{-2}	3.79×10^{-2}	1.31×10^{-2}
350	1.99×10^{-2}	9.22×10^{-3}	-	-	-	-
400	4.42×10^{-2}	1.99×10^{-2}	4.39×10^{-2}	1.82×10^{-2}	4.39×10^{-2}	1.82×10^{-2}
500	9.02×10^{-2}	4.32×10^{-2}	-	-	-	-
600	0.114	6.05×10^{-2}	4.67×10^{-2}	2.43×10^{-2}	5.07×10^{-2}	2.65×10^{-2}
700	0.131	7.31×10^{-2}	-	-	-	-
800	0.141	8.09×10^{-2}	-	-	-	-
1000	0.145	8.49×10^{-2}	4.57×10^{-2}	2.57×10^{-2}	4.64×10^{-2}	2.77×10^{-2}
1200	0.137	8.80×10^{-2}	-	-	-	-
1500	0.126	8.79×10^{-2}	3.71×10^{-2}	2.22×10^{-2}	4.48×10^{-2}	2.61×10^{-2}
2000	0.115	8.42×10^{-2}	3.00×10^{-2}	1.85×10^{-2}	3.74×10^{-2}	2.47×10^{-2}
2500	9.91×10^{-2}	7.32×10^{-2}	2.40×10^{-2}	1.54×10^{-2}	3.58×10^{-2}	2.30×10^{-2}

Table D.1.2.: List of acceptance times efficiency values measured in the $\tau_{\text{had}}\tau_{\text{had}}$ and $\tau_{\text{lep}}\tau_{\text{had}}$ signal regions for Higgs samples produced via b-associated production.

D.2. Model Independent Limit Tables

Limits set on the cross-section times branching ratio are given in terms of the fraction of signal from b-associated production relative to the total production cross-section, called $f_{b\text{-frac}}$, as well as the mass of the neutral Higgs-like resonance. Tables D.2.1 to D.2.5 list the values of m_ϕ-$f_{b\text{-frac}}$ of the $\tau_{\text{had}}\tau_{\text{had}}$ search channel results presented in this thesis while Tables D.2.6 to D.2.10 show the limit values of the combination of the $\tau_{\text{had}}\tau_{\text{had}}$ channel with the $\tau_{\text{lep}}\tau_{\text{had}}$ channel from Reference [24].

The ± 1 and $\pm 2\sigma$ bands of expected exclusion limit is quoted in terms of the relative difference with respect to the median expected value:

$$x_{\text{exp.}}{}^{+1\sigma_{\text{rel.}}/+2\sigma_{\text{rel.}}}_{-1\sigma_{\text{rel.}}/-2\sigma_{\text{rel.}}},$$

with $\pm N\sigma_{\text{rel.}}$ defined by:

$$\pm N\sigma_{\text{rel.}} = \frac{x_{\pm N\sigma} - x_{\text{exp.}}}{x_{\text{exp.}}}, \qquad N \in \{1, 2\},$$

where $x_{\text{exp.}}$ is the expected limit value and $x_{\pm N\sigma}$ the limit value of the $\pm N^{\text{th}}\sigma$ band.

m_ϕ	200 GeV		250 GeV		300 GeV	
$f_{b\text{-frac}}$	obs. [pb]	exp. [pb]	obs. [pb]	exp. [pb]	obs. [pb]	exp. [pb]
0	6.89	$3.87^{+43/+103\,\%}_{-27.9/-46.3\,\%}$	1.63	$1.02^{+42.9/+102\,\%}_{-27.9/-46.3\,\%}$	0.256	$0.354^{+41.9/+99.4\,\%}_{-27.9/-46.3\,\%}$
0.05	6.76	$3.87^{+42.9/+103\,\%}_{-27.9/-46.3\,\%}$	1.58	$1.02^{+42.9/+102\,\%}_{-27.9/-46.3\,\%}$	0.253	$0.355^{+41.9/+99.5\,\%}_{-27.9/-46.3\,\%}$
0.1	6.59	$3.84^{+43.1/+103\,\%}_{-27.9/-46.3\,\%}$	1.52	$1.01^{+42.9/+102\,\%}_{-27.9/-46.3\,\%}$	0.248	$0.354^{+42/+99.9\,\%}_{-27.9/-46.3\,\%}$
0.15	6.42	$3.79^{+43.4/+105\,\%}_{-27.9/-46.3\,\%}$	1.46	$1^{+43.1/+103\,\%}_{-27.9/-46.3\,\%}$	0.242	$0.35^{+42.2/+101\,\%}_{-27.9/-46.3\,\%}$
0.2	6.22	$3.72^{+43.9/+107\,\%}_{-27.9/-46.3\,\%}$	1.39	$0.985^{+43.4/+104\,\%}_{-27.9/-46.3\,\%}$	0.236	$0.345^{+42.7/+102\,\%}_{-27.9/-46.3\,\%}$
0.25	6.02	$3.65^{+44.6/+110\,\%}_{-27.9/-46.3\,\%}$	1.33	$0.965^{+43.8/+105\,\%}_{-27.9/-46.3\,\%}$	0.23	$0.339^{+43.2/+105\,\%}_{-27.9/-46.3\,\%}$
0.3	5.8	$3.57^{+45.5/+113\,\%}_{-27.9/-46.3\,\%}$	1.26	$0.943^{+44.2/+107\,\%}_{-27.9/-46.3\,\%}$	0.224	$0.331^{+43.9/+107\,\%}_{-27.9/-46.3\,\%}$
0.35	5.57	$3.48^{+46.7/+116\,\%}_{-27.9/-46.3\,\%}$	1.19	$0.919^{+44.7/+109\,\%}_{-27.9/-46.3\,\%}$	0.217	$0.323^{+44.7/+110\,\%}_{-27.9/-46.3\,\%}$
0.4	5.33	$3.39^{+47.8/+120\,\%}_{-27.9/-46.3\,\%}$	1.12	$0.894^{+45.3/+111\,\%}_{-27.9/-46.3\,\%}$	0.211	$0.315^{+45.6/+113\,\%}_{-27.9/-46.3\,\%}$
0.45	5.07	$3.29^{+49/+125\,\%}_{-27.9/-46.3\,\%}$	1.05	$0.868^{+46/+114\,\%}_{-27.9/-46.3\,\%}$	0.205	$0.306^{+46.5/+117\,\%}_{-27.9/-46.3\,\%}$
0.5	4.8	$3.2^{+50.3/+129\,\%}_{-27.9/-46.3\,\%}$	0.985	$0.842^{+46.7/+117\,\%}_{-27.9/-46.3\,\%}$	0.198	$0.297^{+47.5/+120\,\%}_{-27.9/-46.3\,\%}$
0.55	4.54	$3.1^{+51.4/+134\,\%}_{-27.9/-46.3\,\%}$	0.924	$0.815^{+47.4/+120\,\%}_{-27.9/-46.3\,\%}$	0.192	$0.287^{+48.4/+124\,\%}_{-27.9/-46.3\,\%}$
0.6	4.27	$3.01^{+52.6/+139\,\%}_{-27.9/-46.3\,\%}$	0.864	$0.789^{+48.2/+122\,\%}_{-27.9/-46.3\,\%}$	0.186	$0.278^{+49.2/+127\,\%}_{-27.9/-46.3\,\%}$
0.65	4	$2.91^{+53.8/+144\,\%}_{-27.9/-46.3\,\%}$	0.809	$0.763^{+48.8/+125\,\%}_{-27.9/-46.3\,\%}$	0.18	$0.269^{+49.9/+131\,\%}_{-27.9/-46.3\,\%}$
0.7	3.75	$2.82^{+55.1/+149\,\%}_{-27.9/-46.3\,\%}$	0.762	$0.737^{+49.4/+128\,\%}_{-27.9/-46.3\,\%}$	0.175	$0.26^{+50.7/+135\,\%}_{-27.9/-46.3\,\%}$
0.75	3.51	$2.72^{+56.2/+154\,\%}_{-27.9/-46.3\,\%}$	0.716	$0.712^{+50/+130\,\%}_{-27.9/-46.3\,\%}$	0.169	$0.251^{+51.4/+138\,\%}_{-27.9/-46.3\,\%}$
0.8	3.3	$2.63^{+57.3/+209\,\%}_{-27.9/-46.3\,\%}$	0.675	$0.688^{+50.5/+133\,\%}_{-27.9/-46.3\,\%}$	0.164	$0.242^{+52/+141\,\%}_{-27.9/-46.3\,\%}$
0.85	3.1	$2.55^{+58.2/+370\,\%}_{-27.9/-46.3\,\%}$	0.636	$0.665^{+51/+135\,\%}_{-27.9/-46.3\,\%}$	0.159	$0.234^{+52.6/+144\,\%}_{-27.9/-46.3\,\%}$
0.9	2.91	$2.46^{+59.1/+579\,\%}_{-27.9/-46.3\,\%}$	0.602	$0.642^{+51.4/+137\,\%}_{-27.9/-46.3\,\%}$	0.154	$0.226^{+53.2/+147\,\%}_{-27.9/-46.3\,\%}$
0.95	2.74	$2.38^{+59.8/+860\,\%}_{-27.9/-46.3\,\%}$	0.57	$0.621^{+51.8/+139\,\%}_{-27.9/-46.3\,\%}$	0.149	$0.218^{+53.6/+149\,\%}_{-27.9/-46.3\,\%}$
1	2.58	$2.3^{+60.5/+1210\,\%}_{-27.9/-46.3\,\%}$	0.541	$0.6^{+52.1/+140\,\%}_{-27.9/-46.3\,\%}$	0.145	$0.211^{+53.9/+151\,\%}_{-27.9/-46.3\,\%}$

Table D.2.1.: List of upper limit values on the cross-section times branching ratio for masses $m_\phi = 200, 250, 300\,\text{GeV}$ of the $\tau_{\text{had}}\tau_{\text{had}}$ channel. Expected limits on $\sigma \times \text{Br}\,(\phi \to \tau\tau)|_{\text{exp.}}$ are quoted with the relative values of the $\pm 1\,\sigma$ and $\pm 2\,\sigma$ confidence bands in the format: $\text{median}^{+1/+2\,\sigma}_{-1/-2\,\sigma}$.

m_ϕ	350 GeV		400 GeV		500 GeV	
$f_{b\text{-frac}}$	obs. [pb]	exp. [pb]	obs. [pb]	exp. [pb]	obs. [pb]	exp. [pb]
0	0.0769	$0.12^{+39.8/+92.7\,\%}_{-27.9/-46.3\,\%}$	0.0522	$0.0565^{+40.6/+93.8\,\%}_{-27.9/-46.3\,\%}$	0.0529	$0.0292^{+42.1/+97.7\,\%}_{-27.9/-46.3\,\%}$
0.05	0.08	$0.121^{+39.9/+93.1\,\%}_{-27.9/-46.3\,\%}$	0.0547	$0.0573^{+40.8/+94.2\,\%}_{-27.9/-46.3\,\%}$	0.0552	$0.0298^{+42.3/+98.2\,\%}_{-27.9/-46.3\,\%}$
0.1	0.0829	$0.121^{+40.1/+93.7\,\%}_{-27.9/-46.3\,\%}$	0.0571	$0.0578^{+41/+94.8\,\%}_{-27.9/-46.3\,\%}$	0.0573	$0.0304^{+42.5/+98.8\,\%}_{-27.9/-46.3\,\%}$
0.15	0.0856	$0.121^{+40.4/+94.8\,\%}_{-27.9/-46.3\,\%}$	0.0593	$0.0581^{+41.2/+95.5\,\%}_{-27.9/-46.3\,\%}$	0.059	$0.0307^{+42.7/+99.5\,\%}_{-27.9/-46.3\,\%}$
0.2	0.0881	$0.12^{+40.8/+96.3\,\%}_{-27.9/-46.3\,\%}$	0.061	$0.058^{+41.5/+96.6\,\%}_{-27.9/-46.3\,\%}$	0.0601	$0.0308^{+42.9/+100\,\%}_{-27.9/-46.3\,\%}$
0.25	0.0903	$0.118^{+41.4/+98\,\%}_{-27.9/-46.3\,\%}$	0.0628	$0.0576^{+41.9/+98\,\%}_{-27.9/-46.3\,\%}$	0.0607	$0.0308^{+43.1/+101\,\%}_{-27.9/-46.3\,\%}$
0.3	0.0925	$0.117^{+42.1/+101\,\%}_{-27.9/-46.3\,\%}$	0.0639	$0.057^{+42.4/+99.7\,\%}_{-27.9/-46.3\,\%}$	0.0608	$0.0305^{+43.4/+102\,\%}_{-27.9/-46.3\,\%}$
0.35	0.0941	$0.115^{+42.9/+103\,\%}_{-27.9/-46.3\,\%}$	0.0647	$0.0562^{+43/+102\,\%}_{-27.9/-46.3\,\%}$	0.0602	$0.0301^{+43.6/+103\,\%}_{-27.9/-46.3\,\%}$
0.4	0.0955	$0.112^{+43.7/+106\,\%}_{-27.9/-46.3\,\%}$	0.0651	$0.0552^{+43.6/+104\,\%}_{-27.9/-46.3\,\%}$	0.0592	$0.0296^{+43.8/+103\,\%}_{-27.9/-46.3\,\%}$
0.45	0.0966	$0.11^{+44.6/+109\,\%}_{-27.9/-46.3\,\%}$	0.0653	$0.0541^{+44.3/+107\,\%}_{-27.9/-46.3\,\%}$	0.0577	$0.0289^{+44.1/+104\,\%}_{-27.9/-46.3\,\%}$
0.5	0.0974	$0.107^{+45.4/+113\,\%}_{-27.9/-46.3\,\%}$	0.0652	$0.0528^{+45/+110\,\%}_{-27.9/-46.3\,\%}$	0.0559	$0.0281^{+44.3/+105\,\%}_{-27.9/-46.3\,\%}$
0.55	0.098	$0.104^{+46.4/+116\,\%}_{-27.9/-46.3\,\%}$	0.0649	$0.0514^{+45.7/+112\,\%}_{-27.9/-46.3\,\%}$	0.0538	$0.0272^{+44.4/+106\,\%}_{-27.9/-46.3\,\%}$
0.6	0.0984	$0.101^{+47.2/+119\,\%}_{-27.9/-46.3\,\%}$	0.0643	$0.05^{+46.5/+115\,\%}_{-27.9/-46.3\,\%}$	0.0515	$0.0263^{+44.5/+107\,\%}_{-27.9/-46.3\,\%}$
0.65	0.0984	$0.0982^{+48/+123\,\%}_{-27.9/-46.3\,\%}$	0.0636	$0.0486^{+47.1/+118\,\%}_{-27.9/-46.3\,\%}$	0.0491	$0.0254^{+44.6/+107\,\%}_{-27.9/-46.3\,\%}$
0.7	0.0979	$0.0952^{+48.8/+126\,\%}_{-27.9/-46.3\,\%}$	0.0627	$0.0471^{+47.7/+120\,\%}_{-27.9/-46.3\,\%}$	0.0467	$0.0245^{+44.6/+108\,\%}_{-27.9/-46.3\,\%}$
0.75	0.0976	$0.0922^{+49.4/+129\,\%}_{-27.9/-46.3\,\%}$	0.0616	$0.0456^{+48.2/+123\,\%}_{-27.9/-46.3\,\%}$	0.0443	$0.0236^{+44.7/+108\,\%}_{-27.9/-46.3\,\%}$
0.8	0.0971	$0.0892^{+50/+132\,\%}_{-27.9/-46.3\,\%}$	0.0606	$0.0441^{+48.6/+125\,\%}_{-27.9/-46.3\,\%}$	0.0419	$0.0227^{+44.7/+108\,\%}_{-27.9/-46.3\,\%}$
0.85	0.0966	$0.0863^{+50.5/+134\,\%}_{-27.9/-46.3\,\%}$	0.0593	$0.0427^{+49/+127\,\%}_{-27.9/-46.3\,\%}$	0.0397	$0.0218^{+44.7/+109\,\%}_{-27.9/-46.3\,\%}$
0.9	0.0957	$0.0835^{+51/+137\,\%}_{-27.9/-46.3\,\%}$	0.0581	$0.0413^{+49.3/+129\,\%}_{-27.9/-46.3\,\%}$	0.0375	$0.0209^{+44.7/+109\,\%}_{-27.9/-46.3\,\%}$
0.95	0.0949	$0.0807^{+51.3/+138\,\%}_{-27.9/-46.3\,\%}$	0.0567	$0.0399^{+49.6/+130\,\%}_{-27.9/-46.3\,\%}$	0.0355	$0.0201^{+44.6/+109\,\%}_{-27.9/-46.3\,\%}$
1	0.0939	$0.0781^{+51.6/+140\,\%}_{-27.9/-46.3\,\%}$	0.0554	$0.0386^{+49.9/+131\,\%}_{-27.9/-46.3\,\%}$	0.0336	$0.0194^{+44.6/+109\,\%}_{-27.9/-46.3\,\%}$

Table D.2.2.: List of upper limit values on the cross-section times branching ratio for masses $m_\phi = 350, 400, 500\,\text{GeV}$ of the $\tau_{\text{had}}\tau_{\text{had}}$ channel. Expected limits on $\sigma \times \text{Br}\,(\phi \to \tau\tau)|_{\text{exp.}}$ are quoted with the relative values of the $\pm 1\,\sigma$ and $\pm 2\,\sigma$ confidence bands in the format: $\text{median}^{+1/+2\,\sigma}_{-1/-2\,\sigma}$.

m_ϕ	600 GeV		700 GeV		800 GeV	
$f_{b\text{-frac}}$	obs. [pb]	exp. [pb]	obs. [pb]	exp. [pb]	obs. [pb]	exp. [pb]
0	0.0167	$0.0173^{+41.9/+97.5\,\%}_{-27.9/-46.3\,\%}$	0.00601	$0.0113^{+41.7/+97.1\,\%}_{-27.9/-46.3\,\%}$	0.00429	$0.00753^{+41.5/+96.4\,\%}_{-27.9/-46.3\,\%}$
0.05	0.0168	$0.0176^{+42.1/+98\,\%}_{-27.9/-46.3\,\%}$	0.006	$0.0114^{+41.9/+97.4\,\%}_{-27.9/-46.3\,\%}$	0.0043	$0.00757^{+41.6/+96.6\,\%}_{-27.9/-46.3\,\%}$
0.1	0.0168	$0.0179^{+42.2/+98.5\,\%}_{-27.9/-46.3\,\%}$	0.00595	$0.0114^{+42.1/+98\,\%}_{-27.9/-46.3\,\%}$	0.00427	$0.00751^{+41.7/+97\,\%}_{-27.9/-46.3\,\%}$
0.15	0.0167	$0.018^{+42.5/+99.3\,\%}_{-27.9/-46.3\,\%}$	0.00587	$0.0112^{+42.4/+98.9\,\%}_{-27.9/-46.3\,\%}$	0.00423	$0.00735^{+41.9/+97.6\,\%}_{-27.9/-46.3\,\%}$
0.2	0.0166	$0.0179^{+42.8/+100\,\%}_{-27.9/-46.3\,\%}$	0.00577	$0.0109^{+42.8/+100\,\%}_{-27.9/-46.3\,\%}$	0.00415	$0.00713^{+42.3/+98.7\,\%}_{-27.9/-46.3\,\%}$
0.25	0.0163	$0.0178^{+43.2/+102\,\%}_{-27.9/-46.3\,\%}$	0.00565	$0.0105^{+43.3/+102\,\%}_{-27.9/-46.3\,\%}$	0.00407	$0.00687^{+42.7/+100\,\%}_{-27.9/-46.3\,\%}$
0.3	0.016	$0.0175^{+43.6/+103\,\%}_{-27.9/-46.3\,\%}$	0.00551	$0.0101^{+43.9/+104\,\%}_{-27.9/-46.3\,\%}$	0.00397	$0.00658^{+43.1/+102\,\%}_{-27.9/-46.3\,\%}$
0.35	0.0156	$0.0172^{+44.1/+104\,\%}_{-27.9/-46.3\,\%}$	0.00537	$0.00971^{+44.5/+106\,\%}_{-27.9/-46.3\,\%}$	0.00386	$0.00628^{+43.7/+104\,\%}_{-27.9/-46.3\,\%}$
0.4	0.0152	$0.0168^{+44.6/+106\,\%}_{-27.9/-46.3\,\%}$	0.00521	$0.00928^{+45.1/+109\,\%}_{-27.9/-46.3\,\%}$	0.00374	$0.00598^{+44.2/+106\,\%}_{-27.9/-46.3\,\%}$
0.45	0.0148	$0.0164^{+45/+108\,\%}_{-27.9/-46.3\,\%}$	0.00506	$0.00885^{+45.8/+111\,\%}_{-27.9/-46.3\,\%}$	0.00362	$0.00568^{+44.7/+108\,\%}_{-27.9/-46.3\,\%}$
0.5	0.0144	$0.0159^{+45.4/+109\,\%}_{-27.9/-46.3\,\%}$	0.00491	$0.00843^{+46.6/+113\,\%}_{-27.9/-46.3\,\%}$	0.0035	$0.00539^{+45.3/+110\,\%}_{-27.9/-46.3\,\%}$
0.55	0.0139	$0.0153^{+45.8/+110\,\%}_{-27.9/-46.3\,\%}$	0.00476	$0.00802^{+47.2/+116\,\%}_{-27.9/-46.3\,\%}$	0.00338	$0.00512^{+45.7/+112\,\%}_{-27.9/-46.3\,\%}$
0.6	0.0134	$0.0148^{+46.2/+112\,\%}_{-27.9/-46.3\,\%}$	0.0046	$0.00764^{+47.7/+118\,\%}_{-27.9/-46.3\,\%}$	0.00327	$0.00486^{+46.2/+114\,\%}_{-27.9/-46.3\,\%}$
0.65	0.013	$0.0143^{+46.5/+113\,\%}_{-27.9/-46.3\,\%}$	0.00446	$0.00727^{+48.2/+120\,\%}_{-27.9/-46.3\,\%}$	0.00316	$0.00462^{+46.6/+116\,\%}_{-27.9/-46.3\,\%}$
0.7	0.0125	$0.0137^{+46.9/+114\,\%}_{-27.9/-46.3\,\%}$	0.00432	$0.00693^{+48.6/+121\,\%}_{-27.9/-46.3\,\%}$	0.00306	$0.0044^{+46.9/+117\,\%}_{-27.9/-46.3\,\%}$
0.75	0.012	$0.0132^{+47.1/+115\,\%}_{-27.9/-46.3\,\%}$	0.00419	$0.00661^{+49/+123\,\%}_{-27.9/-46.3\,\%}$	0.00295	$0.00419^{+47.2/+118\,\%}_{-27.9/-46.3\,\%}$
0.8	0.0116	$0.0127^{+47.3/+116\,\%}_{-27.9/-46.3\,\%}$	0.00406	$0.00631^{+49.3/+124\,\%}_{-27.9/-46.3\,\%}$	0.00286	$0.00399^{+47.5/+120\,\%}_{-27.9/-46.3\,\%}$
0.85	0.0111	$0.0122^{+47.4/+116\,\%}_{-27.9/-46.3\,\%}$	0.00393	$0.00603^{+49.6/+125\,\%}_{-27.9/-46.3\,\%}$	0.00276	$0.00381^{+47.7/+121\,\%}_{-27.9/-46.3\,\%}$
0.9	0.0107	$0.0117^{+47.5/+117\,\%}_{-27.9/-46.3\,\%}$	0.00382	$0.00576^{+49.8/+126\,\%}_{-27.9/-46.3\,\%}$	0.00268	$0.00364^{+47.9/+121\,\%}_{-27.9/-46.3\,\%}$
0.95	0.0103	$0.0112^{+47.6/+117\,\%}_{-27.9/-46.3\,\%}$	0.0037	$0.00552^{+50/+127\,\%}_{-27.9/-46.3\,\%}$	0.00259	$0.00349^{+48.1/+122\,\%}_{-27.9/-46.3\,\%}$
1	0.00989	$0.0108^{+47.7/+117\,\%}_{-27.9/-46.3\,\%}$	0.0036	$0.00529^{+50.3/+128\,\%}_{-27.9/-46.3\,\%}$	0.00251	$0.00334^{+48.3/+123\,\%}_{-27.9/-46.3\,\%}$

Table D.2.3.: List of upper limit values on the cross-section times branching ratio for masses $m_\phi = 600, 700, 800\,\text{GeV}$ of the $\tau_\text{had}\tau_\text{had}$ channel. Expected limits on $\sigma \times \text{Br}\left(\phi \to \tau\tau\right)|_\text{exp.}$ are quoted with the relative values of the $\pm 1\,\sigma$ and $\pm 2\,\sigma$ confidence bands in the format: $\text{median}^{+1/+2\,\sigma}_{-1/-2\,\sigma}$.

m_ϕ	1000 GeV		1200 GeV		1500 GeV	
$f_{b\text{-frac}}$	obs. [pb]	exp. [pb]	obs. [pb]	exp. [pb]	obs. [pb]	exp. [pb]
0	0.00327	$0.00469^{+41.8/+97.6\,\%}_{-27.9/-46.3\,\%}$	0.0032	$0.00317^{+43.1/+102\,\%}_{-27.9/-46.3\,\%}$	0.00265	$0.00191^{+45.3/+109\,\%}_{-27.9/-46.3\,\%}$
0.05	0.00328	$0.00469^{+41.8/+97.7\,\%}_{-27.9/-46.3\,\%}$	0.00321	$0.00318^{+43.1/+102\,\%}_{-27.9/-46.3\,\%}$	0.00268	$0.00194^{+45.3/+109\,\%}_{-27.9/-46.3\,\%}$
0.1	0.00326	$0.00463^{+41.9/+97.9\,\%}_{-27.9/-46.3\,\%}$	0.00319	$0.00317^{+43.1/+102\,\%}_{-27.9/-46.3\,\%}$	0.0027	$0.00195^{+45.2/+109\,\%}_{-27.9/-46.3\,\%}$
0.15	0.00322	$0.00454^{+42/+98.3\,\%}_{-27.9/-46.3\,\%}$	0.00314	$0.00313^{+43.1/+102\,\%}_{-27.9/-46.3\,\%}$	0.0027	$0.00196^{+45.2/+109\,\%}_{-27.9/-46.3\,\%}$
0.2	0.00316	$0.0044^{+42.2/+99.1\,\%}_{-27.9/-46.3\,\%}$	0.00308	$0.00307^{+43.2/+102\,\%}_{-27.9/-46.3\,\%}$	0.00269	$0.00197^{+45.1/+109\,\%}_{-27.9/-46.3\,\%}$
0.25	0.00309	$0.00425^{+42.5/+100\,\%}_{-27.9/-46.3\,\%}$	0.003	$0.003^{+43.3/+103\,\%}_{-27.9/-46.3\,\%}$	0.00267	$0.00196^{+44.9/+108\,\%}_{-27.9/-46.3\,\%}$
0.3	0.003	$0.00409^{+42.8/+101\,\%}_{-27.9/-46.3\,\%}$	0.00291	$0.00292^{+43.5/+103\,\%}_{-27.9/-46.3\,\%}$	0.00264	$0.00195^{+44.8/+108\,\%}_{-27.9/-46.3\,\%}$
0.35	0.00291	$0.00391^{+43.2/+103\,\%}_{-27.9/-46.3\,\%}$	0.00282	$0.00283^{+43.7/+104\,\%}_{-27.9/-46.3\,\%}$	0.0026	$0.00193^{+44.7/+108\,\%}_{-27.9/-46.3\,\%}$
0.4	0.00282	$0.00374^{+43.5/+104\,\%}_{-27.9/-46.3\,\%}$	0.00272	$0.00273^{+43.9/+105\,\%}_{-27.9/-46.3\,\%}$	0.00255	$0.00191^{+44.7/+108\,\%}_{-27.9/-46.3\,\%}$
0.45	0.00272	$0.00357^{+44/+106\,\%}_{-27.9/-46.3\,\%}$	0.00262	$0.00264^{+44.1/+106\,\%}_{-27.9/-46.3\,\%}$	0.0025	$0.00188^{+44.7/+108\,\%}_{-27.9/-46.3\,\%}$
0.5	0.00263	$0.0034^{+44.3/+107\,\%}_{-27.9/-46.3\,\%}$	0.00252	$0.00254^{+44.3/+107\,\%}_{-27.9/-46.3\,\%}$	0.00244	$0.00185^{+44.8/+108\,\%}_{-27.9/-46.3\,\%}$
0.55	0.00254	$0.00324^{+44.6/+109\,\%}_{-27.9/-46.3\,\%}$	0.00242	$0.00244^{+44.5/+108\,\%}_{-27.9/-46.3\,\%}$	0.00238	$0.00181^{+44.8/+109\,\%}_{-27.9/-46.3\,\%}$
0.6	0.00245	$0.00309^{+45/+110\,\%}_{-27.9/-46.3\,\%}$	0.00232	$0.00235^{+44.7/+109\,\%}_{-27.9/-46.3\,\%}$	0.00232	$0.00178^{+44.9/+109\,\%}_{-27.9/-46.3\,\%}$
0.65	0.00236	$0.00295^{+45.2/+111\,\%}_{-27.9/-46.3\,\%}$	0.00223	$0.00226^{+44.9/+110\,\%}_{-27.9/-46.3\,\%}$	0.00225	$0.00174^{+45/+109\,\%}_{-27.9/-46.3\,\%}$
0.7	0.00227	$0.00281^{+45.5/+112\,\%}_{-27.9/-46.3\,\%}$	0.00214	$0.00217^{+45.1/+111\,\%}_{-27.9/-46.3\,\%}$	0.00218	$0.0017^{+45.1/+110\,\%}_{-27.9/-46.3\,\%}$
0.75	0.00219	$0.00269^{+45.7/+113\,\%}_{-27.9/-46.3\,\%}$	0.00206	$0.00209^{+45.3/+111\,\%}_{-27.9/-46.3\,\%}$	0.00211	$0.00166^{+45.2/+110\,\%}_{-27.9/-46.3\,\%}$
0.8	0.00212	$0.00257^{+45.9/+114\,\%}_{-27.9/-46.3\,\%}$	0.00198	$0.00201^{+45.5/+112\,\%}_{-27.9/-46.3\,\%}$	0.00205	$0.00162^{+45.3/+111\,\%}_{-27.9/-46.3\,\%}$
0.85	0.00205	$0.00246^{+46/+115\,\%}_{-27.9/-46.3\,\%}$	0.0019	$0.00193^{+45.7/+113\,\%}_{-27.9/-46.3\,\%}$	0.00198	$0.00158^{+45.4/+111\,\%}_{-27.9/-46.3\,\%}$
0.9	0.00198	$0.00236^{+46.2/+115\,\%}_{-27.9/-46.3\,\%}$	0.00183	$0.00186^{+45.8/+113\,\%}_{-27.9/-46.3\,\%}$	0.00192	$0.00154^{+45.5/+112\,\%}_{-27.9/-46.3\,\%}$
0.95	0.00192	$0.00226^{+46.3/+116\,\%}_{-27.9/-46.3\,\%}$	0.00176	$0.00179^{+45.9/+114\,\%}_{-27.9/-46.3\,\%}$	0.00185	$0.0015^{+45.7/+112\,\%}_{-27.9/-46.3\,\%}$
1	0.00185	$0.00217^{+46.4/+116\,\%}_{-27.9/-46.3\,\%}$	0.0017	$0.00173^{+46/+114\,\%}_{-27.9/-46.3\,\%}$	0.00179	$0.00146^{+45.8/+113\,\%}_{-27.9/-46.3\,\%}$

Table D.2.4.: List of upper limit values on the cross-section times branching ratio for masses $m_\phi = 1000, 1200, 1500\,\mathrm{GeV}$ of the $\tau_{\mathrm{had}}\tau_{\mathrm{had}}$ channel. Expected limits on $\sigma \times \mathrm{Br}\,(\phi \to \tau\tau)|_{\mathrm{exp.}}$ are quoted with the relative values of the $\pm 1\,\sigma$ and $\pm 2\,\sigma$ confidence bands in the format: $\mathrm{median}^{+1/+2\,\sigma}_{-1/-2\,\sigma}$.

m_ϕ	2000 GeV		2500 GeV	
$f_{b\text{-frac}}$	obs. [pb]	exp. [pb]	obs. [pb]	exp. [pb]
0	0.0019	$0.00124^{+46.4/+114\,\%}_{-27.9/-46.3\,\%}$	0.00169	$0.00109^{+46.7/+116\,\%}_{-27.9/-46.3\,\%}$
0.05	0.00193	$0.00126^{+46.4/+114\,\%}_{-27.9/-46.3\,\%}$	0.00172	$0.00111^{+46.7/+116\,\%}_{-27.9/-46.3\,\%}$
0.1	0.00195	$0.00128^{+46.2/+114\,\%}_{-27.9/-46.3\,\%}$	0.00175	$0.00113^{+46.7/+116\,\%}_{-27.9/-46.3\,\%}$
0.15	0.00197	$0.00129^{+46.2/+114\,\%}_{-27.9/-46.3\,\%}$	0.00178	$0.00115^{+46.6/+116\,\%}_{-27.9/-46.3\,\%}$
0.2	0.00198	$0.0013^{+46.1/+113\,\%}_{-27.9/-46.3\,\%}$	0.0018	$0.00117^{+46.6/+115\,\%}_{-27.9/-46.3\,\%}$
0.25	0.00199	$0.00132^{+46/+113\,\%}_{-27.9/-46.3\,\%}$	0.00183	$0.00119^{+46.5/+115\,\%}_{-27.9/-46.3\,\%}$
0.3	0.002	$0.00132^{+45.9/+113\,\%}_{-27.9/-46.3\,\%}$	0.00185	$0.00121^{+46.5/+115\,\%}_{-27.9/-46.3\,\%}$
0.35	0.00199	$0.00133^{+45.9/+112\,\%}_{-27.9/-46.3\,\%}$	0.00186	$0.00122^{+46.4/+115\,\%}_{-27.9/-46.3\,\%}$
0.4	0.00199	$0.00134^{+45.8/+112\,\%}_{-27.9/-46.3\,\%}$	0.00188	$0.00124^{+46.3/+114\,\%}_{-27.9/-46.3\,\%}$
0.45	0.00198	$0.00134^{+45.7/+112\,\%}_{-27.9/-46.3\,\%}$	0.00189	$0.00125^{+46.3/+114\,\%}_{-27.9/-46.3\,\%}$
0.5	0.00196	$0.00134^{+45.7/+112\,\%}_{-27.9/-46.3\,\%}$	0.00189	$0.00126^{+46.2/+114\,\%}_{-27.9/-46.3\,\%}$
0.55	0.00194	$0.00133^{+45.6/+112\,\%}_{-27.9/-46.3\,\%}$	0.0019	$0.00127^{+46.2/+114\,\%}_{-27.9/-46.3\,\%}$
0.6	0.00192	$0.00133^{+45.6/+112\,\%}_{-27.9/-46.3\,\%}$	0.0019	$0.00128^{+46.1/+114\,\%}_{-27.9/-46.3\,\%}$
0.65	0.0019	$0.00132^{+45.6/+112\,\%}_{-27.9/-46.3\,\%}$	0.0019	$0.00129^{+46.1/+114\,\%}_{-27.9/-46.3\,\%}$
0.7	0.00187	$0.00131^{+45.6/+112\,\%}_{-27.9/-46.3\,\%}$	0.00189	$0.0013^{+46.1/+114\,\%}_{-27.9/-46.3\,\%}$
0.75	0.00184	$0.0013^{+45.7/+113\,\%}_{-27.9/-46.3\,\%}$	0.00189	$0.0013^{+46.2/+114\,\%}_{-27.9/-46.3\,\%}$
0.8	0.00181	$0.00129^{+45.7/+113\,\%}_{-27.9/-46.3\,\%}$	0.00188	$0.0013^{+46.2/+115\,\%}_{-27.9/-46.3\,\%}$
0.85	0.00178	$0.00128^{+45.8/+113\,\%}_{-27.9/-46.3\,\%}$	0.00186	$0.00131^{+46.2/+115\,\%}_{-27.9/-46.3\,\%}$
0.9	0.00174	$0.00127^{+45.9/+114\,\%}_{-27.9/-46.3\,\%}$	0.00185	$0.0013^{+46.3/+115\,\%}_{-27.9/-46.3\,\%}$
0.95	0.00171	$0.00125^{+46/+114\,\%}_{-27.9/-46.3\,\%}$	0.00183	$0.0013^{+46.4/+116\,\%}_{-27.9/-46.3\,\%}$
1	0.00167	$0.00123^{+46.1/+115\,\%}_{-27.9/-46.3\,\%}$	0.0018	$0.0013^{+46.5/+116\,\%}_{-27.9/-46.3\,\%}$

Table D.2.5.: List of upper limit values on the cross-section times branching ratio for masses $m_\phi = 2000, 2500\,$GeV of the $\tau_{\text{had}}\tau_{\text{had}}$ channel. Expected limits on $\sigma \times \text{Br}\,(\phi \to \tau\tau)|_{\text{exp.}}$ are quoted with the relative values of the $\pm 1\,\sigma$ and $\pm 2\,\sigma$ confidence bands in the format: $\text{median}^{+1/+2\,\sigma}_{-1/-2\,\sigma}$.

m_ϕ	200 GeV		250 GeV		300 GeV	
$f_{b\text{-frac}}$	obs. [pb]	exp. [pb]	obs. [pb]	exp. [pb]	obs. [pb]	exp. [pb]
0	0.22	$0.427^{+39.6/+88.9\,\%}_{-27.9/-46.3\,\%}$	0.147	$0.207^{+39.8/+89.6\,\%}_{-27.9/-46.3\,\%}$	0.137	$0.117^{+40/+90.3\,\%}_{-27.9/-46.3\,\%}$
0.05	0.219	$0.428^{+39.6/+88.9\,\%}_{-27.9/-46.3\,\%}$	0.144	$0.209^{+39.8/+89.6\,\%}_{-27.9/-46.3\,\%}$	0.137	$0.119^{+40/+90.3\,\%}_{-27.9/-46.3\,\%}$
0.1	0.217	$0.43^{+39.6/+88.8\,\%}_{-27.9/-46.3\,\%}$	0.142	$0.21^{+39.8/+89.5\,\%}_{-27.9/-46.3\,\%}$	0.136	$0.12^{+40/+90.3\,\%}_{-27.9/-46.3\,\%}$
0.15	0.216	$0.431^{+39.6/+88.8\,\%}_{-27.9/-46.3\,\%}$	0.139	$0.212^{+39.7/+89.5\,\%}_{-27.9/-46.3\,\%}$	0.136	$0.122^{+40/+90.3\,\%}_{-27.9/-46.3\,\%}$
0.2	0.214	$0.432^{+39.6/+88.8\,\%}_{-27.9/-46.3\,\%}$	0.137	$0.213^{+39.7/+89.5\,\%}_{-27.9/-46.3\,\%}$	0.134	$0.123^{+40/+90.3\,\%}_{-27.9/-46.3\,\%}$
0.25	0.213	$0.433^{+39.6/+88.8\,\%}_{-27.9/-46.3\,\%}$	0.134	$0.214^{+39.7/+89.4\,\%}_{-27.9/-46.3\,\%}$	0.133	$0.124^{+40/+90.4\,\%}_{-27.9/-46.3\,\%}$
0.3	0.211	$0.434^{+39.6/+88.8\,\%}_{-27.9/-46.3\,\%}$	0.131	$0.215^{+39.7/+89.4\,\%}_{-27.9/-46.3\,\%}$	0.132	$0.125^{+40.1/+90.5\,\%}_{-27.9/-46.3\,\%}$
0.35	0.21	$0.434^{+39.6/+88.8\,\%}_{-27.9/-46.3\,\%}$	0.129	$0.215^{+39.7/+89.4\,\%}_{-27.9/-46.3\,\%}$	0.13	$0.126^{+40.2/+90.7\,\%}_{-27.9/-46.3\,\%}$
0.4	0.208	$0.433^{+39.6/+88.8\,\%}_{-27.9/-46.3\,\%}$	0.126	$0.216^{+39.7/+89.4\,\%}_{-27.9/-46.3\,\%}$	0.128	$0.126^{+40.2/+90.9\,\%}_{-27.9/-46.3\,\%}$
0.45	0.206	$0.433^{+39.6/+88.9\,\%}_{-27.9/-46.3\,\%}$	0.123	$0.215^{+39.7/+89.4\,\%}_{-27.9/-46.3\,\%}$	0.126	$0.127^{+40.3/+91.1\,\%}_{-27.9/-46.3\,\%}$
0.5	0.205	$0.432^{+39.6/+88.9\,\%}_{-27.9/-46.3\,\%}$	0.12	$0.215^{+39.7/+89.5\,\%}_{-27.9/-46.3\,\%}$	0.123	$0.127^{+40.4/+91.5\,\%}_{-27.9/-46.3\,\%}$
0.55	0.203	$0.431^{+39.7/+89\,\%}_{-27.9/-46.3\,\%}$	0.118	$0.214^{+39.8/+89.5\,\%}_{-27.9/-46.3\,\%}$	0.121	$0.127^{+40.5/+91.9\,\%}_{-27.9/-46.3\,\%}$
0.6	0.201	$0.429^{+39.7/+89.1\,\%}_{-27.9/-46.3\,\%}$	0.115	$0.213^{+39.8/+89.6\,\%}_{-27.9/-46.3\,\%}$	0.119	$0.127^{+40.7/+92.4\,\%}_{-27.9/-46.3\,\%}$
0.65	0.199	$0.427^{+39.7/+89.2\,\%}_{-27.9/-46.3\,\%}$	0.113	$0.212^{+39.8/+89.7\,\%}_{-27.9/-46.3\,\%}$	0.116	$0.126^{+40.8/+92.9\,\%}_{-27.9/-46.3\,\%}$
0.7	0.197	$0.425^{+39.7/+89.3\,\%}_{-27.9/-46.3\,\%}$	0.11	$0.21^{+39.8/+89.8\,\%}_{-27.9/-46.3\,\%}$	0.114	$0.126^{+41/+93.4\,\%}_{-27.9/-46.3\,\%}$
0.75	0.196	$0.423^{+39.8/+89.4\,\%}_{-27.9/-46.3\,\%}$	0.107	$0.209^{+39.8/+89.9\,\%}_{-27.9/-46.3\,\%}$	0.111	$0.125^{+41.2/+94.1\,\%}_{-27.9/-46.3\,\%}$
0.8	0.194	$0.42^{+39.8/+89.5\,\%}_{-27.9/-46.3\,\%}$	0.105	$0.207^{+39.8/+90\,\%}_{-27.9/-46.3\,\%}$	0.108	$0.124^{+41.4/+94.8\,\%}_{-27.9/-46.3\,\%}$
0.85	0.192	$0.417^{+39.8/+89.6\,\%}_{-27.9/-46.3\,\%}$	0.102	$0.204^{+39.9/+90.1\,\%}_{-27.9/-46.3\,\%}$	0.106	$0.123^{+41.6/+95.5\,\%}_{-27.9/-46.3\,\%}$
0.9	0.19	$0.414^{+39.9/+89.8\,\%}_{-27.9/-46.3\,\%}$	0.1	$0.202^{+40/+90.2\,\%}_{-27.9/-46.3\,\%}$	0.103	$0.122^{+41.8/+96.2\,\%}_{-27.9/-46.3\,\%}$
0.95	0.188	$0.411^{+39.9/+89.9\,\%}_{-27.9/-46.3\,\%}$	0.0978	$0.2^{+40/+90.3\,\%}_{-27.9/-46.3\,\%}$	0.0999	$0.121^{+42/+97\,\%}_{-27.9/-46.3\,\%}$
1	0.186	$0.408^{+39.9/+90\,\%}_{-27.9/-46.3\,\%}$	0.0955	$0.197^{+40.1/+90.5\,\%}_{-27.9/-46.3\,\%}$	0.0971	$0.12^{+42.2/+97.7\,\%}_{-27.9/-46.3\,\%}$

Table D.2.6.: List of upper limit values on the cross-section times branching ratio for masses $m_\phi = 200,\,250,\,300\,\text{GeV}$ of the combined $\tau_{\text{lep}}\tau_{\text{had}}$ and $\tau_{\text{had}}\tau_{\text{had}}$ channel. Expected limits $\sigma \times \text{Br}\,(\phi \to \tau\tau)|_{\text{exp.}}$ are quoted with the relative values of the $\pm 1\,\sigma$ and $\pm 2\,\sigma$ confidence bands in the format: $\text{median}^{+1/+2\,\sigma}_{-1/-2\,\sigma}$.

m_ϕ	350 GeV		400 GeV		500 GeV	
$f_{b\text{-frac}}$	obs. [pb]	exp. [pb]	obs. [pb]	exp. [pb]	obs. [pb]	exp. [pb]
0	0.0853	$0.0654^{+40.8/+92.4\,\%}_{-27.9/-46.3\,\%}$	0.0601	$0.0391^{+41/+93\,\%}_{-27.9/-46.3\,\%}$	0.0412	$0.0205^{+40.5/+91.5\,\%}_{-27.9/-46.3\,\%}$
0.05	0.0884	$0.0663^{+40.8/+92.4\,\%}_{-27.9/-46.3\,\%}$	0.0633	$0.0398^{+41/+93.2\,\%}_{-27.9/-46.3\,\%}$	0.0432	$0.0209^{+40.5/+91.7\,\%}_{-27.9/-46.3\,\%}$
0.1	0.0914	$0.0671^{+40.8/+92.5\,\%}_{-27.9/-46.3\,\%}$	0.0663	$0.0403^{+41.1/+93.4\,\%}_{-27.9/-46.3\,\%}$	0.0448	$0.0212^{+40.6/+91.9\,\%}_{-27.9/-46.3\,\%}$
0.15	0.0941	$0.0678^{+40.8/+92.6\,\%}_{-27.9/-46.3\,\%}$	0.0688	$0.0407^{+41.2/+93.6\,\%}_{-27.9/-46.3\,\%}$	0.046	$0.0214^{+40.7/+92.2\,\%}_{-27.9/-46.3\,\%}$
0.2	0.0966	$0.0682^{+40.9/+92.7\,\%}_{-27.9/-46.3\,\%}$	0.071	$0.0409^{+41.2/+94\,\%}_{-27.9/-46.3\,\%}$	0.0467	$0.0214^{+40.8/+92.4\,\%}_{-27.9/-46.3\,\%}$
0.25	0.0987	$0.0685^{+41/+92.9\,\%}_{-27.9/-46.3\,\%}$	0.0726	$0.0409^{+41.4/+94.5\,\%}_{-27.9/-46.3\,\%}$	0.0469	$0.0214^{+40.9/+92.8\,\%}_{-27.9/-46.3\,\%}$
0.3	0.1	$0.0686^{+41/+93.3\,\%}_{-27.9/-46.3\,\%}$	0.0738	$0.0408^{+41.5/+95.3\,\%}_{-27.9/-46.3\,\%}$	0.0466	$0.0211^{+41.1/+93.3\,\%}_{-27.9/-46.3\,\%}$
0.35	0.102	$0.0686^{+41.1/+93.7\,\%}_{-27.9/-46.3\,\%}$	0.0744	$0.0405^{+41.8/+95.5\,\%}_{-27.9/-46.3\,\%}$	0.0459	$0.0208^{+41.2/+93.8\,\%}_{-27.9/-46.3\,\%}$
0.4	0.103	$0.0684^{+41.3/+94.3\,\%}_{-27.9/-46.3\,\%}$	0.0746	$0.0401^{+42/+96.7\,\%}_{-27.9/-46.3\,\%}$	0.0449	$0.0204^{+41.4/+94.5\,\%}_{-27.9/-46.3\,\%}$
0.45	0.104	$0.068^{+41.5/+95\,\%}_{-27.9/-46.3\,\%}$	0.0745	$0.0395^{+42.2/+97.8\,\%}_{-27.9/-46.3\,\%}$	0.0437	$0.0199^{+41.5/+95.1\,\%}_{-27.9/-46.3\,\%}$
0.5	0.104	$0.0675^{+41.7/+95.7\,\%}_{-27.9/-46.3\,\%}$	0.074	$0.0389^{+42.5/+99.1\,\%}_{-27.9/-46.3\,\%}$	0.0422	$0.0193^{+41.8/+95.9\,\%}_{-27.9/-46.3\,\%}$
0.55	0.104	$0.0669^{+42/+96.6\,\%}_{-27.9/-46.3\,\%}$	0.0732	$0.0382^{+42.9/+101\,\%}_{-27.9/-46.3\,\%}$	0.0406	$0.0187^{+42/+96.7\,\%}_{-27.9/-46.3\,\%}$
0.6	0.104	$0.0662^{+42.2/+97.6\,\%}_{-27.9/-46.3\,\%}$	0.0721	$0.0374^{+43.3/+102\,\%}_{-27.9/-46.3\,\%}$	0.0389	$0.0181^{+42.2/+97.5\,\%}_{-27.9/-46.3\,\%}$
0.65	0.103	$0.0653^{+42.5/+98.6\,\%}_{-27.9/-46.3\,\%}$	0.0709	$0.0365^{+43.7/+104\,\%}_{-27.9/-46.3\,\%}$	0.0372	$0.0175^{+42.4/+98.2\,\%}_{-27.9/-46.3\,\%}$
0.7	0.103	$0.0644^{+42.9/+99.7\,\%}_{-27.9/-46.3\,\%}$	0.0694	$0.0356^{+44.1/+105\,\%}_{-27.9/-46.3\,\%}$	0.0354	$0.0168^{+42.6/+99.1\,\%}_{-27.9/-46.3\,\%}$
0.75	0.102	$0.0634^{+43.2/+101\,\%}_{-27.9/-46.3\,\%}$	0.0678	$0.0347^{+44.4/+106\,\%}_{-27.9/-46.3\,\%}$	0.0336	$0.0162^{+42.7/+99.7\,\%}_{-27.9/-46.3\,\%}$
0.8	0.101	$0.0623^{+43.5/+102\,\%}_{-27.9/-46.3\,\%}$	0.0661	$0.0338^{+44.9/+108\,\%}_{-27.9/-46.3\,\%}$	0.0319	$0.0156^{+43/+100\,\%}_{-27.9/-46.3\,\%}$
0.85	0.0993	$0.0612^{+43.8/+103\,\%}_{-27.9/-46.3\,\%}$	0.0643	$0.0328^{+45.2/+109\,\%}_{-27.9/-46.3\,\%}$	0.0303	$0.015^{+43.1/+101\,\%}_{-27.9/-46.3\,\%}$
0.9	0.0978	$0.06^{+44.1/+104\,\%}_{-27.9/-46.3\,\%}$	0.0624	$0.0319^{+45.6/+111\,\%}_{-27.9/-46.3\,\%}$	0.0287	$0.0144^{+43.3/+102\,\%}_{-27.9/-46.3\,\%}$
0.95	0.0962	$0.0588^{+44.4/+105\,\%}_{-27.9/-46.3\,\%}$	0.0605	$0.0309^{+45.9/+112\,\%}_{-27.9/-46.3\,\%}$	0.0272	$0.0139^{+43.4/+102\,\%}_{-27.9/-46.3\,\%}$
1	0.0945	$0.0576^{+44.7/+106\,\%}_{-27.9/-46.3\,\%}$	0.0585	$0.03^{+46.3/+113\,\%}_{-27.9/-46.3\,\%}$	0.0258	$0.0134^{+43.5/+102\,\%}_{-27.9/-46.3\,\%}$

Table D.2.7.: List of upper limit values on the cross-section times branching ratio for masses $m_\phi = 350, 400, 500$ GeV of the combined $\tau_{\text{lep}}\tau_{\text{had}}$ and $\tau_{\text{had}}\tau_{\text{had}}$ channel. Expected limits $\sigma \times \text{Br}\,(\phi \to \tau\tau)|_{\text{exp.}}$ are quoted with the relative values of the $\pm 1\,\sigma$ and $\pm 2\,\sigma$ confidence bands in the format: $\text{median}^{+1/+2\,\sigma}_{-1/-2\,\sigma}$.

m_ϕ	600 GeV		700 GeV		800 GeV	
$f_{b\text{-frac}}$	obs. [pb]	exp. [pb]	obs. [pb]	exp. [pb]	obs. [pb]	exp. [pb]
0	0.0136	$0.0125^{+40.7/+92.2\,\%}_{-27.9/-46.3\,\%}$	0.00523	$0.00844^{+40.5/+91.8\,\%}_{-27.9/-46.3\,\%}$	0.00349	$0.00586^{+40.8/+93\,\%}_{-27.9/-46.3\,\%}$
0.05	0.0139	$0.0127^{+40.8/+92.5\,\%}_{-27.9/-46.3\,\%}$	0.00529	$0.00852^{+40.5/+92.1\,\%}_{-27.9/-46.3\,\%}$	0.00353	$0.00588^{+40.9/+93.2\,\%}_{-27.9/-46.3\,\%}$
0.1	0.0141	$0.0129^{+40.9/+92.8\,\%}_{-27.9/-46.3\,\%}$	0.00531	$0.00852^{+40.7/+92.4\,\%}_{-27.9/-46.3\,\%}$	0.00355	$0.00583^{+41/+93.6\,\%}_{-27.9/-46.3\,\%}$
0.15	0.0142	$0.0129^{+41/+93.1\,\%}_{-27.9/-46.3\,\%}$	0.00531	$0.00844^{+40.8/+93\,\%}_{-27.9/-46.3\,\%}$	0.00355	$0.00572^{+41.2/+94.2\,\%}_{-27.9/-46.3\,\%}$
0.2	0.0143	$0.0129^{+41.1/+93.6\,\%}_{-27.9/-46.3\,\%}$	0.00528	$0.0083^{+41.1/+93.9\,\%}_{-27.9/-46.3\,\%}$	0.00352	$0.00557^{+41.5/+95.2\,\%}_{-27.9/-46.3\,\%}$
0.25	0.0142	$0.0128^{+41.2/+94.1\,\%}_{-27.9/-46.3\,\%}$	0.00522	$0.0081^{+41.4/+94.9\,\%}_{-27.9/-46.3\,\%}$	0.00348	$0.00539^{+41.8/+96.4\,\%}_{-27.9/-46.3\,\%}$
0.3	0.014	$0.0126^{+41.4/+94.7\,\%}_{-27.9/-46.3\,\%}$	0.00515	$0.00786^{+41.8/+96.1\,\%}_{-27.9/-46.3\,\%}$	0.00342	$0.00519^{+42.2/+97.7\,\%}_{-27.9/-46.3\,\%}$
0.35	0.0138	$0.0123^{+41.6/+95.4\,\%}_{-27.9/-46.3\,\%}$	0.00506	$0.00759^{+42.2/+97.5\,\%}_{-27.9/-46.3\,\%}$	0.00335	$0.00498^{+42.6/+99.2\,\%}_{-27.9/-46.3\,\%}$
0.4	0.0135	$0.012^{+41.9/+96.2\,\%}_{-27.9/-46.3\,\%}$	0.00495	$0.00731^{+42.6/+98.9\,\%}_{-27.9/-46.3\,\%}$	0.00327	$0.00476^{+43/+101\,\%}_{-27.9/-46.3\,\%}$
0.45	0.0131	$0.0116^{+42.1/+97.1\,\%}_{-27.9/-46.3\,\%}$	0.00483	$0.00702^{+43/+100\,\%}_{-27.9/-46.3\,\%}$	0.00319	$0.00455^{+43.4/+102\,\%}_{-27.9/-46.3\,\%}$
0.5	0.0127	$0.0113^{+42.3/+97.9\,\%}_{-27.9/-46.3\,\%}$	0.00471	$0.00674^{+43.4/+102\,\%}_{-27.9/-46.3\,\%}$	0.00311	$0.00434^{+43.8/+104\,\%}_{-27.9/-46.3\,\%}$
0.55	0.0123	$0.0109^{+42.6/+98.8\,\%}_{-27.9/-46.3\,\%}$	0.00459	$0.00645^{+43.8/+103\,\%}_{-27.9/-46.3\,\%}$	0.00302	$0.00414^{+44.2/+105\,\%}_{-27.9/-46.3\,\%}$
0.6	0.0118	$0.0105^{+42.9/+99.7\,\%}_{-27.9/-46.3\,\%}$	0.00446	$0.00617^{+44.1/+104\,\%}_{-27.9/-46.3\,\%}$	0.00293	$0.00395^{+44.5/+106\,\%}_{-27.9/-46.3\,\%}$
0.65	0.0113	$0.0101^{+43.1/+100\,\%}_{-27.9/-46.3\,\%}$	0.00433	$0.00591^{+44.5/+106\,\%}_{-27.9/-46.3\,\%}$	0.00285	$0.00376^{+44.8/+108\,\%}_{-27.9/-46.3\,\%}$
0.7	0.0109	$0.00969^{+43.3/+101\,\%}_{-27.9/-46.3\,\%}$	0.00421	$0.00565^{+44.7/+107\,\%}_{-27.9/-46.3\,\%}$	0.00276	$0.00359^{+45.1/+109\,\%}_{-27.9/-46.3\,\%}$
0.75	0.0104	$0.00931^{+43.4/+102\,\%}_{-27.9/-46.3\,\%}$	0.00408	$0.00541^{+45/+108\,\%}_{-27.9/-46.3\,\%}$	0.00268	$0.00343^{+45.3/+110\,\%}_{-27.9/-46.3\,\%}$
0.8	0.01	$0.00894^{+43.6/+102\,\%}_{-27.9/-46.3\,\%}$	0.00396	$0.00518^{+45.2/+109\,\%}_{-27.9/-46.3\,\%}$	0.0026	$0.00328^{+45.7/+111\,\%}_{-27.9/-46.3\,\%}$
0.85	0.00958	$0.00859^{+43.7/+103\,\%}_{-27.9/-46.3\,\%}$	0.00385	$0.00496^{+45.5/+110\,\%}_{-27.9/-46.3\,\%}$	0.00253	$0.00314^{+45.9/+112\,\%}_{-27.9/-46.3\,\%}$
0.9	0.00918	$0.00826^{+43.8/+103\,\%}_{-27.9/-46.3\,\%}$	0.00374	$0.00476^{+45.6/+110\,\%}_{-27.9/-46.3\,\%}$	0.00245	$0.00301^{+46/+113\,\%}_{-27.9/-46.3\,\%}$
0.95	0.0088	$0.00794^{+43.9/+104\,\%}_{-27.9/-46.3\,\%}$	0.00363	$0.00456^{+45.9/+111\,\%}_{-27.9/-46.3\,\%}$	0.00238	$0.00288^{+46.2/+113\,\%}_{-27.9/-46.3\,\%}$
1	0.00844	$0.00763^{+44/+104\,\%}_{-27.9/-46.3\,\%}$	0.00352	$0.00438^{+46/+111\,\%}_{-27.9/-46.3\,\%}$	0.00231	$0.00277^{+46.3/+114\,\%}_{-27.9/-46.3\,\%}$

Table D.2.8.: List of upper limit values on the cross-section times branching ratio for masses $m_\phi = 600, 700, 800$ GeV of the combined $\tau_{\text{lep}}\tau_{\text{had}}$ and $\tau_{\text{had}}\tau_{\text{had}}$ channel. Expected limits $\sigma \times \text{Br}\,(\phi \to \tau\tau)|_{\text{exp.}}$ are quoted with the relative values of the $\pm 1\,\sigma$ and $\pm 2\,\sigma$ confidence bands in the format: $\text{median}^{+1/+2\,\sigma}_{-1/-2\,\sigma}$.

m_ϕ	1000 GeV		1200 GeV		1500 GeV	
$f_{b\text{-frac}}$	obs. [pb]	exp. [pb]	obs. [pb]	exp. [pb]	obs. [pb]	exp. [pb]
0	0.00228	$0.00376^{+41.1/+94.1\,\%}_{-27.9/-46.3\,\%}$	0.00207	$0.00263^{+42.1/+97.6\,\%}_{-27.9/-46.3\,\%}$	0.00188	$0.00163^{+43.2/+102\,\%}_{-27.9/-46.3\,\%}$
0.05	0.00231	$0.00375^{+41.2/+94.3\,\%}_{-27.9/-46.3\,\%}$	0.00209	$0.00263^{+42.1/+97.6\,\%}_{-27.9/-46.3\,\%}$	0.00191	$0.00165^{+43.2/+101\,\%}_{-27.9/-46.3\,\%}$
0.1	0.00233	$0.0037^{+41.3/+94.7\,\%}_{-27.9/-46.3\,\%}$	0.0021	$0.00261^{+42.2/+97.6\,\%}_{-27.9/-46.3\,\%}$	0.00193	$0.00165^{+43.2/+101\,\%}_{-27.9/-46.3\,\%}$
0.15	0.00233	$0.00361^{+41.5/+95.3\,\%}_{-27.9/-46.3\,\%}$	0.0021	$0.00257^{+42.2/+97.8\,\%}_{-27.9/-46.3\,\%}$	0.00194	$0.00166^{+43.1/+101\,\%}_{-27.9/-46.3\,\%}$
0.2	0.00232	$0.00351^{+41.7/+96.2\,\%}_{-27.9/-46.3\,\%}$	0.00209	$0.00252^{+42.3/+98.3\,\%}_{-27.9/-46.3\,\%}$	0.00194	$0.00165^{+43.1/+101\,\%}_{-27.9/-46.3\,\%}$
0.25	0.0023	$0.00339^{+42/+97.3\,\%}_{-27.9/-46.3\,\%}$	0.00206	$0.00245^{+42.5/+98.9\,\%}_{-27.9/-46.3\,\%}$	0.00194	$0.00164^{+43.2/+101\,\%}_{-27.9/-46.3\,\%}$
0.3	0.00226	$0.00326^{+42.3/+98.6\,\%}_{-27.9/-46.3\,\%}$	0.00203	$0.00238^{+42.6/+99.6\,\%}_{-27.9/-46.3\,\%}$	0.00193	$0.00163^{+43.2/+102\,\%}_{-27.9/-46.3\,\%}$
0.35	0.00222	$0.00313^{+42.7/+99.9\,\%}_{-27.9/-46.3\,\%}$	0.00199	$0.0023^{+42.9/+101\,\%}_{-27.9/-46.3\,\%}$	0.00191	$0.00161^{+43.3/+102\,\%}_{-27.9/-46.3\,\%}$
0.4	0.00218	$0.00299^{+43.1/+101\,\%}_{-27.9/-46.3\,\%}$	0.00194	$0.00222^{+43.1/+102\,\%}_{-27.9/-46.3\,\%}$	0.00188	$0.00158^{+43.5/+103\,\%}_{-27.9/-46.3\,\%}$
0.45	0.00213	$0.00286^{+43.4/+103\,\%}_{-27.9/-46.3\,\%}$	0.0019	$0.00214^{+43.4/+103\,\%}_{-27.9/-46.3\,\%}$	0.00185	$0.00155^{+43.6/+103\,\%}_{-27.9/-46.3\,\%}$
0.5	0.00208	$0.00273^{+43.7/+104\,\%}_{-27.9/-46.3\,\%}$	0.00185	$0.00206^{+43.7/+104\,\%}_{-27.9/-46.3\,\%}$	0.00182	$0.00152^{+43.8/+104\,\%}_{-27.9/-46.3\,\%}$
0.55	0.00203	$0.00261^{+44.1/+105\,\%}_{-27.9/-46.3\,\%}$	0.00179	$0.00198^{+43.9/+105\,\%}_{-27.9/-46.3\,\%}$	0.00178	$0.00149^{+43.9/+104\,\%}_{-27.9/-46.3\,\%}$
0.6	0.00197	$0.00249^{+44.4/+107\,\%}_{-27.9/-46.3\,\%}$	0.00174	$0.0019^{+44.2/+106\,\%}_{-27.9/-46.3\,\%}$	0.00174	$0.00146^{+44.1/+105\,\%}_{-27.9/-46.3\,\%}$
0.65	0.00192	$0.00238^{+44.7/+108\,\%}_{-27.9/-46.3\,\%}$	0.00169	$0.00183^{+44.4/+107\,\%}_{-27.9/-46.3\,\%}$	0.0017	$0.00143^{+44.3/+106\,\%}_{-27.9/-46.3\,\%}$
0.7	0.00187	$0.00227^{+44.9/+109\,\%}_{-27.9/-46.3\,\%}$	0.00164	$0.00176^{+44.6/+108\,\%}_{-27.9/-46.3\,\%}$	0.00166	$0.00139^{+44.4/+107\,\%}_{-27.9/-46.3\,\%}$
0.75	0.00181	$0.00217^{+45.1/+110\,\%}_{-27.9/-46.3\,\%}$	0.00159	$0.00169^{+44.8/+109\,\%}_{-27.9/-46.3\,\%}$	0.00162	$0.00136^{+44.6/+108\,\%}_{-27.9/-46.3\,\%}$
0.8	0.00176	$0.00208^{+45.3/+110\,\%}_{-27.9/-46.3\,\%}$	0.00154	$0.00163^{+45/+109\,\%}_{-27.9/-46.3\,\%}$	0.00158	$0.00132^{+44.8/+108\,\%}_{-27.9/-46.3\,\%}$
0.85	0.00172	$0.00199^{+45.5/+111\,\%}_{-27.9/-46.3\,\%}$	0.0015	$0.00157^{+45.2/+110\,\%}_{-27.9/-46.3\,\%}$	0.00153	$0.00129^{+44.9/+109\,\%}_{-27.9/-46.3\,\%}$
0.9	0.00167	$0.00191^{+45.7/+112\,\%}_{-27.9/-46.3\,\%}$	0.00145	$0.00151^{+45.4/+111\,\%}_{-27.9/-46.3\,\%}$	0.00149	$0.00125^{+45.1/+110\,\%}_{-27.9/-46.3\,\%}$
0.95	0.00162	$0.00184^{+45.8/+112\,\%}_{-27.9/-46.3\,\%}$	0.00141	$0.00145^{+45.6/+111\,\%}_{-27.9/-46.3\,\%}$	0.00145	$0.00122^{+45.3/+111\,\%}_{-27.9/-46.3\,\%}$
1	0.00158	$0.00176^{+45.9/+113\,\%}_{-27.9/-46.3\,\%}$	0.00136	$0.0014^{+45.7/+112\,\%}_{-27.9/-46.3\,\%}$	0.00141	$0.00119^{+45.5/+111\,\%}_{-27.9/-46.3\,\%}$

Table D.2.9.: List of upper limit values on the cross-section times branching ratio for masses $m_\phi = 1000, 1200, 1500$ GeV of the combined $\tau_{\text{lep}}\tau_{\text{had}}$ and $\tau_{\text{had}}\tau_{\text{had}}$ channel. Expected limits $\sigma \times \text{Br}\,(\phi \to \tau\tau)|_{\text{exp.}}$ are quoted with the relative values of the $\pm 1\,\sigma$ and $\pm 2\,\sigma$ confidence bands in the format: $\text{median}^{+1/+2\,\sigma}_{-1/-2\,\sigma}$.

m_ϕ	2000 GeV		2500 GeV	
$f_{b\text{-frac}}$	obs. [pb]	exp. [pb]	obs. [pb]	exp. [pb]
0	0.00147	$0.0011^{+45/+109\,\%}_{-27.9/-46.3\,\%}$	0.00135	$0.000979^{+45.8/+112\,\%}_{-27.9/-46.3\,\%}$
0.05	0.0015	$0.00112^{+44.9/+109\,\%}_{-27.9/-46.3\,\%}$	0.00138	$0.000996^{+45.8/+112\,\%}_{-27.9/-46.3\,\%}$
0.1	0.00152	$0.00113^{+44.9/+109\,\%}_{-27.9/-46.3\,\%}$	0.00141	$0.00101^{+45.7/+112\,\%}_{-27.9/-46.3\,\%}$
0.15	0.00154	$0.00114^{+44.9/+108\,\%}_{-27.9/-46.3\,\%}$	0.00143	$0.00103^{+45.7/+111\,\%}_{-27.9/-46.3\,\%}$
0.2	0.00156	$0.00115^{+44.8/+108\,\%}_{-27.9/-46.3\,\%}$	0.00145	$0.00104^{+45.6/+111\,\%}_{-27.9/-46.3\,\%}$
0.25	0.00157	$0.00115^{+44.8/+108\,\%}_{-27.9/-46.3\,\%}$	0.00147	$0.00105^{+45.6/+111\,\%}_{-27.9/-46.3\,\%}$
0.3	0.00158	$0.00116^{+44.7/+108\,\%}_{-27.9/-46.3\,\%}$	0.00149	$0.00107^{+45.5/+111\,\%}_{-27.9/-46.3\,\%}$
0.35	0.00158	$0.00116^{+44.7/+108\,\%}_{-27.9/-46.3\,\%}$	0.0015	$0.00108^{+45.5/+111\,\%}_{-27.9/-46.3\,\%}$
0.4	0.00158	$0.00116^{+44.7/+108\,\%}_{-27.9/-46.3\,\%}$	0.00152	$0.00108^{+45.5/+110\,\%}_{-27.9/-46.3\,\%}$
0.45	0.00158	$0.00115^{+44.7/+108\,\%}_{-27.9/-46.3\,\%}$	0.00153	$0.00109^{+45.4/+110\,\%}_{-27.9/-46.3\,\%}$
0.5	0.00157	$0.00115^{+44.8/+108\,\%}_{-27.9/-46.3\,\%}$	0.00153	$0.0011^{+45.4/+110\,\%}_{-27.9/-46.3\,\%}$
0.55	0.00156	$0.00114^{+44.8/+108\,\%}_{-27.9/-46.3\,\%}$	0.00154	$0.0011^{+45.4/+110\,\%}_{-27.9/-46.3\,\%}$
0.6	0.00155	$0.00113^{+44.9/+109\,\%}_{-27.9/-46.3\,\%}$	0.00154	$0.0011^{+45.5/+111\,\%}_{-27.9/-46.3\,\%}$
0.65	0.00153	$0.00112^{+45/+109\,\%}_{-27.9/-46.3\,\%}$	0.00154	$0.00111^{+45.5/+111\,\%}_{-27.9/-46.3\,\%}$
0.7	0.00152	$0.00111^{+45/+109\,\%}_{-27.9/-46.3\,\%}$	0.00153	$0.00111^{+45.5/+111\,\%}_{-27.9/-46.3\,\%}$
0.75	0.0015	$0.0011^{+45.1/+110\,\%}_{-27.9/-46.3\,\%}$	0.00153	$0.0011^{+45.6/+111\,\%}_{-27.9/-46.3\,\%}$
0.8	0.00148	$0.00108^{+45.3/+110\,\%}_{-27.9/-46.3\,\%}$	0.00152	$0.0011^{+45.6/+112\,\%}_{-27.9/-46.3\,\%}$
0.85	0.00145	$0.00107^{+45.4/+111\,\%}_{-27.9/-46.3\,\%}$	0.00151	$0.0011^{+45.7/+112\,\%}_{-27.9/-46.3\,\%}$
0.9	0.00143	$0.00105^{+45.6/+111\,\%}_{-27.9/-46.3\,\%}$	0.00149	$0.00109^{+45.8/+112\,\%}_{-27.9/-46.3\,\%}$
0.95	0.0014	$0.00104^{+45.7/+112\,\%}_{-27.9/-46.3\,\%}$	0.00148	$0.00108^{+45.9/+113\,\%}_{-27.9/-46.3\,\%}$
1	0.00138	$0.00102^{+45.8/+112\,\%}_{-27.9/-46.3\,\%}$	0.00146	$0.00108^{+46/+113\,\%}_{-27.9/-46.3\,\%}$

Table D.2.10.: List of upper limit values on the cross-section times branching ratio for masses $m_\phi = 2000, 2500\,\text{GeV}$ of the combined $\tau_\text{lep}\tau_\text{had}$ and $\tau_\text{had}\tau_\text{had}$ channel. Expected limits $\sigma \times \text{Br}\,(\phi \to \tau\tau)|_\text{exp.}$ are quoted with the relative values of the $\pm 1\,\sigma$ and $\pm 2\,\sigma$ confidence bands in the format: $\text{median}^{+1/+2\,\sigma}_{-1/-2\,\sigma}$.

D.3. Neutral Higgs Boson Mass Splitting in the m_h^{125} Benchmark Models

Figure D.3.1 shows the mass splitting between the A and H boson observed in the m_h^{125}, $m_h^{125}(\tilde{\chi})$, and $m_h^{125}(\tilde{\tau})$ benchmark scenarios. Based on the resolution measured in the $\tau_{had}\tau_{had}$ and $\tau_{lep}\tau_{had}$ channel signal regions, the phase-space is determined in which the mass degeneracy hypothesis is assumed to be invalid. The corresponding area in the m_A-$\tan\beta$ phase space is indicated by the hatched surface.
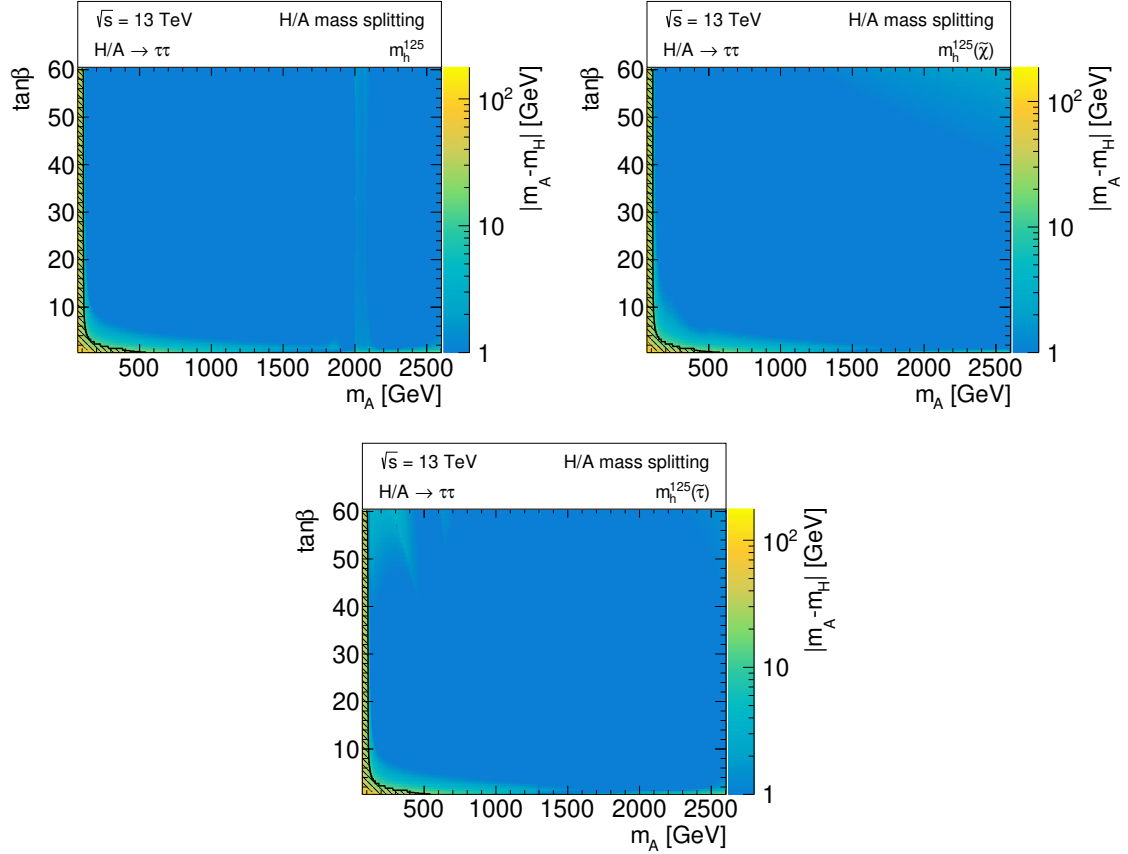
Figure D.3.1.: Mass splitting and resolution exclusion region of the m_h^{125}, $m_h^{125}(\tilde{\chi})$, and $m_h^{125}(\tilde{\tau})$ models [74]. In these models the Higgs masses are calculated with FEYNHIGGS [44, 64–70]. The shaded contour line highlights the resolution exclusion region where upper limits are assumed to be not valid.

Abbreviations

ATLAS . . . . A Toroidal LHC ApparatuS

BTD . . . . Boosted Decision Tree

CCE . . . . Categorical Cross Entropy

CL . . . . Confidence Level

CME . . . . Center of Mass Energy

CT . . . . Conversion Tracks

DSID . . . . Dataset Identifier

DT . . . . Direct Tracks

ECAL . . . . EM Calorimeter

EW . . . . Electro-Weak

EWSB . . . . Electro Weak Symmetry Breaking

FCal . . . . Forward Calorimeter

FSR . . . . Final State Radiation

GRL . . . . Good Run List

GUT . . . . Grand Unified Theory

HCAL . . . . Hadronic Calorimeter

HLT . . . . High-Level Trigger

IBL . . . . Innermost B-Layer

ID . . . . Inner Detector

ISR . . . . Initial State Radiation

JER . . . . Jet Energy Resolution

JES . . . . Jet Energy Scale

JVT . . . . Jet Vertex Tagger

LEP . . . . Large Electron-Positron Collider

LHC . . . . Large Hadron Collider

LO . . . . Leading Order

LSTM . . . . Long Short-term Memory

ME . . . . Matrix Element

MLE . . . . Maximum Likelihood Estimator

MPI . . . . Multi Parton Interaction

MS . . . . Muon Spectrometer

MSSM . . . . Minimal Supersymmetric Standard Model

N^{4}LO . . . . Next-to-Next-to NNLO

NC . . . . Not Classified tracks

NLO . . . . Next-to Leading Order

NNLO . . . . Next-to-Next-to Leading Order

NP . . . . Nuisance Parameters

OT . . . . Other Tracks

p.d.f. . . . . Probability Density Function

PDF . . . . Parton Density Function

PS . . . . Parton Shower

QCD . . . . Quantum Chromo Dynamic

QED . . . . Quantum Electro Dynamic

ReLu . . . . Rectified Linear units

RNN . . . . Recurrent Neural Networks

SCT . . . . Semiconductor Tracker

SM . . . . Standard Model of particle physics

ST . . . . Secondary Tracks

SUSY . . . . Supersymmetry

TRT . . . . Transition Radiation Tracker

TT . . . . Tau Tracks

UT . . . . Underlying Event Tracks

VEV . . . . Vacuum Expectation Value

List of Tables

List of Figures

Danksagung

Versicherung

Hiermit versichere ich, dass ich die vorliegende Arbeit ohne unzulässige Hilfe Dritter und ohne Benutzung anderer als der angegebenen Hilfsmittel angefertigt habe; die aus fremden Quellen direkt oder indirekt übernommenen Gedanken sind als solche kenntlich gemacht. Die Arbeit wurde bisher weder im Inland noch im Ausland in gleicher oder ähnlicher Form einer anderen Prüfungsbehörde vorgelegt.

Die vorliegende Dissertation wurde am Institut für Kern- und Teilchenphysik der Technischen Universität Dresden unter der wissenschaftlichen Betreuung von Prof. Dr. Arno Straessner angefertigt.

Es haben keine früheren erfolglosen Promotionsverfahren stattgefunden.

Ich erkenne die Promotionsordnung des Bereichs Mathematik und Naturwissenschaften an der Technischen Universität Dresden vom 23.02.2011 in der Fassung vom 23.05.2018 an.

———————————————
Ort, Datum

———————————————
M. Sc. Max Märker

'